Research Report

2000-1 January 2000

ISSN 0110 - 3326

Seismic Behaviour and Design of Reinforced Concrete Interior Beam Column Joints

Cheng-Ming Lin

Supervised by J. I. Restrepo and R. Park

Civil Engineering

UNIVERSITY OF CANTERBURY
CHRISTCHURCH • NEW ZEALAND

ISSN 0110-3326

SEISMIC BEHAVIOUR AND DESIGN OF REINFORCED CONCRETE INTERIOR BEAM COLUMN JOINTS

by

Cheng-Ming Lin

Supervised by J. I. Restrepo and R. Park

A report to the Sponsor

Research Foundation of EQC New Zealand
EQC project no. 97 / 294

Research Report 2000-1
Department of Civil Engineering
University of Canterbury
Christchurch
New Zealand

January 2000

ABSTRACT

The physical model of shear transfer mechanism in reinforced concrete beam-column joints in which the New Zealand Concrete Structures Standard NZS 3101:1995 is based provides a good insight into the seismic behaviour of joints. However there are still some issues observed in the laboratory work that can not be fully explained with such model. This research project is aimed at improving the understanding of the seismic behaviour of joints. The research work seeks the endorsement of the design recommendations for interior joints given by the Concrete Structures Standard.

The lower bound theorem of plasticity was applied to find the internal force trajectories within the joint panel. The diagonal compressive stress field of the joint was modeled with variable angle struts-and-ties. Relative importance of parameters influencing the shear strength of the joint panel was identified through the series of parametric analysis.

The database consisting of 60 tests were processed to be used in conjunction with the analytical work. It was found that a clear trend exists between the ductility of the frame subassemblies and the joint shear stress ratios equivalent to a reference joint. This relationship was used to derive the design recommendations for the requirements of horizontal joint shear reinforcement of joints of ductile frames and limited ductility frames.

An experimental programme was conducted to validate the analytical results with particular emphasis given to parameters that were found to be in disagreement between the analysis and the current design recommendations. Eight cruciform subassemblies were tested under simulated earthquake loading. Precast concrete was incorporated in the fabrication of the test units to simulate the design practice. There are five units in which beam bars are lumped at the top and bottom beam chords, while three units incorporate distributed longitudinal beam reinforcement. Grade 500 reinforcing bars were used as beam and column longitudinal reinforcement in all units. Test results showed good agreement with the analytical model within reasonable accuracy. Some of the important findings are summarized below.

First, column compressive loads are not always beneficial to the joint strength. When the column axial load level exceeds $0.3f_cA_g$, it becomes detrimental to the joint. Second, according to the results obtained in this study, the design recommendations given by NZS

3101:1995 are conservative in general and could be relaxed, except for some rare cases. Third, the horizontal joint reinforcement is strongly influenced by the ratio v_{jh} / f'_c rather than by the bond force of the longitudinal beam bars. Forth, the requirement of horizontal joint reinforcement given by NZS 3101:1995 for joints in which the amount of top and bottom beam bars is unequal was found to be unduly stringent. Fifth, the shear strength of the joints in which beam bars are distributed along the web is very similar to that of the conventionally reinforced joints. Therefore, no relaxation of amount of horizontal joint reinforcement can be expected when using this design alternative.

Test results showed that the theoretical model established in this study is able to predict the joint strength in correlation with the ductility. Joint design procedures based on the traditional forced based and displacement based design are discussed in this work. The effect of using high-grade reinforcement on the bond strength within the joint is also studied.

Test results and theoretical predictions conclusively showed that the yield drift of the frame subassembly becomes large when Grade 500 longitudinal reinforcement is incorporated. As a result, full ductility can seldom be achieved before reaching the interstorey drift limitation of 2.5% given for the ultimate limit state by the loadings code, NZS 4203:1992. Drift limitations are expected to control the design of reinforced concrete moment resisting frames when Grade 500 reinforcement is used as longitudinal bars in columns and beams. It is suggested that, except for low-rise structures in which the drift limit can be easily met, moment resisting frames designed using Grade 500 bars be designed only for limited ductility response.

ACKNOWLEDGMENTS

The research work reported in this thesis was carried out in the Department of Civil Engineering, University of Canterbury, New Zealand under Dr.s N. Cooke and K. M$_c$Manus as heads of Department.

I express my deepest gratitude to Dr. J. Restrepo and Professor R. Park, supervisors of this project, for their invaluable advice and encouragement.

The financial support and the scholarship provided by the Research Foundation of the Earthquake Commission of New Zealand (project 97/294) is greatly acknowledged. Also acknowledged is the donation of the Grade 500 reinforcing steel by Pacific Steel Ltd.

The excellent assistance of the technical staff of the Department of Civil Engineering under the direction of Mr. G. Clarke is acknowledged. Thanks are given to Mr. J. Maley, S. Toase, R. McConchie and G. Harvey for their contribution to the construction of the test specimens, reaction frames and the testing. Thanks are also given to Mr. N.H. Hickey for his advice and friendship.

I also wish to thank Emeritus Professor T. Paulay for his interest and fruitful discussions on some of the topics in this project and Dr. N. Cooke for his time on correcting English writing on some of chapters. Warm gratitude is given to my fellow postgraduate students for their friendship and discussions.

Thanks are also given to the Department and the University for the opportunity they gave to me to study here. Being the first Ph.D. student came from Taiwan in this Department conducting seismic reinforced concrete research, what I have learned here and the life in New Zealand will be always in my mind.

Finally, I would like to thank my wife, Sherry Huang for her continuous support, care and encouragement during the past years. Also thanks our parents for their understanding and encouragement of my studying here. And, most importantly, thanks to the Lord, Jesus Christ.

CONTENTS

CHAPTER 3 TEST PROGRAMME

CHAPTER 6 TEST RESULTS OF UNITS 5, 6 AND 7

CHAPTER 8 DISCUSSION OF TEST RESULTS AND DESIGN RECOMMENDATIONS

NOTATION

A_{sh}	=	area of horizontal joint shear reinforcement
A_g	=	gross section area of a column
A_s	=	area of top beam bars
A_s'	=	area of bottom beam bars
$A_{j,e}$	=	effective joint shear area
b_c	=	column width
b_j	=	joint width
b_w , b_b	=	beam width
C	=	neutral axis depth
$C_{b,s}$	=	beam steel compressive force
$C_{b,c}$	=	beam concrete compressive force
$d_{b,t}$	=	diameter of top beam bar passing through joint region
$d_{b,b}$	=	diameter of bottom beam bar passing through joint region
d^-	=	effective beam depth measured from the centroid of the top beam bars to the bottom beam chord
d^+	=	effective beam depth measured from the centroid of the bottom beam bars to the top beam chord
E_c	=	Young's Modulus of concrete
E_s	=	Young's Modulus of steel
f_y	=	tensile yield strength of reinforcing steel
f_u	=	ultimate tensile yield strength of reinforcing steel
f_c'	=	concrete compressive strength
$f_{c,s}$	=	average uniaxial compressive stress in the central strut of the joint
f_{cr}'	=	joint diagonal tension cracking stress
f_t	=	diagonal tensile strength of the concrete
f_g'	=	grout compressive strength
G	=	shear modulus of concrete
h_c	=	overall column depth in the direction of lateral loading
H_D	=	dependable lateral load capacity
H_a	=	theoretical ultimate lateral storey shear force calculated using measured properties
h_b	=	overall beam depth
H_o	=	measured storey shear force at over-strength

H_o'	=	storey shear force at over-strength after the correction for P- delta effect
H_i	=	ideal storey shear force
I_e	=	effective section moment of inertia
I_g	=	moment of inertia of gross section area of structure members
jd^+	=	internal level arm of beams, measured from the centroid of the bottom beam bars to the centroid of concrete stress block
jd^-	=	internal level arm of beams, measured from the centroid of the top beam bars to the centroid of concrete stress block
jd^{*-}, jd^{*+}	=	distance between the centroids of top and bottom beam bars, = ($d-d'$)
K_{joint}	=	joint stiffness
K_{pv}	=	normalization factor for evaluation $v_{jh,e} / f_c'$
l_b	=	beam span length between two pin ends
l_b'	=	half beam span length measured from one pin end to the column face
l_b''	=	half beam span length measured from one pin end to the controid of column exterior bars
l_c'	=	half column height measured from one pin end to the column face
M_i^+	=	ideal beam moment capacity, calculated from $T^+(jd^+)$
M_i^-	=	ideal beam moment capacity, calculated from $T^-(jd^-)$
N^*	=	column axial load
P	=	tensile longitudinal reinforcement ratio
P'	=	compressive longitudinal reinforcement ratio
P_t	=	total longitudinal reinforcement ratio
r^2	=	coefficient of correlation
S_r	=	clear spacing between the deformations of deformed bar
S_c	=	compressive force of the central strut in the joint
S_o	=	circumference of beam bar
$T_{b,1}$	=	top beam bars tensile force
$T_{b,2}$	=	bottom beam bars tensile force
T_i^+	=	tensile force of bottom beam bars based on measured properties without counting over-strength
T_i^-	=	tensile force of top beam bars based on measured properties without counting over-strength
$\dot{U}$	=	calculated bond stress
U_a	=	unit bond stress of reinforcing bars
V_i^+	=	beam shear force associated to M_i^+, calculated from M_i^+ / l_b'
V_i^-	=	beam shear force associated to M_i^-, calculated from M_i^- / l_b'
V_b	=	beam shear force

V_{col}	=	column shear force
V_{jh}	=	nominal joint shear force
$V_{jh,o}$	=	joint shear force at over-strength
V_{sh}	=	joint shear force taken by the provided joint hoops
$V_{jh,i}$	=	ideal joint shear force
$V_{sh,eff}$	=	joint shear force taken by the effective joint hoops
V_N	=	horizontal joint shear resistance due to column axial load
V_C	=	horizontal joint shear resistance due to joint concrete
V_{SV}	=	vertical joint shear force taken by the vertical joint reinforcement
V_{jv}	=	vertical joint shear force
v_{jh}	=	nominal joint stress
$v_{jh,i}$	=	ideal joint shear stress
v_{jh} / f_c'	=	joint shear stress ratio
$v_{jh,e} / f_c'$	=	joint shear stress equivalent to a reference joint
W_S	=	width of the diagonal concrete central strut in the joint
Δ_y	=	reference yield displacement
Δ_c	=	column displacement as a component of yield displacement
$\Delta_{b,fl}$	=	storey displacement due to beam flexural deformation
$\Delta_{b,fe}$	=	storey displacement due to beam fixed-end rotation
$\Delta_{b,sh}$	=	storey displacement due to beam shear
Δ_j	=	storey displacement due to joint shear distortion
μ_Δ	=	displacement ductility factor
μ_θ	=	rotational ductility factor
μ_ϕ	=	curvature ductility factor
ϕ_y	=	reference yield curvature of beams
ϕ_p	=	plastic curvature developing in beam plastic hinge
ϕ_u	=	beam ultimate curvature
$\phi_{c,3/4}$	=	column curvature at joint face associated to 0.75 H_a
δ_{b1}	=	left beam end vertical displacement
δ_{b2}	=	right beam end vertical displacement
δ_{c1}	=	top column end lateral displacement
δ_{c2}	=	bottom column end lateral displacement
δ_{el1}	=	elongation of beams taking place in the first load cycle toward a new displacement ductility
δ_{el2}	=	accumulated beam elongation in the reversed load cycle
$\delta_{c,fe}$	=	column displacement associated to 0.75 H_a due to fixed-end rotation
$\delta_{c,fl}$	=	column flexure displacement associated to 0.75 H_a
$\theta_{c,fe}$	=	column fixed-end rotation

θ_y	=	reference yield drift
θ_{by}	=	yield drift due to deformations in beams
θ_u	=	inter-storey drift ratio in ultimate limit state
γ_{75}	=	joint shear distortion associated to 0.75 H_a
γ_j	=	joint shear distortion
ε_y	=	yield strain of reinforcing bars
ε_{sh}	=	tensile strain at onset of work hardening
ε_u	=	ultimate tensile strain of reinforcing bars
β	=	As' / A_s
λ_o	=	over-strength factor
λ_{jo}	=	over-strength factor for evaluating joint shear stress at over-strength

CHAPTER 1
INTRODUCTION

1.1 SEISMIC DESIGN PHILOSOPHY OF REINFORCED CONCRETE MOMENT RESISTING FRAMES IN NEW ZEALAND

Moment resisting frames are broadly recognized as an efficient structural system for providing the lateral load resistance in reinforced concrete building structures. Frames are generally designed and detailed for ductility to survive a major seismic event.

In New Zealand, with the incorporation of precast structural concrete, designers often separate the structural system into a lateral force resistance system and a gravity load carrying system. Normally the lateral load resistance system is allocated to perimeter frames, which have squat beams and columns, while the interior frames are more flexible and predominately carry gravity loads. The use of perimeter moment resisting frames has the advantage of simplifying the structural analysis and design as well as the detailing of the structural members. This is particularly the case when precast structural concrete is used. Another advantage is that as beams of perimeter frames carry little gravity loads, consequently the gravity beam shear is relatively less than that induced by the lateral force. Hence, under the action of reversed lateral loads, positive and negative plastic hinges can form in beams at the same location adjacent to column faces; thus, uni-directional plastic hinges can easily be avoided. The displacement capacity of moment resisting frames with reversing plastic hinges in beams is generally larger than that of frames with uni-directional plastic hinges. This is because the curvature ductility demands of uni-directional plastic hinges are much larger than those of reversal plastic hinges [D4].

Some concepts of the seismic design of moment resisting frames of multistorey buildings are broadly recognized in the New Zealand Concrete Structures Standard, NZS 3101:1995 [S1] [A6]. First, it is preferable to ensure "strong column-weak beam" response so that the adverse "soft-storey mechanism" can be avoided. Second, the interstorey drift under the design lateral action needs to be restricted to below a certain limit. This is to prevent excessive non-structural damage and P-delta effects.

In New Zealand, a further step has been taken with the use of a deterministic capacity design procedure [P2]. According to this procedure, a suitable sway mechanism is chosen for the structure. Plastic hinge regions are detailed to be ductile and other undesirable failure modes are precluded to ensure that the preferable sway mechanism can develop and be sustained. The input actions for structural members have to be quantified with some accuracy. In order to provide adequate protection against the formation of plastic hinges in columns, a dynamic magnification factor is introduced to magnify the column design moment and shear resulting from input actions of adjacent members to account for the higher mode effects [P2] [S1].

This research project concentrates on the seismic design and behaviour of interior joints. **Figure 1.1** shows a displaced frame structure under the action of lateral load with the classification of exterior and interior beam-column joints. Reinforced concrete beam-column joints are very important because of their role in the behaviour of moment resisting frames designed for earthquake resistance. Joints are subjected to reversing bending moments on opposite adjacent members, and also the input shear force in the joint region is typically of the order of 5 times the column shear force. This can be seen in **Fig. 1.2** which depicts the bending moments and shear force along the column of a frame throughout the joint region. Recent earthquakes, such as El-Asnam (1980) [C6], San Salvador(1986) [S14], Loma Prieta (1989) [S12], Guam (1993) [B7] and Northridge (1994) [N3], have shown that beam-column joints can be vulnerable elements in frames of buildings and bridges. Some photographs showing the damage of reinforced concrete beam-column joints are highlighted in **Fig. 1.3**. It follows that adequate design and detailing are necessary.

1.2 DESIGN CRITERIA FOR BEAM-COLUMN JOINTS

Reinforced concrete beam-column joints have limited energy dissipation characteristics and suffer from rapid strength degradation when they undergo inelastic deformations. As a result, inelastic deformations in ductile moment resisting frame structures designed for earthquake resistance must be located in regions other than the beam-column joints. Some design criteria for beam-column joints were suggested in New Zealand some years ago

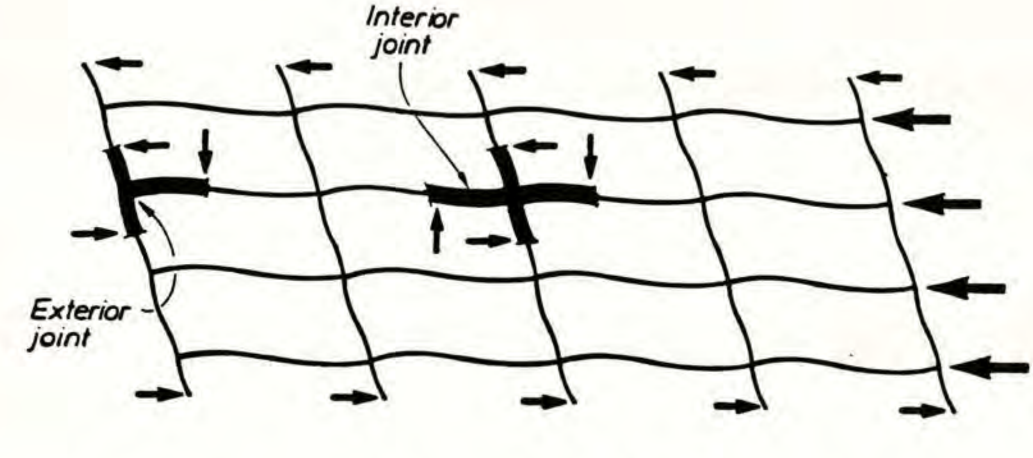

Figure 1.1 - Exterior and Interior Beam-Column Join t Subassemblies of a Ductile Moment Resisting Frame Subjected to Lateral Loads [C1].

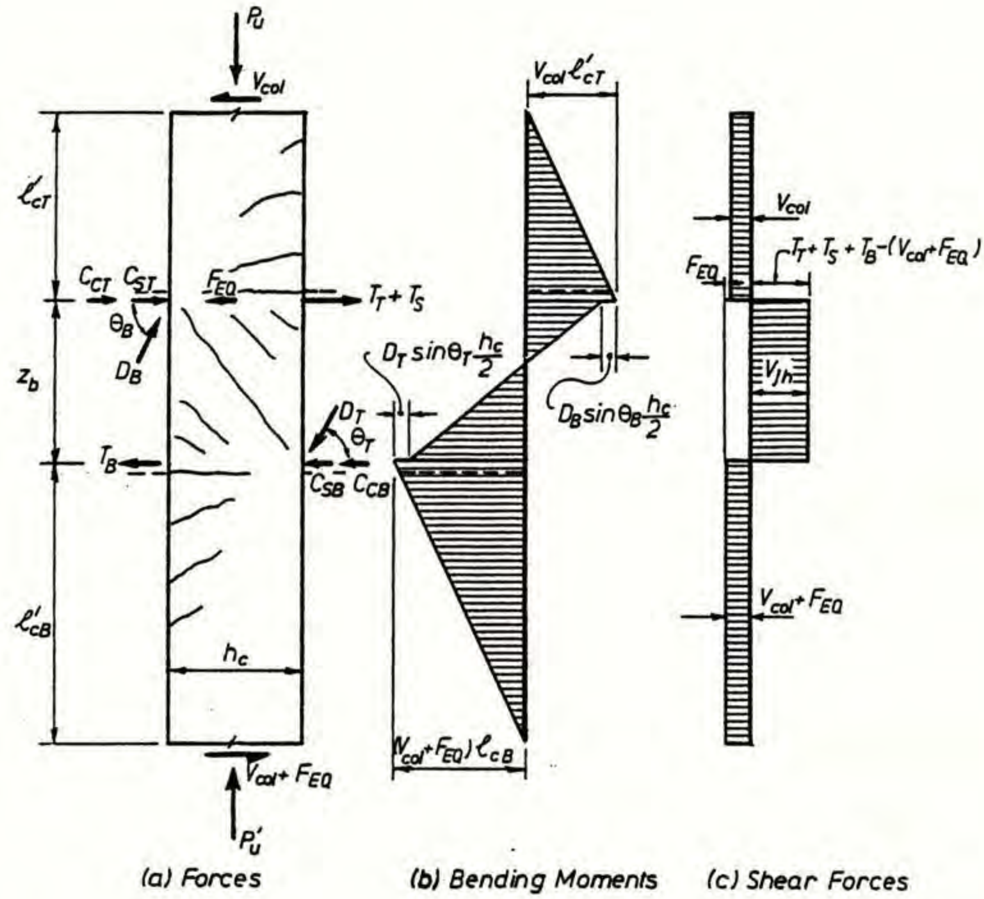

Figure 1.2 - Forces Acting on a Column of Reinforced Concrete Moment Resisting Frames [R1].

(a) Luzon, Philippines (1990)

(b) El-Asnam(1980) [C6]

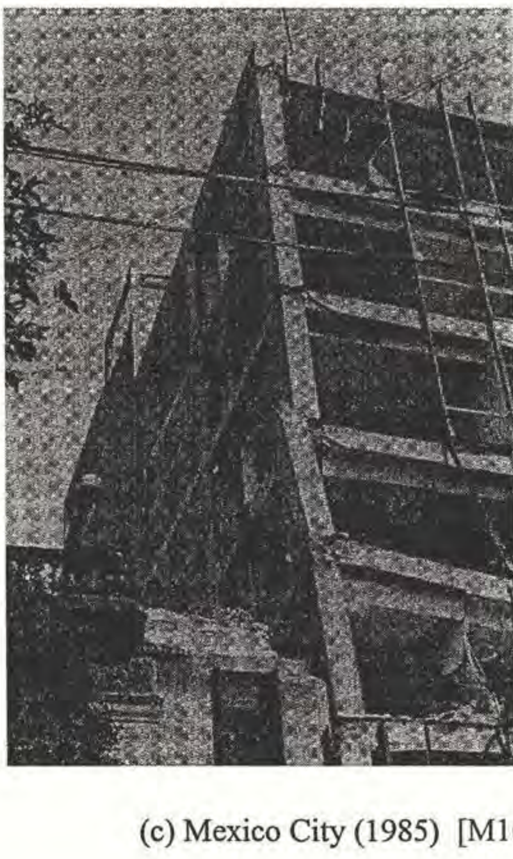

(c) Mexico City (1985) [M10]

Figure 1.3 - Failure of Beam-column Joints in the Past Earthquakes.

by Paulay and Park [P19]. They are described as follows.

1. The strength of a joint should not be less than the maximum strength of the weakest members it connects, to eliminate the need for repair in a relatively inaccessible region and to prevent the need for energy dissipation by mechanisms that undergo strength and stiffness degradation when subjected to cyclic loading in the inelastic range.
2. The capacity of a column should not be jeopardized by possible strength degradation within the joint.
3. During a moderate seismic disturbance, a joint should preferably respond within the elastic range. Joint deformations should not significantly affect stiffness of a building and hence inter-storey drift.
4. The joint reinforcement necessary to ensure satisfactory performance should not cause undue construction difficulties.

Criterion 2 ensures that at the ultimate limit state, the strength of beam-column joints will not compromise the inelastic deformation capacity of the frame nor the vertical carrying capacity of the columns. This criterion recognizes the strength hierarchy of capacity design and consequently beam-column joints should possess sufficient strength to allow plastic hinges to be sustained in adjacent beams. At the ultimate limit state, the inelastic sway mechanism should still be sustained to avoid collapse and in order to achieve this, the gravity load carrying capacity of the columns should not be jeopardized because of the degradation of the joint shear strength.

Criterion 3 ensures that the frames have adequate stiffness at the serviceability limit state. To achieve this, joint deformation must be well controlled and be preferably within the elastic range. Premature bond slip within the joint region can cause a significant reduction of stiffness in the joint at the serviceability limit state. Consequently, the anchorage of beam bars passing through the joint region is an important aspect in the seismic design of beam-column joints.

1.3 REVIEW OF THE SEISMIC DESIGN METHOD OF BEAM-COLUMN JOINTS IN NZS 3101:1995

1.3.1 Background

The design of beam-column joints in the New Zealand Concrete Structures Standard [S1] [C1] is based on a refinement of the model proposed by Park and Paulay in 1974 [P5]. This model, composed of diagonal concrete struts and a parallel steel truss mechanism, has been used in New Zealand for over 25 years. The fundamental concept of this model is that some of the joint shear force together with the column concrete compressive force are transmitted through the diagonal concrete strut by virtue of the bond force in the beam bars. The rest of the joint shear force is carried by a truss consisting of horizontal joint reinforcement and column interior bars. Thus this model depends primarily on the bond distribution along longitudinal beam bars.

In 1977, a lower bound approach based on the model proposed by Park and Paulay was presented by Blakeley [B1]. This macro model was refined further by subsequent researchers. These refinements are all mainly based on the assumption of different profiles of the bond stress distribution along the beam longitudinal bars. In 1978, this approach was revised by Paulay et al. [P5]. A parabolic shape of bond stress profile concentrating towards the centre of the column was proposed. At this stage, the use of code design recommendations had led to rather congested joint reinforcement and strict limitation of diameter of beam bars. Some efforts were made to decongest the joint region. An alternative design approach was to relocate the plastic hinges in the beams away from the column faces. Another design alternative presented by Fenwick and Nguyen [F2] was to use bond plates welded on longitudinal beam bars at locations adjacent to the column faces. Both methods are able to prevent premature bond deterioration taking place within joint region so that the design of an "elastic" joint could be achieved. However, both methods led to construction difficulties.

Park and Dai [D1] indicated in 1987 that the code design requirements could be relaxed and still ensure satisfactory seismic performance. The limitation on beam bar diameter was also refined by introducing the ratio of the quantity between the top and bottom longitudinal beam reinforcement and the square root of the concrete compressive strength. In 1991, Cheung et al. [C1] attempted to relax the design requirements of joint shear reinforcement further by proposing a trapezoidal bond force distribution for estimating the compressive force in the beam longitudinal reinforcement. The bond force within the neutral axis depth of the column was allocated to the concrete strut mechanism and the rest was allocated to the truss mechanism. The influence of column axial load was accounted for by considering the increase of the neutral axis depth associated with an increase in axial load.

In 1992, Paulay and Priestley [P2] followed the same procedure of Cheung et al. and used another idealized bond force distribution to derive the design equations for joint reinforcement and limitation of beam bar diameter. This procedure forms the basis of the design of beam-column joint in the current New Zealand Concrete Structures Standard, NZS 3101:1995 [S1].

1.3.2 The Design Provisions of Interior Beam-Column Joints in NZS 3101:1995

The New Zealand Concrete Structures Standard, NZS 3101:1995 [S1] provides design requirements for the joints of fully ductile frames and for the joints in frames designed for limited ductility response. The design approach for joints of ductile and limited ductility frames are similar except that some relaxation is allowed for the design of beam-column joints in frames with limited ductility. This relaxation is based on the recognition that a lesser degree of deterioration within the joint core can be expected due to the reduced inelastic strains of longitudinal reinforcement passing through the joint region [S2]. In addition, joint shear transfer mechanisms, other than those relying on joint reinforcement, are likely to improve in comparison with those for ductile frames [S2] because of increased residual tensile strength of the concrete core.

The external actions and internal forces of a typical interior beam-column joints are depicted in **Fig. 1.4**. The current design provisions in NZS 3101:1995 are presented as follows.

The area of total effective horizontal joint shear reinforcement corresponding to each direction of horizontal joint shear force shall be:

For interior joints of ductile frames

$$A_{jh} = \frac{6\,v_{jh}}{f_c'} \alpha_j \frac{f_y}{f_{yh}} A_s^* \qquad (1.1)$$

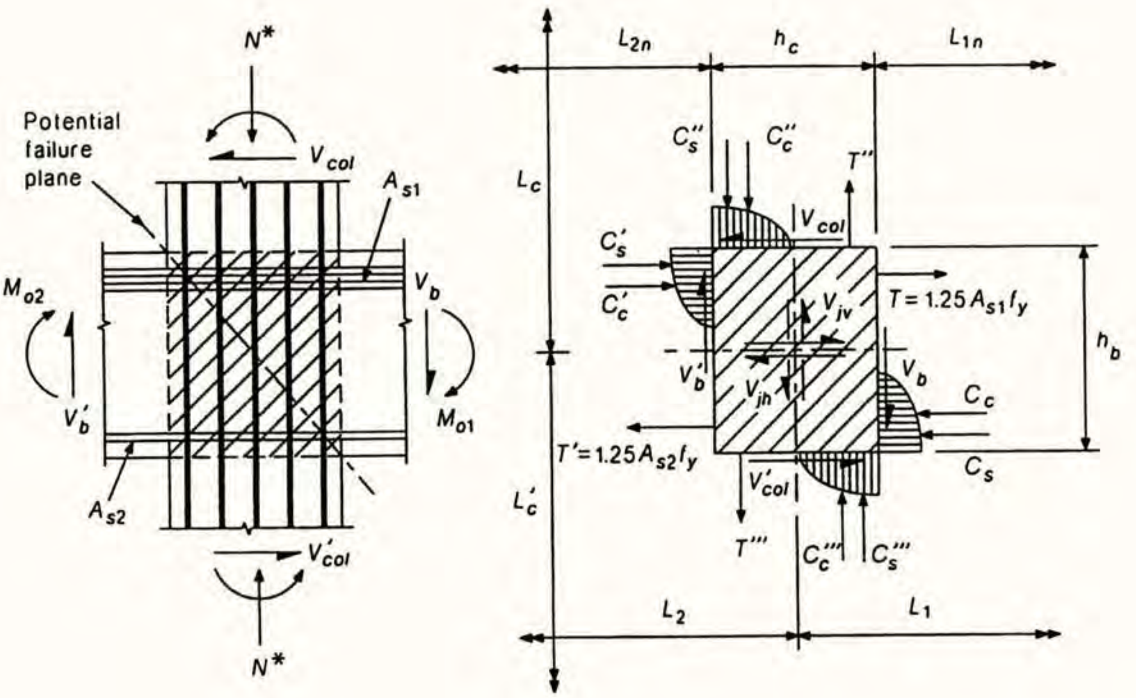

(a) (b)

Figure 1.4 - External Actions And Joint Shear Forces of a Typical Interior Joint [S2].

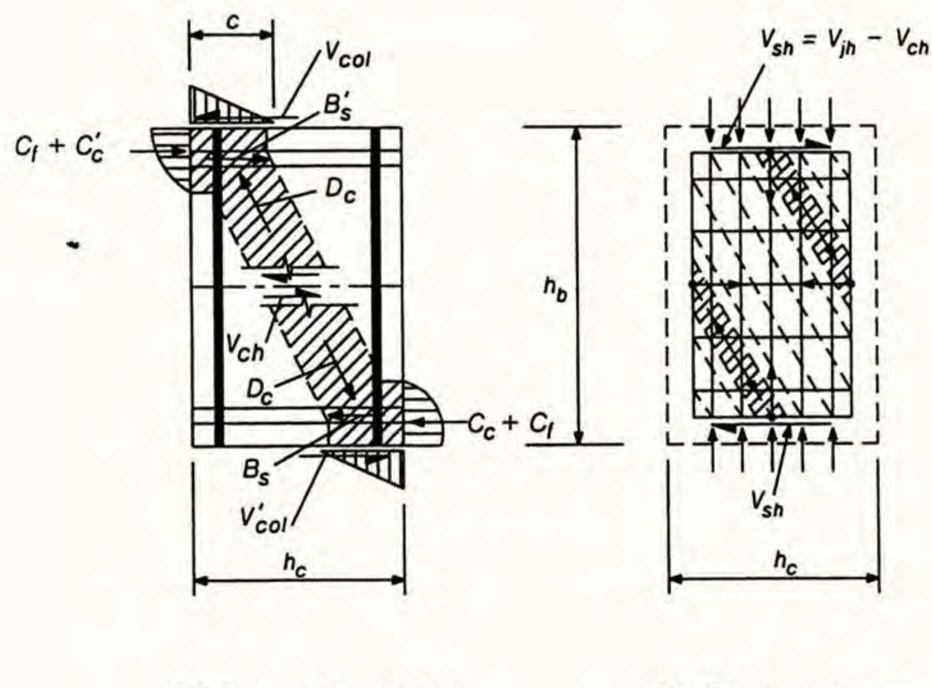

(a) Diagonal concrete strut (b) Truss mechanism

Figure 1.5 - Joint Shear Transfer Mechanism in NZS 3101:1995 [S2].

where

(i) $\alpha_j = 1.4$

or

$$\alpha_j = 1.4 - 1.6\frac{C_j N^*}{f_c' A_g} \tag{1.2}$$

whereby the beneficial effects of the axial compression load acting on the column above the joint may be included. N^* is positive in compression. C_j is a factor that apportions beneficial effects of the axial compression N^* in the x and y directions [P2].

(ii) As^* is the greater of the area of top or bottom beam reinforcement passing through the joint. It excludes bars in effective tension flanges.

The area A_{jh} to be provided in accordance with Eq.1.1 shall not be less than 0.4 V_{jh} / f_{yh}, and the ratio $6v_{jh}/f'_c$ in Eq.1.1 shall not be taken less than 0.85 nor more than 1.2.

For interior joints of limited ductility frames

The A_{jh} may be calculated from Eq. 1.1, where α_j shall be taken as follows:

$\alpha_j = 1.2$

or

$$\alpha_j = 1.2 - 1.4\frac{C_j N^*}{f_c' A_g} \tag{1.3}$$

Using the NZS 3101:1995 design provisions, the horizontal joint reinforcement in frames with limited ductility is about 85% of that required in ductile frames. However, joints of gravity dominated frames in which the bottom beam reinforcement will not yield during a seismic attack, is an exception.

Figure 1.5 illustrates the diagonal concrete strut and parallel steel truss mechanisms of joint shear force transfer in an interior beam-column joint that form the basis of the Standard Provisions. Details of the derivation of the design equations are given in the Commentary to the Concrete Structures Standards (NZS 3101:1995) [S2].

In **Fig. 1.5**, the concrete strut resists forces transmitted from the beam and the column concrete compression regions at the joint faces, together with some bond force in the top or bottom beam bars passing through a joint region which has no shear reinforcement. The horizontal and vertical joint shear reinforcement forms a truss mechanism that resists the remaining joint shear force. Bond force is necessary for the development of the truss mechanism. It is evident that in this model the required quantity of horizontal joint shear reinforcement depends on the bond force being allocated to the concrete mechanism. Significant effort have been made by previous researchers at the University of Canterbury to quantify this portion of bond force.

This model has two distinct features. First, the amount of horizontal joint shear reinforcement is strongly governed by the amount of the bond force in the top or bottom beam bars allocated to the diagonal concrete strut. As a result, it is sensitive to the assumed profile of bond force distribution of beam bars in the joint region. Second, as the column compressive loads increase, the neutral axis depth of the column also increases and this reduces the required amount of horizontal joint shear reinforcement. The results obtained from this research project will be compared with the requirements given by NZS 3101:1995 in order to seek an endorsement of this model. The inherent features of this model described above will be investigated in this study.

1.4 INCORPORATION OF GRADE 500 LONGITUDINAL REINFORCEMENT

Part of this research project is devoted to the seismic design of frames when Grade 500 steel is used as longitudinal reinforcement in beams and columns.

During the prosperous 1980's, many multi-storey reinforced concrete frame buildings were built in New Zealand. The beams of the frames were typically reinforced with Grade 275 longitudinal bars while the columns were reinforced with Grade 380 longitudinal bars. The grade of the reinforcement in the 1980's was referred to as the minimum yield strength. In 1989 the meaning of the grade of reinforcement was changed to represent the 5% value of the lower characteristic yield strength of the steel [S5]. As a result, Grade 275 became Grade 300 reinforcement even though its chemical composition and mechanical properties remained unchanged. Grade 380 reinforcement, which had moderate ductility, high equivalent carbon content and a large ultimate tensile to yield strength ratio, was superseded by Grade 430 reinforcement. Grade 430 is very ductile and readily weldable. Owing to cost savings and encouraged by its excellent properties, Grade 430 reinforcement has been widely used as longitudinal reinforcement in beams and columns of frames in New Zealand since the early 1990's.

With the harmonization of the New Zealand and Australian standards, Grade 430 reinforcement is likely to be superseded by Grade 500 reinforcement [P9]. The new grade may be produced by slightly modifying the current Grade 430 steel. As it is likely that designers will use the new grade of reinforcing for beams and columns of frames, the experimental programme conducted as part of this research programme used Grade 500 reinforcement. Grade 500 reinforcement is currently available in New Zealand in the way of threaded bars.

1.5 AIMS OF THE RESEARCH PROJECT

Reinforced concrete beam-column joints are still one the few structural components for which the behaviour is not fully understood, despite significant amount of research that has been conducted since the first beam-column joint subassembly was tested 30 years ago [H3]. Significant discrepancies still exist in the design and detailing requirements of joints in different Codes [A7]. This is possibly because of the different philosophies of earthquake resistant structural design and the inherent complexity of this problem.

Most of the approaches in overseas Code provisions [A5][A6] are essentially empirical and attempt to provide satisfactory design rather than to predict the joint strength. In New Zealand, the model proposed by Park and Paulay [P4], and refined by later researchers [S1] [C1], have thrown some light into the problem of joint shear transfer. Nevertheless, this method cannot be used to predict the shear strength of beam-column joints.

The capacity design philosophy adopted in New Zealand is based on a strength hierarchy. There is a need to seek more understanding of joint behaviour so that the joint shear strength can be predicted with some degree of accuracy. A more accurate prediction of the joint shear strength could lead to a reduction in the required amount of joint shear reinforcement, which still causes congestion in practice. Furthermore, an accurate prediction of the joint shear strength is essential when conducting seismic assessment of older buildings and bridges.

This study is aimed at predicting the shear strength of beam-column joints. An assessment of the main variables is carried out using the lower bound theorem of the theory of plasticity. Equilibrium and the stress trajectories are found using the strut-and-tie approach.

At the start of this project, a trend was developing in New Zealand to use higher grade reinforcing steel in reinforced concrete design. A new Grade 500 reinforcing steel is to be released to supersede the Grade 430 reinforcement and designers may find some difficulty in anchoring the high grade reinforcing bars in the joint region if the bar diameter limitations given by NZS 3101:1995 are to be satisfied. In order to meet these requirements, designers may need to enlarge the size of the columns or to use many smaller diameter bars. A design alternative, aimed at improving bond performance, is to distribute the longitudinal beam bars along the beam web. It can be proved theoretically that the ultimate flexural strength of beams in which longitudinal bars are distributed through the webs is very similar to that of the conventional beams [W1]. It was deemed to have some potential merits when applied on seismic design of moment resisting frames, i.e. better shear transfer capacity in beam plastic hinge region, less shear deformation, reduction in the amount of joint shear reinforcement and reduction in beam elongation. This design innovation suggested by Priestley [P18] recently, has been tested once in 1980's [W1] at University of Canterbury. This research project incorporates this design innovation in order to seek more understanding of its seismic behaviour. An attempt is made to provide more experimental evidence so that design recommendations regarding this design method can be made.

This research project also provides experimental evidence to verify some design aspects when using Grade 500 reinforcing bars in the beams and columns of moment resisting frames.

1.6 SCOPE OF THE THESIS

The scope of the thesis is outlined as follows.

Chapter 1 : Introduces the background of this research project and the research significance.

Chapter 2 : Presents the analytical approach and results using strut-and-tie models on the shear strength of interior beam-column joints.

Chapter 3 : Describes the details of design consideration of test units. Details of the testing setup and data measuring methods are presented.

Chapter 4 : Discusses test results of Units 1 and 2.

Chapter 5 : Discusses test results of Units 3 and 4.

Chapter 6 : Discusses test results of Units 5, 6, 7.

Chapter 7 : Discusses test results of Unit 8.

Chapter 8 : Some important test results are discussed and compared with the findings of the analytical work. Aspects of seismic design of reinforced concrete moment resisting frames using Grade 500 reinforcement are discussed. Design recommendations based on ductility and drift criteria are given. Assessment of joint shear strength using the established model is also discussed.

Chapter 9 : Contains the conclusions of this research project and some suggestions for future research.

CHAPTER 2
ASSESSMENT OF THE STRENGTH OF INTERIOR BEAM-COLUMN JOINTS

2.1 INTRODUCTION

This chapter describes the analytical part of this research on the shear strength of interior beam-column joints.

The lower bound theorem of plasticity has been used in the analysis and design of reinforced concrete structures by some pioneers [M5] [N1] [M6] [M7]. Later researchers [M3] [S8] [M4] advanced the theory and were able to obtain equilibrium solutions on rather complex problems in a simple way. While elastic analysis can accurately model the flow of stresses prior to cracking, it is unable to predict the redistribution of stresses after cracking, especially in disturbed regions which are characterized by a complex joint stress flow. However, considerable insight into the flow of forces in distributed regions can be gained by the use of simple strut-and-tie models [S8]. Beam-column joints subjected to cyclic lateral loads are typically in the category of disturbed regions. Owing to the inherent complexity, most of the strut-and-tie model analyses were previously only applied to members subjected to static loading, except for a few cases being applied to bridge column-footing joints [P3]. An attempt has been made in this study to investigate the equilibrium between the loads and the internal forces in the concrete and reinforcement using a strut-and-tie model.

Restrepo et al. [R1] suggested using a variable angle truss mechanism and this motivated the development of a strut-tie-model to investigate the stress flow in joints under varied conditions. Since cracked reinforced concrete carries load principally by compressive stresses in the concrete and tensile stresses in the reinforcement, the principal compressive stress trajectories in the concrete tend towards straight lines and hence can be approximated by straight struts. The internal flow of forces in joint panels can be modeled using concrete struts to represent the concrete in uniaxial compression, and ties to model the reinforcement. Therefore it becomes possible to investigate the compression stress fields of joint panels using strut-and-tie models. Some parameters which are likely to influence the stress flows in joints are later investigated in this thesis to identify their relative importance.

The behaviour of reinforced concrete members subjected to cyclic shear is known to be strongly affected by diagonal compression failure of the concrete because the tensile strains in the transverse direction have been shown to reduce the diagonal compressive strength of the concrete [S7]. Recently, in light of the trends described above, Kamimura [K1] calculated the compressive stress of the concrete struts in the joint panel. The strut compressive stresses of some test units did not agree very well with empirical equations obtained from panel shear tests for predicting the reduced compressive strength of cracked concrete. This is because beam-column joints are characterized as non-uniform compression stress fields resulting from joint shear stresses compounded with stresses resulting from column axial load. The result is that due to the non-uniformity and the effect of reversed cyclic loading, the proposed equations, such as modified compression field theory for shear design developed by Collins et al. [V1], cannot be applied directly to the seismic design of joints.

The compressive strength of the cracked concrete in the joint core needs to be established by other means. Extensive experimental work has been conducted to develop empirical equations for design. Alternatively, as in this study, an examination of test results of a series of existing tests conducted under a similar loading sequence is made. The details of this analytical procedure of joints incorporating beams with traditional reinforcement layout is described in the following sections. The same methodology is also applied to analyze beam-column joints incorporating beams with distributed reinforcement. Some typical joints in this category are analyzed and compared with joints incorporating beams with lumped reinforcement.

2.2 ANALYTICAL WORK OF JOINTS INCORPORATING BEAMS WITH LUMPED REINFORCEMENT

2.2.1 General

Beam longitudinal reinforcement that is placed at the top and bottom beam chords is called "lumped reinforcement" is this project. Prior to the analysis of joint panels, input forces from adjacent beams and columns need to be evaluated. For structures designed to develop a beam-sway mechanism according to capacity design procedure adopted in New Zealand, columns remain elastic while plastic hinges form in beams framing into joints. Hence the input forces transmitted from the columns at beam faces can be reasonably estimated using moment-curvature section analysis under the action of beam flexural over-strength and specified column axial load.

The tensile forces in longitudinal beam bars at column faces when beam over-strength is developed, are calculated from the nominal steel yield force multiplied by an over-strength factor of 1.25, according to New Zealand Concrete Structures Standard, NZS 3101:1995 [S1]. The compressive force in the beam compression zone acting at the column faces consist of two components; one due to the concrete, the other due to the beam compressive steel. The centroid of concrete compressive stress in the beam section at column faces is very close to the level of the compressive longitudinal reinforcement when the beam flexural capacity is reached, therefore the beam concrete compressive force is simulated as a single force coinciding with the compressive reinforcement. Note that the magnitude of the concrete compressive force depends on the bond strength of the beam bars passing through the joint region; the more bond force the beam bars can develop, the less is the beam concrete compressive force. The sum of the compressive forces taken by the concrete and the steel should be equal to the steel tensile force at the same section. Thus in the joints studied, the concrete compressive force and the steel compressive force were added together as one compressive force.

All beam-column joints in this study are modeled as plane panels simulating the conditions in one-way perimeter frames.

2.2.2 Basic Assumptions

Some of the basic assumptions made in the strut-and-tie model analysis are:

(a) The concrete in the joint panel is cracked;

(b) All beams framing into the joint, including transverse beams if they exist, form plastic hinges at the column faces;

(c) The columns framing into the joint remain elastic;

(d) The concrete compressive force resulting from flexure in the beam acts at the level of the longitudinal reinforcement closest to the extreme fibre in compression;

(e) The column shear force at the joint face is distributed only within the region of the column concrete compressive stress block.

(f) The beam shear force at the column face enters the beam-column joint as a concentrated force at a location close to the beam compressive steel.

(g) Bond forces along the longitudinal beam bars passing through the joint region cannot exceed those computed from a given bond stress law.

There are several bond stress profiles available to model the bond stress distribution of a longitudinal beam bar passing through a joint core. A bond stress law proposed by Restrepo et al. [R1] was chosen in this analysis, where the partial bond stress distributes linearly from zero to $2.2\sqrt{f_c'}$ across the column effective length (see **Fig.2.1**). Another portion, concentrated in the column concrete compressive region, is superimposed on the linear distribution. It is assumed that the latter portion will mobilize once the concrete surrounding the bars begins to dilate, and it is therefore related to f_c'. It should be noted that this is not an attempt to predict the bond strength using this bond stress law. However, applying this law in all joints analyzed makes the assessment of parameters influencing joint strength feasible.

(h) The horizontal joint reinforcement behaves as perfectly plastic material.

It has been observed in the laboratory tests [R1] that after plastic hinges formed in beams, the whole horizontal joint reinforcement usually reaches its yield strength when the beam-column subassembly is displaced cyclically to a large displacement ductility. There are two exceptions to this, (i) when high strength steel is used for the hoops and cross-ties, [N2] [S11] and (ii) the provided resistance associated with the transverse

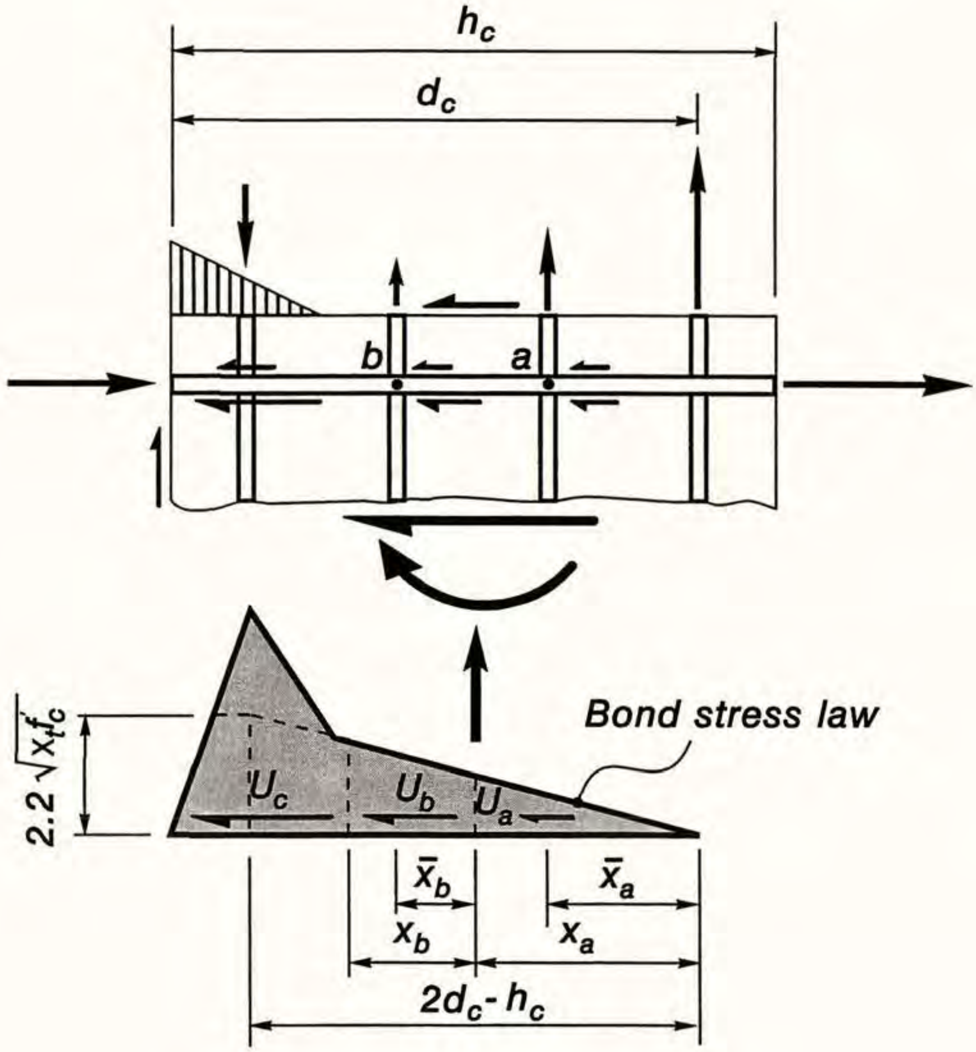

Discrete potential bond forces

$$U_a = 2.2\sqrt{x_t f_c'}\ \frac{(x_a)^2}{2d_c - h_c}\ \frac{S_o}{2}$$

$$U_b = 2.2\sqrt{x_t f_c'}\ \left(\frac{x_a + x_b}{2d_c - h_c}\right)^2 \frac{S_o}{2} - U_a$$

Figure 2.1 - **Bond Stress Law of Beam Bars Passing Through Joint Region Proposed by Restrepo et. al. [R1].**

reinforcement, V_{sh}, exceeds V_{jh}. Therefore, it is assumed in this analysis that all the horizontal joint reinforcement yields, so performing as a perfectly plastic material and exerting constant pressure along two side of the joint panel.

It has also been observed that plain round joint hoops placed very close to the longitudinal beam bars develop low strains, often below the yield limit. In this investigation, the modeling of the pressure applied by the hoops is taken into consideration.

(i) An equivalent rectangular stress block replaces the column concrete compressive stress block at the faces of the joint with the centroid coinciding with that of the original triangular profile.

2.2.3 General Trends

Figure 2.2 shows a typical interior beam-column joint analyzed using the methodology proposed in this study. An example of strut-and-tie model analysis showing the step-by-step procedure to determine the strut forces and positions is also depicted in **Appendix D**.

In each joint, the internal struts and ties meet the external loads at the joint boundary and equilibrium between the input forces, struts and reinforcement or ties must be ensured in the joint. The diagonal compression field in the joint panel is modeled with five to seven discrete struts. Bond forces in the beam longitudinal bars are allocated initially at the nodes where beam bars meet column interior bars based on the prescribed profiles of bond distribution. The remaining bond force is allocated to other struts to satisfy equilibrium.

The angles of the struts are determined by the level of the nodes on column exterior bars where lateral pressure exerting from horizontal joint reinforcement is taken. The vertical component of the compressive force taken by the struts so as the tensile force of column interior bars within joint region can be calculated once the angles are determined. It should be noted that the calculated tensile force of column interior bars can not exceed the steel yield force.

Struts close to the joint centre are also determined following a similar procedure. Interior nodes where the struts crossing the column interior bars may be required for equilibrium. A few iterations are usually required to achieve equilibrium.

The average uniaxial stress in the centre of the joint panel, $f_{c,s}$, is established as the force carried by the central strut divided by the half of distance between the struts at either side of the strut (see **Fig. 2.2**). The uniaxial compressive stress in the joint centre does not represent the maximum uniaxial stress in the joint; this occurs in the region close to the column and beam compression zones. However, experimental work nearly always shows that joint failure occurs by crushing of the concrete at the joint centre [P2]. Therefore, the uniaxial stress in the joint centre is deemed critical to the joint shear strength and will be used as an index to predict failure.

The uniaxial compressive stress of the diagonal strut, $f_{c,s}$, which is computed according to the method depicted above, may vary with the numbers of struts used in a joint. Whereas in the series of strut-and-tie model analysis carried out to establish the analytical models, the numbers of struts are kept as relatively constant (see **Appendix A-1**). As a result, the influence of this sensitivity can be limited as little as possible and the stress, $f_{c,s}$, computed using the methodology described above can be used to measure the relative importance of the different variables.

The strut-and-tie system used to model the force flow in a joint is statically determinate, and only requires equilibrium to seek the solution and does not require strain compatibility or the constitutive law to be considered. With prescribed bond stress and numbers of struts used, several solutions satisfying admissible equilibrium may exist. However, the strut-and-tie models must conform with the lower bound theorem of plasticity and so the objective of the analysis is to seek a solution with the lowest $f_{c,s}$.

The configuration and reinforcing details of the analyzed beam-column subassembly can be found in **Fig. App-1** in **Appendix A-1**. Note that this unit was selected from an example in the report of ACI 351-Committee [A1] for beam-column joint design. All the strut-and-tie model analyses on this unit are presented in **Appendix A-1**. Both the shear force carried by the joint hoops, V_{sh}, and the column axial load ratio $N^* / A_g f_c'$ were varied. However, the diameter of the beam bars passing through the joint region in this example do not meet the limitation required by NZS 3101:1995, so another series of joints in which beam bars were replaced by 9-HD16 at the top and bottom was analyzed as well. Results show very little difference between the two series and these results are presented in **Appendix A-2**.

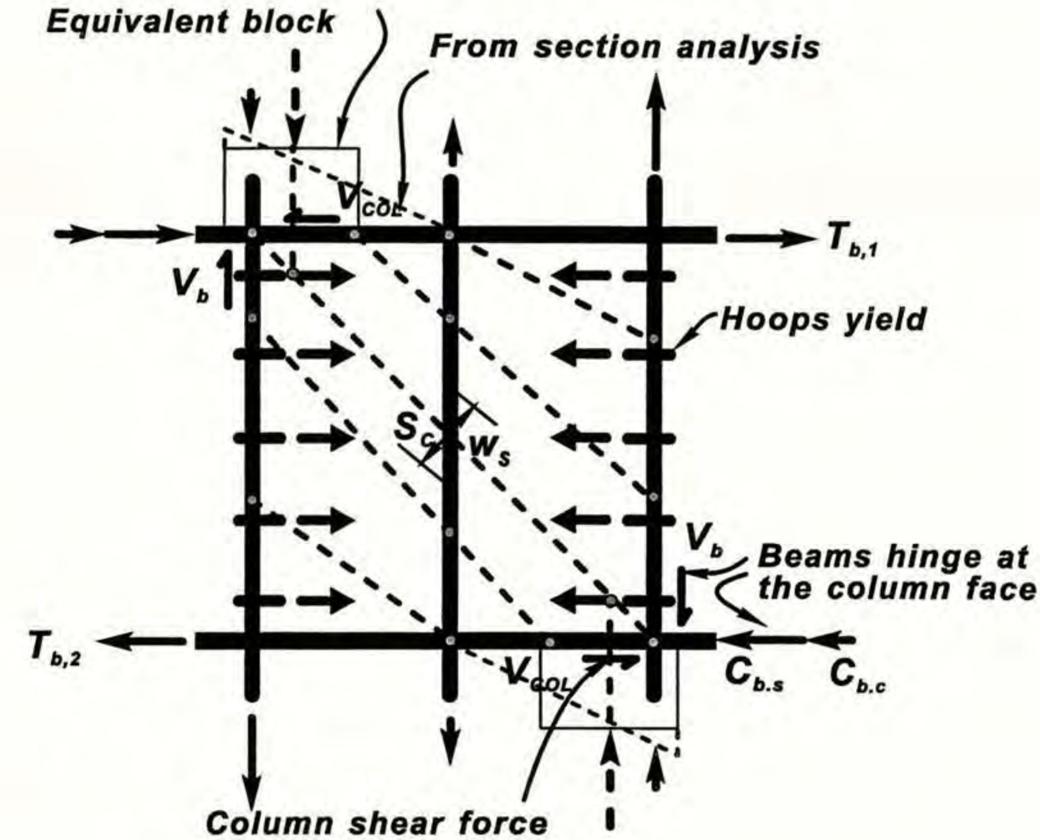

$$\boxed{f_{c,s} = \frac{S_C}{w_s\ b_j}}$$

Figure 2.2 - Analysis of Reinforced Interior Beam-Column Joints Using Strut-and-tie Models.

The strut-and-tie models of joints in **Appendix A-1**, reveal that as the V_{sh} / V_{jh} ratios increases, more joint shear force is resisted by the pressure resulted from joint hoops (V_{jh} is the total nominal horizontal shear force across a joint) and as a result, the struts in the joint tend to be flatter. In contrast, with no joint hoops, most of the joint shear is taken by "concrete" struts, with both ends located in the column concrete compressive region and a few struts bearing against column interior bars carry the remainder. Consequently, the diagonal compression field in the joint tends to concentrate in the joint centre rather than be distributed. It was also revealed that as column compression load increasse, the struts in the joint become steeper because more column concrete compressive force needs to be transmitted through the joint.

It is also observed that struts bearing against the constant pressure provided by V_{sh}, the maximum inclination tends to occur at mid-depth of the joint i.e. the maximum bond stress along column exterior bars occurs near the mid-depth of the joint. Note that this trend was also observed in the test results presented in Chapters 4-7.

2.2.4 Parametric Study

There are many parameters that are likely to influence the behaviour of reinforced concrete beam-column joints. Despite a significant amount of research, a systematic identification of the main parameters influencing the strength of beam-column joints has not yet been done. Since the parameters involved in different tests usually vary, it is impossible to keep some variables constant and compare others. Recently, Bonacci and Pantazopoulou [B2] made an effort to investigate the parameters having an influence on the joints, based on previous research results but no conclusive trends were found.

The analytical part of this research commenced from the strut-and-tie model analysis on many " idealized " joints. This makes feasible the identification of parameters and their influence. Once the important variables are identified, the trends of influence can be clarified further.

The main variables that may influence the stress distribution in the diagonal compression field of interior beam-column joints with beams hinging at the faces of the column are listed below:

(a) The bond force distribution along the longitudinal beam bars;

(b) The V_{sh} / V_{jh} ratio, where V_{sh} is the horizontal shear resistance provided by the horizontal joint reinforcement and V_{jh} is the horizontal joint shear force which can be found as $V_{jh} = (T_{b,1}+T_{b,2}) - V_{col}$; where $T_{b,1}$ and $T_{b,2}$ are the top and bottom beam bars tensile forces at the joint face taking into account the over-strength, and V_{col} is the column shear force;

(c) The $N^*/ A_g f_c'$ ratio, where N^* is the axial compressive force applied on the joint, A_g is the horizontal cross section area of the joint and f_c' is the concrete cylinder compressive strength;

(d) The v_{jh} / f_c' ratio, where v_{jh} is the nominal horizontal joint shear stress, defined as the horizontal joint shear force divided by the effective joint area [S1], ie

$$v_{jh} = \frac{V_{jh}}{b_j h_c}$$

where h_c is the overall depth of column in the direction of the horizontal joint shear to be considered, and b_j is the effective joint width. According to the definition in NZS 3101:1995 [S1], b_j shall be taken as

I. where $b_c > b_w$:

Either $b_j = b_c$, or $b_j=b_w+0.5h_c$, whichever is the smaller,

II. where $b_c < b_w$:

Either $b_j = b_w$, or $b_j = b_c+0.5h_c$, whichever is the smaller;

(e) The ratio of the quantity of top and bottom beam longitudinal reinforcement;

(f) The ductility demand in the plastic hinge developing in the beams next to the joint.

The effect of the above variables was studied by assessing the change in the uniaxial compressive stress in the central diagonal strut within the joint panel using strut-and-tie models. Results of the parametric investigation are presented in the following sections.

2.2.4.1 The Role of Bond Stress of Beam Bars

In order to assess the sensitivity of bond force effect in strut-and-tie model analysis, the bond stress law of beam bars passing through joint region proposed by Restrepo et al. [R1] was chosen and two extreme cases with different bond force distribution was analyzed and compared with each other. Details of the bond stress law and the method to allocate it are shown in **Fig. 2.1**, where x_t is a factor to account for the top bar effect and is taken as 1.0 in all the analysis; S_0 is the circumference of the top or bottom beam bars; X_a and X_b are the distances measured from the centroid of the area of the bond stress profile to the nodal reference lines.

The results of two cases are shown in **Fig. 2.3**. Both joints are identical except for the size of the longitudinal beam bars. The joint shown in **Fig. 2.3(a)** has 3-HD28.7 bars at the top and bottom while the joint in **Fig. 2.3(b)** has 9-HD16 top and bottom bars, so that the sectional areas of longitudinal reinforcement are very similar in both joints. The main difference in the two joints is the bond force distribution. Joint (a) with the HD28.7 bars represents an extreme case, and does not meet NZS 3101:1995 bar anchorage requirement [S1]. The concrete compressive strength, f_c', is 58.2 MPa in both joints. This f_c' value means that in joint (b) all the bond force develops in the triangular profile, without the need of additional bond in the column concrete compressive region. In contrast, bond failure is likely to occur at some stage in joint (a). The bars in tension will be partly anchored on the opposite side of the joint and hence the bond force distribution in the joint is expected to concentrate around the column concrete compression block.

According to the refined Park and Paulay model [S1] [C1], in the beam-column joint with large beam longitudinal bars, the diagonal strut should carry a significantly larger portion of the joint shear than the joint with small bar sizes. A comparison of results (see **Fig. 2.3**) shows that the average uniaxial stress $f_{c,s}$ is very similar in both cases. This suggests that the bond force distribution may not be such an important variable affecting the strength of an interior beam-column joint. In other words, for joints incorporating normally used deformed bar sizes, the ultimate joint strength will not be overly sensitive to the bar diameter. Further, the requirement of transverse joint reinforcement would be more governed by other parameters, such as the joint shear stress ratio, v_{jh}/f_c'. However, it should be noted that this finding does not refer to the joints in which bond failure occurs prematurely, prior to reaching

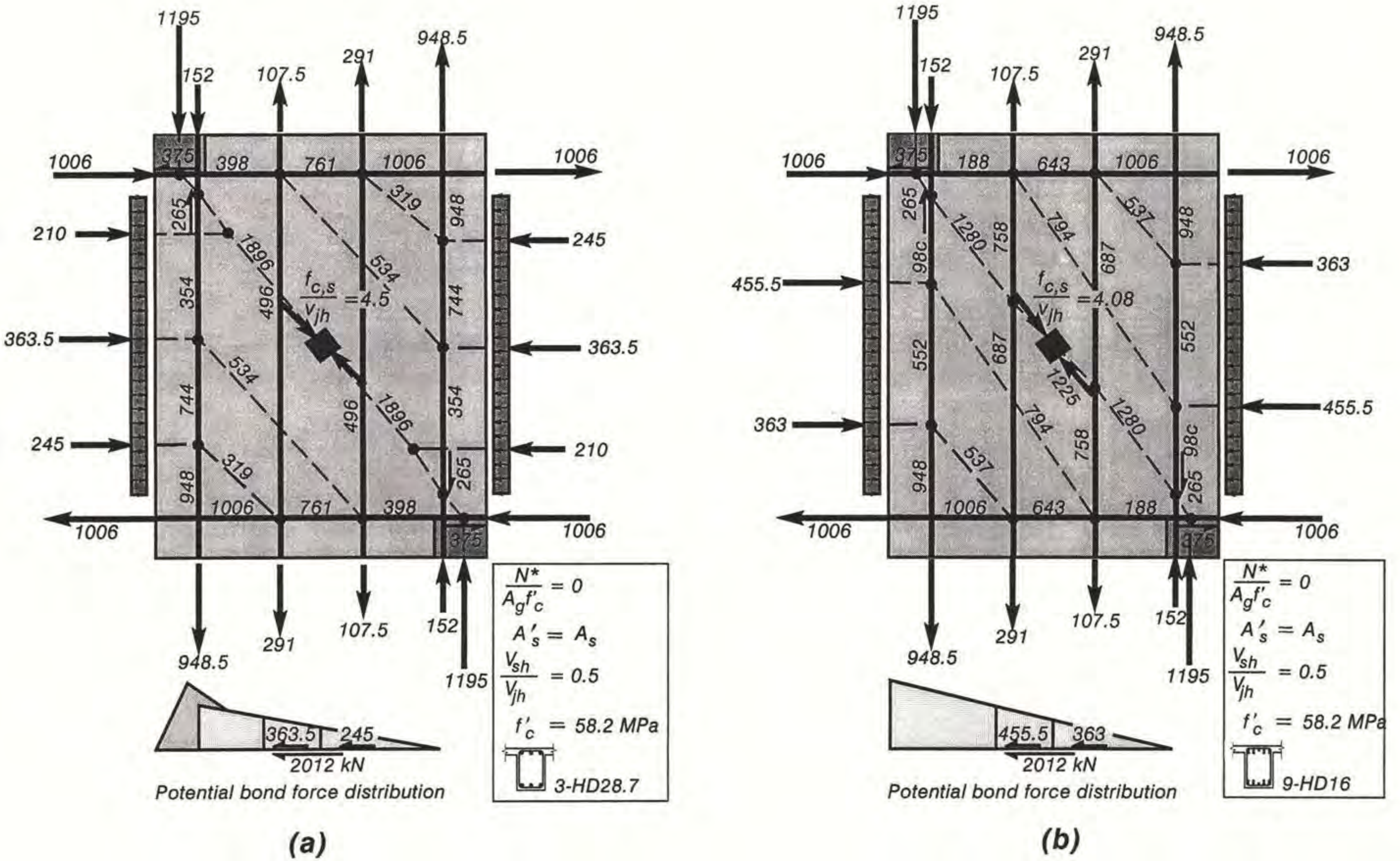

Strtie1.cdr

Figure 2.3 - Comparison of Strut at-and-Tie Model Analysis on Joints Having Good And Poor Bond of Beam Bars.

the theoretical ultimate lateral load capacity.

It should also be noted that the bond requirement, which limits the diameter of the longitudinal beam bars passing through the joint, is still required in the design of reinforced concrete moment resisting frames. This is to prevent excessive inter-storey drift at the serviceability state and ensure good hysteresis loops with good energy dissipation.

2.2.4.2 Effects due to the Column Axial Load and the Horizontal Joint Reinforcement Ratio, V_{sh}/V_{jh}

The variation of $f_{c,s}$ in joints subjected to different column axial compressive load levels were studied. The applied column axial loads varied from 0 to $0.4f_c'A_g$ and the V_{sh} / V_{jh} ratio of joints were varied from 0 to 1. Analyzed joints are presented in **Appendix A-1**. Values of $f_{c,s}$ of cases depicted in **Appendix A-1** are plotted in **Fig. 2.4** against to column axial load ratios for different V_{sh} / V_{jh} ratios.

The influence of the axial load level, $N^*/ f_c'A_g$, and the ratio V_{sh} / V_{jh} can be observed in **Fig. 2.4**. It was found that both ratios have significant effects on the magnitude of the stress $f_{c,s}$. The horizontal axis in **Fig 2.4** is the axial load ratio and the vertical axis at the left of the graph indicates the ratio $f_{c,s} / v_{jh}$. The dots in the figure represent results obtained using strut-and-tie model analysis depicted in **Appendix A-1.** Other curved between the dots were interpolated. There are three distinct regions in this figure; between $N^* / A_gf_c' = 0$ and 0.1, the curves in this region are quite flat, indicating that the effect of the column axial load on the uniaxial compressive stress of diagonal strut is not pronounced in this region. The only important variable in this region is the V_{sh} / V_{jh} ratio, which when the V_{sh} / V_{jh} ratio increases, the magnitude of the ratio $f_{c,s} / v_{jh}$ decreases.

Between $N^* / A_gf_c' = 0.1$ and 0.3, both the axial compression load level and the ratio V_{sh} / V_{jh} significantly influence the ratio $f_{c,s} / v_{jh}$ which decreases when either N^* / A_gf_c' or V_{sh} / V_{jh} ratio increase. This trend is particularly accentuated if little horizontal joint reinforcement is provided. This is because a corner-to-corner diagonal strut, that can very easily be overloaded, carries most of the joint shear force.

Between $N^* / A_gf_c' = 0.3$ and 0.4, when V_{sh} / V_{jh} increases the ratio $f_{c,s} / v_{jh}$ decreases as in previous regions. However, when N^* / A_gf_c' increases the ratio $f_{c,s} / v_{jh}$ also increases i.e.

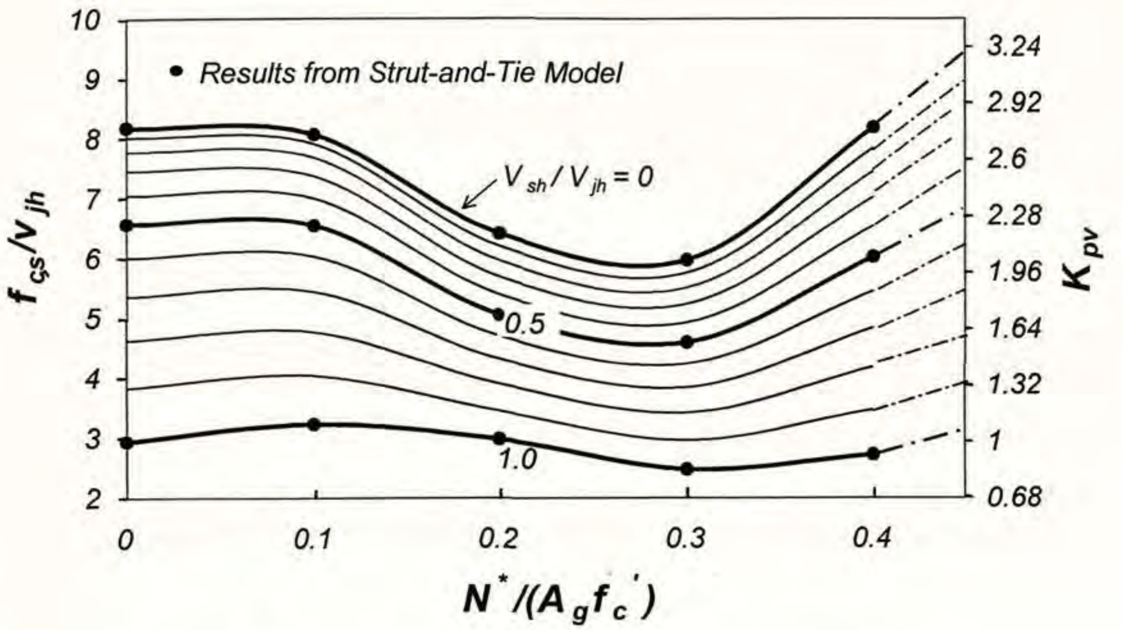

Figure 2.4 - Influence of V_{sh}/V_{jh} and Column Axial Load on $f_{c,s}$.

axial compression in excess of $N^* / A_g f_c' \geq 0.3$ becomes detrimental to the joint. Note that this trend is in contrast to the current NZS 3101:1995 recommendations for the design of beam-column joints [S1].

The analysis also clearly showed that the ratio V_{sh} / V_{jh} influences the stress ratio $f_{c,s} / v_{jh}$. When the ratio V_{sh} / V_{jh} is small the internal forces flow mainly through a corner-to-corner diagonal strut. A more evenly internal force flow is observed when the ratio V_{sh} / V_{jh} is moderate or large.

2.2.4.3 Horizontal Joint Shear Stress Ratio, v_{jh} / f_c'

It was pointed out by Restrepo et al. [R1] that the relevant fraction of joint force ratio, V_{sh} / V_{jh}, might be a function of the horizontal joint shear stress ratio. Code design equations in NZS 3101:1995 for the design of joint reinforcement adopted this finding by means of a scaling factor equal to $6v_{jh} / f_c'$ [S1]. The ratio v_{jh} / f_c' is also recognized as an important factor in Modified Compression Field Theory [V1] for shear design since it is associated with diagonal compression failure. Given that the v_{jh} / f_c' ratio has a pronounced influence on the diagonal compression failure of beam-column joints, v_{jh} of each existing test collected in the database (see Section 2.3 and Appendix B) was expressed in terms of $f_c^{'}$. It will be shown later that after a normalization process associated with the results obtained from strut-and-tie model analysis, the trends of influence of the normalized $v_{jh} / f_c^{'}$ ratios can be clearly observed.

2.2.4.4 Effect of Unequal Top and Bottom Beam Longitudinal Reinforcement

One of the features of refined Park and Paulay's model [S1] [C1] for beam-column joint design is that the requirement of joint reinforcement depends on the maximum input force resulting from top and bottom beam bars. As a result, joints in which the framing beams have unequal top and bottom beam reinforcement, the amount of joint shear reinforcement given by the Concrete Standard [S1] will be considerably larger than that of joints in which beams are reinforced with equal top and bottom steel provided their joint shear stress ratios are similar. Note that this is due to the bond dependent characteristics of the model.

As the non-sensitivity of bond force distribution has been justified, as described in Section 2.3.4.1, it is of interest to investigate the influence of the ratio of top to bottom beam reinforcement, $A_s^{'} / A_s$, on the internal force flow and ultimately on the shear strength of joints. Three joints were analyzed and results are presented in **Figs. 2.5 (a), (b), and (c)**. These joints are identical except for the ratio of $A_s^{'} / A_s$ of the beam bars. Joint (a) has equal top and bottom beam steel, while joints (b) and (c) have $A_s^{'} / A_s$ equal to 0.75 and 0.4 respectively. The three joints have the same joint shear stress ratios in spite of the different $A_s^{'} / A_s$ ratios. The diagonal compression stress field of each joint was modeled as five struts. It can be observed in joints (b) and (c) that the struts are unsymmetrical which is more pronounced with the decreasing of $A_s^{'} / A_s$ ratio. However, the magnitude of all the strut forces are very similar among three joints and the maximum uniaxial compressive stresses ratio $f_{c,s} / v_{jh}$ taken from the central strut are all very close in magnitude, ranging from 3.31 to 3.58.

The analytical results depicted above strongly imply that the influence of $A_s^{'} / A_s$ ratio on the shear strength of joints is insignificant. As a result, the joint strength is more dependent on the joint shear stress ratios than the maximum input force of the top or bottom beam longitudinal reinforcement. This finding implies that the design of joint reinforcement given by NZS 3101:1995 for joints incorporating beams with unequal top and bottom beam reinforcement is unduly stringent. The experimental programme in this study has incorporated this finding to seek further validation.

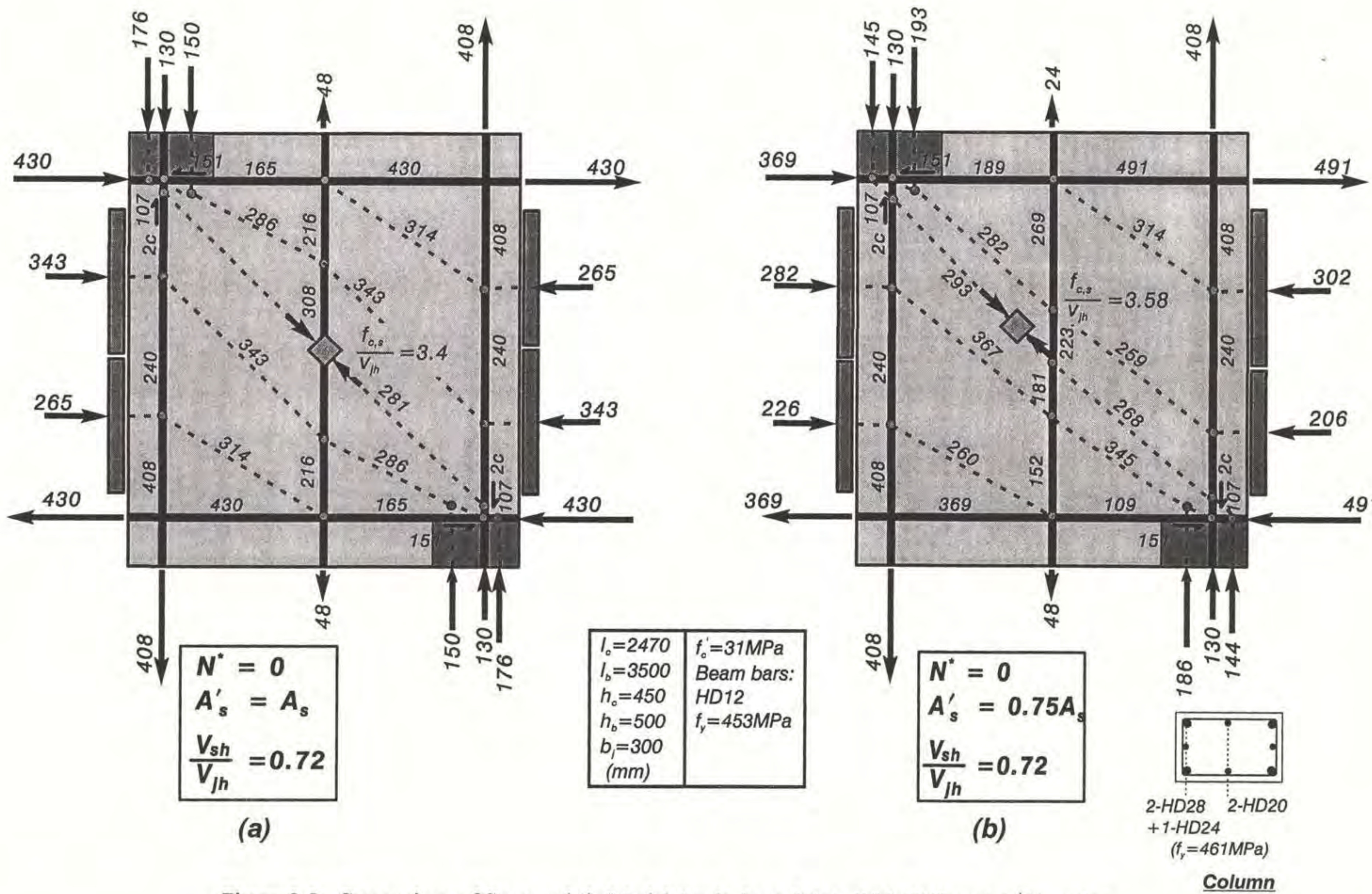

Figure 2.5 - Comparison of Strut-and-tie Model Analysis on Joints With Different A_s'/A_s ratios.

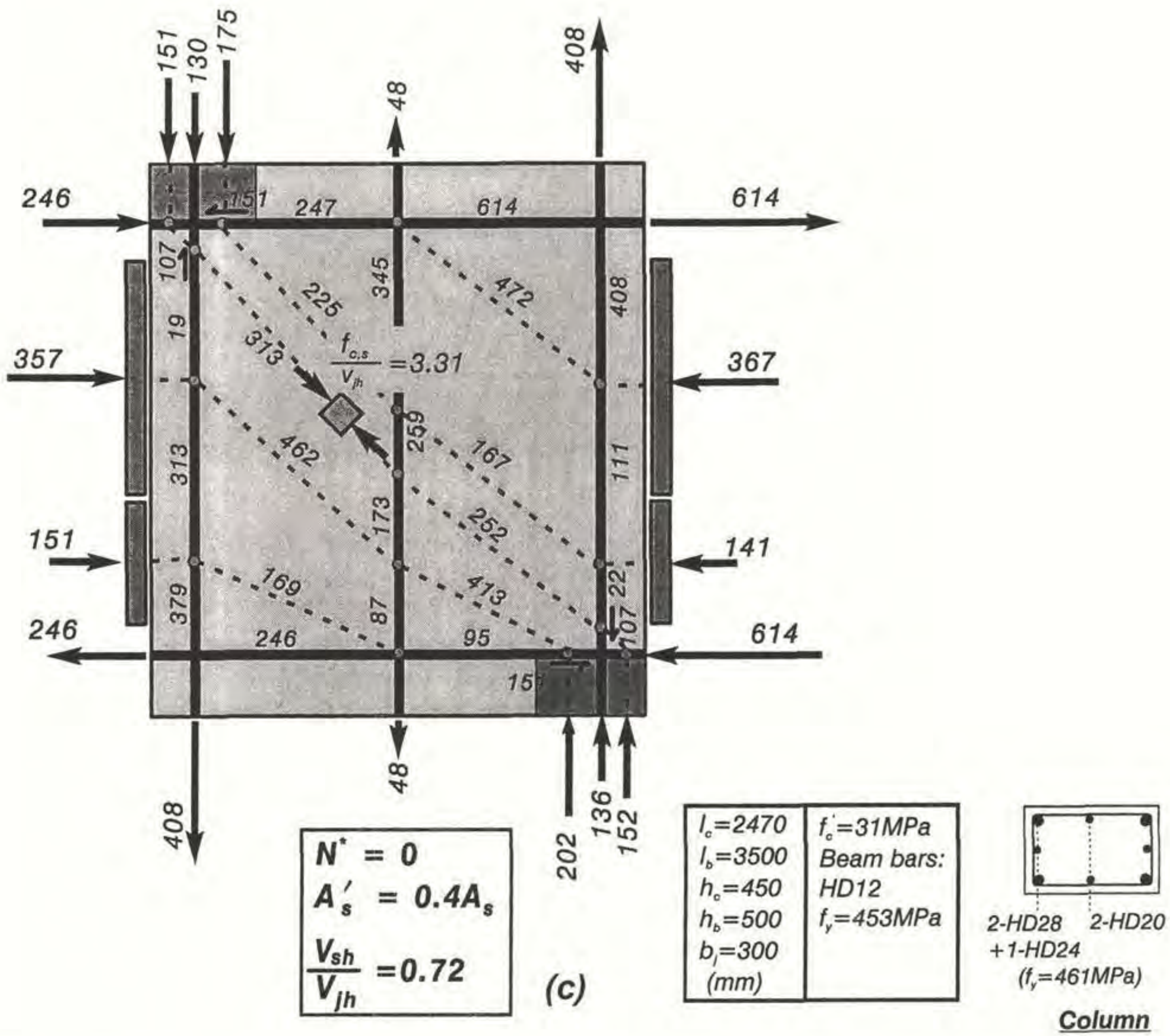

Figure 2.5 (Conti.) - Comparison of Strut-and-tie Model Analysis on Joints With Different A_s'/A_s ratios.

2.2.5 Data Reduction

Figure 2.4 indicates that for a joint with $V_{sh} / V_{jh} = 1$, zero column axial load and $v_{jh} = 0.1 f_c'$, the stress $f_{c,s}$ is approximately equal to $0.3f_c'$. Taking another example, for a given shear stress ratio v_{jh} / f_c', the stress ratio $f_{c,s} / f_c'$ in a beam-column joint without horizontal joint shear reinforcement ($V_{sh} / V_{jh} = 0$) with $N^* / A_g f_c' = 0.4$ is approximately 2.67 times the stress ratio $f_{c,s} / f_c'$ of a joint with $V_{sh} / V_{jh} = 1$ and $N^* / A_g f_c' = 0$. Assuming that the strength of the diagonal compression field in the centre of joint panel is the critical variable for joint failure, it can be interpreted that the reinforced joint can sustain approximately 2.67 times the stress ratio v_{jh} / f_c' of the un-reinforced joint to attain the same stress ratio $f_{c,s} / f_c'$.

According to this rationale, it is possible to relate the strength ratio v_{jh} / f_c' of a beam column joint with given values of $N^* / A_g f_c'$ and V_{sh} / V_{jh} to the shear stress ratio v_{jh} / f_c' of a joint with $N^* / A_g f_c' = 0$ reinforced to carry the whole of the horizontal joint shear force, so that both joints have equal stress ratio $f_{c,s} / f_c'$. This transformation can be achieved using factor K_{pv} shown in the vertical axis at the right hand side of **Fig. 2.4** and can be expressed as following:

$$\frac{v_{jh,e}}{f_c'} = K_{PV} \frac{v_{jh}}{f_c'} \tag{2.1}$$

where $v_{jh,e}$ is referred to as the horizontal joint shear stress of the equivalent joint, which has $N^* / A_g f_c' = 0$ and $V_{sh} / V_{jh} = 1$.

2.3 DATA PROCESSING OF EXISTING TEST RESULTS

A collection of data from similar cyclic reversed load tests on interior beam-column assemblies was carried out in this study. The data investigated did not include tests in which beam-column joints failed prior to yielding of the beam longitudinal reinforcement.

Tests results in which beam-column joints reinforced with transverse hoops without a defined yield plateau region were classified in another category and plotted in different graphs ($V_{jh,e} / f_c'$ versus μ_θ). Uzumeri and Seckin [U1] first reported that this type of reinforcement can have a marked effect on the strength of a beam-column joint. The trend of the influence will be further discussed in Chapter 8.

This database comprises 47 existing tests. With the 8 units conducted in this research project being included the total numbers of tests are 55. The experiments in the database included a wide range of possibly relevant parameters, including:

Column axial load ratio ($N^*/A_g f_c'$): 0-0.483

Concrete compressive strength f_c' : 22.5-88 MPa

Beam reinforcement yield strength (f_y): 276-611 MPa

Joint shear stress ratio (v_{jh} / f_c') : 0.08-0.42

V_{sh}/V_{jh} ratio : 0.09-1.00

h_c /d_b ratio : 14.5 - 37.5

$\beta = A_s' / A_s$: 0.4 –1.0

Details of the procedure to process the test results in the database are described in the following sections. Extracted information of test results of each test is tabulated in **Appendix B**.

2.3.1 Evaluation of the Joint Shear Stress at Overstrength, $v_{jh,o}$, of Tests

An over-strength factor equal to 1.25 is suggested in capacity design in New Zealand to account the beam flexural over-strength when large curvature ductility is developed [S1]. This over-strength factor is in recognition to two sources. One is the actual yield strength of steel in excess of the lower characteristic yield strength, and the other is the strain hardening of steel or strength enhancement of the confined concrete. This factor is used as an upper bound of input force for beam-column joint design. When reviewing the results acquired from laboratory tests, the real over-strength developed in the test subassemblies may vary due to the material properties or reinforcing details. In order to assess the joint strength adequately, it is necessary to compute the real over-strength factor developed in the test assemblies rather than using the factor 1.25, which is applied in the design. The procedure used to determine the maximum joint shear stress in existing tests is now described.

The joint shear force associated with the theoretical ultimate lateral load is calculated as:

$$V_{jh} = (T_{b,1} + T_{b,2}) - H_a \tag{2.2}$$

where H_a is the theoretical ultimate lateral load calculated using measured material properties and no over-strength is taken into account. $T_{b,1}$ and $T_{b,2}$ are the tensile yield forces of beam top and bottom steel passing through the joint, calculated using measured properties. Note that P-Δ influences the calculation procedures as described below.

1. *Test set up without P-Δ effect*

Figure 2.6 shows an interior beam-column subassembly tested without P-Δ effects. V_{jh} in Eq.2.2 can also be expressed as

$$V_{jh} = (V_b^+ + V_b^-)\frac{l_b'}{jd} - H_a \tag{2.3}$$

where H_a can be expressed as

$$H_a = (V_b^+ + V_b^-)\frac{l_b}{2l_c} \tag{2.4}$$

By substituting Eq. 2.4 into Eq. 2.3, we obtain

$$V_{jh} = \left(V_b^+ + V_b^-\right)\left(\frac{l_b'}{jd} - \frac{l_b}{2l_c}\right) \qquad or$$

$$V_{jh} = H_a \frac{2l_c}{l_b}\frac{l_b'}{jd} - H_a = H_a\left(\frac{2l_c}{l_b}\frac{l_b'}{jd} - 1\right) \tag{2.5}$$

Symbols in the above equations are given in **Fig. 2.6** and the notation list at the front of this thesis. Note that when the over-strength is developed, due to the yield penetration of longitudinal beam reinforcement into the joint, the maximum beam flexural strength tends to develop at a section close to the column centre and it would be realistic to assume that it develops at the centroid of the column exterior bars; thus, lb′ will increase to lb″ at over-strength.

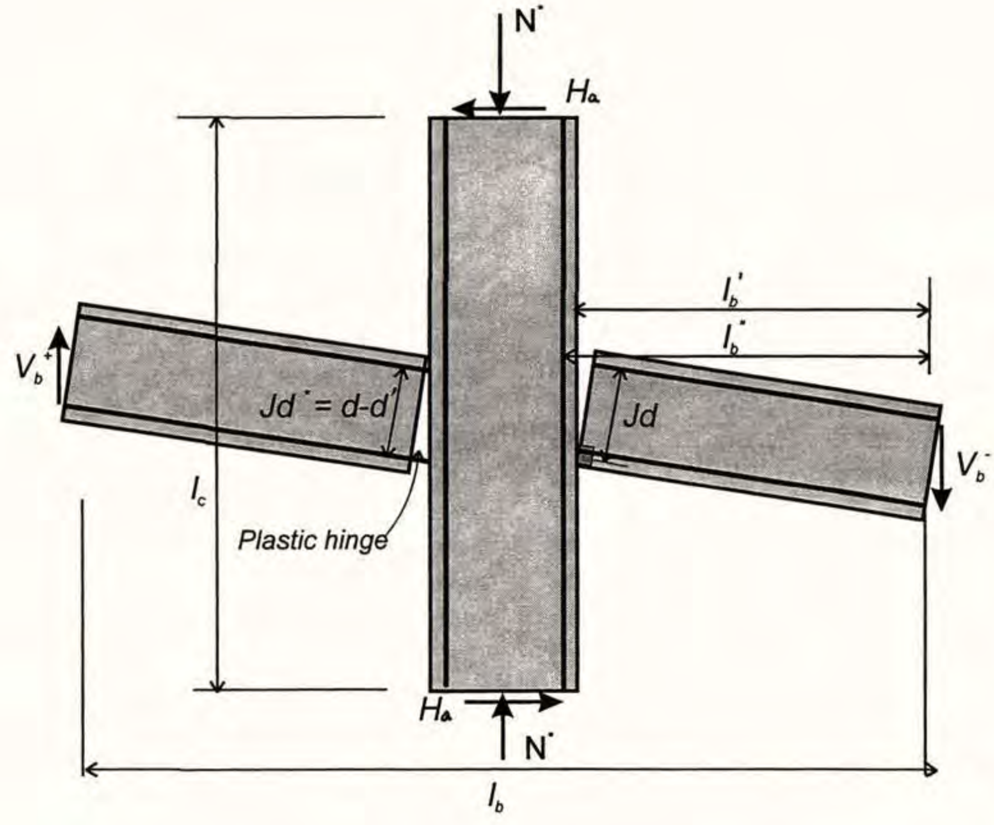

Figure 2-6 Geometrical Configuration of a Beam-column Assembly Tested Without P-Δ Effect.

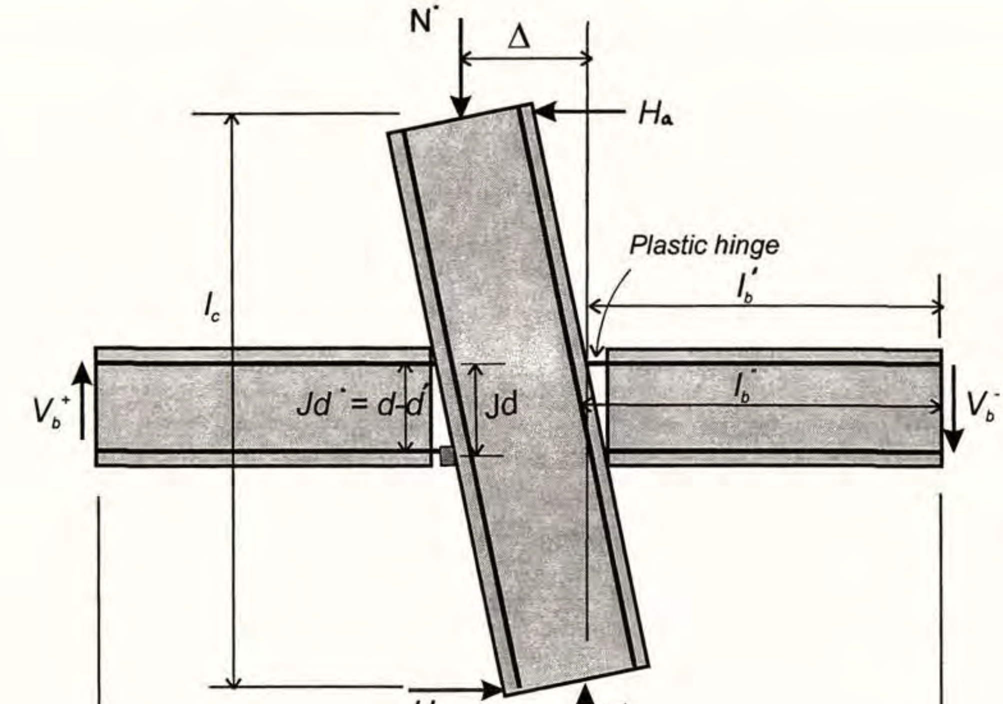

Figure 2.7 - Geometrical Configuration of a Beam-column Assembly Tested With P-Δ effect.

Further, when the beam is developing its over-strength, the beam concrete compressive area usually tends to diminish so that jd will decrease slightly to jd^*, which is the distance measured between the centroid of tensile and compressive beam steel. Meanwhile, the lateral load capacity will increase to H^0 due to the developed over-strength. Note that H^0 here is taken as the maximum lateral load measured during the test. Taking these factors into account, the joint shear force at over-strength can be calculated as

$$V_{jh,o} = H^0\left(2\frac{l_c}{l_b}\frac{l_b''}{jd^*}-1\right) \tag{2.6}$$

If $\lambda_o = \dfrac{H^o}{H_a}$

Then the over-strength factor of joint shear force can be written as

$$\lambda_{jo} = \frac{V_{jh,o}}{V_{jh}} = \lambda_o\left(2\frac{l_c}{l_b}\frac{l_b''}{jd^*}-1\right)\bigg/\left(2\frac{l_c}{l_b}\frac{l_b'}{jd}-1\right) \tag{2.7}$$

The joint shear force at over-strength, $V_{jh,o}$ can then be calculated using Eq. 2.6 or based on λ_o in Eq. 2.7.

2. *Test Set-up with P–Δ effect*

Figure 2.7 shows a beam-column subassembly tested with P-Δ effects. Note that in this set-up, the measured lateral load capacity, H, needs to be corrected by adding the lateral shear induced by the P-Δ moment. The corrected lateral load capacity, H', can be expressed as

$$H' = H + \frac{N^*\Delta}{l_c} \tag{2.8}$$

With reference to **Fig. 2.7**, equilibrium requires that

$$\left(V_b^+ + V_b^-\right)\frac{l_b}{2} = Hl_c + N^*\Delta = H'l_c \tag{2.9}$$

Thus

$$\left(V_b^+ + V_b^-\right) = 2\frac{l_c}{l_b}H' \tag{2.10}$$

Substituting Eq. 2.10 into Eq. 2.3, the joint shear force, V_{jh}, can be expressed as

$$V_{jh} = 2\frac{l_c}{l_b}\frac{l_b'}{jd}H' - H \tag{2.11}$$

when over-strength developed, the joint shear force becomes

$$V_{jh,o} = 2\frac{l_c}{l_b}\frac{l_b''}{jd^*}H_o' - H_o \tag{2.12}$$

where H_o and H_o' are the measured lateral load capacity and the corrected lateral load respectively. $V_{jh,o}$ for tests in which P-Δ effect was induced can be calculated using Eq. 2.12.

Then the joint shear stress corresponding to $V_{jh,o}$ for both cases is

$$v_{jh,o} = V_{jh,o} / \left(b_j h_c\right) \tag{2.13}$$

where b_j and h_c are taken as that defined in NZS 3101:1995 and have been presented in Section 2.2.4. The joint shear stress for each test unit was divided by f_c' to obtain the joint shear stress ratio at overstrength, $v_{jh,o}/f_c'$. This ratio was subsequently transformed to $v_{jh,e}/f_c'$ by multiplying the corresponding K_{pv} value using Eq.2.1. Table 2.1 summaries the parameters used to evaluate the $v_{jh,e}/f_c'$ ratio of each test in the database.

Table 2.1 - Evaluation of Equivalent Joint Shear Stress Ratios of Existing Tests.

Test Code	Researcher	Test	$N^*/A_g f_c'$	$(V_{sh})_{eff}/V_{jh,o}$	$v_{jh,o}/f_c'$	K_{pv}	$v_{jh,e}/f_c'$
B1	Beckingsale [B3]	B11	0.043	1.000	0.140	1.000	0.140
B2		B12	0.045	1.000	0.147	1.000	0.147
B3		B13	0.442	0.879	0.155	1.460	0.226
B4	Birss [B4]	B1	0.053	0.463	0.220	2.280	0.502
B5		B2	0.439	0.139	0.197	3.030	0.597
C1	Cheung [C1]	1D-1	0.000	0.639	0.119	1.960	0.233
D1	Durrani [D2]	X1	0.055	0.332	0.204	2.520	0.514
D2		X2	0.056	0.485	0.213	2.220	0.473
D3		X3	0.053	0.437	0.171	2.360	0.404
D4	Dai [D1]	U1	0.000	0.911	0.076	1.250	0.095
D5		U2	0.000	0.831	0.132	1.449	0.191
D6		U3	0.000	0.450	0.094	2.300	0.216
D7		U4	0.000	0.472	0.113	2.280	0.258
J1	Joh [J2]	JXO-B1	0.161	0.188	0.144	2.310	0.333
J2		JXO-B2	0.161	0.177	0.157	2.290	0.360
J3		JHO-BB-HH	0.153	1.000	0.128	1.080	0.138
J4		JHO-BB-HL	0.143	1.000	0.124	1.000	0.124
J5		JHO-BB-LH	0.153	0.215	0.123	2.280	0.280
J6		JHO-BB-MH	0.153	0.412	0.119	2.040	0.243
L1	Lawrance & Beattie[L1]	HSC	0.000	0.595	0.079	2.030	0.160
M1	Milburn & Park [M8]	U1	0.100	0.843	0.209	1.480	0.309
M2	Menheit & Jirsa	II	0.254	0.128	0.261	1.900	0.496
M3	[M9]	VI	0.483	0.124	0.307	3.110	0.955
M4		XII	0.300	0.388	0.420	1.640	0.689
O1	Otani, Kobayashi,	J1	0.077	0.093	0.252	2.710	0.683
O2	Aoyama [O1]	J2	0.082	0.184	0.272	2.660	0.724
O3		J3	0.082	0.412	0.299	2.410	0.721
O4		J4	0.305	0.082	0.275	1.960	0.539
O5		J6	0.205	0.190	0.169	2.070	0.350
O6	Otani, Kitayama,	C1	0.077	0.116	0.200	2.710	0.542
O7	Aoyama [O2]	C2	0.077	0.367	0.204	2.440	0.498
O8		C3	0.077	0.848	0.198	1.480	0.293
P1	Priestley [P1]	IBC	0.030	1.000	0.080	1.000	0.080
R1	Restrepo, Park [R1]	U6	0.000	0.897	0.090	1.320	0.119
S1	Stevenson [S6]	U1	0.237	0.346	0.253	1.750	0.443
T1	Teraoka et al. [T2]	HNO 1	0.167	0.240	0.172	2.090	0.359
T2		HNO 3	0.167	0.183	0.227	2.260	0.513
T3		NO 43	0.200	0.279	0.109	1.960	0.214
T4		NO 47	0.200	0.183	0.166	2.020	0.335
V1	Viwathanatepa [V1]	BC3	0.361	0.312	0.149	2.120	0.316
X1	Xin [X1]	X1	0.000	0.642	0.167	1.960	0.327
X2		X2	0.000	0.645	0.097	1.960	0.190
X3		X3	0.000	0.663	0.128	1.900	0.243
X4		X4	0.000	0.742	0.083	1.720	0.143
X5		X5	0.000	0.513	0.124	2.230	0.277
X6		X6	0.000	0.554	0.118	2.120	0.250
W1	P.K.C. Wong [W1]	Unit 1	0.000	0.065	0.237	2.730	0.647

2.3.2 Evaluation of $(V_{sh})_{eff}$

As had been mentioned in the item (h) in Section 2.2.2, it has been observed in the laboratory that the sets of joint hoops which are close to the top and bottom beam longitudinal bars usually do not develop the yield strength, while inner sets do. The tensile stress developing in sets of joint hoops is sensitive to the distance from the top and bottom beam bars. As a result, the effective joint shear resistance provided by the joint hoops can be less than that calculated from the yield strength of all the joint reinforcement. This study recognizes this effect and aims to quantify its influence.

Originally $V_{sh,eff}$ of each test was evaluated using judgement. In the majority of tests the top and bottom sets of joint reinforcement was assumed to develop 50% of the yield strength. However, a strain profile across the joint height is proposed, see Section 8.2.1. The proposed profile was based on the results of the test units conducted in this study and it is presented in **Fig. 8.15**. $V_{sh,eff}$ of each existing test was then re-calculated using this profile.

It should be noted that there are a few tests in the database in which the information regarding the position of joint hoops in the joint region is not given. For such joints, realistic assumptions regarding the yield stress developed in joint hoops close to the top and bottom beam bars have to be made based on the available information. This uncertainty accounts for the scatter on the results and observed trends, particularly when the joint reinforcement consists of few sets.

The assumptions which had been made were noted in the table of each test depicted in Appendix B. Tests without any notes regarding $(V_{sh})_{eff}$ indicate that it was calculated using the proposed profile.

2.3.3 Failure Criterion and Measurement of Available Displacement Ductility Factors

The failure criterion for judging failure of a specimen tested in the laboratory generally used in New Zealand is based on a 20% drop from the maximum measured lateral load. The criterion is that test specimen should be able to sustain at least 2 complete load cycles to the same displacement ductility without loss of lateral load capacity larger than 20% with respect to the maximum recorded load [P1] [S4]. The available displacement ductility factor is often referred to as the factor that the specimen has achieved without violation of the criteria.

Another alternative is to use accumulated displacement ductility factor which was proposed by Park [P1].

Another criterion for measuring the ultimate displacement ductility of structural components is proposed and used in this study. In order to make the maximum use of the database, the ultimate displacement was defined as that corresponding to a 10% strength degradation because the usefulness of the database would have been very limited had the 20% strength degradation concept been used in the study. The achieved ultimate displacement ductility factor was measured on the envelope of hysteresis loops associated with a 10% degradation of lateral strength.

The ultimate displacement ductility of each test measured using this criterion and the corresponding failure mode is listed in Table 2.2. Tests in which bond failure was observed are classified as " other failure modes " in the table but not shown in the **Fig. 2.9** which will be discussed in the later section. Data extracted of each test collected in the database used in this study was tabulated in **Appendix B**.

2.3.4 Ductility Relationships

The ultimate displacement ductility was transformed to the ultimate rotational ductility. The rotational ductility defined in this research is similar to the displacement ductility, while the elastic component of the column displacement is subtracted from the ultimate displacement and the yield displacement. This implies that the elastic column displacement at yield is approximately equal to that at ultimate. This implication is valid as columns should always remain elastic in the capacity designed frames. The ultimate rotational ductility relationship is:

$$\mu_\theta = \frac{\Delta_u - \Delta_c}{\Delta_y - \Delta_c} \tag{2.14}$$

where Δ_u is the ultimate displacement measured according to prescribed failure criterion , Δ_c is the column elastic displacement corresponding to the development of the theoretical ultimate strength of the test assembly and Δ_y is the yield displacement measured using the standard procedure [P1]. Details of this procedure to obtain Δ_y are described in Section 3.6. The methodology used to calculate the column displacement is discussed in the next section.

Table 2.2 - Equivalent Joint Shear Stress Ratios, Failure Modes and Rotational Ductility. of Existing Tests.

Code	Researcher	Test	$v_{jh,e}/f'_c$	Measured Ultimate Rotational Ductility					
				Joint reinforcement with Y.P. *			Joint reinforcement without Y.P. *		
				Joint Failure	Other Failure Modes	Beam Hinging Failure	Joint Failure	Other Failure Modes	Beam Hinging Failure
B1	Beckingsale [B3]	B11	0.140			10.0			
B2		B12	0.147			10.0			
B3		B13	0.227			7.4			
B4	Birss [B4]	B1	0.502	6.6					
B5		B2	0.596	4.4					
C1	Cheung [C1]	1D-1	0.230			12.0			
D1	Durrani [D2]	X1	0.513	4.5					
D2		X2	0.473	5.2					
D3		X3	0.404	6.3					
D4	Dai [D1]	U1	0.095			12.3			
D5		U2	0.192		7.2				
D6		U3	0.217			15.2			
D7		U4	0.260					7.6	
J1	Joh [J2]	JXO-B1	0.333				10.5		
J2		JXO-B2	0.359				18.9		
J3		JHO-BB-HH	0.138						8.5
J4		JHO-BB-HL	0.136						7.6
J5		JHO-BB-LH	0.280						7.3
J6		JHO-BB-MH	0.242					8.33	
L1	Lawrance & Beattie[L1]	HSC	0.160		5.2				
M1	Milburn & Park [M8]	U1	0.309	8.2					
M2	Menheit & Jirsa	II	0.496	# 2.64					
M3	[M9]	VI	0.956	# 2.6					
M4		XII	0.690	3.9					
O1	Otani, Kobayashi,	J1	0.680				5.6		
O2	Aoyama [O1]	J2	0.720				5.9		
O3		J3	0.720				6.3		
O4		J4	0.538				7.7		
O5		J6	0.351					7	
O6	Otani, Kitayama,	C1	0.541						9.6
O7	Aoyama [O2]	C2	0.497						8.4
O8		C3	0.294		9.6				
P1	Priestley [P1]	IBC	0.080			11.5			
R1	Restrepo, Park [R1]	U6	0.119			12.9			
S1	Stevenson [S6]	U1	0.442	4.8					
T1	Teraoka et al. [T2]	HNO 1	0.362				9.3		
T2		HNO 3	0.360				4.7		
T3		NO 43	0.213			10.2			
T4		NO 47	0.335	7.0					
V1	Viwathanatepa [V1]	BC3	0.320		4.7				
X1	Xin [X1]	X1	0.327	8.2					
X2		X2	0.191		9.7				
X3		X3	0.244		8.9				
X4		X4	0.140		9.0				
X5		X5	0.276		9.0				
X6		X6	0.250		8.6				
W1	P.K.C. Wong [W1]	Unit 1	0.648	2.3					

Note: * Yield plateau shown by the horizontal joint reinforcement

Beam bars did not yield, excluded in Fig. 2.9

The rotational ductility factor was chosen as a base for assessing existing test results because it is anticipated that joint behaviour depends on the rotational ductility of the adjoining beams and itself, rather than on the displacement ductility achieved by the whole frame assembly.

The rotational ductility in Eq. 2.14 can also be expressed in terms of the displacement ductility ratio $\mu_\Delta = \Delta_u / \Delta_y$ as

$$\mu_\theta = \frac{\mu_\Delta - \dfrac{\Delta_c}{\Delta_y}}{1 - \dfrac{\Delta_c}{\Delta_y}} \tag{2.15}$$

Note that for practical structures, the component of column displacement is likely to range between 20% ~ 30% of the system yield displacement. Table 2.3 shows the relationship between μ_θ and μ_Δ for values of Δ_c / Δ_y typically found in moment resisting frames. This table indicates that if a structure is designed for a limited ductility ($\mu_\Delta = 3$), the equivalent rotational ductility is approximately equal to 3.7. Similarly, if a structure is designed for full ductility ($\mu_\Delta = 6$), the equivalent rotational ductility is approximately equal to 7.7.

Table 2.3 - Relationship between Rotation and Displacement Ductility for Typical Frame Dimensions

Limited Ductility			
μ_Δ	Δ_c / Δ_y	μ_θ	Average μ_θ
3	0.2	3.5	3.7
3	0.3	3.9	

Full Ductility			
μ_Δ	Δ_c / Δ_y	μ_θ	Average μ_θ
6	0.2	7.3	7.7
6	0.3	8.1	

2.3.5 Calculation of Column Deformation as a Component of System Yield Displacement

Three main sources, flexural deformation, shear deformations and fixed-end rotation at the beam face, contribute to the column displacement. The column shear deformation component is generally insignificant and can be neglected. The flexural deformation and fixed-end rotation are calculated using procedures described below. In order to seek consistency with the measured yield displacement, values corresponding to 75% of the theoretical lateral strength are calculated first and then extrapolated to the values associated with H_a.

The flexural deformation is calculated by integrating the curvatures along columns up to the joint face. The curvature was determined from a section moment-curvature analysis with a column compressive load and bending moment corresponding to the 75% of the theoretical ultimate lateral strength, H_a. The curvature of the column critical section at the joint face is $\phi_{c,3/4}$, and the flexural deformation of a single column when laterally loaded with 0.75 H_a (see **Fig. 2.8**) is :

$$\delta_{c,fl} = \frac{\phi_{c,3/4}\, l'}{2} \frac{2l'}{3} = \frac{\phi_{c,3/4}\, l'^2}{3} \qquad (2.16)$$

Since the columns are designed to remain elastic, significant yielding of column longitudinal reinforcement at the beam faces when the theoretical ultimate lateral strength develops is unlikely to occur. Thus the column fixed-end rotation would develop only from the elastic deformation of the column reinforcement within the joint height. **Figure 2.8** shows a beam-column subassembly with fixed-end rotations. The stress profile of column exterior bars is assumed to be a parabolic distribution crossing the joint height, see **Fig. 2.8** where f_{st} and f_{sc} are found from the section moment-curvature analysis described above. With this profile, the " pull-out " of column exterior bars at joint face can be estimated as

$$d\varepsilon = \frac{2}{3} d_x \frac{f_{st}}{E_s} \qquad (2.17)$$

d_x is defined in **Fig. 2.8** and E_s is the Young's Modulus of steel. Then the angle of fixed-end rotation estimated at joint face is

$$\theta_{c,fe} = \frac{d\varepsilon}{d - C} \tag{2.18}$$

where C is the neutral axis depth of column critical section obtain from M-ϕ analysis. By substituting Eq. 2.17 into Eq. 2.18,

$$\theta_{c,fe} = \frac{2}{3}\sqrt{\frac{1}{1 - f_{sc}/f_{st}}}\frac{(d - d')}{d - C}\frac{f_{st}}{E_s} \tag{2.19}$$

Then the column end deflection resulting from the fixed-end rotation can be estimated

$$\delta_{c,fe} = \frac{2}{3}\sqrt{\frac{1}{1 - f_{sc}/f_{st}}}\frac{(d - d')}{d - C}\frac{f_{st}}{E_s}l_c'' \tag{2.20}$$

as

l_c'' is the half column height measured from the mid-storey height to the centroid of longitudinal beam reinforcement. Once $\delta_{c,fl}$, $\delta_{c,fe}$ have been found, the total column deformation corresponding to the development of the theoretical ultimate lateral strength is

$$\Delta_c = 2\left(\frac{4}{3}\right)\left(\delta_{c,fl} + \delta_{c,fe}\right) \tag{2.21}$$

2.3.6 Observed Trends

Figure 2.9 plots the test results from the database in terms of the equivalent beam-column joint. The horizontal axis in **Fig. 2.9** is the rotational ductility, μ_θ, of the test units while the vertical axis is the transformed equivalent joint shear stress ratios. A clear trend can be observed in this graph and it is that joints with measured equivalent joint shear stress ratios less than 0.3 never fail in the joint. This is in spite of the large ductility demands imposed in plastic hinges developing in beams at the column faces. **Figure 2.9** also shows a clear trend for those joints that causes failure in the test subassemblies. The data points show a reasonably linear trend. It will be shown in Chapter 8 that with the tests conducted in this

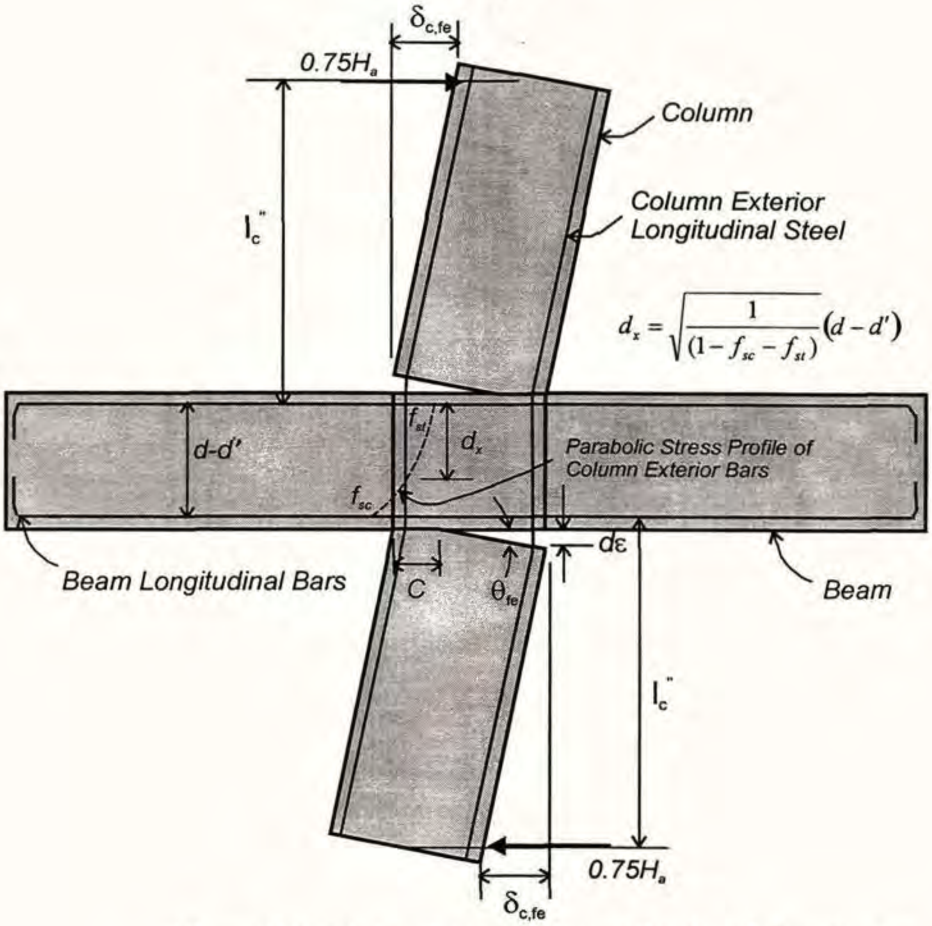

Figure 2.8 - Estimation of Column Fixed-end Rotation as a Component of Yield Displacement.

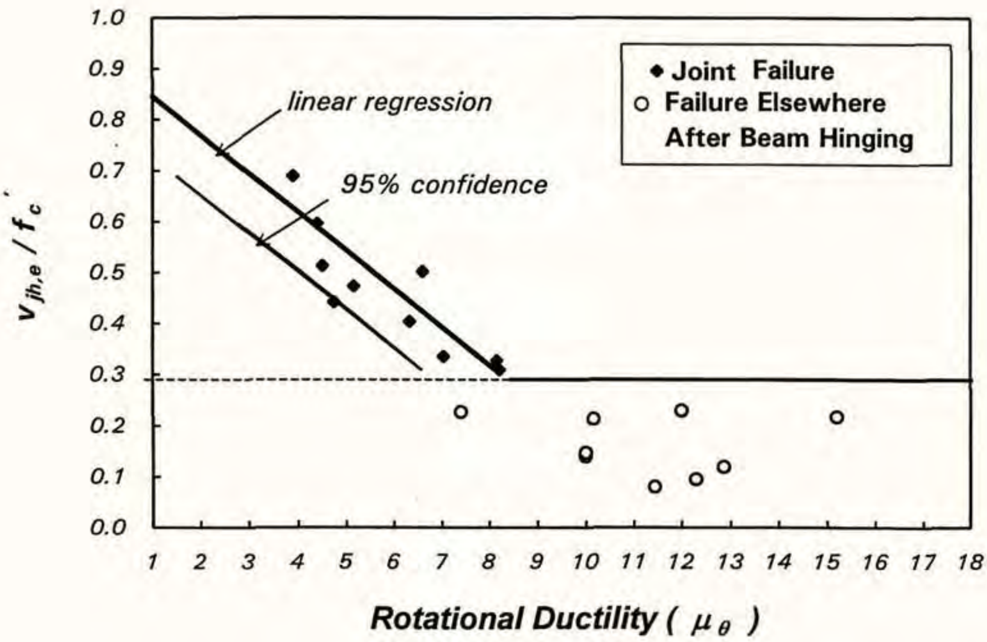

Figure 2.9 - Equivalent Joint Shear Stress Ratio Versus Rotational Ductility Factor of Existing Tests in the Database.

research project being included, the linear regression line gives a mean value of the ratio of measured μ_ϕ divided by predicted μ_ϕ equal to 0.97 and a standard deviation of 0.16. Considering the wide range of parameters existing in the tests, this scatter is relatively small.

It is noted that in tests coded M2 and M3 in the database (see **Appendix B**), the beams did not reach their nominal strength during the test. Apparently joints of the two tests failed prior to the yielding of beam bars. As a result, they were excluded in **Fig. 2.9**.

The trend found in **Fig. 2.9** can be used for the prediction of the strength and deformation capacity of beam-column joints of frames. Furthermore, design recommendations to establish the horizontal joint reinforcement can also be derived for joints of ductile and limited ductility frames using the trends shown in this graph.

2.4 ANALYTICAL RESULTS OF INTERIOR JOINTS INCORPORATING LUMPED BEAM BARS

2.4.1 Design of the Horizontal Joint Reinforcement

Design charts for joints of ductile and limited ductility frames can be formulated using the straight lines shown in **Fig. 2.9**. For instance, for moment resisting frames designed to form a beam side-sway mechanism, curvature ductility factors of μ_θ equal to 7.7 and 3.7 may be used in **Fig. 2.9** for the joint design of a full ductile structure and a limited ductility structure. These rotational ductility factors imply equivalent joint shear stress ratios of 0.3 and 0.52 when using the 95% confidence limit line. The design charts in **Figs. 2.10(a)** and **(b)** were produced by substituting the equivalent joint shear stress ratio corresponding to joints in ductile frames into Eq. 2.1 to find the corresponding K_{pv} for joints with a given v_{jh} / f_c'. The requirements of V_{sh} / V_{jh} can then be found by working back to **Fig. 2.4** with the given K_{pv} and the applied column axial load. The same procedures were applied on joints in limited ductility structures and the requirements of horizontal joint shear reinforcement are presented in **Fig. 2.10(c)**.

There are three distinct regions in **Fig. 2.10(a)**. With column axial load ratios ranging from 0 to 0.1, the required amount of hoop reinforcement does not change significantly. When the column axial load ratio increases further, the required design joint reinforcement decreases

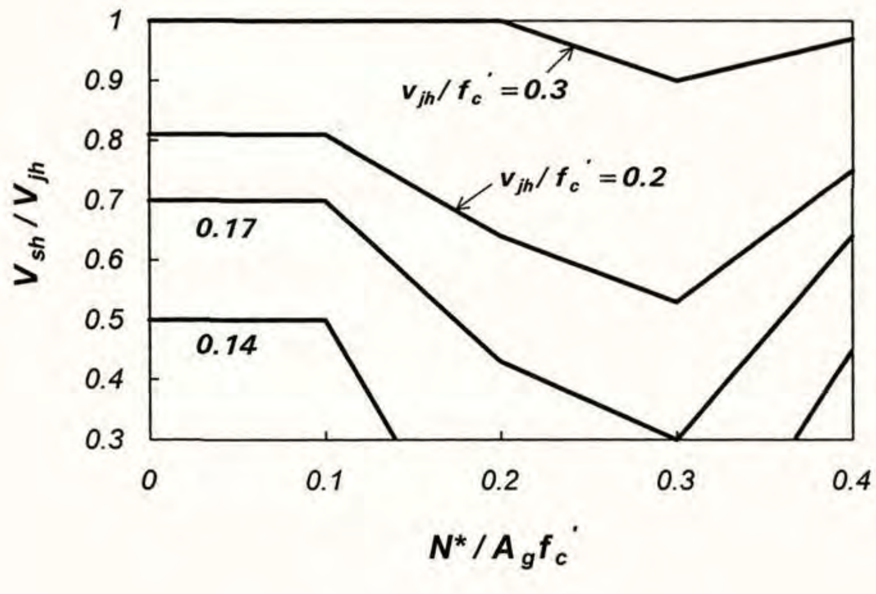

(a) Joints of Ductile Frames ($\mu_\Delta = 6$)

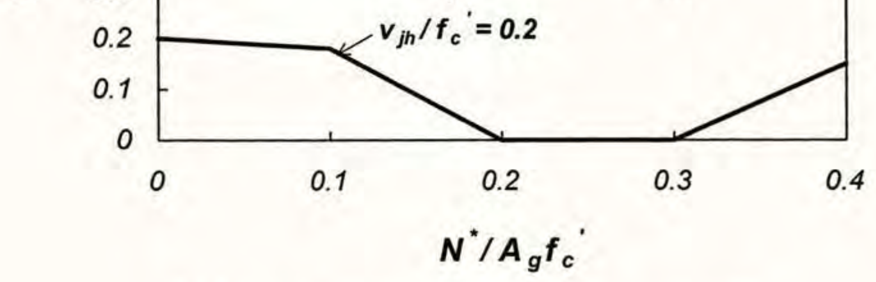

(b) Joints of Limited Ductility Frames (μ_Δ=3)

Figure 2.10 - Design of Horizontal Joint Shear Reinforcement Based on the Analytical Results (95% confidence limit).

until $N^* / A_g f_c'$ reaches 0.3. Then the required joint reinforcement ratio begins to increase when column axial load ratios exceed 0.3. This finding is in contrast to the design recommendations in NZS 3101:1995 in which the column compressive load is always considered beneficial to the strength of the joint. The increasing trend of V_{sh} / V_{jh} when $N^* / A_g f_c'$ exceeds 0.3 is caused by the increasing of uniaxial compressive stress in the central diagonal strut in the diagonal compression field of the joint.

Another trend indicated in **Fig. 2.10(a)** is that when the joint shear stress ratio v_{jh} / f_c' increases, the effect of column axial load on reducing the requirement of V_{sh} / V_{jh} diminishes. Also observed in **Fig. 2.10(b)** for joints in ductile frames having $v_{jh} / f_c' = 0.14$, the required amount of horizontal joint shear reinforcement is much less than that given by NZS 3101:1995.

In **Fig. 2.10(c)**, it can be seen that for joints in limited ductility frames with joint shear stress ratios less or equal than 0.2, the requirements of V_{sh} / V_{jh} are below 0.4 for all ranges of column axial load levels.

2.4.2 Evaluation of Cracking of the Joint Panel

It is accepted that reinforced concrete behaves like homogeneous isotropic material prior to cracking. When cracking initiates, the reinforcement is mobilized so that the member can sustain deformation and loads. A basic assumption, that the joint concrete is cracked, has been made in this project. Therefore, the cracking of joint concrete within all the domains in **Fig. 2.10** must be investigated. If there are some domains in which the joint concrete remains uncracked under the given column axial loads and joint shear stress, results obtained from the strut-and-tie models are not applicable because joints problems are no longer of concern.

There are several equations have been proposed to evaluate cracking of the joint concrete. Procedures adopted by Hakuto et al. [H1] were used in this research. Hakuto et al. [H1] equations are based on a series of existing tests and proposed a mean value equation for the diagonal tensile strength of joint concrete, f_t, is

$$f_t = 0.17 f_c'^{2/3} \tag{2.22}$$

The joint diagonal tension cracking stress f_{cr}' can be found from the principal tensile stress in the joint from the following equation.

$$f'_{cr} = -\frac{N^*}{2A_g} + \sqrt{\left(\frac{N^*}{2A_g}\right)^2 + v_j^2} \tag{2.23}$$

When f_t reaches f_{cr}', i.e. $f_t = f_{cr}'$, the above equation can be derived as

$$v_j = \sqrt{f_t\left(f_t + \frac{N^*}{A_g}\right)} \tag{2.24}$$

or

$$\frac{v_j}{f_c'} = \sqrt{\frac{f_t}{f_c'}\left(\frac{f_t}{f_c'} + \frac{N^*}{A_g f_c'}\right)} \tag{2.25}$$

For different f_c' values, different f_t / f_c' ratios can be obtained from Eq. 2.25. For example, when f_c' is 50 MPa, f_t / f_c' is 0.046 and, when f_c' is 25 MPa, f_t / f_c' is 0.058. To be conservative, the corresponding joint shear stress ratios which cause the initial cracking of joint core are evaluated by choosing f_t / f_c' as 0.06, 0.07, and 0.08 respectively and are listed in the following Table 2.4.

Table 2.4 - Diagonal Tension Cracking Stresses Associated with Different f_c'.

f_t / f_c'=0.06		f_t / f_c'= 0.07		f_t / f_c'=0.08	
$N^*/A_g f_c'$	v_{jh} / f_c'	$N^*/A_g f_c'$	v_{jh} / f_c'	$N^*/A_g f_c'$	v_{jh} / f_c'
0	0.06	0	0.07	0	0.08
0.267	0.14	0.21	0.14	0.165	0.14
0.422	0.17	0.34	0.17	0.281	0.17
0.61	0.20	0.5	0.20	0.42	0.20

According to Table 2.4, the envelope of region of uncracked joint concrete does not appear on the design chart, **Fig. 2.10**, and it indicates that for all the ranges of value v_{jh} / f_c' and column compressive loads shown in **Fig. 2.10**, the joint concrete was cracked. Therefore the assumption made in the analysis that the joint concrete was cracked is justified.

2.4.3 Comparison of Analytical Results With Requirements of NZS 3101:1995

The findings of this analytical work are compared with the requirements given by the design recommendations in NZS 3101:1995[S1] in **Fig. 2.11**. The analytical results were derived from $\mu_\theta = 7.7$ and 3.7 for joints in full ductility and limited ductility frames. **Fig. 2.11(a)** shows that current NZS 3101:1995 recommendations for joints of ductile frames with $v_{jh} = 0.2f_c'$ and beams having equal top and bottom reinforcement appear adequate up to $N^* / A_g f_c' \leq 0.34$ but are unconservative for higher axial load ratios. Note that, these calculations have been carried out for joints with typical geometry and the reinforcement required for confinement is unlikely to govern the design of the joint transverse reinforcement for $N^* / A_g f_c' \leq 0.45$. Note also that there are very few tests available on interior beam-column joints subjected to high axial load levels. The disparity of the requirements of horizontal joint reinforcement between the NZS 3101:1995 recommendations and the analytical results for joints subject to column axial load ratios beyond 0.34, is the subject of study in this research through experimental work.

Figure 2.11(b) compares analytical findings and NZS 3101:1995 recommendations for joints in ductile frames with $v_{jh} = 0.14f_c'$ and beams having equal top and bottom reinforcement. The analytical results are well below NZS 3101:1995 requirements for the entire ranges of column axial loads, suggesting that NZS 3101:1995 recommendations could be relaxed. This also will be confirmed through experimental work.

Figure 2.11(c) compares the analytical findings and the NZS 3101:1995 recommendations for joints in frames designed for limited ductility when $v_{jh} = 0.2f_c'$ and the framing beams have equal top and bottom reinforcement. The comparison indicates that NZS 3101:1995 recommendations are unduly conservative and could be relaxed.

2.4.4 Proposed Design Recommendations

In accordance with the analytical results, design recommendations were made for joints designed for ductile and limited ductility structures.

The contribution to the horizontal shear resistance of interior beam-column joints can be expressed as the sum of three different mechanisms of the form:

$$V_{jh} = V_{sh} + V_N + V_c \tag{2.26}$$

where V_{jh} is the horizontal joint shear force, which can be calculated as $(T_{b,1}+T_{b,2})-V_{col}$; $T_{b,1}$ and $T_{b,2}$ are the tensile force of top and bottom beam bars at over-strength respectively; $T_{b,1}=\alpha_o A_{s,b} f_y$, $T_{b,2}=\alpha_o A_{s,t} f_y$, where α_o is the over-strength factor which is equal to 1.25 in accordance with the design recommendations in NZS 3101:1995 [S1]; $A_{s,b}$, $A_{s,t}$ are the section areas of the bottom and top beam bars respectively and f_y is the yield strength of the beam longitudinal bars.

V_{sh} is the shear resisted by horizontal reinforcement in the joint; V_N is the component of shear resisted by column axial load and V_c is the shear resisted by concrete.

An equation representing the component of the concrete contribution to the shear resistance of interior beam-column joints of ductile frames was derived by the author based on the observed curves in **Fig. 2.10**.

$$\frac{V_c}{V_{jh}} = \frac{1}{660\left(\frac{v_{jh}}{f'_c}\right)^3} \tag{2.27}$$

Similarly, equations representing the joint shear resistance due to column axial compression was derived by the author from the analytical results depicted in **Fig. 2.10**. They are

$$\frac{V_N}{V_{jh}} = 0 \quad when \quad \frac{N^*}{A_g f'_c} \leq 0.1$$

$$\frac{V_N}{V_{jh}} = 1.0 - 2.27\frac{N^*}{A_g f'_c} \quad when \quad \frac{N^*}{A_g f'_c} > 0.3$$

$$\frac{V_N}{V_{jh}} = 1.6\left(\frac{N^*}{A_g f'_c} - 0.1\right) \quad when \quad 0.1 < \frac{N^*}{A_g f'_c} \leq 0.3 \tag{2.28}$$

Once the shear component of concrete and column axial load contribution have been found, that provided by the horizontal joint reinforcement can be easily found from $V_{sh} = V_{jh} - V_N - V_c$.

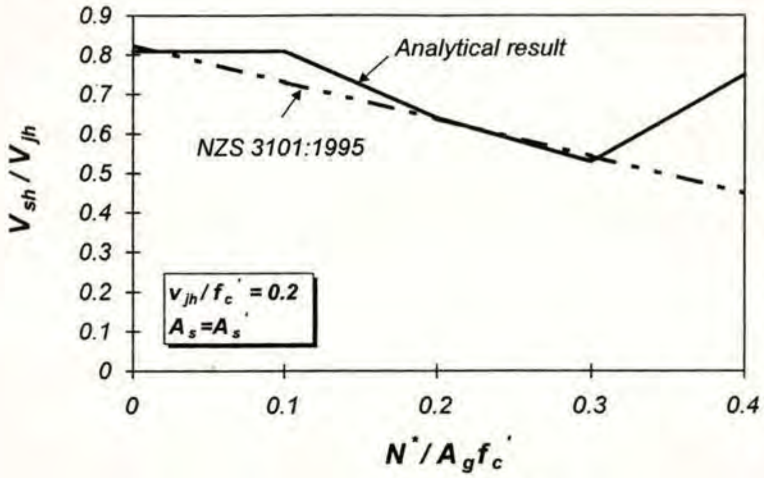

(a) Joints of Ductile Frames (μ_Δ=6)

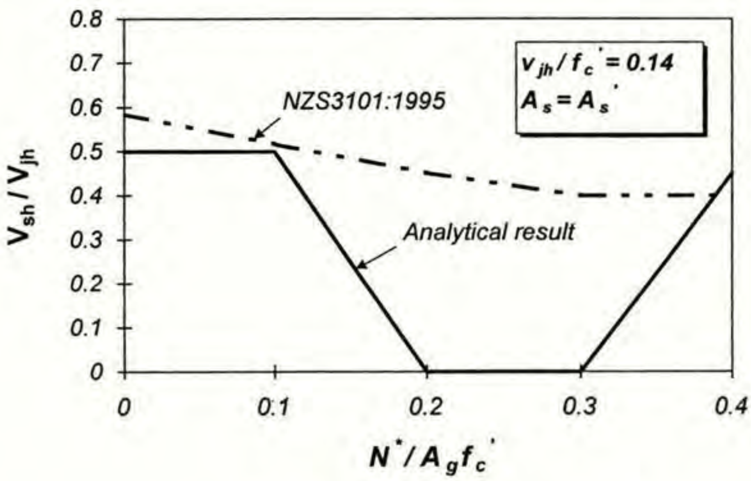

(b) Joints of Ductile Frames (μ_Δ=6)

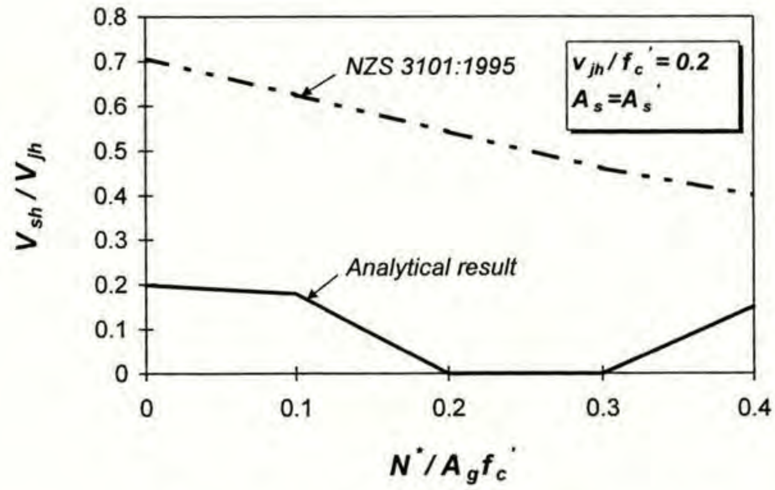

(c) Joints of Limited Ductility Frames (μ_Δ=3)

Note: The analytical result is based on the 95% confidence line

Figure 2.11 - Comparison of the Requirements of Horizontal Joint Reinforcement Given by NZS 3101:1995 and the Analytical Result for Joints in Ductile And Limited Ductility Frames.

It is recommended that the minimum requirement of horizontal joint reinforcement given by Code [S1] is satisfied:

$$0.4 \le V_{sh}/V_{jh} \le 1 \tag{2.29}$$

and the joint shear stress should be limited within:

$$v_{jh} \le 0.2 f_c' \tag{2.30}$$

Although the analytical results depict that joint shear failure can be prevented for joints with v_{jh} larger than $0.2f_c'$ if an adequate quantity of horizontal joint shear reinforcement is provided, the author would suggest that the above joint shear stress limit is used until further experimental evidence with $v_{jh}>0.2 f_c'$ is available.

For interior beam-column joints of frames designed for limited ductility, it can be seen in **Fig. 2.10(b)** that the required horizontal joint shear reinforcement (V_{sh}) for joints with $v_{jh} \le 0.2 f_c'$ is far less than $0.4V_{jh}$. Thus, it is recommended that the minimum requirement of joint reinforcement is satisfied i.e. $V_{sh} = 0.4 V_{jh}$ when $v_{jh} \le 0.2f_c'$.

2.5 VERTICAL JOINT SHEAR REINFORCEMENT

The requirement of vertical joint shear reinforcement in the joint region was initially highlighted by Park and Paulay [P4]. Subsequent researchers [S6] [P10] in the University of Canterbury concluded that vertical joint shear reinforcement is required to form the truss mechanism resisting joint shear so that joint shear failure can be prevented.

Despite that an attempt has been made to relax the requirement on vertical joint shear reinforcement [C1], but the current code recommendations [S1] still often result in vertical joint shear reinforcement in addition to the interior column bars for joints undergoing relatively high shear stress. This results in construction difficulties.

The formulations of design equations for vertical joint reinforcement in NZS 3101:1995 is a refinement of Park and Paulay's macro model [S1]. According to this model, the presence of vertical joint reinforcement is necessary in order to sustain the diagonal compression field by virtue of a truss mechanism. Current design recommendations in NZS 3101:1995 derived the vertical joint shear force from the input horizontal joint shear multiplied by the aspect ratio of the joint. This derivation implies that the vertical joint shear force is similar to horizontal joint shear in magnitude for typical joints. A reduction factor was then introduced into the design equation of vertical joint shear reinforcement. This factor is based on the estimation that the reserved strength of column interior bars which can be used as vertical joint reinforcement is about 30% of the yielding strength when the capacity design procedure, including the dynamic moment magnification, is incorporated. The advantage of column axial load is also taken into account in this factor. However, additional vertical joint shear reinforcement is still likely to be required for joints when the column axial loads are low.

Recently, it was pointed out by Restrepo et al. [R1] that the main function of interior column bars in the joint regions is to enable some bond force to be developed along the longitudinal beam bars beyond the column concrete compressive region. The column interior bars usually have some reserve strength to provide clamping effects which improve the bond transfer of beam bars in the joint region, if the capacity design procedure is used. The design of vertical joint reinforcement should therefore be reconsidered.

In practical design, column interior bars are usually required for the purpose of confinement, unless the column section is very small. Designers would expect that the existing column interior bars required by column design can meet the requirements of vertical joint reinforcement. Most of the strut-and-tie model analysis which have been shown in this study possessing 2 column interior bars on each column face between corner bars but without additional vertical joint reinforcement.

In order to further clarify the role of vertical joint reinforcement, two joints were analyzed and compared. **Figure 2.12** show the results of analysis. The two joints are identical except for the addition of a column interior bar in joint (b).

Note that in joint (a), due to the absence of column interior bars, the bond force of beam bars would tend to concentrate at the column concrete compressive region. Bond failure of beam bars can be expected as the large bond stress cannot sustained within the region of concrete compressive stress block. As a result, C_s, the force in the beam reinforcement can be very small or even in tension in the compression region, whereas the total compressive force (C_s+C_c) should be equal to 430 kN for equilibrium. It is assumed that C_s and C_c are still co-linear with the centroid of the beam compressive reinforcement in this study. In contrast, in joint (b), the bond of beam bars beyond the column compressive region is considerably

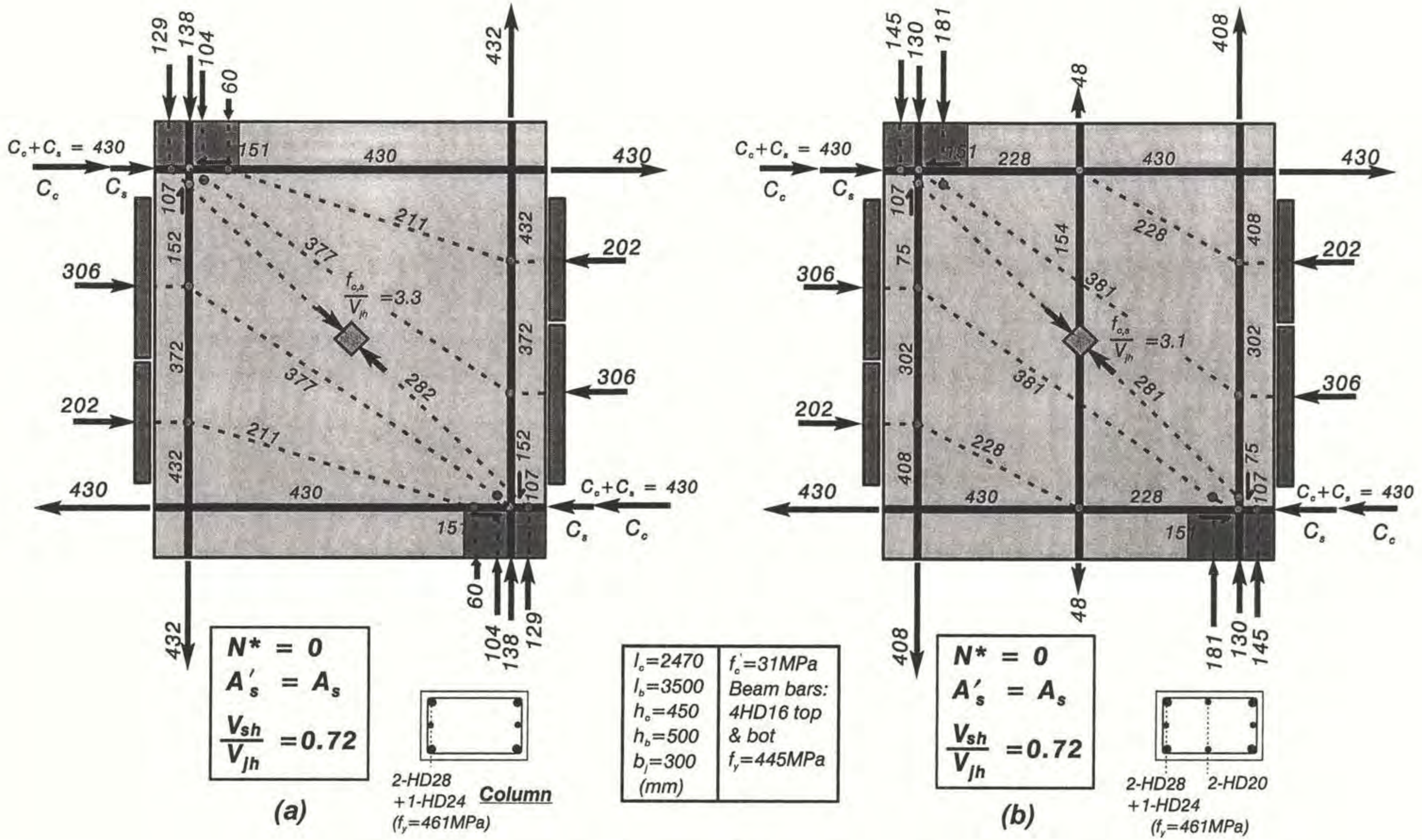

Figure 2.12 - Comparison of Strut-and-tie Model Analysis of Joints With or Without Column Interior Bars.

Strcint.cdr

improved due to the presence of a column interior bar. As a result, bond failure is less likely to occur and C_s is expected to be larger than that in joint (a).

Both joints were modeled using five struts so that comparison is possible. Results show that not only the strut patterns but also the compressive forces taken by the struts of two joints are very similar. The only appreciable difference is the angle of inclination of the outer struts. This analysis strongly implies that the presence of vertical joint shear reinforcement does not have a significant effect on the compressive stress in the middle of the joint.

Furthermore, it is not difficult to find tests in which the amount of vertical joint shear reinforcement provided is less than that is required by NZS 3101:1995 and which performed satisfactorily. Table 2.5 shows a collection of tests which performed satisfactorily in a ductile manner without failure. There is only one exception, test M1, which showed joint shear failure in the late stage when the ultimate displacement ductility was very close to 6.

Table 2.5 - Parameters of Vertical Joint Reinforcement of Existing Tests

Test Code	v_{jh}/f_c'	V_{sv}/V_{jv} provided	V_{sv}/V_{jv} NZS 3101:1995	Note
B1	0.140	0.478	0.497	*
B2	0.147	0.466	0.376	
B3	0.155	0.486	0.157	
C1	0.119	0.413	0.364	
D4	0.076	0.422	0.585	*
D6	0.094	0.240	0.592	*
M1	0.209	0.383	0.469	*
P1	0.080	0.580	0.58	
T3	0.109	0.454	0.243	
T4	0.166	0.52	0.285	
R1	0.090	0.705	0.402	
X5	0.124	0.245	0.380	*

*Note: * Provided vertical joint reinforcement is less than the requirements of NZS 3101:1995*

It can be seen in Table 2.5 that in 6 of 12 tests, the provided vertical joint reinforcement does not satisfy the requirement of NZS 3101:1995. Note that all the tests shown in the Table 2.5 had column interior bars as vertical joint reinforcement and no additional vertical joint reinforcement was used.

Note that the test on the Unit 3 by Thompson [T1], has been quoted by a previous researcher [S6] as an example showing joint failure caused by the lack of vertical joint shear reinforcement. This unit was investigated again in this study in light of the analytical finding regarding the effect of vertical joint shear reinforcement.

The columns of this unit were only reinforced with four corner bars. This unit had a joint shear stress ratio measured at ultimate strength, $v_{jh,o}$ = 0.242 $f_c^{'}$ and $(V_{sh})_{eff}/V_{jh}$ ratio equal to 0.74. The column compressive load applied on it was 0.216 $f_c^{'}A_g$. The K_{pv} value obtained from **Fig. 2.4** is 1.43, which results in a $v_{jh,e}/ f_c^{'}$ ratio of 0.345. This unit failed in the joint at a displacement ductility factor of 4.8, which corresponds to $\mu_\theta = 6$, when the criterion for judging failure proposed in this study was used.

The analytical model predicts failure at a rotational ductility, μ_θ, of 7.7 for this unit. This μ_θ corresponds to a displacement ductility factor, μ_Δ= 6.1. According to the above description, it is evident that this unit tested by Thompson [T1] did not have satisfactory ductile performance despite that the analytical model predicts a satisfactory behaviour. However, it should be noted that for a joint possessing a $v_{jh,e}/ f_c^{'}$ ratio of 0.345, joint failure is bound to occur eventually, although the provided horizontal joint shear reinforcement can defer the occurrence of joint failure until a displacement ductility factor of 6 had been achieved.

It should be noted that this unit was tested under an unusual loading sequence that is different from what was adopted and customized for the quasi-static laboratory tests in New Zealand [P1]. This unit was displaced drastically toward very large lateral displacement after finishing the elastic load cycles. It is believed that such drastic applied lateral displacement could result in faster joint strength degradation than joints tested under normal loading sequence. As a result, measured ultimate rotational ductility is smaller than the predictive value.

2.6 ANALYTICAL WORK OF JOINTS INCORPORATING BEAMS WITH DISTRIBUTED REINFORCEMENT

2.6.1 Moment-Curvature Analysis on Beam Sections Reinforced with Lumped and Distributed Bars

Wong et al. [W1], pointed out that the ultimate flexural strength of beams in which beam bars are distributed along webs is very close to that of beams in which same numbers of longitudinal bars are lumped on the top and bottom chords. Some of the features of the beams in which distributed reinforcement is incorporated are further investigated in this study.

Moment-curvature analysis on three beams were carried out using the programme *RESPONSE* developed by Collins and Mitchell [C2]. The concrete model used in this analysis is a parabolic function. **Figure 2.13** shows the results of the analysis and the details of the three beams. Note that the section area of beam bars in beam (3) is slightly less that in beam (1) and (2). It can be seen in this figure that three beams reached similar ultimate strengths. This result is in agreement with what was found by Wong et al. [W1].

The extreme case, beam (3), in which all of the beam bars are distributed along the web, shows a rapid drop of strength after the ultimate strength has been reached. This indicates beam (3) does not have enough curvature ductility and capacity very little over-strength was observed. The reduction of flexural strength occurs when the compressive strain at the extreme fibre of the concrete exceeds the maximum permissible strain and spalls off. The numbers of beam bars in compression is relatively small and the neutral axis depth of the beam section increases to compensate for the compressive force in the beam section. As a result, the internal lever arm of the beam section is reduced and therefore so is the flexural capacity. In contrast, in beams in which the longitudinal beam bars are lumped on the top and bottom of beams, the beam bars in compression are enough to take most of the beam compressive force when the concrete cover spalls off. With the increase of curvature ductility, the flexural capacity would increase, as the tensile bars are strained into the strain-hardening region.

According to the analysis described above, it is evident that the higher the quantity of beam reinforcement is distributed along the web, the greater the compressive force relies on the concrete. As a result, the adverse effect of reducing curvature ductility of beams occurs. It

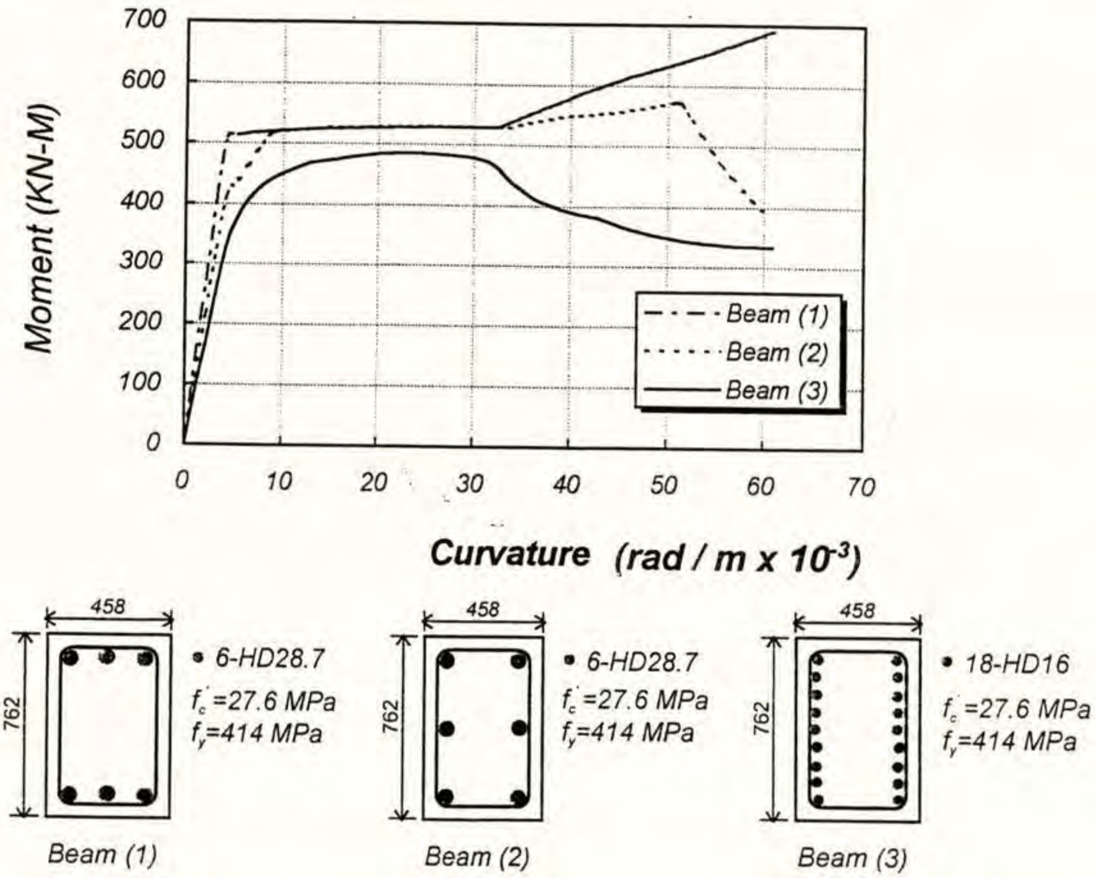

Figure 2.13 - Comparison of Moment-Curvature Analysis of Beams.

is suggested that at least an additional longitudinal bar be placed between corner bars when an attempt is made to distribute beam bars vertically along the web. This is to ensure enough curvature ductility. This kind of beam section should be designed as a wall section and the additional longitudinal beam bars placed between the corner bars should be restrained by cross ties to prevent buckling.

2.6.2 Strut-and-Tie Model Analysis

A series of strut-and-tie model analyses were carried out on joints in which the framing beams have distributed reinforcement. The applied axial compressive loads on the joints range from 0 to 0.2 $N^* / A_g f_c'$ for two ratios of V_{sh} / V_{jh} of 0 and 0.5. Three types of joints incorporating beams with different portions of distributed reinforcement were studied. Details of beam reinforcement layout in these three types of joints examined can be referred to **Fig. 2.13**.

The column internal forces were determined using the same method as in other analysis. Based on the assumption that plastic hinges form in beams at the column faces, the beam internal forces at the column faces were obtained from the results of a section moment curvature analysis at ultimate strength and then multiplied by an over-strength factor 1.25. The forces so found show that most of the layers of longitudinal beam bars yield in tension at over-strength except for one or two layers located near the neutral axis which are either in tension below yielding or in compression. Note that when over-strength in the beams develops on both sides of column faces, most of the interior layers of distributed beam bars passing through the joint region yielded in tension on both sides. This implies that the bond forces of the intermediate layers of beam bars in the joint region are not needed for anchorage.

When calculating V_{jh} of joints in this category, it was found that except for the joint regions close to the top and bottom beam bars, the V_{jh} of joints incorporating distributed beam reinforcement is nearly the same as that of joints with the same amount of beam reinforcement lumped at beam top and bottom chords. This is because the ultimate flexural capacities of beams incorporating lumped and distributed reinforcement are very similar to each other.

The concrete compressive forces of beams are also assumed to act at the level of extreme layer of compressive steel. Each joint was modeled using 6 or 7 struts. The maximum compressive stress of the diagonal strut of each unit was calculated and compared to the results acquired from the conventional joints. Details of all of the analyzed joints are presented in **Appendix A-3**.

2.6.3 <u>General Trends Observed</u>

Table 2.6 tabulates the $f_{c,s}$ / v_{jh} ratios of the joints studied. Results are also compared with joints having conventionally reinforced beams. Note that the three types of joints have very similar section areas of longitudinal beam reinforcement (see **Fig. 2.13**), as well as joint shear stress ratios. Several trends were observed. First, the maximum uniaxial compressive stress in the diagonal compression field in the centre of the joint is always smaller than that in conventional joints. Second, it seems that the greater the portion of beam steel distributed along the webs, the less $f_{c,s}$ / v_{jh} becomes. The extreme case of all longitudinal beam reinforcement distributed along webs leads to a drop of $f_{c,s} / v_{jh}$ ratio up to 34.3% with respect to that was found from the conventional joints. Third, when joint reinforcement ratios increase, the strut compressive stress diminishes. As $V_{sh} / V_{jh} = 1$, the results show little difference between conventional joints and joints with distributed reinforcement.

Table 2.6 - Comparison of $f_{c,s}/v_{jh}$ of Joints

$N^*/A_g f_c'$	V_{sh}/V_{jh}	$f_{c,s}/v_{jh}$			
		Lumped	Distributed [1]*	Distributed [2]*	Distributed [3]*
0	0.5	6.61	5.05/(23.6%)#	5.47/(17.25%)	4.34(34.34%)
0.2	0.5	5.09	4.38/(13.95%)	4.57/(10.22%)	-
0	1	2.93	3.1/(-5.8%)	-	-
0.2	1	2.96	2.93/(1.01%)	-	-

* Referring to beam (1) (2) (3) in Fig. 2.13

\# the percentage of drop with respect to the value in " lumped" joint

The beneficial effect on the diagonal compression stress field of joints in which framing beams having distributed reinforcement, can be observed from this analysis. However, the reduction percentages are scattered. On the other hand, it should be noted that the strength of the cracked concrete of the joint might decrease due to the yielding of intermediate layers of beam reinforcement passing through joint region. Due to the lack of test results of joints in this category, experimental work will be conducted to validate and calibrate the observed trends.

2.7 CONCLUSIONS

1. The lower bond theorem of plasticity was used to analyze interior beam-column joints in this study. Parameters influencing the joint behaviour were studied using this analysis and the relative importance of them has been identified.

2. Form the analytical work, the bond stress profiles of longitudinal beam bars passing through the joint region did not greatly affect the joint shear strength.

3. The joint shear stress ratio, v_{jh}/f'_c, the quantity of horizontal joint shear reinforcement (V_{sh}/V_{jh} ratio), and the column axial loads were found to have a significant influence on the strength and deformation capacity of interior joints.

4. It was found that the trend of influence of column compressive loads on the joint shear strength is different from NZS 3101:1995 when $N^*/A_g f'_c$ exceeds 0.3. The analytical work indicates that axial compression is detrimental to the joint when $N^*/A_g f'_c$ exceeds 0.3.

5. The analytical work shows that for joints incorporating unequal top and bottom beam bars, the requirement of horizontal joint shear reinforcement is very similar to that for joints incorporating equal top and bottom beam bars, provided that the v_{jh}/f'_c ratios of them are the same. This finding justifies that the joint shear strength more depends on the joint shear stress level, v_{jh}/f'_c, than the bond stress of the top or bottom beam bars.

6. A database set, collected from interior beam-column joints tested under similar loading sequences, were processed and correlated to the results from strut-and-tie model analyses. As a result, a theoretical framework for the design of interior beam-column joints has now been established.

7. Design recommendations for reinforced interior beam-column joints in ductile and limited ductility frames have been made on the basis of the established theoretical model. The new design approach aims to simplify the current design provisions in New Zealand. It was found that by applying this new approach, the requirements of horizontal joint reinforcement for the majority of interior joints can be relaxed except for some rare cases.

8. The analytical work indicates that vertical joint shear reinforcement does not unduly influence joint shear strength.

9. A design innovation for reinforced concrete perimeter moment resisting frames, in which beams in the primary frames are reinforced with distributed reinforcement was studied. Some aspects of beam detailing were suggested based on moment-curvature analyses.

10. Joints in which framing beams having distributed reinforcement were analyzed using strut-and-tie models. A slight reduction of strut compressive forces in the joints with respect to the conventional joints was observed.

CHAPTER 3
TEST PROGRAMME

3.1 INTRODUCTION

There are three main objectives in this experimental programme. First, to validate some of the recommendations given for the design of beam-column joints in NZS 3101:1995 3101:1995, especially in those areas where the analytical model discussed in Chapter 2 significantly differ from the recommendations. Second, to provide experimental investigation of beam-column sub-assemblages incorporating distributed longitudinal beam bars. Third, to observe the seismic behaviour of frame units when designed using Grade 500 longitudinal reinforcement in beams and columns.

The main difference between the trends given by the analytical model and NZS 3101:1995 were : first, the required quantities of horizontal joint reinforcement for joints under the combination of high joint shear stress and high column axial load; second, the design recommendations in NZS 3101:1995 for joints subjected to low shear stress ratios; third, the requirement of horizontal joint reinforcement in interior joints with the framing beams having an unequal quantity of top and bottom longitudinal reinforcement.

Due to the limited number of former tests in which beams with distributed longitudinal reinforcement were incorporated, an attempt was also made to understand the behaviour of such alternative method for the seismic design of perimeter moment resisting frames. Initial research work was carried out by Wong [W1]. Analytical assessment on the strength of this kind of joints by means of the strut-and-tie model analysis examined in Chapter 2 was also adopted in the design of the test specimens.

3.2 DESCRIPTION OF THE TEST UNITS

3.2.1 Design Considerations

The testing programme in this project comprises two series, designated as L and D series. Five units in which beams were conventionally reinforced constitute the L series. The

D series comprises three units with beams in which the longitudinal reinforcement is distributed through the web.

All the tests units were 70% scale cruciform, one way beam-column sub-assemblages of a typical perimeter moment resisting frame. With most of the gravity load sustained by interior gravity frames, the bending moment induced by gravity load is small relative to that induced by seismic loading. As a result, the point of inflection in the beams is located very close to the beam mid-span. All units were built using precast concrete elements commonly employed in New Zealand for the construction of equivalent monolithic high-rise multi-storey buildings. The precast concrete system (system 2 [G1]) used incorporates the beam and beam-column joint in one unit. The beams are connected at mid-span in a cast-in-place joint. Ducts are left in the beam-column joint region to enable the column longitudinal bars to pass through the joint. As the precast beam is seated on the lower column, the ducts are then grouted. The upper precast concrete column is lifted in position and the column bars protruding from the beam-column joint region are embedded in corrugated ducts placed in the upper column. A second grouting operation is performed to connect the column bars. Further details of the construction with this precast reinforced concrete system can be found elsewhere [G1].

The current trend in the design of reinforced concrete structures in New Zealand is to use Grade 500 longitudinal steel having f_y = 500 MPa [P9]. Nevertheless, design recommendations in the Concrete Design Standard, NZS 3101:1995 [S2] are mainly based on test results in which Grade 300 or 430 longitudinal steel was incorporated. Therefore, it was decided to use Grade 500 steel as the longitudinal steel in the beams and columns of all of the test units to provide experimental verification for the design of reinforced concrete moment resisting frames.

All test specimens had the same dimensions and member sizes but different reinforcement detailing. **Figures 3.1** to **3.6** shows the reinforcing details of the units tested. A description of the units is given in the following section. According to the Loadings Code, NZS 4203:1992 [S3], the inter-storey drifts of the building structure under the action of design seismic lateral load need to be under certain limits. The theoretical inter-storey drifts were calculated based on the dimensions of the test subassemblies using elastic theory. An effective moment of inertia, I_e, was used in this analysis in recognition of cracking as recommended by the Concrete Structures Standard [S2]. Table 3.1 presents the theoretical inter-storey drifts calculated to each test unit. The design seismic lateral loads at the ultimate limit state used in the calculations were based on the dependable lateral load capacity of the test units. The dependable lateral load capacity was calculated assuming that plastic hinges would develop in the beams at the column faces. The beam flexural strength was computed using the equivalent rectangular stress block method, nominal material properties and a strength reduction factor of $\phi = 0.85$. As the test units were designed to be fully ductile, inter-storey drifts obtained using elastic theory need to be multiplied by a displacement ductility factor $\mu_\Delta = 6$ to obtain the drifts corresponding to the ultimate limit state on the basis of the " equal displacement " concept which is adopted in Loadings Code [S3] for medium to long period structures.

Note that in this calculation, joint flexibility was ignored and drifts were obtained by integrating curvature along members up to joint faces.

Table 3.1 - Theoretical Inter-storey Drift of the Test Units Subjected to the Design Seismic Lateral Load.

Specimen Designation	Dependable Lateral Load Capacity H_D (kN)	Effective Moment of inertia ($I_{e,beam} : I_{e,column}$)	Theoretical Inter-storey Drift Ratio, θ_y' (%)	Inter-storey Drift Ratio in Ultimate Limit State $\theta_u = \theta_y' \mu_\Delta$ (%) *
Unit 1	176	$0.4I_g : 0.75I_g$	0.29	1.73
Unit 2	176	$0.4I_g : 0.75I_g$	0.29	1.73
Unit 3	133	$0.4I_g : 0.48I_g$	0.26	1.59
Unit 4	133	$0.4I_g : 0.48I_g$	0.26	1.59
Unit 5	170	$0.4I_g : 0.48I_g$	0.34	2.00
Unit 6	170	$0.4I_g : 0.48I_g$	0.34	2.00
Unit 7	174	$0.4I_g : 0.6I_g$	0.31	1.86
Unit 8	176	$0.4I_g : 0.48I_g$	0.35	2.10

* $\mu_\Delta = 6$

The Loadings Code [S3] stipulates that inter-storey drift ratios obtained from an elastic analysis should be less than 1.5% or 2.0% depending upon the height of the building when the equivalent static or modal response spectrum method of analysis is used. Where inelastic time history is used the drift limit is increased to 2.5%. The inter-storey drift ratios of the test units, see Table 3.1, are all within the maximum limit of 2.5%.

" Capacity design " procedure [P4] was applied to the design of the units to ensure that plastic hinges would occur in beams at the column faces. All the design requirements of transverse reinforcement in beams and columns given by the Concrete Structures Standard, NZS 3101:1995 [S2] were satisfied. Design dynamic magnification factors were taken as 1.0 since only static loads were applied to the units.

The diameter of the longitudinal beam bars passing through the beam-column joints satisfied the limitation of the bar diameter-to-column depth ratio given in NZS 3101:1995 for a specified concrete cylinder compressive strength $f_c' = 30$ MPa. Such limitation allowed the use of 12 mm diameter bars when using Grade 500 reinforcement steel. The limitation on beam bar diameter given by NZS 3101:1995 could lead to the use of many small diameter bars, and result in reinforcement congestion. One strategy to solve this difficulty, which forms part of this research programme, is to use beams incorporating distributed longitudinal reinforcement in moment resisting frames. Note that all beams were cast upright as is commonly done in practice.

3.2.2 Description of Test Units in the L-Series

3.2.2.1 Units 1 and 2

Two units were designed to reconcile the discrepancy between the theoretical model and the design recommendations given by NZS 3101:1995 [S1] for joints subjected to high column compressive loads in combination with high joint shear stresses.

Figure 3.1 shows the reinforcing details of Units 1 and 2. Both units have identical reinforcing details, except for the quantity of horizontal joint reinforcement. The joint reinforcement placed in Unit 1 exceeded the minimum requirements given by NZS 3101:1995 for ductile frames, whereas the horizontal joint reinforcement in Unit 2 was found from the analytical model described in Chapter 2. The axial load level, $N^* / A_g f_c'$ and joint shear stress

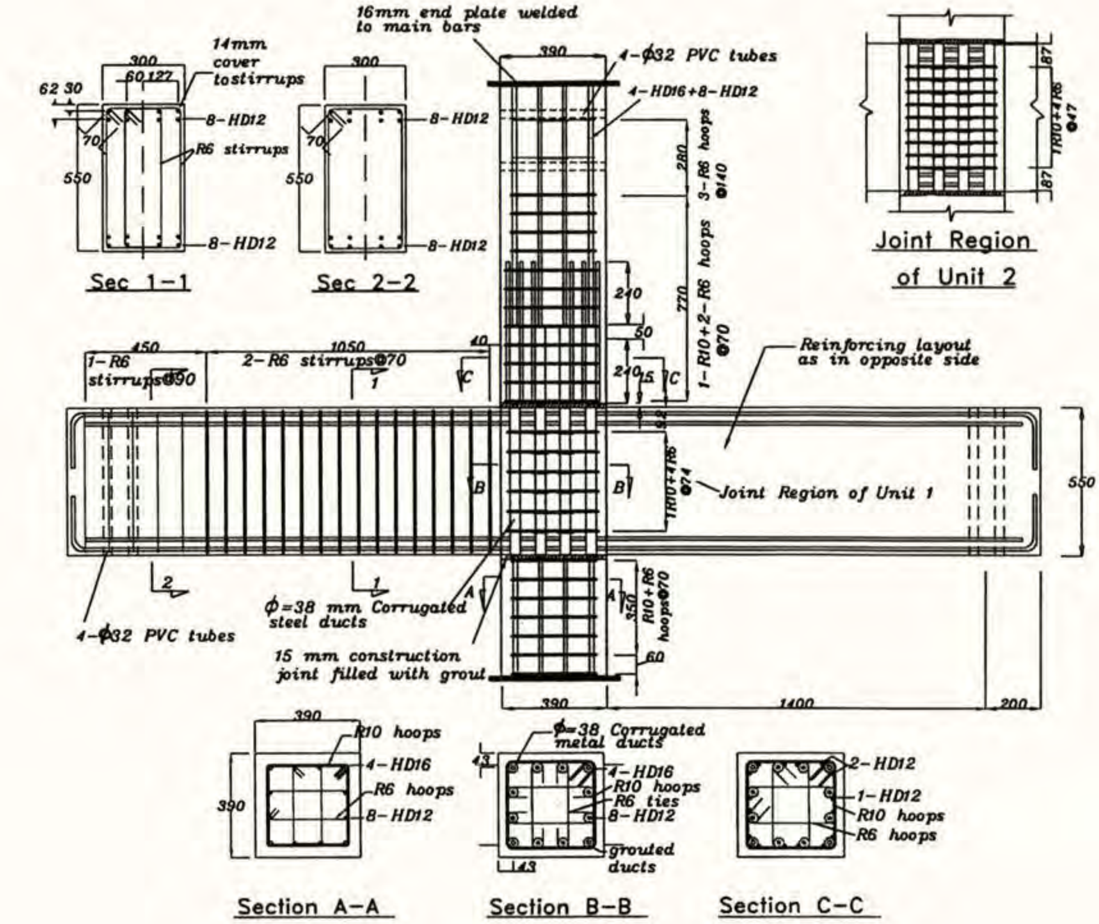

Figure 3.1 – Reinforcing Details of Units 1 and 2.

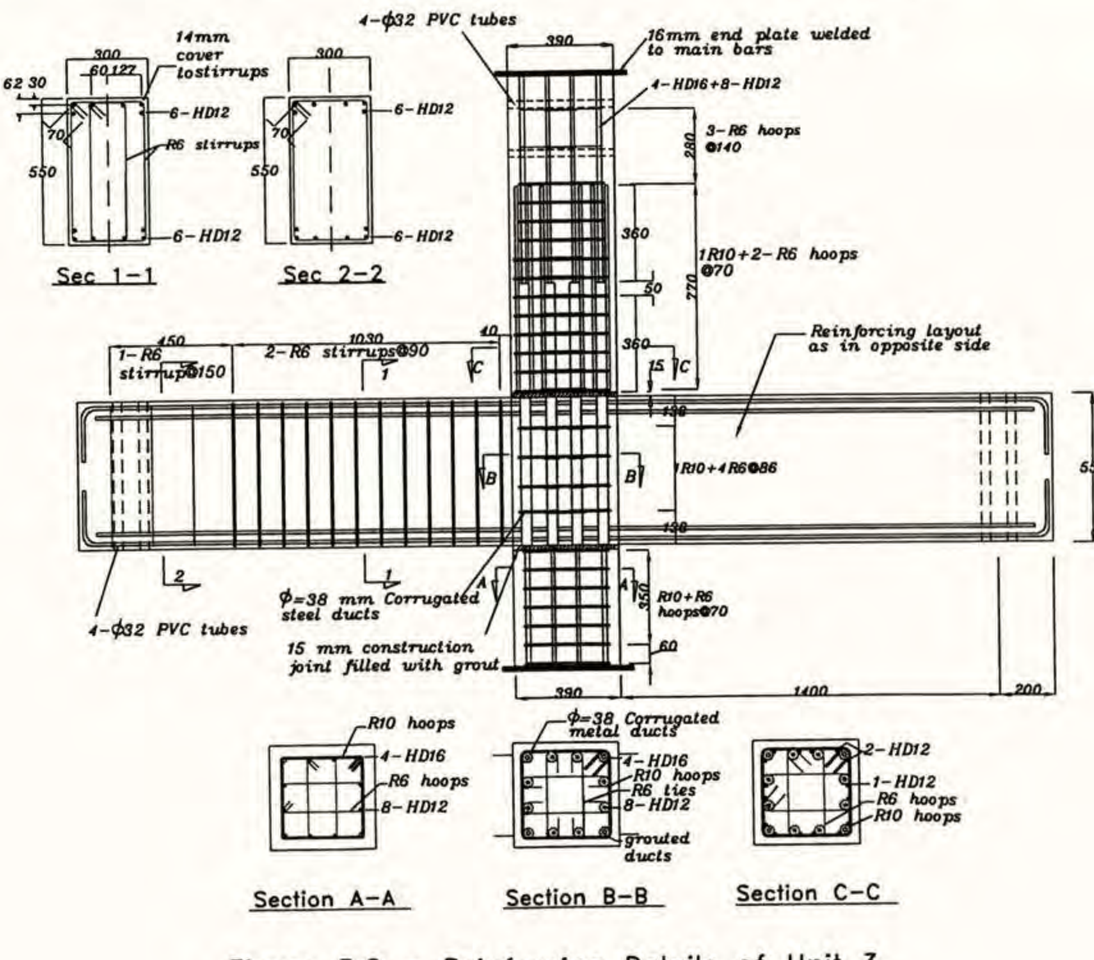

Figure 3.2 – Reinforcing Details of Unit 3.

ratio v_{jh} / f_c' for these units were 0.4 and 0.19, respectively.

HD12 and HD16 bars were used as longitudinal beam and column reinforcement. The beam longitudinal reinforcement ratio was $p = p' = 0.006$. R10 and R6 plain round bars were used as transverse reinforcement in the beams, columns and joints. Units 1 and 2 were cast simultaneously in order to achieve the identical concrete compressive strength so that results of them could be compared.

Six and nine sets of perimeter R10 hoops plus 2 legged R6 inner ties were placed in the joint region as horizontal joint reinforcement in Units 1 and 2, respectively. Table 3.2 tabulates the V_{sh} / V_{jh} ratios provided in the test units and that required to achieve ductile performance by NZS 3101:1995 and the analytical model. V_{sh} is referred to as the horizontal joint shear force carried by the transverse reinforcement and V_{jh} is the horizontal joint shear force. Note that V_{sh} was calculated using the measured material properties of the joint hoops and V_{jh} was calculated based on the development of 25% flexural over-strength of the beam plastic hinges calculated using the 5% value of the lower characteristic yield strength of the longitudinal reinforcement, that is using $\lambda_o = 1.25$ and $f_y = 500$ MPa.

Table 3.2 - Ratio V_{sh} / V_{jh} in Units 1 and 2.

Unit		$(V_{sh}) / V_{jh}$ Required		Provided	
	$N^* / A_g f_c'$	NZS 3101:1995	Analytical Model (1)	V_{sh} / V_{jh}	$(V_{sh})_{eff} / V_{jh}$ (2)
1	0.4	0.45	0.61	0.53	0.46
2	0.4	0.45	0.61	0.79	0.72

Notes : (1) Based on the prediction of mean value straight line in **Fig. 2.9** using nominal value of $v_{jh} / f_c' = 0.19$ and assuming $\mu_\theta = 7.7$.

(2) $(V_{sh})_{eff} / V_{jh}$ as was defined in Section 2.3.2

It can be seen in Table 3.2 than the ratio V_{sh} / V_{jh} in both units is larger than that required by NZS 3101:1995. Nevertheless, the ratio $V_{sh,eff}$ / V_{jh} provided in Unit 1 is less than the value required by the analytical model to achieve ductile behavior. The joint reinforcement in Unit 2 satisfies quantity required by the analytical model. According to the prediction of the analytical model, Unit 1 can only have limited ductility with joint failure occurring and Unit 2 is able to have a fully ductile performance.

3.2.2.2 Units 3 and 4

Figures 3.2 and **3.3** show complete reinforcing details of Units 3 and 4. These units were built to provide experimental evidence to the finding of the analytical model that the ratio between the areas of the top and bottom reinforcement has little influence on the behaviour of the joint, which is not implied by NZS 3101:1995 [S1]. Also, it was intended to demonstrate that the joint shear stress ratio, v_{jh} / f_c', is a main parameter affecting the strength of joints. The current Concrete Structures Standard, NZS 3101:1995 includes v_{jh} / f_c' as a design parameter, but the importance of it is not significant.

Units 3 and 4 are identical except for the arrangement of the beam longitudinal reinforcement. The beams of Unit 3 had equal top and bottom longitudinal reinforcement whereas the amount of top longitudinal reinforcement in the beam of Unit 4 was twice the amount of the bottom longitudinal reinforcement. In quantitative terms, the beams of Unit 3 had $p = p' = 0.0044$ while the beams of Unit 4 had $p = 0.0060$ and $p' = 0.0030$. It can be shown that the theoretical joint shear stress ratio v_{jh} / f_c' is identical for these two units.

Table 3.3 compares the V_{sh} / V_{jh} ratios required by NZS 3101:1995 and the analytical model. Also shown in this Table is the ratio V_{sh} / V_{jh} of the joint reinforcement provided. Note that to avoid any variation in the concrete compressive strength, these two units were cast simultaneously.

Table 3.3 - Ratio of V_{sh} / V_{jh} in Units 3 and 4.

Unit		V_{sh} / V_{jh} Required		Provided	
	$N^* / A_g f_c'$	NZS 3101:1995	Analytical Model	V_{sh} / V_{jh}	$(V_{sh})_{eff} / V_{jh}$
3	0.1	0.55	0.4	0.46	0.46
4	0.1	0.73	0.4	0.46	0.46

Notes : (1) Based on the prediction of mean value straight line in **Fig. 2.9** using nominal value of $v_{jh} / f_c' = 0.145$ and assuming $\mu_\theta = 7.7$.
(2) $(V_{sh})_{eff} / V_{jh}$ as was defined in Section 2.3.2.

It can be seen in above table that provided V_{sh} / V_{jh} in Unit 3 does not meet the requirement by NZS 3101:1995 and neither does that in Unit 4. Note that the value required by the analytical model was based on the minimum requirement recommended in

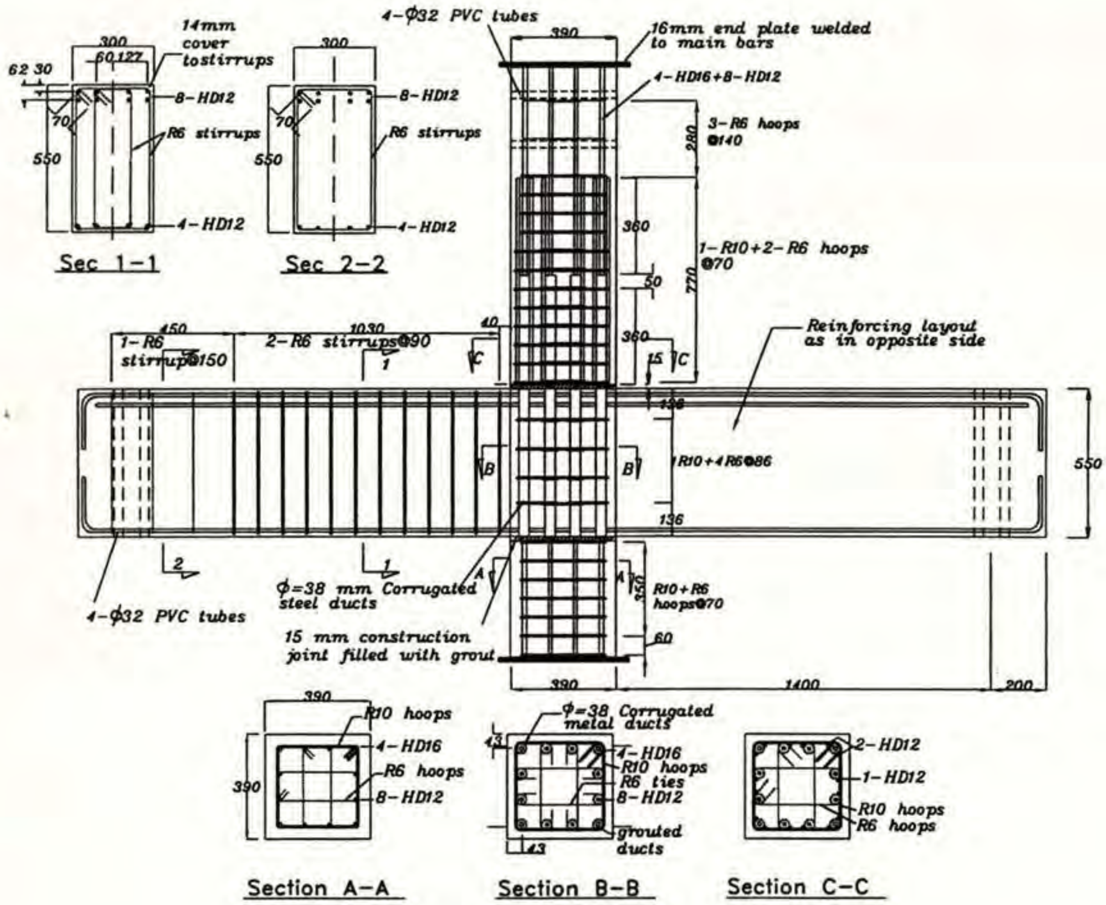

Figure 3.3 – Reinforcing Details of Unit 4.

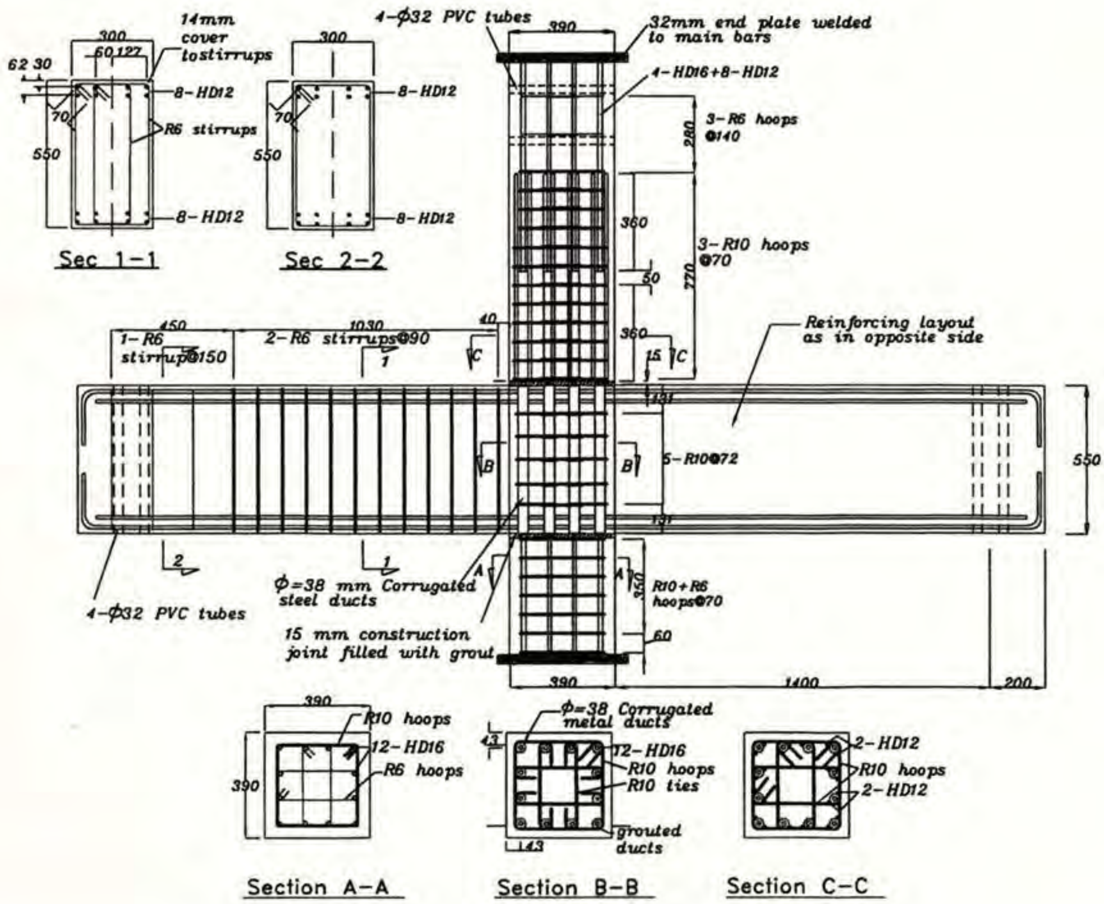

Figure 3.4 – Reinforcing Details of Unit 8.

NZS 3101:1995. For a joint with a nominal ratio $v_{jh} / f_c' = 0.145$, the mean value straight line in **Fig. 2.9** leads to $V_{sh} / V_{jh} = 0.3$. The horizontal joint reinforcement in both units satisfy the minimum requirement of $V_{sh} / V_{jh} = 0.4$ recommended in NZS 3101:1995. It is worth noting that the amount of horizontal joint reinforcement in Unit 4 is even less than that required by NZS 3101:1995 for a joint of a frame designed for limited ductility response. According to the analytical model, Units 3 and 4 should have a ductile performance with plastic hinges forming in the beams.

3.2.2.3 Unit 8

Unit 8 is a benchmark unit built for comparing the behaviour with that of the test units, in the D-series, where distributed longitudinal reinforcement was incorporated in the beams. The beam longitudinal reinforcement ratio in Unit 8 is the same as that of Units 1 and 2, $p = p' = 0.006$, but the column has more longitudinal reinforcement than the two units as a result of the smaller axial compressive load, $N^* / A_g f_c' = 0.1$ applied to this unit.

The horizontal joint reinforcement consisted in 5 sets of perimeter R10 plus 2 legged R10 inner ties. The joint reinforcement was designed according to the analytical model to ensure joint failure before full ductility was achieved. This allowed the database to be more comprehensive in terms of the number of tests displaying beam-column joint failure.

Unit 8 was cast at the same time as Units 5 to 7 to avoid the concrete compressive strength from becoming a variable.

3.2.3 Description of Test Units in the D-series

3.2.3.1 General Considerations

Several considerations were studied for the design of this test series because of the lack of existing design recommendations. First, the analytical model examined in Section 2.6.3 indicates that the greater the amount of longitudinal beam steel is distributed through the webs, the lesser is the magnitude of the compressive stress in the joint panel. This indicates that the most extreme case in which all the longitudinal reinforcement is distributed through the web is most beneficial to the joint. However, this beneficial effect has the adverse effect on the curvature ductility capacity in the beams as it is reduced. As has been discussed in

Section 2.6.1, a reduction in the compressive reinforcement places more reliance on the concrete. To ensure sufficient curvature ductility capacity it is suggested that beams having the longitudinal reinforcement distributed through the web be detailed as a wall, where the intermediate longitudinal reinforcement in tension do not have to be restrained with a cross tie.

Complete reinforcing details of Units 5 and 6 are presented in **Fig. 3.5**. Unit 7 is shown in **Fig. 3.6**.

3.2.3.2 Units 5 and 6

Figure 3.5 displays complete reinforcing details of Units 5 and 6. These two units are very similar to Unit 8 (see **Fig. 3.4**), which was described in Section 3.2.2.3, except that the beam longitudinal reinforcement is distributed through the beam web rather than lumped at the top and bottom.

According to the analytical model examined in Section 2.6.3, the maximum stress in the diagonal compression field in joints incorporating beams with distributed reinforcement is slightly less than in joints with conventionally reinforced beams. However, reduction in the capacity of the diagonal compression field in the joint is also expected owing to the tensile strains beyond yielding imposed by the distributed reinforcement. The trends given by the analytical model were used for the design of the horizontal joint reinforcement in these two units. A large database with experimental results, which would have led to an estimate of the capacity of joints with beams incorporating distributed longitudinal reinforcement was not available. Data from the tests carried out by Wong [W1] showed a similar trend to those joints having conventionally reinforced beams, see **Fig. 8.16**. To gain more experimental data on the capacity of joints with beam incorporating distributed reinforcement, it was decided to design the joint to fail before a ductile response could be attained. About 85% of the amount of horizontal joint reinforcement required by the analytical model was provided in Units 5 and 6. The normal axial load for the units was $N^* / A_g f_c' = 0.1$ and the joint shear stress ratio was $v_{jh} / f_c' = 0.19$.

The only difference between Units 5 and 6 was the type of horizontal joint reinforcement used. The joint reinforcement in Unit 5 consisted of plain round bars as it has

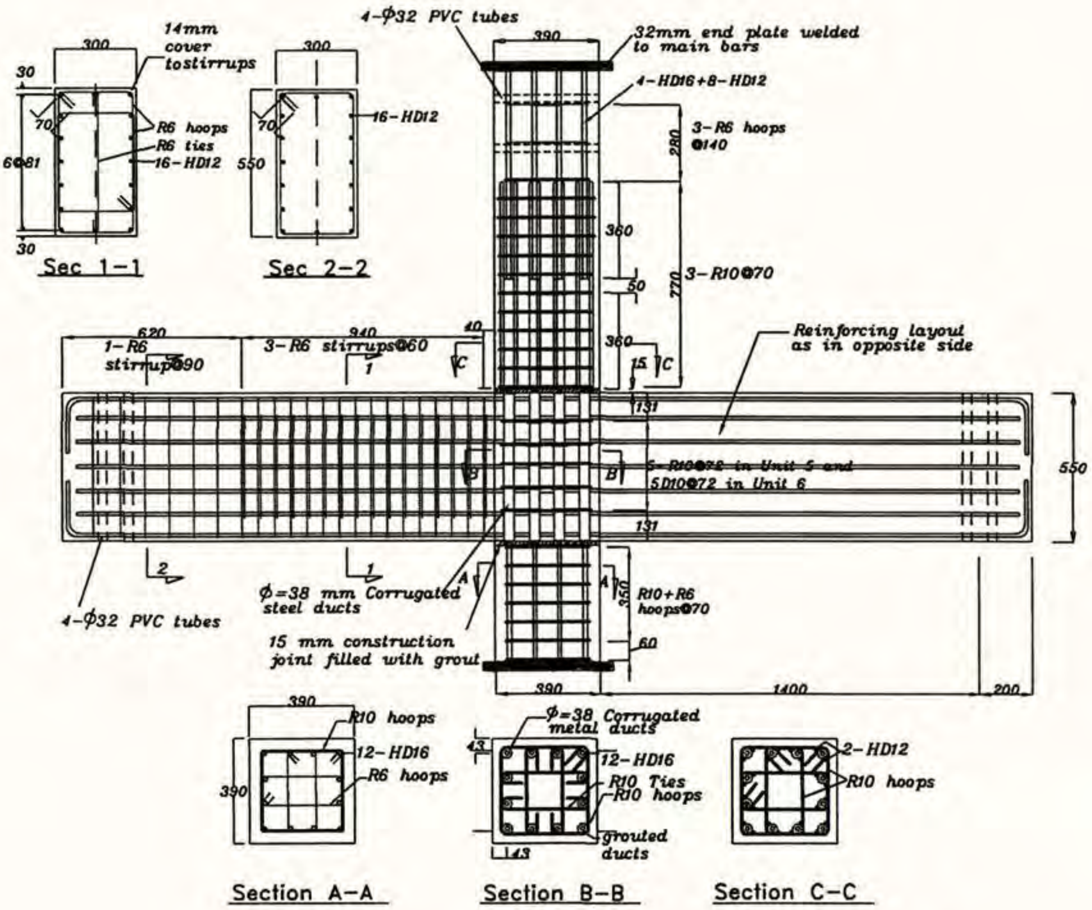

Figure 3.5 – Reinforcing Details of Units 5 and 6.

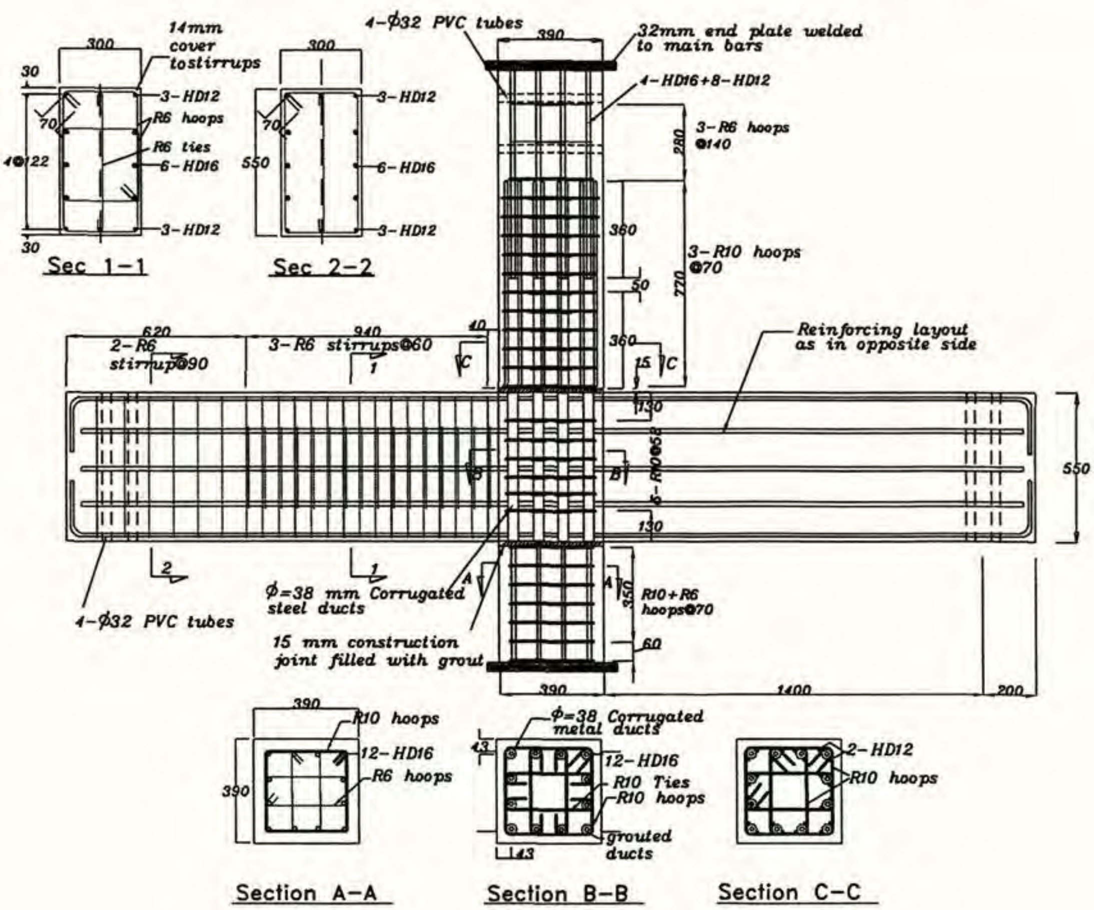

Figure 3.6 – Reinforcing Details of Unit 7.

been common practice for many years. Five sets of R10 hoops and R10 ties were placed in Unit 5. Unit 6 was reinforced using deformed reinforcement, which could be used to overlap with the beam inner longitudinal reinforcement and reduce the tensile strain in the centre of the joint. The overlapping effect would enhance the capacity of the joint. The nominal axial load for testing these units was $N^* / A_g f_c' = 0.1$.

3.2.3.3 Unit 7

According to the moment-curvature analyses on beam sections incorporating distributed reinforcement carried out in Chapter 2, nearly all of the inner longitudinal beam bars distributed through the beam web are in tension. These bars yield in tension when plastic hinges from in the beams at both sides of the joints and, consequently, bond forces are not required to be developed in the joint to ensure equilibrium. Therefore, a consequence of this behaviour is that the diameter of the inner bars does not have to be limited to avoid bond failure from occurring.

The beams of Unit 7 were designed with larger inner diameter bars while those on the top and bottom met the limitation d_b / h_c imposed by NZS 3101:1995. The inner beam longitudinal reinforcement consisted of HD16 bars while the top and bottom reinforcement were HD12 bars, see **Fig. 3.6**. The area of reinforcement in the beams of Unit 7 was slightly larger than that provided in Units 5 and 6. The horizontal joint reinforcement consisted in six sets of R10 hoops and R6 ties. A nominal axial load of $N^* / A_g f_c' = 0.1$ was chosen for this test, but as discussed in Section 6.4.1 the level of loading was increased to $N^* / A_g f_c' = 0.25$ for the test of this unit.

3.3 LOADING FRAME AND TEST SET-UP

The units were tested in the structures laboratory of the Civil Engineering Department. As relatively large axial loads were to be applied to Units 1 and 2 it was decided to apply this load through the 10 MN DARTEC Universal Testing Machine. The self-balanced steel reaction frame shown in **Fig. 3.7** was designed and built for the testing of the units in this programme.

Two pairs of steel cast fittings with 5000 kN allowable tensile / compressive load were designed and cast in A4 Medium Maganese Steel to BS 3100 A4, which has 0.2% proof tensile strength of 412 MPa. Appendix C gives complete details of the fittings. Each pair of fittings are used as connections between the column ends of the test specimen and the DARTEC Universal Testing Machine. One of the fittings was bolted down to the DARTEC actuator using 60 mm diameter bolts machined from high strength alloy; while the other piece connected the steel end plates on column ends through bolts. Two 160 mm diameter pins made of AISI 1045 high strength alloy were pinned through the central holes in each pair of the fittings. The bottom pin was also inserted through the holes cut on the webs of the two steel I-beams. Two steel rings were machined and bolted together with the webs of I beams surrounding the holes through 6-24 mm diameter high strength grip friction bolts. This design enables the bottom pin to bear against the steel rings instead of the web of the steel I-beams when the lateral load is applied. As a result, the lateral force can be directly transmitted into webs of the I-beams and local buckling and excessive deformation on the webs of the I-beams are prevented.

Each test specimen was lifted to position in the reaction frame outside the DARTEC Universal Testing Machine. Then the reaction frame was rolled under the universal testing

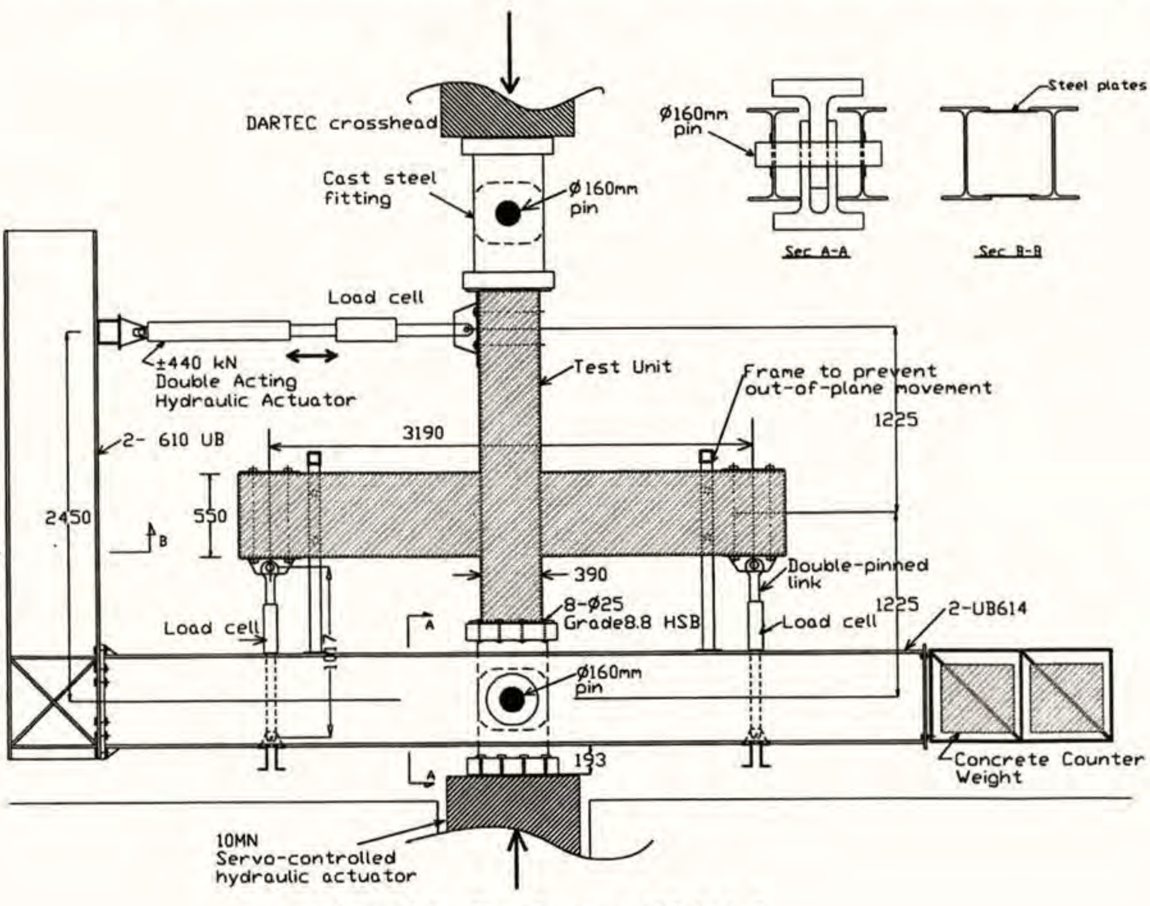

Figure 3.7 - Test Set-up of Unit 1-8.

machine in a simple and swift operation.

A 440 kN capacity double acting hydraulic actuator was used to apply reversed cyclic lateral loads. Two steel brackets were used as connections on both ends of the hydraulic jack to allow freedom of rotation. One end was connected to the side of the top end of the column using four threaded steel rods passing through PVC sleeves embedded in the column while the other end was fastened to the reaction frame using steel bolts. Two double pinned links were connected to the bottom of the beams at their ends. These links were fitted with load cells to monitor the shear force induced by the loading frame.

The top and bottom column ends were connected to the steel cast fittings using high strength bolts. Since the lower half column in the test specimen was terminated a distance away from the centre of the bottom steel pin, it was necessary to design the bottom steel base plate, on which the column main reinforcing was welded, to possess enough stiffness to avoid any significant deformation from occurring. Owing to different lateral load capacities and applied column axial loads in each test unit, the numbers of high strength bolts and thickness of steel base plates in Units 1-4 is different to that of the plates in Units 5-8. A thin steel plate was provided at the top of the columns as no significant stresses were expected in this region.

In order to prevent out-of-plane deformation from occurring in the beams of test units, especially at the stage of large displacement ductilites, a small steel frame was erected on each side of steel I-beams to guide the movement of RC beams and ensure that they displaced in their plane. Four rollers were bolted on each side of steel frame to bear against the concrete surfaces of beam webs.

The lateral load applied with the hydraulic actuator deforms the loading frame and the test specimen as depicted in **Fig. 3.8**. The loading frame pivots around the lower ϕ 160 mm diameter pin and the links connected at the beam ends push and pull the beams, inducing bending moment and shear.

A study was made to quantify the effect of the flexibility of the loading frame on the loading and imposed deformation on a test specimen. **Figure 3.9** shows the bending moment diagram on the reaction frame when the lateral load is applied. It can be seen in **Fig. 3.8** that if the loading frame and the end links have infinite rigidity, the imposed displacements on both

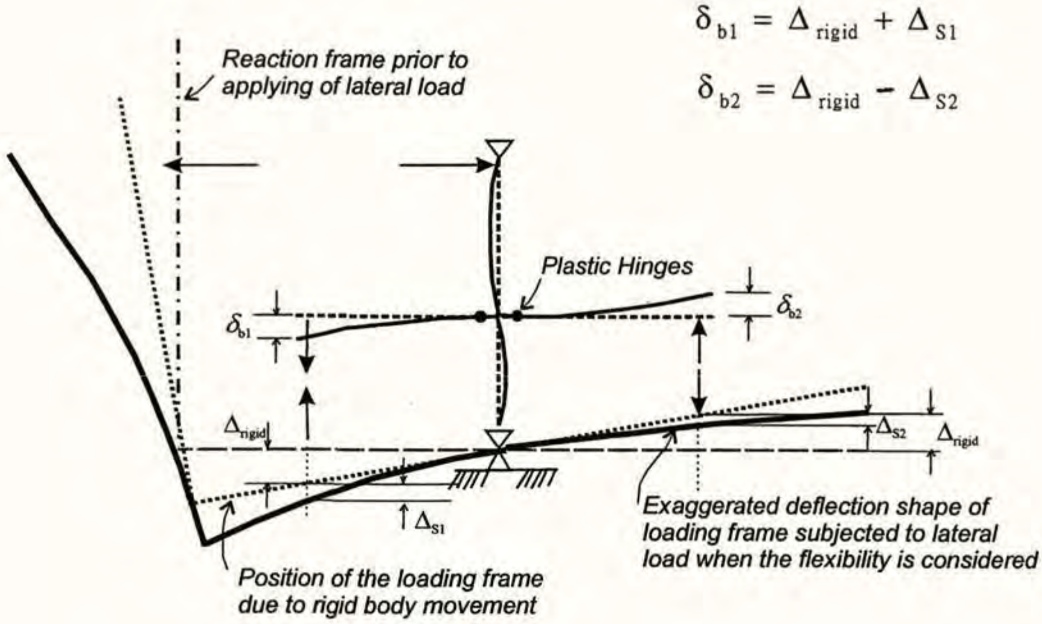

Figure 3.8 - Imposed Deflection on Test Specimen by Reaction Frame.

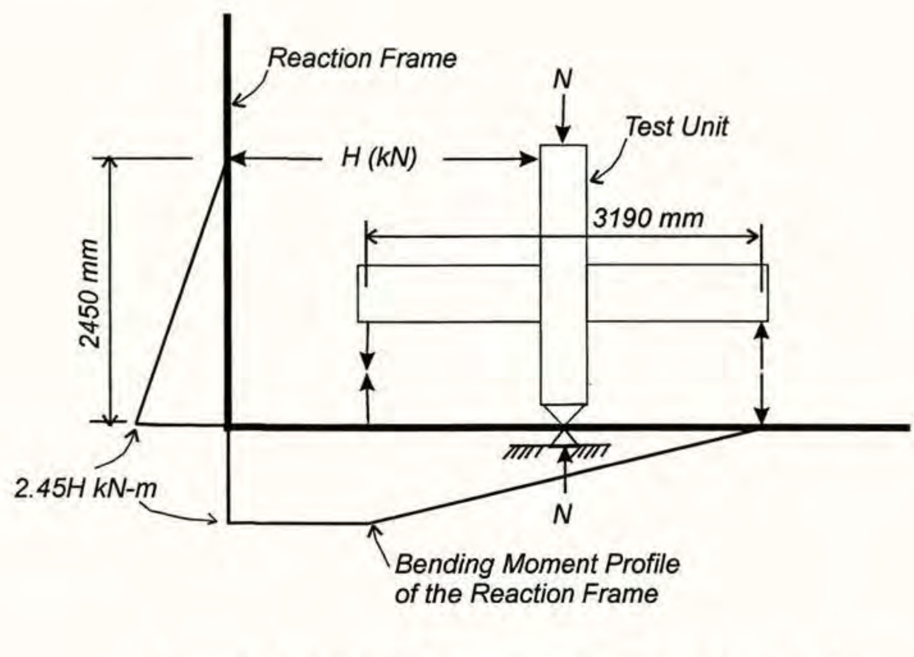

Figure 3.9 - Bending Moment Diagram on Reaction Frame When the Lateral Load is Applied.

beam ends must be equal to the movement of loading frame at the location of the links due to rigid body rotation. However, if the flexibility of reaction frame is considered, the relation between the beam end movement of test specimen and movement of reaction frame can be expressed as

$$\begin{aligned} \delta_{b1} &= \Delta_{rigid} + \Delta_{s1} \\ \delta_{b2} &= \Delta_{rigid} - \Delta_{s2} \end{aligned} \qquad (3.1)$$

where Δ_{rigid} is the vertical movement of reaction frame at the position of steel link due to rigid body rotation. Δ_{s1} and Δ_{s2} are the flexural deformation of the pair of steel I beams at the same locations. For a specific lateral inter-storey displacement, δ_{b1} should be equal to δ_{b2}. The differential displacement between δ_{b1} and δ_{b2} is $\Delta_{s1} + \Delta_{s2}$. The flexural deformation of steel reaction beams corresponding to the applied lateral load, H(kN), was calculated using traditional elastic theory and depicted below.

$$\Delta_{s1} = 2.08H/E_sI_s x\, 10^{12}\text{mm}, \quad \Delta_{s2} = 1.04H/E_sI_s x 10^{12}\ \text{mm}$$

where E_s is the Young's Modulus of steel ($2x10^5$MPa), I_s is the moment of inertia of I beam section ($2x1316.4x10^6$ mm^4). For Units 1 and 2, the maximum lateral load H = 270 kN, Δ_{s1}, Δ_{s2} equal 1.07, 0.53 mm, respectively. The differential displacement between two beam ends caused by the flexibility of the steel reaction frame is equal to $\Delta_{s1} + \Delta_{s2} = 1.6$ mm. For Units 3 and 4 with which the maximum lateral load is approximate H = 206 kN, the differential beam displacement is 1.2 mm.

The consequence of the differential displacement is that the rig will make two beams of the test unit yield at slightly different drift ratios. However, the " top bar " effect existing in all units has the adverse effect on the yielding of left and right beams and compensates so that the two beams would likely yield simultaneously.

Another aspect of the loading system which was studied was the effect of friction acting around the bottom 160 mm diameter pin. The friction stresses that exist around the bottom 160 mm diameter pin cannot be avoided with the result that bending moments develop in this region, which was originally expected to be zero in-theory. The estimation of this moment due to the friction stresses is depicted in **Fig. 3.10**. According to this figure, if the coefficient of friction C_f is assumed to be 0.1, the bending moment at the pin, M_{pin}, resulting from friction is

$M_{pin} = 4$ kN - m, when $N^* / A_g f_c' = 0.1$

$M_{pin} = 17.6$ kN - m, when $N^* / A_g f_c' = 0.43$

Figure 3.11 shows the actual bending moment distribution in the column of a test unit. Compared with the column moment occurring at the beam face at the development of the theoretical ultimate lateral load in the unit, M_{pin} is small. Therefore, the influence of M_{pin} on the response of test unit is considered insignificant.

3.4 CONSTRUCTION OF THE TEST SPECIMENS

3.4.1 Formwork

The formwork for casting the beams and the columns were built using plywood. Timber block and steel angles were used to stiffen the formwork to minimize the bowing of the plywood sheets during the casting of fresh concrete. The inner surfaces of the formwork were painted with oil based paint to prevent water absorption by the plywood. All the intersection edges of plywood were sealed with Silicon to prevent leaking of water of fresh concrete. After each cast, the moulds were re-painted and re-sealed.

3.4.2 Reinforcing Cages

All the longitudinal bars in this project were cut and bent in the Structures Laboratory. Stirrups, hoops and ties were all cut and bent by a local firm. All the hooks of stirrups and ties were bent through 135 or 180 degrees with an extension beyond the end of the hook of not less than $8d_b$.

The main bars and stirrups selected for instrumentation had either studs welded or strain gauges attached before the reinforcing cages were assembled.

Corrugated steel ducts of 36 mm inner diameter were left in the beam-column joint region at the position of the column bars. Joint hoops were tied to ducts to form the cage in this region.

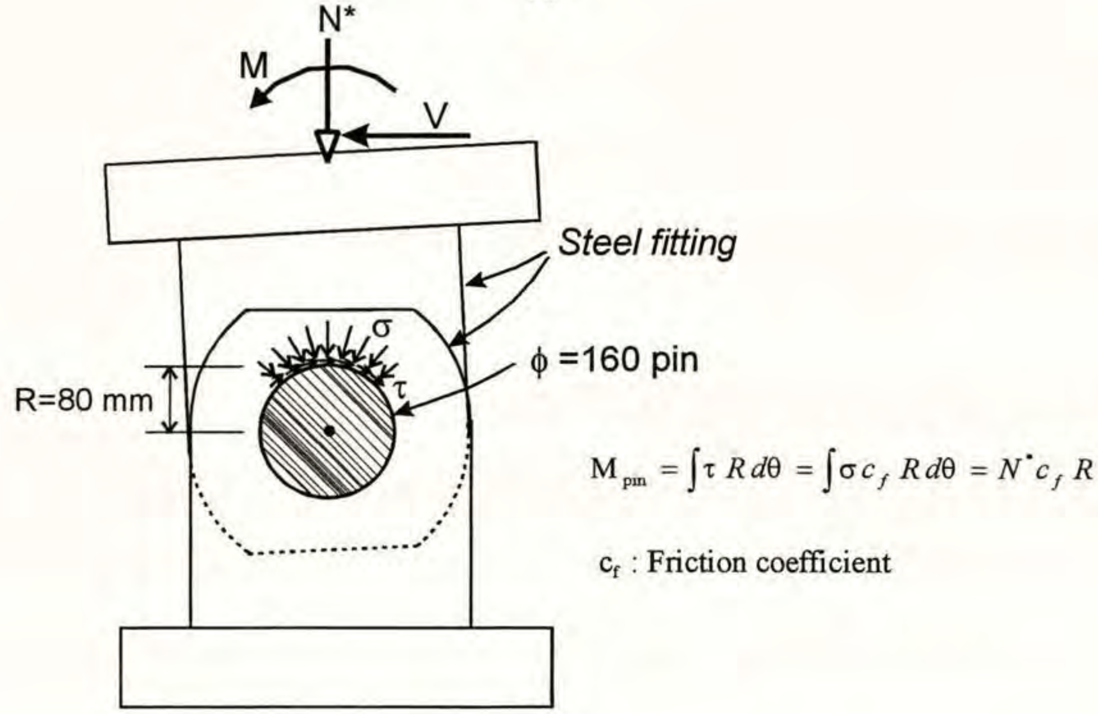

Figure 3.10 - Estimation of Moment on the Bottom Pin Due to Friction.

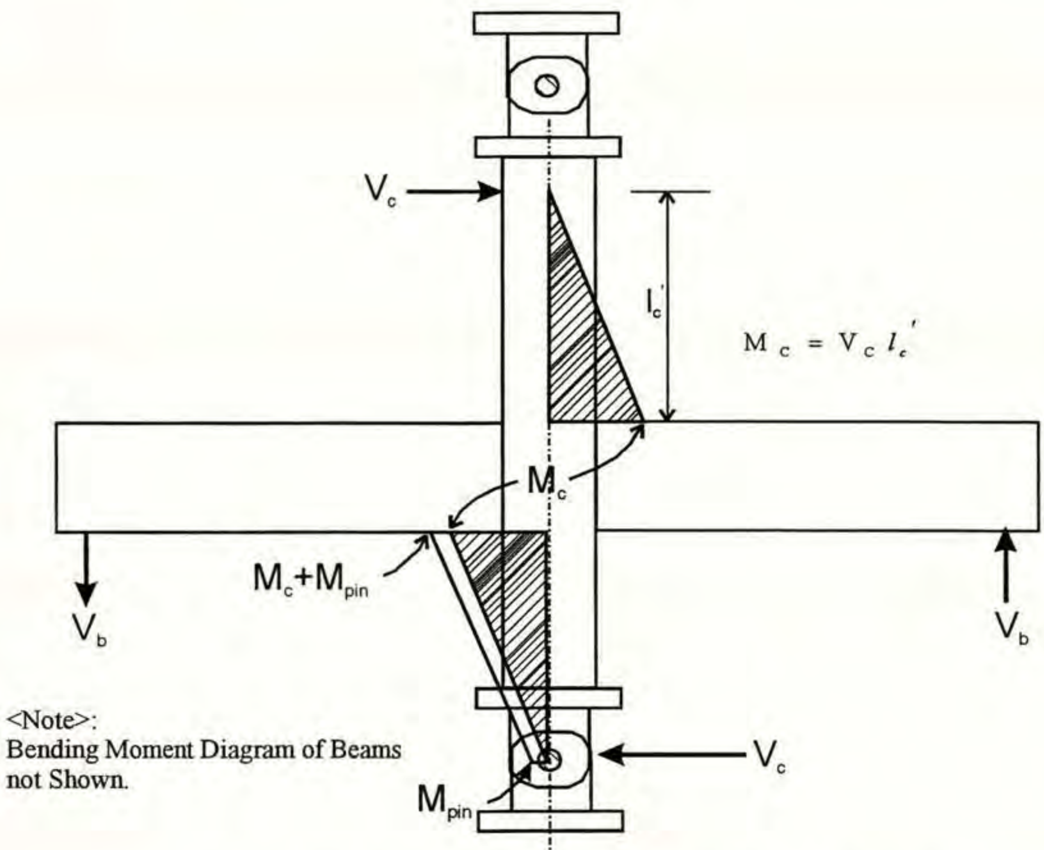

Figure 3.11 - Influence of M_{pin} on the Profiles of Column Bending Moment of Test Specimen.

Beam cages were built first and placed in the formwork. The joint cages were made subsequently. Special attention was taken with the location of the corrugated ducts in the joint region. Circular wood blocks with diameter equal to the inner diameter of ducts were screwed down to the bottom of the molds to fix the ducts at the right location. A plywood board with the same circular wood blocks was fixed to the ducts on the top of the joint when the cages of the joint reinforcement was assembled. This central part of this wood template was cut out to allow concrete to be cast into this region. After the whole cages had been assembled completely, 10 mm diameter potentiometer rods, to be used later on to fit the instrumentation, were inserted through the cages and moulds. Four PVC sleeves were placed vertically at each end of beams as required by the connection detail to the loading links. **Fig. 3.12** shows a typical reinforcing beam cage.

Column cages were assembled afterwards. Each test unit had two column segments. A steel plate was used as a base for each column segment on which column main bars were welded. The steel plate had holes for connecting the unit to the cast steel fittings.

With reference to the reinforcing details depicted in **Figs. 3.1** to **3.6**, it can be seen that each top column cage segment consists of 12 metal ducts adjacent to the joint connection. The main column longitudinal bars were welded onto a steel plate terminated just above the ends of metal ducts. Some short HD12 bars were placed adjacent to the ducts and extending past them in order to form a lap splice. The metal ducts in the upper column segments have an extra 50 mm reserved for bleeding the grout and to ensure that, in case of plastic settlement, the grout would always embed the reinforcing bars inside the duct.

The reinforcing cage of the bottom column only had a short portion within the moulds with longitudinal column bars protruding outward. These long protruding bars were inserted through the ducts in the joint region and extended into the ducts in the top column. Typical cages for the top and bottom columns are shown in **Fig. 3.13**.

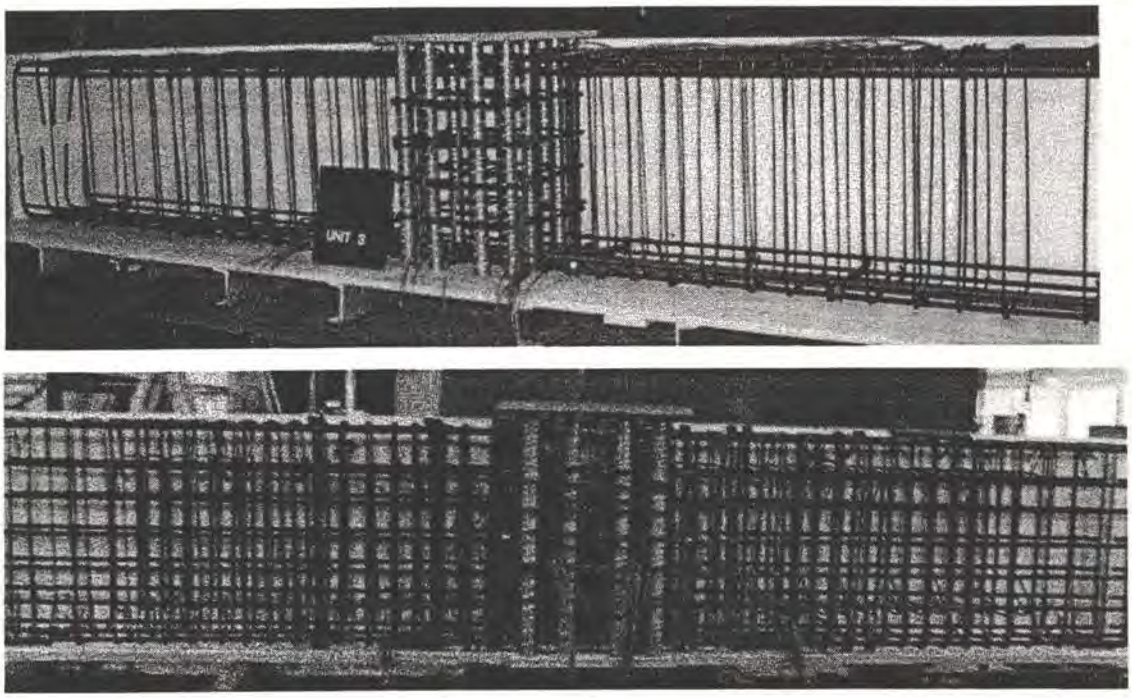

Figure 3.12 - Beam Reinforcing Cages.

(a) Bottom
Columns

(b) Top
Columns

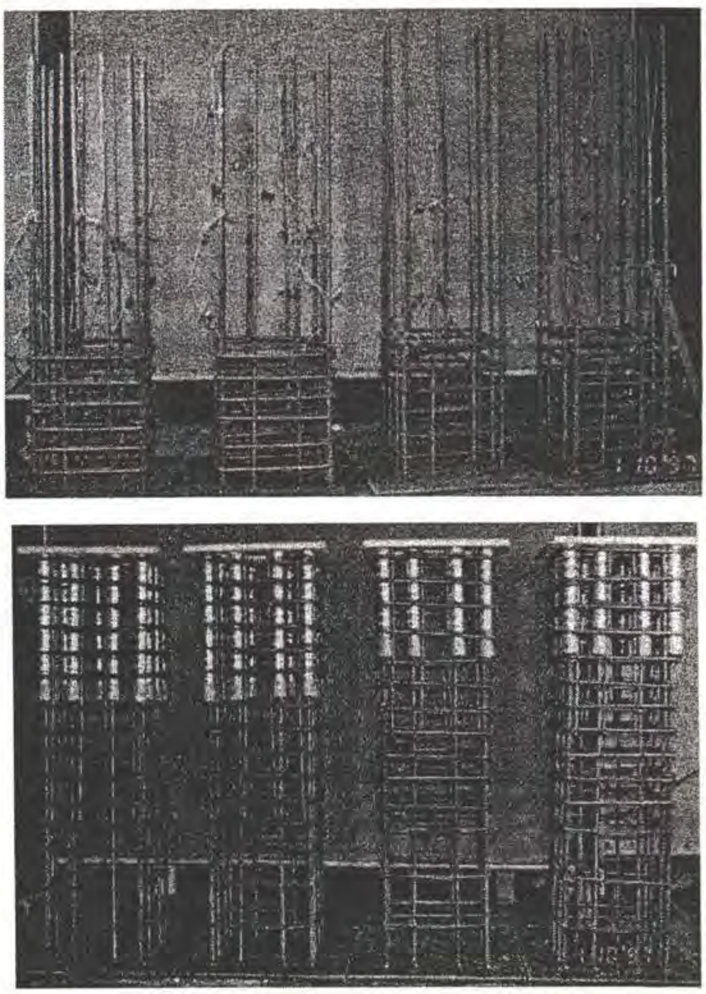

Figure 3.13 - Column Reinforcing Cages.

3.4.3 Casting of the Concrete

The concrete used to construct the test specimens was purchased from a local supplier. The average compressive strength was specified to be 30 MPa at 28 days for all the beams and 35 MPa for the columns. The specified maximum aggregate size and slump were 13 mm and 100 mm, respectively. The beams and columns were cast upright simulating actual conditions in a precast concrete yard.

After casting the concrete, components of test specimens together with sample cylinders were cured with damp hessian sacks and covered with plastic sheets for seven days. The moulds were stripped and the members and concrete cylinders were allowed to dry out.

As it was felt that the concrete compressive strength was an important variable when comparing the results on tests of beam-column joints, it was decided to cast the beams of Units 1 and 2, those of Units 3 and 4 and the beams of Units 5 to 8 simultaneously.

3.4.4 Preparation of Connection Surface

With this precast concrete system the beams and columns are connected by means of grouted joints. In order to obtain a good connection, the jointing surfaces need to be well roughened.

The method used in this project was to spray SIKA Retarder on the connection surfaces just after finishing casting of the concrete. The Retarder is capable of deferring the hardening process of concrete as the surface concrete exposed to air goes off slower than the inner part so that cement paste on such surfaces can be scrubbed out using a wire brush on the next day. This procedure exposes the coarse aggregates and leave a rough surface.

For the connection surface on the bottom of the beam which was inaccessible before mould stripping, an air compressor driven roughen scrubber was used to roughen the surface.

3.4.5 Assembling of the Beam-Column Sub-assemblages

Each test unit was required to be assembled through two grout stages. The first stage commenced by inserting the lower column longitudinal bars through the corrugated steel ducts left in the beam-column joints. The precast concrete beam was lifted above the lower column and positioned slowly once the protruding column bars were guided into the ducts. Special care was taken on protecting the strain gauges attached on the protruding bars during the process of positioning the beams. A 15 mm width gap, which is the 70% scale of that used in practice, was left between the joining surfaces by seating the beam on steel shims plastered on the lower column. Attention was paid on the alignment of the beam and column before commencing to grout to satisfy the tight tolerance [G1].

The joining surfaces were blown with air flow to clean off small particles and dust. Subsequently the perimeter of the gap was sealed using plywood together with the aid of some clamping steel angles. One hole was drilled on the corner of the gap to allow grout to flow in. At this stage care needed to be taken to check if the column bars had been located correctly inside the ducts. Since the long protruding column bars are flexible, a template made of plywood was used on the top beam face to locate them as close to the centre of each duct as possible.

Prior to grouting, the ducts in the joint region and the 15 mm gap were saturated with water for a couple of hours. A pre-mixed cement grout, SIKA 215, and adequate amount of water were weighed and mixed in accordance with the manufacturer's instructions. After the grout was well mixed and stirred, it was poured into a bucket connected through a plastic tube to the corner of the joining gap. The bucket was lifted to a high elevation by an overhead crane to allow grout to flow down to the joint. During this process, the grout in the bucket was stirred regularly. **Fig. 3.14** shows the grouting procedure between the lower column and the beam. Grouting was stopped when it overflowed through several ducts. Due to the loss of the hydraulic pressure, topping off on some ducts was required.

The second stage of assembling the test units commenced at least one day after finishing the first stage. The upper column was positioned over the longitudinal column bars protruding from the joint and then lowered in position as the column bars slipped into the corrugated steel ducts left in the upper column. As in the first stage, a 15 mm gap was left between the two joining members. The perimeter of the gap was sealed with plywood and one inlet port was drilled for grouting. One hole was drilled at the end of each duct to provide outlet ports for bleeding of air and grout. Then the grout mixture was prepared and poured into the bucket to allow it flow into the gap through the plastic tub. Grout was kept flowing until it flowed out

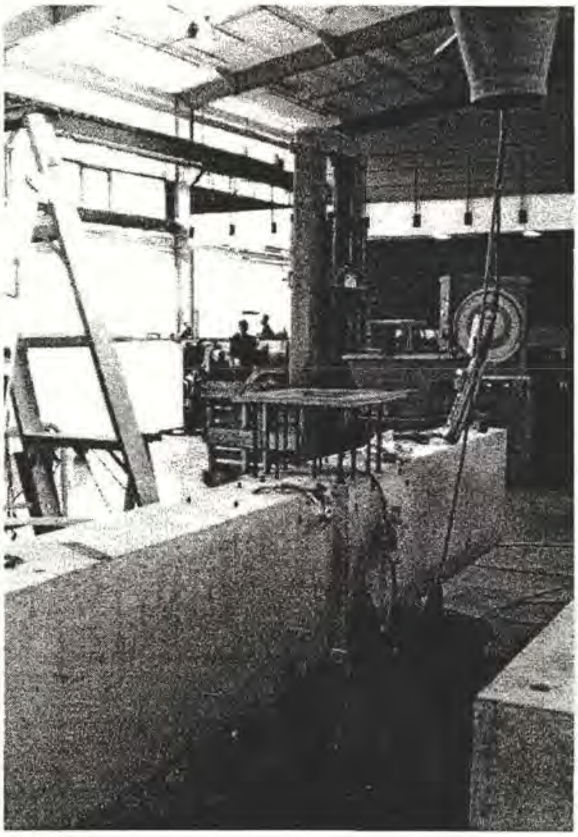

Figure 3.14 - Grouting of Connection Between Beam and Bottom Column.

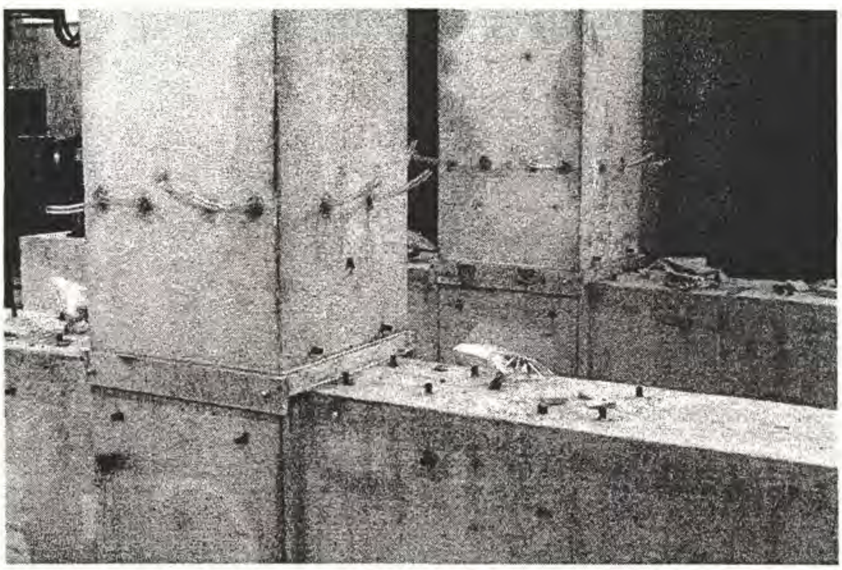

Figure 3.15 - Grouting of Connection Between Beam and Top Column.

of the hole at the end of each duct. Assurance must be made that grout over-flowed through the end of every duct as an indication that the whole volume inside the duct was filled up with grout. **Figure 3.15** presents the second stage of grouting.

Each unit was assembled following the above procedure and the grout was left to dry out at least 7 days before the beginning of a test. Six 50 mm diameter by 100 mm high cylinders were poured in the second step of grouting for obtaining the compressive strength of the grout.

3.5 MATERIALS

3.5.1 Reinforcing Steel

The longitudinal beam and column reinforcement were deformed bars with a 5% value of the lower characteristic yield strength of 500 MPa. Details of the deformations of the reinforcing steel are presented in **Fig. 3.16**. A feature of the Grade 500 reinforcement manufactured in New Zealand is that the bar deformations form a continuous thread. The characteristics of the deformations of HD12, HD16 reinforcing bars were checked with the requirements given by NZS 3402:1989 [S5] and are shown in Tables 3.4 and 3.5.

Table 3.4 - Comparison of Deformations of HD12 bars with NZS 3402:1989 Requirements.

HD12 bars		
Quoted provision in NZS 3402:1989	**Checking of measured data with requirements**	**Results**
10.2.2	$\theta = 75.8^\circ > 45^\circ$ $> 70^\circ$	Satisfactory
10.2.3	Average spacing of deformations = 7.8 mm < 70% x 12 = 8.4 mm	Satisfactory
10.2.4	Gap between the extreme ends of deformations = 3.4 mm < 12.5% x 37.7 = 4.7 mm	Satisfactory
10.2.5	Average height of deformations = 0.54 mm > 0.48 mm	Satisfactory

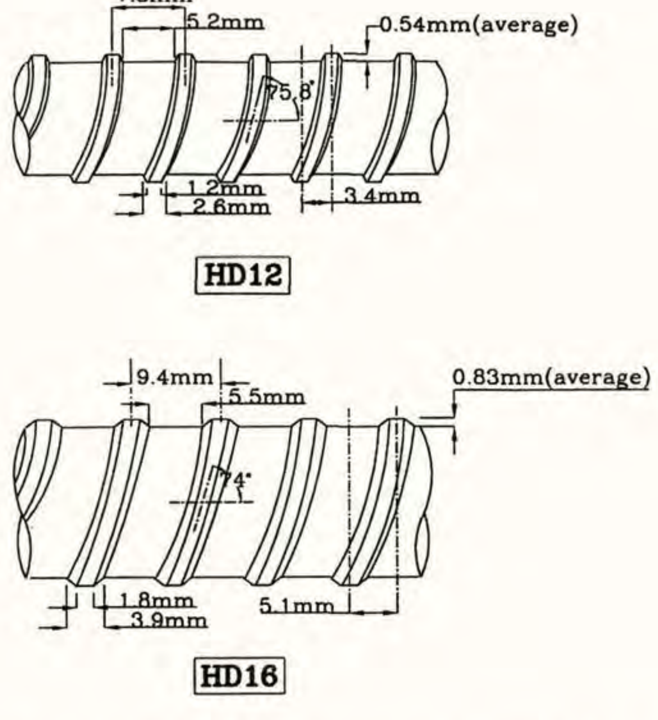

Figure 3.16 – Details of Deformations of Grade 500 Reinforcing Steel.

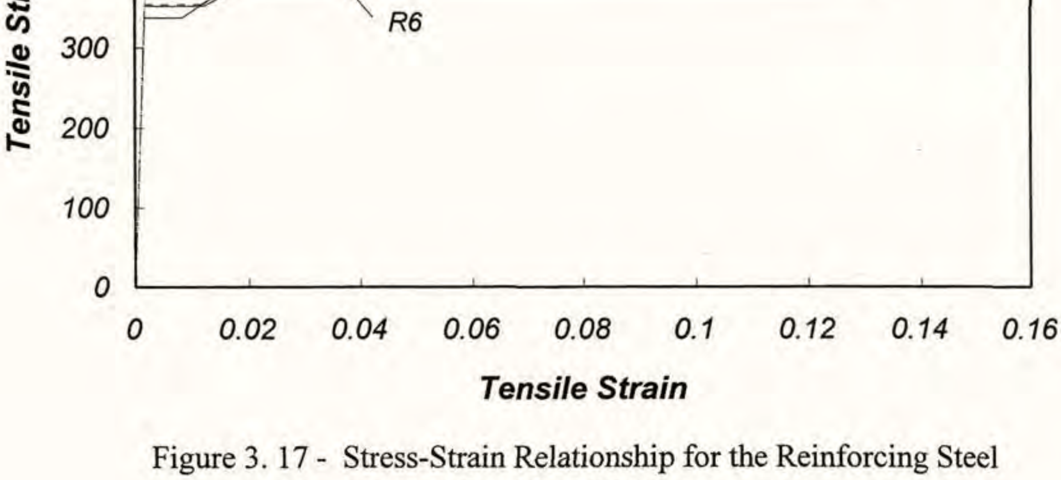

Figure 3. 17 - Stress-Strain Relationship for the Reinforcing Steel
Used in All Units.

Table 3.5 - Comparison of Deformations of HD16 bars with NZS 3402:1989 Requirements.

	HD16 bars	
Quoted provision in NZS 3402 : 1989	**Checking of measured data with requirements**	**Results**
10.2.2	$\theta = 74^{\circ} > 45^{\circ}$ $> 70^{\circ}$	satisfactory
10.2.3	Average spacing of deformations = 9.4 mm < 70% x 16 = 11.2 mm	satisfactory
10.2.4	Gap between the extreme ends of deformations = 5.1 mm < 12.5% x 50.3 mm = 6.3 mm	satisfactory
10.2.5	Average height of deformations = 0.83 mm > 0.72	satisfactory

Results tabulated above reveal that, in spite of the different characteristics of ribs to standard deformed bars, the bar deformations on threaded bars used in this project satisfy the requirements given by NZS 3402:1989 [S5].

Stirrups, hoops and ties were plain round steel bars with a lower characteristic yield strength of 300 MPa in all units except for Unit 6, where deformed bar with lower characteristic strength of 300 MPa was used as horizontal joint reinforcement.

Steel samples cut from straight bars or as-bent stirrups or ties were tested monotonically in a 100 kN or 1000 kN Avery Universal Testing Machine. A clip extensometer was used to measure strains. Table 3.6 and **Fig. 3.17** present the measured mechanical properties and stress-strain relationship of the reinforcing steel used in the test units, the values shown in this table are the average from the results measured in three samples. All stress-strain curves showed a well defined yielding plateau. However results from six samples of R6 bars indicated that both the yielding and the ultimate strengths varied and tended to two different values. It is supposed that R6 stirrups delivered to the project were from two different heats. The values presented in Table 3.6 for R6 bars were obtained by averaging the measured data from 6 sample tests. It is believed that the influence of disparity on measured yield stress of R6 bars is insignificant.

Table 3.6 Measured Mechanical Properties of Reinforcing Bars.

Bar Size	Grade	Type	Locations	f_y (MPa)	ε_y	ε_{sh}	f_u (MPa)	ε_u
R6	300	Plain round	Units 1-8	352	0.00176	0.0123	502	0.113
R10	300	Plain round	Units 1-8	354	0.00177	0.0120	488	0.126
D10	300	Deformed	Unit 6	337	0.00169	0.0084	447	0.062
HD12	500	Deformed	Units 1-8	525	0.00263	0.0257	652	0.160
HD16	500	Deformed	Units 1-8	518	0.00259	0.0197	668	0.175

3.5.2 Concrete and Grout Compressive Strengths

Eight 100 mm diameter by 200 mm high concrete test cylinders were prepared for each beam and column member, respectively. All sample cylinders were cured under the same conditions as the test specimens. Cylinder compressive tests were carried out on 28 days for each cast and on testing day for beam and column members.

Six 50 mm diameter by 100 mm of grout cylinders prepared during the second step of grouting process for each test unit were tested on the testing day to determine the compressive strength of the cement based grout mixture. All compressive tests were carried out in an Avery Universal Testing Machine. Measured properties of the concrete and grout are tabulated in Tables 3.7 and 3.8. Due to the refurbishment of structural laboratory, the Avery Universal Testing Machine was inaccessible when the age of cast 1 and 2 was 28 days. As a result, f_c' at 28 days for cast 1 and 2 was not measured. However, the compressive strength of the concrete measured on testing day provided sufficient information. Note that in this precast construction method the joint is cast together with the beam, so that the concrete compressive strength corresponding to the joint region should be that of the beam. It can be seen from Table 3.8 that the grout strength of every unit is much larger than that of the concrete. The Guidelines for Precast Structural Concrete [G1] recommend the grout to be at least 10 MPa stronger than the concrete of the members being jointed.

Table 3.7 Concrete Properties of Each Cast.

Cast No.	Location	Slump (mm)	Unit	f_c' at 28 days (MPa)	Age at Test (days)	Compressive Strength on testing day (MPa)
1	Beams of Units 1 and 2	120	Unit 1	-	310	33.3
			Unit 2	-	325	33.3
2	Beams of Units 3 and 4	75	Unit 3	-	324	37.0
			Unit 4	-	339	37.0
3	Columns of Units 1 to 4	80	Unit 1	33.1	80	36.8
			Unit 2	33.1	95	36.8
			Unit 3	33.1	115	35.0
			Unit 4	33.1	130	35.0
4	Beams of Units 5 to 8	95	Unit 5	29.2	57	31.5
			Unit 6	29.2	68	32.7
			Unit 7	29.2	84	33.1
			Unit 8	29.2	78	33.2
5	Columns of Units 5 and 6	140	Unit 5	45.3	28	45.3
			Unit 6	45.3	39	49.1
6	Columns of Units 7 and 8	75	Unit 7	47.2	38	51.0
			Unit 8	47.2	32	51.7

Note: Loading rate of the compressive test = 23% of 500kN.

Table 3.8 Compressive Strength of Grout in the Connection of Each Unit.

	Unit 1	Unit 2	Unit 3	Unit 4	Unit 5	Unit 6	Unit 7	Unit 8
Grout f_g'on testing day(MPa)	49.8	49.8	50.5	55	55.7	59.6	59.6	58.6
Age at test(days)	43	58	16	31	15	26	22	16

Notes: 1. Tabulated were average values from 6 sample cylinders.

2. Size of the sample cylinder is 50 mm x100 mm(diameter x height).

3. Loading rate of the compressive test = 15 MPa/min = 29 kN/min

3.6 INSTRUMENTATION

3.6.1 Measurement of Loads

Electrical resistance strain gauge load cells were used to measure the reactions at the two beam ends and the applied load from the hydraulic actuator. The location of these load cells is shown in **Fig. 3.7**. Two 300 kN capacity load cells were designed and manufactured in this project for measuring the shear force at the beam ends. They were machined from AISI 4140 high strength steel alloy. The cross section area of the central region of the load cell was designed based on the principle that the tensile stress developing in the steel in this region is kept to be approximate 50% of the yield strength when the applied load reaches 300 kN. Two complete independent full bridge circuits which were built with electrical strain gauges into each load cell. Tokyo Sokki QFCB-6350 strain gauges, containing double 5-mm 350 Ω resistance gauges in each set, were used to build the electrical bridges in the load cells.

Another load cell with 400 kN capacity was placed between the horizontal hydraulic actuator and the steel bracket to measure the applied lateral load. This load cell also has two independent full bridge circuits. All the load cells were calibrated in an Avery Universal Testing Machine both in tension and compression prior to testing. The resolution of load measurement of 400 kN and 300 kN capacity load cells are 0.48 and 0.44 kN per division, respectively.

In this experimental programme, only one circuit in each 300 kN capacity load cell was used to monitor the load through the data logger. In the 400 kN capacity load cell, one circuit was connected to the data logger while another one was connected to a strain indicator. During the test, readings of loads monitored from the two circuits in the 400 kN load cell were compared with each other. In addition, the reaction forces measured from two 300 kN load cells were used to calculate the lateral storey shear force of the test sub-assemblage and compared with the lateral load measured from the 400 kN load cell. Readings obtained from two circuits in 400 kN capacity load cell were very consistent with a disparity of less than 3%. The difference between the calculated lateral storey shear based on two reactions of two beam ends and that measured directly from 400 kN capacity load cell was below 3% at peak loading. Therefore the reliability of the load measurement by means of load cells in this experimental programme is warranted.

3.6.2 Measurement of Displacements and Deformations

3.6.2.1 Measurement of Displacements

The inter-storey lateral displacement of the test specimen was obtained from measurement using two 10 kΩ resistance of linear potentiometers. The arrangement of linear potentiometers for measuring the lateral displacement of all test units is shown in **Fig. 3.18**.

Linear potentiometers used to obtain the inter-storey lateral displacement in this project included two with a travel of 300 mm which were placed vertically on top of the beam at both ends in line with the centre line of links. Two 15 mm travel potentiometers were placed near the column ends at the same level of input of lateral loads. The 300 mm travel linear potentiometers were used to monitor the vertical movement of beam ends against the strong floor. Each of them was mounted on a steel frame which was bolted down to the strong floor. The beam displacements obtained this way are absolute values and are not affected by the flexibility of the links loading frame and beam links. The beam end displacements were used to compute the inter-storey displacement of the unit when loaded similarly to a building component.

The small rigid body rotation of the test unit was monitored through two 15 mm travel linear potentiometers placed at the level of the top and bottom 160 mm diameter pins through the column as **Fig. 3.18** shows. With reference to **Fig. 3.18**, the lateral storey displacement in terms of column displacement, Δ_c ,can be obtained using the following equation if the rigid body movement of the test specimen is taken into account,

$$\Delta_c = \frac{2450}{3190}(\delta_{b1} - \delta_{b2}) - (\delta_{c1} - \delta_{c2}) \qquad (3.2)$$

It was found that the column lateral displacements δ_{c1} and δ_{c2} were very small and could be ignored in most cases, especially when the units were loaded beyond the elastic limit. Consequently, Eq. 3.2 was simplified to be

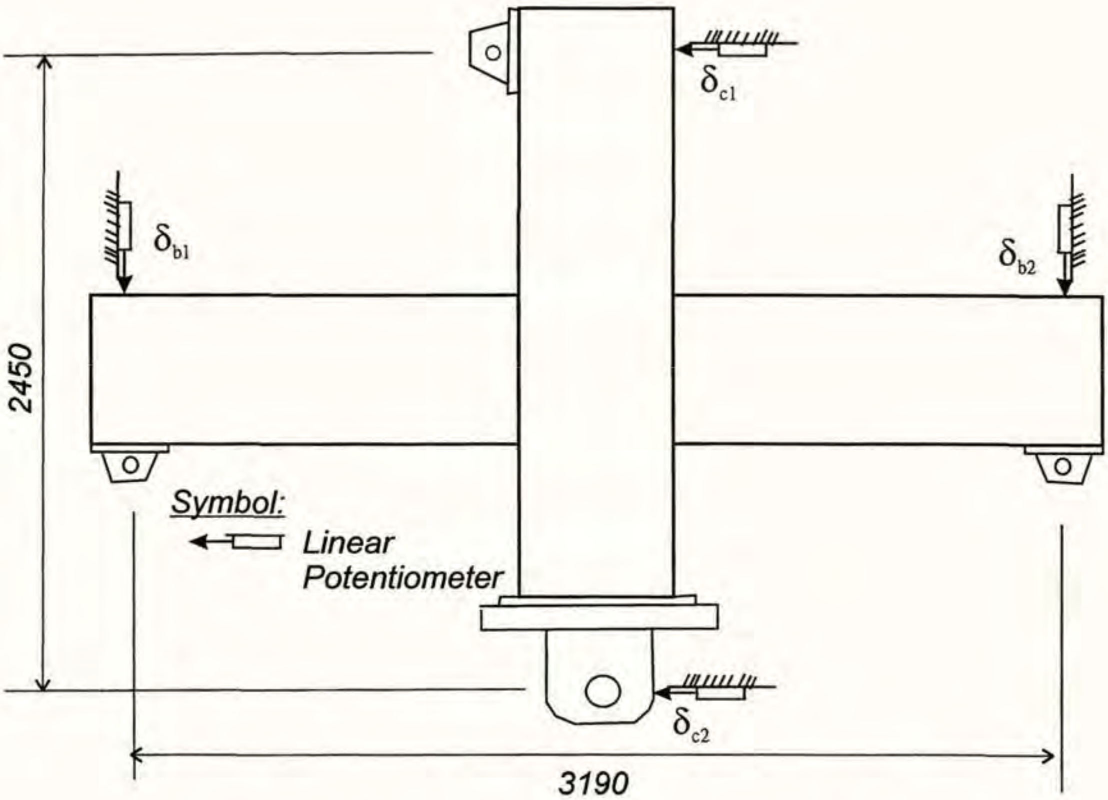

Figure 3.18 - Positions of Linear Potentiometers to Measure the Lateral Storey Displacement.

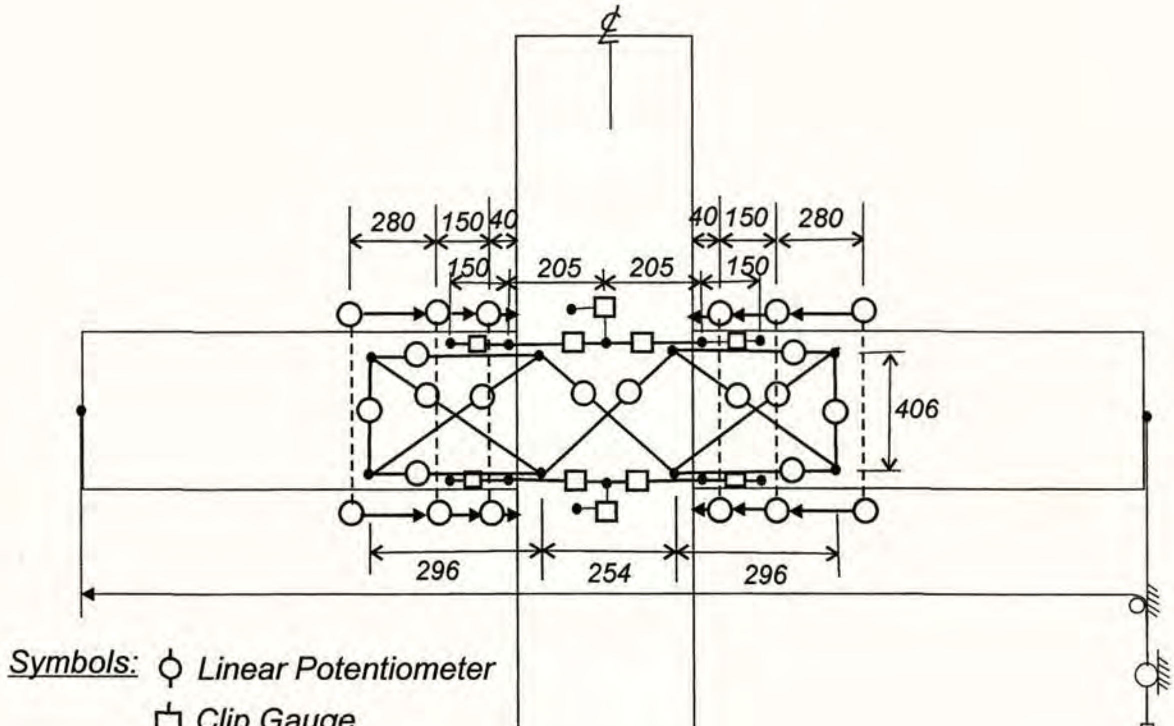

Figure 3.19 - Lay out of Linear Potentiometers and Clip Gauges Measuring Internal Deformation of Unit 1-4.

$$\Delta = \frac{2450}{3190}(\delta_{b1} - \delta_{b2}) \qquad (3.3)$$

3.6.2.2 Measurement of Internal Deformations

Figures 3.19 and **3.20** show the location and type of devices used to measure the internal deformation in the test specimens. A series of 10 kΩ resistance-50mm travel Sakae linear potentiometers were used to measured the deformation of the beam chords. They were mounted on steel brackets screwed into R10 steel rods embedded in the concrete. The readings from the first pair of potentiometers immediately adjacent to column faces were used to determine the fixed-end rotation in beams of all units. The rotation of the beam chords and average strains can be determined from the readings of the remaining potentiometers. The procedure used to calculate each component of lateral displacement will be discussed later in Section 3.8.4.

An attempt was also made to determine the average shear distortion in the beam-column joint and the plastic hinge region in the beams through measurement of diagonal deformation. Potentiometers with 15 or 30 mm travel were mounted diagonally on aluminum brackets with universal joints fixed on the R10 steel rods embedded in concrete. The procedure to estimate the shear deformation in the joint and beam region will be discussed in Section 3.8.3.

The elongation of the beams at mid-depth was monitored by a 50 mm travel linear potentiometers attached to the side end of the beam by a steel wire and a pulley.

Note that as the capacity design procedure had been applied in the design process, no plastic hinges were expected to occur in the columns of all units. The elastic deformations of columns can be determined using the standard procedure adopted in the analytical work presented in Chapter 2. Therefore, it was decided to place no instrumentation in the columns.

3.6.2.3 Beam Bar Slippage

The slippage of longitudinal beam bars passing through the beam-column joint region in each unit was monitored as shown in **Fig. 3.21**. This method had been used by previous researchers [R1][H1] and has been accepted as a reasonable accurate method. This measuring system consists of three clip gauges on each top and bottom longitudinal bars. One clip gauge

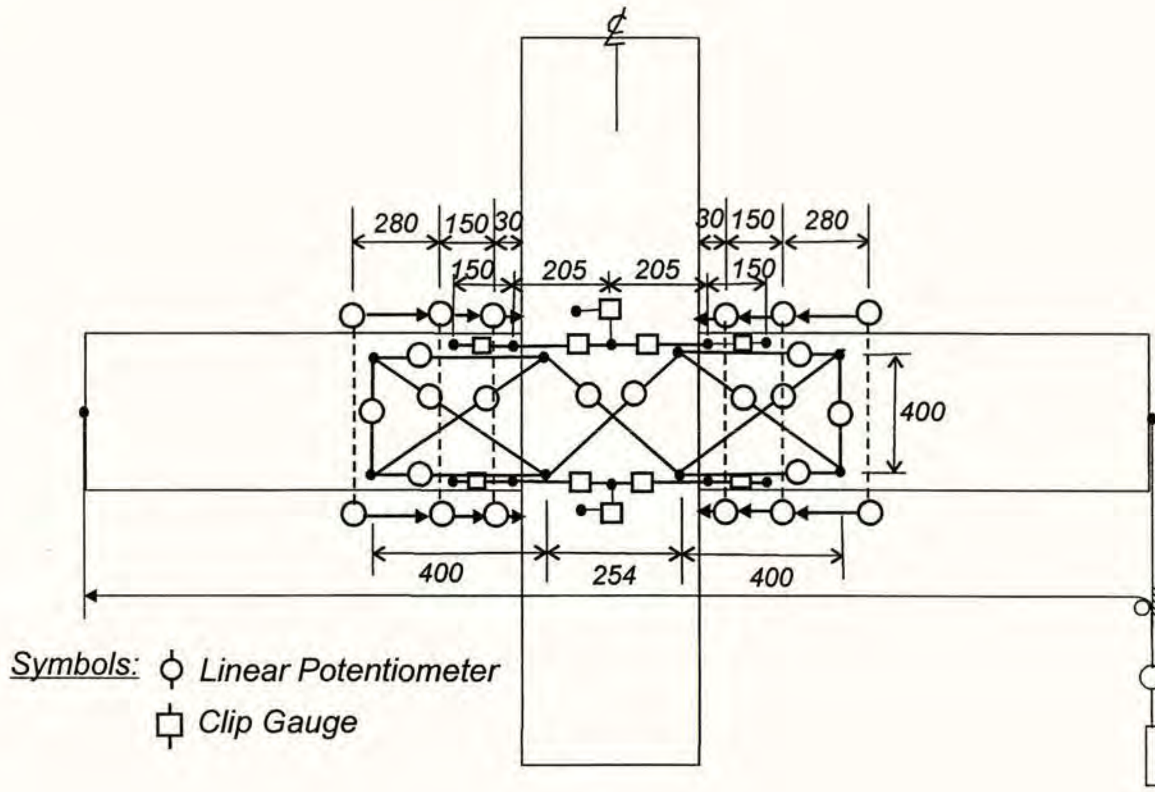

Figure 3.20 - Lay out of Linear Potentiometers and Clip Gauges Measuring Internal Deformation of Unit 5-8.

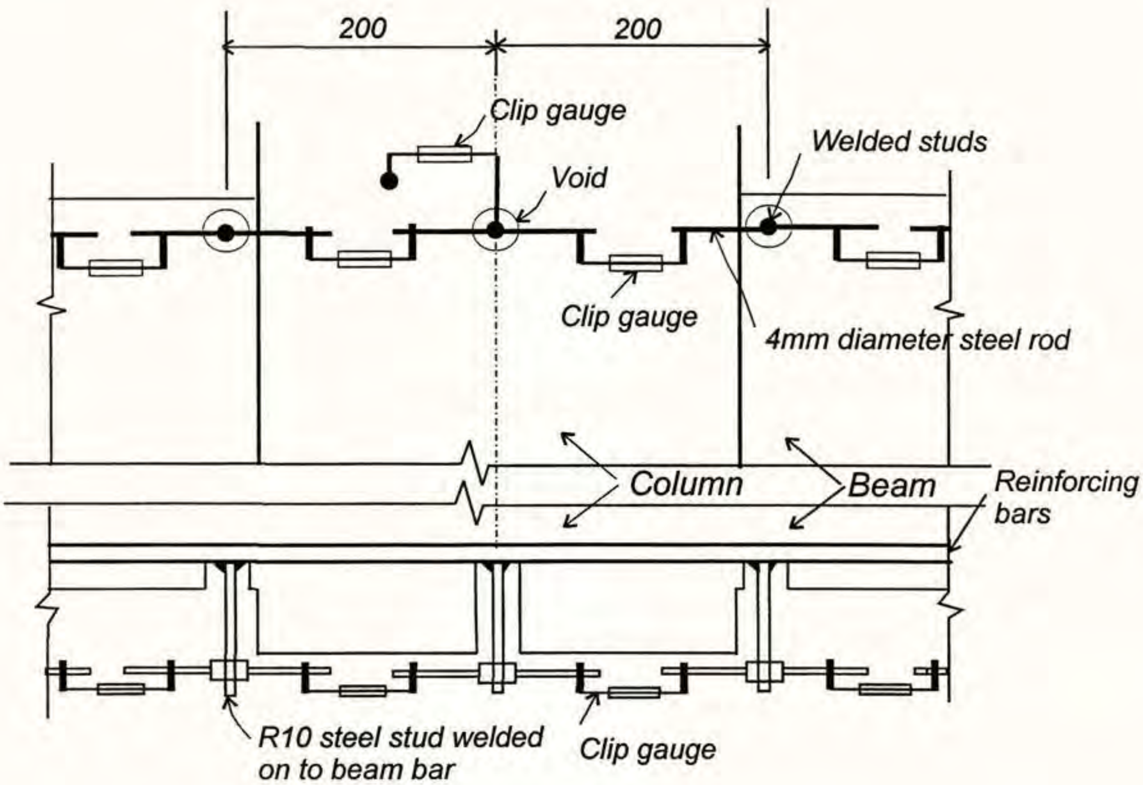

Figure 3.21 - Measurement of Beam Bar Slip Within Joint Region.

was mounted on the concrete surface in the joint region and a target stud welded to the HD12 reinforcing bars at the centre of joint region to measure the relative movement. Two other two clip gauges were used to measure the elongation of the bars between the centre target and targets welded on the same bars at 10 mm away from the column faces. An assumption has been made that the concrete in the vicinity of this measuring system is infinity rigid. The movement of bars at two other locations in the joint region relative to the column centre line can be determined by adding the local bar slip measured at the column centre line to the elongation of bars at the location close to the column faces. Voids were made around the steel studs to allow free movement of the stud and to avoid bearing against the concrete.

3.6.2.4 Measurement of Strains in Reinforcing Bars

Local Strains

The local strains of longitudinal beam bars, column bars and horizontal joint hoops were measured using 2 or 5 mm long electrical resistance strain gauges (Tokyo Sokki FLA-5-11 or FLA-2-11) with 120 Ω resistance and nominal gauge factor of 2.13. All strain gauges have pre-attached electrical leads so that soldering to terminals is not required.

Surface preparation of reinforcing bars before attaching the strain gauges consisted in four steps. First, the deformation of the bar within the range where gauge was to be attached was removed using a file. Care was taken to avoid excessive removal of the ribs and of the bar section in this region. Second, the area prepared was polished using sand cloth. Polishing was carried out until the surface was smooth. Third, The surface of the bar was cross hatched at 45 degrees using new 180 grit sand cloth. Cross hatching is done to provide the bond conditions of the adhesive and the bar. Forth, the surface was cleaned using Methy-Ethyil-Ketone (MEK) applied with cotton swabs. Cleaning procedure repeated at least 3 times until no contaminants were found on the cotton swabs.

Each strain gauge was then spread with a thin layer of ethyl cyanoacrylate adhesive on the back surface and attached immediately on the reinforcing bars and held with pressure for a couple of minutes. A layer of waterproofing glue, Shinkoh SN/4, was placed to cover the attached strain gauge within 24 hours. Another waterproofing layer was spread 8 hours after the spreading of the first layer. Then the portion of wires near the gauge without PVC sleeve was folded back and attached down to the bar adjacent to the sides of strain gauge 15 minutes afterward. This procedure is to provide some flexibility to the wire near the gauge since the movement of the gauged bars relative to the surrounding concrete may cause the loss of the circuit at an early stage. Additional three layers of waterproofing glue were applied afterwards in a time interval of at least 6 hours. Finally, a piece of 3M rubber mastic tape was used to cover each gauged region to provide physical protection against the surrounding concrete. Then the wires of each strain gauge near the gauge was tied down to the bar using thin steel wire under the cover of a small piece of 4 mm PVC sleeve. The function of PVC sleeve is to insulate and protect the leads of strain gauges being cut by the holding wire.

It is known that strain gauges are vulnerable when large strains develop. According to the reliability tests of strain gauges under cyclic loading carried out by Restrepo et al.[R1], creep or de-bonding may cause unreliable strain readings beyond 1.2%. Since it was observed that after the strain gauges de-bond, the gauge is still capable of giving a cyclic response [R1], caution was taken to judge the reliability of strain gauge readings. Readings recorded at the peak of each loading run were compared with that obtained from a scan prior to unloading. The gauge was rendered damaged if a large strain difference was found between the two readings.

Two diametrically opposite strain gauges, one on the top and the other one on the bottom of the bars, were attached to each beam-column joint hoops and ties to cancel out the local bending effect in the bars. Positions of these strain gauges will be presented with the test results in the following chapters.

Average Strains

It is also of interest to measure the average strain on reinforcing bars using other transducers. Two devices were used to obtain the average strains of reinforcement at some localities. Clip gauges were mounted on the R10 steel studs welded to top and bottom beam bars to measure the average strains near the column faces. The positions of them in test unit are shown in **Figs. 3.19** and **3.20**.

Average strain measured from clip gauges can be calculated as,

$$(\varepsilon_i)_{avg} = \frac{\delta_i}{l_i} \tag{3.4}$$

where δi is the displacement measured over the region i by clip gauges and l_i is the gauge length of the region i.

Average strains at the level of the longitudinal reinforcing steel can also be estimated using the readings obtained from the linear potentiometers mounted along the top and bottom chords of the beams. As shown in **Fig. 3.22**, the flexural deformation over a beam segment gauged by a linear potentiometer can be idealized as an crack with the neutral axis coinciding the beam compressive steel. Thus the average strain, ε_{avg} , at the level of the longitudinal reinforcing steel can be given by

$$\varepsilon_{avg} = \frac{\delta_p \dfrac{(d-d')}{d_p}}{l_g} \tag{3.5}$$

where d-d' is the distance between centroids of top and bottom longitudinal beam bars, δ_p is the extension measured from the linear potentiometer over gauge length l_g, d_p is the distance between the linear potentiometer and the centroid of the steel in compression.

It has been found that measurements obtained using this method are sensitive to the cracks forming in the beams near column faces so that some error will be incurred when an attempt is made to represent the strain profiles along the beam longitudinal reinforcement [R1]. In addition, the average strains found in this way may not exactly represent those in the reinforcing bar itself because of relative concrete-to-bar slip. However, it is believed that large errors are unlikely to occur as long as strains are considered as average values. Despite this limitation the data found can provide useful information for obtaining a crude estimate of the strain profiles developed in beams at the level of longitudinal beam bars at large displacement ductility levels when strain gauges have probably failed.

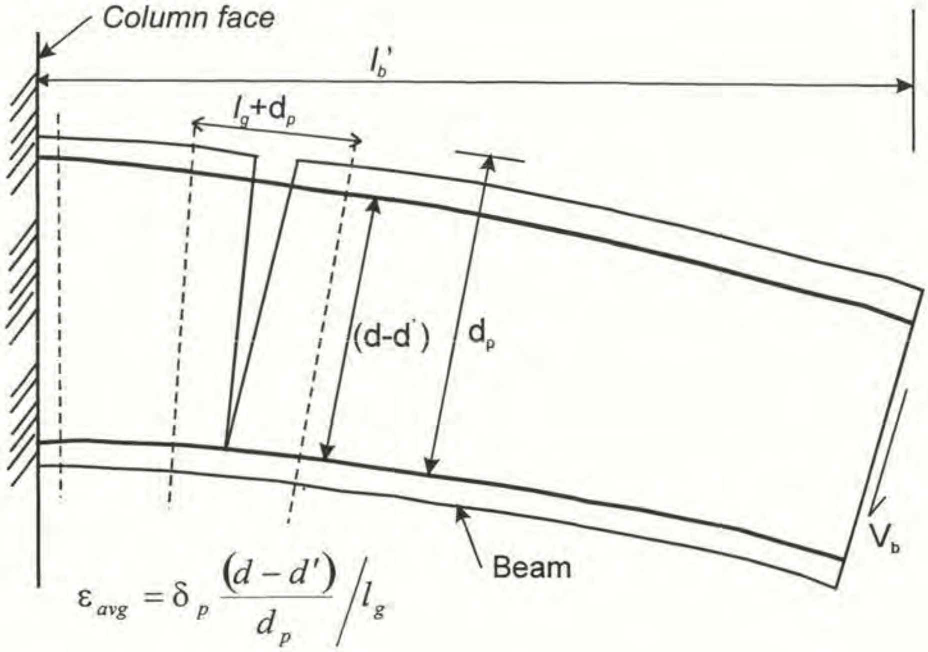

Figure 3.22 - Average Strain at the Level of Longitudinal Beam Bars Obtained from Readings of Linear Potentiometers.

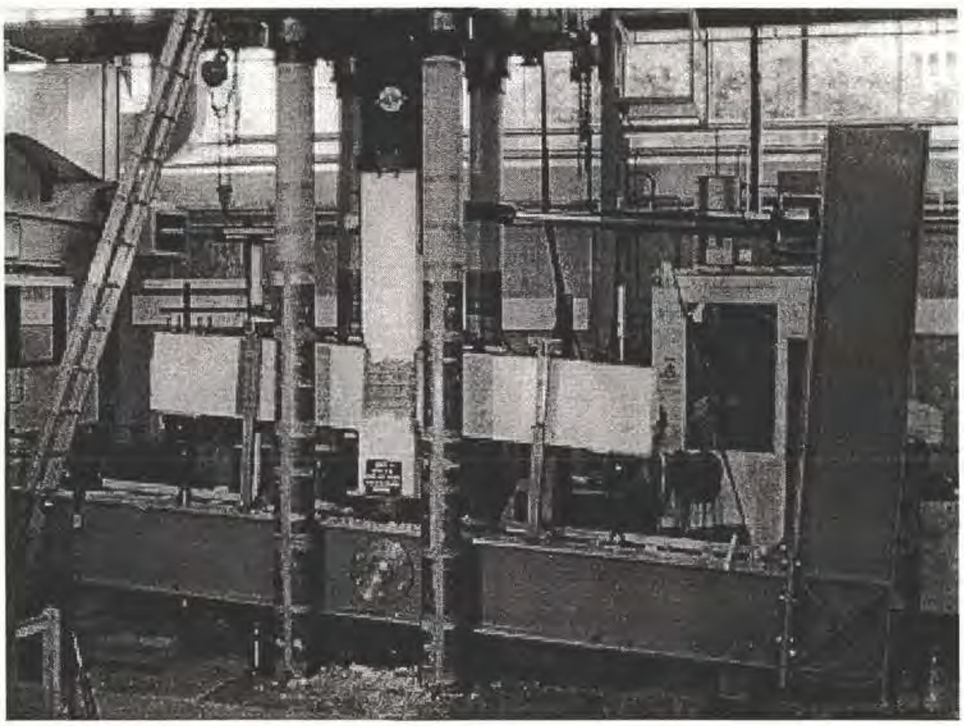

Figure 3.23 - A test Unit Under Testing.

3.7 TEST PROCEDURE AND LOADING SEQUENCE

Before test commenced, all strain gauges were checked for continuity and resistance to earth and all linear potentiometers were calibrated in position using steel spacers. Clip gauges also were calibrated using a metric calibrator and a data logger and then fitted in position in the test specimen. All calibration data was analyzed using linear regression and accepted if the coefficient of correlation was larger than $r^2 = 0.99998$. A 256 channel data logger, PCLAB, was used for data acquisition. Appropriate gain factors associated with specific instrumentation was set up in each channel of the data logger.

The specimen was fitted to the reaction frame first and then moved to the DARTEC machine. Eight steel studs made of high strength alloy were screwed through each steel fitting into the DARTEC ram. Constant axial load was exerted on the column first and then lateral loads were applied according to the loading sequence. **Figure 3.23** shows a unit under testing.

The loading sequence adopted in this testing program follows the typical quasi-static test sequence used at the University of Canterbury for many years. It is believed that the probable seismic resistance of a sub-component evaluated following the simple testing sequence is able to provide a satisfactory behaviour during a real seismic event [P1].

The test specimens were loaded to 3/4 of the theoretical lateral load capacity, which was calculated based on beam flexural strength using measured material properties and the concrete rectangular stress block, to determine the Δ_{75} displacement. When calculating the theoretical lateral strength, the strength reduction factor was taken as 1.0 according to the capacity design principle and over-strength was not considered. The procedure to obtain the lateral storey displacement from the readings of linear potentiometers measuring the displacements in a test specimen was described in Section 3.6.2.1. The lateral storey displacements at the peak of each load controlled cycle corresponding to 75% of the theoretical ultimate lateral load were recorded and averaged following the procedure. If Δ_{75} represents the average value of the recorded displacements mentioned above, the reference yield displacement, Δ_y, of the beam-column sub-assemblage can be obtained by linear extrapolation as,

$$\Delta_y = \frac{4}{3}\Delta_{75} \quad (3.6)$$

The definition of reference yield displacement is expressed graphically in **Fig. 3.24**. Once the yield displacement has been found, the target lateral displacement of the test specimen associated with the intended displacement ductility factor can be determined in proportion to the yield displacement. If μ_Δ is the displacement ductility factor, the relation described above can be expressed in the following equation.

$$\mu_\Delta = \frac{\Delta}{\Delta_y} \quad (3.7)$$

where Δ is the imposed lateral displacement. The complete loading sequence used in this test program is shown in **Fig. 3.25**.

3.8 DECOMPOSITION OF INTERSTOREY DISPLACEMENTS

3.8.1 General

It is of interest to decompose the inter-storey displacement to understand the behaviour of a test unit. The lateral displacement of a test unit comprises several components. In general, they can be classified as, column deformation, beam flexural, beam fixed-end, and beam shear deformations and beam-column joint shear distortion. The total lateral inter-storey displacement can be expressed as the sum of each component:

$$\Delta = \Delta_c + \Delta_{b,fl} + \Delta_{b,fe} + \Delta_{b,sh} + \Delta_j \quad (3.8)$$

The procedure used to determine each component of lateral displacement are described in the following sections.

3.8.2 Column Deformations

As that columns in every unit were expected to behave elastically during the test, no instrumentation was placed on them. The component of the column deformation contributing to the inter-storey displacement, Δ_c, was obtained theoretically. The theoretical prediction, including flexural deformation and fixed-end rotation, were based on the same procedure

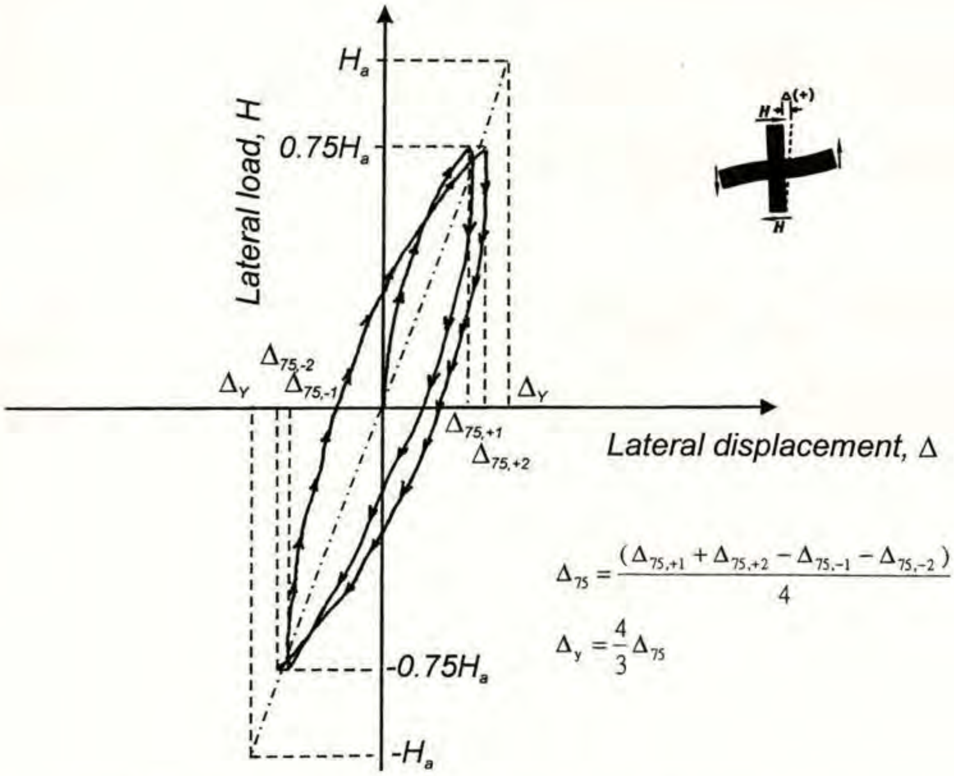

Figure 3.24 - Definition of Reference Yield Displacement.

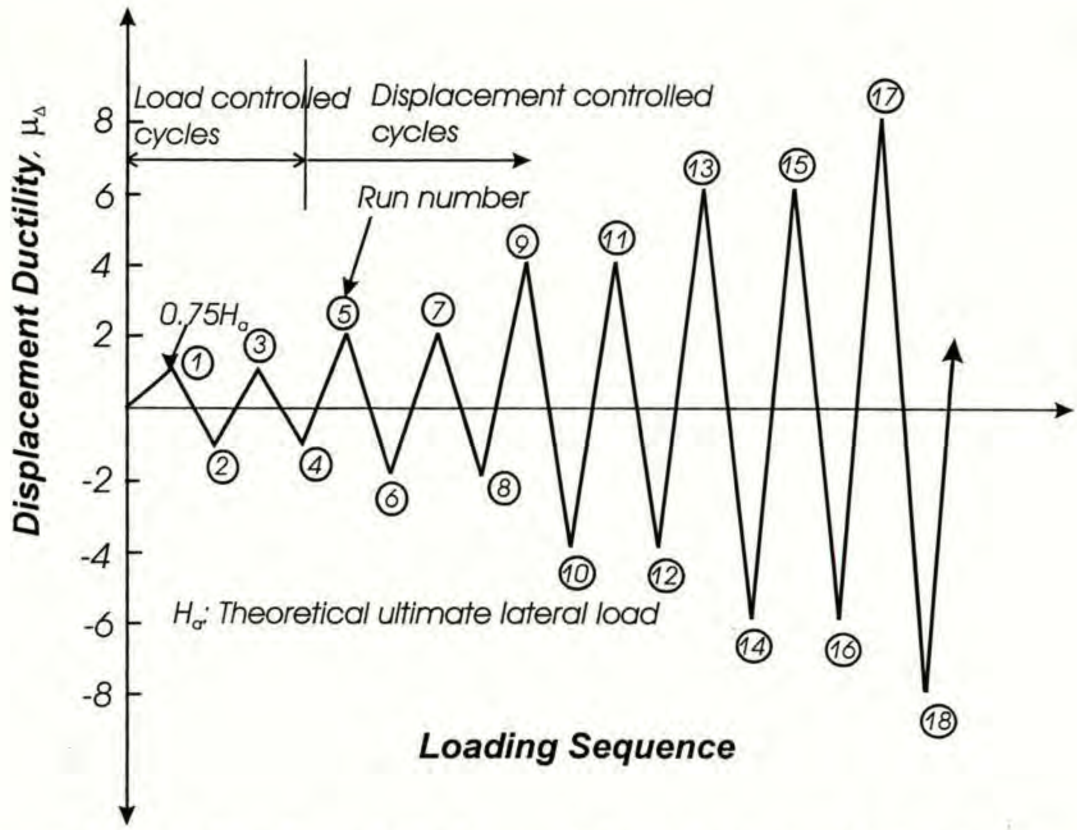

Figure 3.25 - Cyclic Lateral Loading and Displacement History Applied to All Test Specimens.

discussed in Section 2.3.5 to obtain the column deformations of existing database of tests.

3.8.3 Beam-Column Joint Shear Distortion

Two linear potentiometers of 15 mm travel were placed diagonally on the joint panel to estimate the average shear distortion of the joint core. They were fixed to aluminum brackets fitted with spherical joints. The brackets were fixed to steel rods embedded in the corners of the joint. With reference to **Fig. 3.26**, the average joint shear distortion γ_j can be estimated from the deformed shape of the joint panel using the following equation:

$$\gamma_j = \gamma_1 + \gamma_2 = \frac{\delta_j - \delta_j'}{2l_j}(\tan\alpha_j + \frac{1}{\tan\alpha_j}) \tag{3.9}$$

where δ_j and δ_j' are the change in the lengths of the diagonals, l_j is the initial length of the diagonals and α_j is the angle of the diagonals to the horizontal. As depicted in **Fig. 3.27**, the contribution to the lateral storey displacements from joint shear distortion can be estimated from the following equation based on the support conditions of the loading system used in this study,

$$\delta_{b,j} = \gamma_j\left(l_c - h_c\frac{l_c}{l_b}\right) - \gamma_j h_b \tag{3.10}$$

where h_c is the column depth, l_c is the vertical distance between the bottom column end pin and the centre of horizontal hydraulic jack, l_b is the beam span length or horizontal distance between the beam end pins. Note that for the units tested l_c = 2450 mm and l_b = 3200 mm.

In addition, another point to be investigated in this study is the stiffness of the joint panel. This information is essential when modeling the frame structures in a computer analysis taking into account the flexibility of beam-column joint panel. The joint stiffness can be evaluated from the measured joint shear distortion and horizontal joint shear force as,

$$K_{joint} = \frac{(V_{jh})_{75}}{\gamma_{75}} \tag{3.11}$$

where $(V_{jh})_{75}$ is the horizontal joint shear force corresponding to 75% of the theoretical

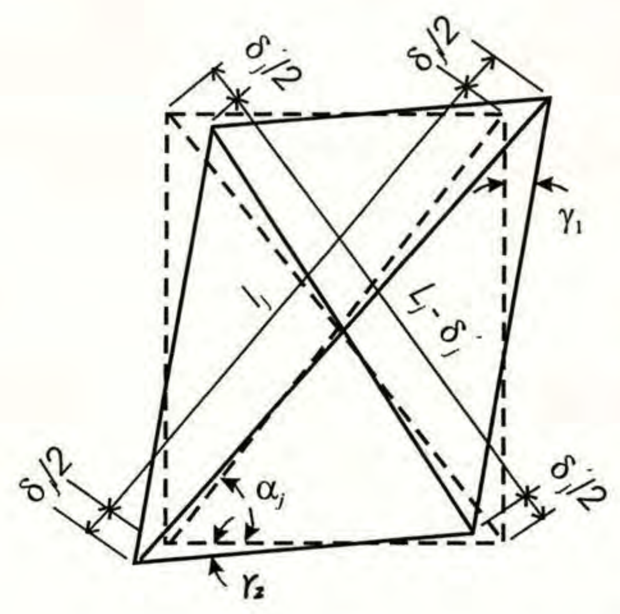

Joint shear distortion :

$$\gamma_j = \gamma_1 + \gamma_2 = \frac{\delta_j - \delta_j'}{2l_j}\left(\tan\alpha_j + \frac{1}{\tan\alpha_j}\right)$$

Figure 3.26 - Measurement of Joint Shear Distortion.

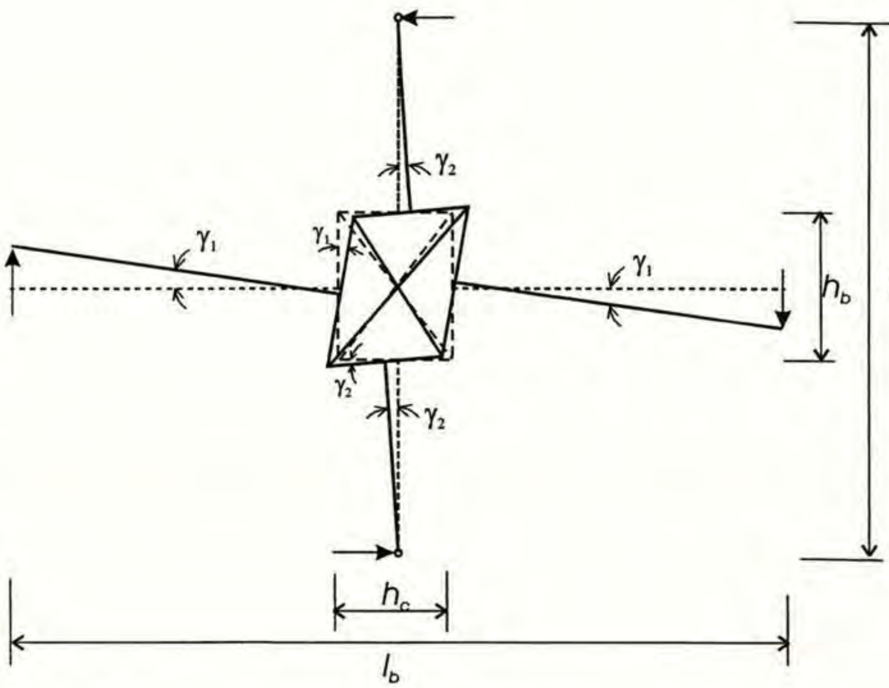

$$\Delta_j = \gamma_1(l_b - h_c)\frac{l_c}{l_b} + \gamma_2(l_c - h_b) - \gamma_2 h_c \frac{l_c}{l_b} - \gamma_1 h_b$$

$$= \gamma_j\left(l_c - h_c\frac{l_c}{l_b}\right) - \gamma_j h_b$$

Figure 3.27 - Lateral Storey Displacement Due to Joint Shear Distortion.

ultimate lateral load H_a, and γ_{75} is the average value of the measured joint shear distortion at the peak of each load controlled cycle corresponding to the 0.75 H_a. The equivalent joint shear area, $A_{j,e}$ can be calculated as

$$A_{j,e} = \frac{(V_{jh})_{75}}{G\gamma_{75}} \tag{3.12}$$

where G is the shear modulus of concrete, which can be estimated as $G = 0.4E_C$. The ratio of equivalent joint shear area with respect to the area of the joint panel is calculated equal to $A_{j,e}$ / (h_b h_c), where h_b and h_c are the overall beam and column depths, respectively.

3.8.4 Beam Deformations

3.8.4.1 Flexural Deformations

Beam flexural deformations can be obtained from the rotation of each segment in the beam measured from a pair of top and bottom linear potentiometers located at the top and bottom chords and based on the Bernoulli hypothesis that plane sections remain plane after deformation. With reference to **Fig. 3.28**, the change of slope between two beam sections, section a and b, in which R10 steel rods were embedded for mounting the linear potentiometers is given by

$$\theta_{ba} = \frac{\left(\delta_{pb} - \delta_{pb}'\right)}{h_p} \tag{3.13}$$

where θ_{ba} is the change of slope between section a and b, δ_{pb} and δ_{pb}' are the extension and shortening of top and bottom beam chords measured by a pair of linear potentiometers at section b relative to point a. Thus, the beam end deflection obtained from the change of slope between sections a and b is:

$$_b\delta_{b,fl} = \frac{(\delta_{pb} - \delta_{pb}')}{h_p}\left(l_b' - x_b\right) \tag{3.14}$$

In accordance with the same procedure described above, another portion of beam flexural deformation obtained from change of slope between sections b and c is:

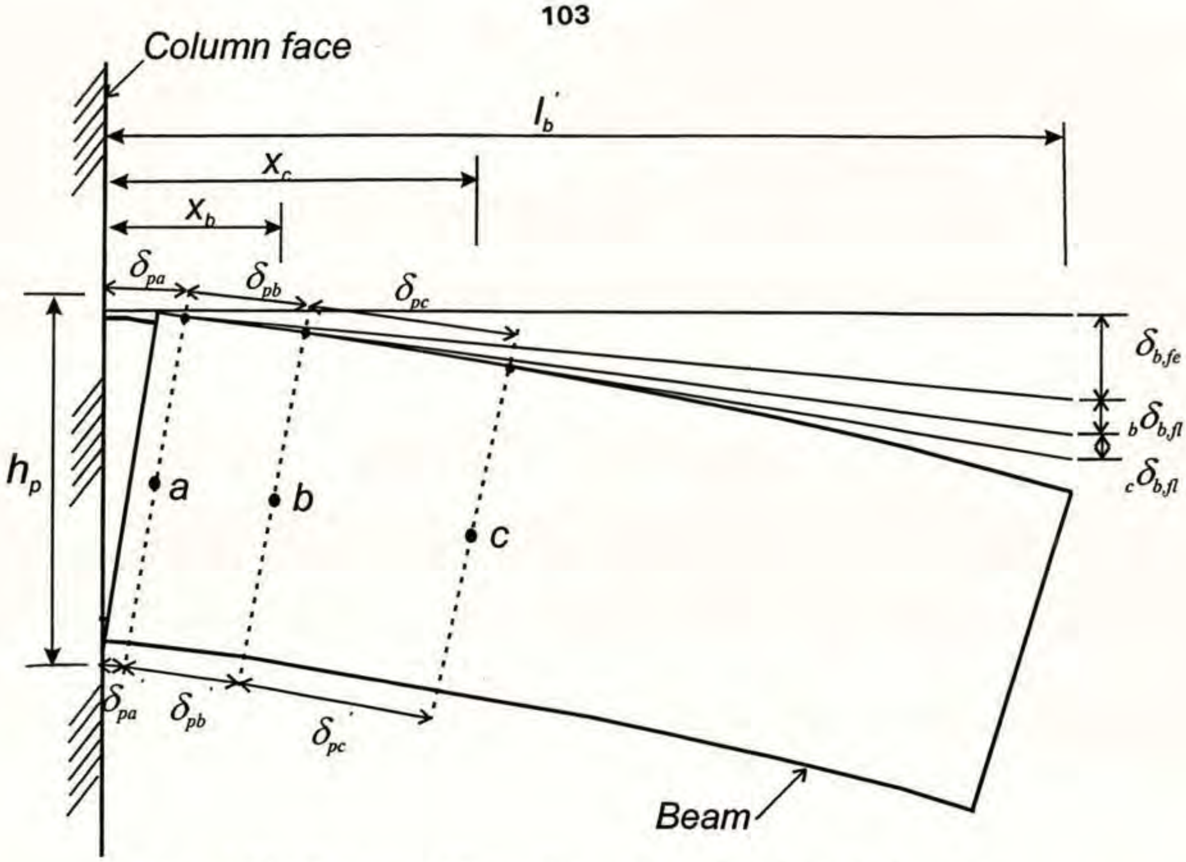

Figure 3.28 - Estimate of Beam Flexural and Fixed-end Deformation.

$$ {}_c\delta_{b,fl} = \frac{(\delta_{pc} - \delta_{pc}')}{h_p}\left(l_b' - x_c\right) \tag{3.15} $$

The sum of the discrete beam flexural deformations gives the total beam flexural displacement, $\delta_{b,fl}$.

$$ \delta_{b,fl} = {}_b\delta_{b,fl} + {}_c\delta_{b,fl} \tag{3.16} $$

The lateral inter-storey displacement due to beam flexural displacement is

$$ \Delta_{b,bfl} = \delta_{b,fl}\frac{l_c}{l_b} \tag{3.17} $$

3.8.4.2 Fixed-End Rotation

The beam fixed-end rotation was estimated from the readings of the pair of linear potentiometers placed in a short distance, 40 mm, away from column faces. As shown in **Fig. 3.28**, the beam end vertical movement due to beam fixed-end rotation can be estimated as

$$\delta_{b,fe} = \theta_{fe}\, l_b{}' = \frac{\left(\delta_{pa} - \delta_{pa}{}'\right)}{h_p} l_b{}' \qquad (3.18)$$

where h_p is the distance between the pair of linear potentiometers nearest to the column face, δ_{pa} and $\delta_{pa}{}'$ are the extension and shortening measured from linear potentiometers on the top and bottom of beam chords. $\delta_{b,fe}$ can be expressed as a component of the lateral inter-storey displacement given by the following equation,

$$\Delta_{b,fe} = \delta_{b,fe} \frac{l_c}{l_b} \qquad (3.19)$$

There are two sources contributing to the beam fixed-end rotation, one is caused by the deformations of the longitudinal bars passing through the joint core, and another one is due to global slippage of these bars. The method adopted here is an approximate method having the disadvantage that some rotation occurs due to the elongation of the beam bars in the region between the column face and the first potentiometer rod was also counted. However, the first set of linear potentiometers were placed as close as possible to the column face to reduce this influence.

3.8.4.3 Beam Shear Deformations

Beam shear deformations were estimated following the methodology suggested by Restrepo et al. [R1]. It was not directly estimated using the kinematics relationship of the deformed polygon depicted in **Fig. 3.29,** because of the change in length of the diagonals in the beam plastic hinge region is also affected by the extension of the tension chord due to flexure in the beam. This is specially important when the diagonal displacement transducers crossing through the column faces, the extension of diagonals due to fixed-end rotations can cause apparent shear deformations. Shear deformations occurring beyond the plastic hinge regions are expected to be so small that they can be ignored, consequently no measurements were taken in this region of the beam. This methodology comprises two components and is represented in the following.

(1) Shear-Flexure Deformation

If flexure shear cracks in the beam plastic hinge region are idealized as an equivalent

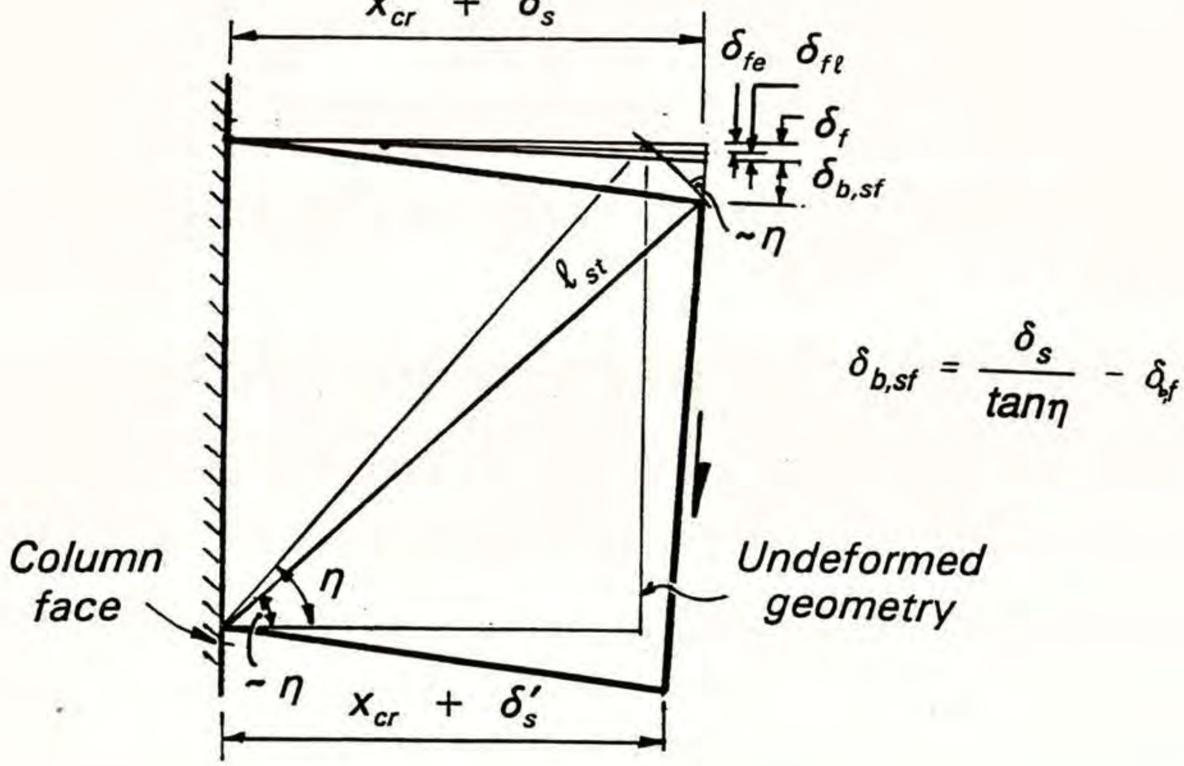

Figure 3.29 - Shear Displacement Due to Shear-Flexure [R1].

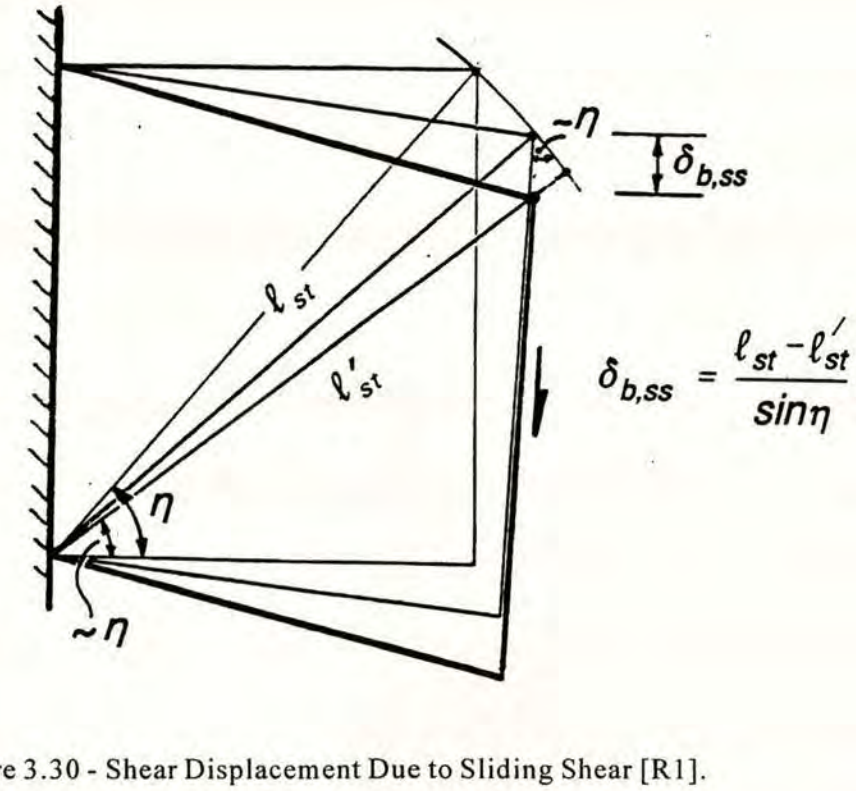

Figure 3.30 - Shear Displacement Due to Sliding Shear [R1].

crack radiating from the centre of the compression steel at the column face, the kinematics of the plastic hinge of a beam is illustrated in **Fig. 3.29**.

The extension of the chords and the beam displacement caused by flexure and fixed-end rotation which occurred at a distance x away from the column face are all known. Consequently, the shear component due to diagonal shear-flexure cracking can be determined from the following equation. This equation was derived by assuming that the length of the compression strut, l_{st}, remains unchanged. From geometry in the figure, the component of shear deformation is given by

$$\delta_{b,sf} = \frac{\delta_s}{\tan\eta} - \delta_{b,f} \qquad (3.20)$$

where $\delta_{b,f} = \delta_{b,fe} + \delta_{b,fl}$, and the critical distance at which the diagonal strut develops was approximated to the position where the diagonal potentiometers in the beam were located. Although theoretically it should be identical or close to the plastic hinge length, it is expected that the experimental flexural-shear deformation would be small so that using an approximate critical distance in this analysis would have a very insignificant influence.

(b) Pure-Shear Deformation

Another source of shear deformation, caused by yielding of the stirrups, disintegration of the diagonal strut or relative sliding between cracks in the plastic hinge region, is shown in **Fig. 3.30**. If this mode of shear deformation occurs, the length of the diagonal strut, l_{st}, will decrease and induce additional vertical displacement, $\delta_{b,ss}$, which can estimated as

$$\delta_{b,ss} = \frac{l_{st} - l_{st}'}{\sin\eta} \qquad (3.21)$$

where l_{st}' is the new length of diagonal strut after shortening. The total shear deformations of the beams in every test unit were estimated using this methodology, summing two modes of deformations together. If $\delta_{b,sh}$ represents the total beam shear deformation then

$$\delta_{b,sh} = \delta_{b,sf} + \delta_{b,ss} \qquad (3.22)$$

The beam shear deformation can be converted into a component of lateral storey displacement using the following relation.

$$\Delta_{b,sh} = \delta_{b,sh} \frac{l_c}{l_b} \qquad (3.23)$$

3.9 CONCLUSIONS

1. This chapter describes the design aspects, including objectives and design considerations of each unit in the test programme.

2. Fabrication of precast concrete members and construction procedures of the beam-column subassemblies are also described.

3. Methods used to measure the loads, internal deformations, displacements and strains of test unit are presented in this chapter.

4. The loading frame, designed for conducting the tests in the experimental programme is described.

CHAPTER 4
TEST RESULTS OF UNITS 1 AND 2

4.1 INTRODUCTION

This chapter presents test results from two cruciform test specimens, designated as Units 1 and 2. The main objective of the tests is to validate the findings of the analytical model described in Chapter 2. In this chapter it was discussed that in the presence of high axial compressive force in the column and high shear stresses in the joint region, the design recommendations given in the Concrete Structure Standard, NZS 3101:1995 [S1] may not result in a satisfactory performance of the joint. Reinforcing details for these two units and a description of the design considerations were presented in Section 3.2.2.1. Basically, both specimens are identical apart from the quantity of horizontal joint shear reinforcement. Unit 1 was designed according to NZS 3101:1995 [S1] for joints of ductile frames, while Unit 2 was designed to achieve a displacement ductility of at least $\mu_\Delta = 6$ according to the method proposed in this study.

Test procedure incorporated in the testing of these two units was described in Section 3.7. All test results are presented in terms of the imposed displacement ductility factor, for which a definition is given in Section 3.7.

4.2 UNIT 1

4.2.1 General

The horizontal joint shear reinforcement of Unit 1 was designed in accordance with NZS 3101:1995 [S1] for a target axial compressive force of $0.4f_c{}'A_g$ and relatively high joint shear stress ratio, $v_{jh} = 0.19\ f_c{}'$. The joint horizontal shear reinforcement consists of 6 sets of perimeter R10 hoops plus four inner R6 cross ties, see **Fig. 4.6**.

To conduct the test, the imposed axial compressive force in this unit was slightly increased to $0.43f_c{}'A_g$ to account for the difference between specified and measured concrete compressive strengths.

4.2.2 Overall Behaviour

This unit did not have satisfactory performance for components designed to be ductile. Failure was caused by crushing of the concrete in the beam-column joint. At the peak of the second load run of $\mu_\Delta = -4$, corresponding to a 2.45% inter-storey drift, the lateral storey shear dropped to 79% of the maximum recorded load. After the completion of loading cycles to $\mu_\Delta = -6x2$, the lateral load capacity dropped to 70% of the recorded maximum value. At the end of the test the joint concrete was badly crushed, indicating a diagonal compression failure in beam-column joint. However, column compressive load was sustained, though shortening of the column of the order of 8 mm had occurred at the end of test.

The observed cracking at different stages during the test and the storey shear versus lateral displacement response are shown in **Figs. 4.1** and **4.2**, respectively.

In the elastic loading cycles, fine cracks spread along the top and bottom chords of the beams. Most cracks were vertical and propagated toward the beam compression zone. Only about four flexural-shear cracks developed in each beam. The vertical cracks in the beams at the column faces were combined together after a reversed cycle to form a full crack through the beam depth. The recorded crack width in the beams at this stage did not exceed 0.1 mm. It is noted that the crack pattern in the beam was un-symmetrical. Cracks on the top beam chord distributed at a shorter distance along span than that on bottom chord. This phenomenon can be attributed to the well-known " top bar effect ". Furthermore, it was observed that the vertical cracks on the beams at the column faces developing as a result of negative bending were much wider than those developing as a result of positive bending moment. This is believed to be another evidence to show the influence of "top bar effect" of the beam bas passing through the joint. Cracks in columns were not seen to develop at this stage of loading. In the second positive loading run of 75% of theoretical ultimate lateral load, one crack located near the construction joint with width about 0.1 mm occurred on tension side of each column. The propagation of these two cracks was restricted only within the thickness of the cover concrete. The first crack in the joint region appeared in the second cycle to $0.75H_a$. At the end of elastic loading cycles, six diagonal cracks, with steep angles had occurred in the joint region and with measured crack widths less than 0.1 mm.

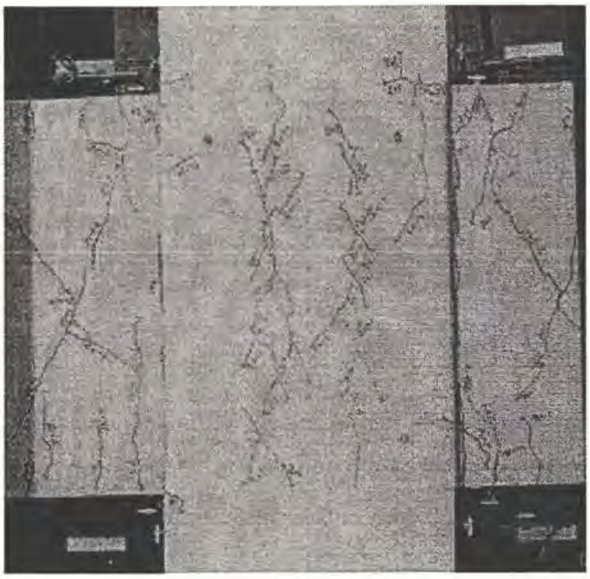

(a) At μ_Δ=-2x1

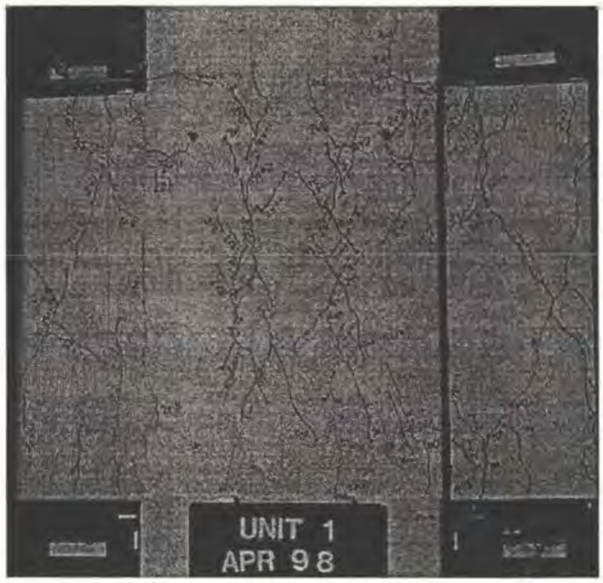

(b) At μ_Δ=-2x2

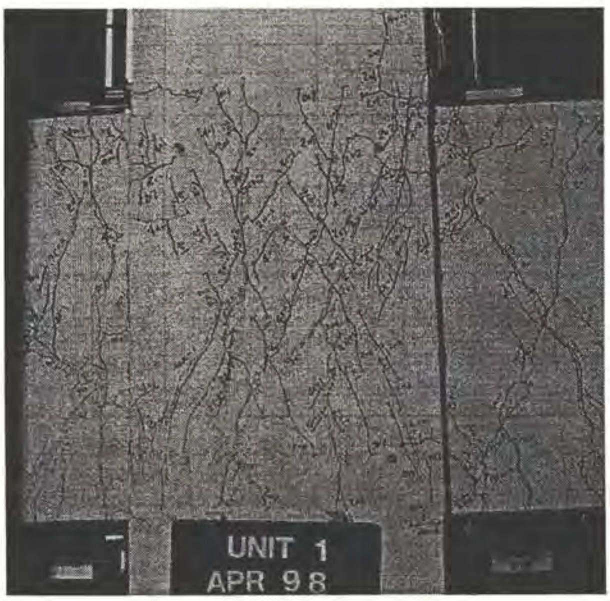

(c) At μ_Δ=-4x1

(d) At μ_Δ=-4x2

Figure 4.1 - Cracking of Unit 1 at Different Stages During the Test.

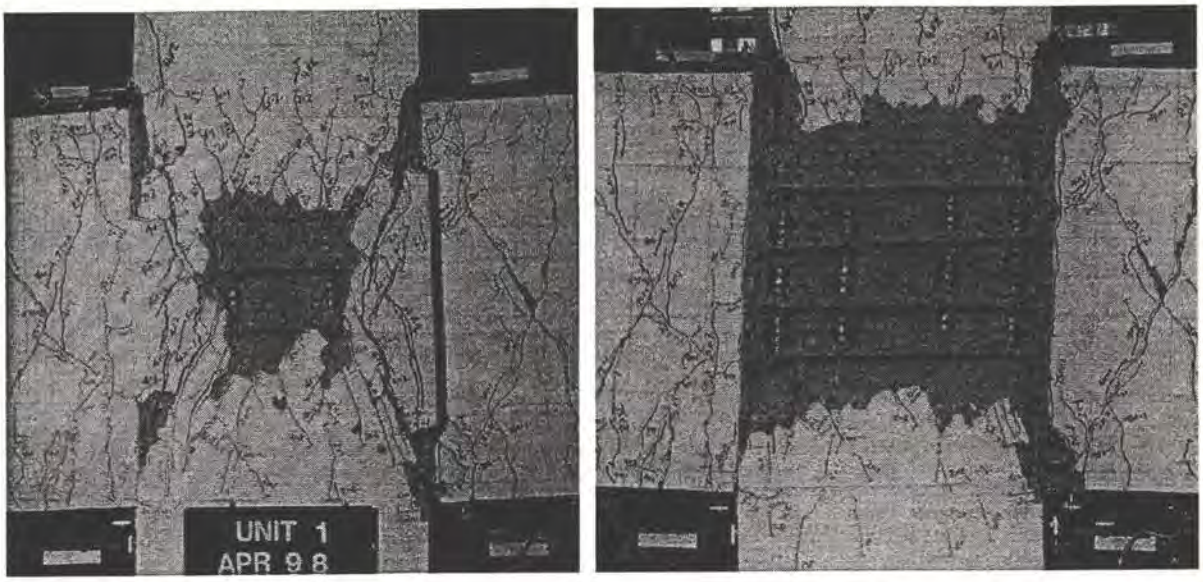

(e) At μ_Δ=-6x1

(f) At μ_Δ=-6x2

Figure 4.1(Contd.) - Cracking of Unit 1 at Different Stages During the Test.

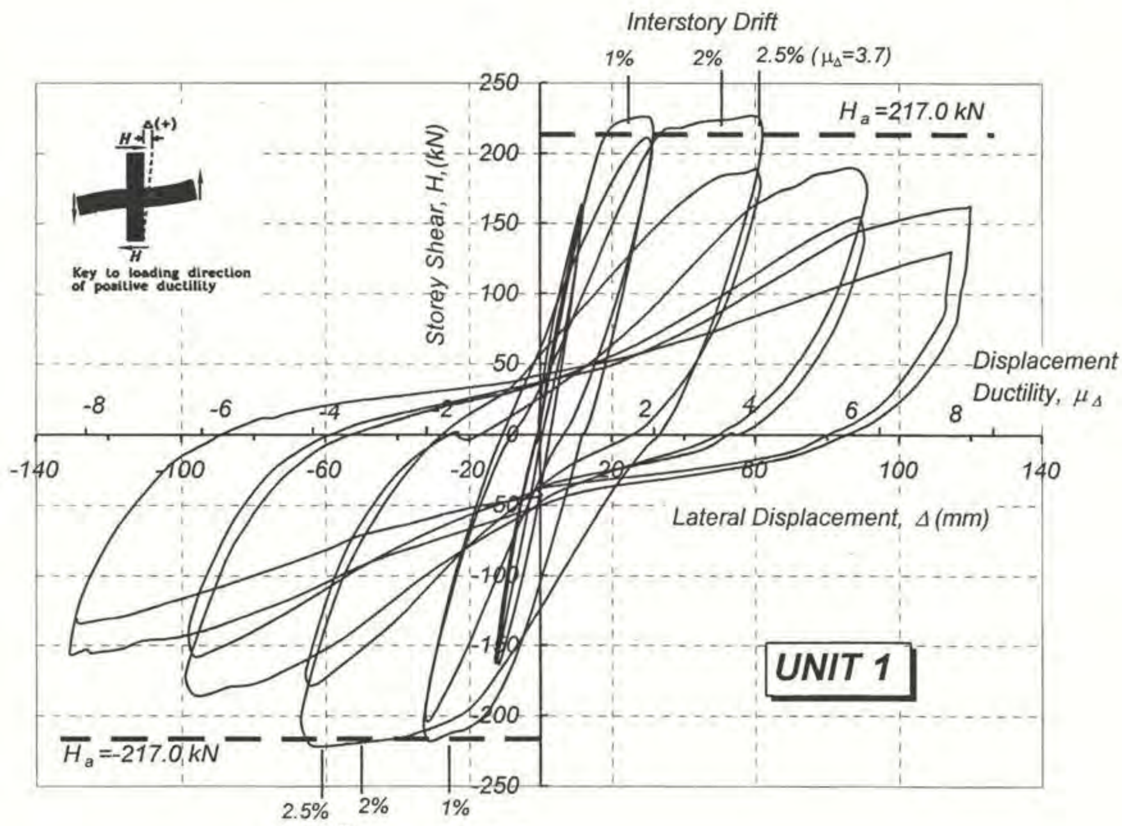

Figure 4.2 - Lateral Load-Displacement Response of Unit 1.

During the loading cycles to $\mu_\Delta = +2$, more flexural-shear cracks propagated through the beam web. Cracks located in the beams at the column faces widened and reached a width of 2.5 mm in the extreme tension chord. The crack pattern in joint region became denser with more short diagonal cracks concentrated in the vicinity of column interior bars, see **Figs. 4.1(a)** and **(b)**. The width of these cracks was small, typically of the order of 0.2 mm. Few cracks in the joint propagated into columns and penetrate a short length into them. The columns remained un-cracked at this loading stage, except at the joint face.

In the loading cycle to $\mu_\Delta = +4$ cracks in the beams and in the joint region continued to grow wider. The cracks in the bottom chord of the beams were more distributed and denser than in the top chord. The cracks in the beams tended to concentrate on two locations, one at the column faces, the other initiated at a distance of 100 mm away from column face and propagated diagonally into beam web. The width of the cracks at column faces reached 3.5 mm, and the maximum diagonal crack in plastic hinge region was 3 mm wide. The horizontal grid lines indicate that some shear deformation had occurred in the beam plastic hinges. The observed maximum crack in the joint region at this stage was 1 mm wide. In the reversed load run, $\mu_\Delta = -4x1$, some incipient damage to the cover concrete in joint region occurred, indicating that the joint had started to deteriorate. In the contrast, cracks in the beams became smaller in comparison with those in the previous loading run. It is evident that, since this loading run, the lateral displacement started to concentrate in the beam-column joint region. This can be further verified with the chart of displacement components presented in **Fig. 4.4**.

As the test proceeded toward the second cycle to $\mu_\Delta = \pm 4$, the cover concrete in the joint continued to spall off. The cracks in the beams remained essentially unchanged and the width of the main cracks decreased. This indicates that the lateral displacement contributed from beams diminished while the component of shear distortion of the deteriorated joint became the main source.

In the loading cycles of $\mu_\Delta = \pm 6x1$, large pieces of cover concrete in joint region fell off. The reinforcing hoops and metallic ducts embedded in the joint region were exposed and apparent distortion of the vertical metallic ducts could be observed. As loading proceeded toward the load cycle to $\mu_\Delta = +6x2$, most of the cover concrete in joint region spalled off. Crushing of the concrete in the joint core was observed. This specimen was loaded until $\mu_\Delta =$ +8x2, when the unit failed in diagonal compression of the joint. Spalling off of the cover concrete in the joint region spread upward to the upper beam face so that the grouted construction joint was exposed. It is noted that during the test, the grouted construction connection performed very well. Neither sliding movement nor crushing of the grout between precast concrete columns and the precast concrete beam unit was observed. After finishing this test, one of the metallic ducts embedded in joint region was cut and partially peeled off. It can be seen in **Fig. 4.3** that the duct was entirely filled with grout without any voids being detected.

During the test, the column axial load was maintained constant and the axial shortening of the column was monitored. As the specimen was loaded till μ_Δ = +8x1, 3 mm vertical shortening of the joint region was recorded. At the end of test, the recorded vertical shortening of the joint core reached 8 mm. However, the large column compressive load, 2180 kN, was still sustained without any diminution.

Figure 4.3 – Close-up of an Exposed Grouted Duct.

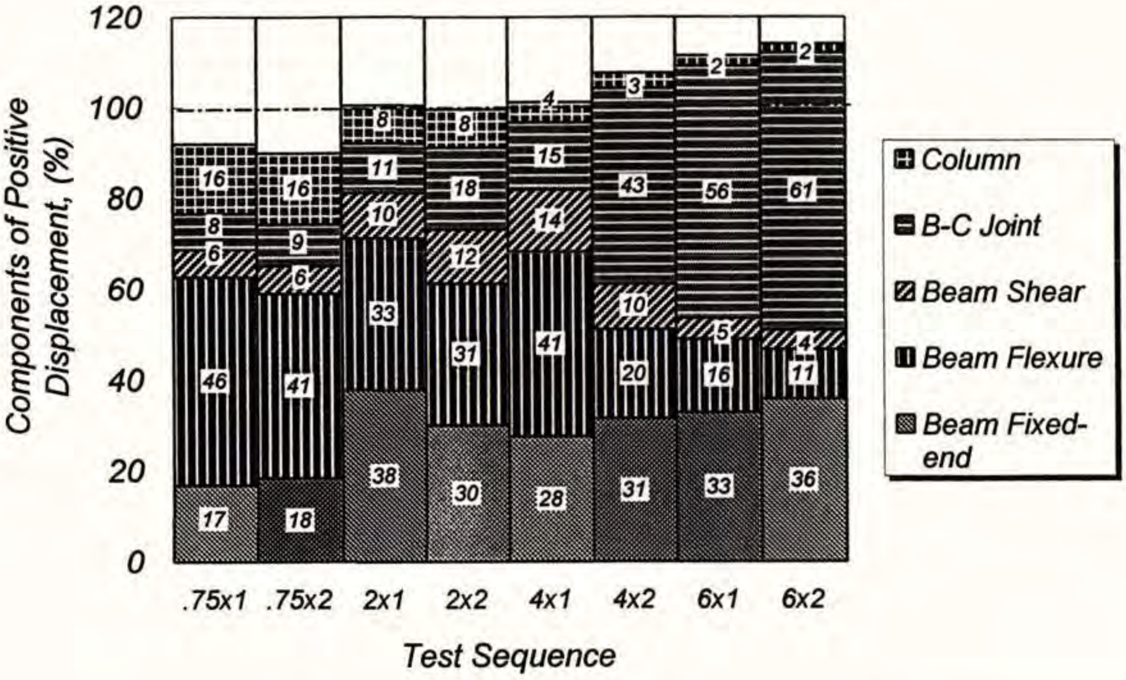

(a) Runs to Positive Ductilities.

UNIT 1

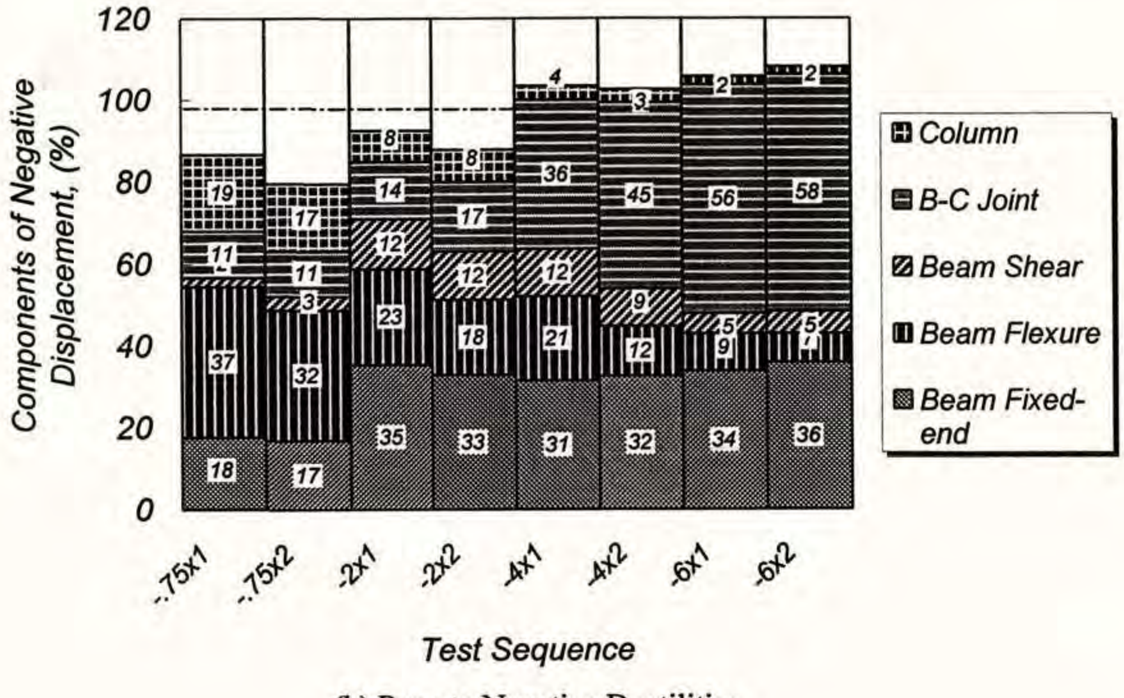

(b) Runs to Negative Ductilities.

Figure 4.4 - Components of Lateral Displacement of Unit 1 at Peaks of Load Cycles.

4.2.3 Load Displacement Response

The lateral load versus lateral displacement response of Unit 1 is presented in **Fig. 4.2**. The measured yield drift of this unit in accordance with the definition given in Section 3.7 was 0.67% . This yield drift level implies displacement ductility equal to $\mu_\Delta = 3.7$ when the drift limit 2.5% imposed by the Loading Standard [S3] is attained.

In the first inelastic loading run of, ($\mu_\Delta = +2$), the lateral load attained was 5% more than the theoretical load; while in the reverse load run, the recorded lateral load exceeded the theoretical value by only 1%. In the second load cycle to the same displacement ductility, the lateral load dropped just below the theoretical value. It is believed that the reduction of lateral load capacity occurred in this load cycle was mainly caused by the stiffness degradation induced from cracking.

The lateral load versus displacement loops in the first cycle to $\mu_\Delta = 4$ were stable without pinching despite that the maximum lateral loads in this cycle were very close to the values attained in the first loading cycle to $\mu_\Delta = 2$. Unlike the good shape of hysteresis loops in the first cycle to $\mu_\Delta = 4$, the loops during the loading cycle to $\mu_\Delta = 4x2$ indicated some problems had occurred in this unit. The lateral loads decreased by 17% and 19% of the maximum values in the positive and the negative loading cycle to $\mu_\Delta = 4x1$, respectively. Besides, the hyeteresis loops in this loading cycle showed apparent pinching. With reference to the crack pattern presented in **Fig. 4.1** and the chart of displacement components in **Fig. 4.4**, it can be concluded that a beam-column joint failure had occurred in this load cycle, causing substantial lateral load drop, loss of stiffness and pinching of the hysteresis loops.

As the test proceeded toward $\mu_\Delta = \pm 6x1$, more pinching of the hysteresis loops, accompanied by significant stiffness degradation, was observed. However, the achieved peak loads at this stage were very similar to the values attained in the previous cycle. In the subsequent loading cycle, $\mu_\Delta = 6x2$, a 33% reduction of lateral load capacity was recorded with continuing stiffness degradation. According to the criteria employed in New Zealand [P1] [S4], this unit failed at this stage and did not satisfy the requirement for ductile components in terms of strength and ductility.

This specimen was displaced further to $\mu_\Delta = 8$. Significant stiffness degradation and loss of lateral load capacity carried on in the loading cycles of $\mu_\Delta = \pm 8$. The test was terminated at this stage because the potentiometers monitoring the beam end deflections were run out of travel.

4.2.4 Decomposition of Lateral Displacements

Figure 4.4 illustrates the components of lateral displacement at each peak of loading run. These components were calculated following the procedure described in Section 3.8 and are presented here as a percentage of the applied lateral displacement.

The flexural deformation of the beams was the main source of lateral displacement during the loading cycles in the elastic range. It contributed to the total lateral displacement from 32% to 46% in elastic loading cycles. Column deformations, calculated from theoretical analysis, contributed from 16% to 19% of the applied lateral displacement. Note that a large error in predicted column deformation is unlikely since the column essentially remained elastic during testing. With reference to **Fig. 4.4**, it can be seen that the closure error is larger in the elastic loading cycles rather than in the inelastic cycle. This can be attributed to the instrumentation used to measure the beam flexure and shear deformations was not distributed throughout the entire span. With plastic deformation occurring in beams, the unaccounted elastic beam flexural deformation became insignificant in inelastic loading cycles. The components of beam-column joint shear distortion in elastic load cycles was 8% to 11%, which appeared to be not yet excessive at this stage.

As the test proceeded into the cycles to $\mu_\Delta = 2$, the component of beam fixed-end rotation became very significant. Beam flexure deformations were still important, though their contribution was less than in the elastic cycles. The remaining component of the lateral displacement was relatively small at this loading stage.

In the load cycle to $\mu_\Delta = 4$, the component of the beam fixed-end rotation was similar to that in the cycles to $\mu_\Delta = 2$. In the cycles beyond $\mu_\Delta = 4x1$, the component of the lateral displacement due to the beam flexural deformation had a notable reduction. Instead, the component of lateral displacement due to the beam-column joint shear distortion became the most important source of deformation in Unit 1. This trend prevailed until the end of the test, where shear deformation in the joint accounted for about 56% - 61% of the total imposed displacement.

4.2.5 Joint Behaviour

4.2.5.1 Strains in the Horizontal Joint Shear Reinforcement

Figures 4.5 and **4.6** show the strains of perimeter R10 hoops and inner R6 ties at the peak of each loading run. It is noted that the values shown were averaged from double strain gauges which were put diametrically opposite on the top and bottom of the reinforcing bars. This layout enables effect of bending of joint hoops to be canceled out. Unfortunately both 1-mm electrical resistance strain gauges placed on the outermost top R6 tie were damaged before commencing the test.

The recorded strains of joint transverse reinforcement show that all hoops and ties exceeded the yield strain once the unit was loaded into $\mu_\Delta = 4$. It can be observed in these figures that, in general, the strain profiles of joint hoops show an arch shape along the height of joint with central hoops reaching larger strains. Those joint hoops and ties close to the top and bottom longitudinal beam bars eventually reached yielding in the final stage of the test.

Yielding of horizontal joint reinforcement justifies the assumption made in the analytical work of using constant pressure on the sides of joints. Also, as mentioned in Section 2.2.2, the entire joint transverse reinforcement eventually yields as long as $V_{sh} < V_{jh}$. However, it is believed two main factors influence the strength degradation of diagonal compressive stress field in the joint. First, the transverse strain of joint, which is governed by the ratio $V_{sh} / V_{jh.}$ Second, the joint shear stress ratio, $v_{jh} / f_c^{'}$. Joints with high $v_{jh} / f_c^{'}$ ratios have more rapid strength degradation than that those with a low $v_{jh} / f_c^{'}$ ratio. It is believed that with the presence of relatively high joint shear stress ratio and column axial load, the provided V_{sh} / V_{jh} in this unit is inadequate. Joint shear failure thus occurred during the test.

4.2.5.2 Joint Shear Distortion

The joint shear distortion versus lateral load is plotted in **Fig. 4.7**. The joint shear distortion was calculated from the readings of two potentiometers diagonally mounted in the joint region in accordance with the procedure described in Section 3.8.3.

The computed joint shear distortion was less than 0.005 radians until the load run to $\mu_\Delta =$ +4x1. During this semi-cycle, the joint shear distortion began to significantly increase. A value of 0.02 radians was reached in the second load cycle to $\mu_\Delta = 4$ and exceeded 0.03 radians in the

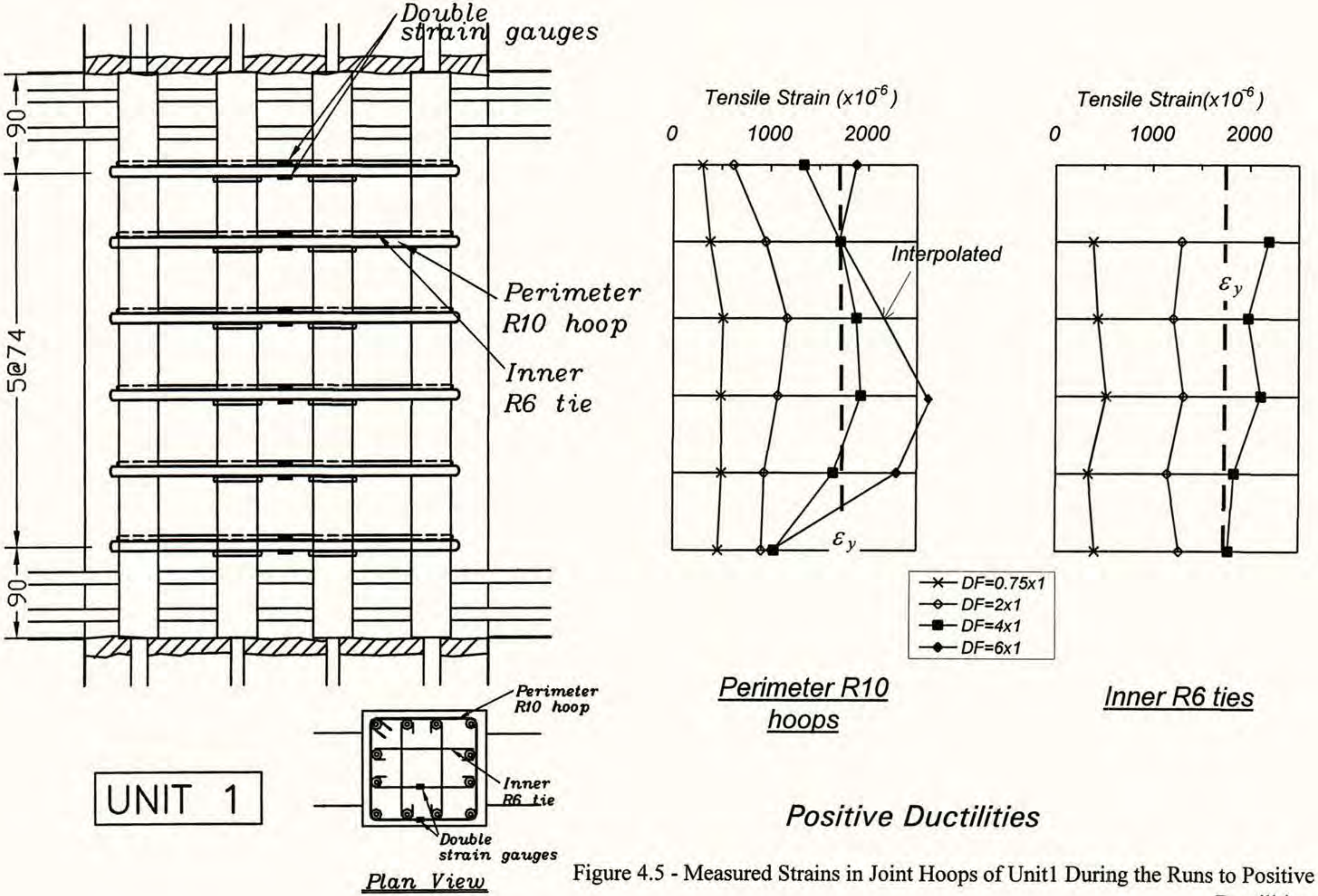

Figure 4.5 - Measured Strains in Joint Hoops of Unit1 During the Runs to Positive Ductilities.

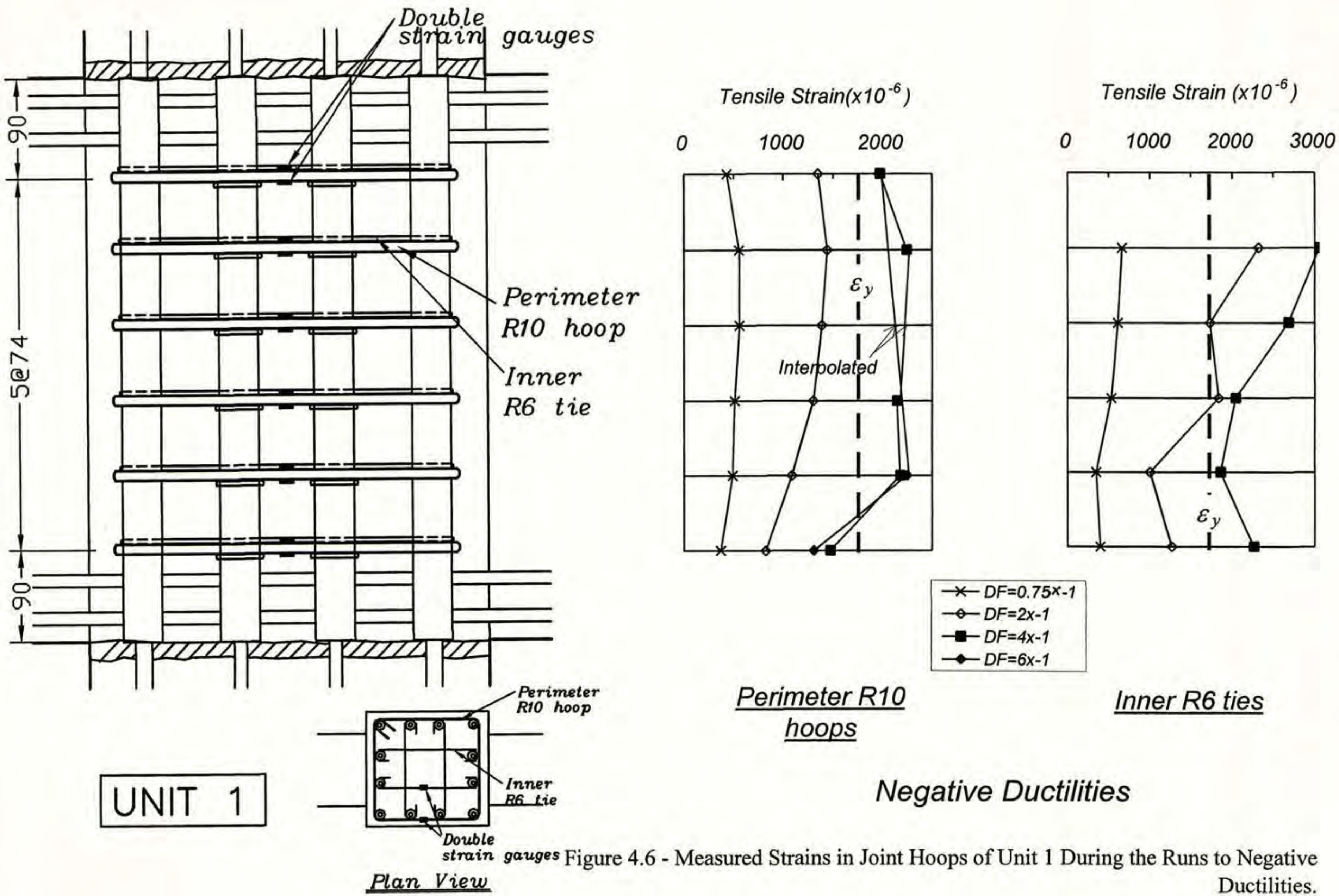

Figure 4.6 - Measured Strains in Joint Hoops of Unit 1 During the Runs to Negative Ductilities.

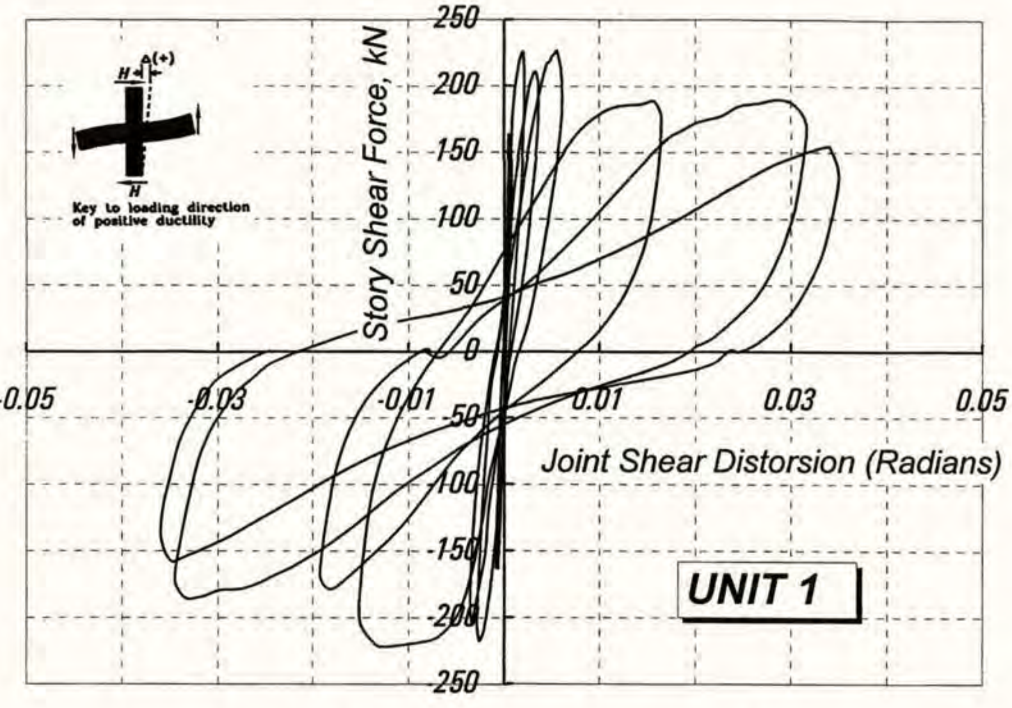

Figure 4.7 - Joint Shear Distorsion Versus Storey Shear Force.

cycle to $\mu_\Delta = 6$.

Obviously the behaviour of the beam-column joint was unsatisfactory, as it did not meet the requirement for ductile components. Excessive joint shear distortion and considerable loss of lateral load capacity took place from the load run to μ_Δ = -4x1. Note that joint failure occurred at this stage, leading to poor energy dissipation and loss of lateral load and ductility capacity, must be precluded.

4.2.5.3 Beam Bar Slip

The local slip of the top and bottom beam reinforcing bars at three locations in joint region is presented in **Fig. 4.8**. Although this method for determining the beam bar slip in the joint region has some limitations, it is believed that the difference between the actual and measured slip is insignificant.

In general, the slip of top and bottom beam bars increased progressively with the test sequence. By comparing the slip of the top and bottom in **Fig. 4.8**, it is evident that the slip of top beam bars is larger than that of the bottom bars due to the " top bar effect " or direction of concrete casting. The maximum slip of top bars reached 7 mm recorded at east location in the load cycle to μ_Δ = -6x1. Meanwhile, the maximum slip of bottom bars reached 5 mm. Note that the maximum slip in the top bars is 7.5 mm, which exceeds the clear distance between the deformations of the HD12 bars, 5.2 mm, indicating local bond stress had deteriorated. However total bond failure did not develop as the measured slip of bars at the column centre line was well below the clear spacing between deformations. Note that total bond failure is defined as the slip of bars measured in the centre of joint region exceeds the clear spacing between bar deformations. The development of a joint failure at μ_Δ = -4x1 precluded total bond failure from occurring as the bond stress decreased at the end of the test.

4.2.5.4 Beam Bar Strains and Bond Stresses in Joint Region

Strain profiles of the two layers of longitudinal beam bars passing through joint region, which were measured from the electrical strain gauges in each peak of loading cycle, are shown in **Figs. 4.9 and 4.10**. **Figure 4.11** shows the bond stresses developed in the top and bottom longitudinal reinforcement, which were calculated from the recorded bar strains. It is noted that strain gauges on beam bars located in the vicinity of column faces are vulnerable to the yield penetration and bar slip in this region. As expected, they were damaged in the early loading cycles. All strain gauge readings were checked to assure reliable data. The general rule to judge the reliability of strain gauge readings was described in Section 3.6.2.4.

In the elastic loading cycles, the tensile strain of the outer layer of beam bars at the column face reached 2000 micro-strain, while the compressive strain on the opposite side was small. The strain profiles of inner layers were smaller than that recorded on outer layers. The peak bond stresses in top and bottom beam bars at this stage was 6 MPa and was reached in the region affected by the column concrete compressive zone. Bond stress decreased toward the tension side.

As the loading sequence progressed into the cycles to μ_Δ = 2, strain profiles of outer and inner layers of beam bars show two distinct trends. First, the compressive strain in the outer layers was small, as expected. Second, the inner layers were subjected to very small compressive strains or even were subjected to tension, suggesting that at this loading stage the neutral axis depth was located very close to the position of the inner layers. The maximum bond

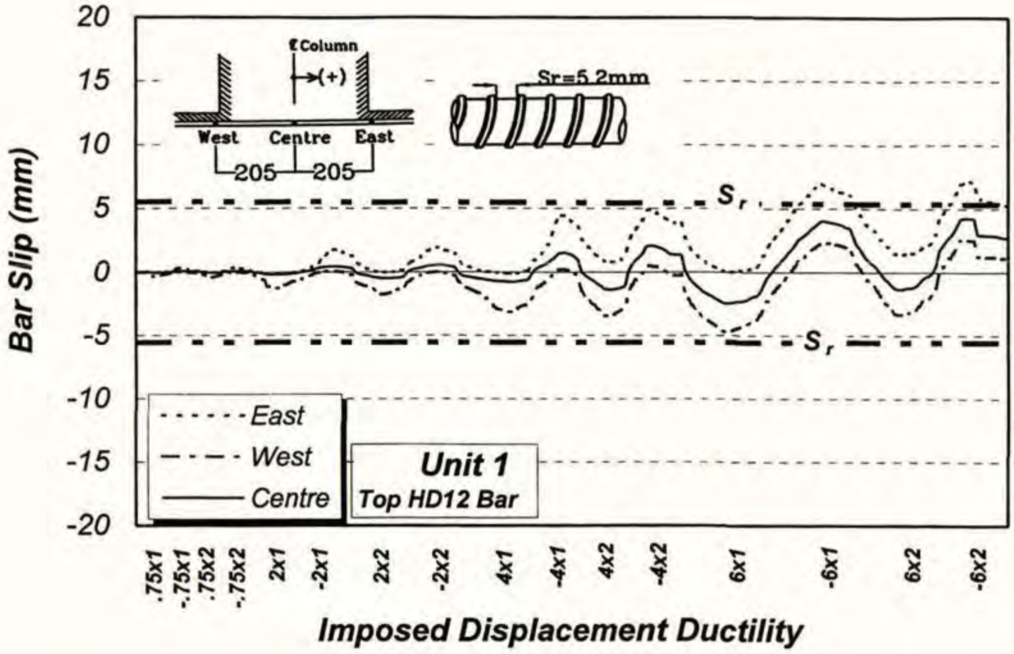

(a) Top Bars

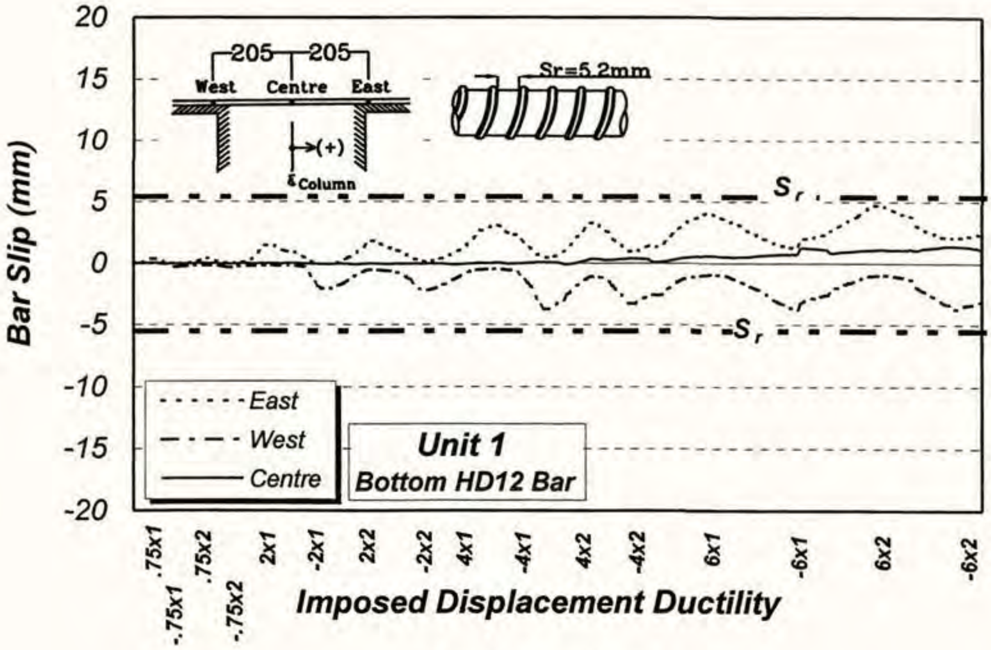

(b) Bottom Bars

Figure 4.8 - Relative Slip of Beam Longitudinal Bars in the Joint Region.

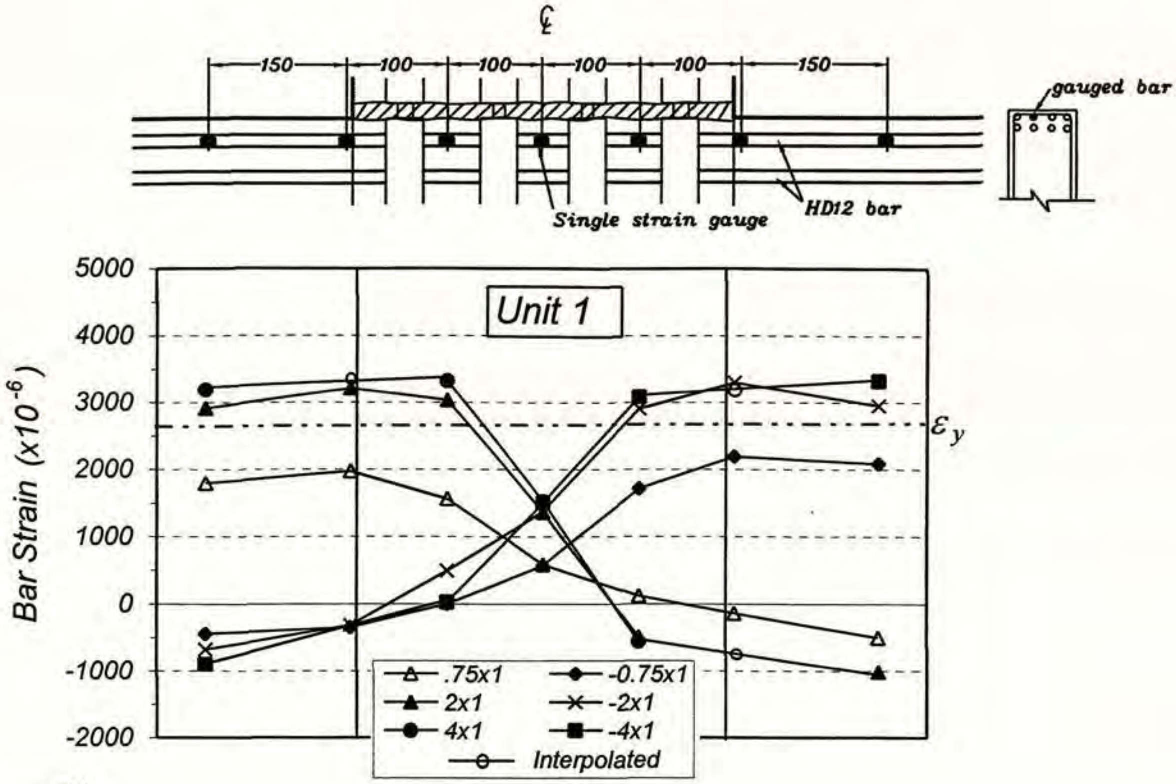

(a) Outer Layer

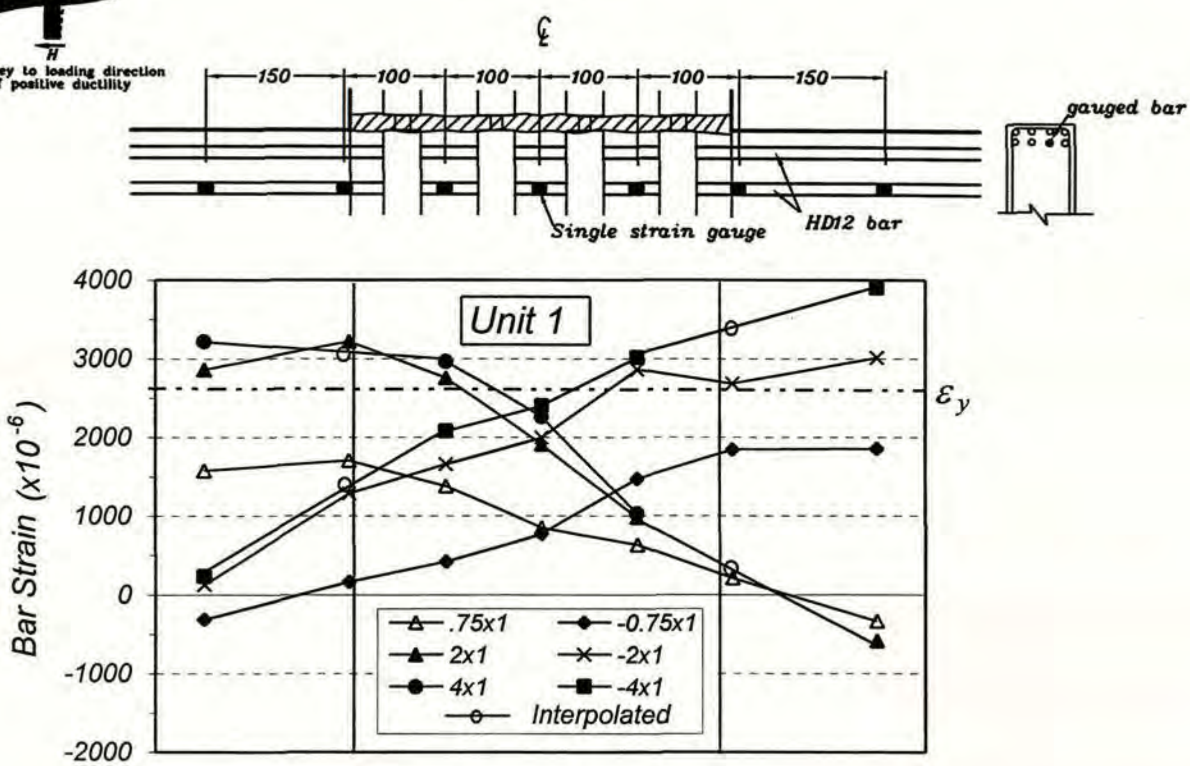

(b) Inner Layer

Figure 4.9 - Top Beam Bar Strain Profiles.

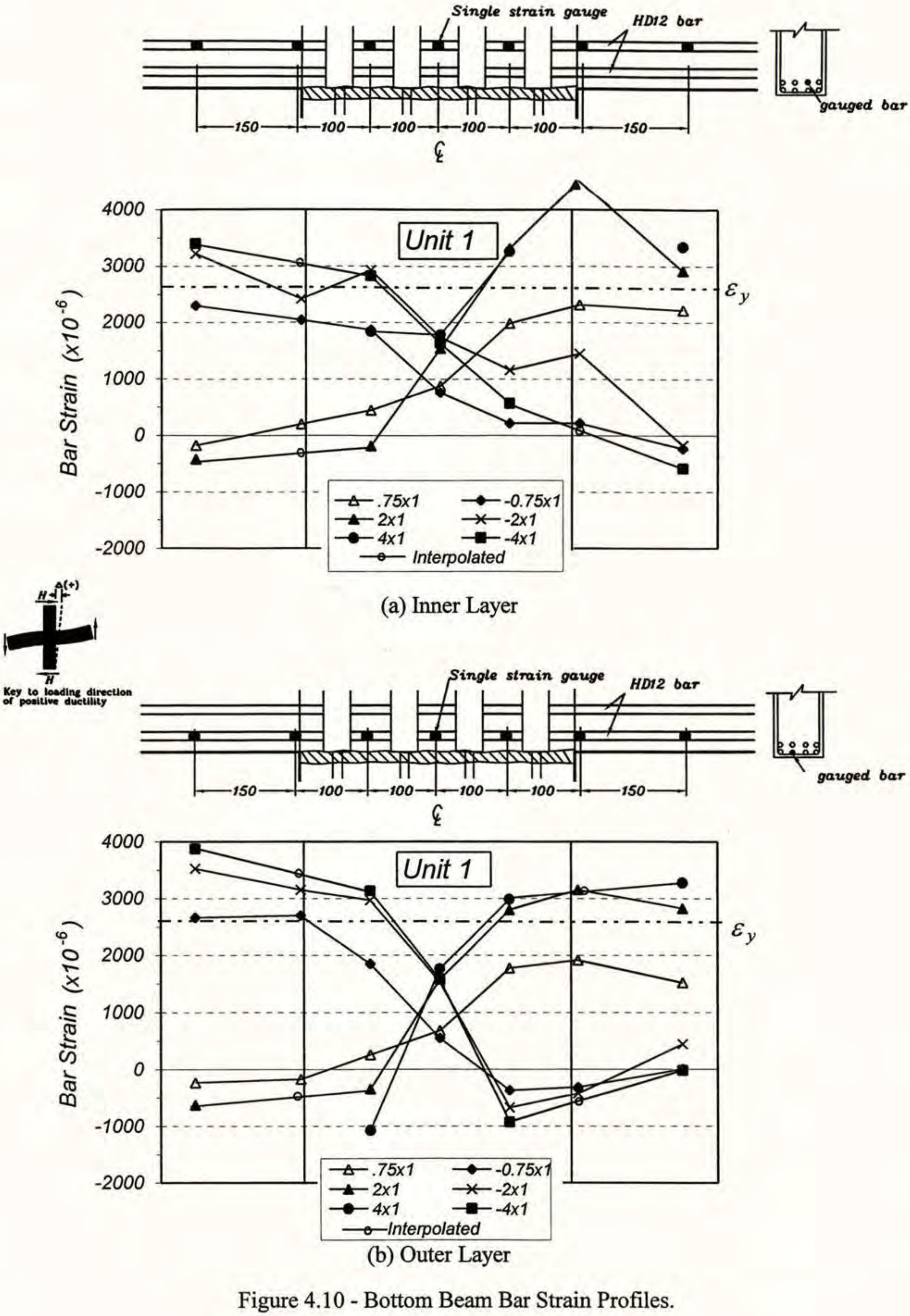

Figure 4.10 - Bottom Beam Bar Strain Profiles.

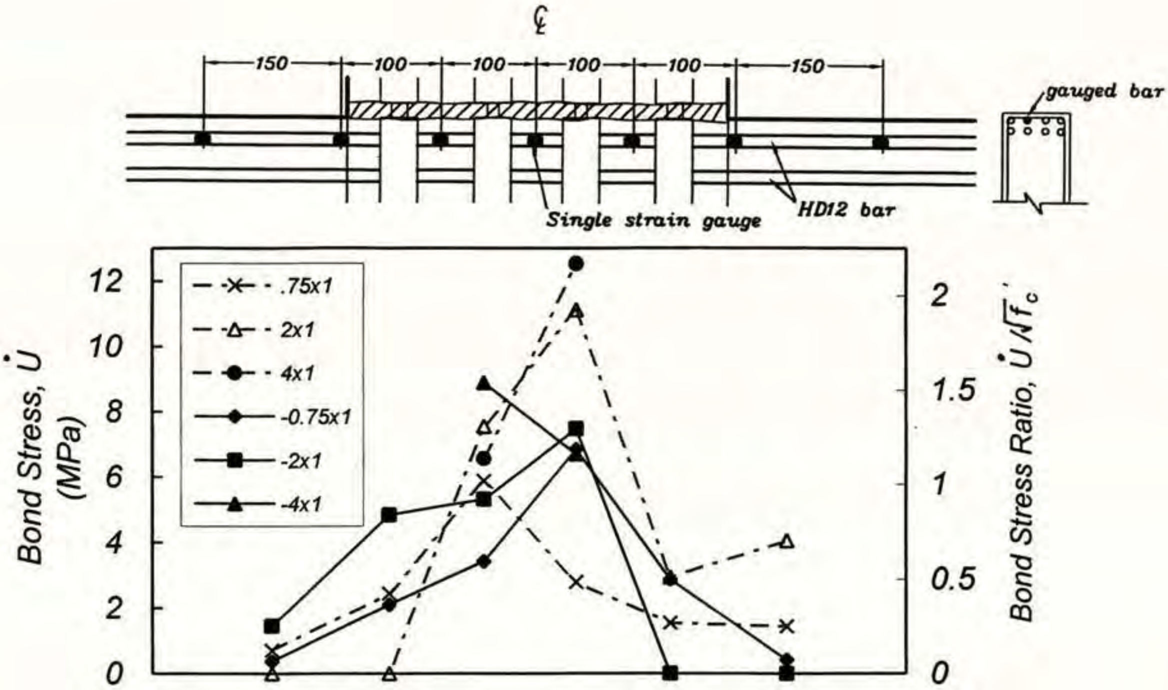

(a) Top Bars

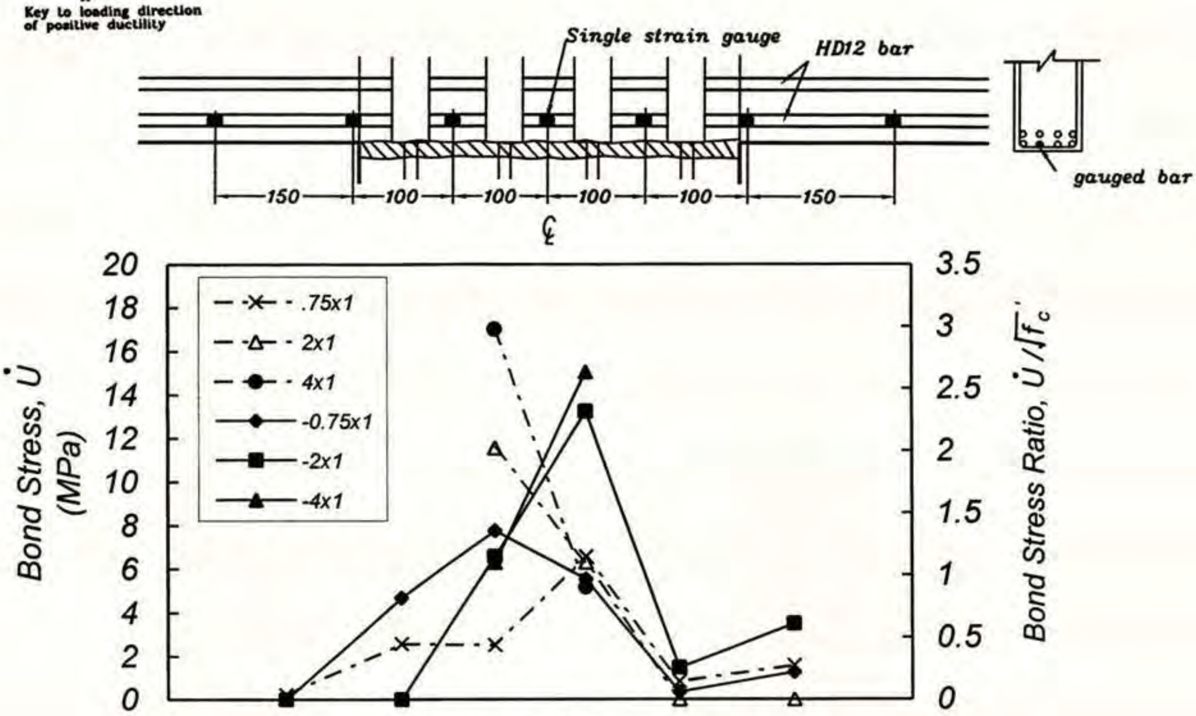

(b) Bottom Bars

Figure 4.11 - Calculated Bond Stresses.

stresses recorded in the outer layers were 11 MPa and 13.5 MPa in the top and bottom bars, respectively. Note that the peak values of bond stresses occurred at a location in the region of column concrete compression zone which shifted in a tendency toward the centre of joint. This is due to the tensile yielding penetration of beam bars subject to cyclic loading. The observed feature of bond stress distribution across the joint core somehow agrees with what was observed in the past by other researchers [P2].

In the load cycles to $\mu_\Delta = 4$, due to gradual damage of the electrical resistance strain gauges, less points used to derive bond stresses became available. The loss of the strain gauges is due to relative bar slip shearing off the wires. However, the maximum bond stresses computed near the centre of joint are 12.5 MPa and 17 MPa, for the top and bottom beam bars respectively. The bond stresses are equivalent to $2.2\sqrt{f_c'}$ and $2.9\sqrt{f_c'}$. It is noted that these recorded values in this unit are close to $2.5\sqrt{f_c'}$, a value that was suggested by Paulay Priestley [P2] for the peak bond stress of longitudinal bars anchored in confined concrete.

Most of the strain gauges attached on the beam bars and embedded in the joint concrete were damaged when the specimen was loaded toward $\mu_\Delta = 6$. Nevertheless, since the lateral load capacity dropped significantly due to the development of joint failure, it is believed that the strains and bond stresses of beam bars were reduced at this stage.

4.2.5.5 Bar Stresses of the Column Vertical Reinforcement Within Joint Region

Longitudinal column bar strains within beam-column joint region were measured using electrical resistance strain gauges. Strains on exterior and interior column bars recorded at each peak load have been converted into bar stresses and are presented in **Fig. 4.12**. It can be observed in this figure that, due to the significant axial load exerted on the column section, exterior column bars were subject to compression within the full height of the joint in the early stages, with stress profiles showing a linear distribution across the joint height. As the load sequence progressed, the compressive stress at the location of beam face rose while the stress on the other face began to get into tension with a maximum compressive stress on column exterior bars reaching 400 MPa. Besides, stress profiles are no longer linear distributed. The rapid change of stress of exterior column bars within joint centre region indicates that maximum bond stress occurred there. This agrees with the trend shown in the strut-and-tie model analysis depicted in Chapter 2.

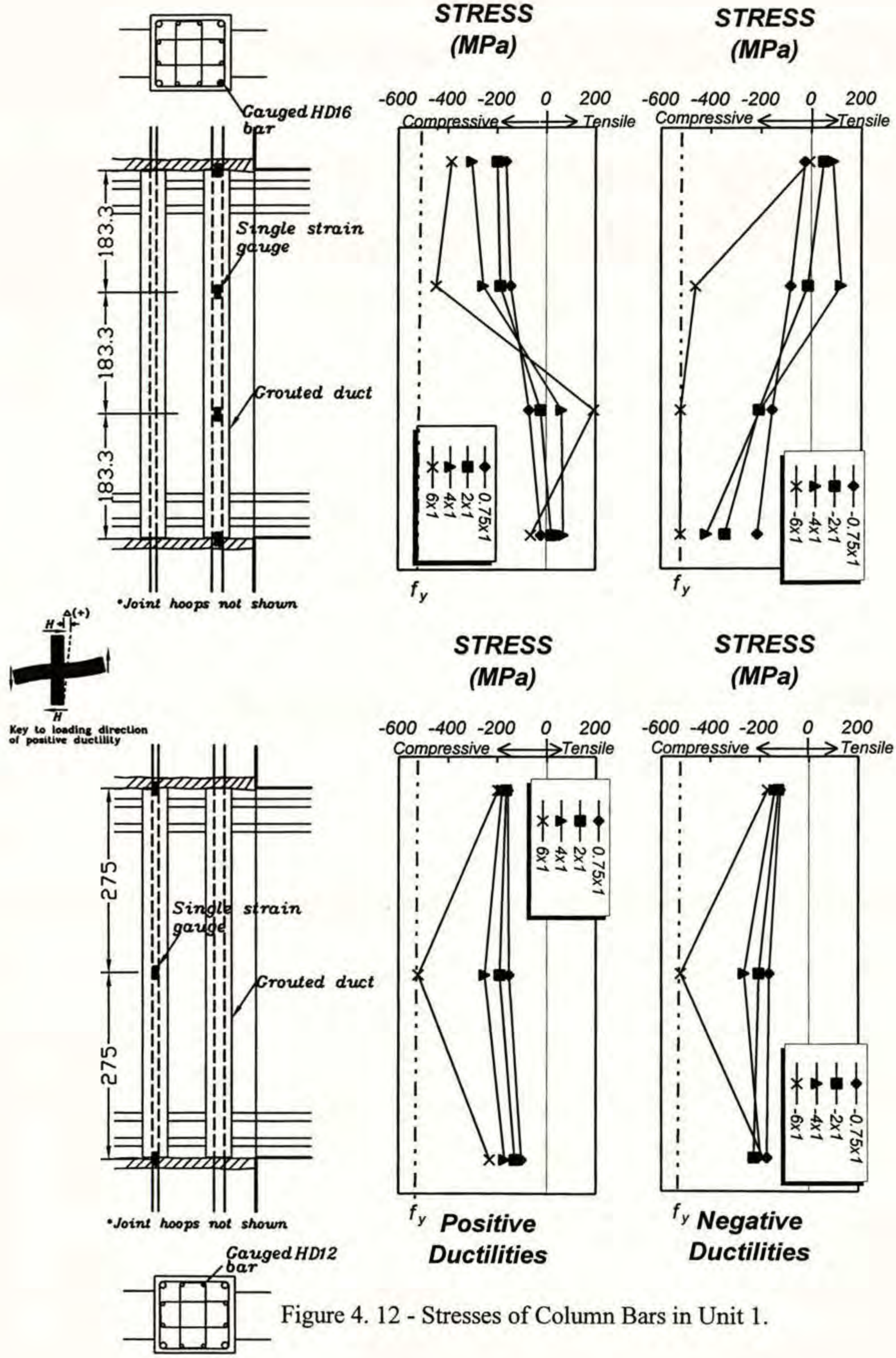

Figure 4. 12 - Stresses of Column Bars in Unit 1.

The stress on interior column bars showed uniform distribution crossing the joint region while no tensile stress was developed. With load sequence progressing toward larger displacement ductilities, the middle portion of the interior column bars was compressed further reaching a compressive stress of 300 MPa. Perhaps due to the axial shortening of the joint when the concrete core began to crush. The stress on the top and bottom end of the gauged interior bar remained essentially unchanged. The observed trends justify the assumption made in the theoretical work of having no intermediate nodes in these bars, unless required for equilibrium.

4.2.6 Beam Behaviour

4.2.6.1 Curvature Ductility Factors in Plastic Hinge

The beam curvature ductility factors presented in **Fig. 4.13** were calculated from the readings of the second pair of linear potentiometers mounted on beams closest to the column face. The gauge length was 150 mm. The yield curvature was obtained based on the same procedure described in Section 3.7 for calculating the yield displacement of a beam column assembly. It can be seen in **Fig. 4.13** that the curvature ductility factors so found showed a considerable scatter. The maximum value was only 6. The low values are partially due to the large beam fixed-end rotation, which accounted for a significant component of the applied

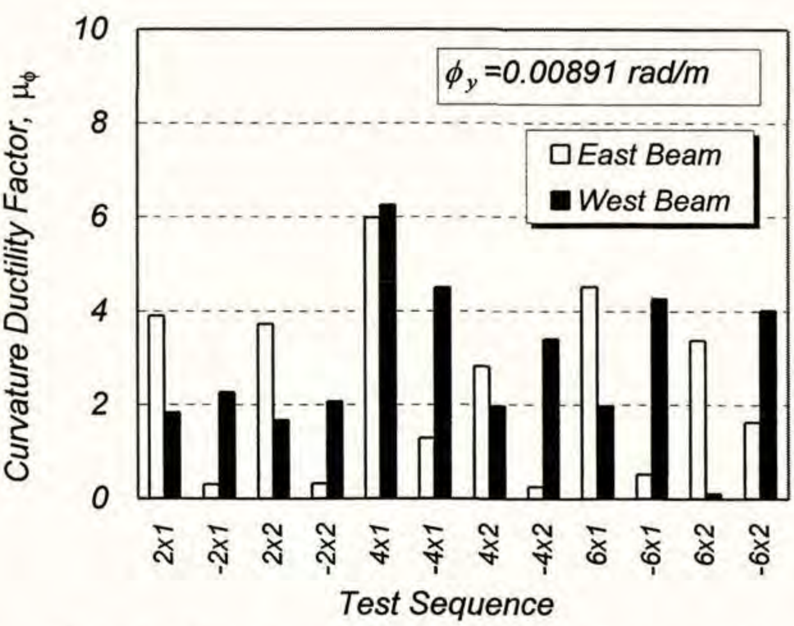

Figure 4.13 - Curvature Ductility Factors of Beam of Unit 1.

lateral displacement (see **Fig. 4.4**). Note also that in the second cycles to a given displacement ductility, there is a reduced demand for curvature ductility in the beams as other sources of displacement increase their contribution, particularly the joint shear distortion.

4.2.6.2 Beam Strain Profiles at the Level of the Longitudinal Reinforcement

Since the electrical strain gauges attached on the longitudinal beam bars are not able to provide reliable readings at large displacement ductility levels, it is of interest to investigate the average strain of longitudinal beam bars estimated from the linear potentiometers mounted along the beam chords. The method adopted here to calculate the beam strain profiles at the level of the longitudinal reinforcement was described in Section 3.6.2.4.

Figures 4.14 and **4.15** depict the train profiles at the level of top and bottom beam longitudinal reinforcement. The tensile strain measured near the column face at the level of outer layer of the top beam bars reached 2.5% in the load run to μ_Δ = +4x1. Note that, in the load runs to μ_Δ = ±6x1, the tensile strain of top and bottom beam bars was smaller than in the load runs to μ_Δ = +4x1. This is because joint failure had occurred and joint shear distortion controlled the lateral displacement of the unit.

4.2.6.3 Beam Elongation

The measured beam elongation against the storey shear is depicted in **Fig. 4.16**. In the elastic cycles, some residual elongation was recorded when the lateral load was released back to zero. This is mainly due to the imperfect closure of flexural cracks. The elongation shown in **Fig. 4.16** includes both beams.

The beam elongation increased rapidly when the specimen was loaded into the inelastic range. There was a feature of the measured beam elongation, which has also been observed by others [Rl], that beam elongation mainly takes place in the first loading cycle to a new displacement ductility. That is the beam did not lengthen in the second loading cycle of the same displacement ductility. Beam elongation accumulated during the cycles when there was a flexurally dominated response. In the final stages of the test beyond μ_Δ = 4, the joint shear distortion began to govern the response of the unit and consequently no further elongation was observed. The recorded maximum beam elongation of this unit was 15 mm at the end of test. This elongation is equal to 2.7 % of the beam depth.

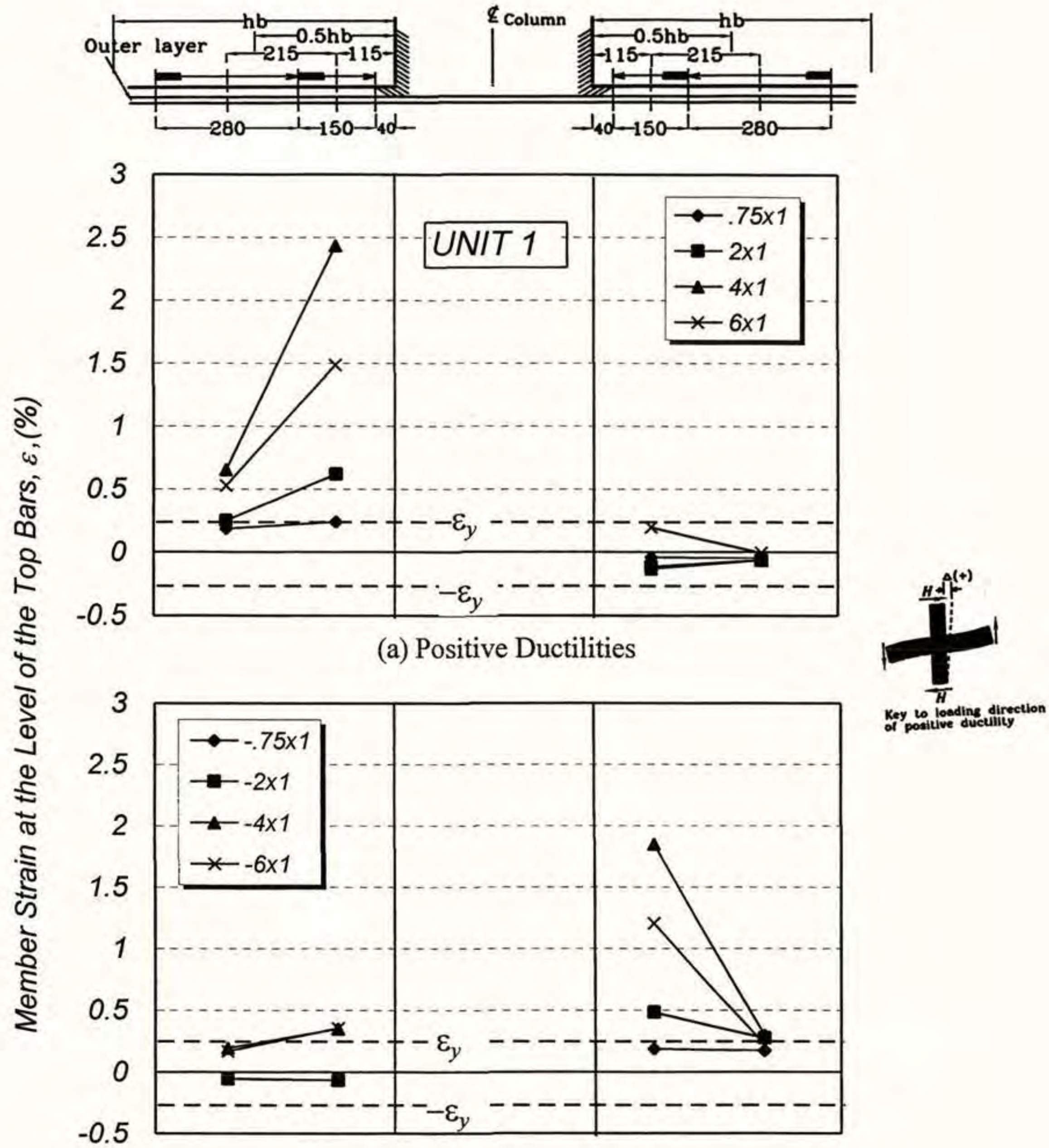

(a) Positive Ductilities

(b) Negative Ductilities

Figure 4.14 - Beam Strain Profiles at the Level of the Outer Layer of the Top Beam Bars of Unit 1.

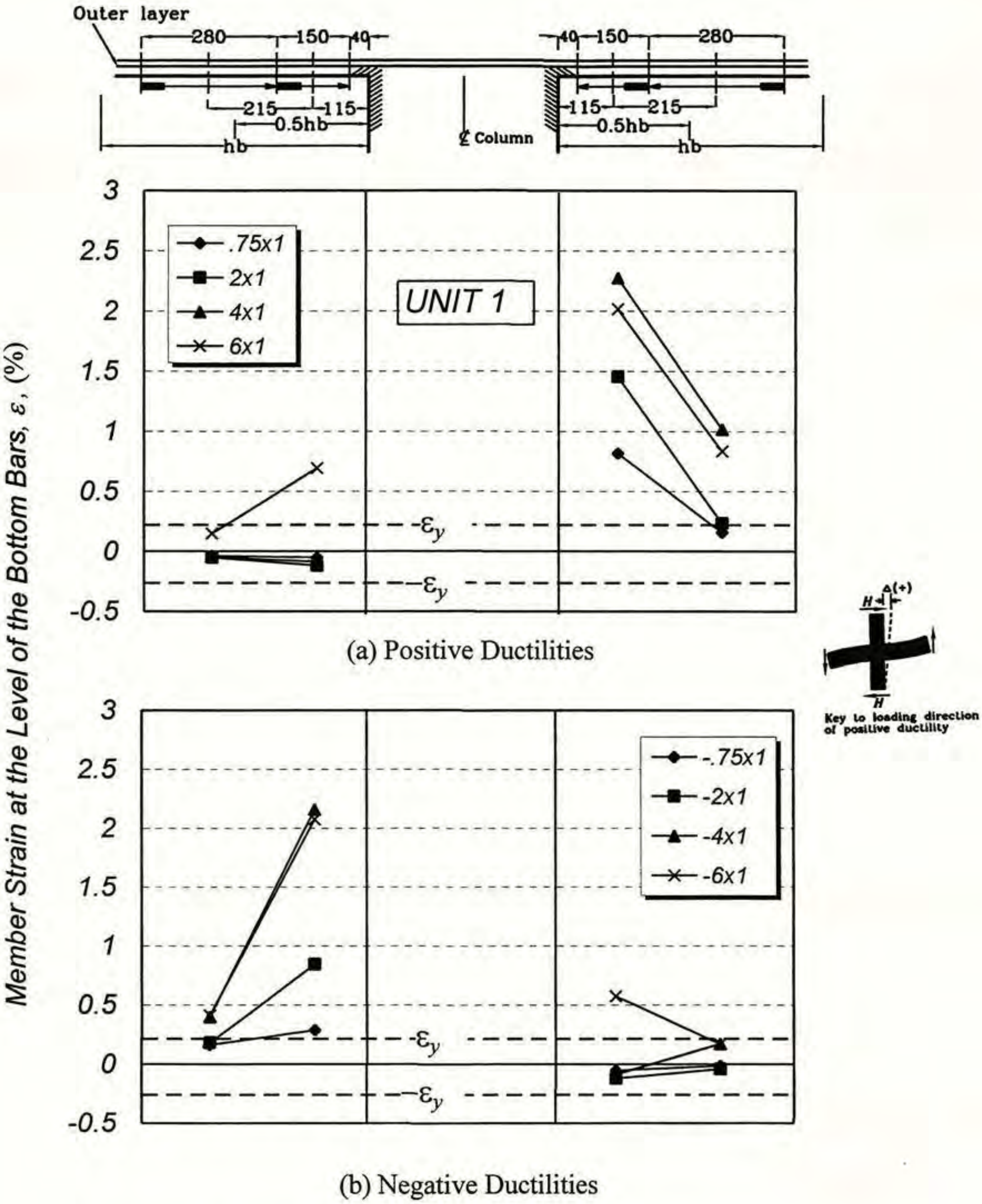

Figure 4.15 - Beam Strain Profiles at the Level of the Outer Layer of the Bottom Beam Bars of Unit 1.

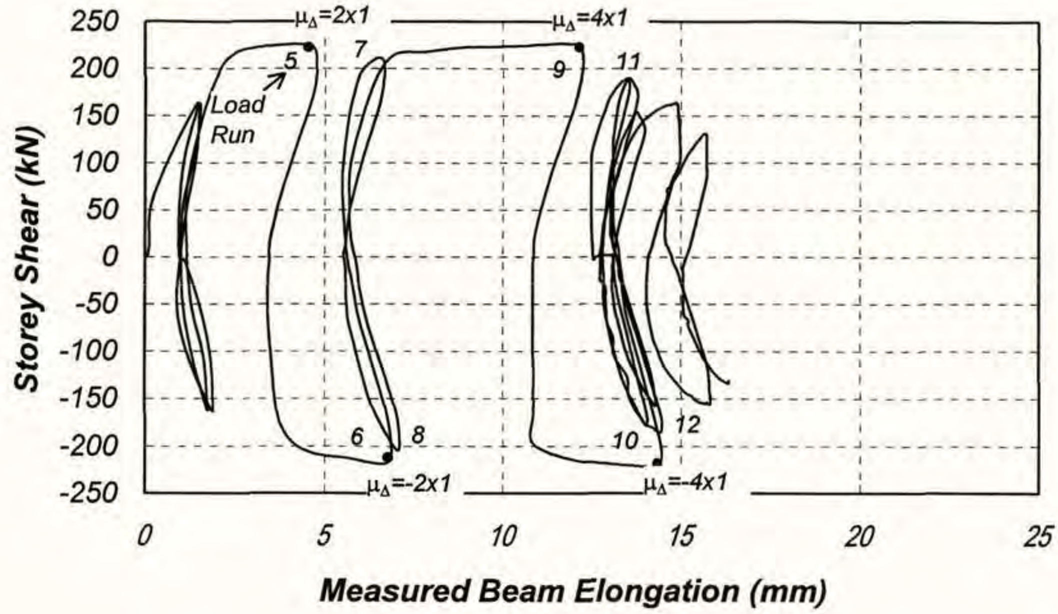

Figure 4.16 - Beam Elongation of Unit 1.

4.2.7 Column Behaviour

As described in Section 4.2.2, very few cracks occurred in columns, which indicated that columns remained elastic during the test. This can also be verified by observing the figures presented in Section 4.2.5.5. in which the stress profiles of column bars are shown.

4.3 UNIT 2

4.3.1 General

The quantity of joint transverse reinforcement of Unit 2 was designed according to the analytical model for a target axial compressive force of $0.4f_c'A_g$ and relatively high joint shear stress ratio, $v_{jh} = 0.19f_c'$. This quantity resulted in 9 sets of perimeter R10 hoops plus R6 cross ties provided in joint region, see **Fig. 4.20**. Comparisons of quantity of horizontal joint reinforcement required by code [S1] and the analytical model and the provided values for Units 1 and 2 could be referred to Table 3.2.

As the concrete compressive strength of precast beams is the same as that of Unit 1, the applied column compressive load in this unit was also increased to $0.43f_c'A_g$ when conducting the test.

4.3.2 General Behaviour

The overall behaviour of this unit was satisfactory in terms of the performance criteria used in New Zealand for components of ductile frames. Some incipient damage to the concrete in the joint panel was observed to occur at the end of test. In the cycle to $\mu_\Delta = 6x1$, bond failure of the top beam bars occurred induce pinching of the hysteresis loops in the subsequent cycles.

The crack pattern at different peak of loading run and the lateral load-displacement response are shown in **Figs. 4.16** and **4.17**, respectively.

In the load-controlled cycles, crack pattern on the beams and the columns was very similar to what was observed in Unit 1. The unsymmetrical developing of cracking along the top and bottom chords of the beams was also observed in this unit. The first crack in the joint panel appeared in the first positive load run to 75% of theoretical ultimate load. More cracks in the joint panel occurred in the second load controlled cycle. Compared with Unit 1, the cracks in the joint of this unit were fewer and shorter. Like those in Unit 1, they also occurred in the vicinity of column intermediate bars as well and were less than 0.1 mm wide.

As the test sequence proceeded into the loading cycle to $\mu_\Delta = 2x1$, two main cracks formed in the beams at column faces. Few other cracks developed in the beams in the region of high bending moment. The two main cracks reached a width of 1.5 mm measured on the extreme tensile fibre and grew to 2.5 mm in the reversed cycle. The remaining crack widths in the beams did not exceed 0.1 mm. Cracking in columns was very limited and showed a pattern similar to that of Unit 1 as it can be seen by comparing **Figs 4.1(b)** and **4.17(b)**. In the joint region, more short and hairline fine cracks progressively occurred, mainly located in the vicinity of the column interior bars.

When Unit 2 was loaded into loading cycle to $\mu_\Delta = 4x1$, diagonal cracks in the expected beam plastic hinge region of the beam grew wider, reaching 2.0 mm while the two main cracks opening along the column faces had a width of 3.5 mm. In the reversed load run, flexural-diagonal cracks in the plastic hinge region continually grew wider to a width of 3.5 mm. Flexural-diagonal cracks initiating from the top and bottom chords of the beams merged. It was evident that plastic hinge had formed in the beams at this stage. The crack pattern in joint panel changed slightly with very few new cracks occurring. A couple of cracks in the joint close to the beam faces extended into the column slightly. However, all of the cracks in joint panel remained fine without any sign of widening, indicating that the joint strength and deformation were well controlled.

In the second load cycle to $\mu_\Delta = 4$, diagonal cracks in the beams grew progressively. The cracks opening along column faces, reaching a maximum width of 5.0 mm. It was observed that some grid lines draw on the beam plastic hinge region were offset due to the diagonal cracks crossing them, indicating that some shear deformation in this region had occurred (see **Fig 4.17(d)**). In the second load cycle to of $\mu_\Delta = 4$, some cover concrete in the locality where diagonal cracks merged was dislodged. This was a sign to indicate that once diagonal cracks which propagating upward and downward merged, cracks were likely to be opened wider. The shear transferring capacity of concrete in plastic hinge region dropped as a consequence of less effective aggregate interlock. Until this stage, plastic hinges in the beams were well developed.

As the test proceeded toward $\mu_\Delta = 6x1$, slip of top beam bars occurred prior to reaching the peak load, causing a sudden bumpy shape of lateral load-displacement response. Furthermore, the cover concrete around the top two corners of joint panel was crushed and spalled off. It is evident that the top beam bars had slipped through the joint region but were anchored on the opposite beam. This suggests that the compression steel on the section adjacent to the column faces could significantly lose its compressive stress or, even worse, be subjected to tension. The consequence was that excessive compressive stress on concrete compressive region of beam sections on column faces was induced, causing crushing of the concrete in the vicinity of highly compressed corner. In the reverse load cycle, $\mu_\Delta = -6x1$, a large gap appeared on the column face and propagated through almost the full depth of west beam. The crack widths elsewhere in the west beam decreased, indicting that fixed-end rotation was the main source of the lateral displacement of this beam with flexural and shear deformation of beam diminishing. In the mean time, cracks in east beam showed different pattern. The main crack opening on the column face initiating from the bottom chord of the east beam did not widen any further, keeping a width of 4 mm, while flexural and diagonal cracks in plastic hinge region became slightly wider. The concrete in compressive region of the east beam located 100 mm away from column face was dislodged. This phenomena indicated that bond deterioration of top beam bars spread into the beam region. According to the above description, it is apparent that, despite the significant slip of top beam bars, the bottom bars were still adequately anchored in the joint region, causing unsymmetrical deformation characteristics of east and west beams.

In the subsequent cycles to $\mu_\Delta = 6$ (see **Figs. 4.17(e)** and **(f)**), the crushed concrete in the vicinity of top corners of the joint spread into the beams further. Incipient crushing of the cover concrete on the bottom chord of the beams at the column faces was observed, indicating that bond of bottom beam bars in joint region had started to deteriorate. Also the main cracks in the bottom chord of the beams at the column faces reached a width of 5 mm. At this stage, a little, and incipient damage on joint concrete was observed.

This specimen was displaced further toward $\mu_\Delta = 8$. The concrete on the bottom corners of beam section adjacent to column faces started to be damaged, revealing that slip of bottom beam bars occurred as well. Some sliding shear deformation on the critical sections was believed to occur since some bending deformation can be observed on the exposed longitudinal beam bars in the vicinity of the main cracks. The bond break-down on both the top and bottom beam bars limited the input shear force in the joint so that damage in joint region was no longer expected.

4.3.3 Load-Displacement Response

The lateral load-displacement response of Unit 2 is shown in **Fig. 4.18**. Measured yield drift of this specimen is 0.66 % of the storey height, which is very close to the value recorded in Unit 1. This yield drift level implies a displacement ductility factor $\mu_\Delta = 3.8$ when the 2.5% drift limit imposed by the Loading Standard [S3] is attained.

In the first load cycle to $\mu_\Delta = 2$, the lateral load reached the theoretical ultimate value in both positive and negative load runs.

The hysteresis loops were stable in the load cycles leading to $\mu_\Delta = 4$, which corresponds to a storey drift ratio of 2.6%. In the first cycle to this ductility level the lateral load exceeded the theoretical value in both load directions. At the peak of $\mu_\Delta = -4x1$, the lateral load exceeded the theoretical value by 8.3%, indicating that little strain hardening on longitudinal steel might start to develop. The response in the cycle that followed was significantly different from that observed in Unit 1. This is because the peak lateral loads exceeded the theoretical value in both

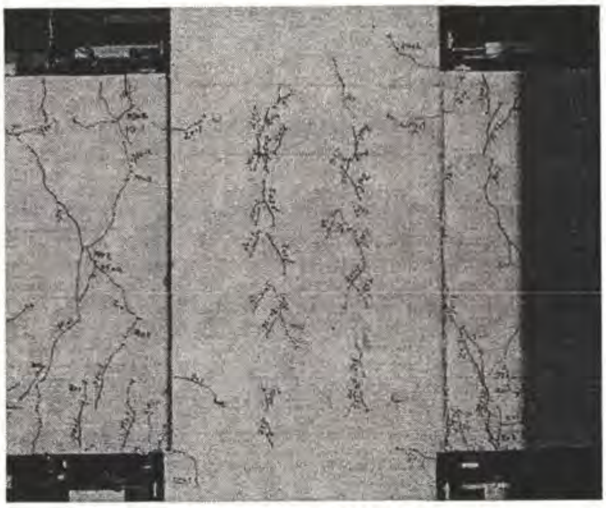

(a) At μ_Δ=-2x1

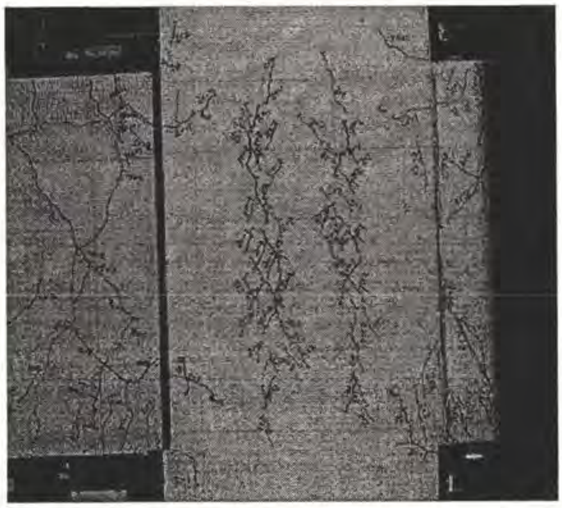

(b) At μ_Δ=-2x2

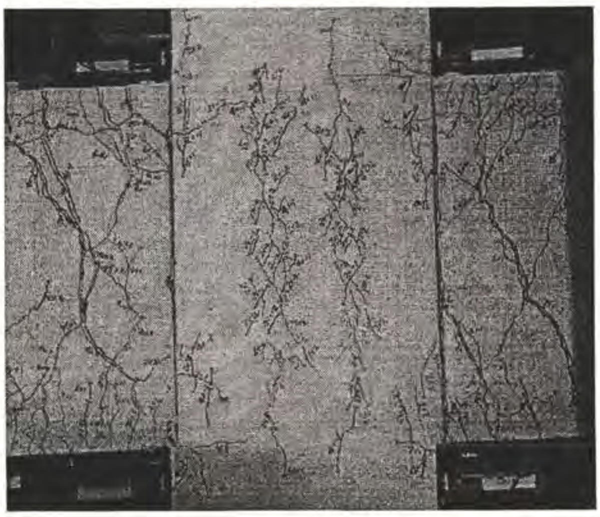

(c) At μ_Δ=-4x1

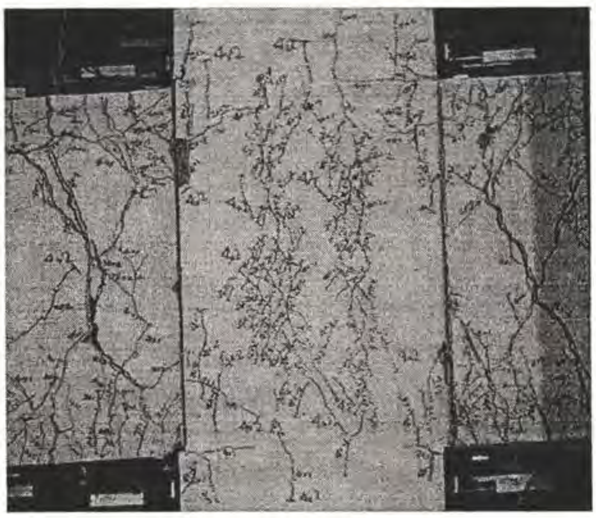

(d) At μ_Δ=-4x2

Figure 4.17 - Cracking of Unit 2 at Different Stages During the Test.

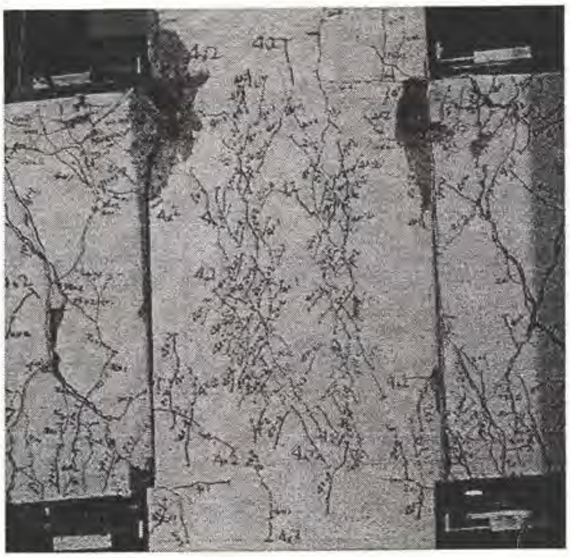

(e) At μ_Δ=-6x1

(f) At μ_Δ=-6x2

Figure 4.17(Contd.) - Cracking of Unit 2 at Different Stages During the Test.

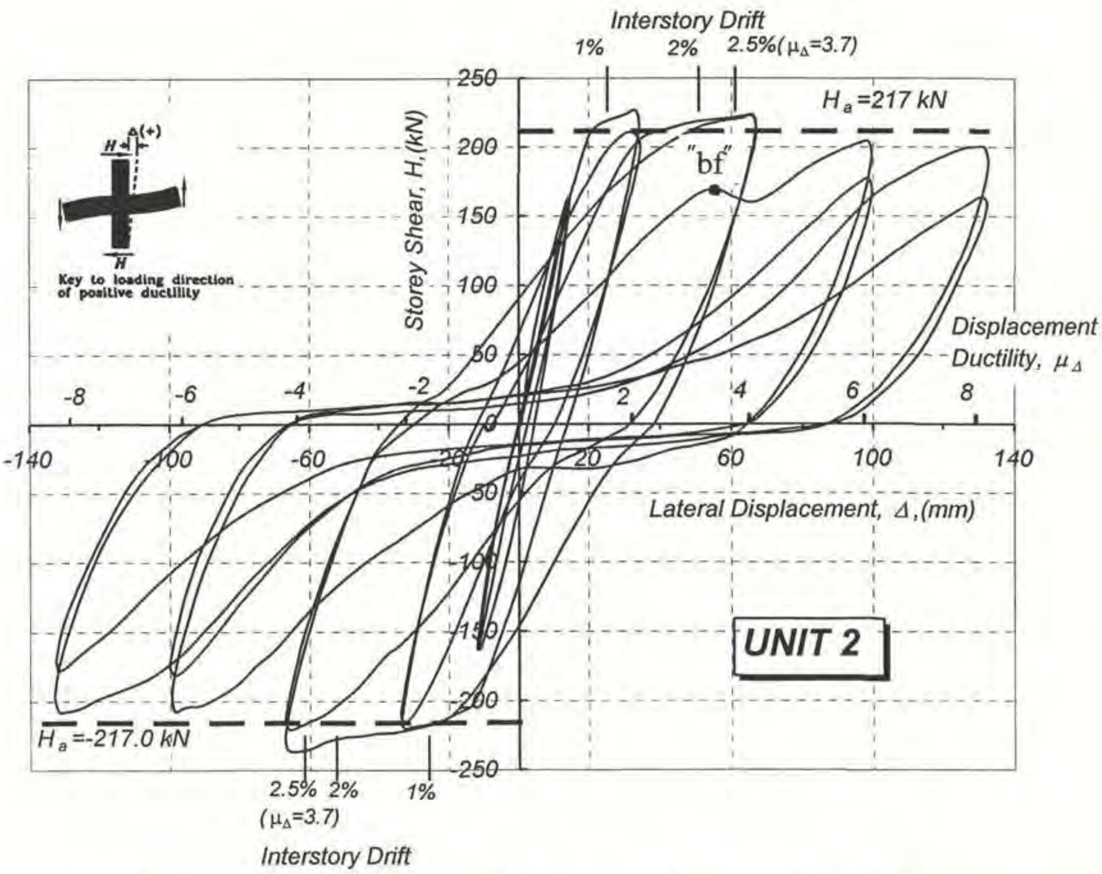

Figure 4.18 - Lateral Load-Displacement Response of Unit 2.

load directions. Slightly pinching of the hysteresis loops was observed at this stage. It is believed that pinching was mainly caused by the closure of cracks in the beam plastic hinge regions.

In the load run to μ_Δ = 6x1, a sudden load drop occurred prior to reaching the target displacement, see **Fig. 4.18**. Then, the lateral load capacity picked up subsequently when the specimen was displaced further. However, the peak load achieved in this load cycle dropped below the theoretical value by 6%. It is believed that significant bond break down of top beam bars occurred in the load run, causing a distortion on the load-response curve and, ultimately, some drop of lateral load capacity.

In the loading run to μ_Δ = 6x2, significant pinching of hysteresis loops and stiffness degradation occurred. The lateral load capacity dropped in the positive and negative load runs respectively by 18% and 17% with respect to the measured maximum value.

When Unit 2 was displaced further to μ_Δ = 8, the lateral load reached a peak value of 89%, and 87% of the maximum measured load in the positive and negative load runs respectively. These load levels are similar to those observed in the loading runs to μ_Δ = 6x1. This is a typical feature of the lateral load-displacement response of beam-column joint assembly in which bond slip had occurred in the joint region. Note that the drop of lateral load capacity in the second load cycle with the same displacement ductility factor was mainly resulted from stiffness degradation which can be gained back once the specimen was displaced further.

This unit met the criteria [P1] [S4] employed in New Zealand for ductile components both in ductility and strength. The satisfactory performance of this unit justifies the adequate design of beam-column joint transverse reinforcement in this unit.

It may probably be argued that the significant stiffness degradation occurring after the bond slip of top beam bars may not satisfy the capacity design principle adopted in New ~~Zealand, owing that the bond~~ failure in beam-column joint was not precluded. Nevertheless, it should be noted that in this beam-column joint assembly, in which G500 steel was incorporated, a displacement ductility factor of 6 corresponds to a storey drift of 3.9%, which is beyond the code specified limit of 2.5 % for failure [S3]. At this storey drift, the structure was obviously in the Survival State, in which the stiffness degradation and beyond repair are no longer necessary to be concerned.

4.3.4 Decomposition of Lateral Displacements

Figure 4.19 depicts the components of lateral displacement of Unit 2 at the peak of each load run. These components were calculated based on the procedure described in Section 3.8.

In the elastic cycles, the beam flexural deformation was the main source of the lateral displacement, ranging between 28 and 41%. Fixed-end rotation had a 17% contribution in the elastic loading cycles. Note that the closure error in elastic stage was larger than that in cycles beyond the elastic range. It is believed that part of the error was due to elastic flexural beam deformation, since the instrumentation in beams using to measure the curvature of beam sections were not distributed through the whole length of beams.

In the inelastic load cycles up to μ_Δ = -4x2, the fixed-end rotation contributed by 32 to 41% of the total applied displacement while the beam flexural deformation was similar to that in the elastic cycles. The contribution of the beam-column joint shear was below 13%, indicating that, unlike in Unit 1, shear distortion was small. Contribution to the displacement from the shear deformation in the beams reached a maximum value of 16%.

By μ_Δ = 6, considerable fixed-end rotation occurred as a consequence of slippage of the top beam bars. As a result 49 and 71 % of the applied displacement were due to this source of deformation in the in the loading runs to μ_Δ = 6x1 and -6x2, respectively. The component of displacement due to beam-column joint distortion did not increase anymore. In fact, it decreased slightly to a value of 10%.

4.3.5 Joint Behaviour

4.3.5.1 Strains in the Horizontal Joint Shear Reinforcement

The strains obtained from the average of double strain gauges attached on the perimeter R10 hoops and inner R6 ties at the peak of each loading cycle are presented in **Figs. 4.20** and **4.21**. In general, the arch shape of the strain profiles along the height of the joint was more obvious at large ductility cycles. At the peak of the load cycle to μ_Δ = 4x1 and μ_Δ = -4x1, most of the joint hoops, including the perimeter R10 and inner R6, approached the yield strain except for the top and bottom sets. However, the unrestricted yielding did not occur, as the

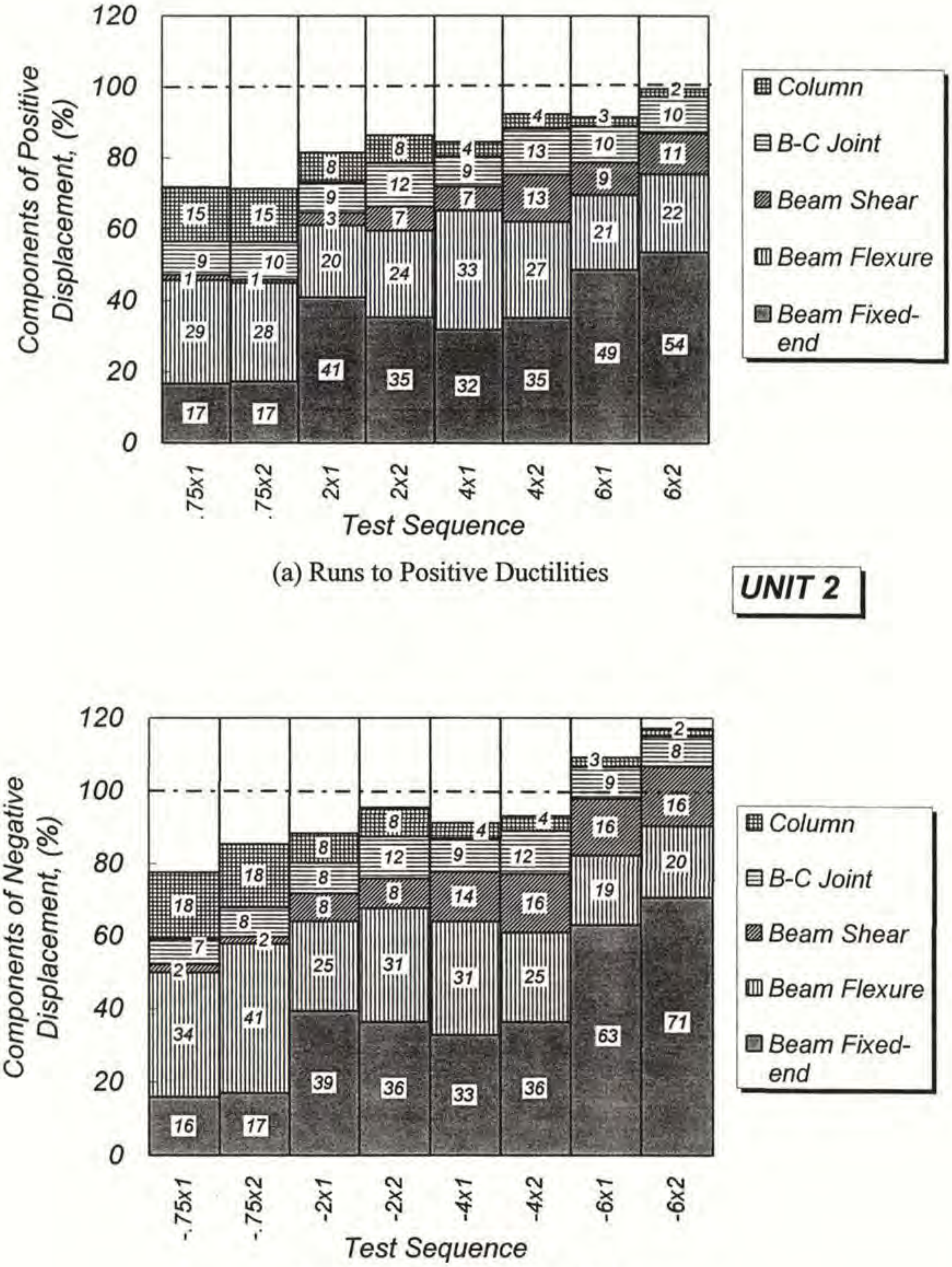

(a) Runs to Positive Ductilities

UNIT 2

(b) Runs to Negative Ductilities

Figure 4.19 - Components of Lateral Displacement of Unit 2
at Peaks of Load Runs.

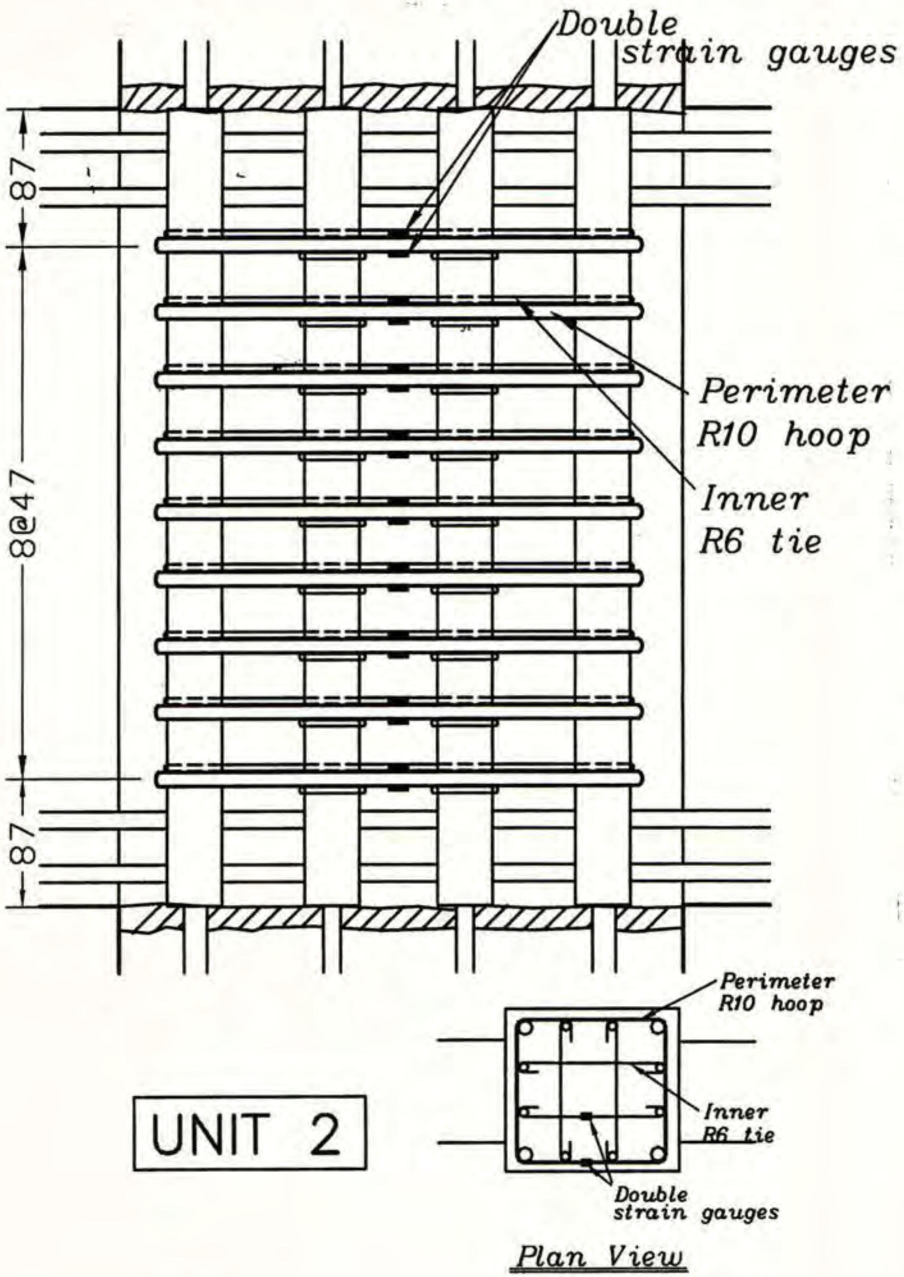

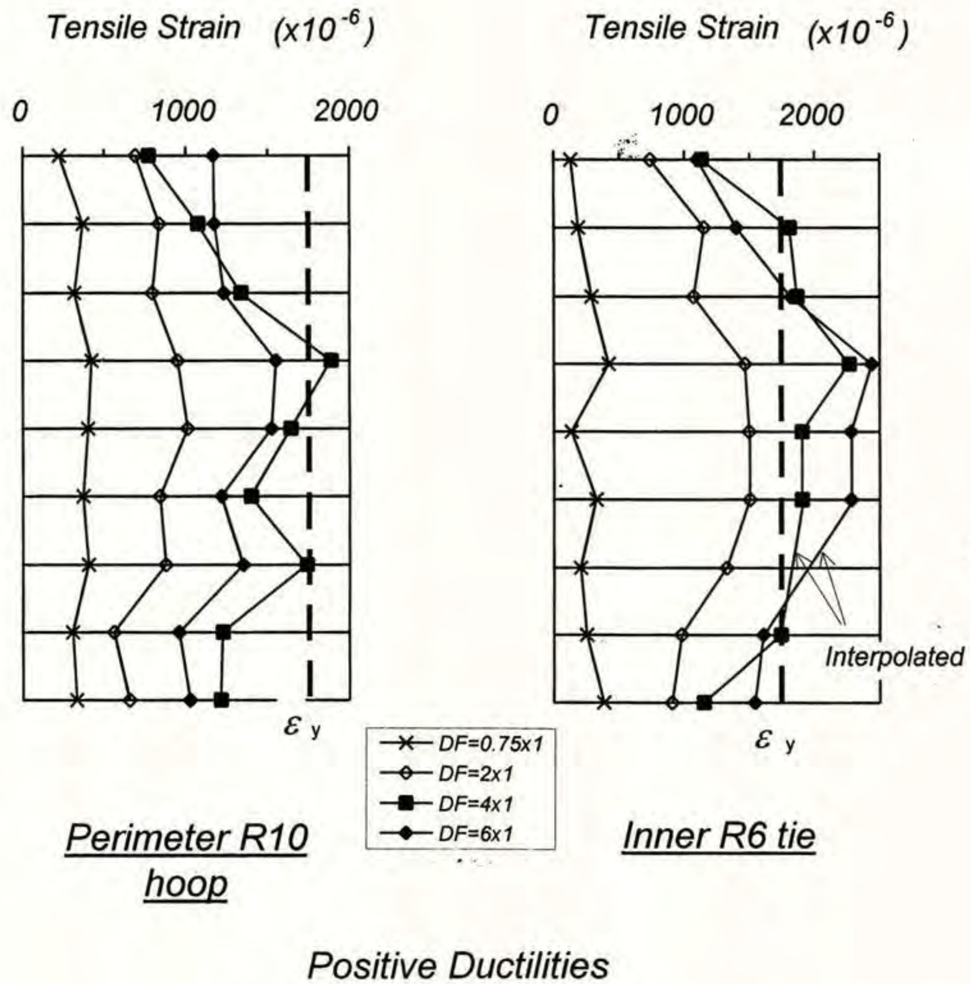

Figure 4.20 - Measured Strains in Joint Hoops of Unit 2 During the Runs to Positive Ductilities.

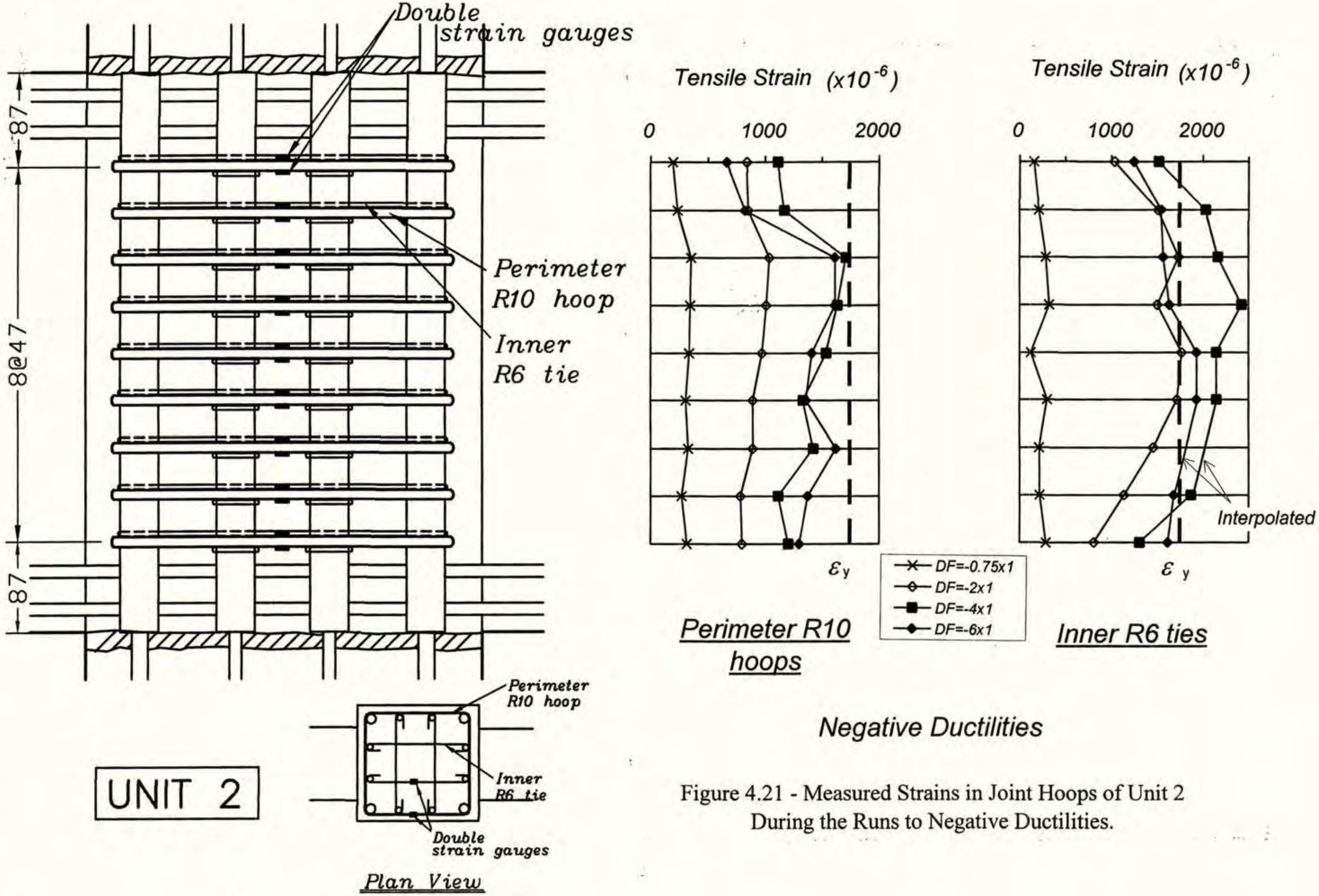

Figure 4.21 - Measured Strains in Joint Hoops of Unit 2
During the Runs to Negative Ductilities.

strain in the transverse reinforcement did not develop much further beyond the yield strain in the subsequent cycles. In general, the inner R6 ties approached larger strains, especially those sets placed in the middle portion of the joint region.

Comparing the strain profiles of Units 1 and 2 (see **Figs. 4.5, 4.6, 4.20**, and **4.21**), the transverse joint reinforcement in Unit 2 yielded at a latter stage. As mentioned in Section 4.2.5.1, the strength of beam-column joints is sensitive to not only the ratio v_{jh} / f_c' but also on the strain in the transverse direction. It is evident that, the provided quantity of joint shear reinforcement in Unit 2 is appropriate for the ratio v_{jh} / f_c' so that rapid strength degradation of joint can be prevented.

4.3.5.2 Joint Shear Distortion

Figure 4.22 shows the measured joint shear distortion plotted against the storey shear force. It can be seen in this figure that the maximum joint shear distortion reached a value slightly beyond 0.005 at the end of load cycle of μ_Δ = 6x2, indicating that joint shear deformation was well controlled. With reference to the **Fig. 4.19**, it is noted that the joint shear distortion contribution to the lateral displacement reached a maximum value of 13% during the

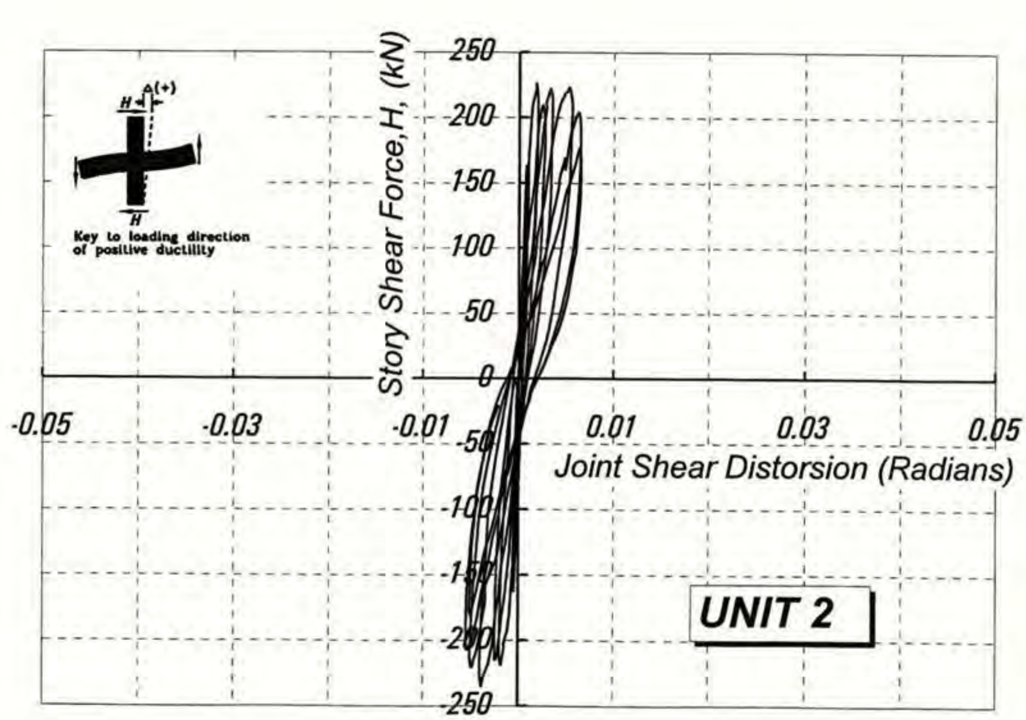

Figure 4.22- Joint Shear Distorsion Versus Storey Shear Force.

test. This percentage is less than the 20% limit, which was suggested for well-designed joint [C1].

4.3.5.3 Beam Bar Slip

Figure 4.23 depicts the local bar slip of the top and bottom beam bars at three locations in the joint region. Again the " top bar effect " is reflected in the measurement of bar slip of top and bottom bars. The slip of the bottom bars measured at three locations was always less than 5 mm during the test. In contrast, the slip of the top bars at the column centreline exceeded the clear spacing between deformation in the HD12 bars of 5.2 mm in the load run to $\mu_\Delta = 6x1$. As a result, significant loss of bond of top beam bars occurred in this load cycle. The total bond failure is defined in this study as the bar slip at column centreline exceeds the clear space between deformations in the bars. Because once the bar slip exceeded the space between deformations in the bars at the column centreline, the concrete surrounding the ribs will be crushed and significant loss of bond will occur [R1]. Note that the dot marked as " bf " in **Fig. 4.23(a)** indicates the total bond failure of top bars occurred half way of load cycle to $\mu_\Delta = 6x1$. This agrees with another " bf " dot marked in **Fig. 4.18** which also located about half way during the load cycle to $\mu_\Delta = 6x1$. Unlike the top bars, the anchorage of bottom bars within joint region behaved satisfactorily during the test without significant deterioration.

4.3.5.4 Bar Strain And Bond Stress of the Beam Longitudinal Reinforcement Passing Through Joint Region

Figures 4.24 and **4.25** present the strain profiles of the longitudinal beam bars passing through the joint. The bond stresses developed in the longitudinal reinforcement are plotted in **Fig. 4.26**. Note that data recorded after the loading cycles of $\mu_\Delta = 6$ were discarded since most of the strain gauges were damaged at that stage.

In general, the strain profiles along longitudinal beam bars follow the similar trends as in Unit 1. The peak values of bond stress of beam bars within joint region calculated from the measured strains are very close to what were recorded in Unit 1 in magnitude. A peak value of 12 and 16 MPa, which are equivalent to 2.1 and $2.8\sqrt{f_c'}$, were recorded in the loading cycles of $\mu_\Delta = 4$ on the top and bottom beam bars respectively.

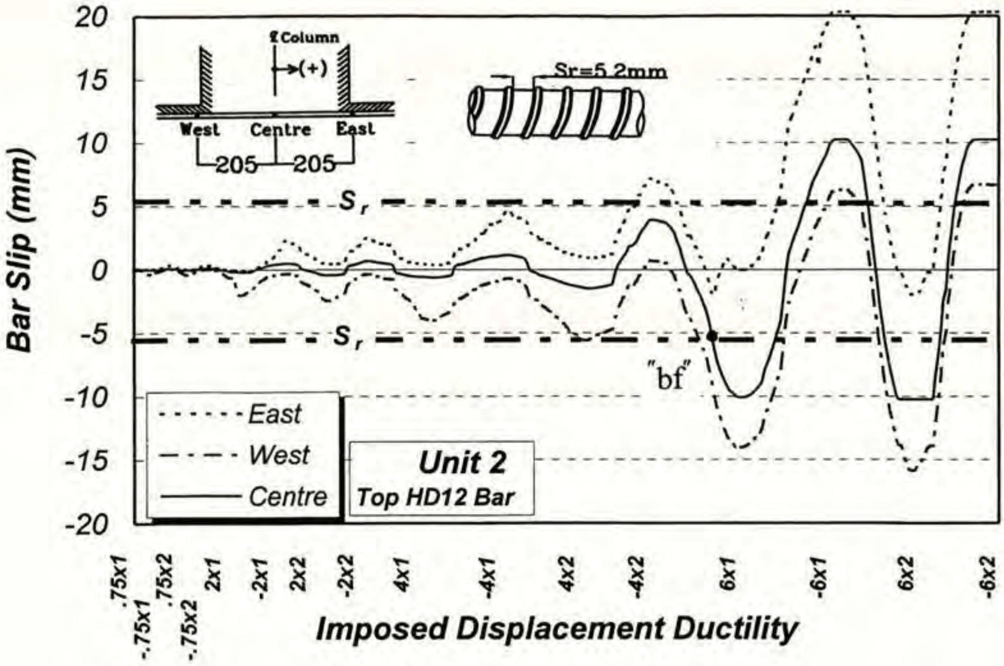

(a) Top Bars

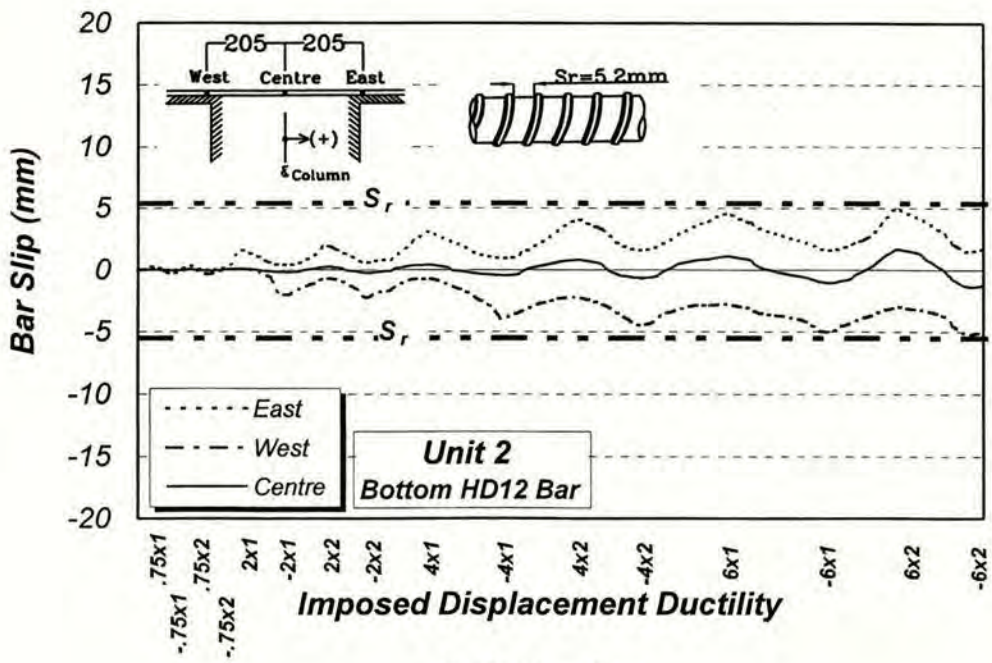

(b) Bottom Bars

Figure 4.23 - Relative Slip of Beam Longitudinal Bars in the Joint Region.

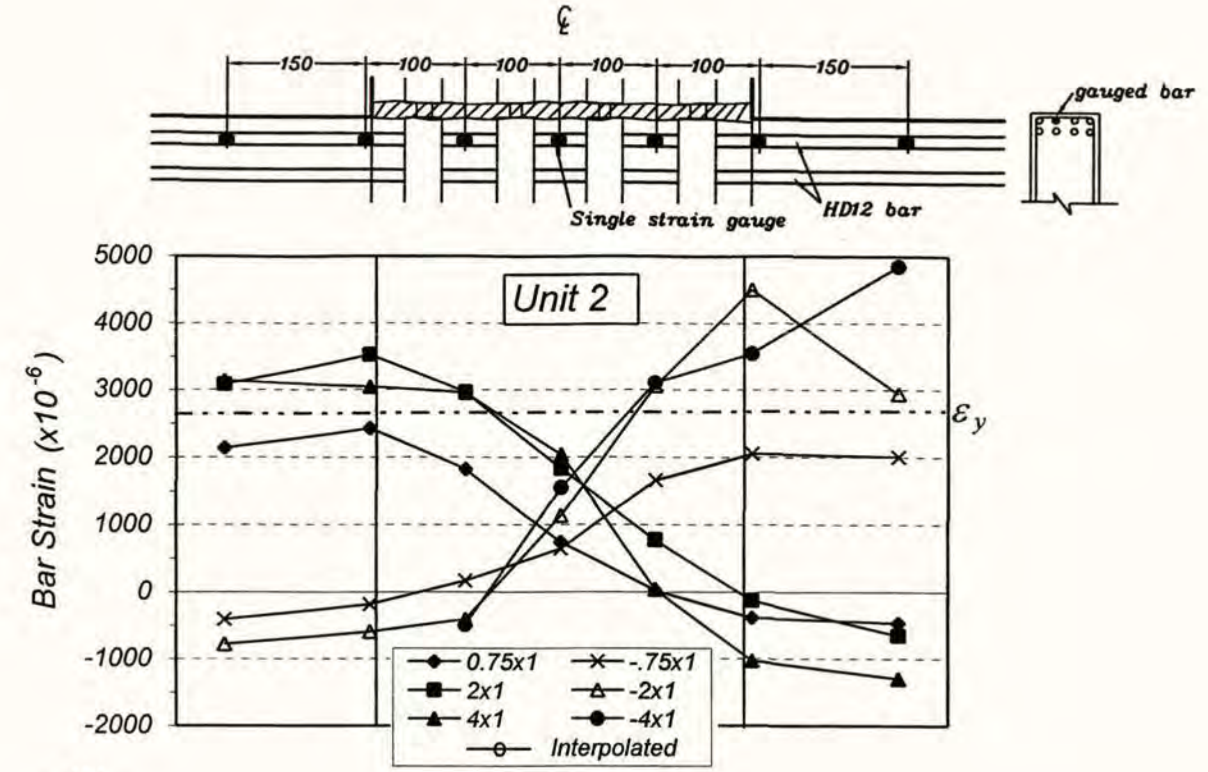

(a) Outer Layer

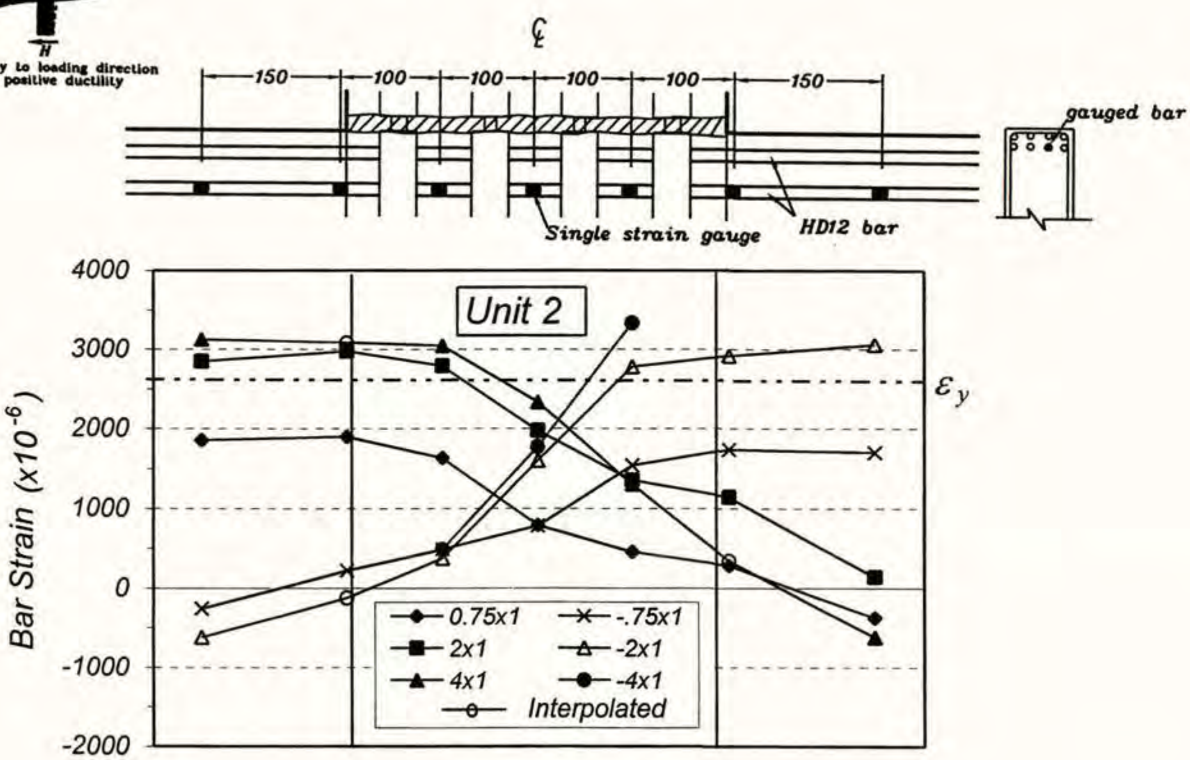

(b) Inner Layer

Figure 4.24 - Top Beam Bar Strain Profiles.

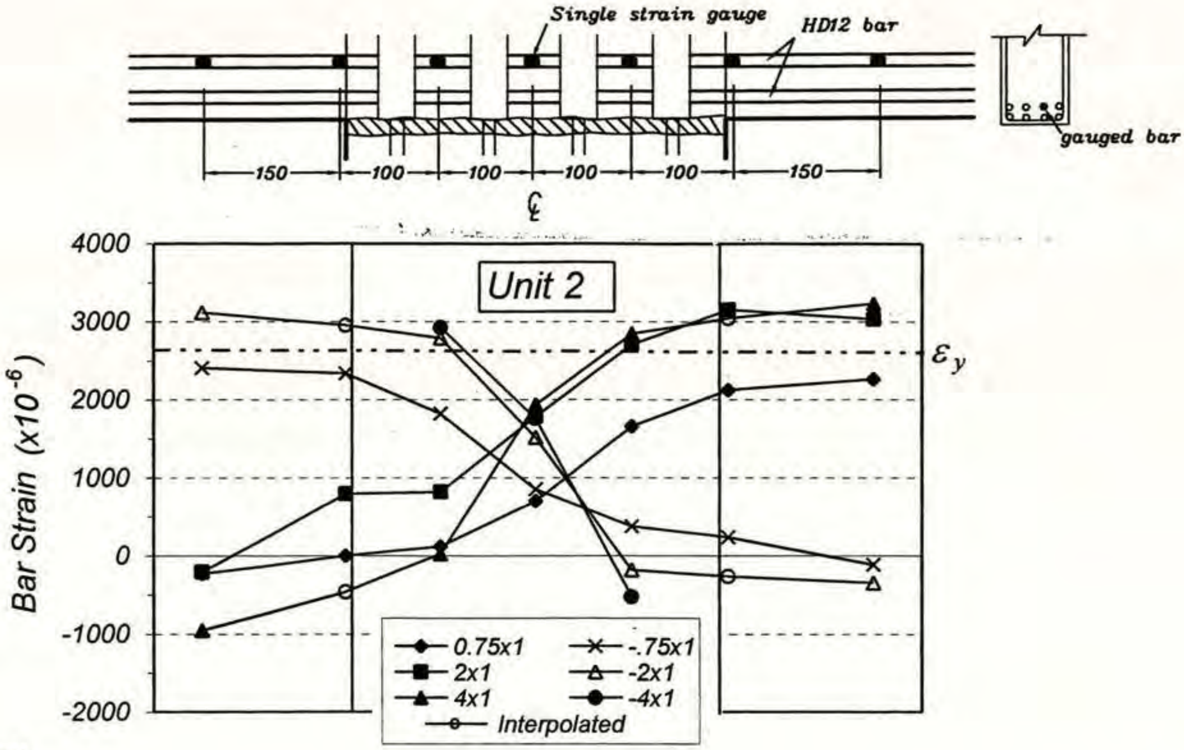

(a) Inner Layer

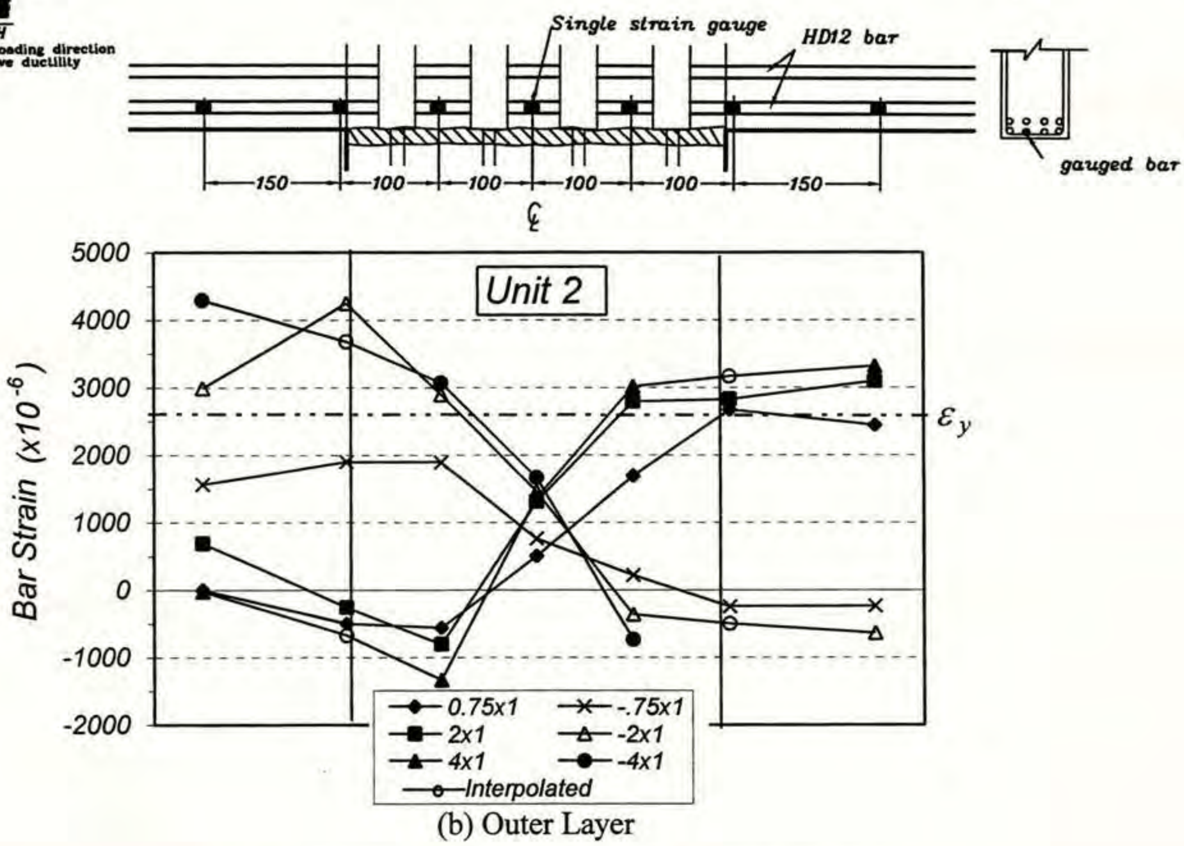

(b) Outer Layer

Figure 4.25 - Bottom Beam Bar Strain Profiles.

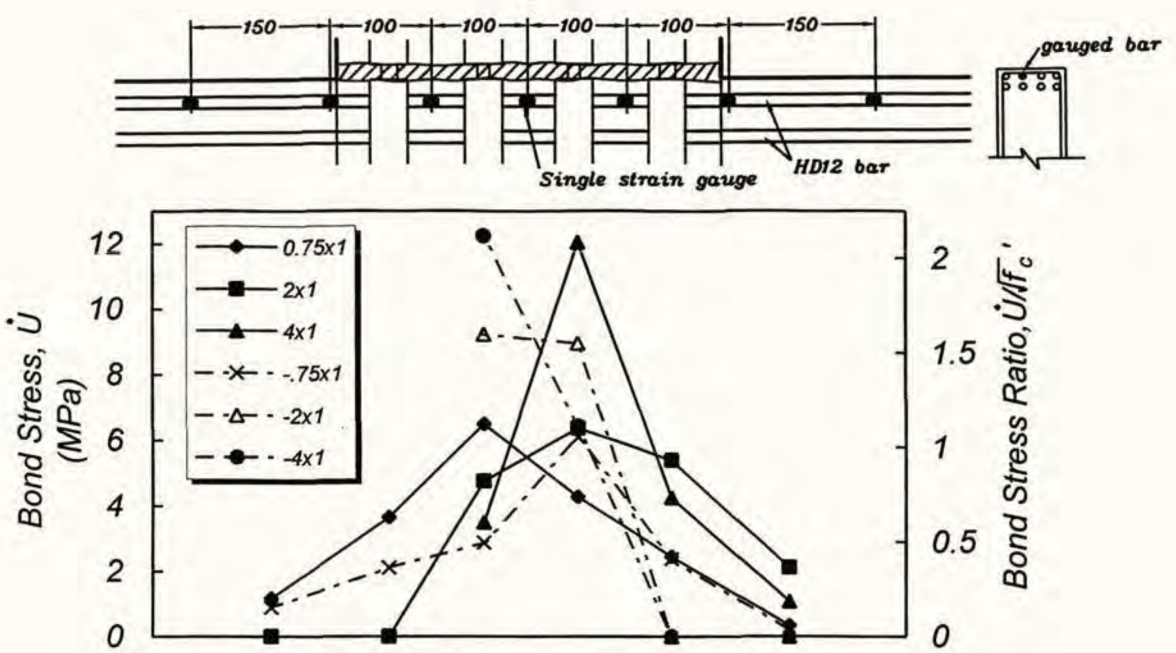

(a) Top Bars

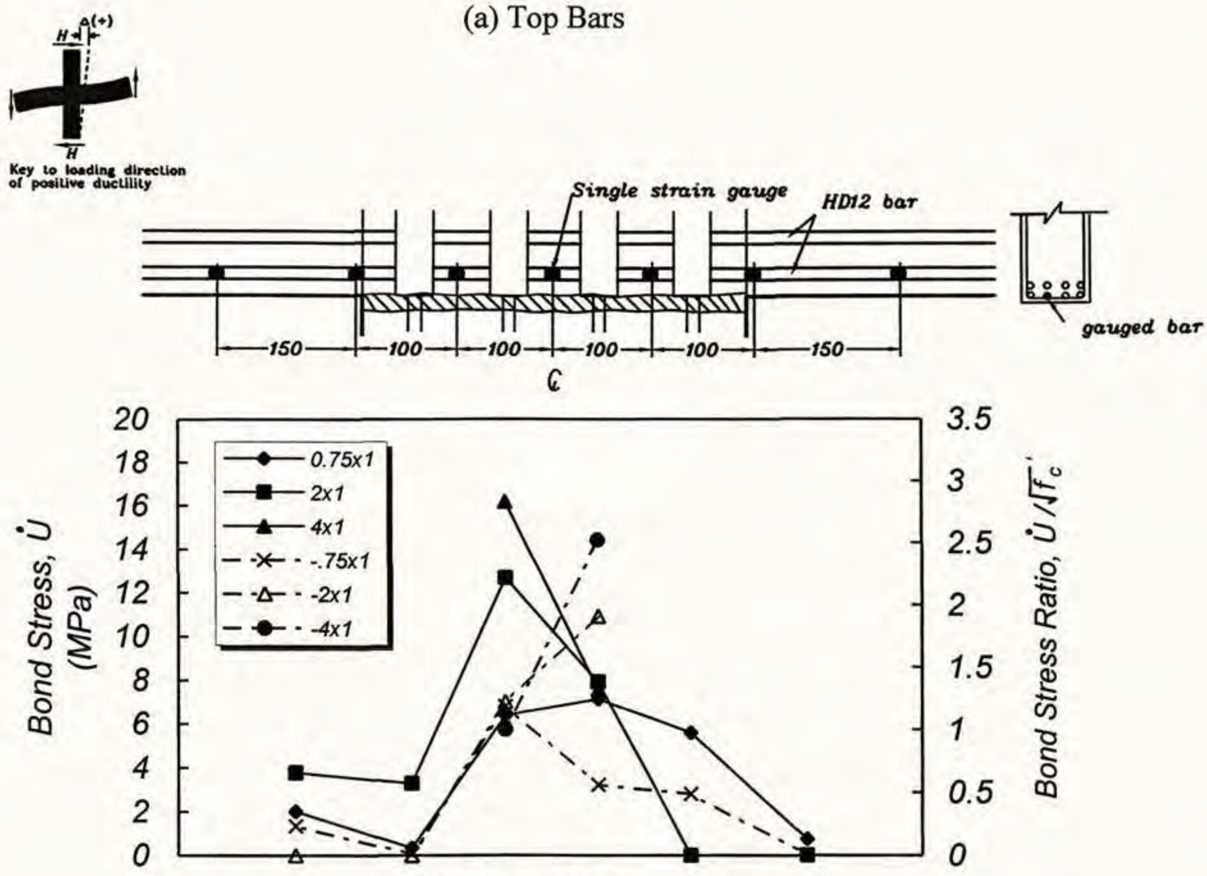

(b) Bottom Bars

Figure 4.26 - Calculated Bond Stresses.

4.3.5.5 Bar and Bond Stresses of the Column Vertical Reinforcement within Joint Region

The stresses on the column bars at each peak of loading cycle calculated from the strain gauge readings are depicted in **Fig. 4.27**. The obtained stress profiles followed the same trends observed in Unit 1. The only difference is that the stresses in the exterior column bars close to the top and bottom beam faces are larger than that in the previous unit. This is because the larger beam flexural strength developed in this unit. However, stresses in column bars are still well below yielding. Further, the stress profiles obtained in the load cycle of $\mu_\Delta = 4$ showed more linear distributed in comparison with that in Unit 1. This indicates that more amount of transverse joint reinforcement provided in Unit 2 enables a better bond stress distribution in the column exterior bar. In other words, the diagonal compression stresses field in the joint region spread more uniformly due to the presence of adequate quantity of transverse joint reinforcement. This justifies the same trend observed in the strut-and-tie model analysis depicted in Chapter 2.

The stresses on interior column bars followed the same trend as in Unit 1. The developed stresses in the middle portion were larger than that recorded on the top and bottom, but the stress gradient is low, indicating that a very low bond stress developed in the bars there.

4.3.6 Beam Behaviour

4.3.6.1 Curvature Ductility Factors in the Plastic Hinges

The curvature ductility factors in the plastic hinges were calculated in accordance with the same procedure used in Section 4.2.6.1. and are presented in **Fig. 4.28**.

The curvature ductility factors developed in plastic hinge region were larger than those observed in Unit 1. A maximum value of $\mu_\phi = 11$ was reached in the loading run to $\mu_\Delta = 6x2$. The values reached in load runs to $\mu_\Delta = 4$ are similar to the corresponding values recorded in Unit 1, see **Figs. 4.13** and **4.28**. The main difference between the curvature ductility factor in the beams of Units 1 and 2 during the final stages in the tests is due to the different sources of lateral displacement in these units. Joint shear distortion was the dominated mode of deformation in the final stages of the test in Unit 1. Whereas fixed-end rotation and flexural deformation in the beams accounted for most of the deformation in the final stages of the test in the Unit 2.

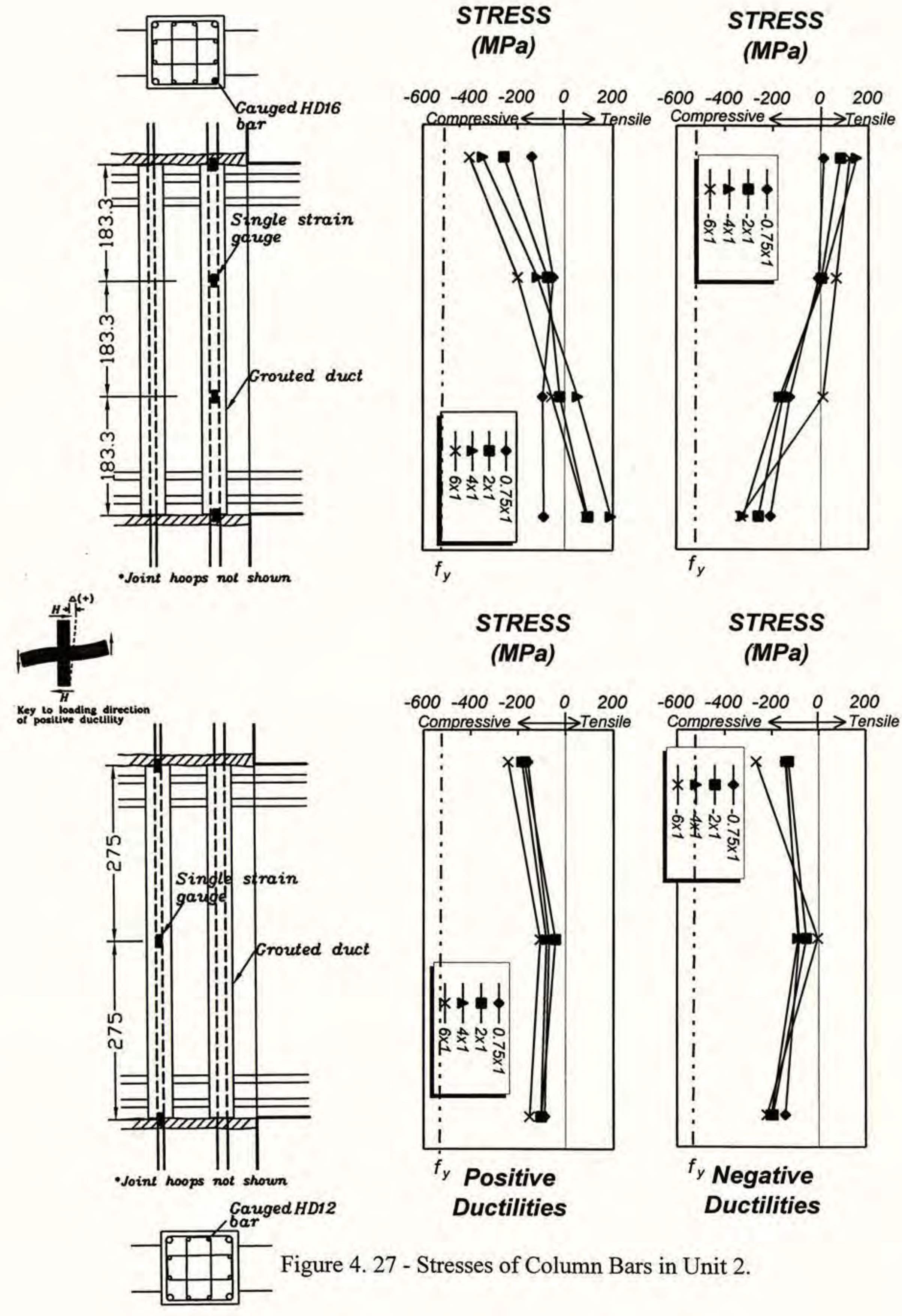

Figure 4. 27 - Stresses of Column Bars in Unit 2.

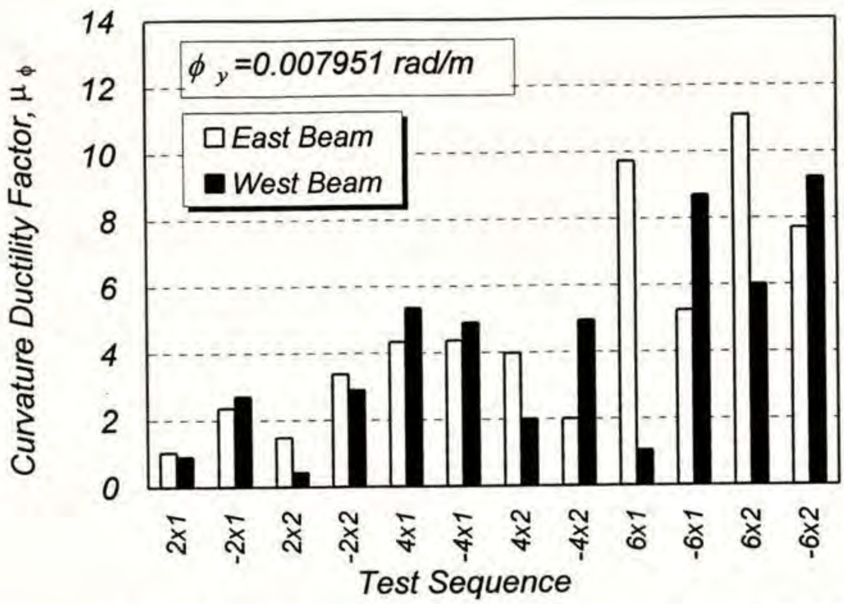

Figure 4.28 - Curvature Ductility Factors of Beam of Unit 2.

The disparity between the curvature ductility factors in the west and east beams in Unit 2 during the load runs to μ_Δ = 6 is appreciable, see **Fig. 4.28**. This difference is due to the difference in response of the beams under positive and negative bending moment. When the beams were loaded to induce negative bending moment, most of the deformation was due to fix-end rotation as a result of " total " bond failure of the top bars. In contrast, the positive plastic hinges were well developed and spread through the beam span as " total " bond failure of the bottom bars did not occur.

4.3.6.2 <u>Beam Strain Profiles at the Level of the Longitudinal Reinforcement</u>

Figures 4.29, **4.30** depict the beam strain profiles at the level of the longitudinal reinforcement. The maximum member strains at the level of top beam bars reached 2%. Note that in the load cycle of μ_Δ = 6x1, there was a reduction of tensile strains at the level of top beam bars on the west beam. In contrast, the top chord of the other beam at the location close to the column face was subjected to high compressive strains, reaching a value of -1.7%.

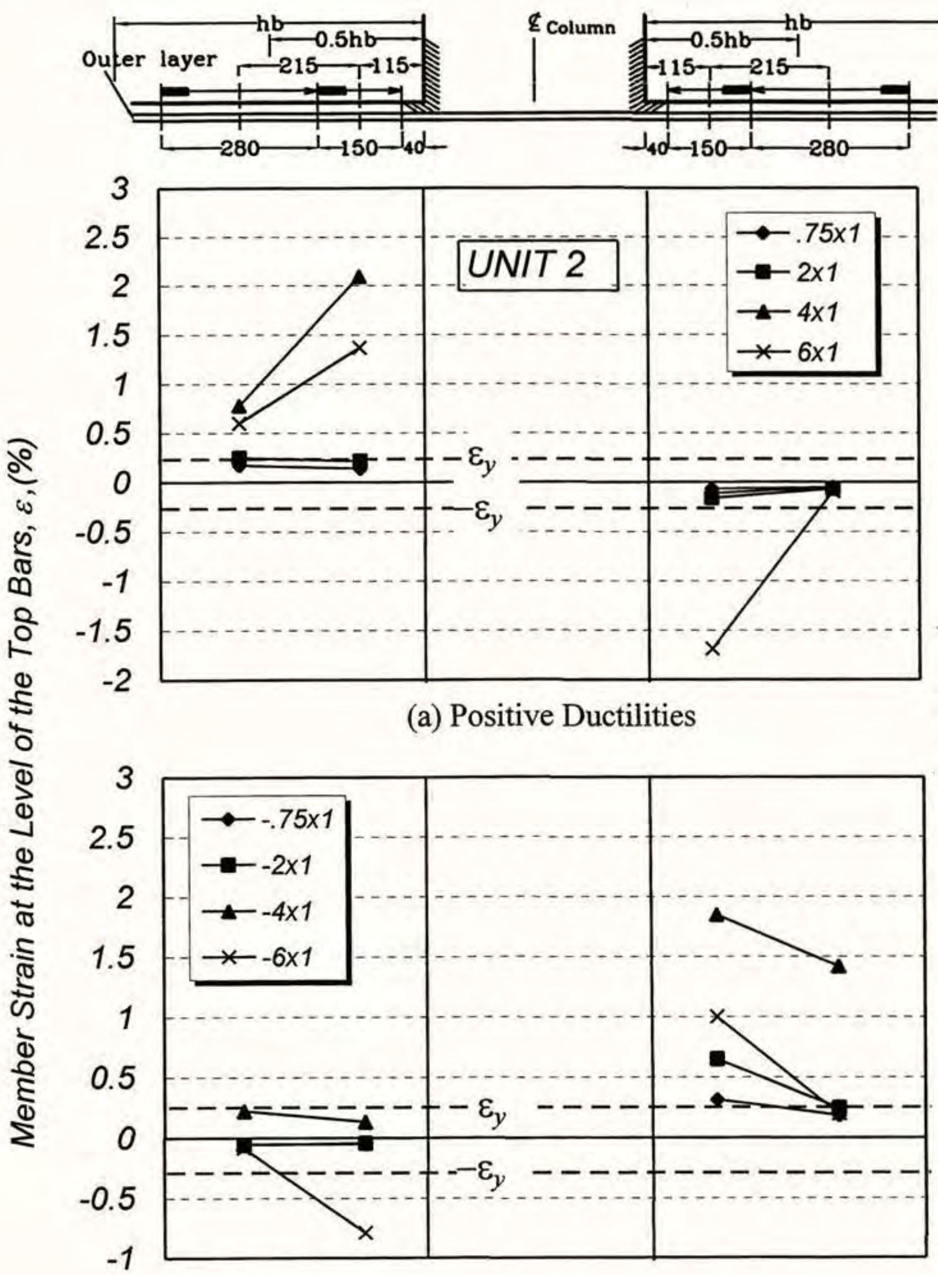

(b) Negative Ductilities

Figure 4.29 - Beam Strain Profiles at the Level of the Outer Layer of the Top Beam Bars of Unit 2.

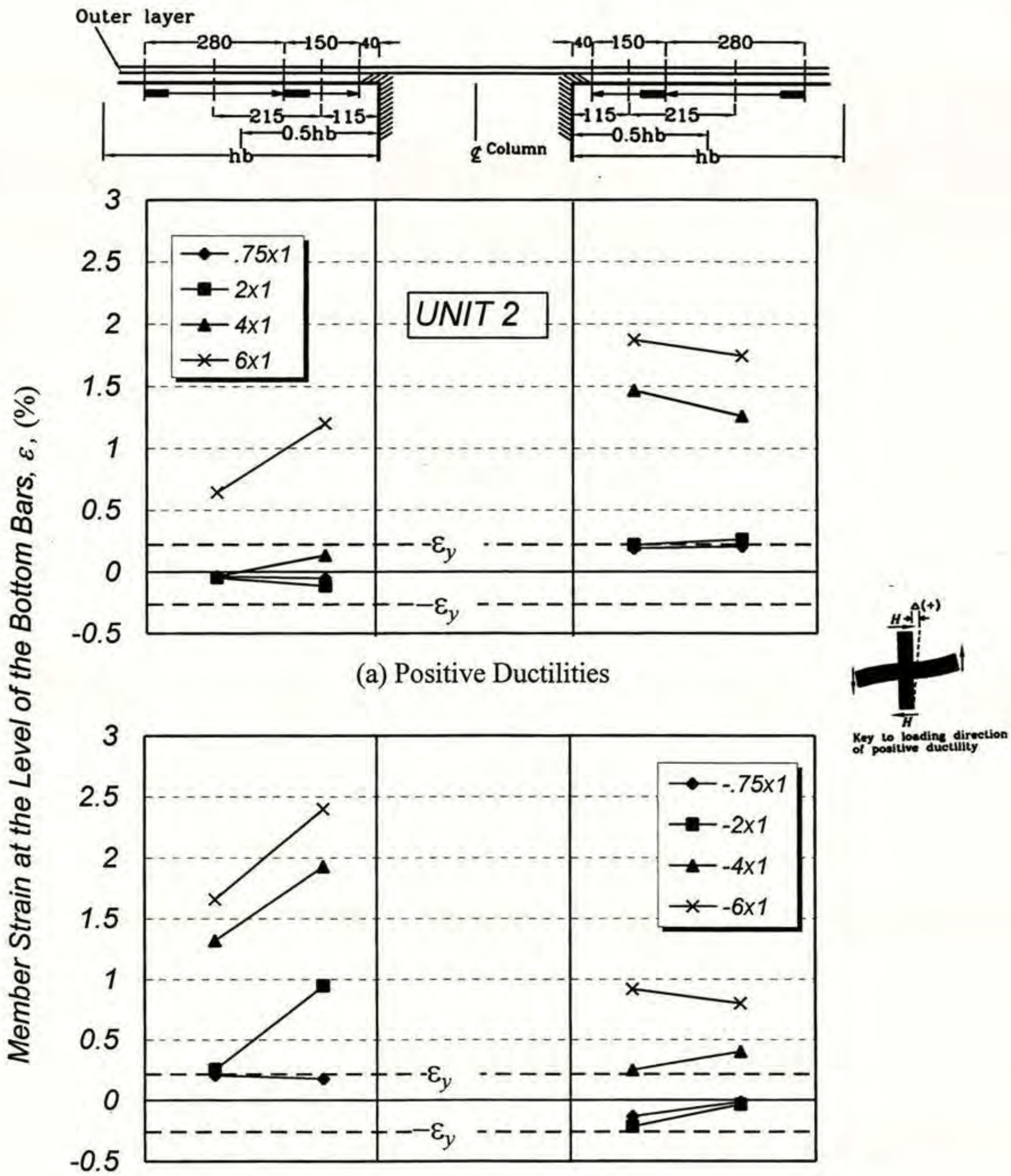

(a) Positive Ductilities

(b) Negative Ductilities

Figure 4.30 - Beam Strain Profiles at the Level of the Outer Layer of the Bottom Beam Bars of Unit 2.

Clearly this is the consequence of slippage of top beam bars. Significant loss of bond of the top beam bars in the joint region caused the bars to slip through out the joint region and be anchored in the beam at the other side of the column. As a consequence the concrete on the top chord of the other beam was therefore subjected to high compressive strains.

The strain profiles at the level of the bottom beam bars showed a different trend. First, the maximum tensile strain of 2.5% was larger than that observed in the top bars. Second, the evidence of the bottom bars slippage did not occurred on the bottom bars. As a result, the plastic hinge developed in the beam and spread away from the column face with the strain in the bars in this region increase with increasing rotation in the hinge.

4.3.6.3 Beam Elongation

Figure 4.31 shows the measured beam elongation against storey shear force. Comparing with Unit 1, Unit 2 has a larger beam elongation, with a maximum value of 23 mm, corresponding to 4.2% of the beam height. It is about 1.5 times of that measured in Unit 1.

Significant beam elongation took place in the first load cycle toward a new displacement ductility until finishing the load runs to $\mu_\Delta = 4$. At the peak of the load run to $\mu_\Delta = -4x1$ the

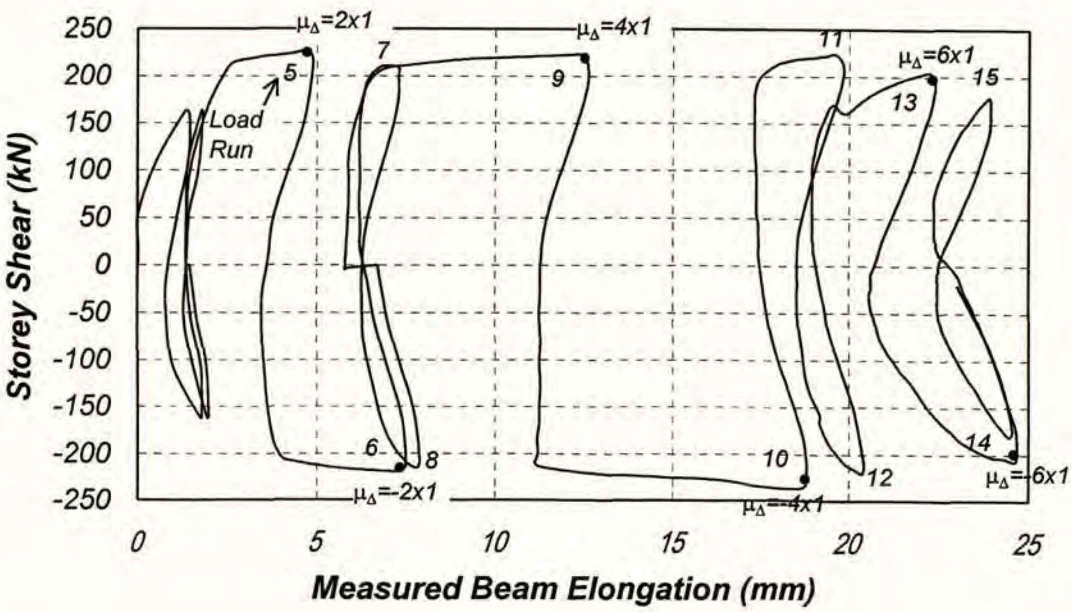

Figure 4.31 - Beam Elongation of Unit 2.

beams had elongated 18 mm. Some more elongation took place in the load runs to $\mu_\Delta = 6$, though it was not as large as that in the load cycles of $\mu_\Delta = 4$. The reason to cause the reduction of beam elongation in the load cycles of $\mu_\Delta = 6$ was the occurrence of bar slippage. The influence of bond slip in joint region on beam elongation can be clearly observed. Once significant bond slip occurs, and fixed-end rotation becomes the dominant mode of deformation, the plastic hinge can not spread and consequently it cannot grow in length.

4.3.7 Column Behaviour

Based on the visual observation and recorded strains on column bars, columns clearly remained elastic during the test.

4.4 CONCLUSIONS

1. The test results of two cruciform interior beam-column joint assemblies, designated as Units 1and 2 with high column axial load up to $0.43f_c'A_g$ was described in this chapter.

2. The tests conclusively indicate that the precast system used to build the test specimens behaves as monolithic. The joints between the pre-cast concrete members did not influence the overall response of the tests.

3. Unit 1, in which the quantity of transverse reinforcement complied with the requirement of the Concrete System Standard, NZS3101:1995 [S1], for ductile frames, showed limited displacement ductility response. Beam-column joint shear failure was observed to occur in this unit.

4. Unit 2, in which the quantity of transverse joint reinforcement complied with the requirements derived from the analytical work in this study, showed an acceptable performance in terms of strength and ductility.

5. Test results of Units1 and 2 justify the analytical finding depicted in Chapter 2 that the current code design recommendations for joints with high column axial load in combination with high joint shear stress ratios is non-conservative due to the overloading of the central part of the diagonal compression field that develops in the joint panel. Review of the design recommendations given in the Concrete Structure Standard [S1] is thus suggested.

6. The tests conducted in Units 1 and 2 have conclusively shown that axial compression does not always enhance the shear strength of beam-column joints. This finding is in line with the trend derived from the analytical work described in Chapter 2.

7. Bar slippage occurred in the test of Unit 2 indicates that the current code requirement of beam bar anchorage in beam-column joint region is not necessarily conservative when G 500 steel is incorporated in longitudinal beam bars and the applied column compressive load is in large level, $0.43f_c'A_g$. Test of Unit 2 in which the margin ratio of d_b/h_c required by Code [S1], is not able to perform competently until displacement ductility of 6 without pinching of hysteresis loops resulted from slippage of beam bars.

CHAPTER 5
TEST RESULTS OF UNITS 3 AND 4

5.1 INTRODUCTION

This chapter presents test results of Units 3 and 4. in which the joint shear stress ratio, v_{jh}/f_c', was kept to below 0.14. The applied column compressive load was $0.1f_c'A_g$. The tests on these two units were aimed at validating some findings of the analytical model that contrasted with the design recommendations given in NZS 3101:1995 [S1]. The two main discrepancies are : firstly, the shear strength of reinforced beam-column joints is sensitive to the joint shear stress ratio, v_{jh}/f_c'. For joints with low v_{jh}/f_c', the current code design recommendations were believed to be too stringent. Secondly, the current code approach for the design of horizontal joint reinforcement is in directly related to the maximum cross section area of the top or bottom longitudinal beam reinforcement. According to the analytical results described in Chapter 2, the required horizontal joint reinforcement is largely dependent on the joint shear stress ratio v_{jh}/f_c' rather than on the maximum section area of longitudinal steel. This discrepancy could lead to unnecessary quantity of horizontal joint reinforcement for joints incorporated beams with unequal top and bottom reinforcement.

Unit 3 was designed to validate the first discrepancy whereas Unit 4 was designed to investigate the design recommendations for beam-column joints incorporated framing beams with unequal top and bottom longitudinal reinforcement.

5.2 UNIT 3

5.2.1 Introduction

In accordance with the analytical results described in Chapter 2, the required amount of horizontal joint reinforcement for joints with v_{jh}/f_c' ratio less than 0.14 is very small and the minimum requirement, $V_{sh} = 0.4V_{jh}$, specified in NZS 3101:1995 [S1] and suggested in this research was adopted for the design of these units. The horizontal joint reinforcement consisted in 4 sets of perimeter R10 plus 2 legged of inner R6 ties.

5.2.2 General Behaviour

The beam-column joint of this unit performed extremely well without any noticeable negative effects on overall behaviour of test unit as a result of the low amount of horizontal joint reinforcement provided, which was only 84% of that required by NZS 3101:1995 [S1]. Significant loss of bond on top beam bars anchored in joint region occurred during the second cycle to $\mu_\Delta = 4$, causing stiffness degradation and pinching of hysteresis loops in the subsequent load cycles. The crack pattern at different stages and the lateral load-displacement response are presented in **Figs. 5.1** and **5.2**.

In elastic load cycles, fine flexural cracks spread along the top and bottom chord of the beams. The first crack in joint region occurred in the first positive load run toward 75% of theoretical ultimate load and located at the left lower corner of the joint panel. A couple of additional fine cracks appeared in joint panel in the subsequent elastic load cycles. Few cracks developed in columns with one horizontal crack appearing on each top and bottom columns along the beam faces.

When the unit was taken to a displacement ductility factor of 2, diagonal cracks developed from corner to corner in joint panel reaching a width of 0.3 mm. Besides, other short diagonal cracks occurred on both sides of the joint panel. It is noted that the cracks pattern observed at this stage were not parallel as implied in Park and Paulay's model [P4]. In fact, it could be observed that the cracks pattern of the joint panel at this stage was similar to the variable angle strut-and-tie model presented in the Chapter 2. Plastic hinges developed in the beams at this stage of loading. The maximum crack width there reached 1.0 mm. Some new cracks along tension side of columns were observed to occur.

By $\mu_\Delta = 4$, corresponding to a storey drift ratio of 2.4 %, the cracks in plastic hinge region of the beams widened further, reaching a maximum width of 4.5 mm at the peak load to $\mu_\Delta = -4x1$. Two central cracks in joint panel reached a width of 0.6 and 1.0 mm, respectively. Few new cracks occurred in columns but these were kept short and fine. In the subsequent load cycles to the same displacement ductility factor, the diagonal cracks in the centre of the joint panel did not grow anymore, though a couple of new cracks appeared. The main cracks along column faces in beams initiated from top the beam chords and had a width of 5.0 mm, which contributed significantly to the beam fixed-end rotation. Also observed was some cover concrete of top column at beam face started to spall off. It is noted that in this load

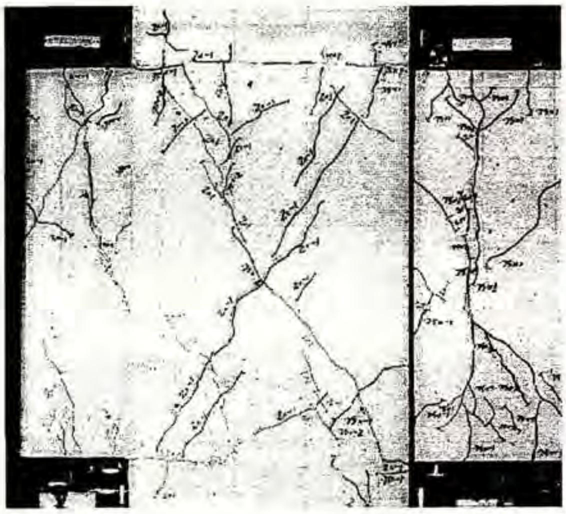

(a) At μ_Δ=-2x1

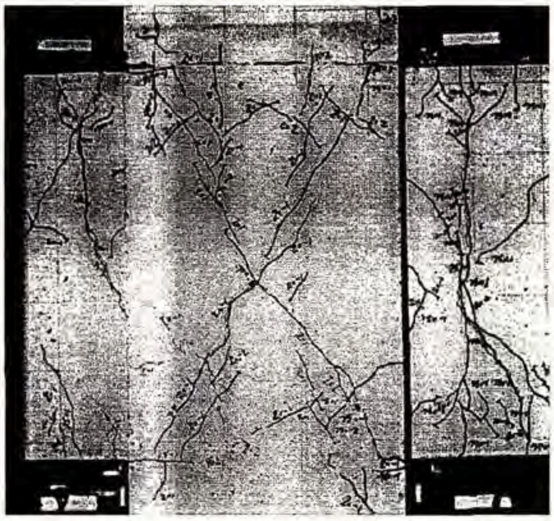

(b) At μ_Δ=-2x2

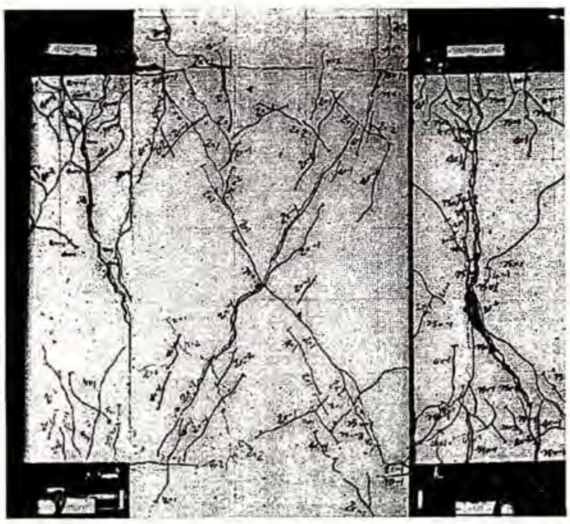

(c) At μ_Δ=-4x1

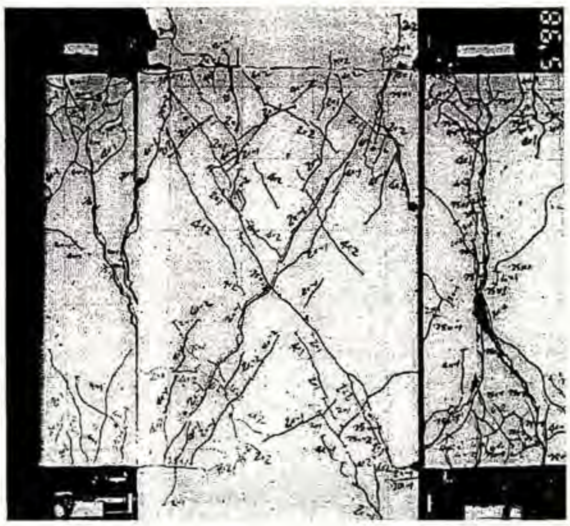

(d) At μ_Δ=-4x2

Figure 5.1 - Cracking of Unit 3 at Different Stages During the Test

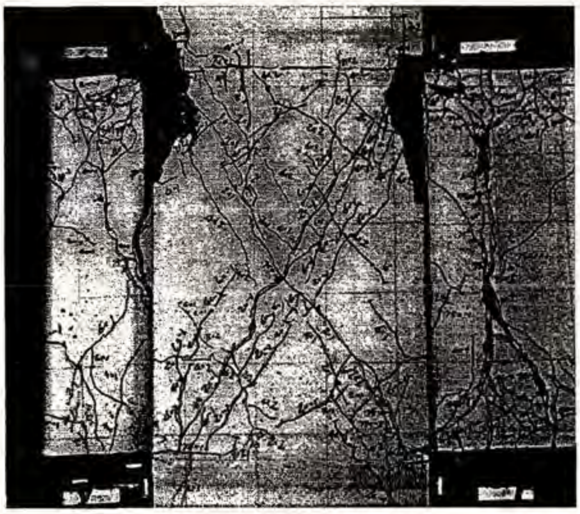

(e) At μ_Δ=-6x1

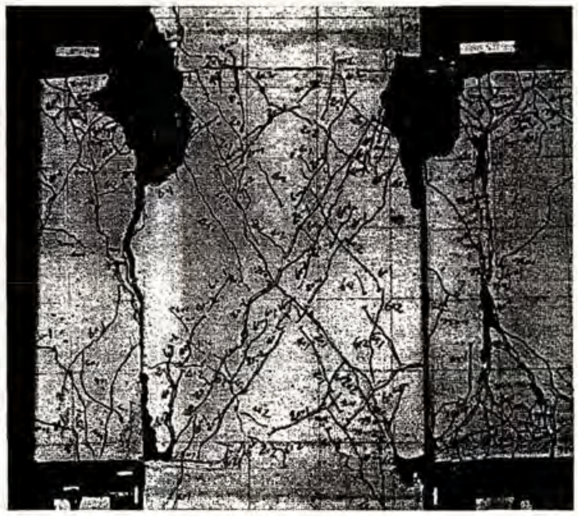

(f) At μ_Δ=-6x2

Figure 5.1 (Cont.) - Cracking of Unit 3 at Different Stages During the Test

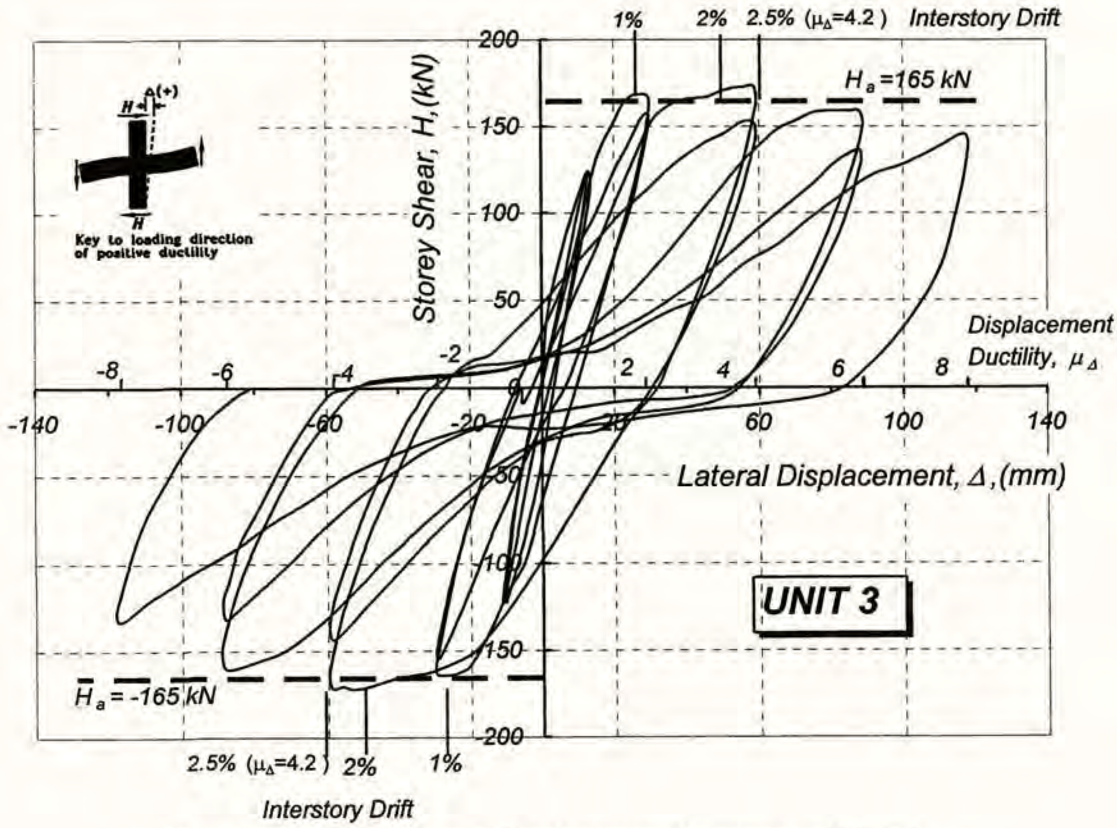

Figure 5.2 - Lateral Load-Displacement Response of Unit 3

cycle, some sliding shear deformation of beams was believed to occur by noticing some shift of the grid lines drawn in the beam plastic hinge regions.

At $\mu_\Delta = 6$, the top corners at the intersection between beam and the column were crushed, indicating that significant bond slip of top beam bars had occurred. Large gaps opening from top and bottom beam chords occurred along column faces reaching 9.0 mm and 4.0 mm, respectively. Cracks elsewhere in beams became narrower indicating that fixed-end rotation had a significant contribution towards the lateral displacement. Input joint shear force decreased as strain hardening of beam longitudinal steel could no longer be developed. Few new cracks occurred in the joint panel whereas the width of existing cracks decreased. Until this stage, the cracked concrete in the joint region did not have any apparent sign of deterioration or damage.

In further loading cycles to $\mu_\Delta = 8$, loss of bond of the bottom beam bars in joint region was noticed since the concrete in the two bottom corners of the joint panel was damaged. In spite of the significant stiffness degradation and pinching of the hysteresis loops as a result of bond slip, it can be said that this unit showed satisfactory performance as a ductile component.

5.2.3 <u>Load-Displacement Response</u>

The lateral load-displacement response of Unit 3 is shown in **Fig. 5.2**. Measured yield drift following the procedure described in Section 3.7 was 0.60%. This yield drift level implies a displacement ductility equal to $\mu_\Delta = 4.2$ when the drift limit of 2.5% imposed by the Loading Standard [S3] is attained.

This unit achieved its theoretical ultimate lateral load in the first load cycle to $\mu_\Delta = 2$. The lateral load capacity exceeded the theoretical value by 4.2% in both positive and negative load cycles of $\mu_\Delta = 4x1$. The hysteresis loops were stable until some pinching initiated in the load run of $\mu_\Delta = \pm 4x2$, which corresponds to a storey drift ratio 2.4%. Stiffness degradation in conjunction with some incipient bond deterioration in joint region gave rise to the decrease of lateral load capacity to 88.3 % and 84.3% of the recorded maximum load in the positive and negative load runs, respectively.

In spite of pinching of hysteresis loops in the following cycles, considerable pick up of lateral load capacity was observed in the first load cycle to $\mu_\Delta = 6$. The achieved peak loads are equivalent to 93% and 95% of the recorded maximum value and very close to the theoretical ultimate load. Unlike Unit 1, in which joint failure had occurred, the reduction of lateral load capacity induced by bond slip in joint region is usually able to be recovered once the specimen is displaced further toward larger lateral displacement level. Therefore, despite that lateral load capacity dropped to 79% and 78% of the maximum value in the second load cycles of $\mu_\Delta = 6$, which are slightly less than the 80% recommended in the Commentary of Loading Code [S4], it is believed that the overall performance of this specimen is still acceptable since the lateral load capacity can be easily brought up to meet the criteria if the imposed lateral displacement carried on slightly further. Furthermore, as illustrated in Sections 4.3.3, the main consequences, such as stiffness degradation and irreparable structures which arose from significant loss of bond in joint region and occurred at a storey drift ratio of 3.6 %, are not necessarily to be of great concern.

The specimen was displaced toward a load cycle to $\mu_\Delta = 8$. The lateral load capacities in this load cycle reached up to 84% and 78% of the maximum load in the positive and negative load run, respectively.

5.2.4 Decomposition of Lateral Displacement

Each component of the applied lateral displacement at the peak of loading run is presented in **Fig. 5.3**.

In the elastic load cycles, column deformation, beam flexure and beam fixed-end rotation each contributed to about one-third of the overall lateral displacement. Note that the component of the column displacement was obtained from theoretical analysis. In comparison with Units 1 and 2 ,in which the applied column axial load was large, the column component rose considerably in this unit. The increasing of column flexibility was caused by the applied light column compressive load, $0.1f_c'A_g$. There is a trend shown in **Fig. 5.3** that the components of the measured beam fixed-end rotation in the positive load runs are relatively larger than that in the negative load runs of elastic cycles. It is believed that the component of beam fixed-end rotation might be somehow overestimated in the positive loading run, causing the occurrence of 15% closure error. On the other hand, beam shear deformation and beam-column joint shear distortion only have a small percentage during the elastic cycles.

The component of beam fixed-end rotation increased continually with the test sequence until reaching a maximum percentage of 65% at the end. Meanwhile, the component of beam flexural deformation gradually diminished with the increasing of beam fixed-end rotation.

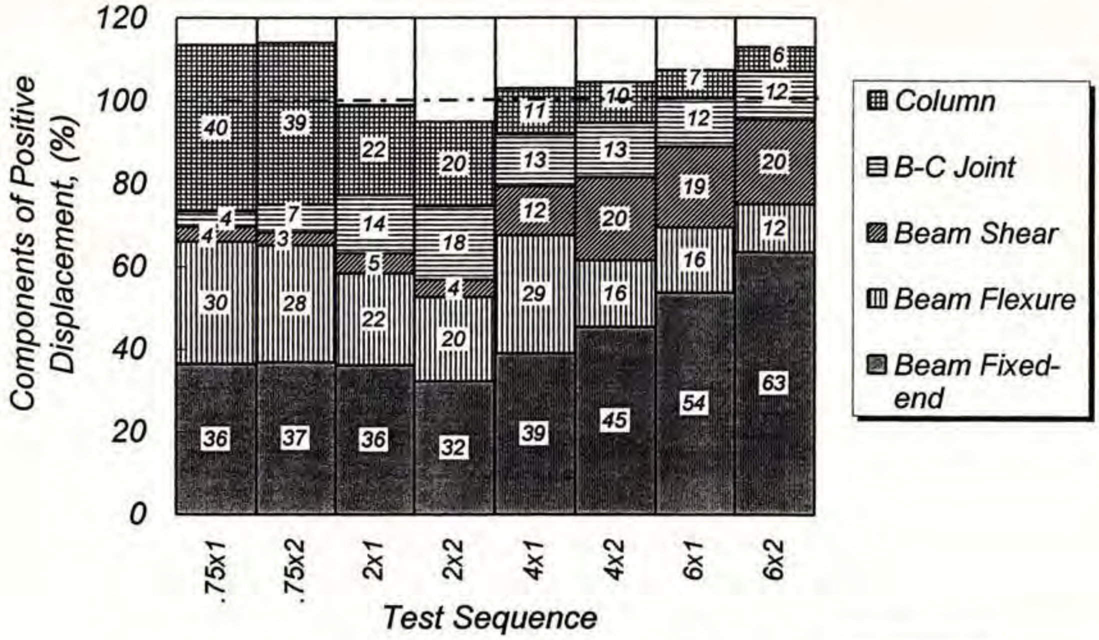

(a) Runs to Positive Ductilities.

UNIT 3

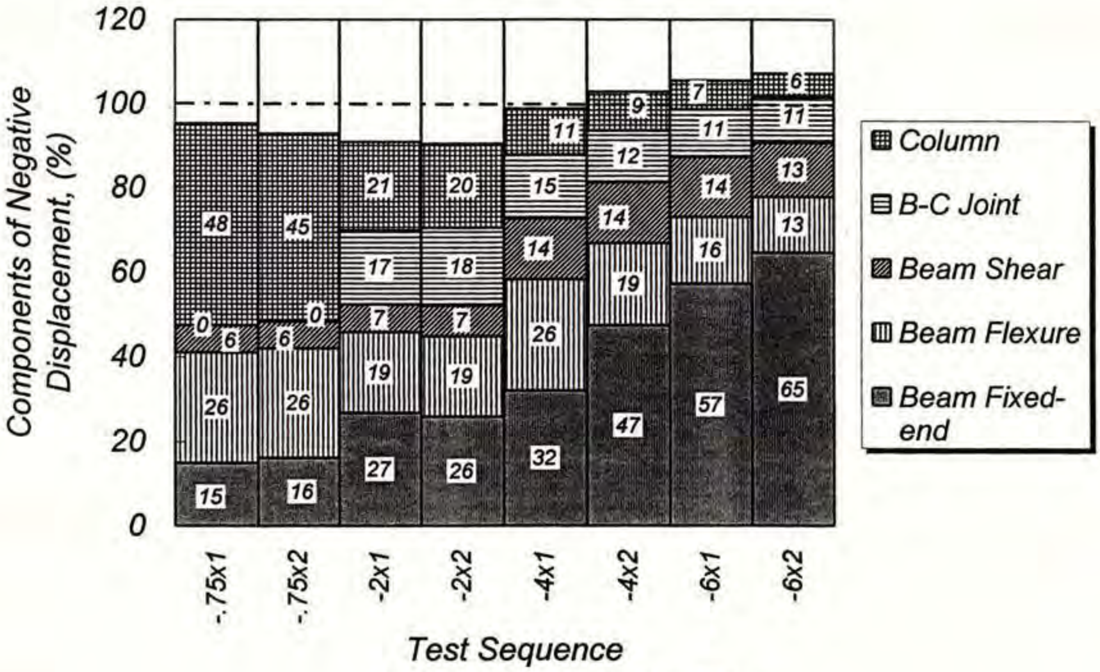

(b) Runs to Negative Ductilities.

Figure 5.3 - Components of Lateral Displacement of Unit 3 at Peaks of Load Runs

Unlike in Units 1 and 2, the component of fixed-end rotation during the test had a trend that it increased gradually instead of sudden rising in a loading run. This is simply due to the different characteristics of bar anchorage in beam-column joint between units with large and light column axial loads.

The maximum percentage of beam-column joint shear distortion occurred in the load cycle to $\mu_\Delta = \pm 2x2$, reaching a value of 18%. Clearly this deformation component was controlled within an acceptable limit. The beam shear deformation, which consists of flexural and sliding shear deformation in beams, increased gradually during the test. It can be observed in this chart that once the beam fixed-end rotation became the largest component of the lateral displacement, unlike the beam flexure, beam shear deformation still had an ascending trend. This is because that once the full depth crack along column faces occurred as a consequence of beam bars slip, shear force transfer along column faces became to rely on dowel action. Therefore, more sliding shear deformation can be induced. However, since the lateral load capacity also diminished as a consequence of the beam bars slip, the increasing trend of beam shear deformation was not considerable. It only reached a maximum value of 20% at the end of the test.

5.2.5 Joint Behaviour

5.2.5.1 Strains in the Horizontal Joint Shear Reinforcement

The average strains of R10 hoops and inner R6 ties at each peak of loading cycles are depicted in **Figs. 5.4** and **5.5**. It can be seen in these figures that the recorded strains in the elastic loading cycles remained very small. In comparison with measured strains in corresponding loading cycles of Units 1 and 2, the recorded strains of joint reinforcement in this unit are much smaller in magnitude. It implies that, as indicated by the proposed theoretical model, the component of the concrete contribution to the joint shear strength is sensitive to the joint shear stress ratio. Note that in all units referred above, cracks had appeared in the joint panels in the elastic load cycles. For joints having low joint shear stress ratios, the strength of joint concrete degrades relatively slow comparing with joints having high shear stress ratios. Therefore, transverse joint shear reinforcement was mobilized in a latter stage.

In the load cycles to $\mu_\Delta = 2$, most of the transverse joint reinforcement, including the

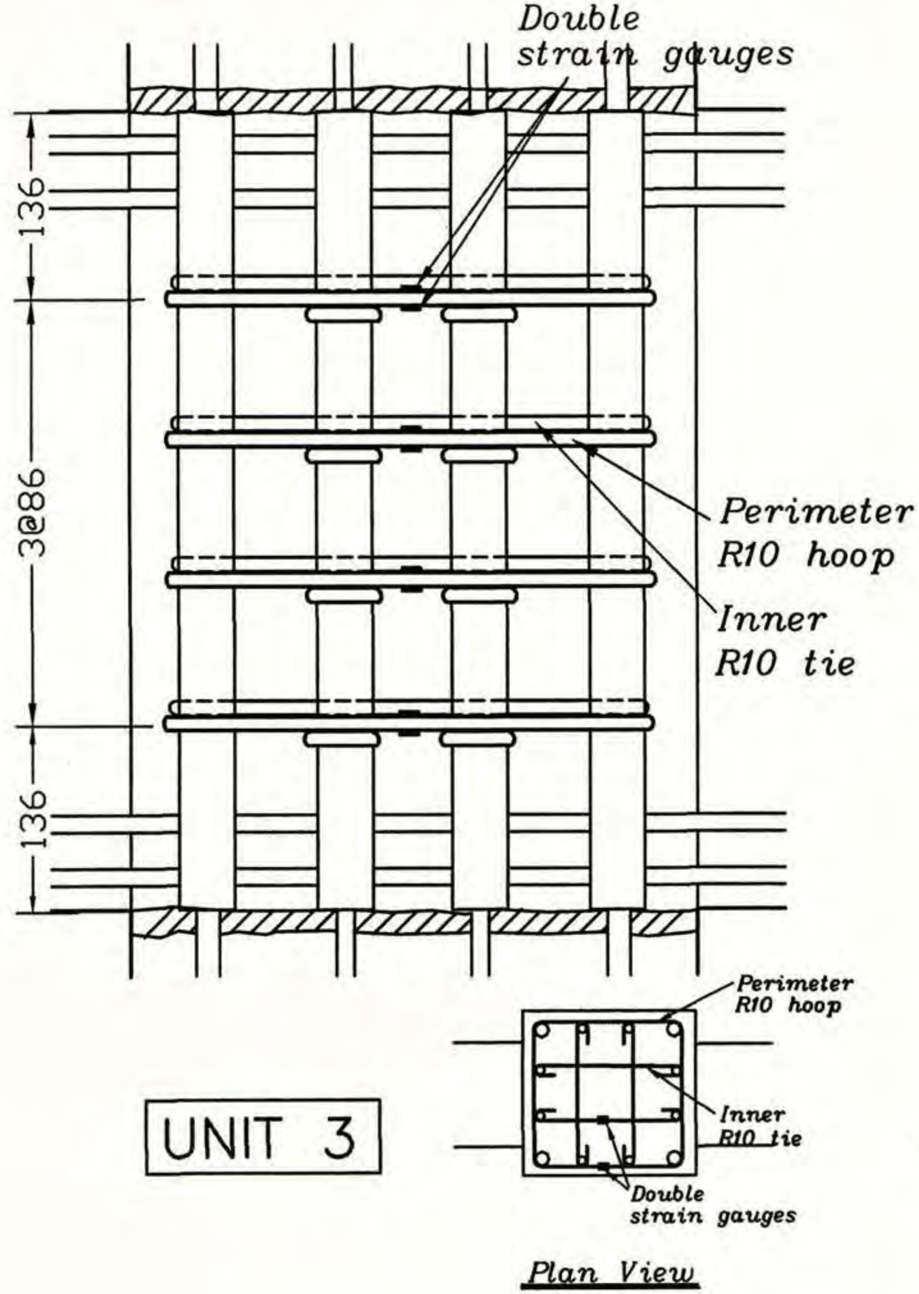

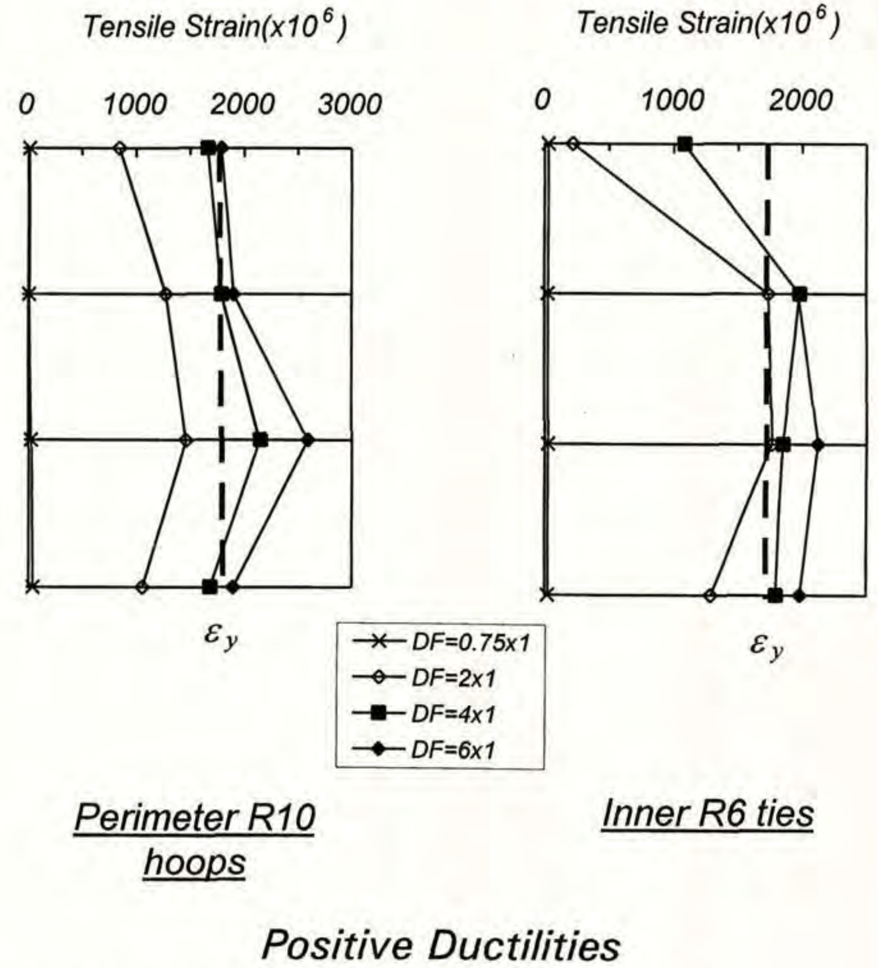

Figure 5.4 - Measured Strains in Joint Hoops of Unit 3 During the Runs to Positive Ductilities.

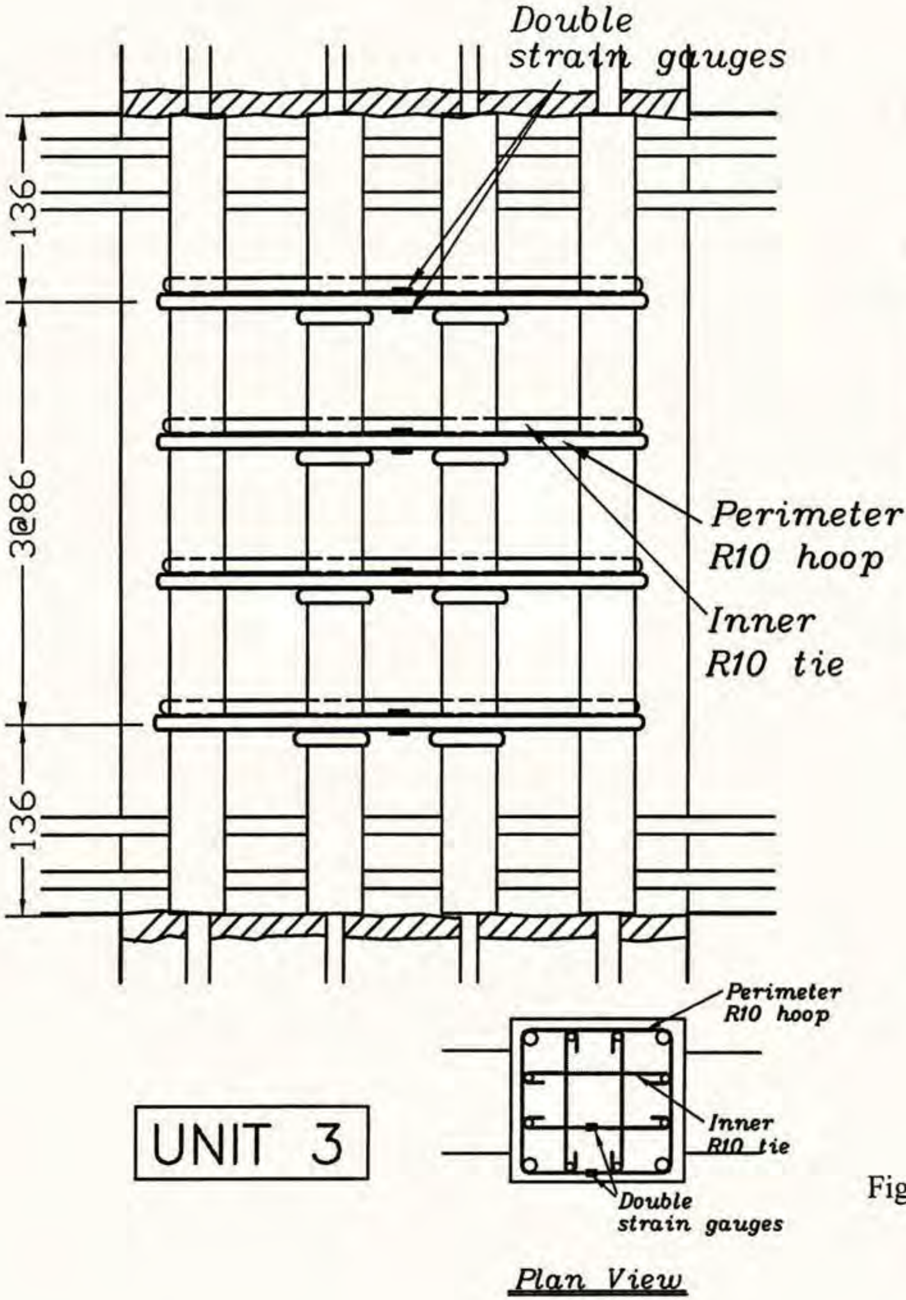

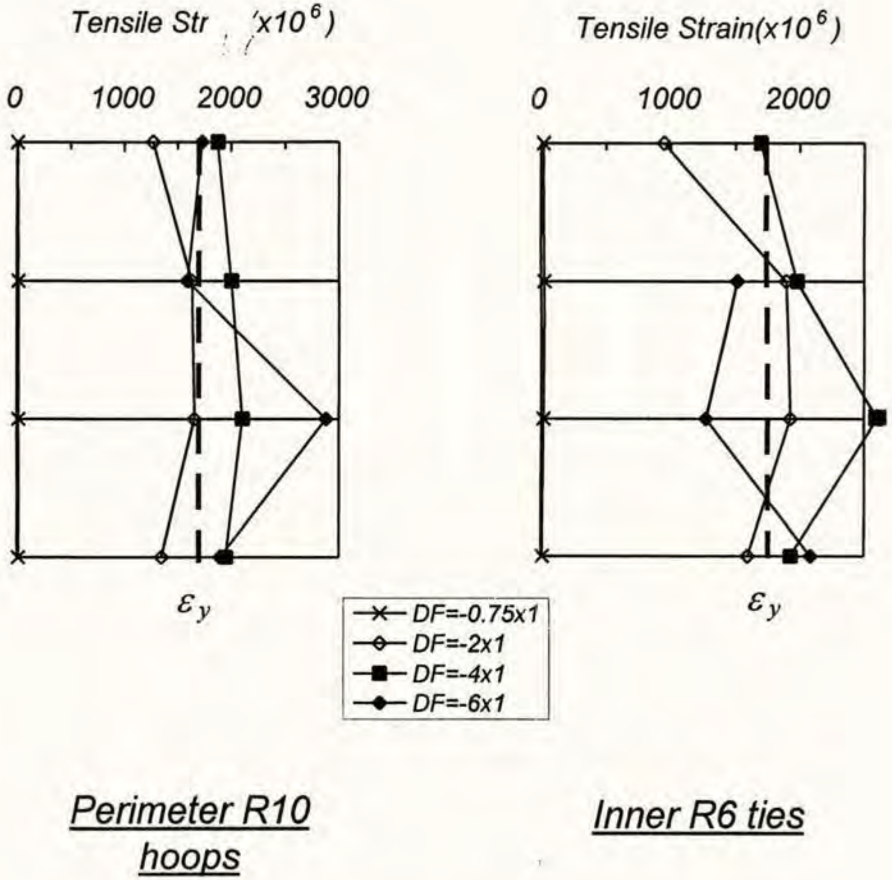

Negative Ductilities

Figure 5.5 - Measured Strains in Joint Hoops of Unit 3 During the Runs to Negative Ductilities.

perimeter R10 hoops and inner R6 ties, approached a value close to the yield strain. Subsequently they reached the yield strain in the load cycles to $\mu_\Delta = 4$ and then remained in the similar level in the load cycles to $\mu_\Delta = 6$.

It is of interest to illustrate further **Figs. 5.4** and **5.5** by looking at the strain distribution of the joint reinforcement. Firstly, the strain distribution in the joint reinforcement along the height of the joint showed a rather uniform distribution. The recorded strains at the top and bottom sets were similar to the inner sets. This is because that top and bottom sets were placed toward to the centre of the joint region as possible so that they can fully participate in resisting of input joint shear force. Comparing the strain profiles with what was observed in Units 1 and 2, it can be realized that if the joint hoops are placed within a short distance away from the top and bottom beam bars, only partial capacity of them can be developed in resisting the input joint shear force. This justifies the need to take into account this factor when the provided effective V_{sh} of existing tests were evaluated. Attempt will be made in the latter chapter to calibrate this influence length based on the test results.

Secondly, it can be confirmed that the assumption made in the theoretical work that the joint transverse reinforcement yield and act as a constant pressure is appropriate.

Thirdly, as described above, the strain profiles in load cycle to $\mu_\Delta = 6$ remained in similar level as in the loading stage to $\mu_\Delta = 4$. This implies that despite slippage of top bars had occurred at this stage, the joint transverse reinforcement still participated in sustaining the compression stress field of joint region. This implication contradicts with the postulate made in Park and Paulay's model [P4] which asserted that the truss mechanism in joint panel relies on the bond stress in longitudinal beam bars. Once the bond stress is lost as a consequence of the bar slippage, the diagonal concrete strut mechanism will resist most of the input joint shear force without the function of transverse reinforcement. The above description may further justify the trend found in the analytical work that the bond stress along longitudinal beam bars does not play a significant role in the distribution of the diagonal compression stress field in joint panel. In fact, the joint transverse reinforcement is still required in order to sustain the strength of the diagonal compression stress field even though some part of bond stress on longitudinal beam bars is lost, as long as the input joint shear force has not diminished significantly.

5.2.5.2 Joint Shear Distortion Versus Lateral Loads

The measured joint shear distortion was plotted against the lateral load in **Fig. 5.6.** It can be observed in this figure that the joint shear deformation was well controlled during the test. The maximum joint shear distortion only reached 0.006 radians at the end of test. Besides, it is evident again that the joint shear distortion was not magnified as the lateral load was diminishing. This may be able to justify that the cause of decrease of lateral load capacity was due to beam bars slip instead of degradation of the joint strength.

5.2.5.3 Beam Bar Slip Within Joint Region

Figure 5.7 present the local slip of top and bottom beam bars at three locations in joint region. The influence of the " top bar effect " on bond of the beam bars was also evident in this unit. The measured slip of top bars was considerably larger than that in the bottom bars, especially in the loading cycles beyond $\mu_\Delta = 4$.

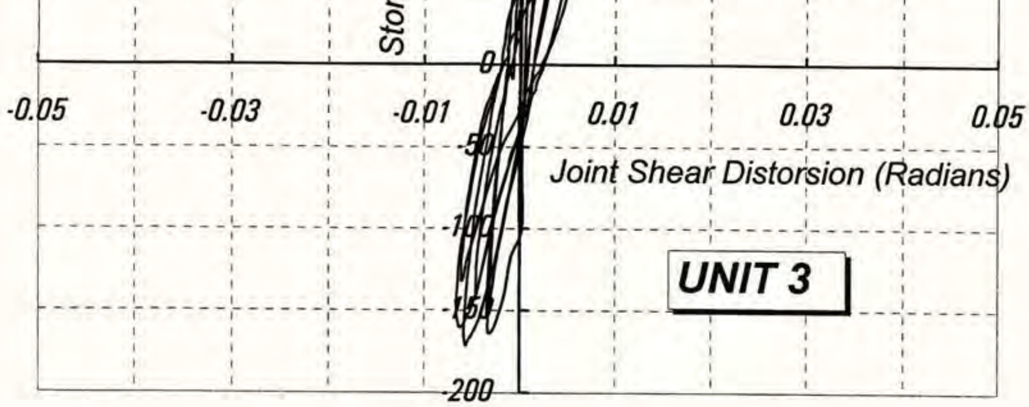

Figure 5.6 - Joint Shear Distorsion Versus Storey Shear Force.

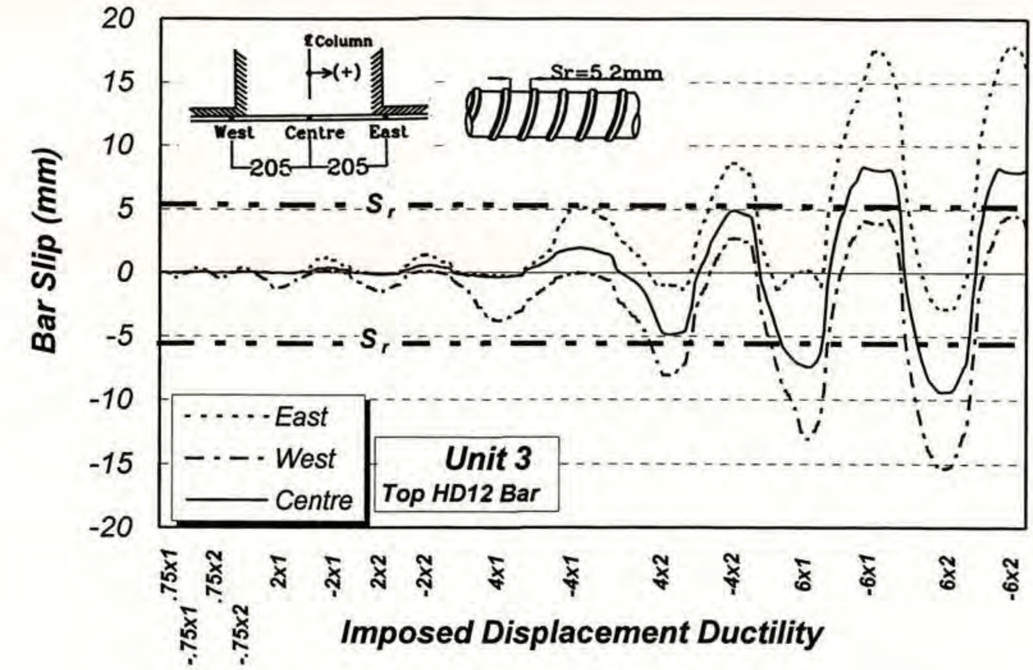

(a) Top Bars

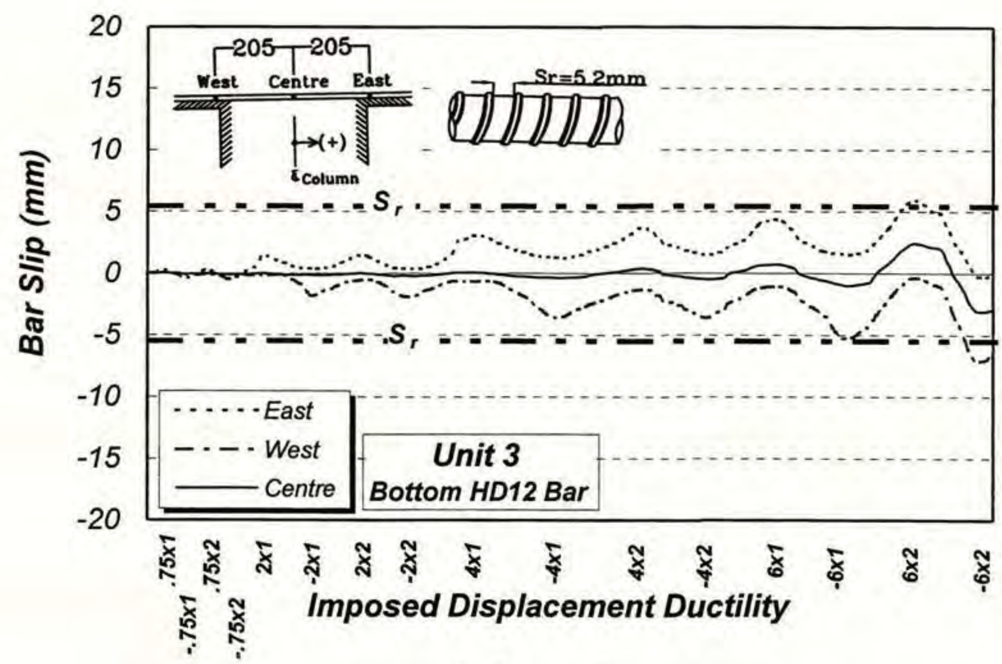

(b) Bottom Bars

Figure 5.7 - Relative Slip of Beam Longitudinal Bars in the Joint Region.

The slip of top beam bars measured at the centre of the joint in the load cycle of $\mu_\Delta = \pm 4x2$ reached 5mm, which just approached the clear ribs spacing of the HD12 bars 5.2 mm, indicating that significant loss of bond on top beam bars was just about to mobilize at this stage. The measured slips in the subsequent load cycle, $\mu_\Delta = 6x1$, significantly increased and exceeded 5.2mm, indicating that total bond failure of top beam bars occurred at this stage. Some readings were affected due to contact between steel studs and the surrounding concrete.

The bottom bars did not show large slip until the end of test. The maximum recorded slip reached 7 mm in the load run to $\mu_\Delta = -6x2$. The slip value measured in the centre of the joint kept less than 5.2mm during the test, indicating that the total bond failure of bottom beam bars did not occur.

5.2.5.4 <u>Bar Strain And Bond Stress of the Beam Longitudinal Reinforcement Passing Through Joint Region</u>

The strain distribution along longitudinal beam bars in joint region are depicted in **Figs. 5.8** and **5.9**. Average bond stress on beam bars calculated from the strains are also presented in **Fig. 5.10**. Note that very limited data was recorded in the loading cycles to $\mu_\Delta = 4$ since at this loading stage most of the strain gauges were damaged.

The maximum recorded tensile strain of top bars approached 3500 micro-strain in the loading run to $\mu_\Delta = -2x1$, while the maximum compressive strain reached -1000 micro-strain. According to inelastic stress-strain relationship of steel, the maximum compressive stress in compression bars was approximate 70-80% of f_y. Measured tensile and compressive strains in the bottom bars are similar in magnitude to that in the top bars.

In general, bond stresses developed in the bottom beam bars were larger than that in top beam bars. A peak value of bond stresses of 5.5 MPa and 16 MPa were recorded on top and bottom beam bars, respectively. Note that the recorded absolute bond stress in the top beam bars may not represent the largest value developed during the test, since data acquired in the load cycle of $\mu_\Delta = 4$ and onwards was no longer available. For the bottom beam bars, again, data is only available up to $\mu_\Delta = 2$. However, the measured peak bond stress 16 MPa is doubtful as the stresses used to calculate seen to be abnormal in comparison with values

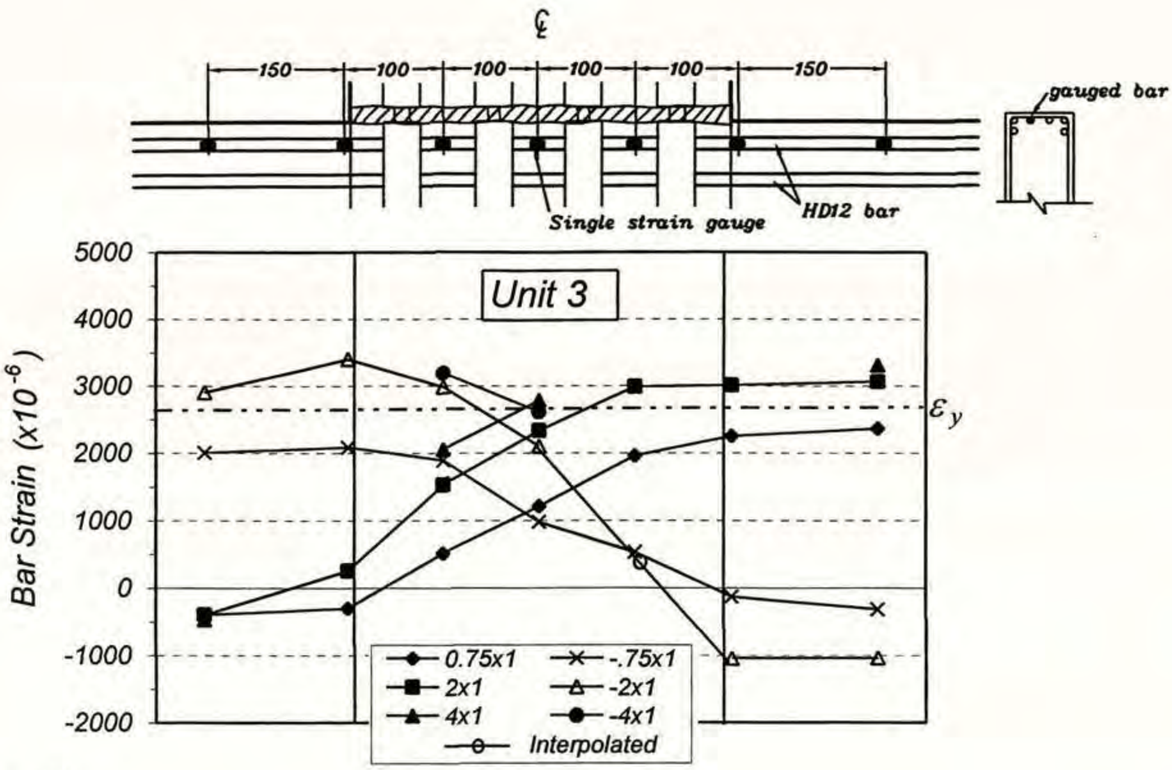

(a) Outer Layer

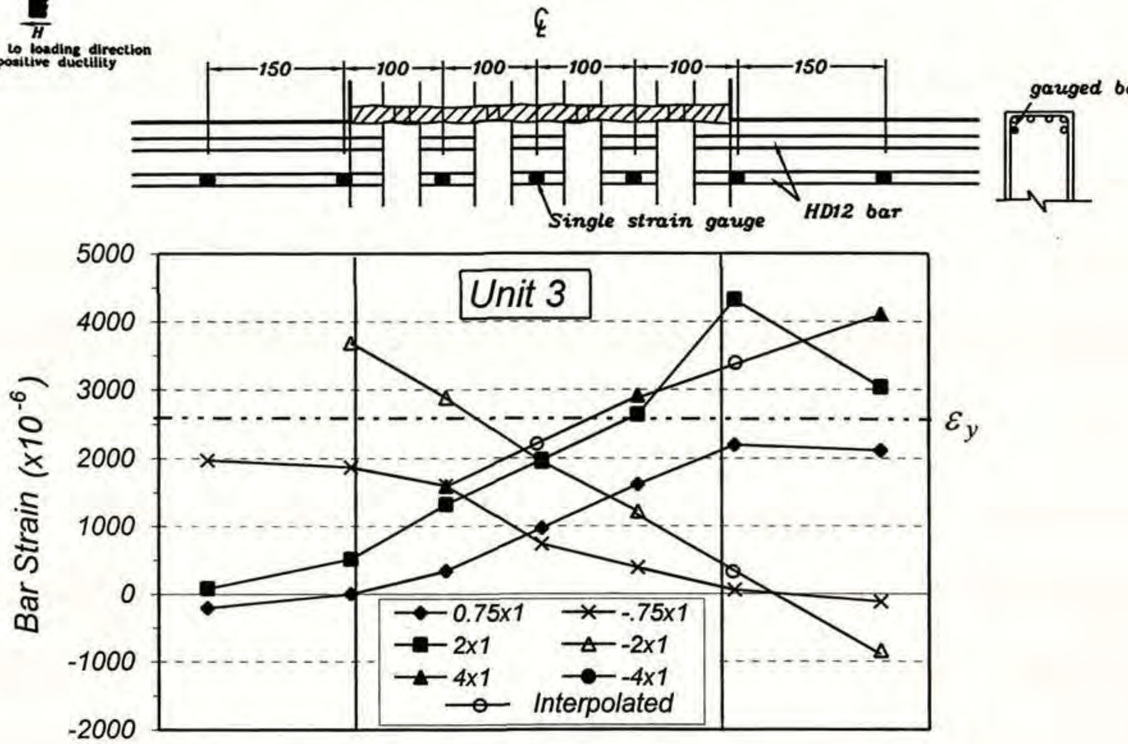

(b) Inner Layer

Figure 5.8 - Top Beam Bar Strain Profiles.

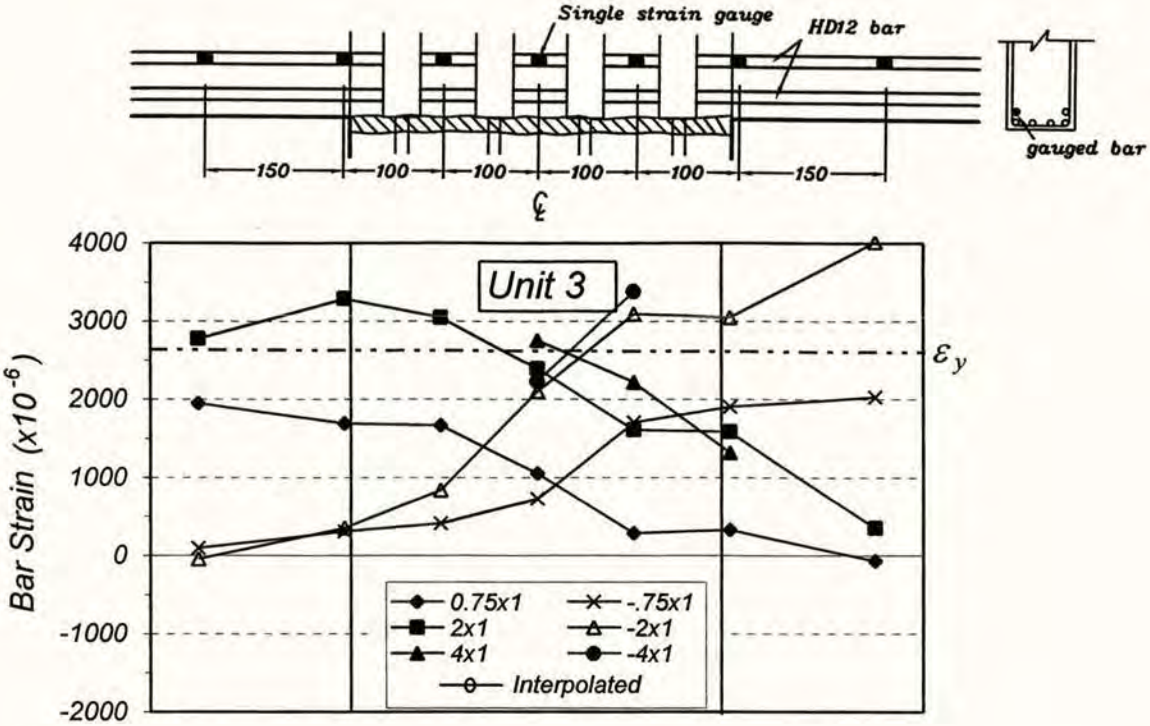

(a) Inner Layer

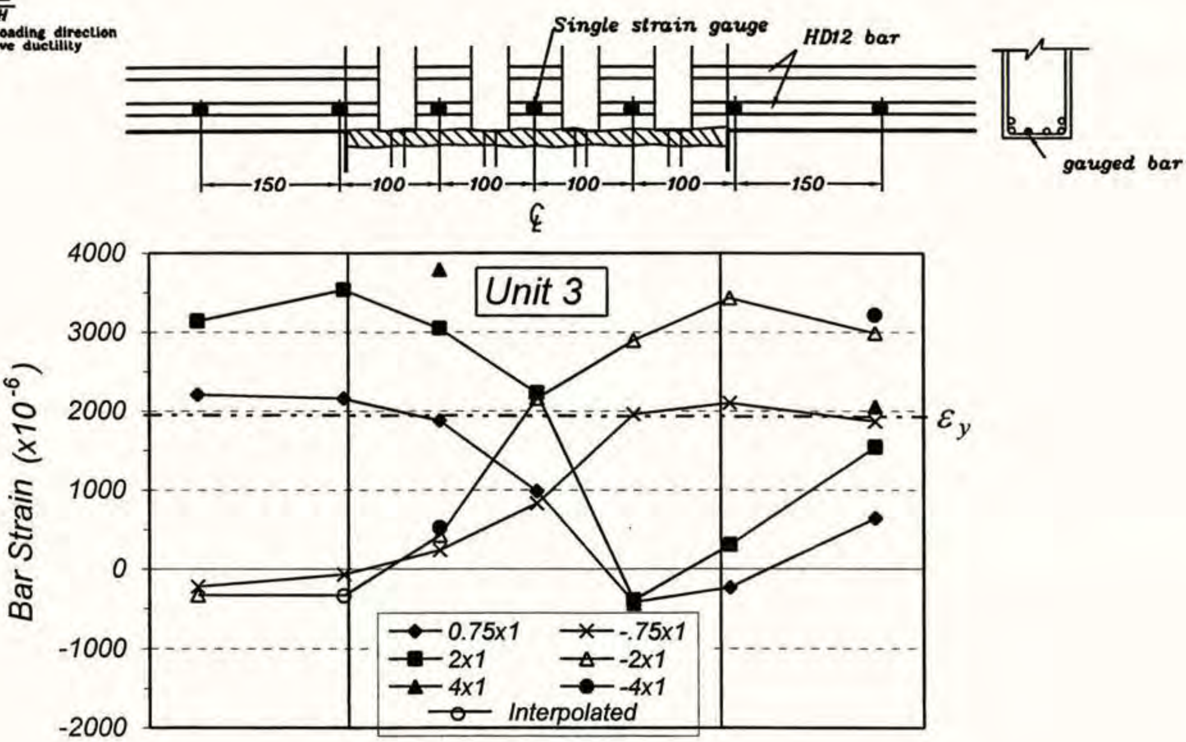

(b) Outer Layer

Figure 5.9 - Bottom Beam Bar Strain Profiles.

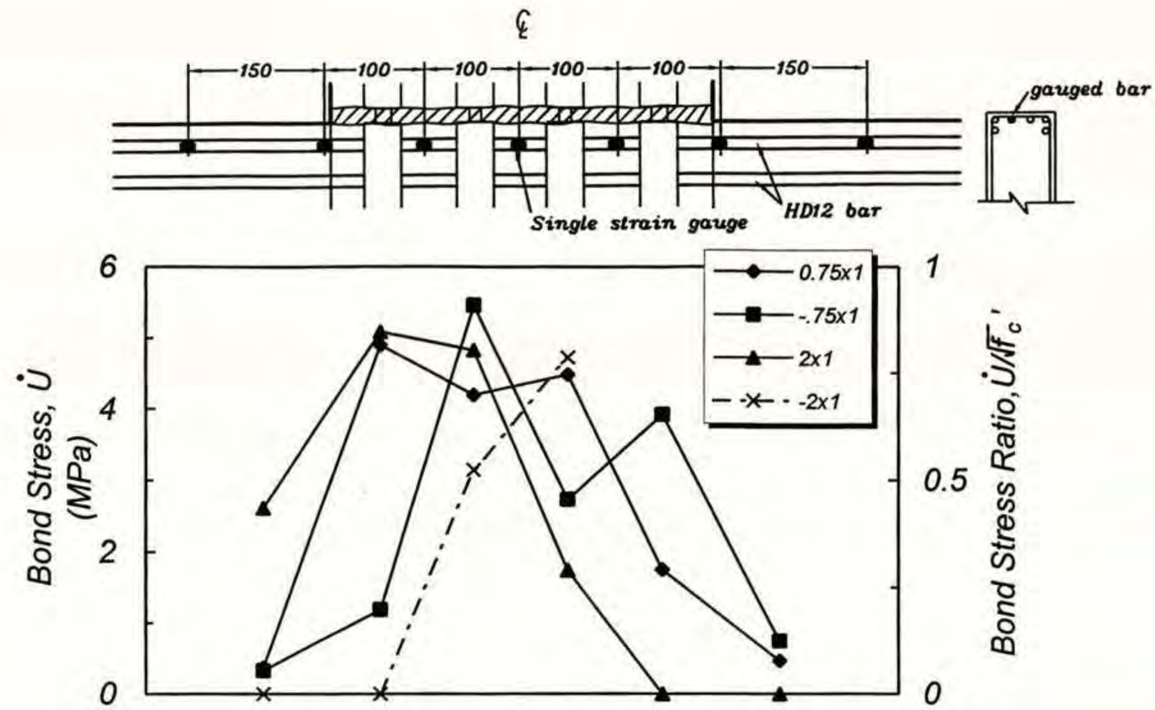

(a) Top Bars

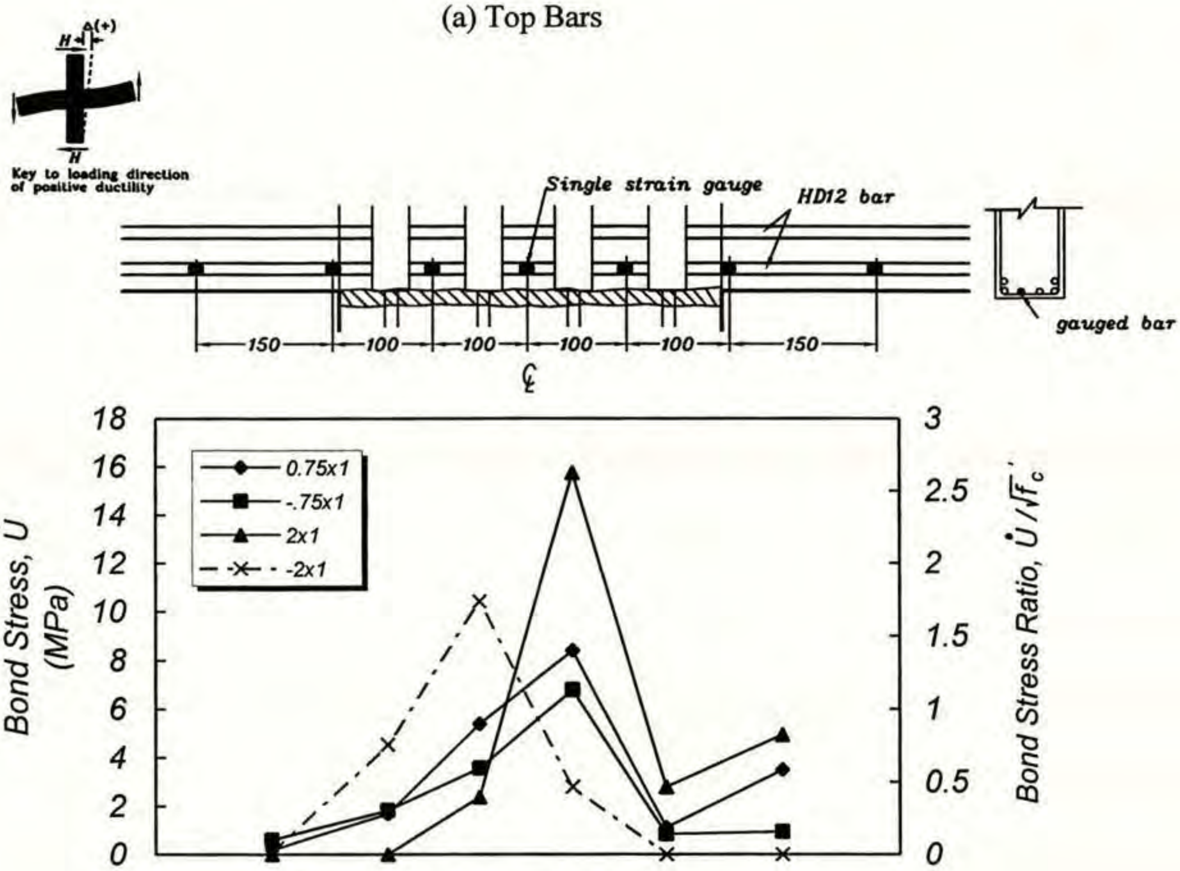

(b) Bottom Bars

Figure 5.10 - Calculated Bond Stresses.

computed for other units. Therefore, another peak value, 11 MPa, obtained in the load run of μ_Δ = -2x1 was recognized as the maximum peak bond stress developed on bottom beam bars. Thus the measured peak bond stresses on top and bottom beam bars are equivalent to 0.9, 1.8 $\sqrt{f_c'}$ respectively.

Apparently the values of absolute bond stress are smaller than that recorded in Units 1 and 2, in which large column axial loads were applied. Based on the results obtained in this study, it can be observed that the peak bond stress developed in the joint region depend on the axial load level applied in the column.

5.2.5.5 Bar Stresses of the Column Vertical Reinforcement Passing Through the Joint Region

All strain gauged bars remain elastic as expected during the design of the units. The stress profiles of the column longitudinal bars passing through joint region were calculated from the strain gauge readings and are presented in **Fig. 5.11**. The stress profiles in a corner bar showed a nearly uniform distribution in elastic load cycles and then showed a linear distribution in the inelastic load cycles. The maximum tensile stress on column bars reached 350 MPa at the beam faces. In contrast, the maximum compressive stress reached a maximum value of -80 MPa.

The stress profiles of interior column bars are also shown in **Fig. 5.11**. More uniformly distributed stresses profiles through the height of the joint can be observed with a maximum recorded stress of 220 MPa.

5.2.6 Beam Behaviour

5.2.6.1 Curvature Ductility Factors in Plastic Hinge Region

Figure 5.12 presents the beam curvature ductility factors obtained using the same procedure as in previous units.

The beam curvature ductility factors so found showed large scatter. However, a general trend that they increased gradually with the test sequence can be observed. The maximum value was 19 recorded on West beam in the loading cycle of μ_Δ = -6x1.

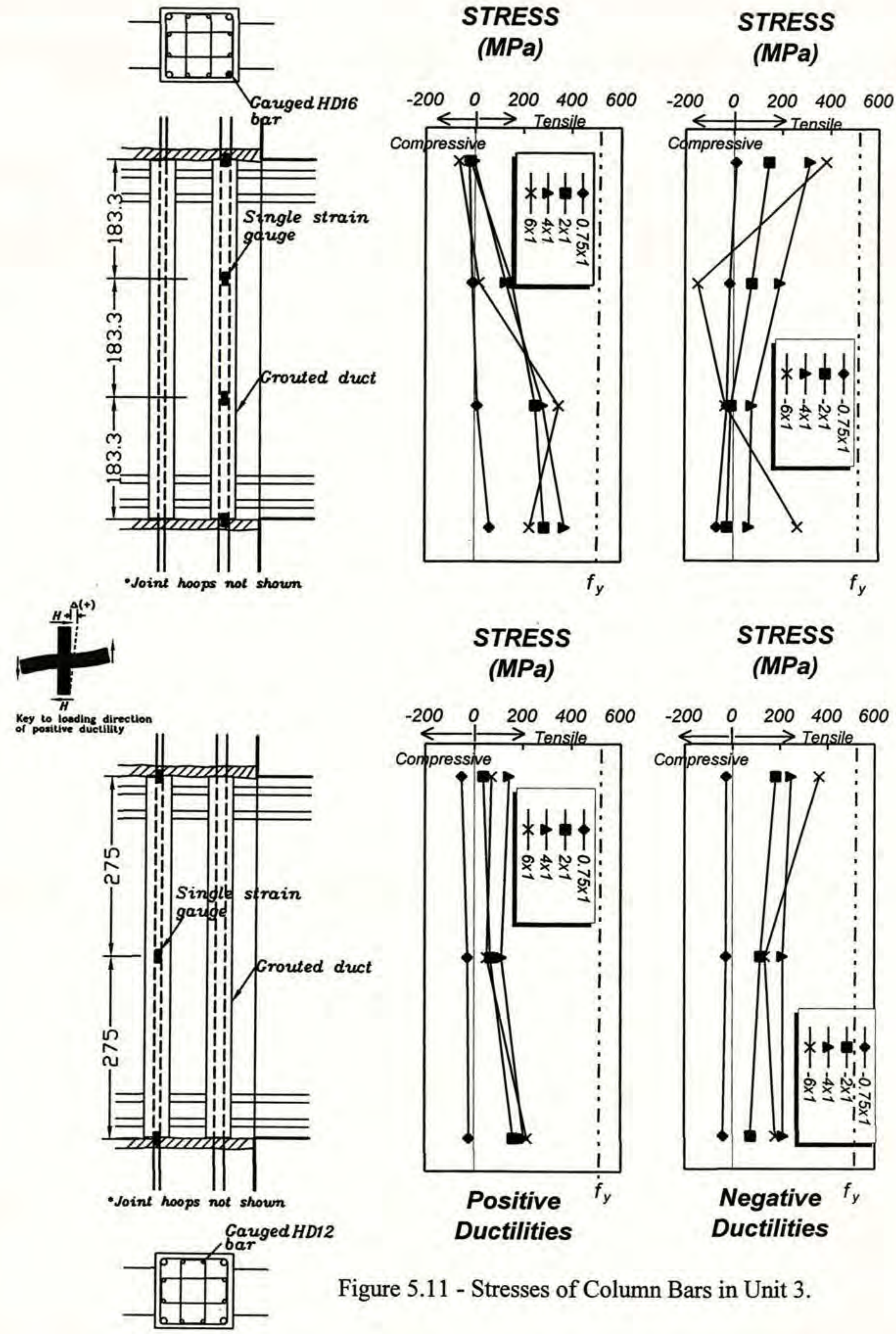

Figure 5.11 - Stresses of Column Bars in Unit 3.

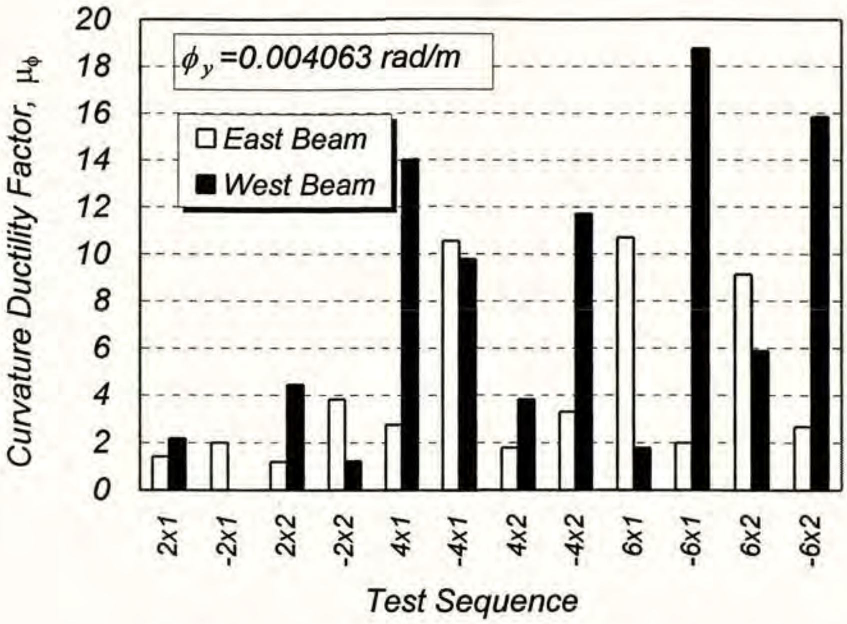

Figure 5.12 Curvature Ductility Factors of Beams of Unit 3

It is noted that the curvature ductility factors measured in East and West beams are rather inconsistent. This phenomena became more obvious from the loading cycles to μ_Δ = -4x2. The main difference observed in the curvature ductility factor in **Fig. 5.12** is attributed to the " top bar effect ". This is because the top beam bars slipped in the joint and as a result the plastic hinge did not spread out through the beam span, whereas the contrary occurred with the plastic hinge developing as a result of positive bending moment where the bottom bars were subjected to tension and had much better bond condition for anchoring in the joint region.

5.2.6.2 Beam Strain Profiles at the Level of the Longitudinal Reinforcement

Figures 5.13 and **5.14** show the strain profiles at the level of top and bottom longitudinal reinforcement of Unit 3. Presented information was calculated from the data readings of the potentiometers mounted along top and bottom beam chords.

The maximum member strains derived from the linear potentiometer reading at the level of top longitudinal reinforcement reached 2.5%. In **Fig. 5.13**, the tensile strain on West beam measured at a location close to the column face reached 2.5% in the loading cycle of μ_Δ = 4x1.

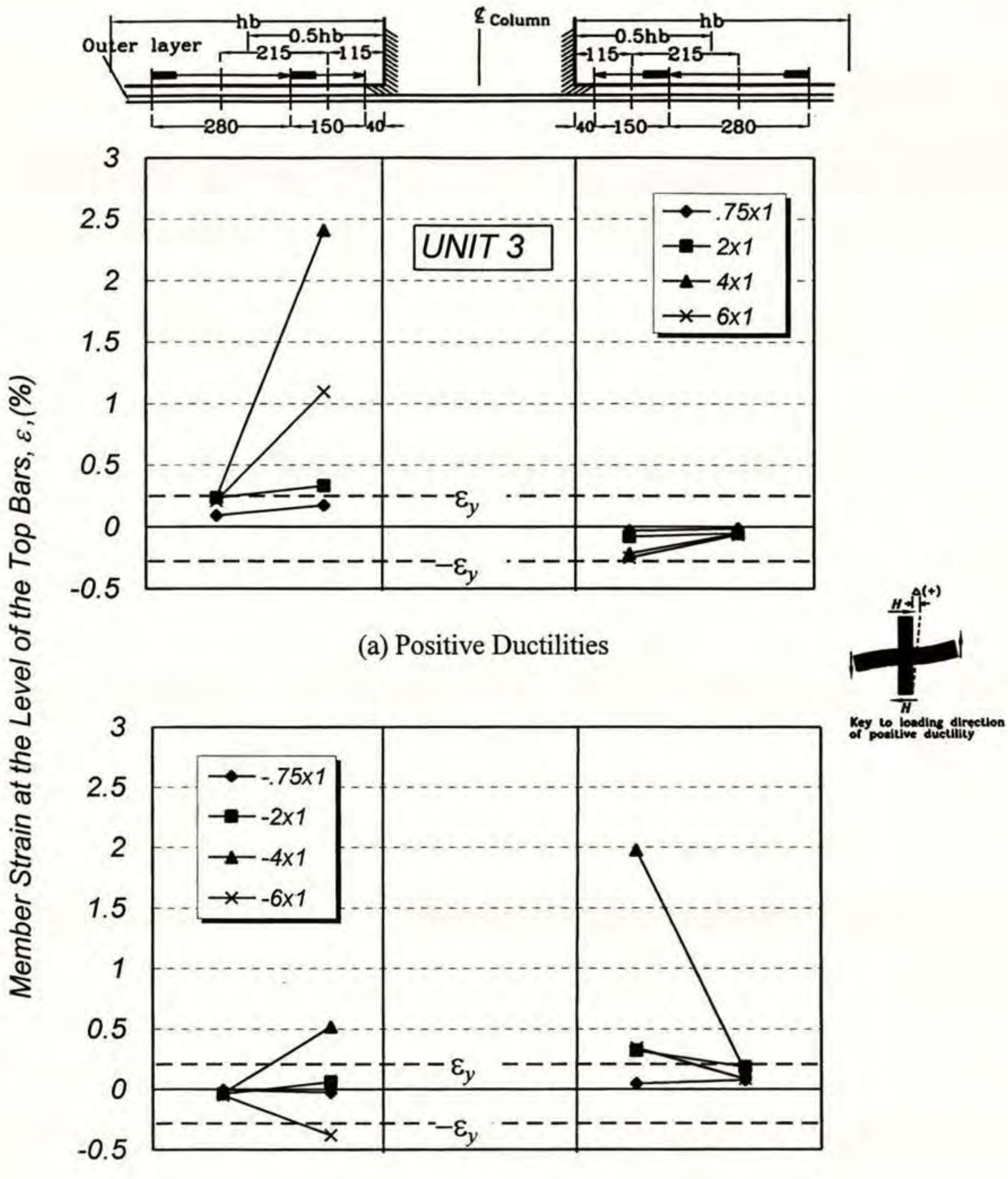

(a) Positive Ductilities

(b) Negative Ductilities

Figure 5.13 - Beam Strain Profiles at the Level of the Outer Layer of the Top Beam Bars of Unit 3.

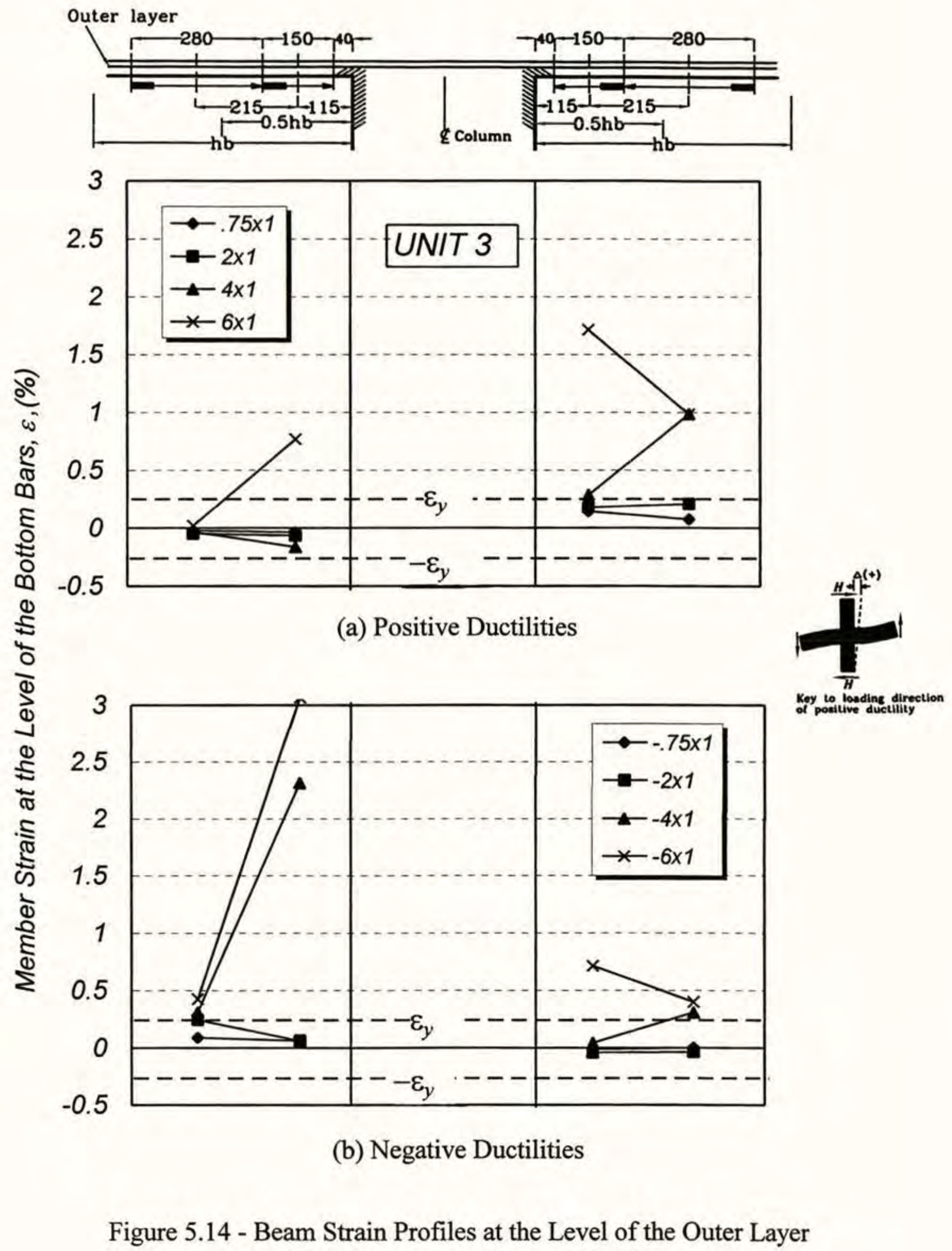

Figure 5.14 - Beam Strain Profiles at the Level of the Outer Layer
of the Bottom Beam Bars of Unit 3.

In the load cycle of μ_Δ = 6x1, it decreased to 1.1% at the same location. Whereas the level of the top bars in East beam recorded a high compressive strain, which is about equal to the yield strain of reinforcing bars. the same phenomenon also can be observed in the load cycle to μ_Δ = -6x1. It is believed that the high compression exists in concrete while the reinforcing bars may be in tension as a result of bond failure. At this stage, the assumption made in Section 3.6.2.4 that the concrete and reinforcement have the same average strain is no longer valid.

The strain profiles at the level of bottom longitudinal reinforcement reached a maximum value of 3%, see **Fig. 5.14**. The high compressive strain observed on top beam bars was not observed on the bottom bars. The strains recorded in the load cycles to μ_Δ = 6 rose continually with respect to the values in the load cycles to μ_Δ = 4. This agrees what had been discussed in Section 5.2.5.3 that the total bond failure of bottom beam bars did not occur eventually.

5.2.6.3 <u>Beam Elongation</u>

Figure 5.15 presents the measured beam elongation against the storey shear. The measured beam elongation followed a similar trend as in other units that most of it took place in the first load cycle toward a new displacement ductility.

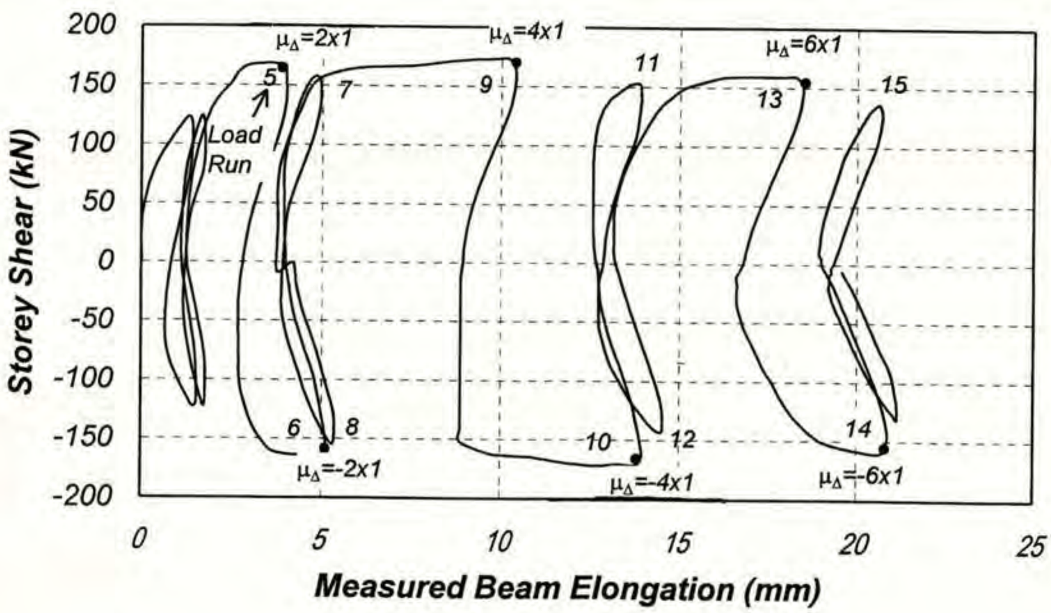

Figure 5.15 - Beam Elongation of Unit 3.

The measured beam elongation reached 18 mm at the peak to $\mu_\Delta = 6x1$. The amount of elongation took place in the load cycle of $\mu_\Delta = -6x1$ was less than that recorded in the previous load run. This indicates that the slippage of top beam bars tended to ease the growth of beam length.

The beam elongation measured at the end of test was 21 mm, which is approximately equivalent to 3.8% of the overall beam depth.

5.2.7 Column Behaviour

Visual observation and the analysis of the observed stresses in column bars presented in **Fig. 5.11**, indicate the column remained elastic throughout the test.

5.3 UNIT 4

5.3.1 Introduction

This unit was identical to Unit 3 except that the amount of top beam reinforcement was twice that of the bottom reinforcement. Identical quantity of horizontal joint reinforcement to that provided in Unit 3, was placed in the joint region of this unit. Provided amount of horizontal joint reinforcement is only 63% of that required by NZS 3101:1995 [S1] to achieve ductile performance. On the basis of the prediction from the analytical model, this unit should be able to have acceptable performance without joint failure.

5.3.2 General Behaviour

The overall behaviour of this unit is very similar to Unit 3. Crack patterns at some peak of loading cycles are illustrated in **Fig. 5.16**. The lateral load-displacement response was very stable until the load run to $\mu_\Delta = -6x1$. Except for the decrease in the lateral load capacity and pinching of hysteresis loops that took place in the final stages of the test, the performance of this specimen was even better than the previous one. The beam-column joint was able to provide enough strength to allow the development of plastic hinges in the beams.

In the elastic cycles, the crack pattern in the beams, columns and in the joint were generally similar to that in Unit 3. A corner to corner diagonal crack in joint panel occurred in the first load run of 75% of theoretical lateral load which appeared earlier than in Unit 3.

However, another corner to corner crack did not appear in another direction in the reversed load run. It was observed that the cracks in joint panel were prone to take place in the vicinity of the top beam bars. Cracking in beams showed a general trend that they spread a longer distance in the top than in the bottom chord.

As the specimen was loaded into inelastic range, $\mu_\Delta = 2$, new cracks occurred in the joint region with the corner to corner diagonal crack reaching a width of 0.5 mm. Cracks in beams occurred in a pattern in which main cracks concentrated vertically on column faces with a width of 2.0 mm. Diagonal cracks also developed in the beams at a distance of 150 mm from column faces. Cracks in columns remained nearly unchanged as in the elastic cycles and concentrated along the top and bottom beam faces. In general, it seems that more cracks occurred in the upper half part of the joint panel than in the lower part at this stage.

By $\mu_\Delta = \pm 4x1$, very few new cracks took place in the joint with the central diagonal ones having a width of 0.5 mm. Cracks in the plastic hinges in the beams developed progressively, with maximum width reaching 4 mm along column face and 2.5 mm elsewhere. A few flexural cracks appeared on the tension side of top and bottom column sections in a distance of 200 mm away from beam faces. In the following load cycle, cracks in beam plastic hinge region increased in width reaching up to 5.0 mm. A corner to corner crack in joint region grew wider to a width of 1.0mm. Comparing the crack patterns in the upper and lower half of the joint panel, it can be seen that more cracks formed in the upper part than that in the lower part. However, there was no sign showing damage on the joint concrete. It is believed that until this stage the joint shear reinforcement was able to resist the input joint shear force adequately and sustain the stresses in the diagonal compression field.

In the load cycle to $\mu_\Delta = +6x1$, the cracking in the joint region remained essentially similar to that in the previous load cycle with crack widths remaining the same. Cracks in plastic hinge region grew to a width of 7.0 mm at column face and 4.5 mm elsewhere. In the reversed load cycle, the cracks in the beams concentrated at the column faces while the width of other cracks decreased. This indicated that slip of top bars and bottom bars took place and the fixed-end rotation predominated the lateral displacement. As test proceeded toward the second cycle of $\mu_\Delta = 6$, slip of beam bars was more obvious by observing that cover concrete around corners at the intersection of beams and columns began to be crushed, especially in the bottom corners. Some split of concrete in beams along bottom beam bars took place which

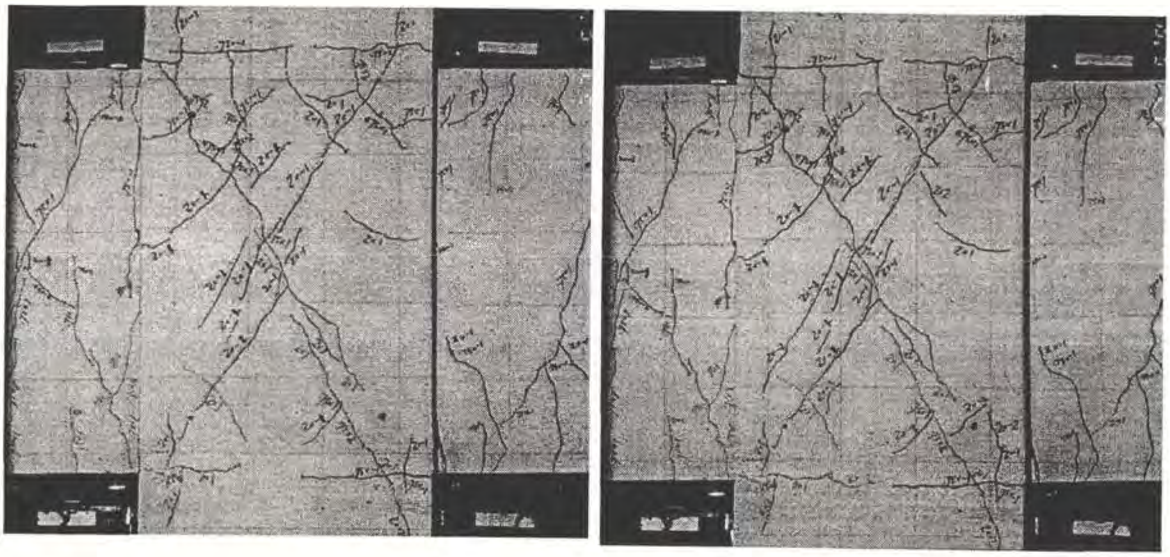

(a) At μ_Δ=-2x1

(b) At μ_Δ=-2x2

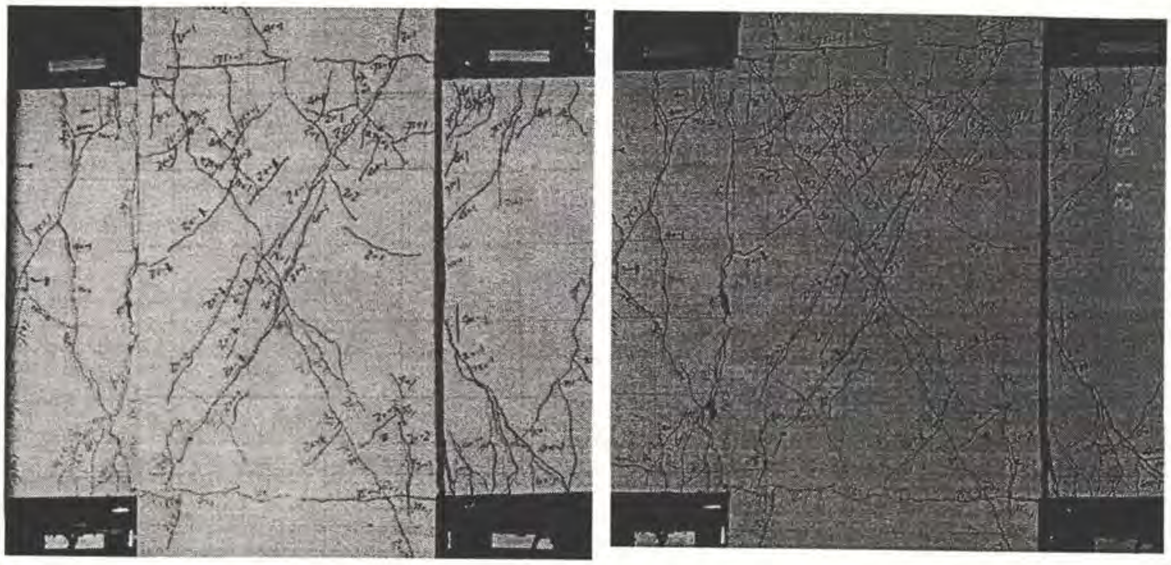

(c) At μ_Δ=-4x1

(d) At μ_Δ=-4x2

Figure 5.16 – Cracking of Unit 4 at Different Stages During the Test.

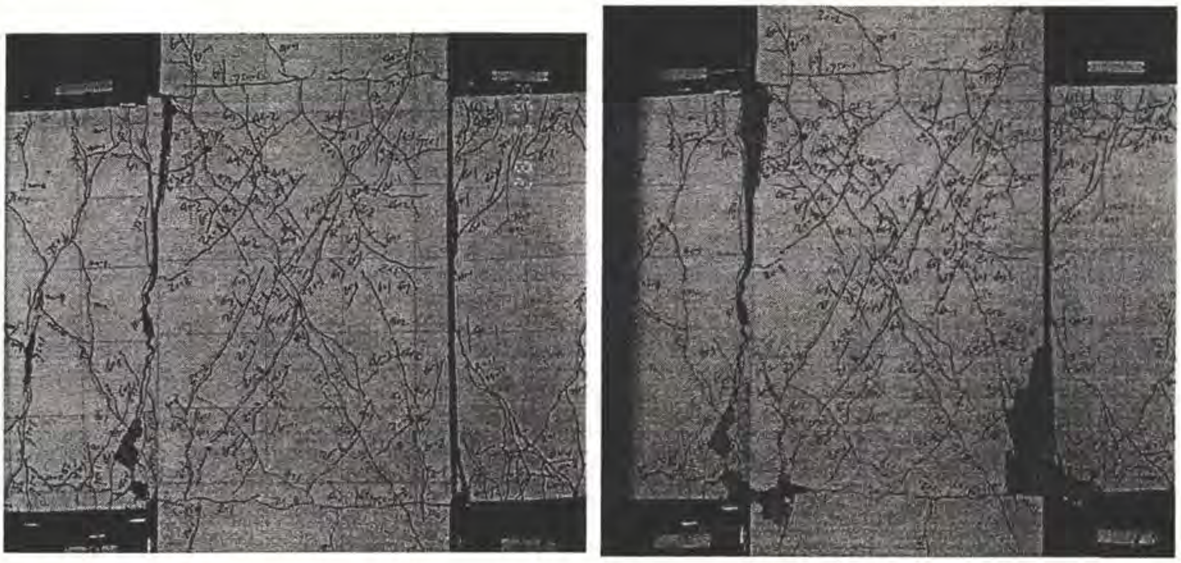

(e) At μ_Δ =-6x1 (f) At μ_Δ =-6x2

Figure 5.16 (Cont.) – Cracking of Unit 4 at Different Stages During the Test.

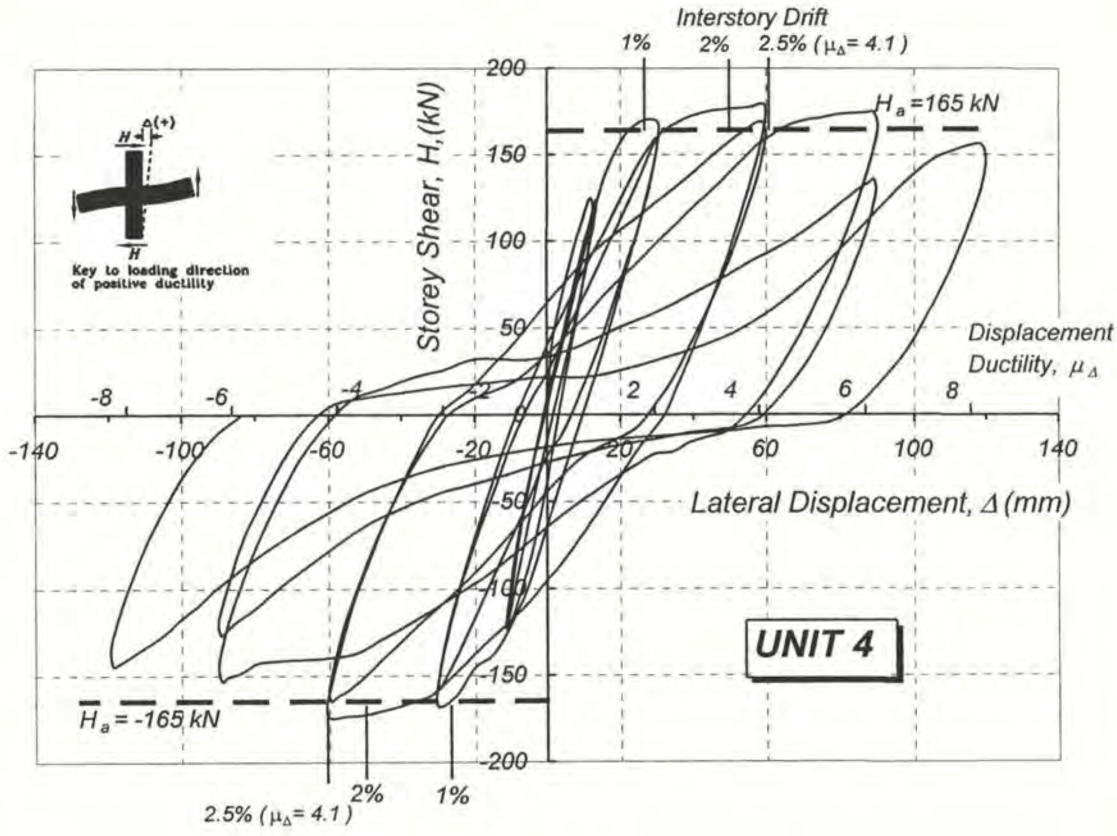

Figure 5.17 - Lateral Load-Displacement Response of Unit 4.

was an indication of spreading of bond deterioration into beam region. Maximum crack width in joint region remained as 1.0mm, similar to that measured in the previous load cycle.

Test was carried on toward $\mu_\Delta = 8$. Cracks in beams along column faces were growing up as two big gaps. Crush of concrete in the four corners and split of cover concrete along top and bottom beam bars which are all indications of bond slip were in progress. Apparent sliding shear deformation at column faces as a consequence of the forming of gaps could be observed. Test was terminated in finishing the load cycle to $\mu_\Delta = 8$x-1.

5.3.3 Load-Displacement Response

The yield inter-storey drift, averaged from the measured values obtained in the four elastic load runs, was 0.61%. The yield drift implies a displacement ductility, $\mu_\Delta = 4.1$ when the 2.5 % drift limit is attained.

The measured lateral load-displacement response for Unit 4 is presented in **Fig. 5.17**. The theoretical ultimate lateral load was achieved in the first inelastic cycle. Note that a slight disturbance in the load-displacement response took place prior to the peak to $\mu_\Delta = -2$x1. It is believed that this was caused by the closure of some cracks in the beams. The lateral load rose at the peak of the following cycle to $\mu_\Delta = 4$x1, and exceeded the theoretical ultimate lateral load by 8.5% and 4.5% in the positive and negative load runs, respectively. Note that the peak loads of this unit at this stage of loading are greater than those attained by Unit 3. In the second cycle to $\mu_\Delta = 4$, unlike in Unit 3 in which significant loss of bond on top beam bars gave rise to a reduction of lateral load capacity below theoretical ultimate value, the lateral load reached the theoretical ultimate value.

In the first load cycle to $\mu_\Delta = 6$, the hysteresis loop was stable with the peak load exceeding the theoretical ultimate value by 5.5%. However, in the reversed load run, $\mu_\Delta = -6$x1, a 11% drop of lateral load capacity with respect to the recorded maximum load was recorded. The lateral load capacity dropped more significantly to 76% and 74% of the maximum measured load in the positive and negative load runs to the second cycle to $\mu_\Delta = 6$, respectively. Significant pinching in the loops was observed from this load cycle onwards. Note that this considerable drop of lateral load capacity was caused by bond slip of both top and bottom beam bars. In the following cycle, $\mu_\Delta = +8$x1, the lateral load capacity was recovered up to 87% and 85% of the recorded maximum value.

Test was terminated at the end of finishing load cycle of μ_Δ = -8x1 corresponding to an inter-storey drift of 4.9 %.

5.3.4 Decomposition of Lateral Displacements

The decomposition of the lateral displacements in this Unit are shown in **Fig. 5.18**.

In general, the components of lateral displacement are very similar to those of Unit 3. The component of beam fixed-end rotation increased gradually during the test. A considerable rise of this component occurred in the load cycles to μ_Δ = -6x1, indicating that significant loss of bond on longitudinal beam bars in joint region took place in that load cycle.

The measured beam flexural deformation tended to be larger in the positive load runs than in the negative runs. This component was basically very similar in magnitude in each load cycle up to μ_Δ = 6x1. An apparent diminution of this component occurred in the subsequent load cycle, μ_Δ = 6x2.

The component of beam-column joint distortion reached a maximum value 19% in the load cycle to μ_Δ = -4x2. Note that this value did not exceed the 20% limit suggested by Cheung et al. [C1].

Beam shear deformation showed an increasing trend with the progress of the test, reaching a maximum value of 18% in the load cycle to μ_Δ = -6x1.

5.3.5 Joint Behaviour

5.3.5.1 Strains in the Horizontal Joint Shear Reinforcement

Readings taken from the double strain gauges attached on the top and bottom of each set of joint transverse reinforcement, including perimeter R10 and inner R6, were averaged and presented in **Figs. 5.19** and **5.20**

The strain distribution in the joint hoops is rather similar to the trend observed in Unit 3. The recorded strains in the elastic loading cycles were smaller in Unit 3. As it was explained in Section 5.2.5.1, this is a feature of joints with low shear stress ratios.

By μ_Δ = 2, the hoop strains approached yielding and then reached yielding strain in the

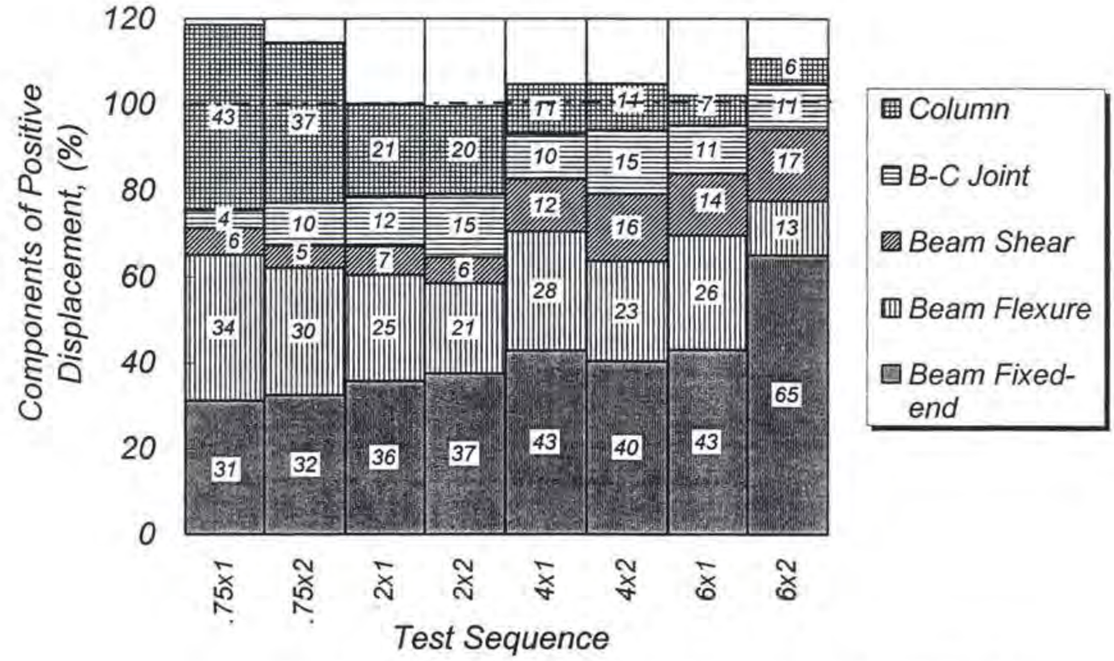

(a) Runs to Positive Ductilities

UNIT 4

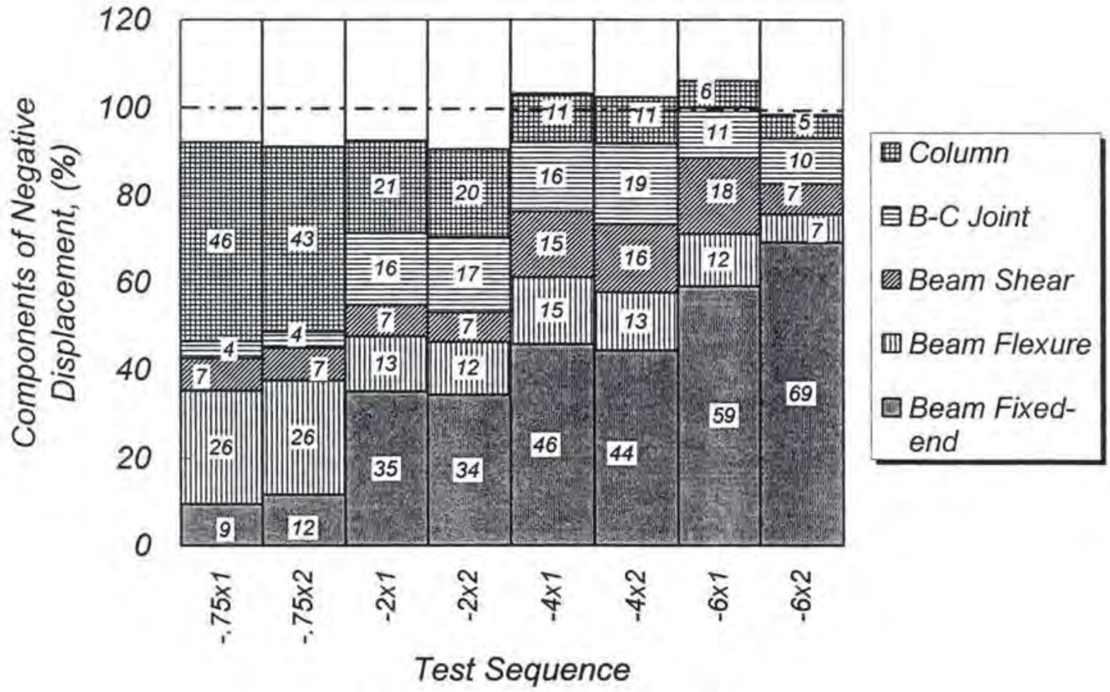

(b) Runs to Negative Ductilities

Figure 5.18 - Components of Lateral Displacement of Unit 4 at Peaks of Load Runs

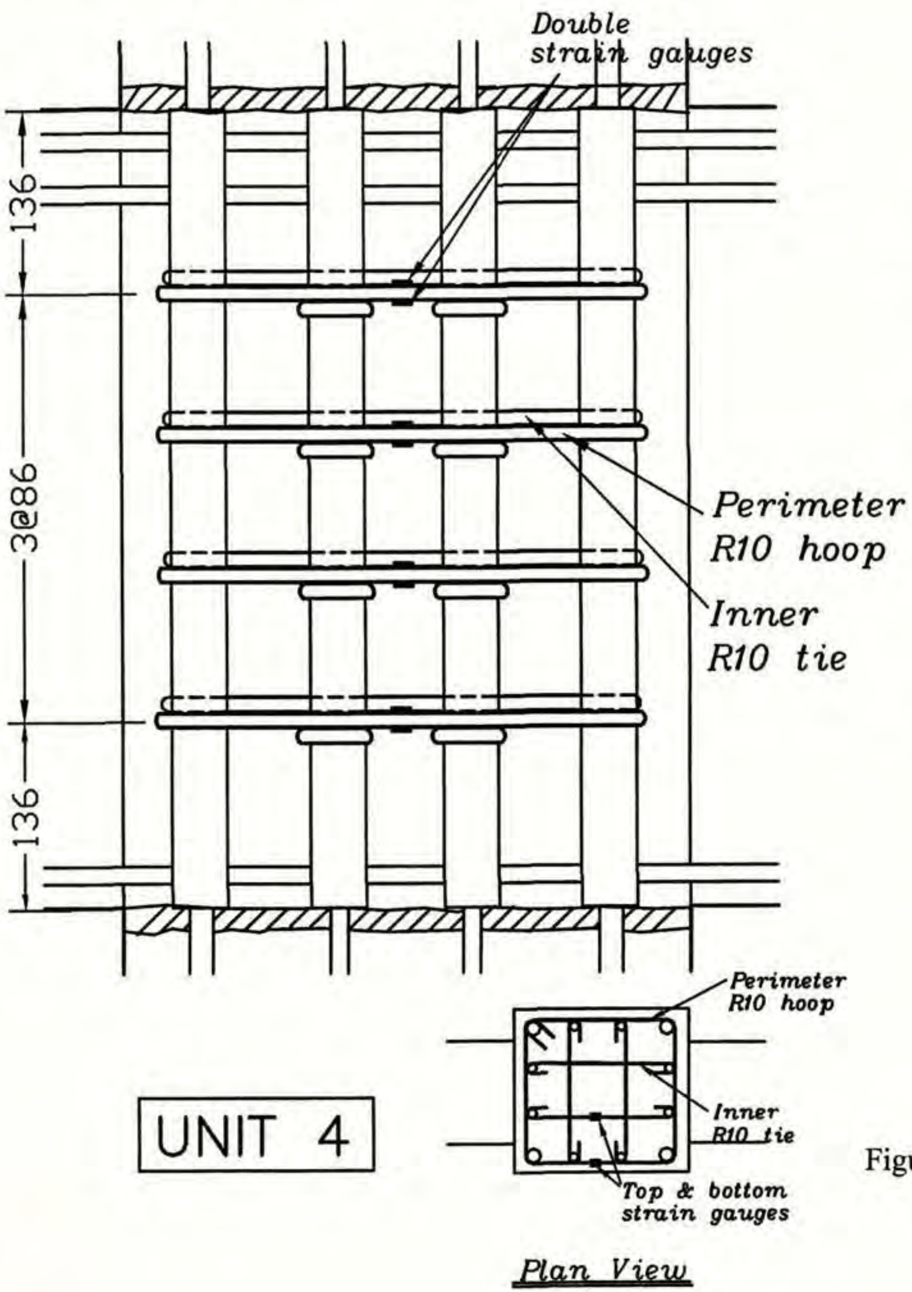

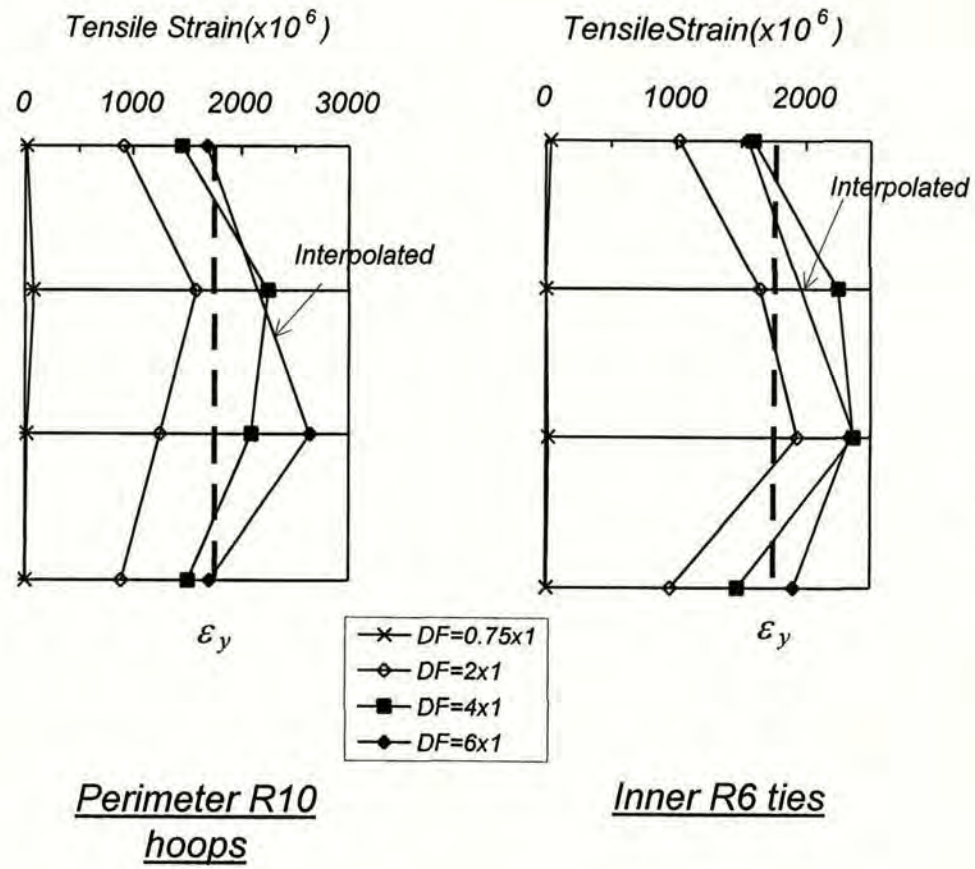

Positive Ductilities

Figure 5.19 - Measured Strains in Joint Hoops of Unit 4 During the Runs to Positive Ductilities.

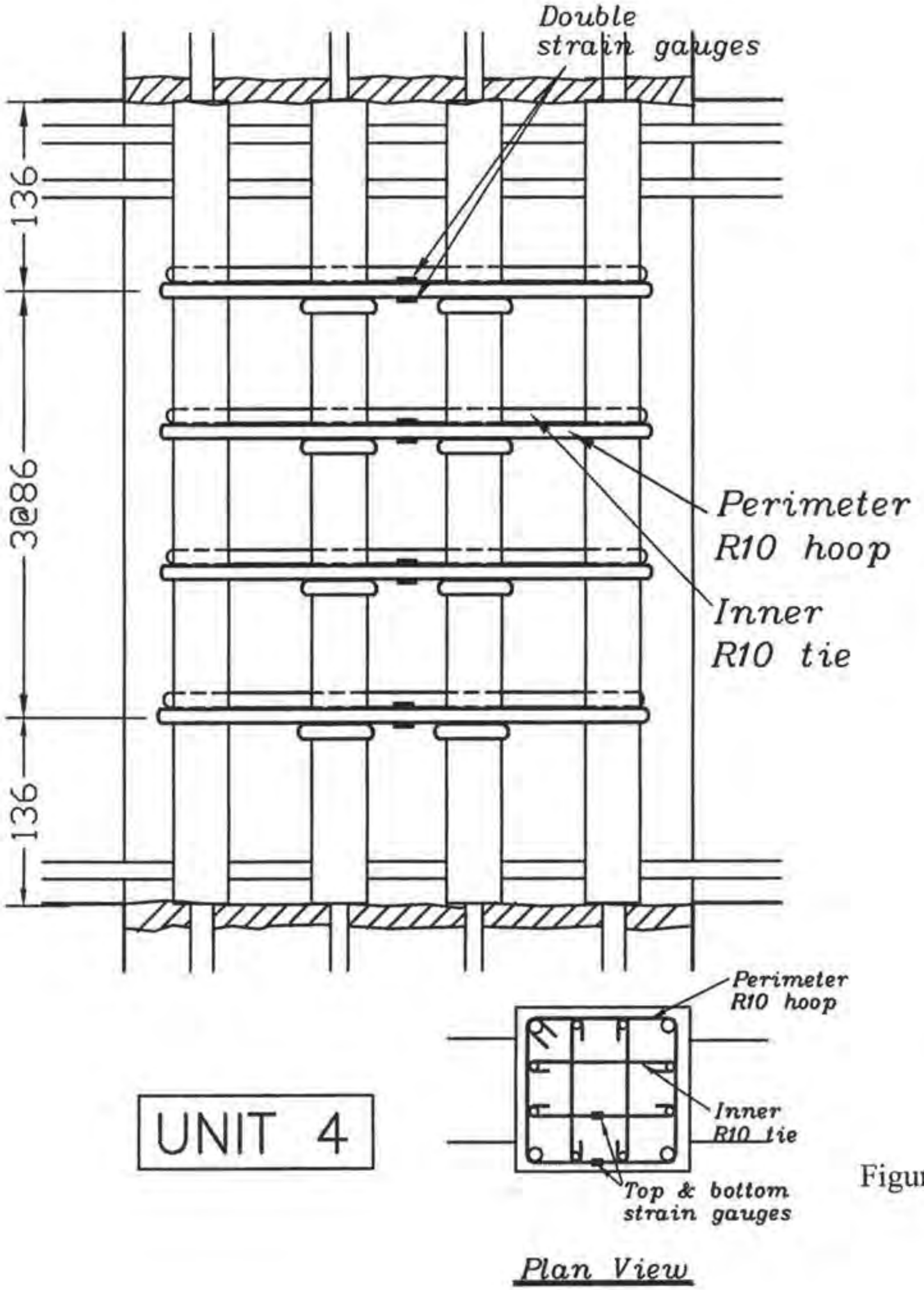

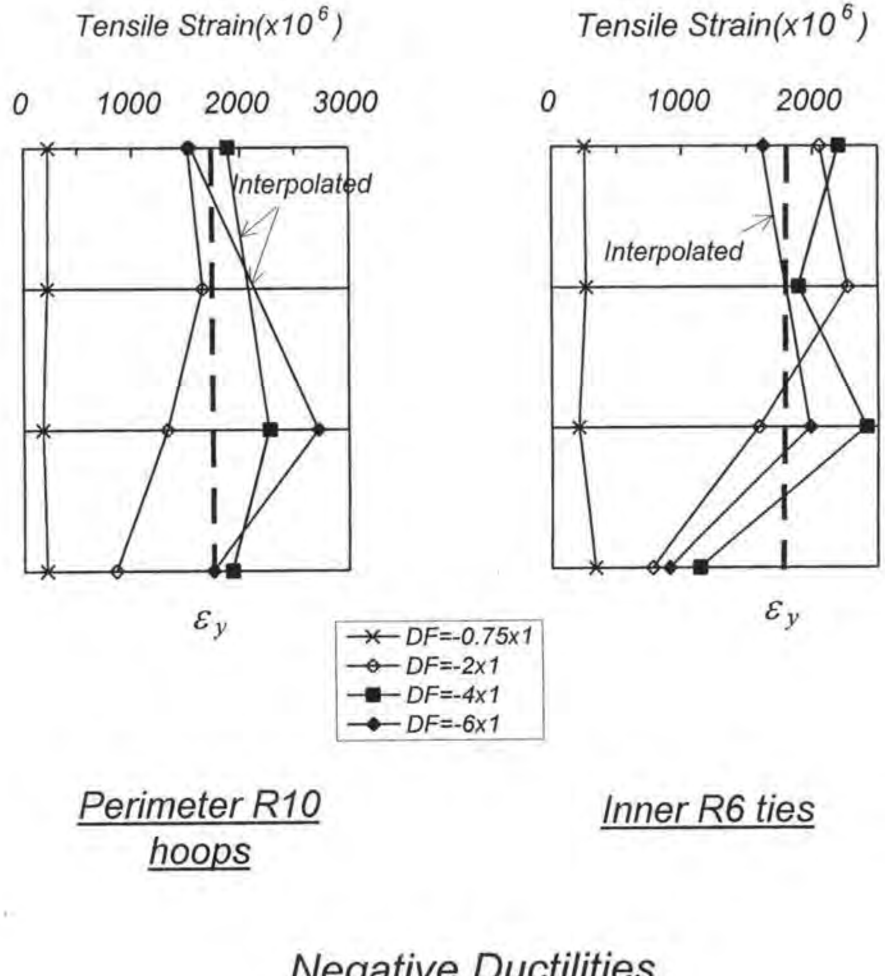

Figure 5.20 - Measured Strains in Joint Hoops of Unit 4 During the Runs to Neagtive Ductilities.

load cycle to $\mu_\Delta = 4$. Similar to what had been found in Unit 3, the strain in the joint hoops in the loading cycles to $\mu_\Delta = 6$ did not significantly change from those strains measured in the load cycles to $\mu_\Delta = 4$.

Although the joint transverse reinforcement eventually yields when the specimen is loaded towards a large displacement ductility, the aim of a joint design is to provide adequate quantity of reinforcement to delay unrestricted yielding, that leads to a deterioration of the strength of the diagonal compression stress field, to occur at relative large ductilities. It is noted that yielding of the joint hoops and ties in the load cycle to $\mu_\Delta = 4$ was proved to be adequate for the design of joints with low $v_{jh} / f_c^{'}$ ratios as the tests in Units 3 and 4 clearly showed.

5.3.5.2 Joint Shear Distortion Versus Lateral Loads

Figure 5.21 presents the measured joint shear distortion against lateral load. The response is very similar to that measured in Unit 3. The maximum joint shear distortion

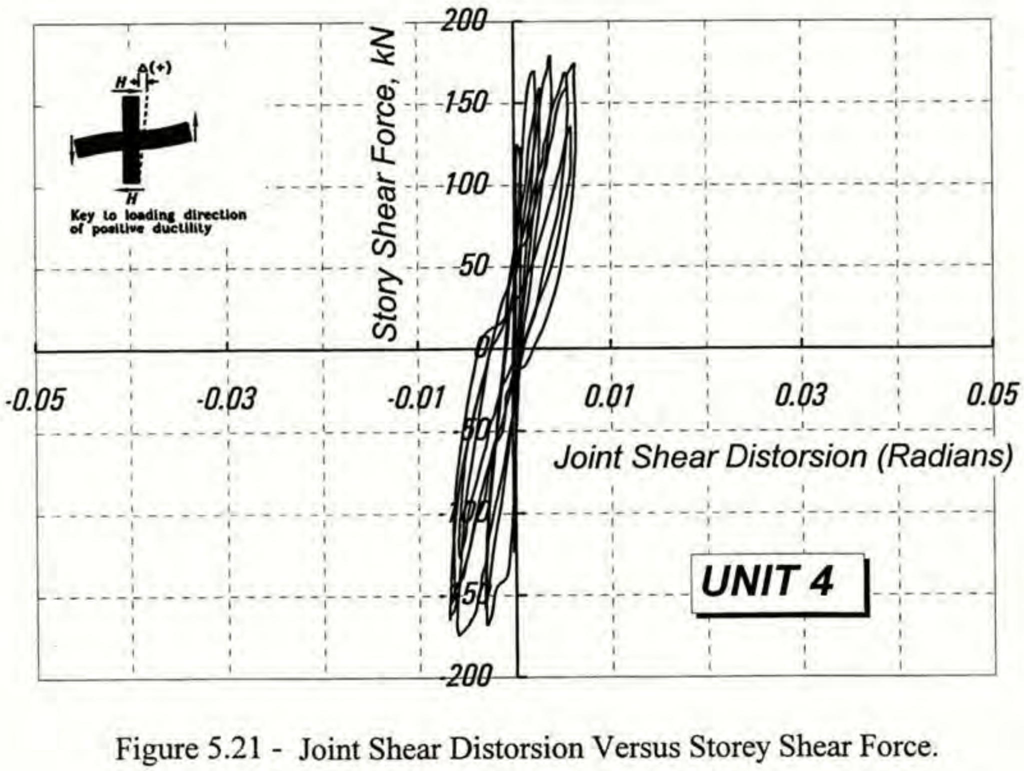

Figure 5.21 - Joint Shear Distorsion Versus Storey Shear Force.

reached 0.006 radians, a value which is approximately equal to that was recorded in Unit 3 (see **Fig. 5.6**).

5.3.5.3 Beam Bar Slip Within Joint Region

Figure 5.22 depicts the local slip of the top and bottom beam bars at three locations in joint region. The top beam bars of Unit 3 showed large bar slip than those in Unit 4. The contrary was observed for the bottom bars. Slip of both top and bottom beam bars measured at the location of joint centre exceeded the rib clear spacing 5.2 mm in the load cycle to $\mu_\Delta = -6x1$, indicating that bond failure of both top and bottom beam bars in joint region had occurred.

Note that at this stages some reading of the slip were affected by the contacting of studs and the surrounding concrete.

With reference to the lateral load-displacement response depicted in **Fig. 5.17**, it can be concluded that the 11% reduction of lateral load capacity recorded in the loading run $\mu_\Delta = -6x1$ was caused by the loss of bond in the top and bottom beam bars described above.

The insignificant discrepancy of slip on top and bottom beam bars observed in this unit can be explained as following. The amount of top beam longitudinal reinforcement is greater than the bottom reinforcement in Unit 4. Compressive stress developed in top bars on one side of column face would be less than that of the case in which equal top and bottom beam bars were incorporated. As a result, the demand of anchorage within joint region for top bars is less severe than for Unit 3 that had equal top and bottom reinforcement. On the other hand, the bottom beam bars will be subjected to larger compressive stress on the other side of column face than the normal joints, imposing a more severe demand of bond stress in joint region for bottom beam bars [R1] [C1].

5.3.5.4 Bar Strain And Bond Stress of the Beam Longitudinal Reinforcement Passing Through Joint Region

The strain profiles on each layer of longitudinal beam bars within joint region are presented in **Figs. 5.23** and **5.24**. **Figure 5.25** plots the absolute bond stresses developed along the top and bottom beam bars.

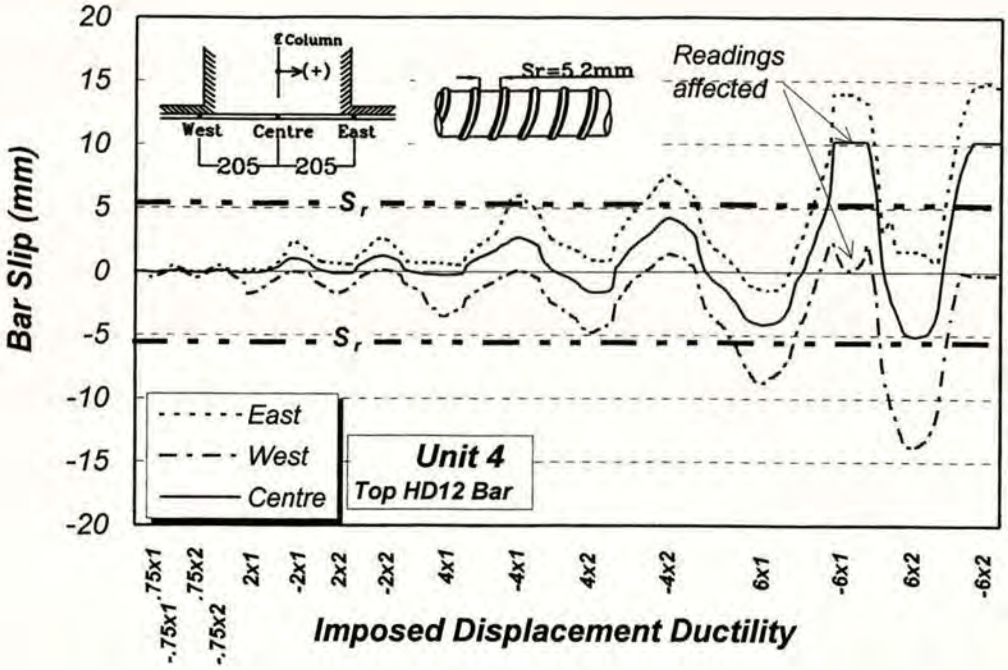

(a) Top Bars

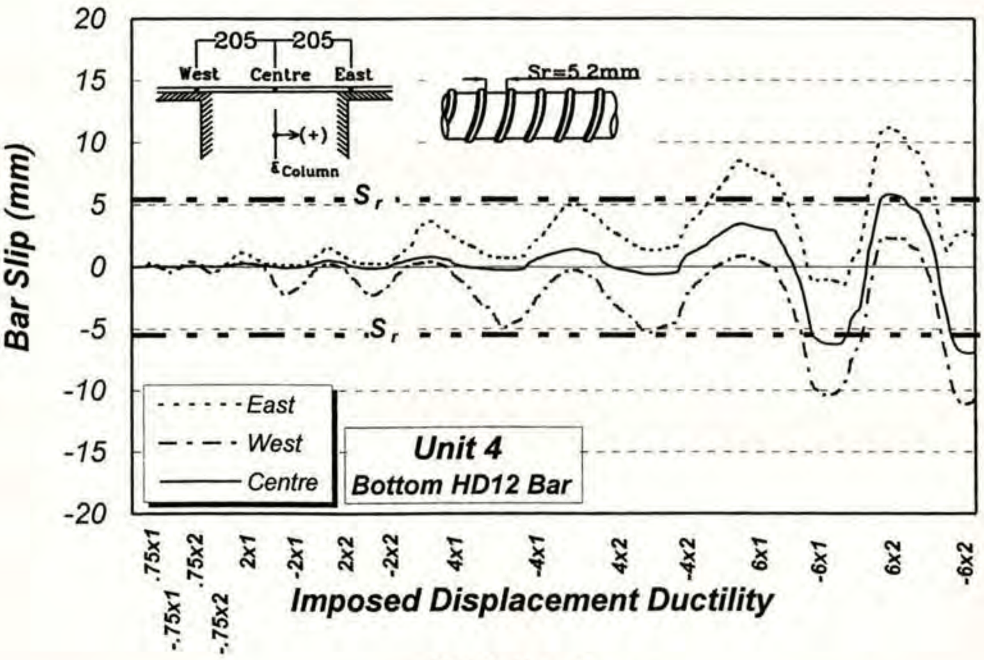

(b) Bottom Bars

Figure 5.22 - Relative Slip of Beam Longitudinal Bars
in the Joint Region.

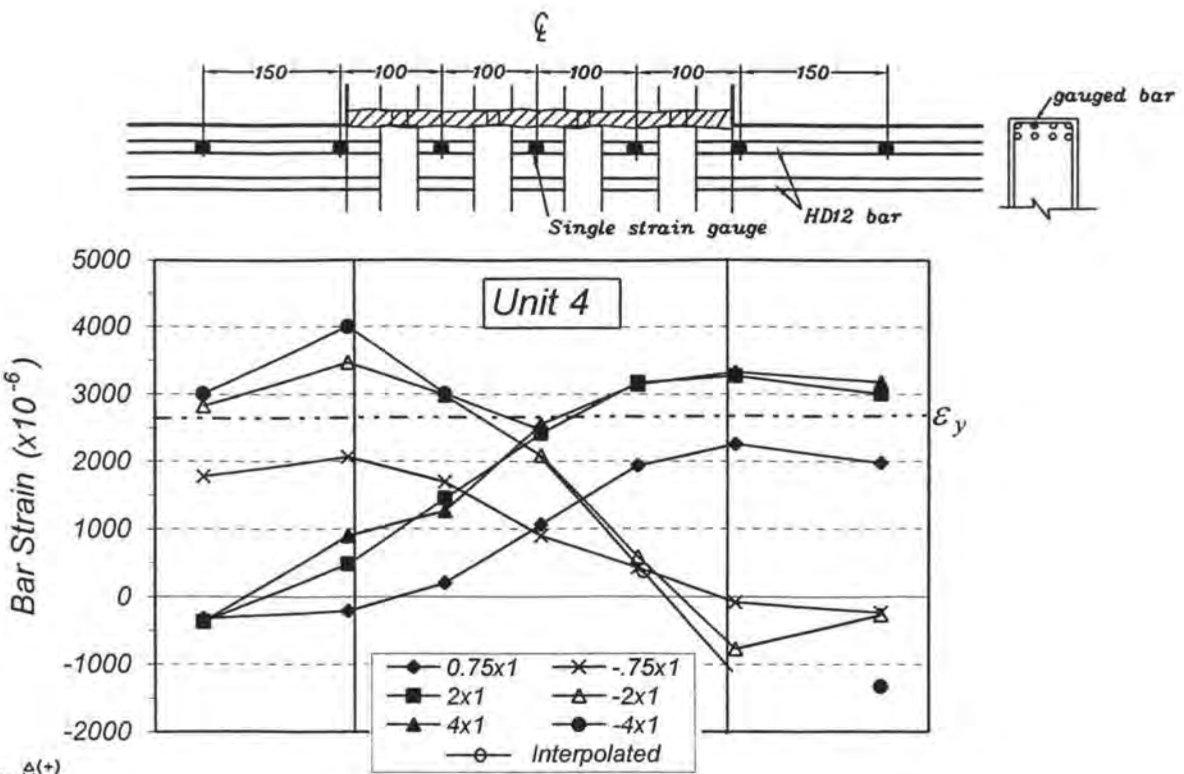

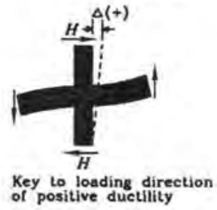

(a) Outer Layer

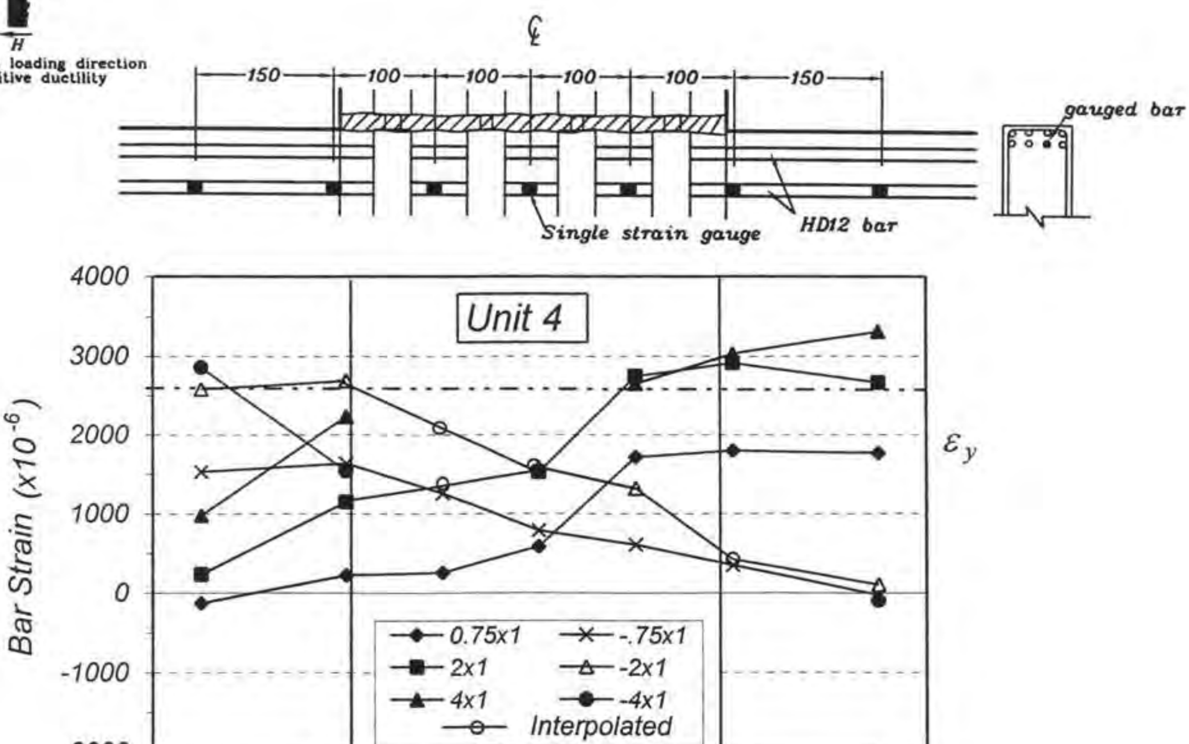

(b) Inner Layer

Figure 5.23 - Top Beam Bar Strain Profiles.

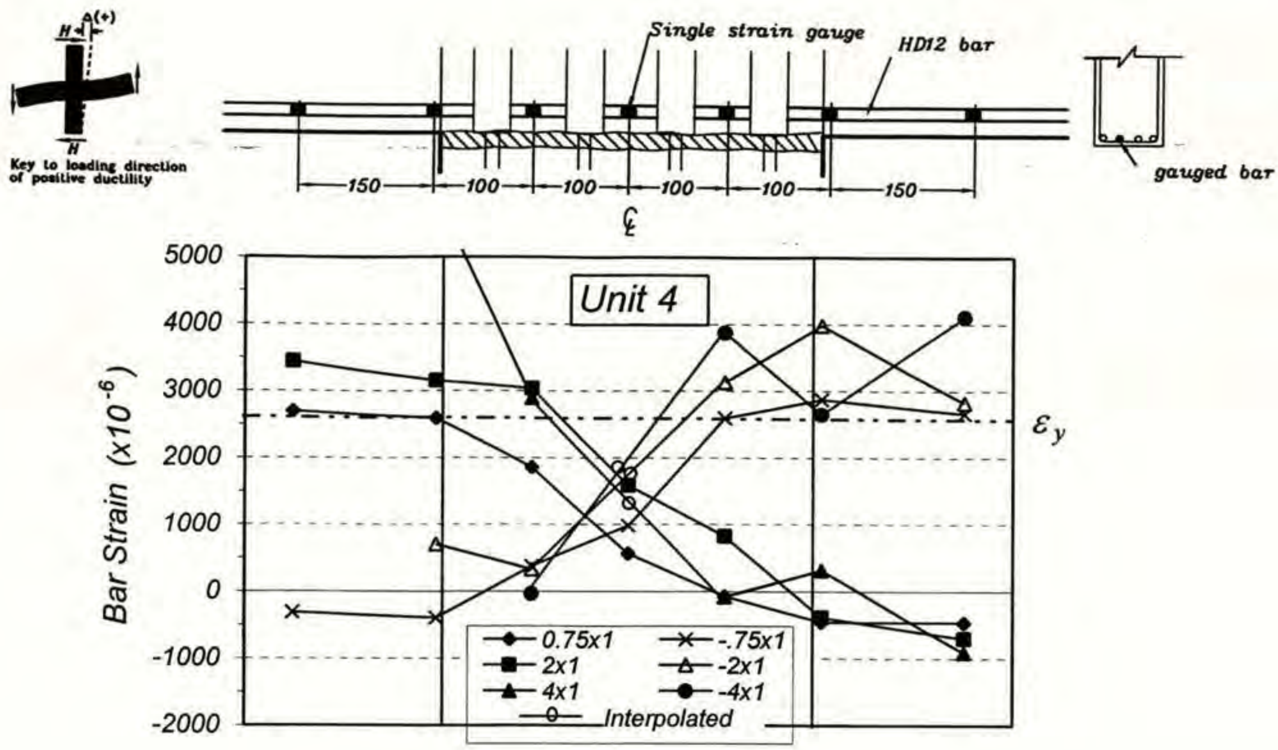

Figure 5.24 - Bottom Beam Bar Strain Profiles.

Maximum tensile strain developed on the first layer of top beam bars reached 4000 micro-strain in the load cycle to μ_Δ = -4x1. The maximum compressive strain on the same layer of beam bars was -1200 micro-strain occurring in the same load cycle, μ_Δ = -4x1.

Both the tensile and compressive strains recorded on the second layer of top beam bars were, as excepted, not as large as that in the first layer. Only very little compressive strain, 100 micro-strain, was recorded on the compressive side in the elastic cycles. Due to the upward shift of neutral axis, the recorded strain profiles along the second layer of top beam bars within the gauged region were all in tension. This implies that the demand of bond stress on the second layer of top beam bars within joint region was not so much as in the first layer.

The strain profiles recorded on bottom beam bars are, in general, larger than that recorded on the first layer of top beam bars in each corresponding cycle. This is due to the reason described in the last section, the layout of unequal top and bottom beam bars imposed a more severe demand of bond stresses in the bottom beam bars.

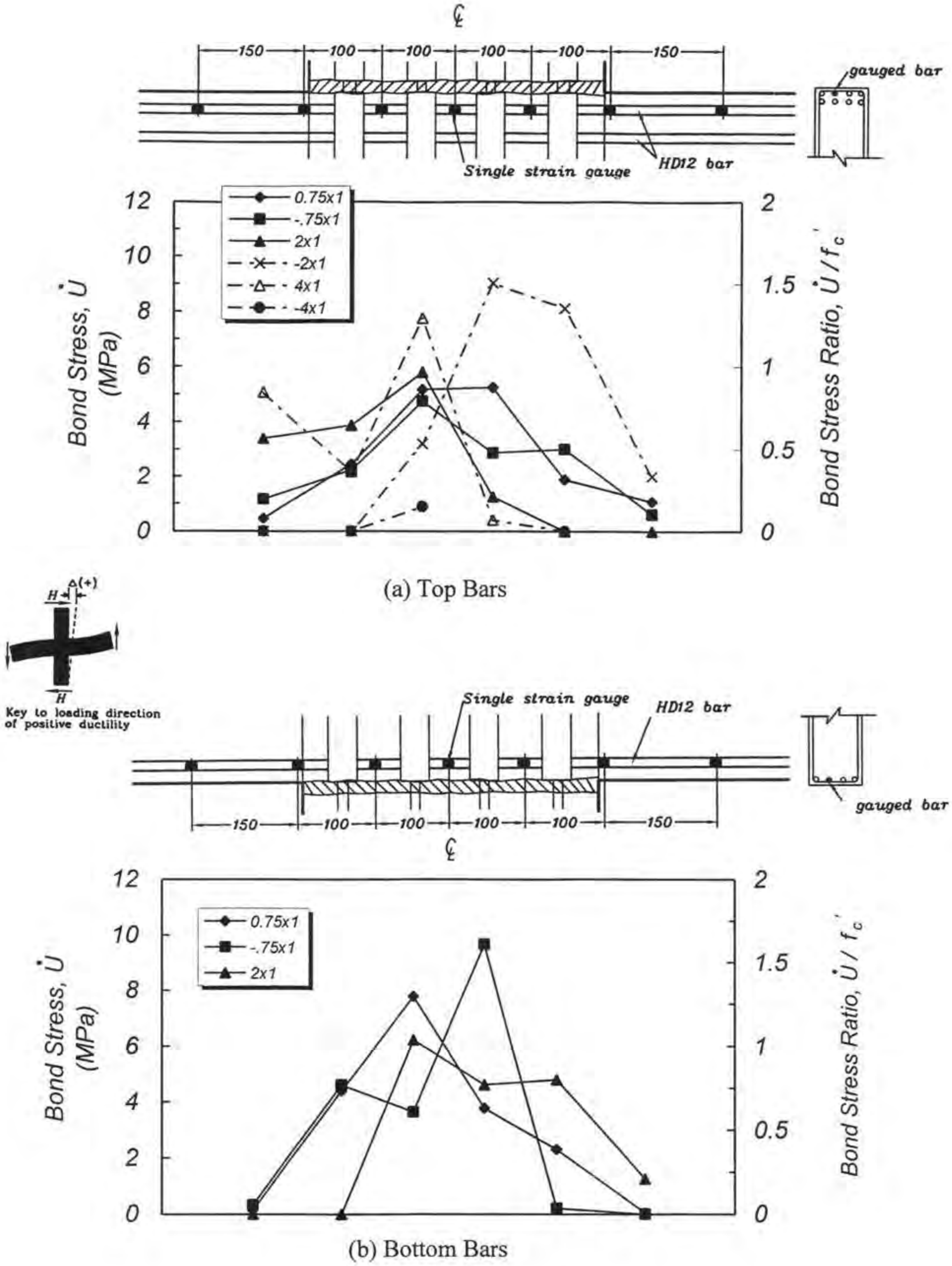

(a) Top Bars

(b) Bottom Bars

Figure 5.25 - Calculated Bond Stresses.

The maximum bond stresses developed in the top and bottom beam bars were 9 and 10 MPa, which are equivalent to 1.5, $1.64\sqrt{f_c'}$, respectively. Data used to calculate the bond stresses in the bottom beam bars were only available until load cycle of $\mu_\Delta = 2x1$ as some of strain gauges were damaged. Therefore it is believed that larger bond stress was likely develop on bottom beam bars though it was not recorded.

5.3.5.5 Bar Stresses of the Column Vertical Reinforcement Passing Through the Joint Region

As the same procedure used in the previous units, the stress profiles of exterior and interior column bars at each peak of load run were plotted in **Fig. 5.26**. In general, the profiles followed a similar trend as in Unit 3.

The maximum tensile stress occurred in exterior column bars at top of beam face were larger than that in Unit 3, with a value approaching the yielding stress in the load run to $\mu_\Delta = -4x1$. Apparently the bending moment in column critical section was larger than that in Unit 3. This is because that larger beam flexural strength was developed in this unit. However, it is believed that the yielding of column bars did not progress further beyond.

Stresses on interior column bars were generally below yielding with a maximum stress of 350 MPa measured in the load cycle to $\mu_\Delta = -4x1$.The stress profiles in interior column bars showed a different trend with Unit 3. The stresses developed in the bars in the middle of joint were less than that obtained in the last unit, making the stress profiles in large ductility level were not as uniformly distributed as that in Unit 3. It is evident that, unlike that in Unit 3, some bond force developed near the joint centre region in these bars. This trend justifies the analytical work depicted in Section 2.2.4.4 (See **Fig. 2.5(a), (b), (c)**) that for joints incorporating unequal top and bottom beam bars, more nodes in the interior column bars are needed for equilibrium.

5.3.6 Beam Behaviour

5.3.6.1 Curvature Ductility Factors in Plastic Hinge Region

The curvature ductility factors of East and West beams calculated at each peak of loading run are presented in **Fig. 5.27**. It was found that the yield curvature for positive moment is larger than that for negative moment. This was probably because of the disparity of

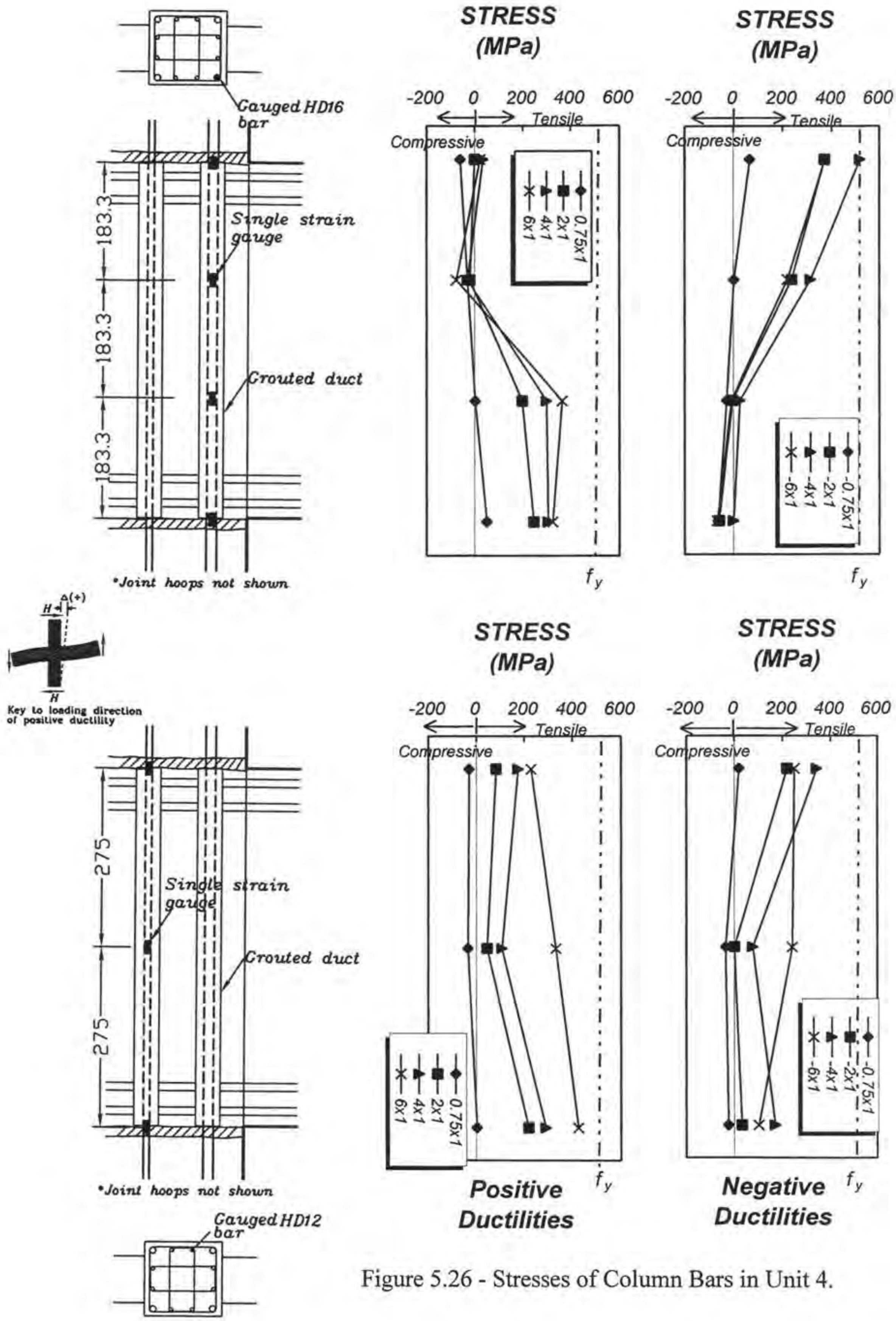

Figure 5.26 - Stresses of Column Bars in Unit 4.

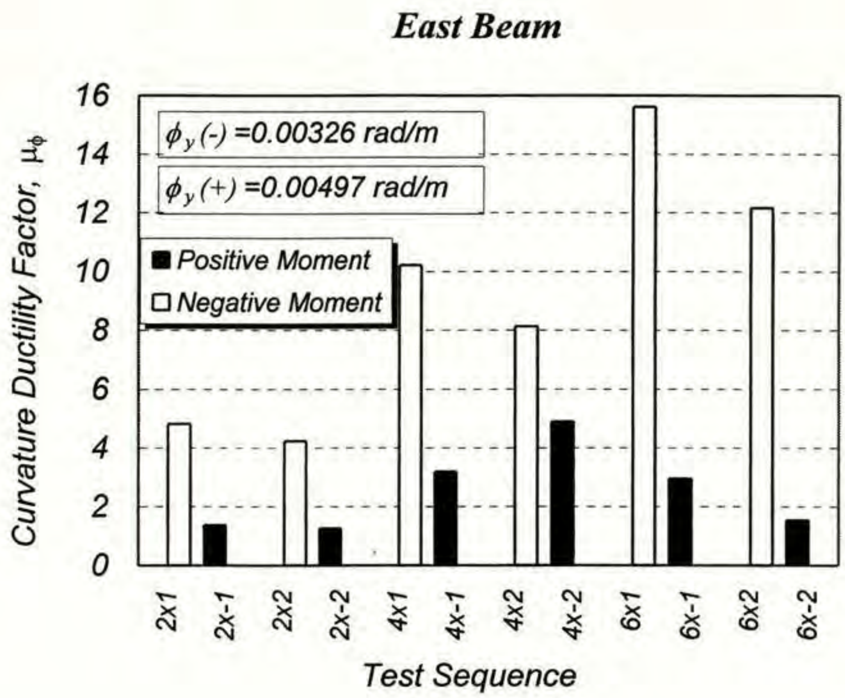

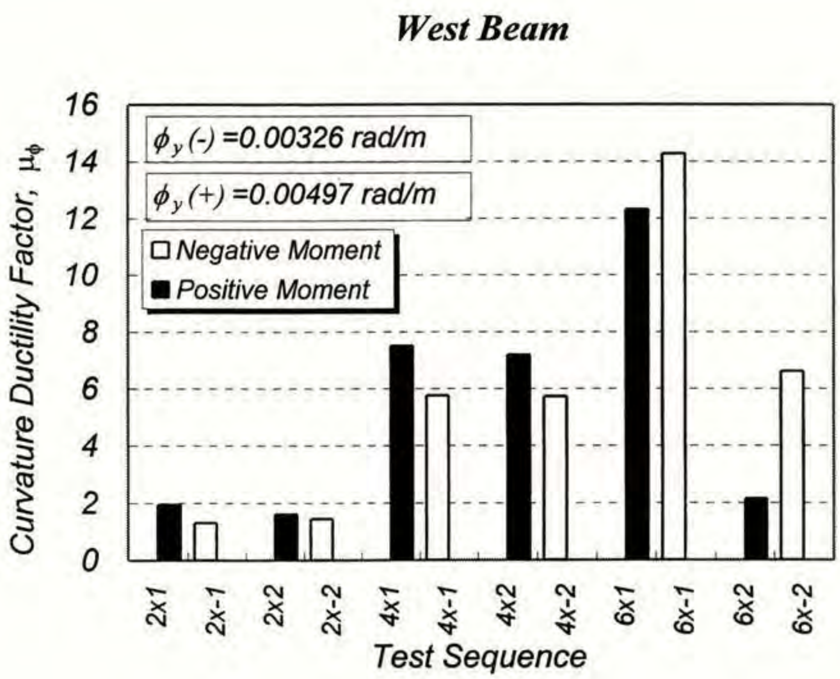

Figure 5.27 - Curvature Ductility Factors of Beams of Unit 4.

the positions of the top and bottom beam bars, or that the cracks in beams did not form within the measured region both in the positive and negative load runs. Note that obtained yield curvatures of two beams are consistent so that values of positive and negative moments measured from two beams were averaged for calculating the curvature ductility factors of both beams.

Note that the curvature ductility factors are quite scatter. The maximum value was μ_ϕ = 16, a value similar to that obtained in Unit 3. In general, it can be observed that curvature ductility factors increased as the test progressed up to μ_Δ = 6x1 and then began to decrease afterwards. Recorded curvature ductility factors in load cycles to μ_Δ = 6x2 were far less than that recorded in the previous load cycle, implying that other source of contribution of lateral displacement became predominant.

5.3.6.2 Beam Strain Profiles at the Level of the Longitudinal Reinforcement

Figures 5.28 and **5.29** present the strain profiles at the level of the beam longitudinal reinforcement obtained following the procedure described in Section 3.6.2.4.

The tensile strain at the level of top beam reinforcement reached a maximum value of 2.8% in the load cycle to μ_Δ = 6x1. In the subsequent load cycle, μ_Δ = -6x1, the recorded strain at the same location was in high compression, reaching the yield strain of longitudinal steel, whereas the tensile strain on the other side of column face only increased slightly comparing with values recorded in the last load cycle. Note that the high compressive strain is probably in the concrete as the bars here may be in tension as a result of loss of bond. The procedure depicted in Section 3.6.2.4 and used here assumes "average" strains in the concrete and reinforcement are equal. This assumption is no longer valid after bond failure. Note that measured bar slip depicted in Section 5.3.5.3 indicates that total bond failure of top beam bars occurred in the load cycle to μ_Δ = -6x1. which agrees with the point discussed above.

The maximum tensile strain at the level of bottom beam bars was 2.5% recorded in the load cycle to μ_Δ = 6x1 that was comparable to the value recorded at the level of top bars.

5.3.6.3 Beam Elongation

The measured overall beam elongation is plotted against storey shear in **Fig. 5.30**. The recorded beam elongation was very similar to that observed in Unit 3 (see **Fig. 5.15**). This

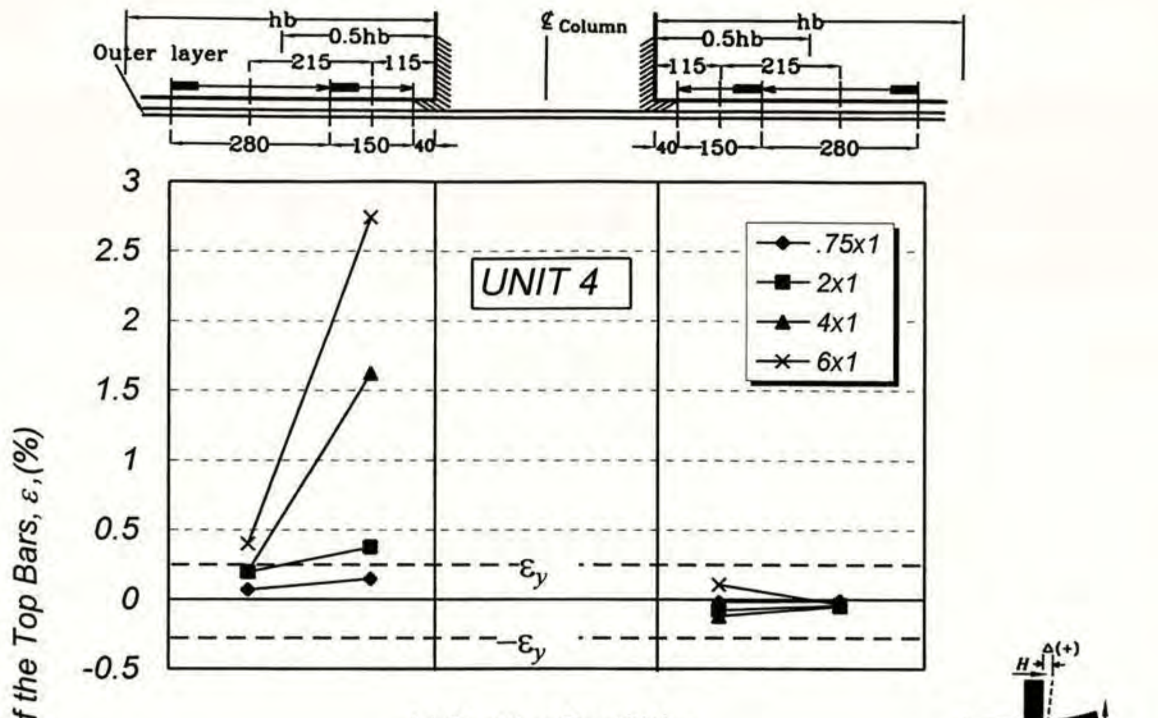

(a) Positive Ductilities

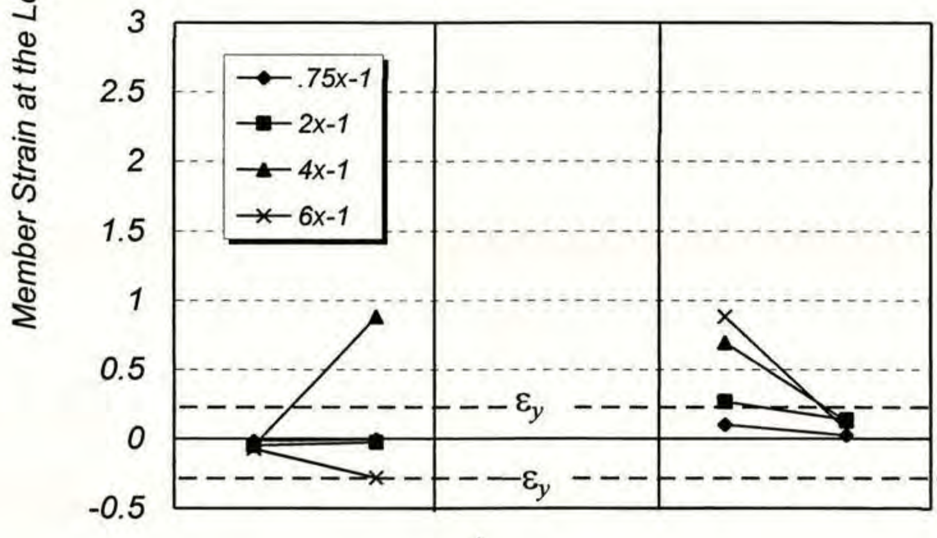

(b) Negative Ductilities

Figure 5.28 - Beam Strain Profiles at the Level of the Outer Layer of the Top Beam Bars of Unit 4.

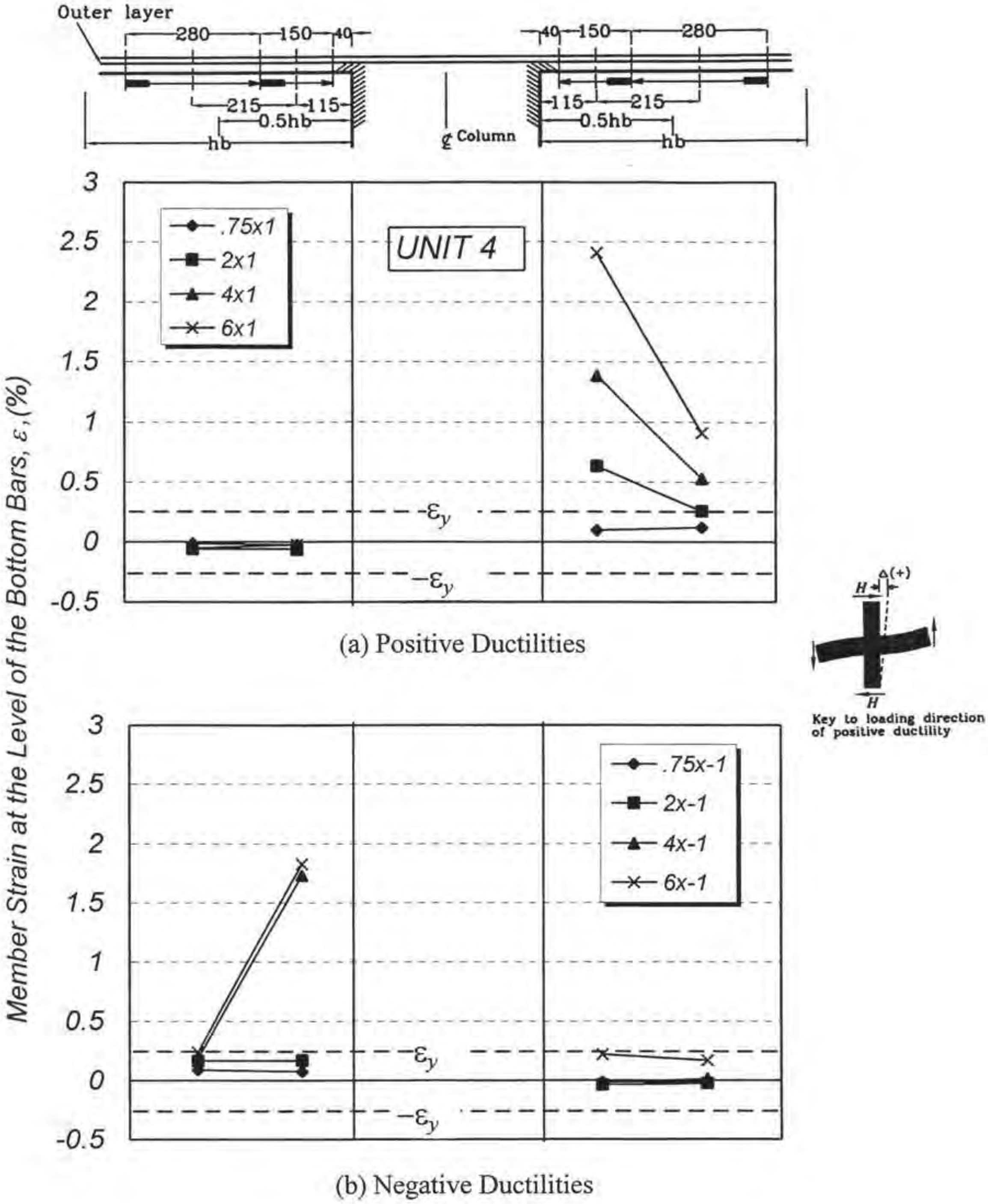

Figure 5.29 - Beam Strain Profiles at the Level of the Outer Layer of the Bottom Beam Bars of Unit 4.

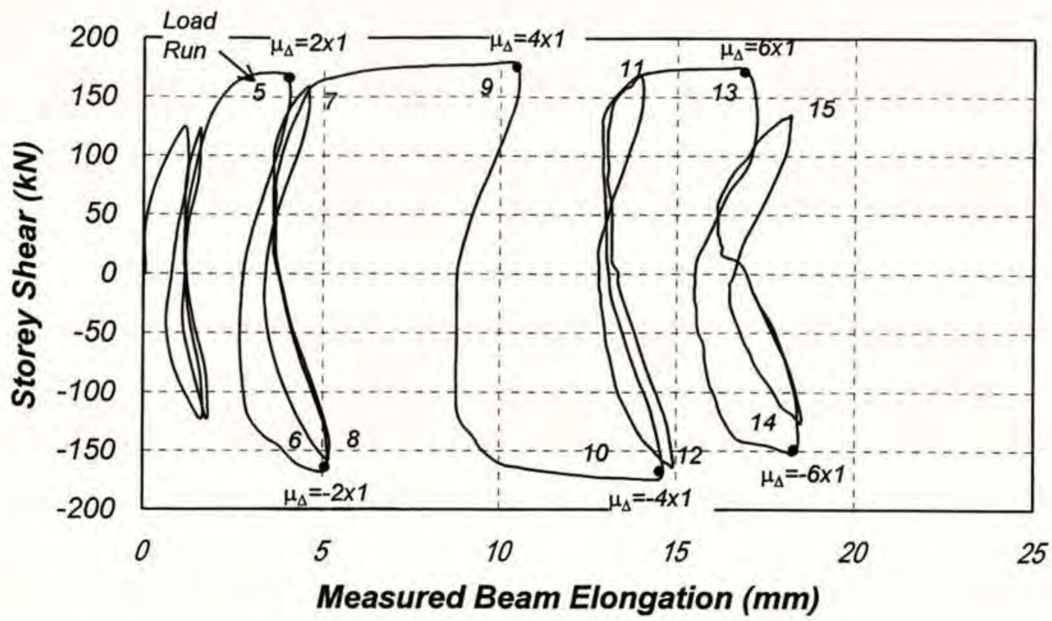

Figure 5.30 - Beam Elongation of Unit 4.

may indicate that unequal top and bottom beam longitudinal reinforcement does not make much difference on the characteristics of beam elongation. The maximum beam elongation measured during the test was 18.5 mm, which is equivalent to 3.4 % of the beam height.

5.3.7 Column Behaviour

By observing the crack pattern in the column of this unit and with reference to the strains depicted in **Fig. 5.25**, it can be concluded that the column remained elastic during the testing. Note that yielding of some column bars, which was observed in Section 5.3.5.5, is not equivalent to the development of plastic hinges in the column.

5.4 CONCLUSIONS

1. Test results of two units, designated as Units 3 and 4, were described in this chapter. Unit 3 is aiming to validate the analytical finding concerning joints having v_{jh} / f_c' ratio less than 0.14, while Unit 4 was designed and tested to verify the analytical results for joints incorporating unequal top and bottom beam reinforcement.

2. Unit 3, in which the provided horizontal joint shear reinforcement was less than that required by NZS 3101:1995 [S1] for ductile frames, showed ductile performance.

3. Unit 4 showed very similar behaviour to Unit 3. This unit also had ductile performance despite that the provided horizontal joint reinforcement is much less than that required by NZS 3101:1995.

4. Test results of Unit 3 and 4 justify the parametric study depicted in Chapter 2 that the joint shear strength, and thus the required horizontal joint shear reinforcement, is strongly influenced by the joint shear stress ratio, v_{jh} / f_c'.

5. Good performance of Unit 3 verified the analytical finding that, for joints having v_{jh} / f_c' ratio less than 0.14, the amount of horizontal joint shear reinforcement given by NZS 3101:1995 still can be relaxed.

6. Satisfactory performance of Unit 4 indicates that the requirement of horizontal joint shear reinforcement given by NZS 3101:1995 for joints incorporating unequal top and bottom beam bars is unnecessarily stringent and can be relaxed.

CHAPTER 6
TEST RESULTS OF UNITS 5, 6 AND 7

6.1 INTRODUCTION

Test results of D-series comprising Units 5, 6 and 7 in which beams with distributed longitudinal reinforcement were incorporated are presented in this chapter. Reinforcing details and design considerations were presented in Section 3.2.3. Note that the quantity of transverse shear reinforcement placed in the joint regions of these units was based on a 15% reduction with respect to the amount required by the analytical model for conventional joints except for that in Unit 7. A comparison between the quantity of horizontal joint reinforcement required by the theoretical model and that provided is given in Table 3.4. Units 5 and 6 were tested under $0.1f_c^{'}A_g$ column compressive load. Prior to commencing test of Unit 7, it was decided to increase the applied column compressive load to $0.25f_c^{'}A_g$.

Test procedure used in the testing of these three units is described in detail in Section 3.7.

6.2 UNIT 5

6.2.1 Overall Behaviour

Joint shear failure in combination with bond failure of extreme layers of longitudinal beam bars passing through joint region led to eventual failure of this unit. In the second load cycle to $\mu_\Delta = 4$, corresponding to a 4.3% inter-storey drift, the lateral load dropped to 70% of the maximum measured value. At the end of test joint shear distortion was evident. Most of the cover concrete in joint panel spalled off together with crushing of concrete on top and bottom beam chords at column faces.

The joint region at different stages during the test is presented in **Fig. 6.1. Figure 6.2** shows the storey shear versus lateral displacement response.

In the elastic load cycles, long cracks vertically propagated beam webs through toward

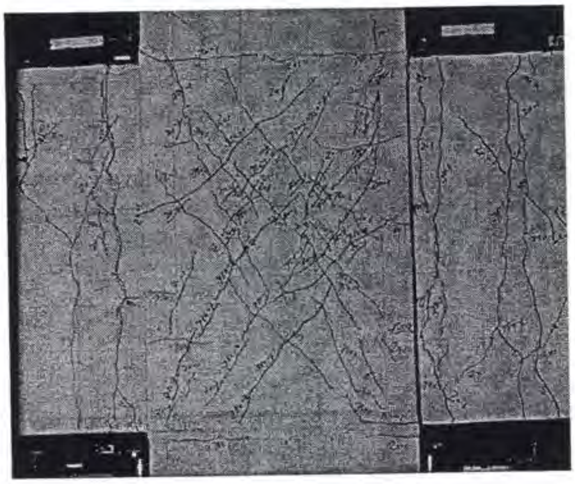

(a) At μ_Δ = -2x1

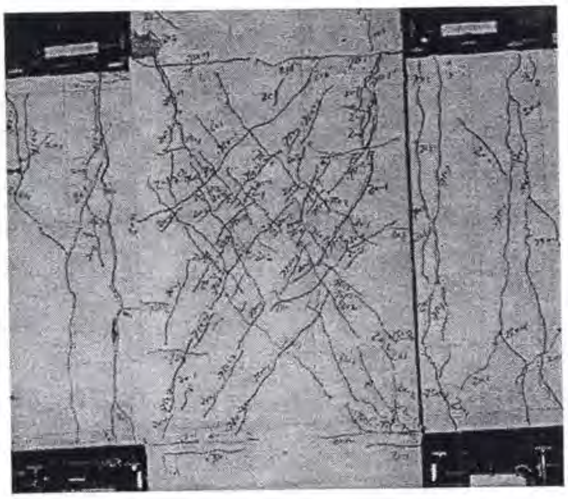

(b) At μ_Δ = -2x2

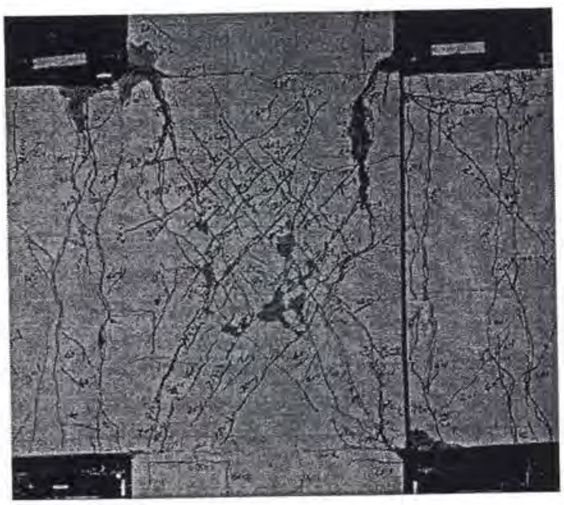

(c) At μ_Δ = -4x1

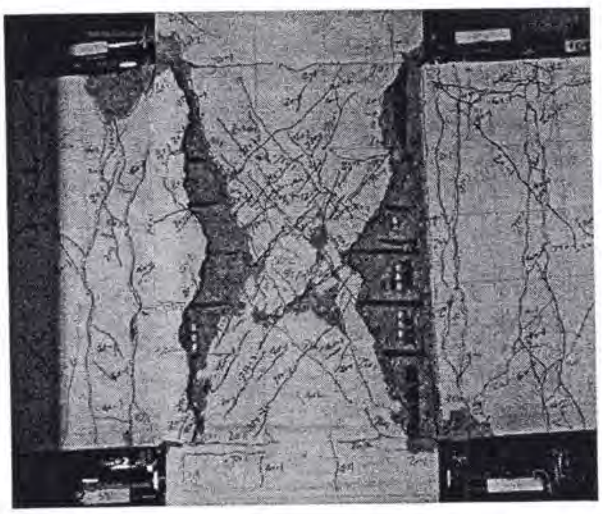

(d) At μ_Δ = -4x2

Figure 6.1 - Cracking of Unit 5 at Different Stages During the Test.

(e) At μ_Δ = -6x1

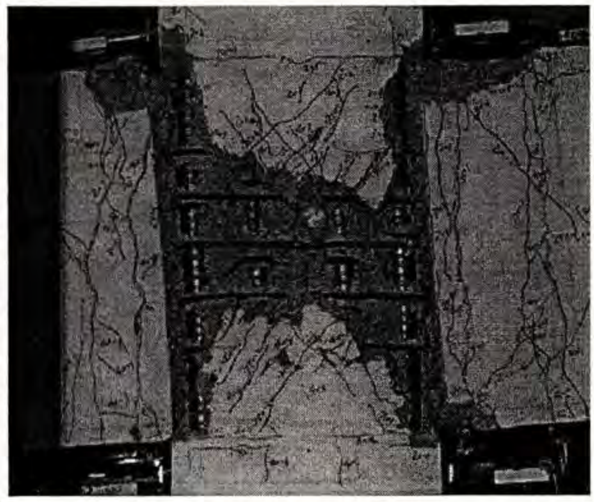

(f) At μ_Δ = -6x2

Figure 6.1(Cont.) - Cracking of Unit 5 at Different Stages During the Test.

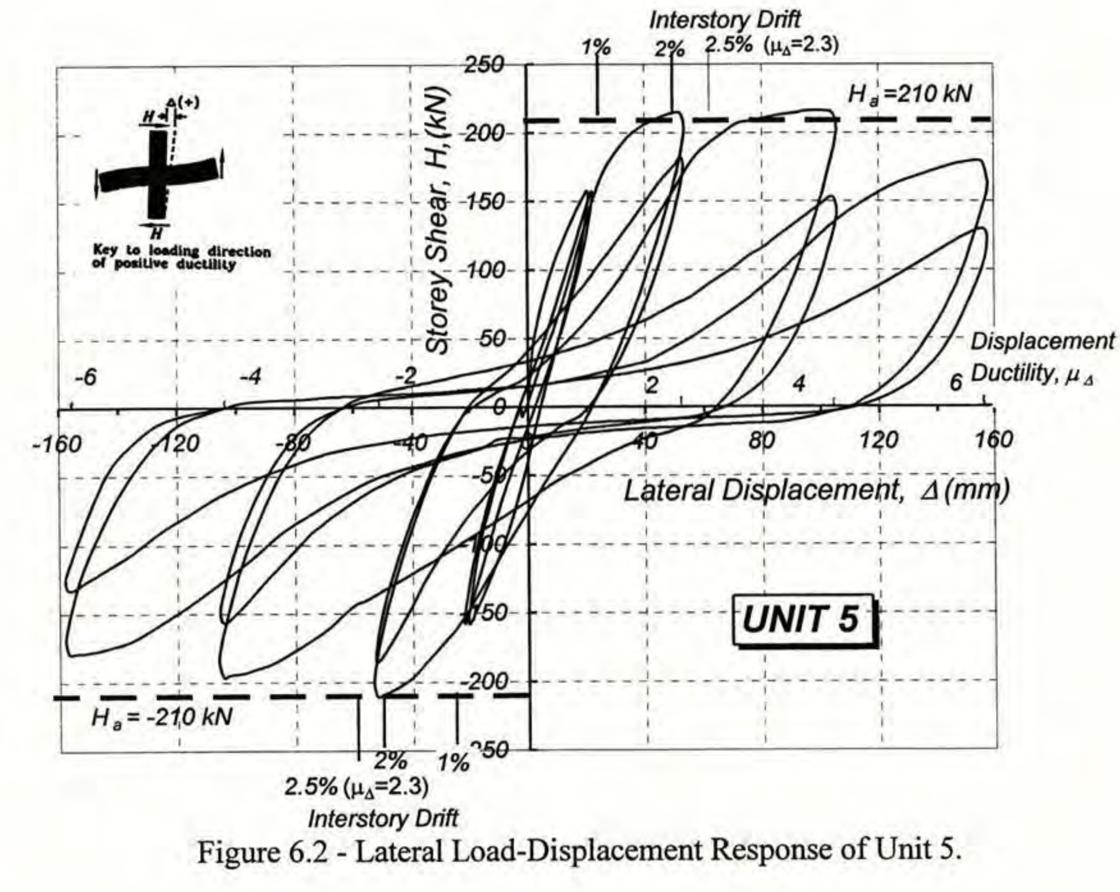

Figure 6.2 - Lateral Load-Displacement Response of Unit 5.

beam compression zone. Most of the vertical cracks in the plastic hinge region propagating from top and bottom beam chords merged in the reversed load run. Diagonal cracks forming in the beams were relatively few in comparison with cracking appearance observed in the L-series of tests. Note that the measured crack width in beams was less than 0.1 mm at this stage. Cracks in columns were limited to approximate 3 cracks forming on each tension side of each column including one located at the beam face. At the end of first load controlled cycle, -0.75x1, several diagonal cracks developed in the joint region. These cracks were less than 0.1 mm wide. In the subsequent load controlled cycle, the crack pattern in joint region remained essentially unchanged.

As the test proceeded to μ_Δ = 2x1, plastic hinges developed in the beams with more flexural cracks forming and widening of existing cracks. The maximum crack width in beams reached 1.0 mm and 2.0 mm in the positive and negative load runs,. The widest cracks were observed to occur at the column faces. Some short diagonal cracks formed in the beam plastic hinge regions. Cracking in the joint region became denser in this loading cycle. The maximum crack width measured in this cycle in the joint panel was 0.3 mm. In the reversed load run, μ_Δ = -2x1, no noticeable change of width of joint cracks was observed except for two 1 mm wide cracks located around the top corners of joint panel. These cracks were restricted to within a short distance of approximate 50 mm away from column faces and did not propagate into the central part of the joint panel. These cracks were the product of the loss of concrete cover around the corrugated steel ducts embedded in the joint. The loss of concrete cover in this region is an indication of initiation of bar slip through joint region. Several more cracks occurred in columns at this stage which were short and with small width less than 0.1 mm.

In the second loading cycle to a displacement ductility of 2, μ_Δ = ±2x2, neither change of crack width nor crack patterns were observed in beam plastic hinges. Some more fine cracks developed in the joint panel and existing cracks were widened slightly, reaching a maximum width of 0.5 mm around the centre of the joint. In the reversed load run, μ_Δ = -2x2, some incipient damage to the concrete cover in the joint panel was observed. The two large cracks located near the top corners of joint panel grow wider, reaching a width of 2.5 mm.

In the loading runs to μ_Δ = ±4x1 the crack pattern in the beams remained without significant change and only the width of the widest crack reached 1.5 mm. In contrast, apparent change of crack patterns in joint panel could be observed, indicating that joint was deteriorating. The change included denser crack pattern, larger cracks and incipient damage to the concrete cover. The widest crack reached 1 mm in the centre of the joint. With the observation on the target studs welded on the top and bottom beam bars contacting the surrounding concrete and the dislodged cover concrete around four corners of joint panel, it is believed that bond failure of both top and bottom beam bars had taken place. Further, some cover concrete on top and bottom beam chords at column faces was crushed at this stage. A few more new cracks occurred in columns but with small width and length.

As the test proceeded to $\mu_\Delta = 4x2$, large pieces of cover concrete surrounding the corner ducts embedded in joint region began to fall apart. Crushing of the concrete in the centre of the joint panel was significant. In contrast, no further cracking in the beams was observed to occur. In fact some beam cracks were noticed to be not so wide as in the previous load runs.

In the load cycles to $\mu_\Delta = 6x1$, metallic ducts and joint hoops were exposed as a result of extensive crushing of the concrete in the joint panel. It can be felt that the joint had failed in shear at this stage. The shear distortion in the joint was apparent in this load run. As was expected, crack width in beams became very small. No change of cracking appearance in columns was observed since bending moment undergoing on columns decreased as a consequence of the reduction of the applied lateral load.

At the end of test, finishing of load cycle to $\mu_\Delta = 6x2$, the joint concrete, was extensively crushed. It is noted that joint failure in this unit is such a similar type as that occurred in Unit 1, in which joint failed by crushing of joint concrete, or in other words, diagonal compression failure.

6.2.2 Load Displacement Response

Figure 6.2 depicts the measured lateral load-displacement response of Unit 5. The yield drift of the beam-column assembly, which was obtained following the procedure described in Section 3.6 was 1.07%. This yield drift level implies a displacement ductility equal to $\mu_\Delta = 2.3$ when the drift limit of 2.5% imposed by the loading standard [S3] attained.

The theoretical ultimate lateral load, calculated from beam flexural strength based on measured material strengths, was achieved and exceeded in the first inelastic cycle, $\mu_\Delta = 2x1$, in both positive and negative load runs. In the second load cycle to the same displacement ductility, the measured lateral load dropped to approximate 84% and 88% of the theoretical ultimate load in positive and negative load runs, respectively. Note that the reduction of lateral load capacity in this load cycle is considerable in comparison with the response of previous units in L-series. It is believed that stiffness degradation and drop of lateral load capacity in this stage were caused by the slip of top and bottom layers of beam bars.

At μ_Δ = 4x1, the measured lateral load exceeded the theoretical ultimate value by 3% in the positive load direction, whereas it was only 94% of the theoretical value in the negative load direction. In the subsequent load cycles, μ_Δ = 4x2, more significant loss of lateral load capacity and serious pinching of hysteresis loops were observed. The measured lateral loads reached only 70% and 74% of the maximum loads in the positive and negative load runs, respectively. According to the criteria commonly employed in New Zealand [P1] [S4], this unit failed at this displacement ductility level.

In the load cycle to μ_Δ = 6x1, the hysteresis loops showed serious pinching, the lateral load capacity reached 83% and 86% of the maximum loads in positive and negative load runs respectively. As the test carried on to μ_Δ = 6x2, the lateral load capacity dropped to very low values, which were only 61% and 63% of the maximum load. Besides, hysteresis response showed extensive pinching and very low stiffness.

6.2.3 Decomposition of the Lateral Displacement

The percentage of each lateral displacement component calculated following the procedure described in Section 3.8 is presented in **Fig. 6.3**.

In elastic load cycles, the beam flexural deformations contributed to 21-26% of the total lateral displacement. Beam fixed-end rotations contributed to the total displacement by 24-29%. Column deformations, calculated from theoretical analysis, was 36-40% of the applied lateral displacement. Surprisingly the component of beam-column joint shear distortion at this stage reached a percentage of 22%, which exceeded the 20% limit for well designed joints suggested by Cheung et al. [C1].

It is evident in **Fig. 6.3** that the component of beam fixed-end rotation and the joint distortion increased as the test progressed. A 38% of beam fixed-end rotation was recorded in the load cycle to μ_Δ = -2x2. The beam flexural deformation commenced to diminish since the

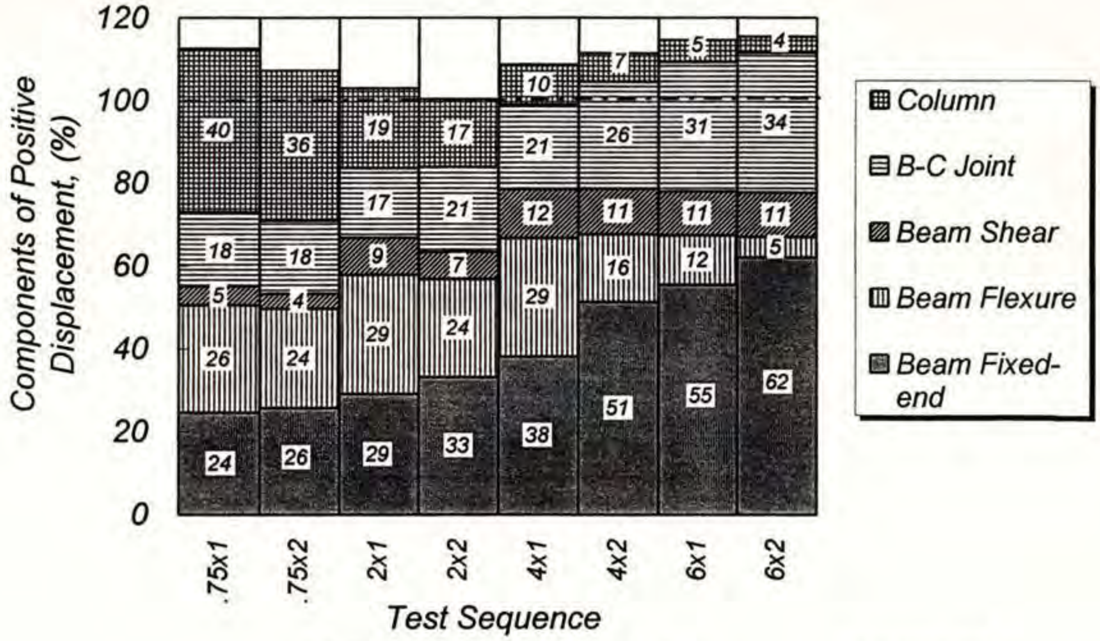

(a) Runs to Positive Ductilities.

UNIT 5

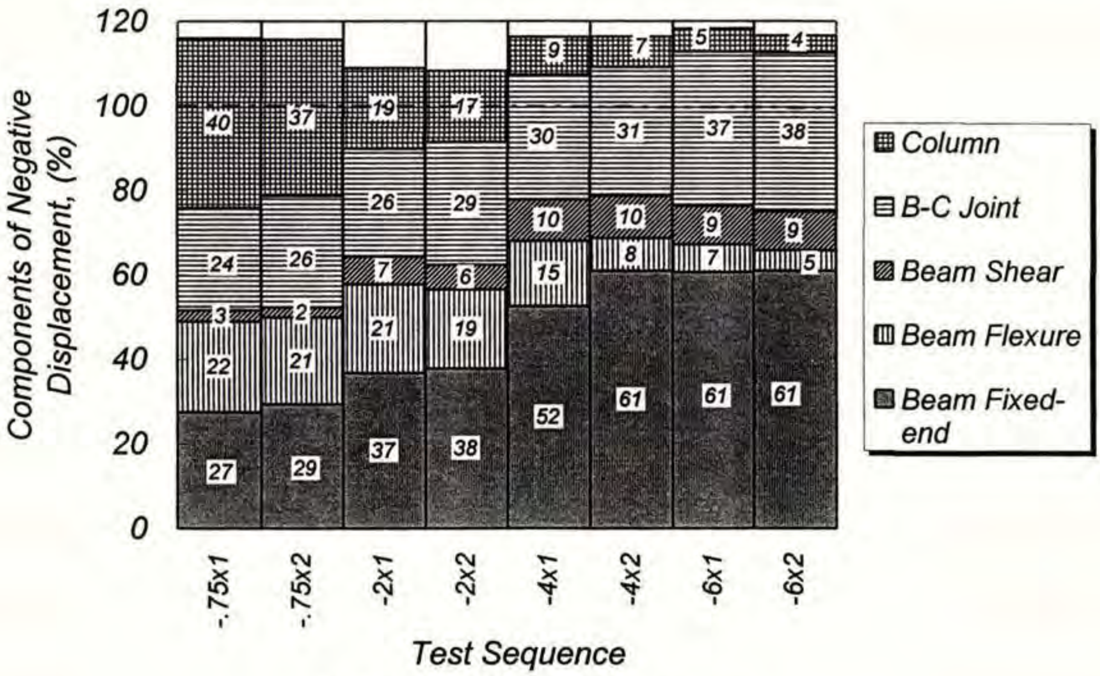

(b) Runs to Negative Ductilities.

Figure 6.3 - Components of Lateral Displacement of Unit 5 at Peaks of Load Runs.

load cycle to μ_Δ = -2x2.

In the load cycles towards the end of the test, the component of beam fixed-end rotation and the joint shear distortion became the dominant model of deformation.

6.2.4 Joint Behaviour

6.2.4.1 Strains in the Horizontal Joint Reinforcement

Joint transverse reinforcement in this unit comprised 5 sets of exterior R10 hoops plus two legged R10 inner ties. Strains obtained by averaging the measured values from double strain gauges at the peak of each load cycle are presented in **Figs. 6.4** and **6.5**.

In the elastic load cycles, the recorded strain profiles were rather uniformly distributed across the height of the joint. The strain approached 1000 micro-strains. Note that the recorded hoop strains are considerably large comparing to the strains recorded in Units 1-4 in the corresponding load cycles.

Strain profiles in the joint hoops and ties measured in the load cycle to μ_Δ = 2x1 showed an arch shape with readings in the mid-height set approaching to yield. In the following load cycles, μ_Δ = 4x1, most of the joint hoops and ties yielded except for the sets closest to the top and bottom beam longitudinal reinforcement. In the cycles to μ_Δ = 6x1 most strain gauges failed as the joint disintegrated. Large tensile strains could have developed at this stage.

6.2.4.2 Joint Shear Distortion

The measured joint shear distortion against storey shear is presented in **Fig. 6.6**. The maximum joint shear distortion measured in this unit in the elastic load cycles was about 0.003 radians. As the specimen was displaced into the inelastic range, the joint shear distortion increased significantly up to 0.01 radians in the load cycle to μ_Δ = 2x2 and reached 0.02 radians in the load cycle to μ_Δ = 4x2. The measured joint shear distortion kept on increasing in the final cycles despite that the lateral load capacity was decreasing. At the end of test, the recorded maximum joint shear distortion was 0.037 radians. **Figure 6.6** clearly shows that the shear deformation occurred in the joint was excessive during the test, indicating that the joint deformation was not well controlled through adequate amount of joint transverse reinforcement provided in this unit.

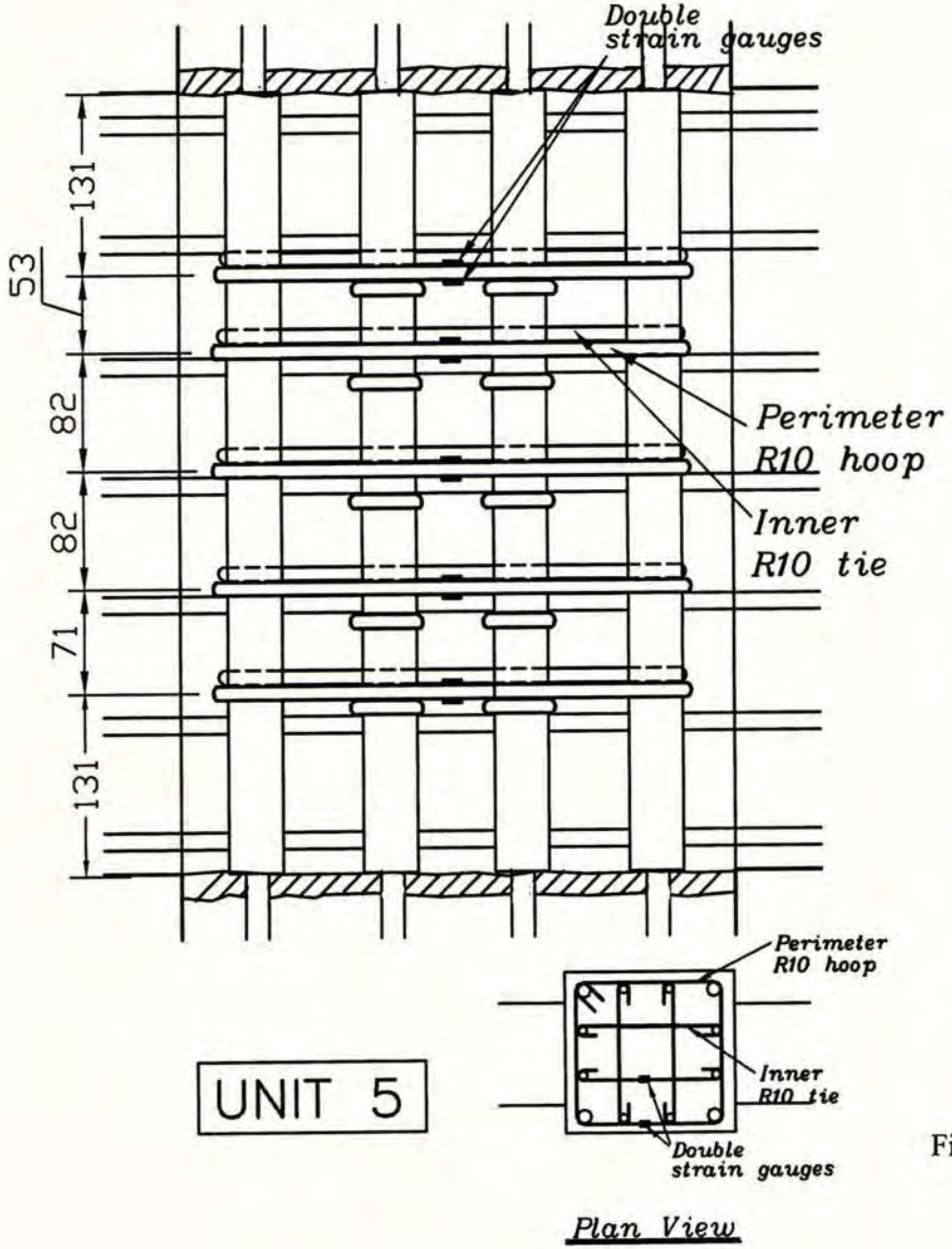

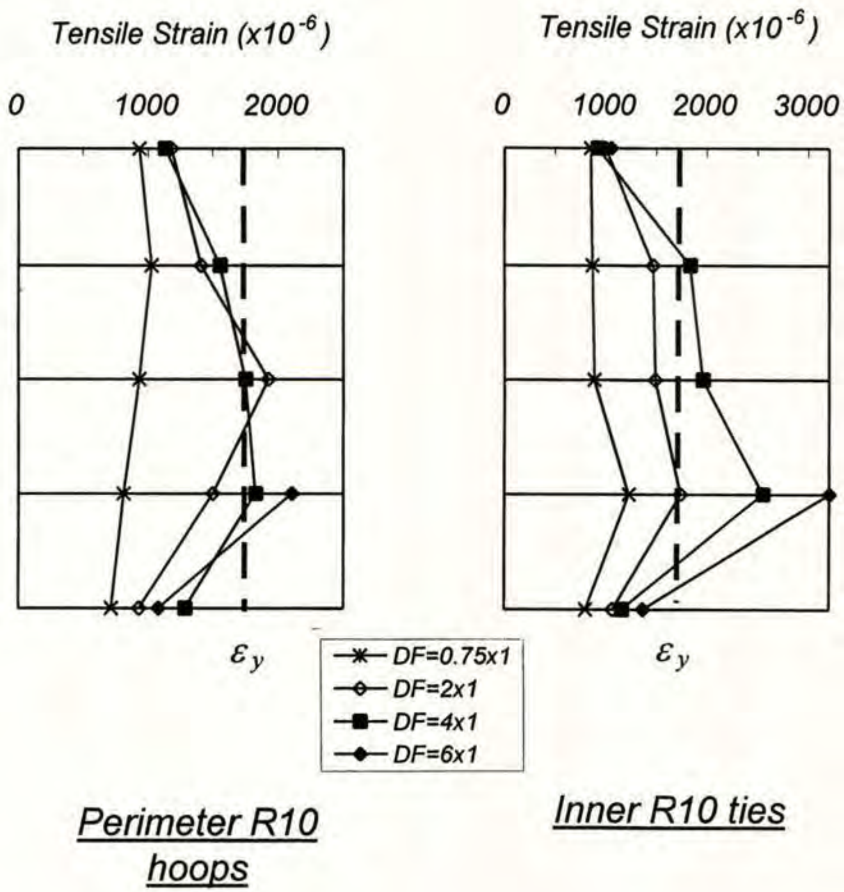

Positive Ductilities

Figure 6.4 - Measured Strains in Joint Hoops of Unit 5
During the Runs to Positive Ductilities.

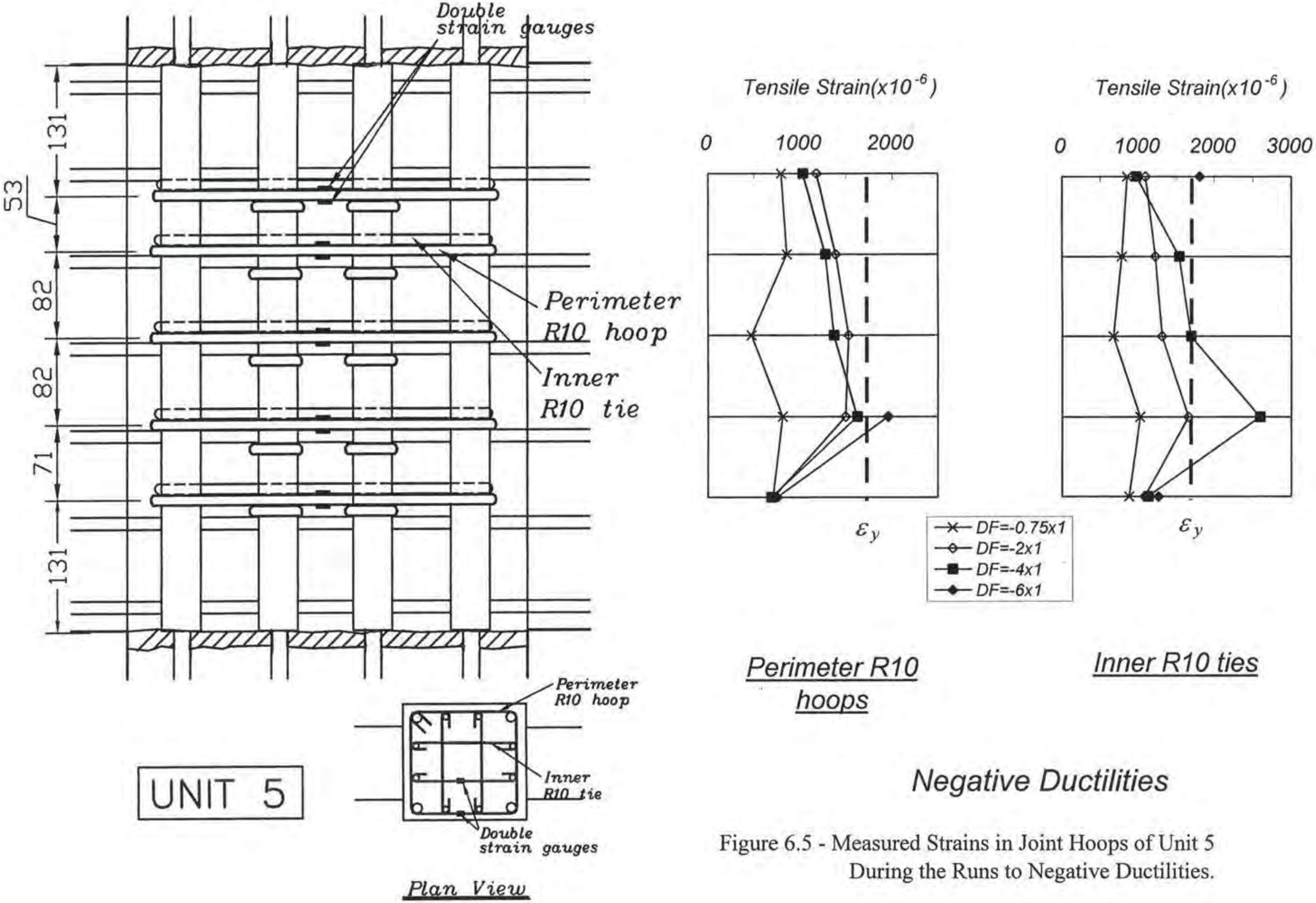

Figure 6.5 - Measured Strains in Joint Hoops of Unit 5 During the Runs to Negative Ductilities.

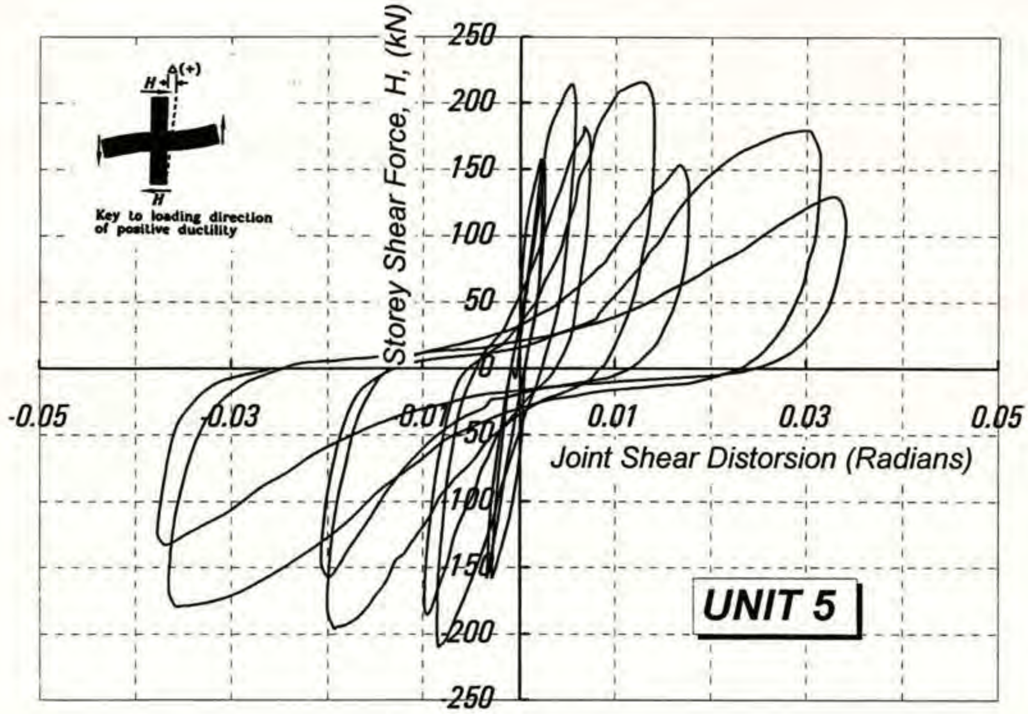

Figure 6.6 - Joint Shear Distorsion Versus Storey Shear Force.

6.2.4.3 Beam Bar Slip

Figure 6.7 shows the local bar slip for the top and bottom beam bars at three locations in the joint. In general, the slip of the top beam bars was larger than that of bottom bars, although the difference was less significant than that in Units 1-4. Once again the main difference in the recorded slip between the top and bottom bars can be attributed to the " top bar " effect caused by the direction of casting of the fresh concrete. The slip of the top beam bars in the centre of joint region approached the clear spacing between deformations in load run μ_Δ = -4x1. It is thus known that total bond failure of top beam bars was just about occurring in this load cycle. The measured slip of the bottom beam bars followed a similar trend. It exceeded the clear spacing in the load run to μ_Δ = -4x1. It is believed that part of the loss of the lateral load capacity that occurred in the load run to μ_Δ = -4x1 was due to total bond failure of both top and bottom beam bars. The measured bar slip will be compared with those found in the benchmark unit, Unit 8, in Chapter 7.

It is noted that once beam bars slipped through B-C joint region as a result of total bone failure, considerable loss of lateral load capacity can occur due to the following reasons.

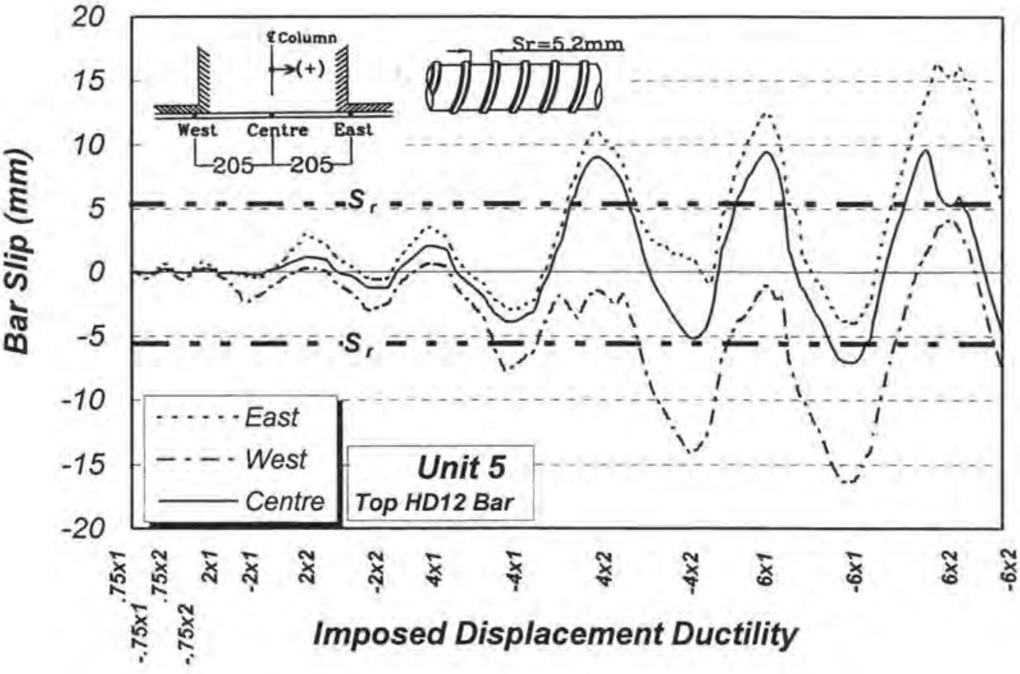

(a) Top Bars

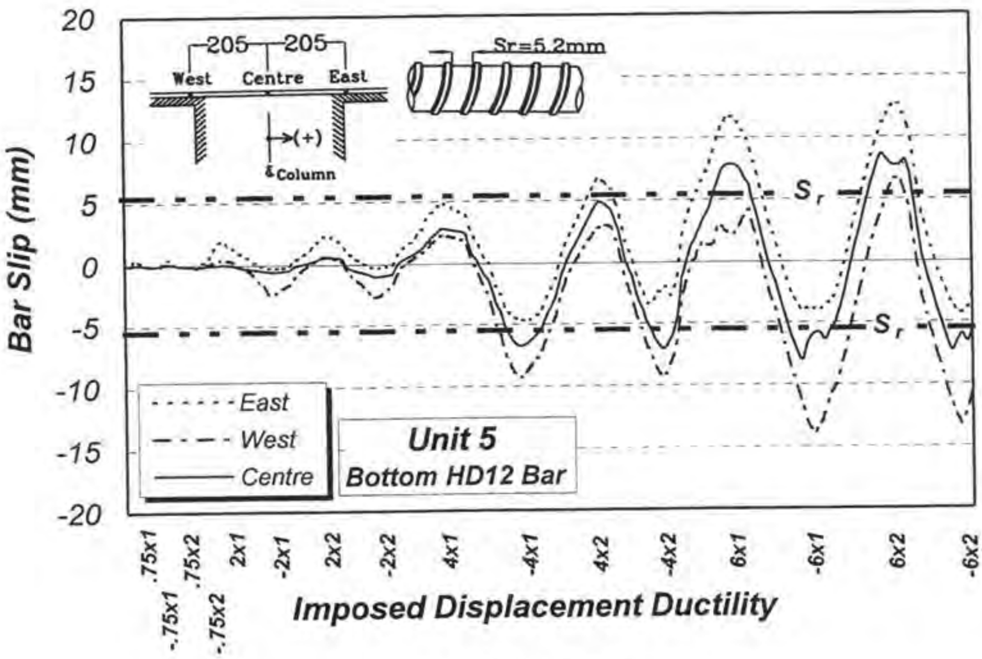

(b) Bottom Bars

Figure 6.7 - Relative Slip of Beam Longitudinal Bars in the Joint Region.

1. As a result of bone failure of extreme layers of beam bars in joint region, compressive bars could be subjected to less compressive strain at column face or even in tension. Thus excessive compressive stress may be induced on concrete surrounding the originally compressed steel so that crushing of concrete on extreme fiber is likely to occur. As a consequence, some drop of beam flexural strength can be induced.

2. Once the compression steel changes to tension as a result of bond failure in joint region, the neutral axis depth in the beam section adjacent to columns must increase to satisfy equilibrium. The moment level arm in beam critical sections is thus reduced. In addition, the layer of distributed beam bar adjacent to top and bottom bars while were originally subjected to tension can change to compression. As a consequence, beam flexural strength can no longer be maintained at the maximum value. Reduction of lateral load capacity occurs as a result.

6.2.4.4 Bar Strain and Bond Stresses in Joint Region

Figures 6.8(a), (b) present the strain profiles of top and bottom extreme layers of longitudinal steel within joint region obtained from the electrical strain gauges readings at each peak of loading cycles. Bond stresses developed on extreme layers of longitudinal steel were also calculated are plotted in **Fig. 6.9**.

Strain readings were only available until $\mu_\Delta = 2$ as damage occurred due to relative slip between concrete and bars. In the elastic load cycles, the maximum tensile stress approached yielding while compressive stress developed on the other side of column faces reaching a maximum value of -600 micro-strains.

In the load cycles to $\mu_\Delta = 2$, both tensile and compressive strains on extreme layers increased, reaching maximum values of 3500 and -2000 micro strain, respectively. Note that the recorded compressive strain implies that the reinforcing bars were just about yielding when the inelastic stress-strain relationship of steel is considered.

The bond stresses depicted in **Fig. 6.9** show a peak value of 14 and 12 MPa developed on top and bottom beam bars respectively. It is noted that the values are equivalent to 2.5 and $2.1\sqrt{f_c'}$, respectively.

Figure 6.10 plots the strain profiles at peaks of loading cycles obtained from inner layers

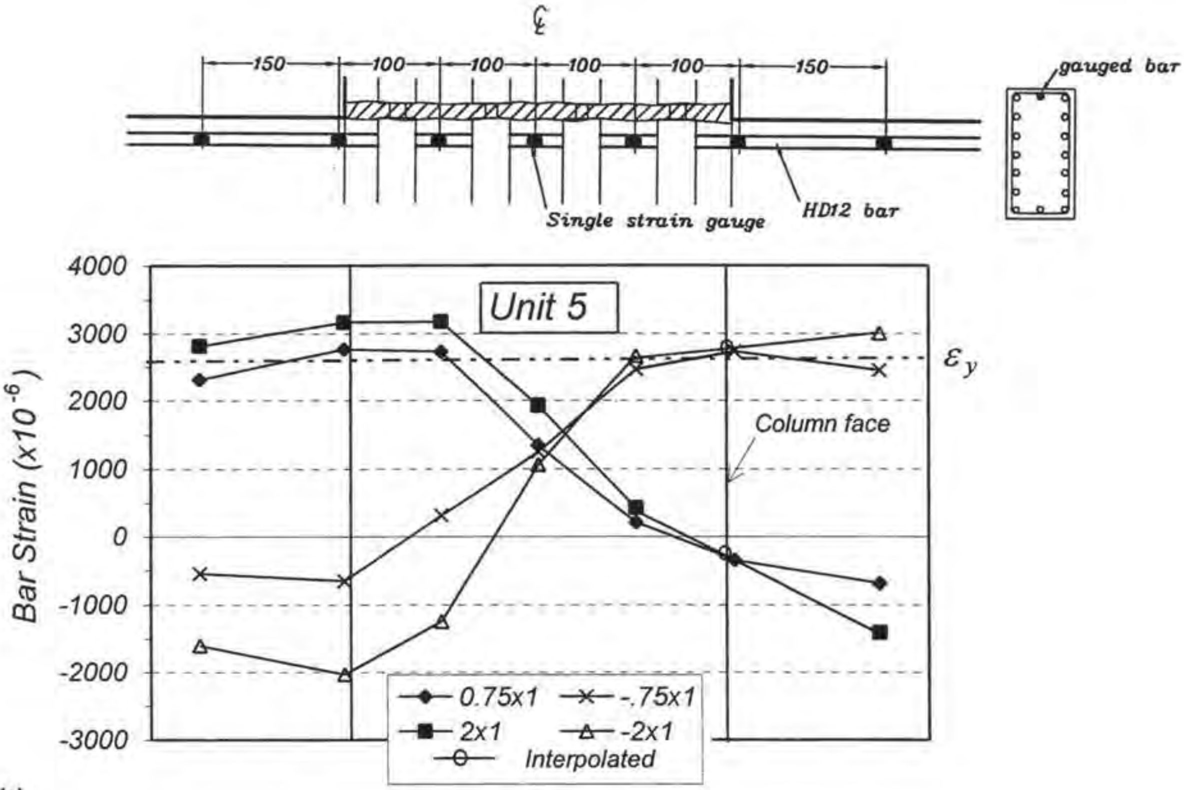

(a) Top Beam Bar

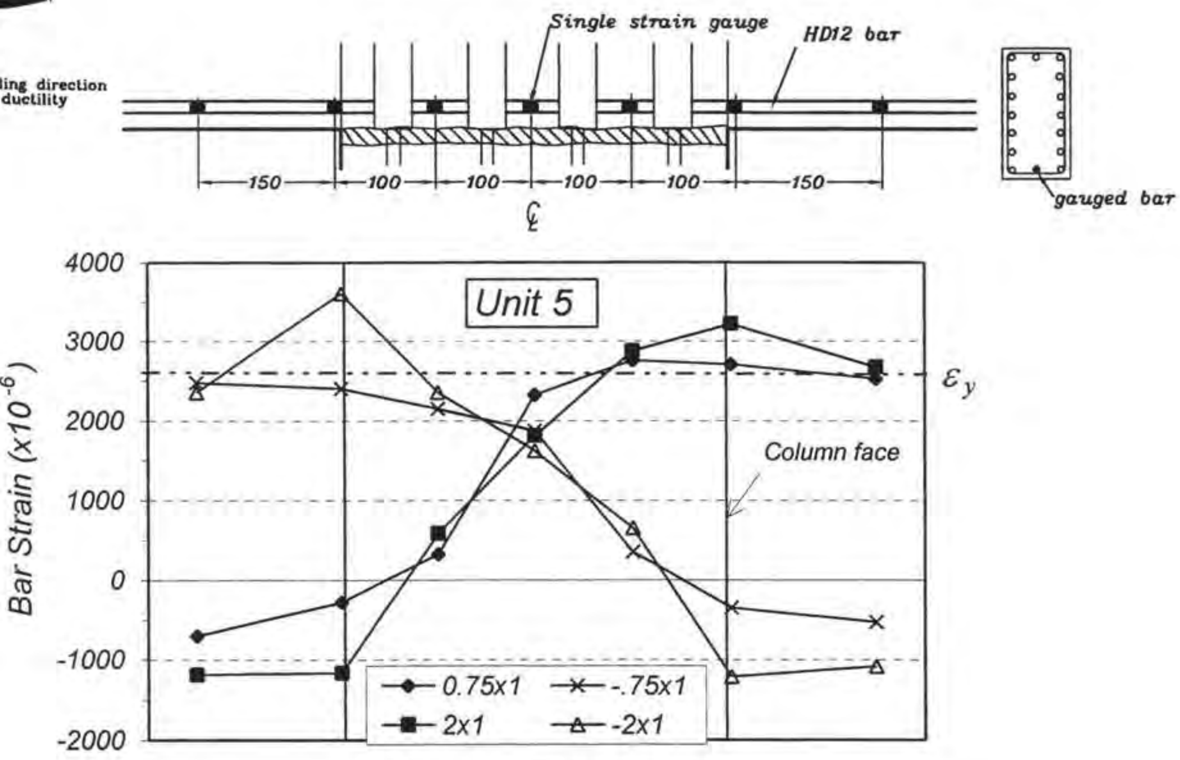

(b) Bottom Beam Bar

Figure 6.8 - Strain Profiles of Outer Layers of Beam Bars.

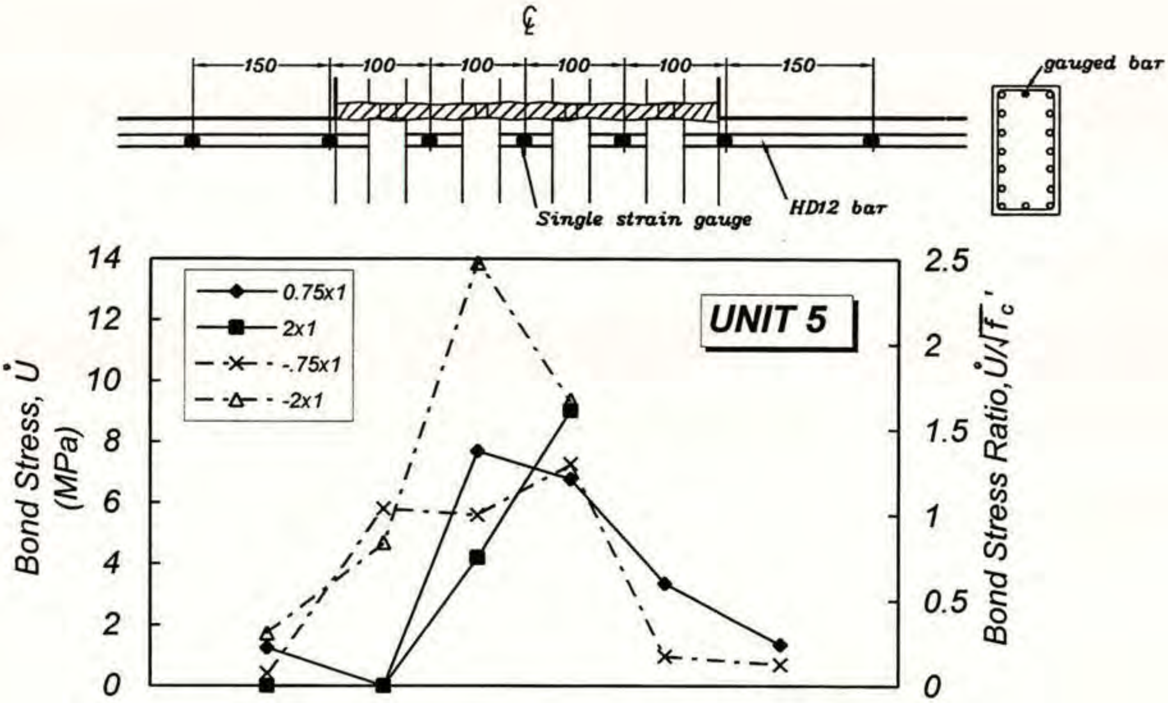

(a) Top Bars

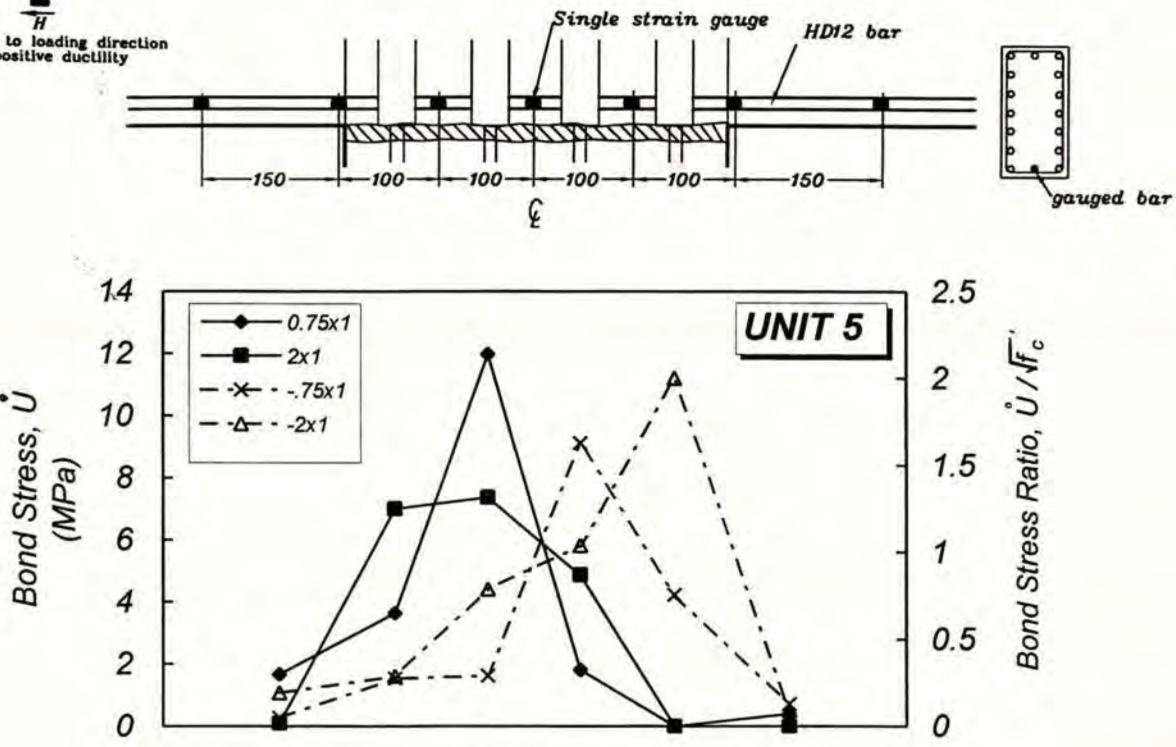

(b) Bottom Bars

Figure 6.9 - Calculated Bond Stresses.

of the longitudinal beam bars. The figures show a general trend that the strain profiles showed some gradient in the elastic load cycles and increased up beyond yielding within the whole range of joint depth in the successive load cycles except for that in the layers adjacent to the top and bottom bars. Note that the trend obtained here that most of the intermediate layers of beam bars were yielding in tension on both sides of column faces, indicating that the development of bond stress on theses bars are not necessary, agrees with what was found in the analytical work carried out prior to testing and described in Chapter 2.

Strain profiles depicted in **Figs. 6.10(a)**, **(e)** show a different trend to that in other interior layers. It can be seen in **Fig. 6.10(e)** that strain profiles in $\mu_\Delta = 2$ still showed linear stain distribution with strain on one side of column faces exceeding the yielding strain whereas on the other side being less than yielding. It indicates that some bond stress may be required along these two layers of beam bars though. This is because the two layers of longitudinal steel located close to the neutral axis of beam critical section at column faces. Nevertheless, as long as significant slip of extreme layers of longitudinal steel did not occur, with the increasing of curvature of beam sections the neutral axis depth would carry on decreasing, resulting in tensile yielding of the two layers of steel on both sides of column faces.

6.2.4.5 Bar Stresses in the Column Vertical Reinforcement Passing Through the Joint Region

Strain variations of column bars within joint region during the test were monitored using single electrical strain gauges. Obtained strains were converted into stresses and are presented in **Fig. 6.11**. The stress profiles of corner bar show in a linear distribution in elastic load cycles with maximum compressive and tensile stresses reaching -100 and 150 MPa, respectively. In the successive load cycles tensile stresses on corner bars approached yielding while compressive stresses developed on the other end decreased to zero. In the load cycles to $\mu_\Delta = \pm 4x1$, stress profiles have abnormal change in the middle portion of the joint. This abnormality that suggests the bars were bent as a result of joint shear distortion.

Stresses profiles of the interior column bars show a uniformly distribution. The stress profiles shifted toward larger tensile with the progressing of load cycles, but they all remained below yielding during the test.

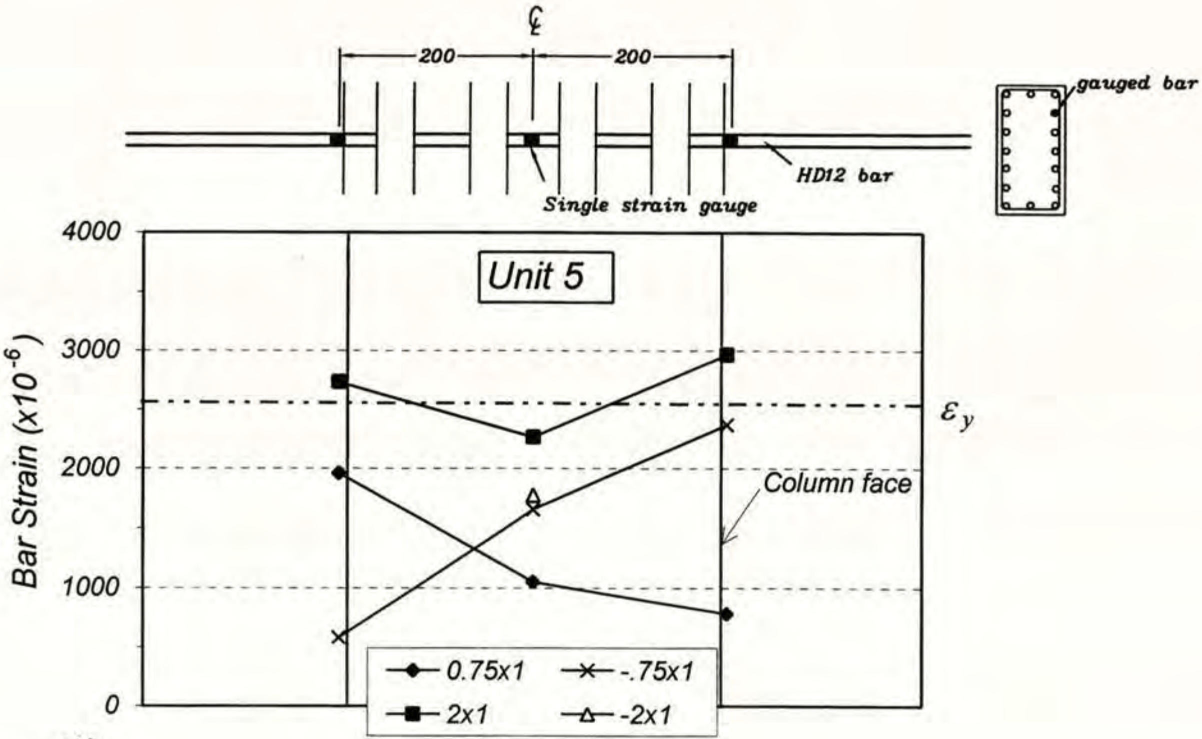

(a) Layer "a"

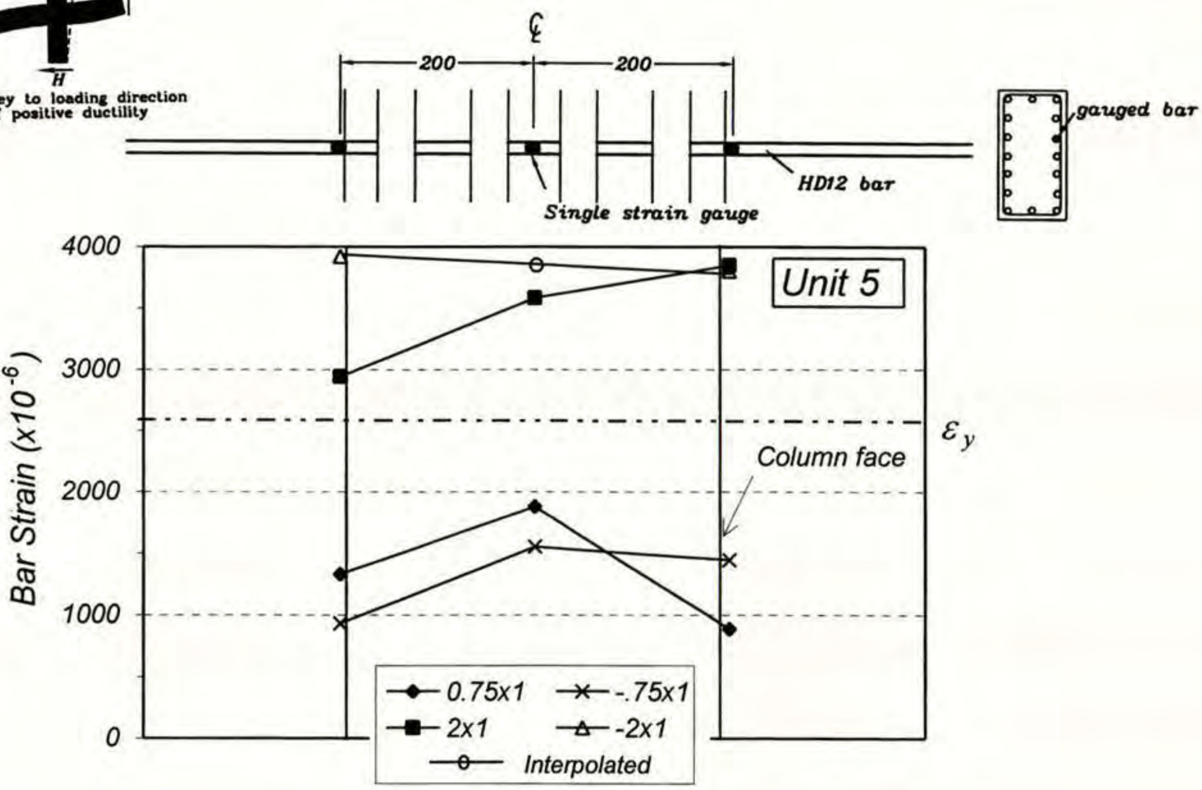

(b) Layer "b"

Figure 6.10 - Strain Profiles of Intermediate Layers of Beam Bars.

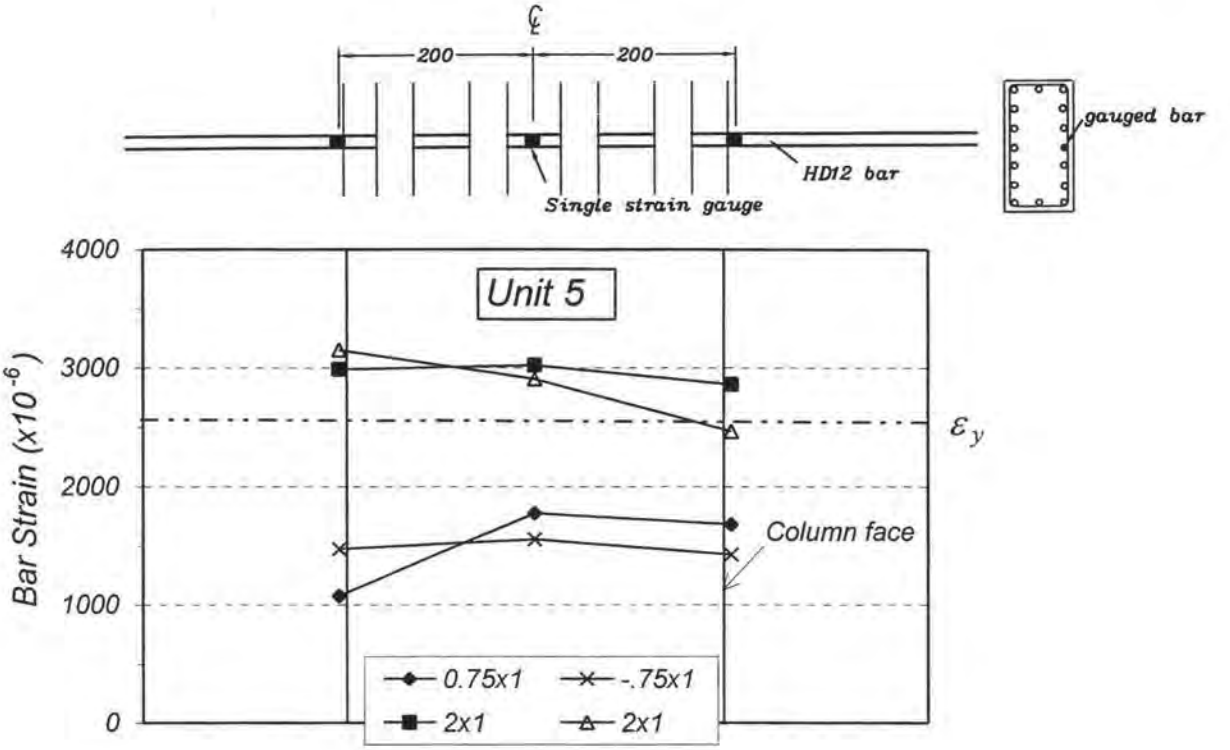

(c) Layer "c"

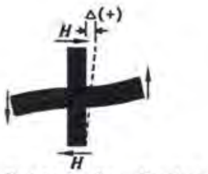

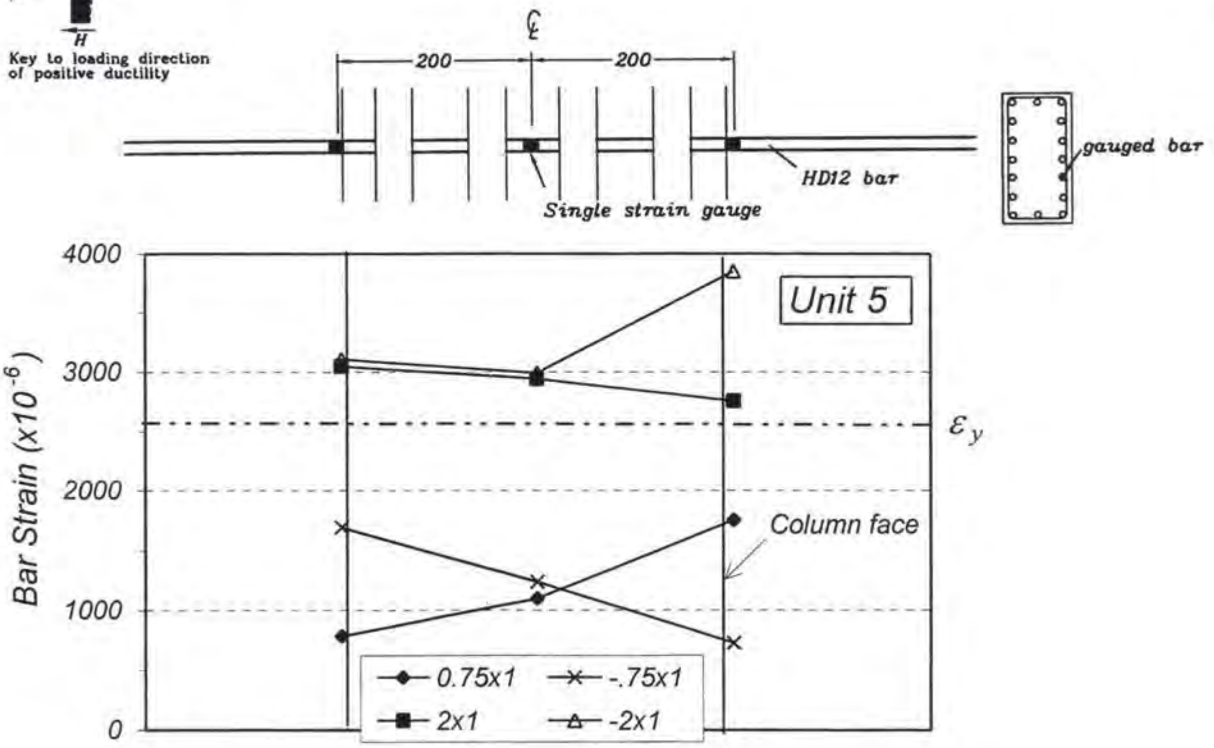

(d) Layer "d"

Figure 6.10 (Cont.) - Strain Profiles of Intermediate Beam Bars.

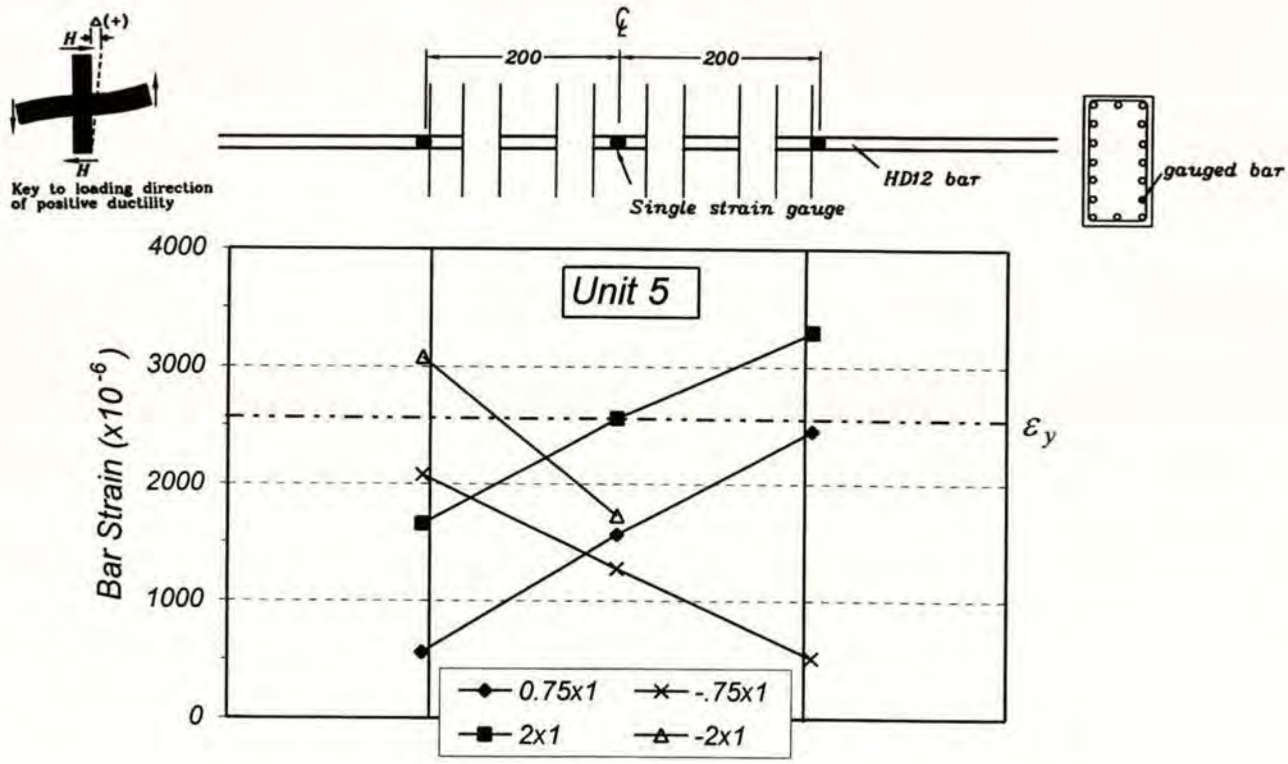

(e) Layer "e"

Figure 6.10 (Cont.) - Strain Profiles of Intermediate Beam Bars.

6.2.5 Beam Behaviour

6.2.5.1 Curvature Ductility Factors in Plastic Hinge

The beam curvature ductility factors obtained by the same procedure as in the previous units are depicted in **Fig. 6.12**.The beam curvature ductility factors show an ascending trend up to a peak value in both East and West beams in the load cycles to $\mu_\Delta = 4x1$ and then descended afterwards. This indicates that since the loading cycles to $\mu_\Delta = 4x1$, other sources of deformation, such as beam fixed-end rotation and joint shear distortion, controlled the deformation of the unit.

6.2.5.2 Beam Strain Profiles at the Level of the Longitudinal Reinforcement

The strain profiles at the level of the longitudinal reinforcement of Unit 5 are shown in **Figs. 6.13** and **6.14**. Presented data was calculated from the readings of the potentiometers mounted along top and bottom beam chords.

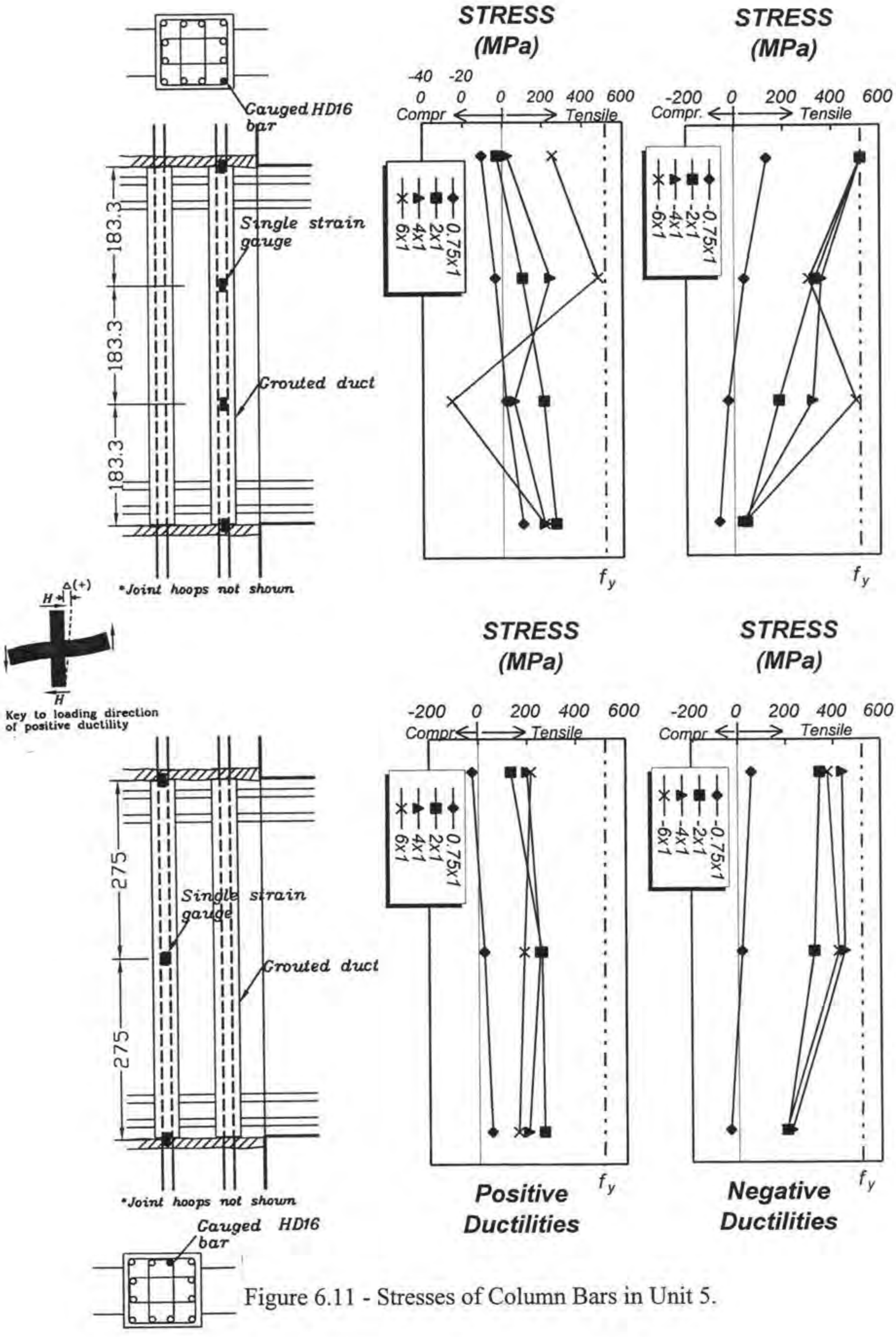

Figure 6.11 - Stresses of Column Bars in Unit 5.

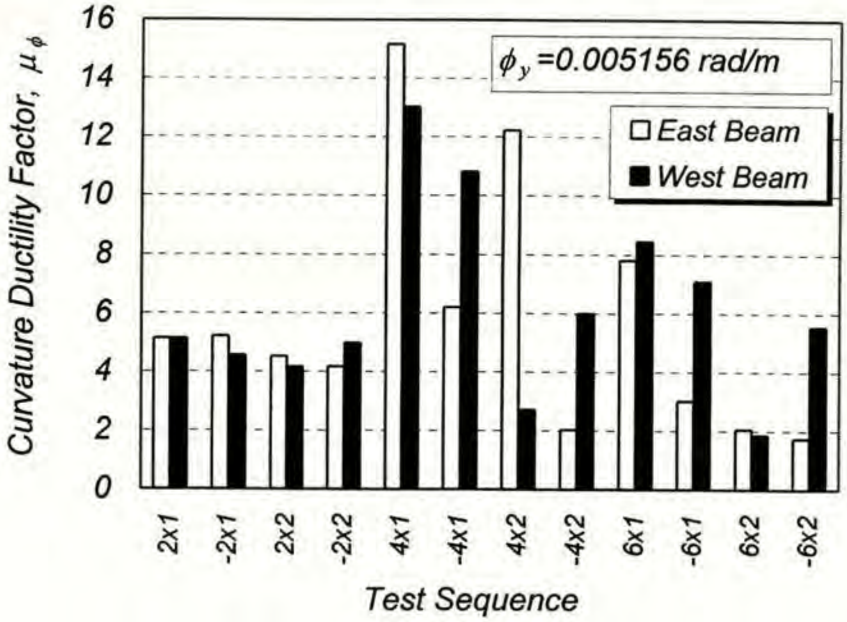

Figure 6.12 - Curvature Ductility Factors of Beam of Unit 5.

The tensile strains at the level of the top beam bars measured close to the column faces increased with the progressing of load cycles until reaching a maximum value of 3.0% in the load cycle to μ_Δ = 4x1. The compressive strain measured on the opposite side also show increasing trend with the progressing of test sequence. It reached the yield strain of longitudinal beam bar in the load cycle to μ_Δ = 2x1 and increased to -0.75% at the peak of μ_Δ = 4x1. From the loading cycle to μ_Δ = -4x1 the tensile strain ceased to increase while the compressive strain on the other side of column face had a sudden increase. This trend was more evident in the successive load cycles. As mentioned in the previous unit, this phenomenon was caused by bar slipping through the joint region. With reference to Section 6.2.4.3, it is known that the trend observed here is in good agreement with what was observed in **Fig. 6.7(a)**, in which total bond failure of top beam bars occurred in the load cycle to μ_Δ = -4x1.

Strain profiles of bottom beam bars show a similar trend as that of top bars. The drop of tensile strain and increasing of compressive strain also occurred in the load cycle to μ_Δ = 6x1.

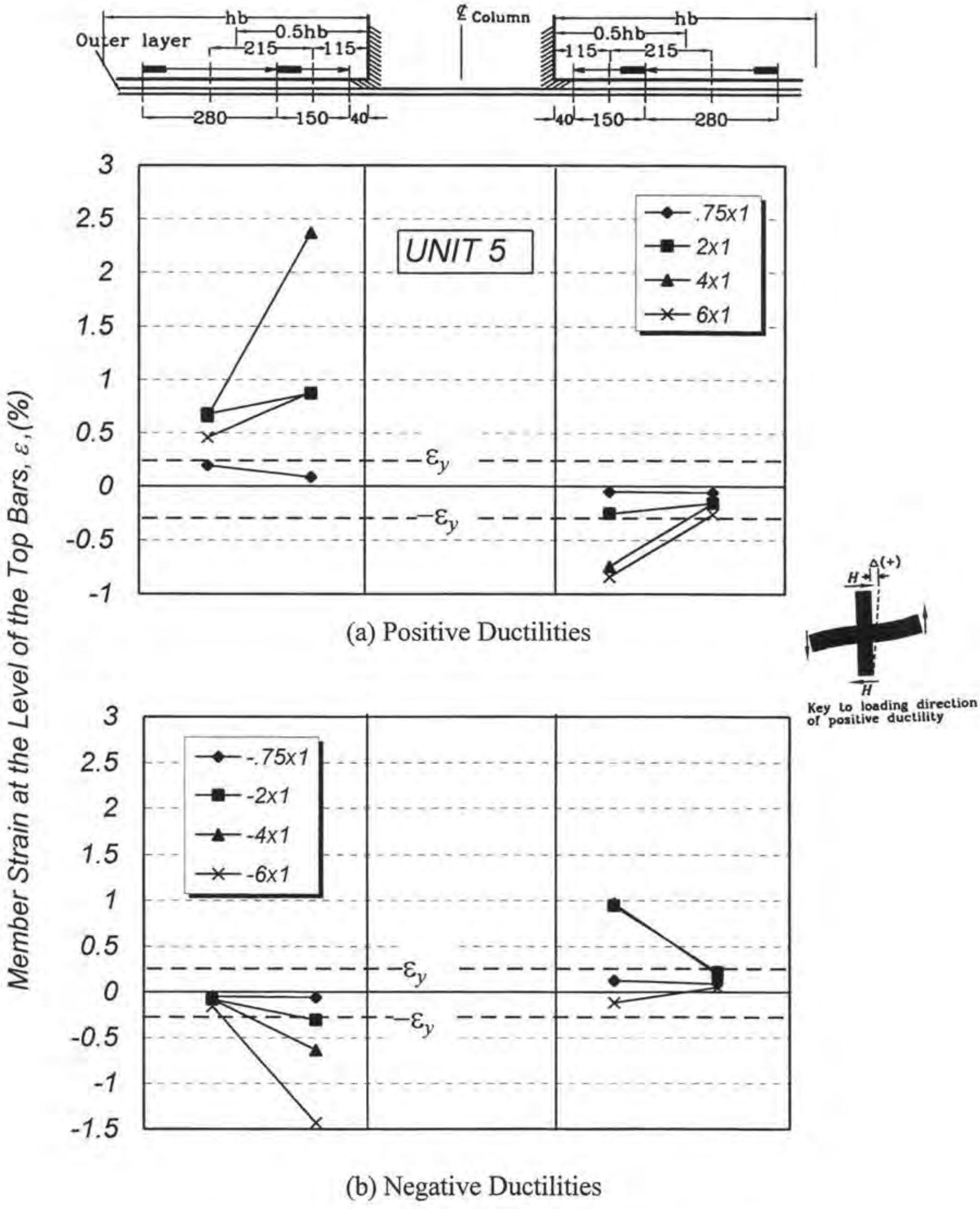

(a) Positive Ductilities

(b) Negative Ductilities

Figure 6.13 - Beam Strain Profiles at the Level of the Outer Layer of the Top Beam Bars of Unit 5.

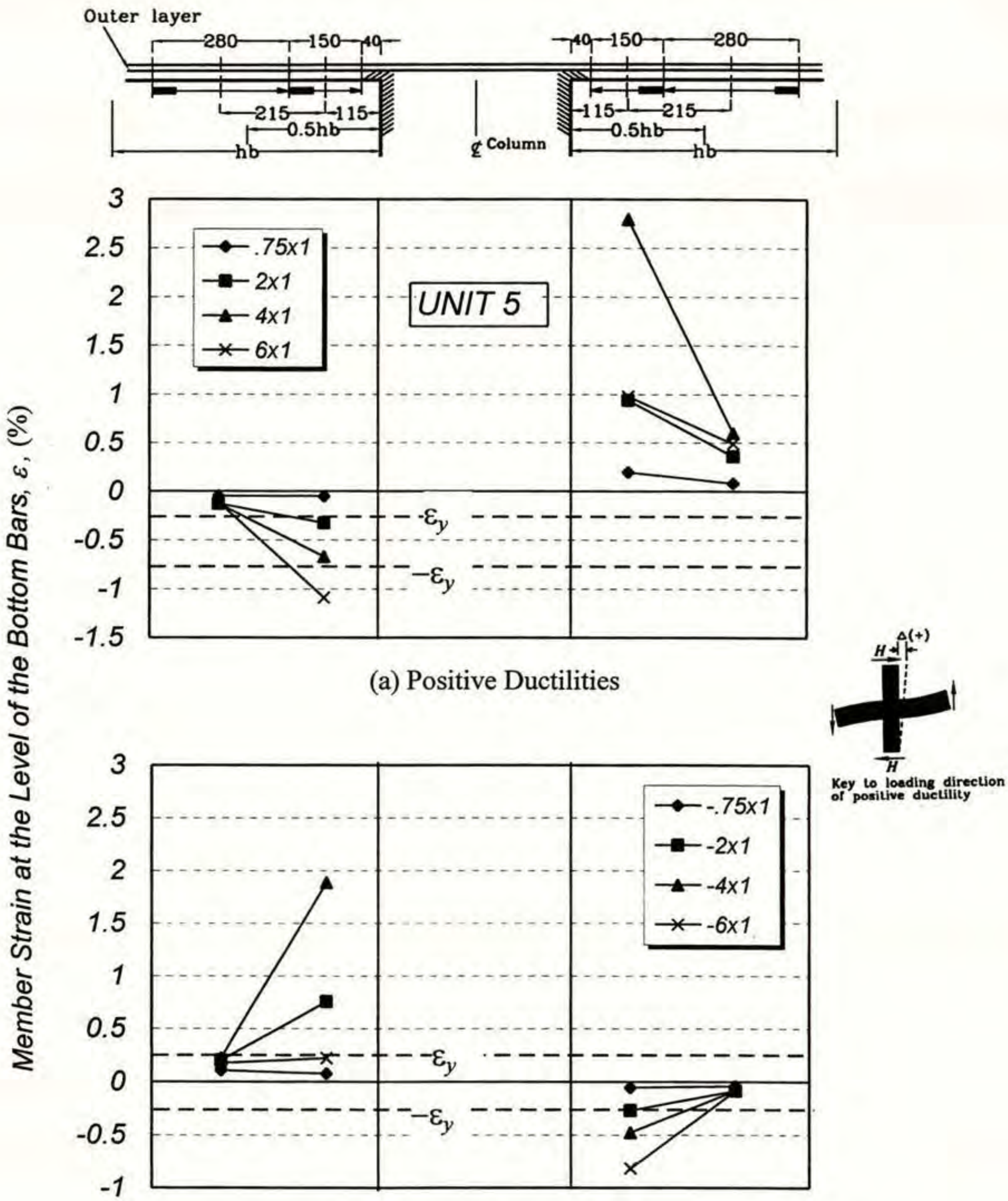

(a) Positive Ductilities

(b) Negative Ductilities

Figure 6.14 - Beam Strain Profiles at the Level of the Outer Layer of the Bottom Beam Bars of Unit 5.

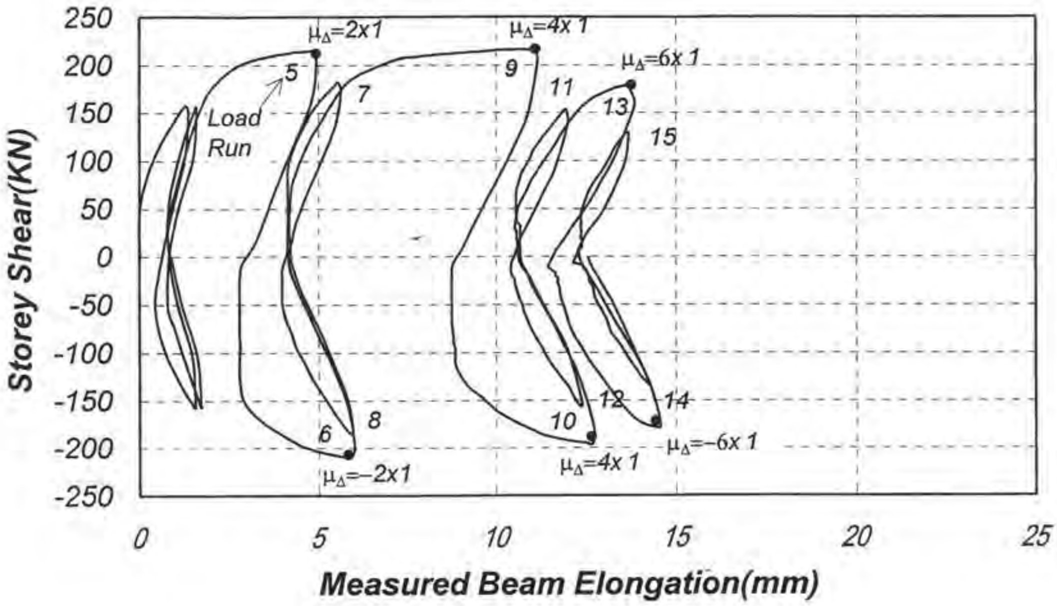

Figure 6.15 - Beam Elongation of Unit 5.

6.2.5.3 Beam Elongation

The measured beam elongation during the test was plotted against the storey shear in **Fig. 6.15**. It can be seen that significant beam elongation took place in each load cycle toward a new displacement ductility until μ_Δ = -4x1. After that, very little elongation was developed since the contribution of beam flexural response to the lateral displacement was diminishing. The recorded maximum beam elongation was 14.5 mm at the end of test, which is equal to 2.6% of the overall beam depth.

6.2.6 Column Behaviour

With observation on the crack patterns in columns and the stress profiles measured on column bars within joint region, it can be concluded that the columns behaved elastically during the test.

6.3 UNIT 6

6.3.1 General

Unit 6 was designed identically to Unit 5 except for incorporating deformed bars as horizontal joint reinforcement. Joint hoops and ties in Unit 5 were replaced by sets incorporating of deformed bars. Attempt was made through this unit to identify the enhancement effect on joint by means of deformed joint hoops and to observe if any lapping action between the joint reinforcement and the longitudinal beam bars would occur, leading to reduction of the tensile strain in the interior longitudinal beam bars and enhancing the strength of the diagonal compression field as a result.

6.3.2 Overall Behaviour

Like the observed behaviour in Unit 5, this unit did not perform satisfactorily for components designed to be ductile. Similar failure modes as found in Unit 5 including loss of anchorage of extreme layers of longitudinal beam bars passing through joint region and joint shear failure were observed. In the load cycle to μ_Δ = +4x2, corresponding to a inter-storey drift of 4.1%, 28% reduction of lateral load capacity with respect to the measured maximum load, was recorded. At the end of test, considerable portion of cover concrete in joint panel spalled off and crushing of concrete on top and bottom beam chords at column faces had occurred. In addition, joint shear distortion could be observed visually. However the use of deformed joint reinforcement did somehow improve the joint behaviour.

Cracking of the test specimen at different stages during the test is presented in **Fig. 6.16.** The lateral load versus lateral displacement response is plotted in **Fig. 6.17**.

In general, the crack pattern observed in the elastic load cycles in Unit 6 was very similar to that of Unit 5 both in the beams and the columns. However, the cracks in Unit 6 spread through the joint panel and were shorter and smaller in width than those observed in Unit 5. While joint cracks in Unit 5 tended to concentrate in the vicinity of diagonal strut. At this stage cracks in joint region was less than 0.1 mm wide.

As the load sequence proceeded to μ_Δ = 2x1, more flexural cracks, up to 1.5 mm wide, developed in the beams. Short and fine diagonal cracks occurred in the joint region, making the difference between joint cracking patterns of Units 5 and 6 more evident. However, at this

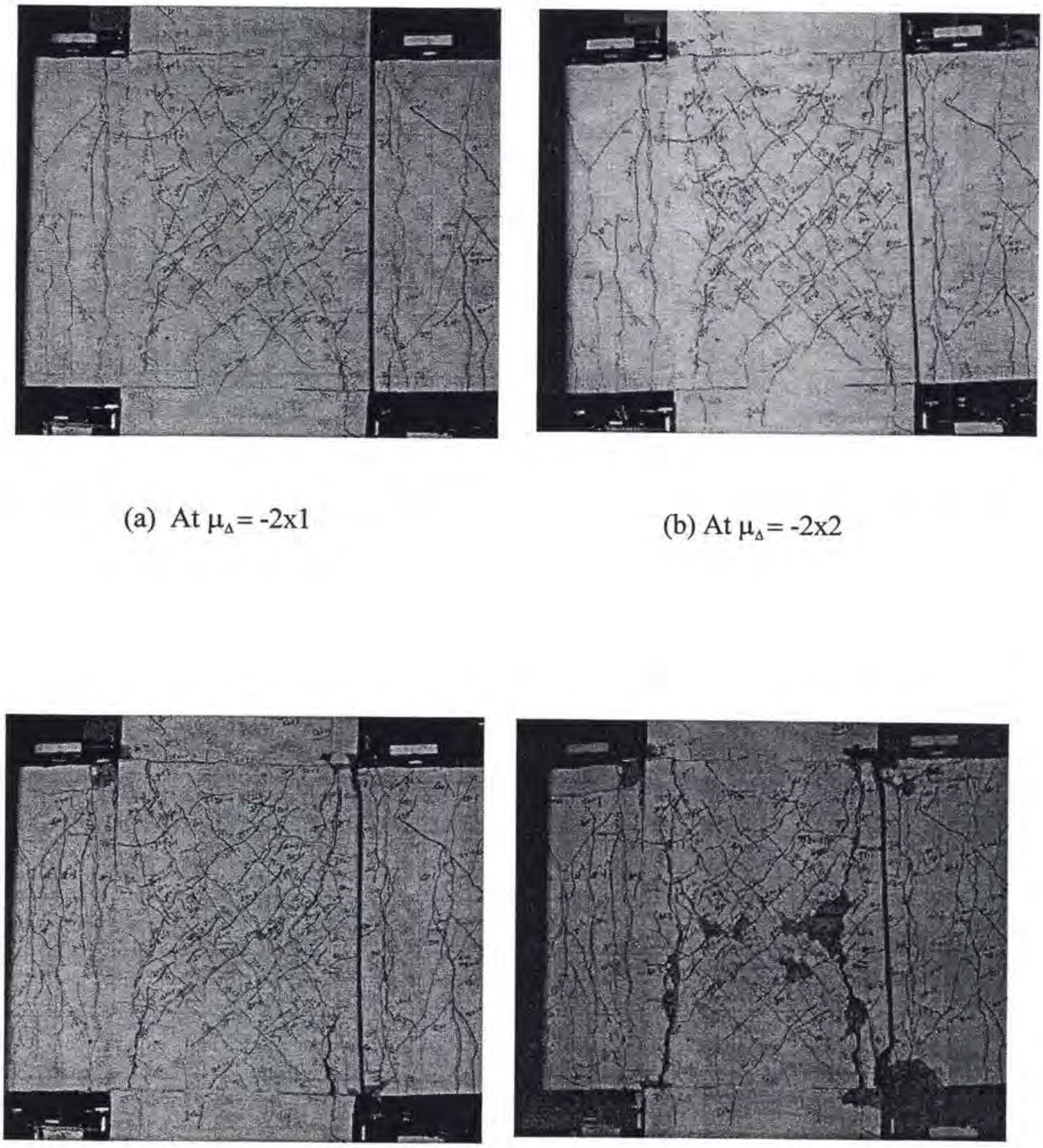

(a) At $\mu_\Delta = -2x1$

(b) At $\mu_\Delta = -2x2$

(c) At $\mu_\Delta = -4x1$

(d) At $\mu_\Delta = -4x2$

Figure 6.16 - Cracking of Unit 6 at Different Stages During the Test.

(e) At μ_Δ = -6x1

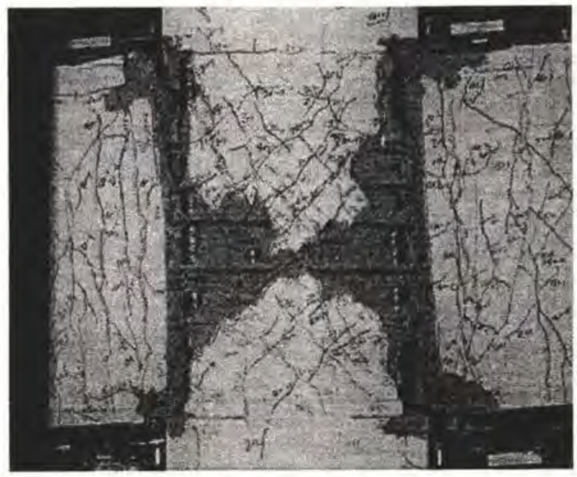

(f) At μ_Δ = -6x2

Figure 6.16(Cont.) - Cracking of Unit 6 at Different Stages During the Test.

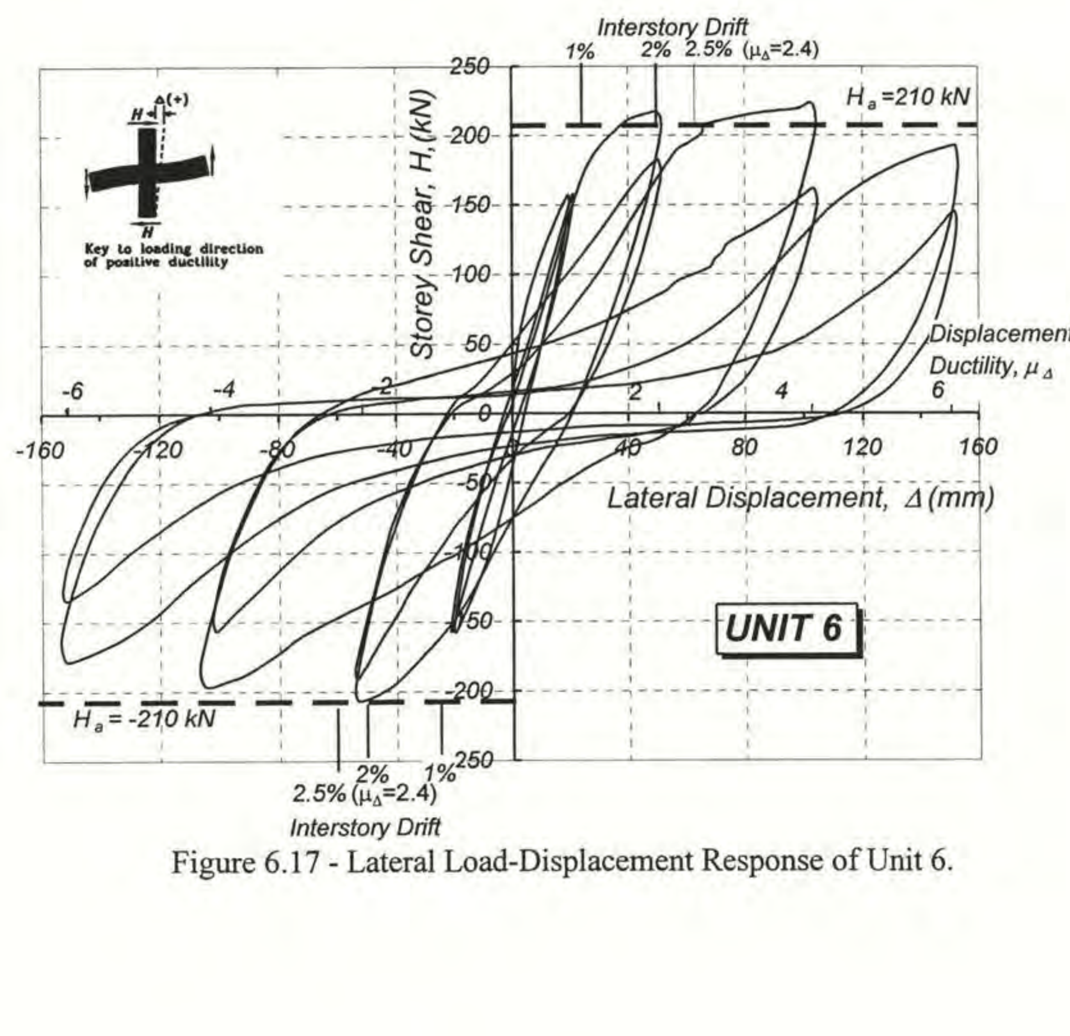

Figure 6.17 - Lateral Load-Displacement Response of Unit 6.

loading stage, cracks in the four corners of joint panel reached 3.5 mm in width, indicating that anchorage of top and bottom beam bars had started to deteriorate. Apart from these large cracks located in corners of joint panel, other joint cracks remained less than 0.3 mm wide.

By μ_Δ = 4x1, cracks in the beam plastic hinge regions became wider, reaching a maximum width of 4 mm. The widest cracks formed in the beam at the column faces. It is noted that significant slip of top beam bars was noticed at this stage as the movement of the target stud welded on longitudinal beam bars in the centreline of the joint became apparent. Cracking patterns in joint region was similar to that in the last load cycle with maximum crack width less than 0.5 mm except for the corner cracks resulted from beam bars slip.

In the load cycles to μ_Δ = 4x2, see **Fig. 6.16(c)**, incipient damage of cover concrete in central part of joint region was observed. In addition, concrete cover surrounding the corner metal ducts embedded in joint region became dislodged. Moreover, cover concrete at the top and bottom beam chords next to the column faces spalled off owing to the significant slip of longitudinal bars.

In the load cycles to μ_Δ = 6x1, cracks in beams at the column faces were quite wide, especially the one propagating from the top beam chord. A large gap at column face propagating from top beam chord could be observed. It is believed that bond failure of top and bottom beam bars had occurred at this stage. At the peak of μ_Δ = -6x1, the corner metallic ducts were exposed due to spalling of the concrete cover.

In the load cycles to μ_Δ = ±6x2, see **Fig. 6.16(d)**, spalling of the cover concrete spread towards the central part of the joint panel. In addition, crushing of concrete on the top and bottom beam chords at column faces was very noticeable. At the end of test, the middle portion of the interior metallic ducts in joint region were also exposed due to spalling of concrete cover. Bond failure of both top and bottom extreme layers of beam bars in combination with joint shear failure led to the eventual failure of Unit 6.

6.3.3 Load-Displacement Response

Figure 6.17 shows the measured lateral load - lateral displacement response of Unit 6. The yield drift of the unit was 1.04%, a value similar to that of Unit 5. Similarly, this yield drift level implies a displacement ductility equal to μ_Δ = 2.4 when the 2.5% drift limit imposed by the loading standard is attained.

In general, the hysteresis loops of this unit were very similar to that of Unit 5. The measured lateral load capacity reached the theoretical ultimate lateral load in the load cycles to $\mu_\Delta = \pm 2x1$. Like that in Unit 5, the lateral load measured in the second load cycle of the same displacement ductility dropped to 84% and 91% of the theoretical ultimate loads in positive and negative load cycles respectively.

In the load cycles to $\mu_\Delta = \pm 4x1$, the measured lateral load exceeded the theoretical ultimate value by 3% in the positive load cycle, while it was 94% of the theoretical value in the reversed load direction. In the successive load cycles, $\mu_\Delta = \pm 4x2$, considerable reduction of lateral load capacity and apparent pinching of hysteresis loops were observed. The measured lateral load capacity only reached 73% and 74% of the maximum loads in the positive and negative load cycles respectively. This unit failed in this load cycle if the criteria commonly used in New Zealand Standard [S4] [P1] was employed.

In the load cycles to $\mu_\Delta = \pm 6x1$, the lateral load - lateral displacement response showed significant pinching, the lateral load capacity picked up to 86% of the maximum loads. Note that the gain of lateral load capacity in this load cycle was noticeable. Thus it is believed that the reduction of lateral load capacity in the load cycles to $\mu_\Delta = 4x1$ was partially caused by bond failure of extreme layers of beam bars. This can be further confirmed in the latter section.

As test carried on to $\mu_\Delta = \pm 6x2$, lateral load capacity dropped further to 64% and 66% of the measured maximum loads with serious pinching of hysteresis loops observed.

6.3.4 Decomposition of Lateral Displacements

Percentage of each component of lateral displacement was calculated and is presented in **Fig. 6.18**. In general, the trends depicted in **Fig. 6.18** are similar to that of Unit 5. The main difference is that in the load cycles near the end of the test the component of joint shear deformation in Unit 6 was smaller than in Unit 5 but that due to beam-fixed rotation was larger. This difference, although not too significant, can be attributed to the presence of deformed joint reinforcement.

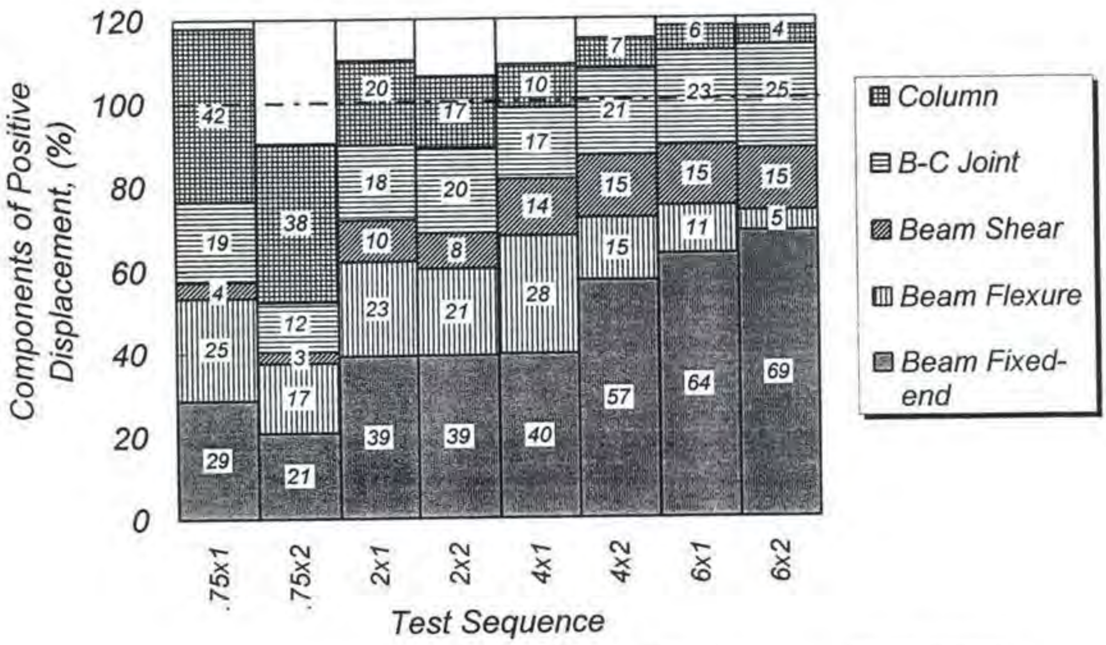

(a) Runs to Positive Ductilities

UNIT 6

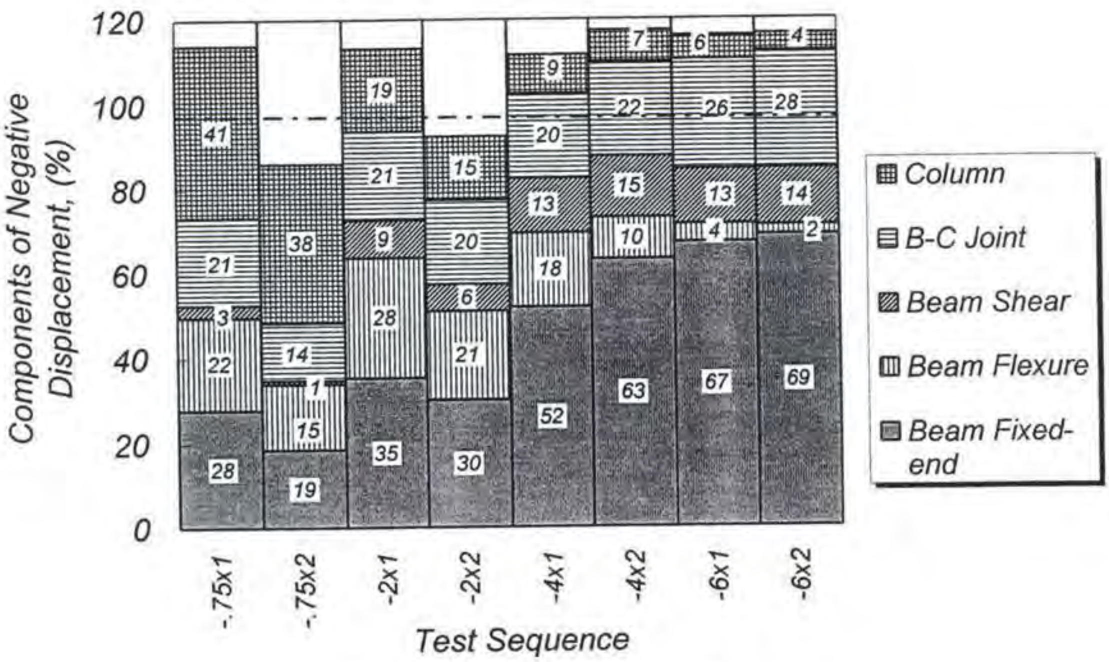

(b) Runs to Negative Ductilities

Figure 6.18 - Components of Lateral Displacement of Unit 6 at Peaks of Load Runs

6.3.5 Joint Behaviour

6.3.5.1 Strains in the Horizontal Joint Reinforcement

The joint transverse reinforcement of Unit 6 comprised 5 sets of perimeter D10 hoops and inner D10 ties. Strain values averaged from readings of each pair of double strain gauges attached on joint hoops and ties are shown in **Figs. 6.19** and **6.20**.

In the elastic load cycles, strains in each joint reinforcement set were quite consistent, reaching about 1000 micro-strains. In the load cycles to $\mu_\Delta = 2$, strains approached yielding in almost all sets. All sets but the extreme perimeter hoops yielded in the cycles to $\mu_\Delta = 4$. Comparing the recorded joint strain profiles of Units 5 and 6 (see **Figs. 6.4, 6.5, 6.19** and **6.20**), it can be observed that the measured strains of sets of joint reinforcement adjacent to top and bottom beam bars in Unit 6 are more consistent with the readings of inner sets than that of Unit 5. In Unit 5 the top and bottom sets did not yield until $\mu_\Delta = 4$. This indicates that the bond stress developing along the deformed joint hoops enable the extreme sets of horizontal joint reinforcement to develop its strength in resisting the input joint shear more effectively. Note that this can be a potential advantage for the design of beam-column joint reinforcement by means of using deformed bars.

6.3.5.2 Joint Shear Distortion

Joint shear distortion at the peak of each load cycle was calculated from readings of potentiometers diagonally mounted on the joint panel and plotted against measured storey shear in **Fig. 6.21**.

In comparison the graph in **Fig. 6.21** with that in **Fig. 6.6** for Unit 5, it can be seen that the joint shear distortion of Unit 6 is smaller than that recorded in Unit 5. Prior to the load cycles to $\mu_\Delta = 4$, the joint shear distortion measured for Unit 6 was of similar order to that observed in the joint of Unit 5. Beyond this level of ductility, the shear distortion measured in the joint of Unit 6 did not increase as significantly as that in Unit 5. At the end of test, maximum measured joint shear distortion in Unit 6 reached 0.025 radians which contrast with 0.035 radians measured in joint of Unit 5. It is evident that deformed joint reinforcement does have some beneficial effect on improving the joint behaviour.

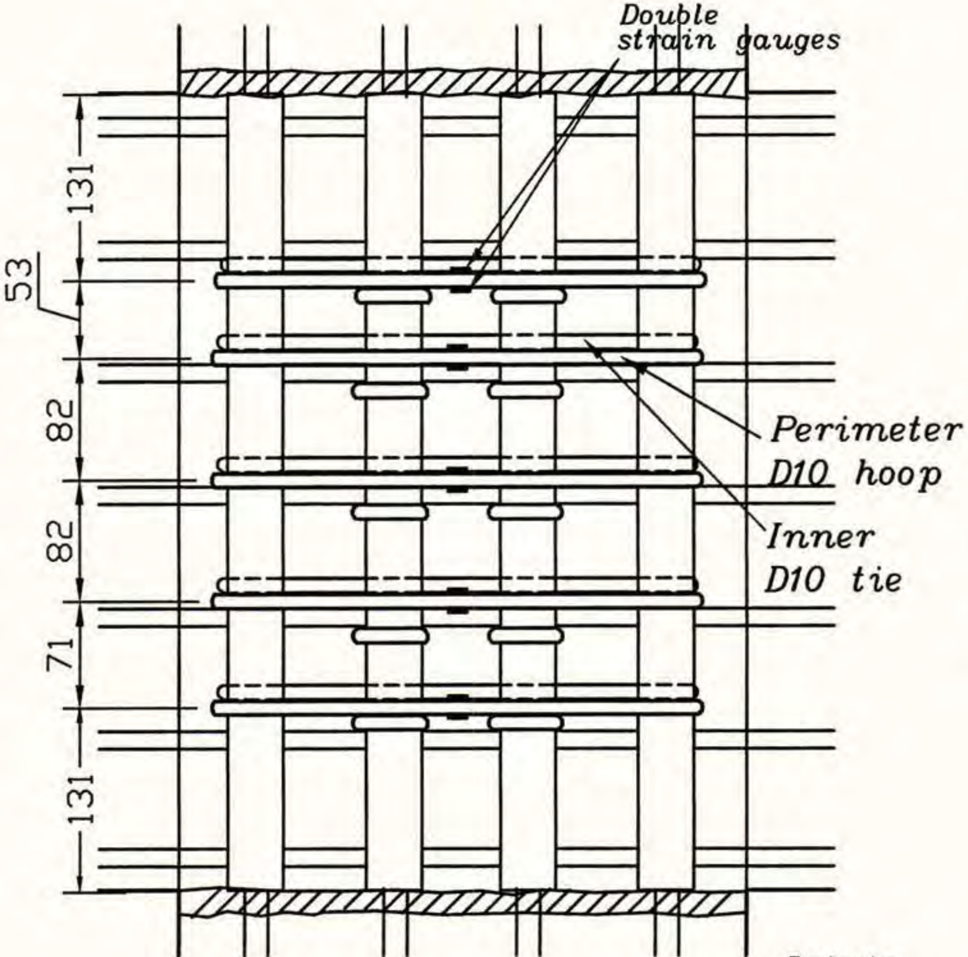

UNIT 6

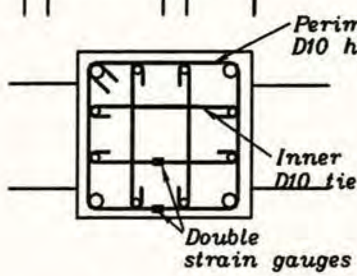

Plan View

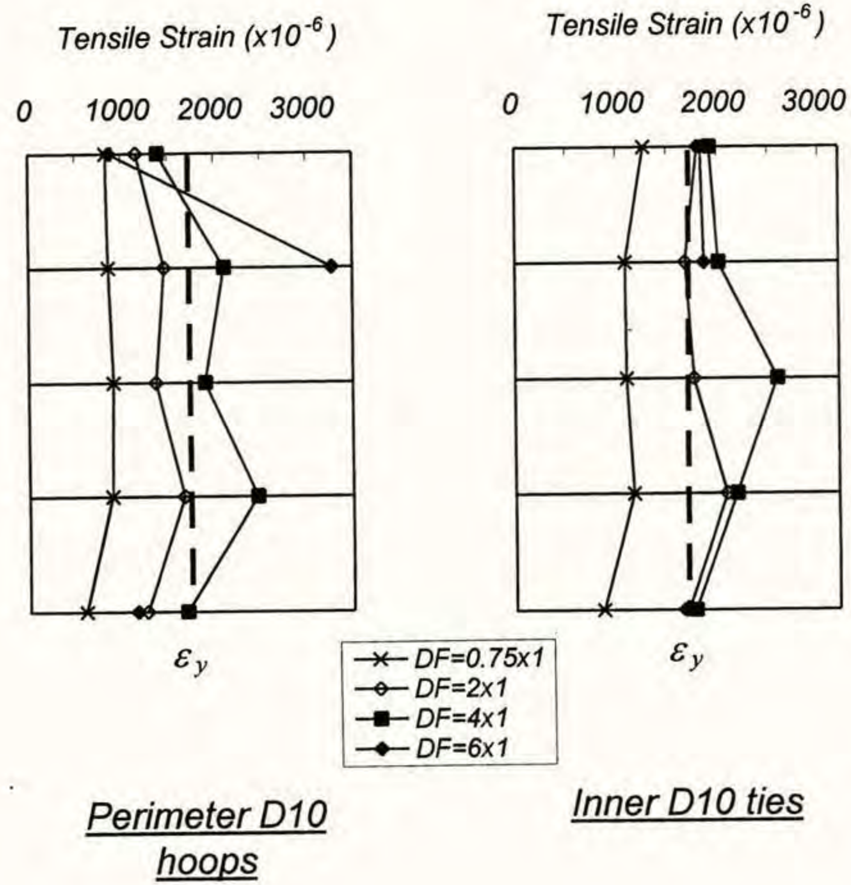

Positive Ductilities

Figure 6.19 - Measured Strains in Joint Hoops of Unit 6 During the Runs to Positive Ductilities.

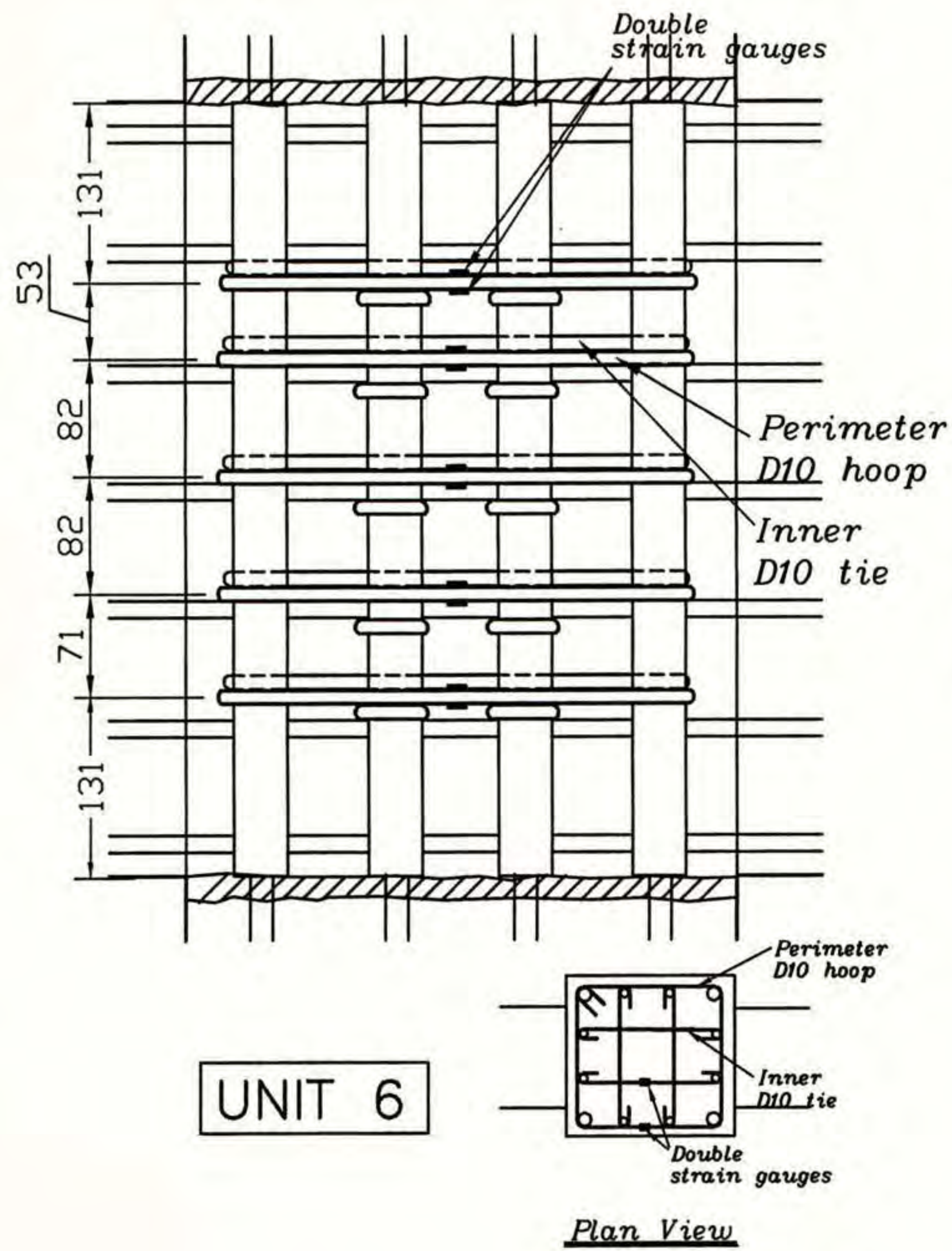

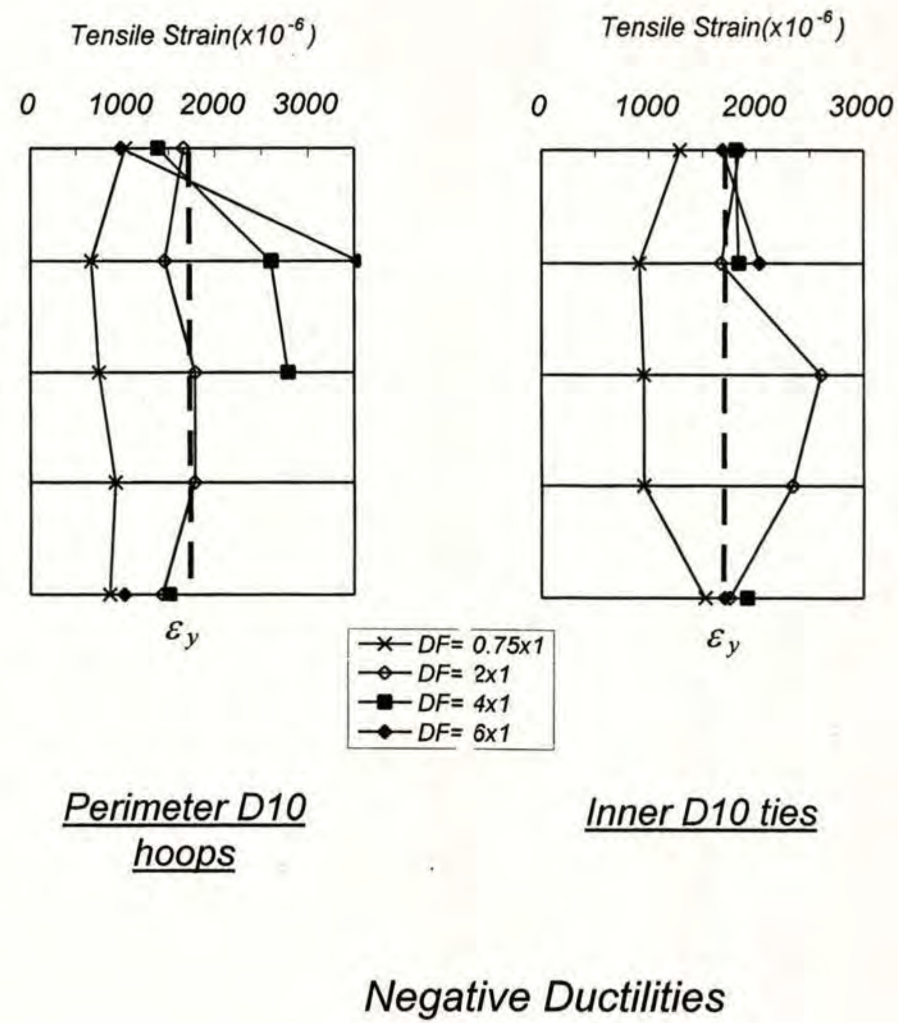

Figure 6.20 - Measured Strains in Joint Hoops of Unit 6 During the Runs to Negative Ductilities.

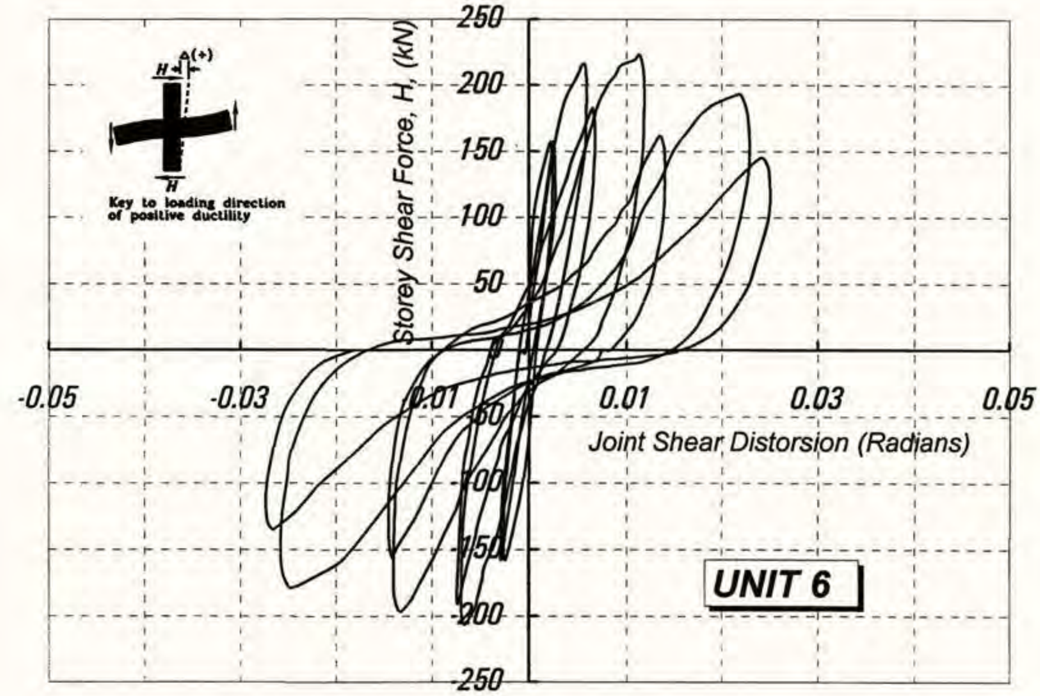

Figure 6.21 - Joint Shear Distorsion Versus Storey Shear Force.

6.3.5.3 <u>Beam Bar Slip</u>

The measured local bar slip of extreme layers of longitudinal beam bars at three locations within joint region is presented in **Figs. 6.22(a), (b)**. Note that the abnormalities in these plots beyond the load cycles to $\mu_\Delta = 4$ are the result of bar slip that resulted from the welded studs bearing against the concrete.

In general, the measured slip of top and bottom beam bars of Unit 6 was very similar to that of Unit 5, see **Figs. 6.7** and **6.22**, which is expected since the two units were cast simultaneously. Slip of top beam bars was larger than that of bottom beam bars, though the difference between them was not obvious. Slip of top beam bars measured in the joint centre exceeded the clear spacing between bar deformations, half way through the load cycle to μ_Δ = -4x1, while the bottom bars reached this threshold near the peak of load cycle to μ_Δ = -4x1. The reduction of lateral load capacity taking place in the load cycle to μ_Δ = -4x1 was partly caused by bond failure of top and bottom beam bars.

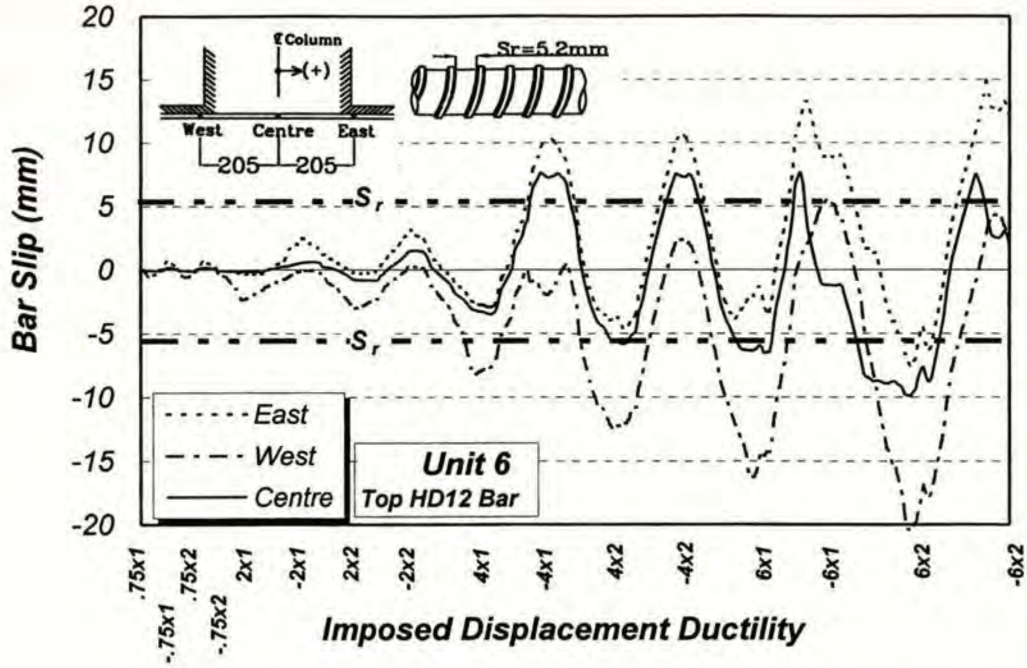

(a) Top Bars

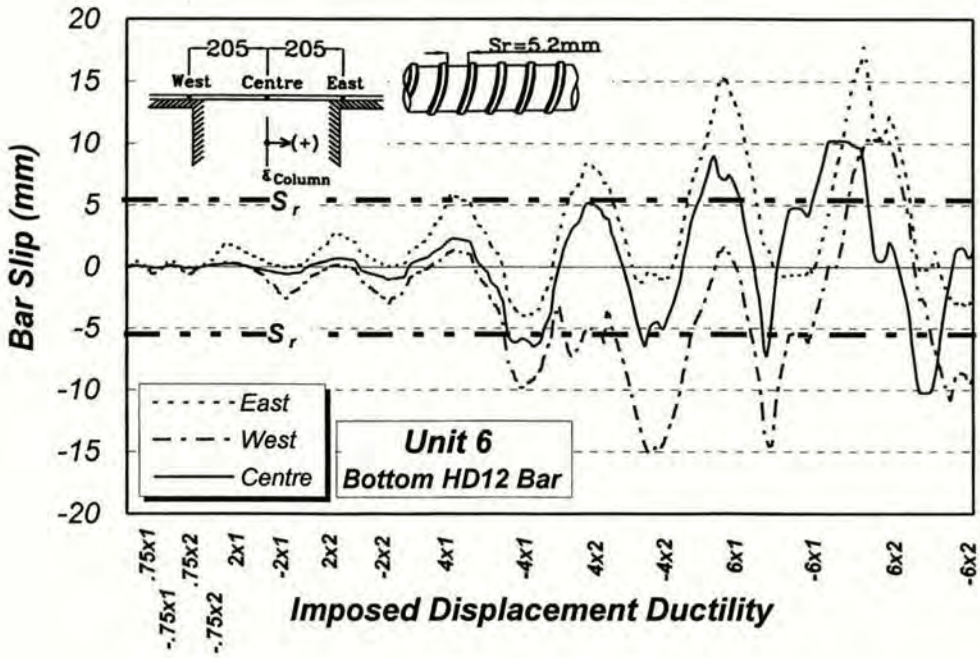

(b) Bottom Bars

Figure 6.22 - Relative Slip of Beam Longitudinal Bars in the Joint Region.

6.3.5.4 Bar Strain and Bond Stress in Joint Region

The strain profiles along extreme layers of longitudinal beam bars obtained from readings of electrical strain gauges are shown in **Fig. 6.23**. **Figure 6.24** plots the bar bond stresses.

Like that in Unit 5, the strain profiles can only be available until $\mu_\Delta = 2$ since most of the strain gauges were damaged due to relative movement between bar and concrete. In general, the strain profiles in the load cycles at the beginning of the test are very much similar to that of Unit 5, see **Figs. 6.8** and **6.23**. They also possess the feature that the tensile strain approached yielding in elastic load cycles. The maximum compressive strain recorded in the load cycle of $\mu_\Delta = 2$ was -2000 micro-strains, a value the same as recorded in Unit 5.

Meanwhile, so found bond stresses depicted in **Fig. 6.24** were very similar to those observed in Unit 5, see **Fig. 6.9**. The peak values on top and bottom beam bars were 9, 12.5 MPa, which are equivalent to 1.61and 2.2 $\sqrt{f_c'}$, respectively. Note that the strain gauge in the centre of the joint region showed abnormal readings, leading abnormal calculated bond stress.

Strain profiles of some bars in the inner layer of longitudinal bean reinforcement web are depicted in **Fig. 6.25**. Generally the trends found here are very much similar to that observed in Unit 5, see Section 6.2.4.4.

6.3.5.5 Bar Stresses of the Column Vertical Reinforcement Passing Through the Joint Region

Figure 6.26 presents the stresses profiles of column bars within joint region. It can be seen that so found stresses profiles are very similar to that are shown in **Fig. 6.11** for Unit 5. It is noted that the stress profiles of corner bars measured in the load cycles to $\mu_\Delta = \pm 4x1$ did not show abnormal change in the middle part of joint panel as was observed in Unit 5. It indicates that the joint shear distortion did not affect the stress profiles of corner column bars as that in Unit 5. This trend agrees with what was observed in Section 6.3.5.2 that the joint shear distortion in Unit 6 was less than in Unit 5.

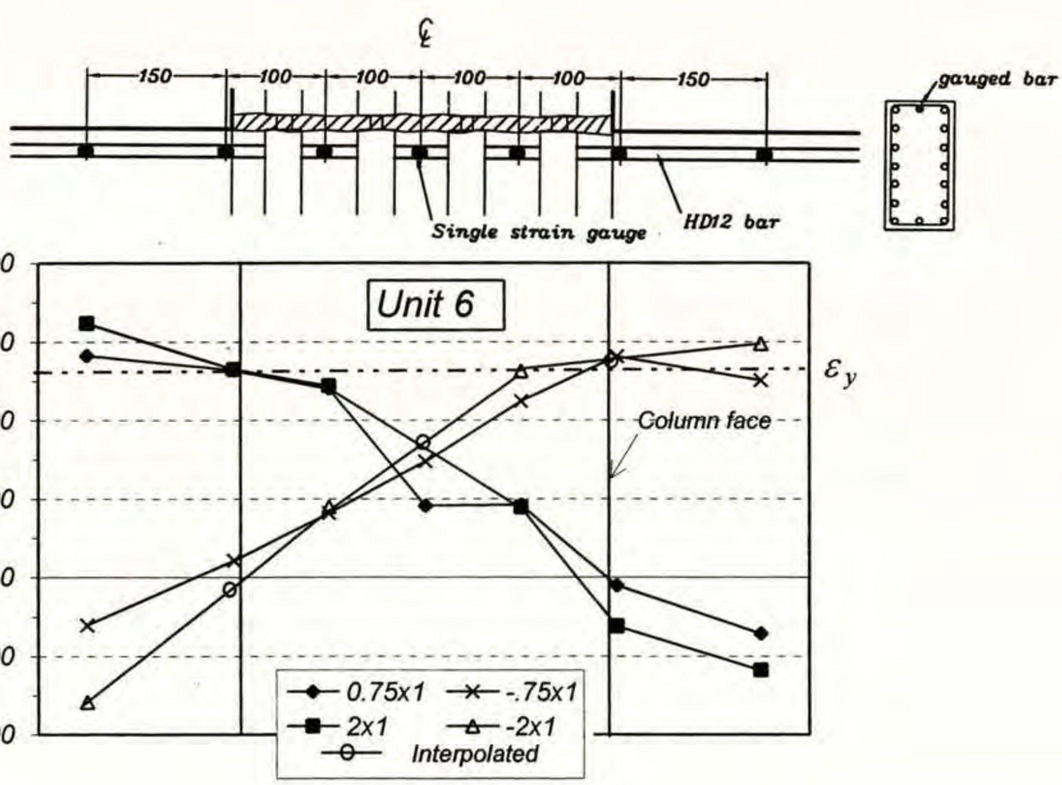

(a) Top Beam Bar

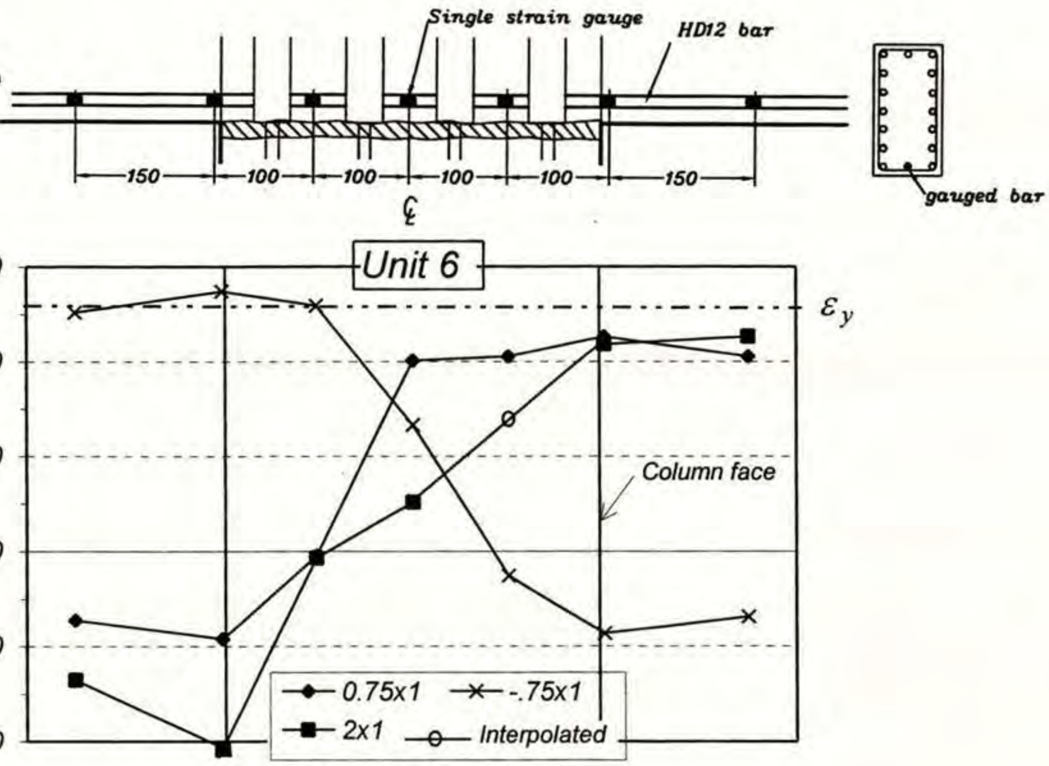

(b) Bottom Beam Bar

Figure 6.23 - Strain Profiles of Outer Layers of Beam Bars.

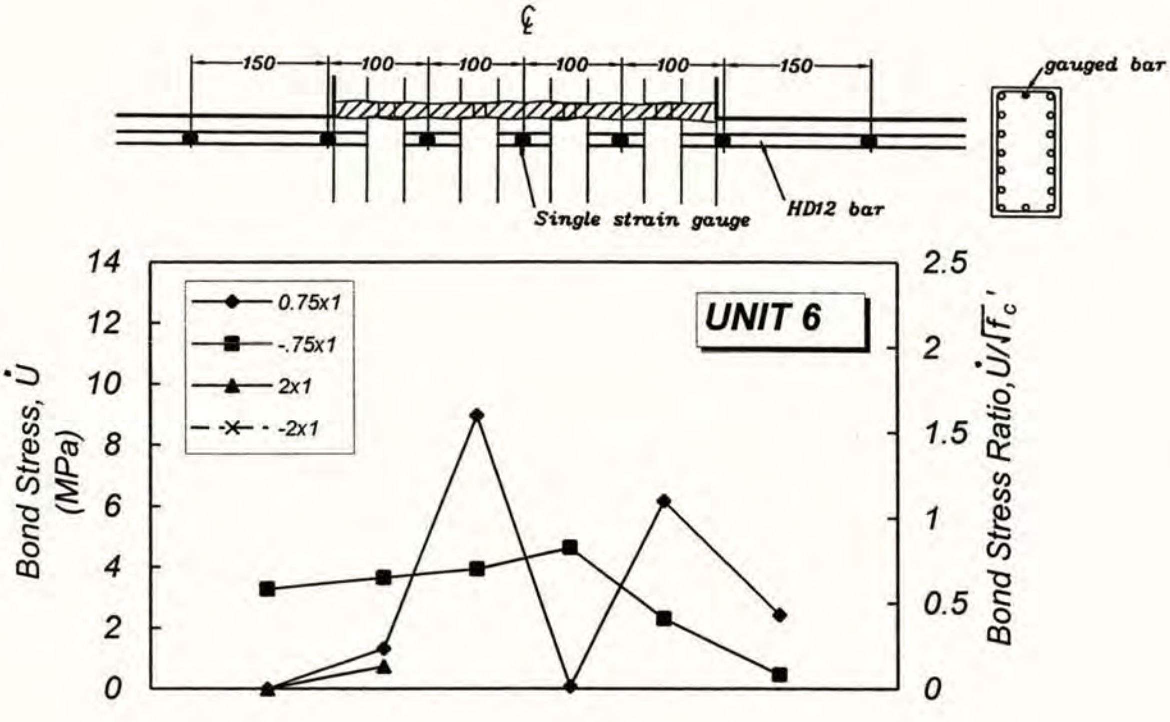

(a) Top Bars

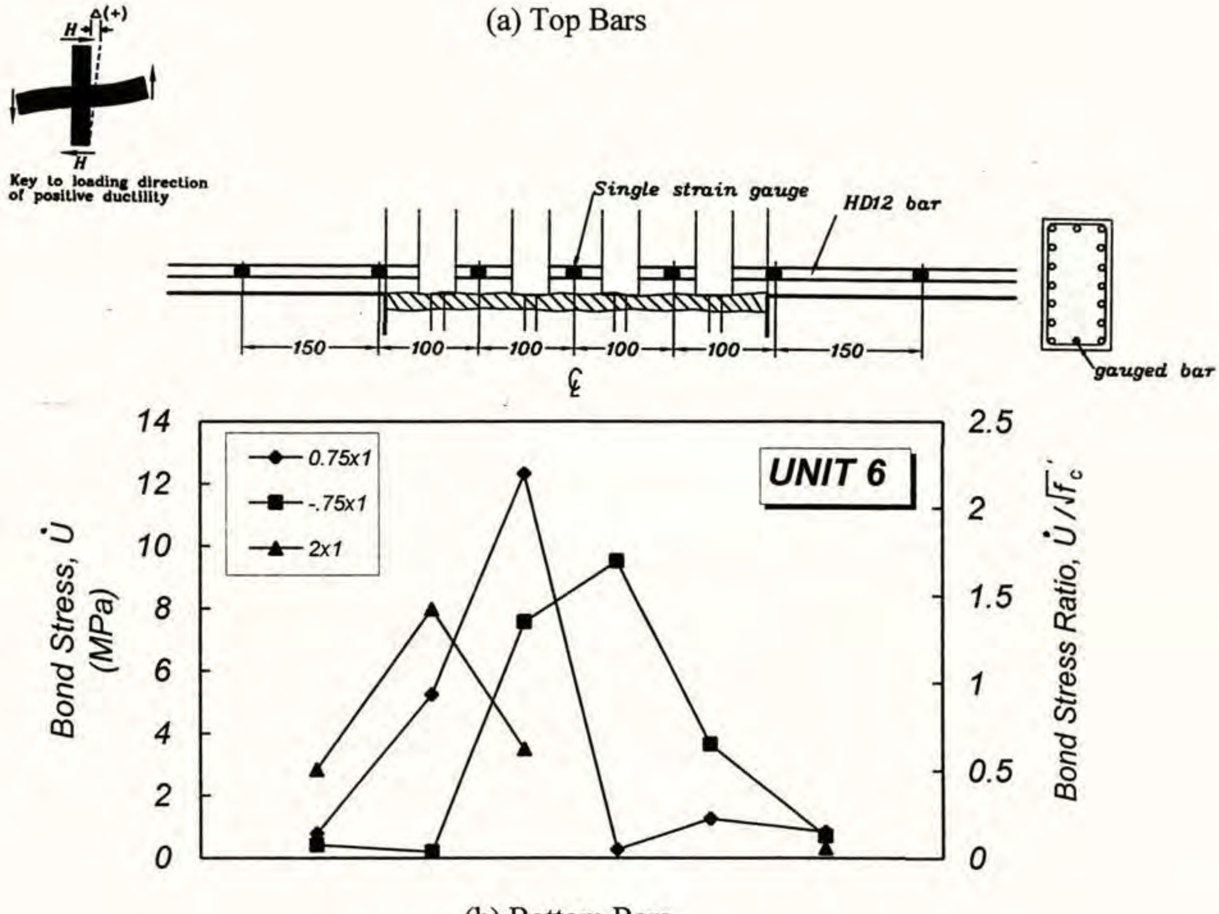

(b) Bottom Bars

Figure 6.24 - Calculated Bond Stresses.

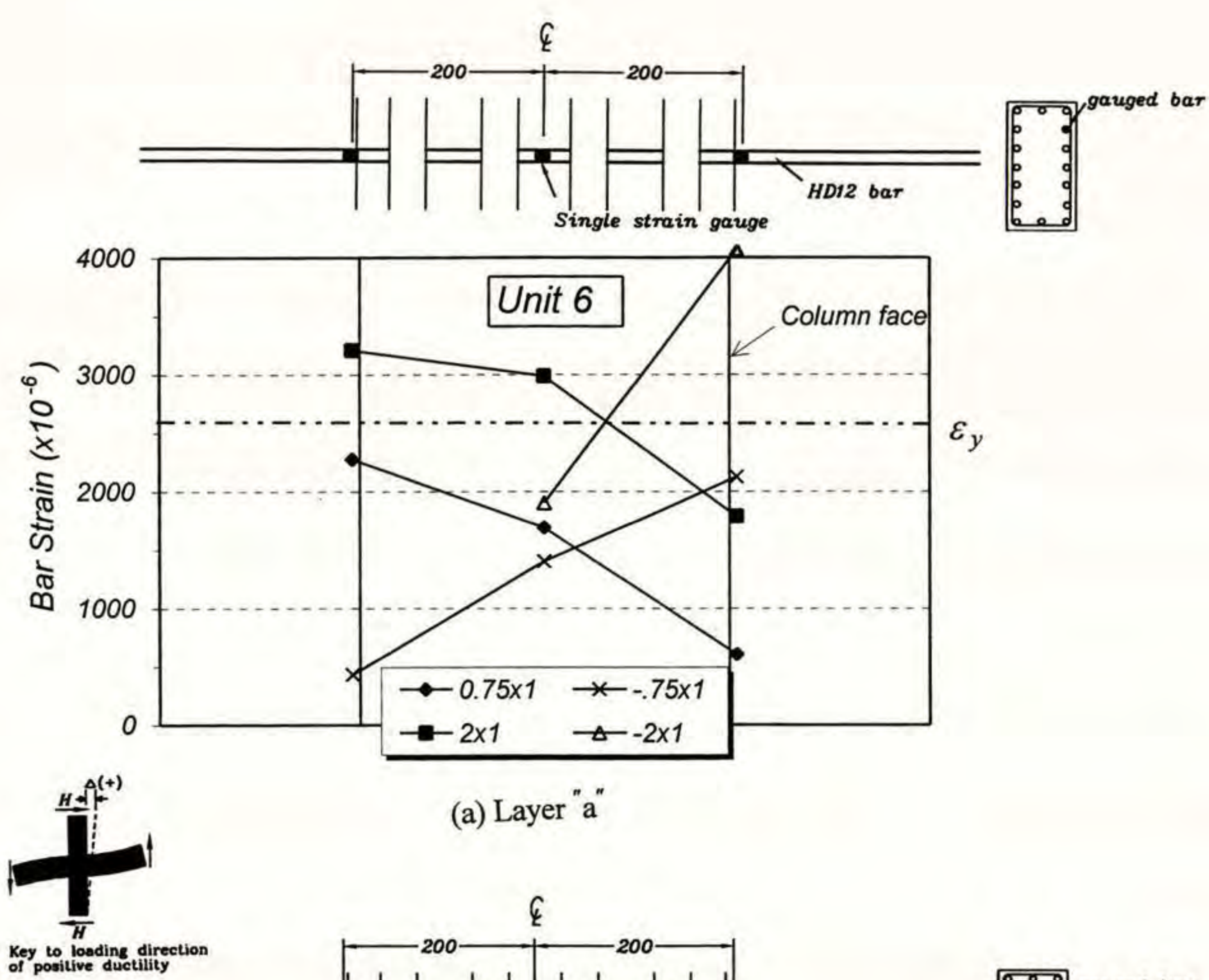

(a) Layer "a"

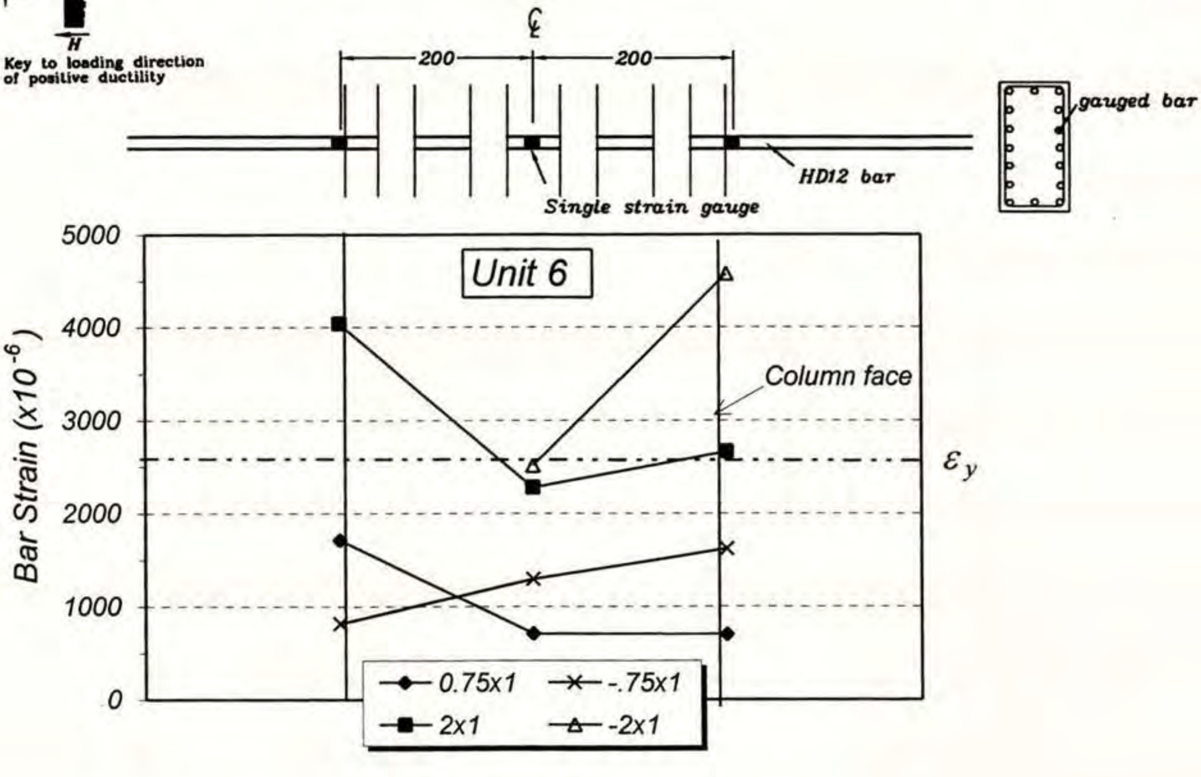

(b) Layer "b"

Figure 6.25 - Strain Profiles of Intermediate Beam Bars of Unit 6.

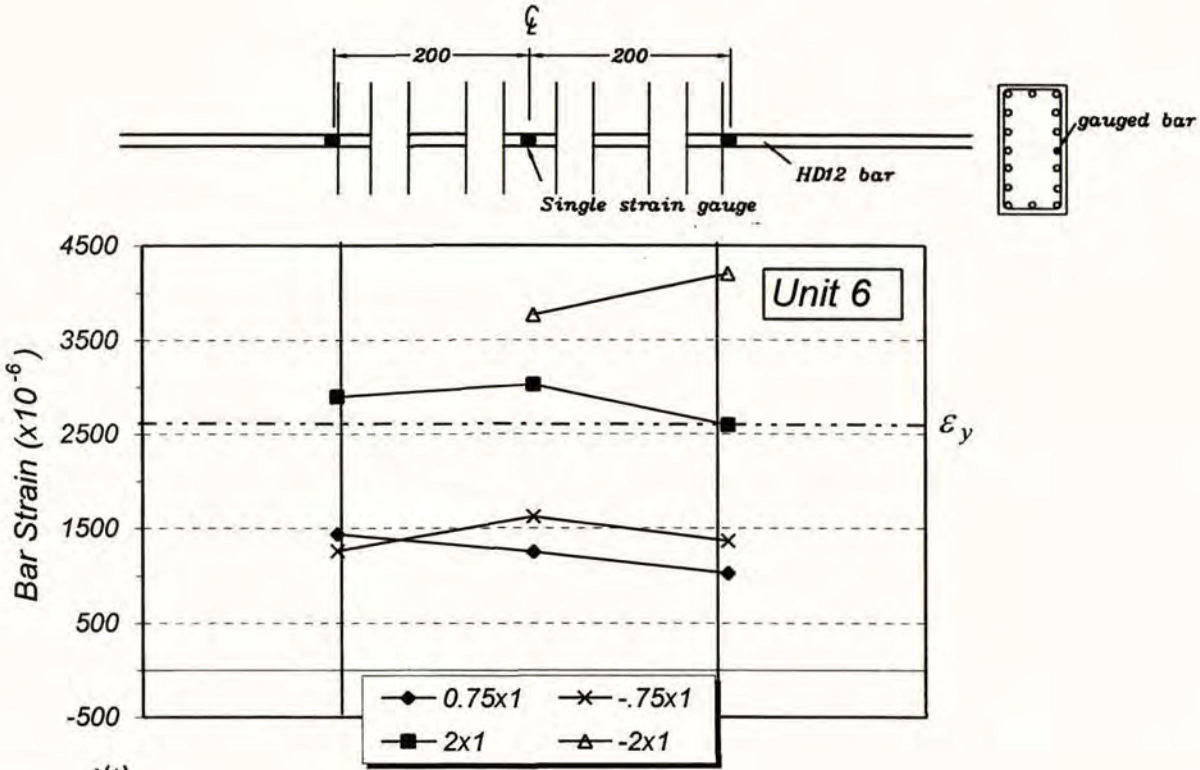

(c) Layer "c"

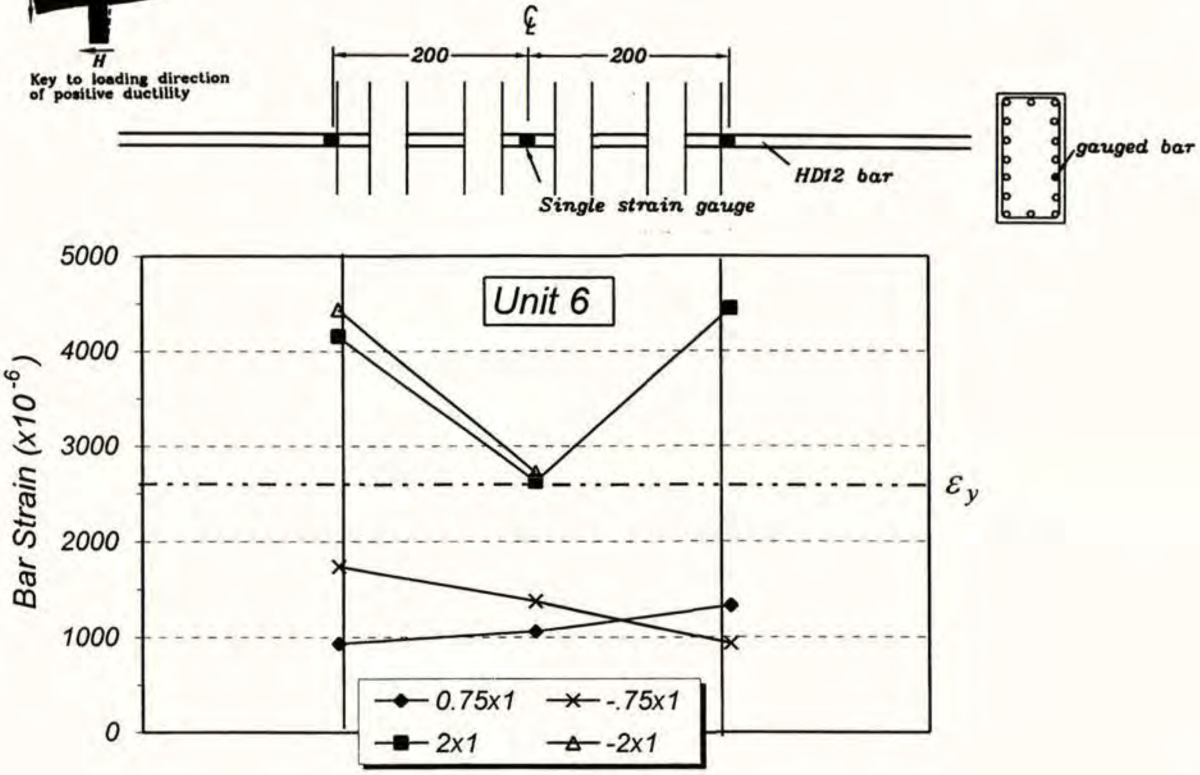

(d) Layer "d"

Figure 6.25 (Cont.) - Strain Profiles of Intermediate Beam Bars of Unit 6.

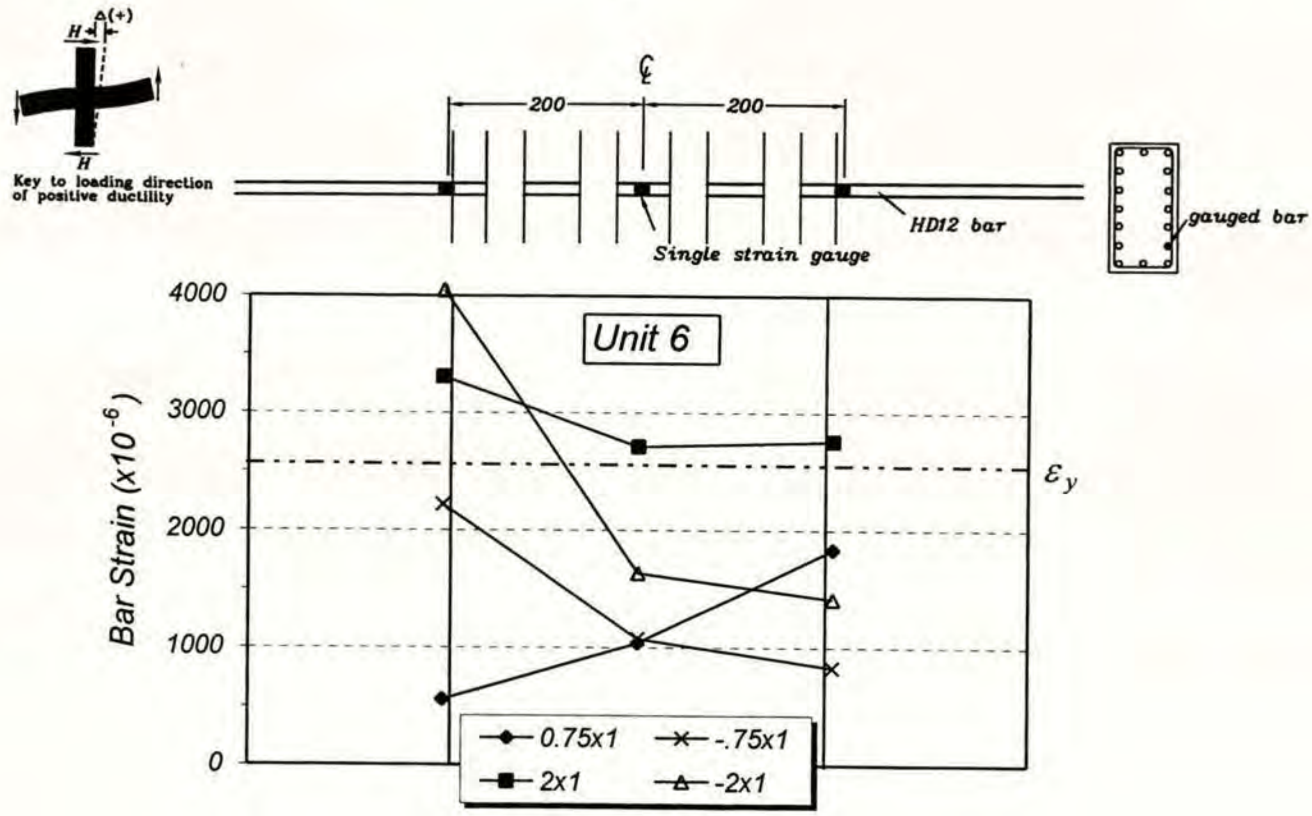

(e) Layer "e"

Figure 6.25 (Cont.) - Strain Profiles of Intermediate Beam Bars of Unit 6.

6.3.6 Beam Behaviour

6.3.6.1 Curvature Ductility Factors in Plastic Hinge

Beam curvature ductility factors in plastic hinge region of this unit were also computed using the same method and presented in **Fig. 6.27**. So found beam curvature ductility factors are very similar to what are found in Unit 5. Maximum value occurred in the load cycle to μ_Δ = 4x1 and diminished afterward as result of bond failure of beam bars.

6.3.6.2 Beam Strain Profiles at the Level of the Longitudinal Reinforcement

Figures 6.28 and **6.29** plot the strain profiles obtained from potentiometer readings and interpolated to the level of the longitudinal reinforcement of Unit 6. Again, so found strains are very similar to that in Unit 5. The trend obtained in Unit 5 and described in Section 6.2.5.2 that a decrease in the tensile strain and an increase of compressive strain on the other side of column face occurred from the load cycle to μ_Δ = -4x1. This phenomena was caused by bar slippage.

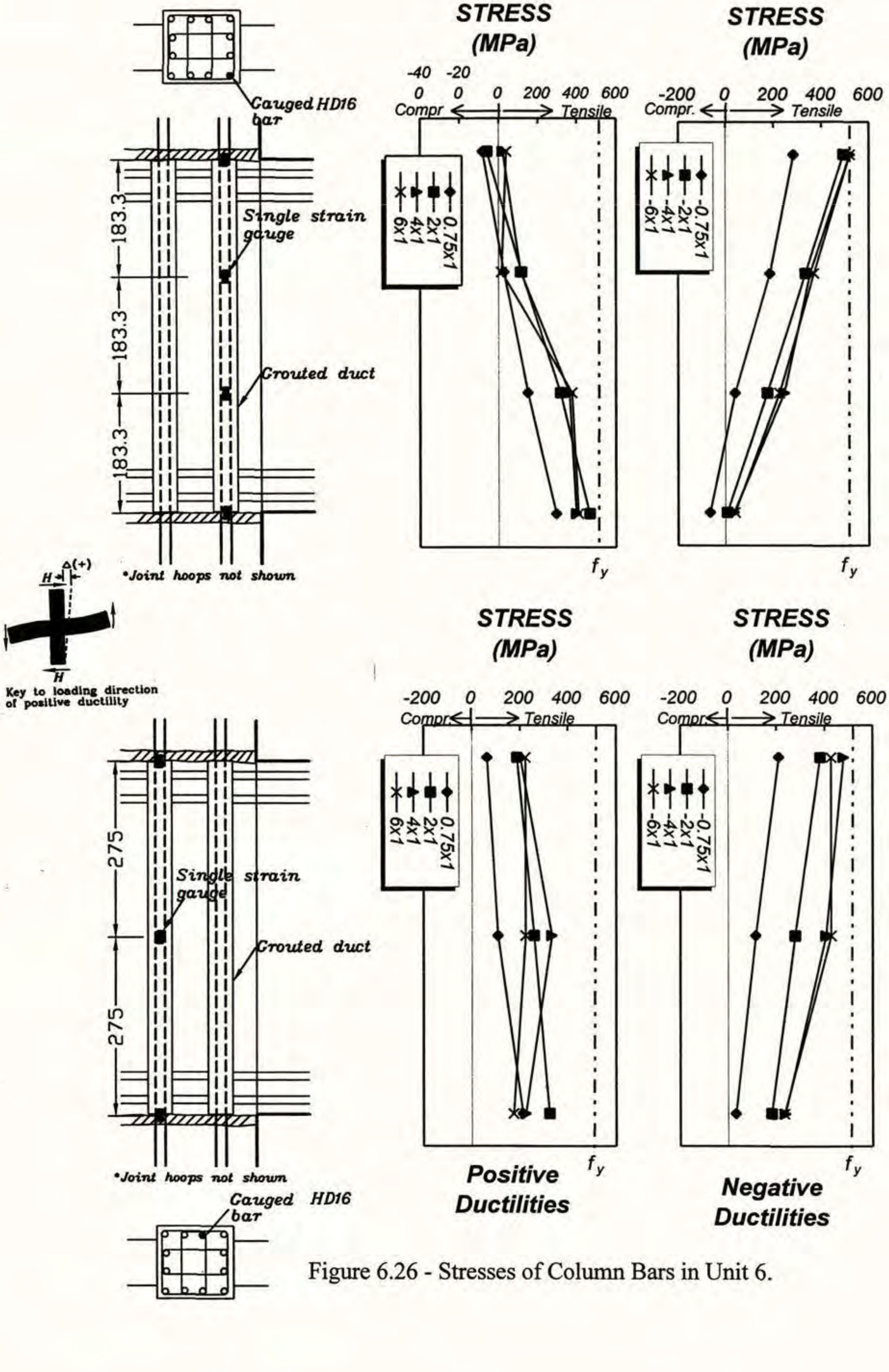

Figure 6.26 - Stresses of Column Bars in Unit 6.

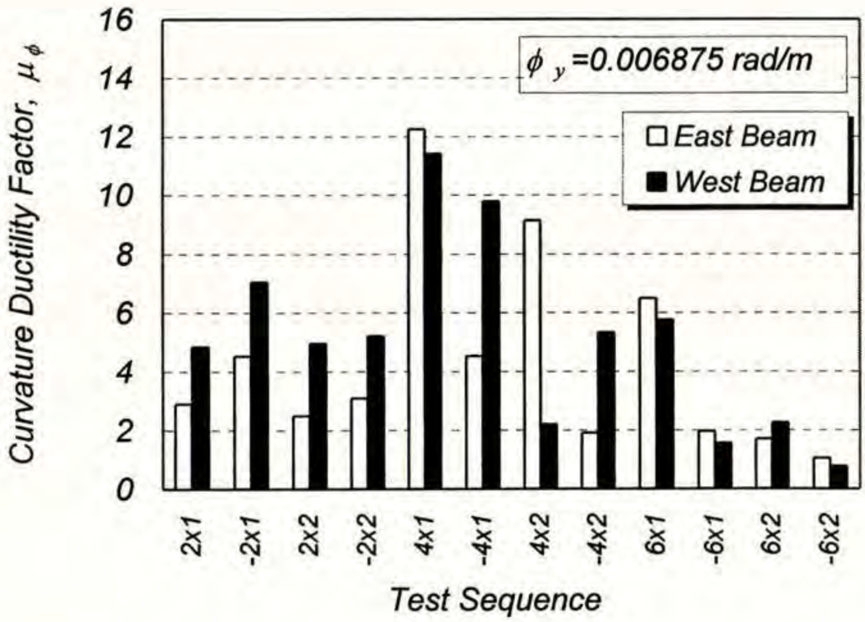

Figure 6.27 - Curvature Ductility Factors of Beam of Unit 6.

6.3.6.3 Beam Elongation

Measured beam elongation is plotted against storey shear and presented in **Fig. 6.30**. It can be seen that, unlike what was recorded in Unit 5, beams of Unit 6 carried on lengthening in each load cycle toward a new displacement ductility until μ_Δ = 6x1. The maximum overall beam elongation was 20 mm, which is equivalent to 3.6% of the overall beam depth, a value larger than that recorded in Unit 5. The main reason for the difference between the beam elongation of two units can be attributed to the stronger beam-column joint of Unit 6 that pushed the plastic deformation to spread along the beams.

6.3.7 Column Behaviour

As the visible crack patterns in columns and recorded stress profiles of column vertical bars within joint region are all very similar to that recorded in Unit 5, it is no doubt that columns behaved elastically during the test.

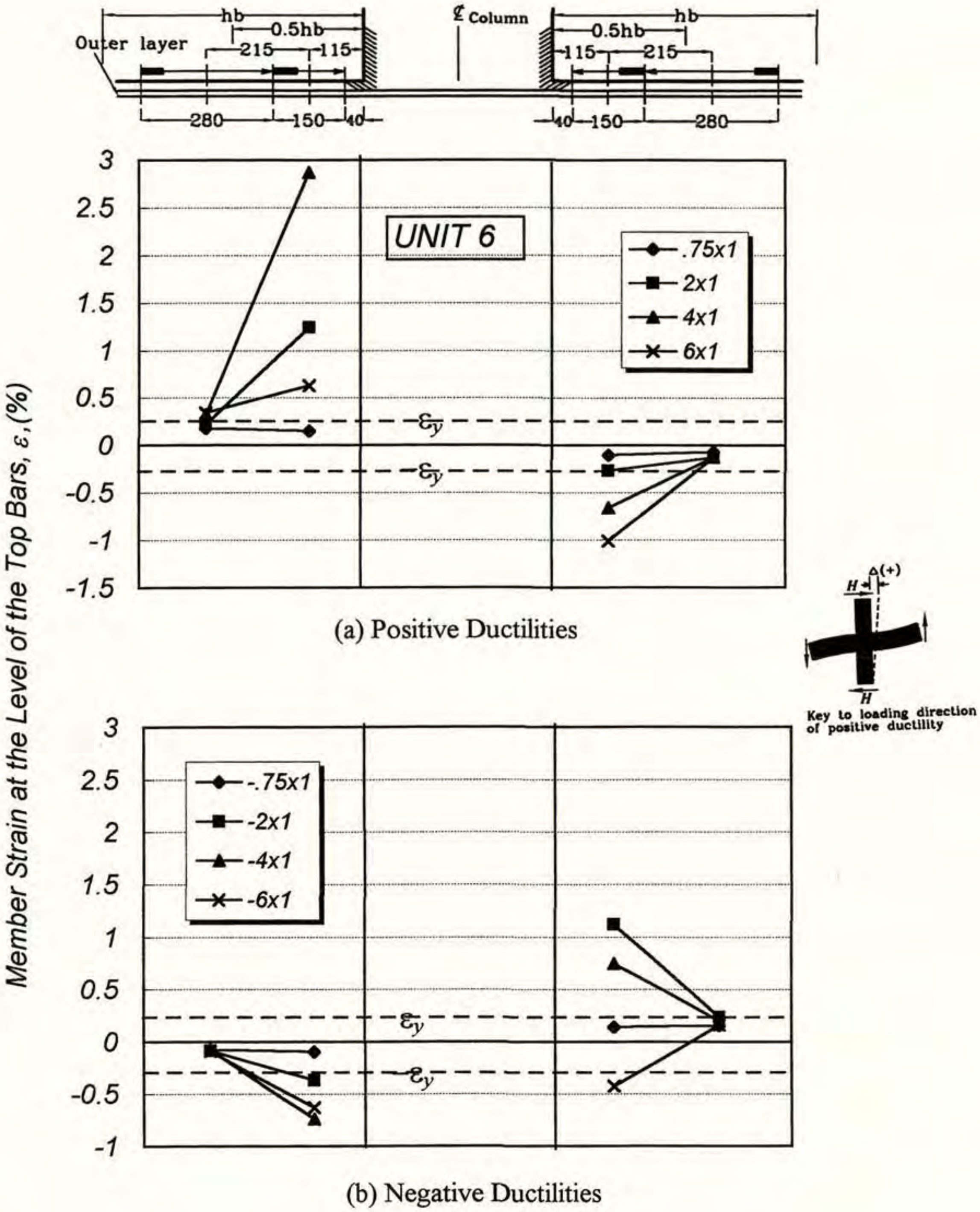

Figure 6.28 - Beam Strain Profiles at the Level of the Outer Layer of the Top Beam Bars of Unit 6.

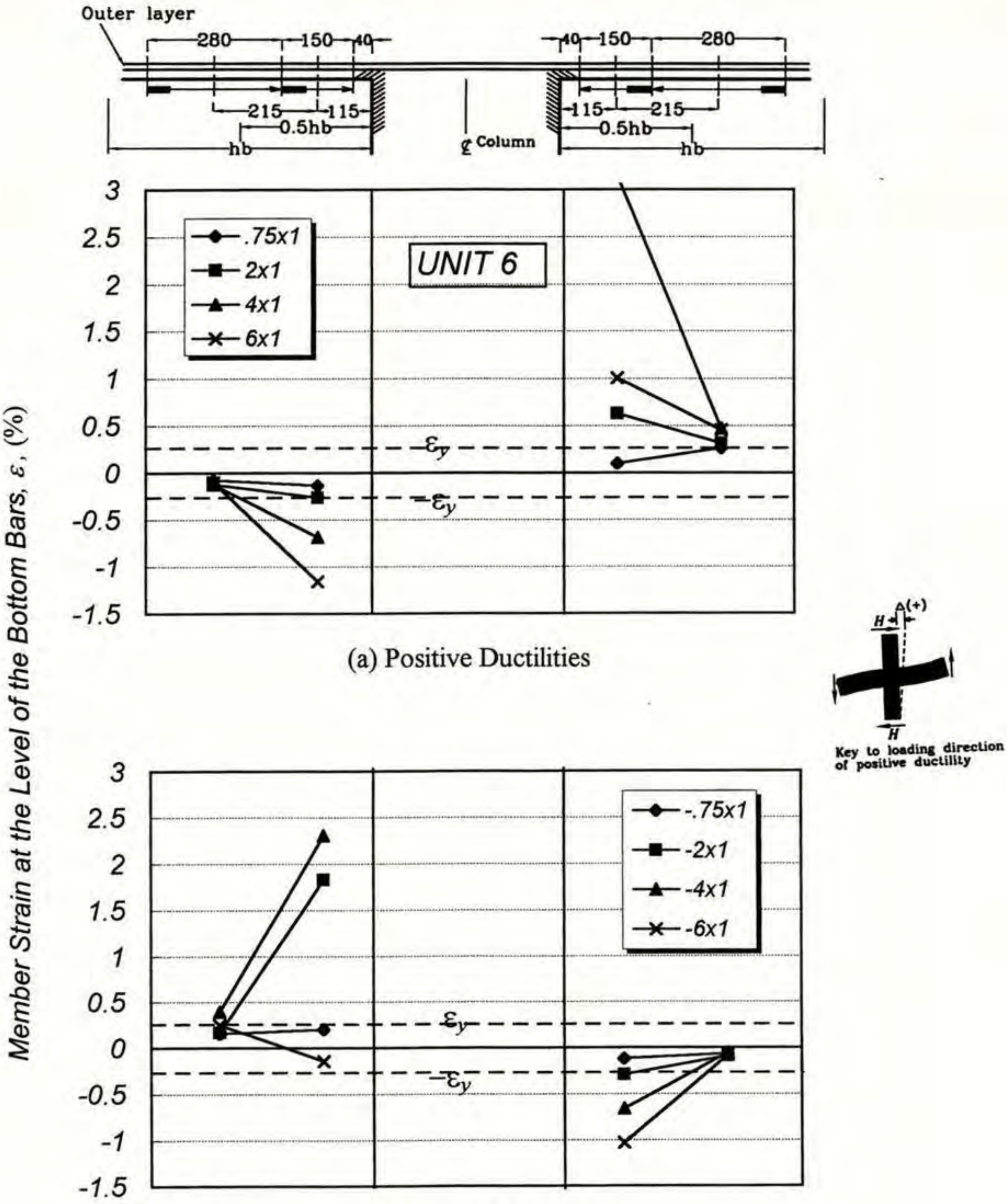

(a) Positive Ductilities

(b) Negative Ductilities

Figure 6.29 - Beam Strain Profiles at the Level of the Outer Layer of the Bottom Beam Bars of Unit 6.

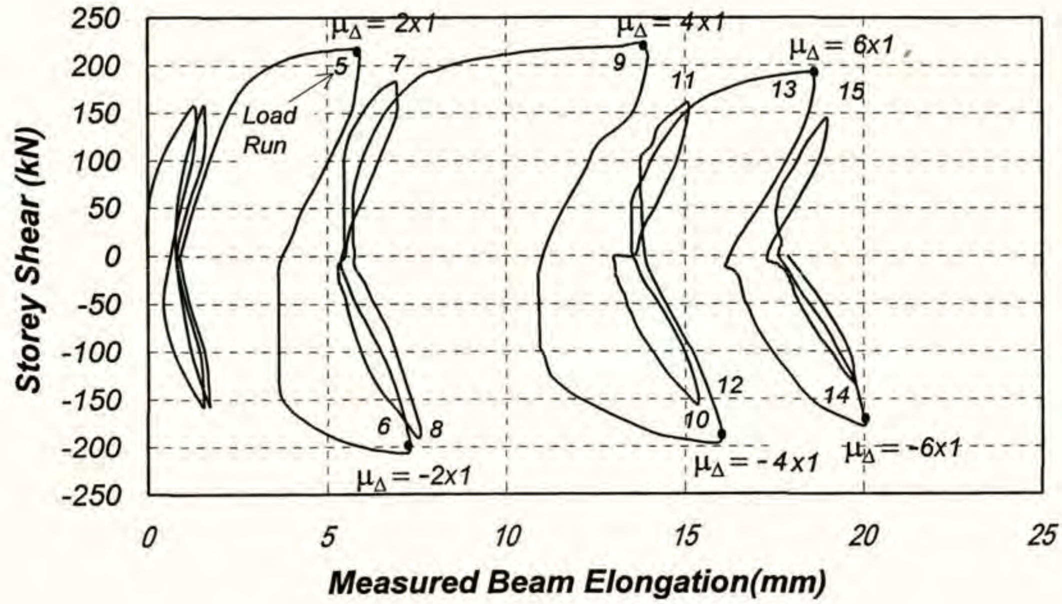

Figure 6.30 - Beam Elongation of Unit 6.

6.4 UNIT 7

6.4.1 General

Another test unit incorporating distributed beam longitudinal reinforcement, designated as Unit 7, was tested under the simulated seismic loading. Test results are presented in the following sections. As it had been mentioned in the analytical work that the bond stresses on the interior layers of distributed beam bars are not needed for equilibrium after hinges forming the beams at the column faces. As a result a design alternative is to use larger diameter bars for the interior layers of reinforcement when beam bars are distributed through the web. The interior layers of reinforcement in Units 5 and 6, 5-HD12 bars on each side of beam web, were replaced by 3-HD16 on each side in Unit 7. One more set of horizontal joint reinforcement was added into the joint of this unit owing to the slightly increase of input joint shear stress. Originally this unit was planned to be tested under the same constant column compressive load, $0.1f_c'A_g$. Nevertheless, prior to testing, based on the observation of joint failures in Units 5 and 6, it was decided to increase the applied column axial load to $0.25f_c'A_g$ to see how the joint strength could be enhanced by the column compressive load when beams with distributed reinforcement are incorporated.

6.4.2 Overall Behaviour

Cracking appearance at different stages and the lateral load displacement response are presented in **Figs. 6.31** and **6.32.**

The overall behaviour of this unit is better than that of Units 5 and 6. Performance of the joint panel was enhanced by the axial load. Only incipient damage in the joint was observed at the end of test. However, bond failure of top and bottom beam bars caused significant loss of lateral load capacity near the end of test. In the load cycle to μ_Δ = 6x2, corresponding to a 5.1% inter-storey drift, the measured lateral load dropped to 61% and 68% of the maximum loads in the positive and negative load cycles respectively.

In the elastic load cycles, cracking mainly concentrated on the beam ends adjacent to the column. Most of the flexural cracks vertically propagated from top and bottom beam chords toward beam compression zone. Yet some cracks changed direction and became diagonally oriented when they penetrated into the central portion of the beam web. Note that the region in which the vertical flexural cracks became diagonal is mainly within the spacing between the distributed longitudinal steel. In the joint panel, some diagonal cracks were distributed in the vicinity of column intermediate bars in a steep angle, see **Fig. 6.31(a)**. Comparing the crack pattern in joint panel with that in Units 5 and 6, joint cracks in this unit are less and shorter. The columns showed only four short cracks along the beam faces.

As the test proceeded into the inelastic range, that is to μ_Δ = 2, see **Fig. 6.31(b)**, more flexural cracks occurred in the beam plastic hinge regions and the maximum crack width reached 2.0 mm. Cracking in joint panel became denser with more fine and short cracks forming. The maximum width of the cracks in joint panel reached a maximum of 0.1 mm at this stage. Cracks in the columns were still very few and fine.

By μ_Δ = 4x1, flexural cracks in beam plastic hinge region continue to widen, reaching a maximum width of 3.0 mm. The concrete at the top beam chord at column faces showed incipient crushing. The joint panel remained in the crack pattern without too much change. The only noticeable change was the slightly increased in crack width to 0.2 mm. At this stage, the concrete surrounding the top and bottom ends of corner metal ducts embedded in joint

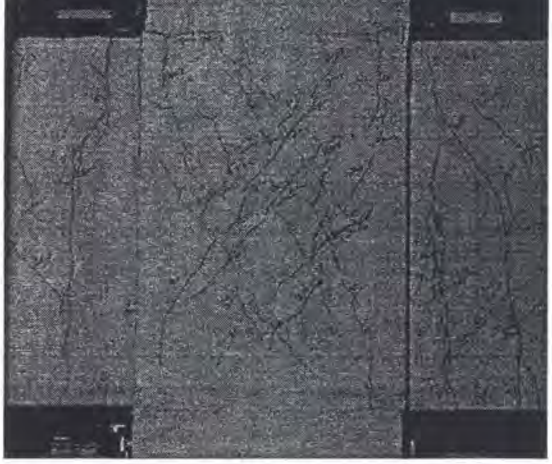

(a) At μ_Δ = -2x1

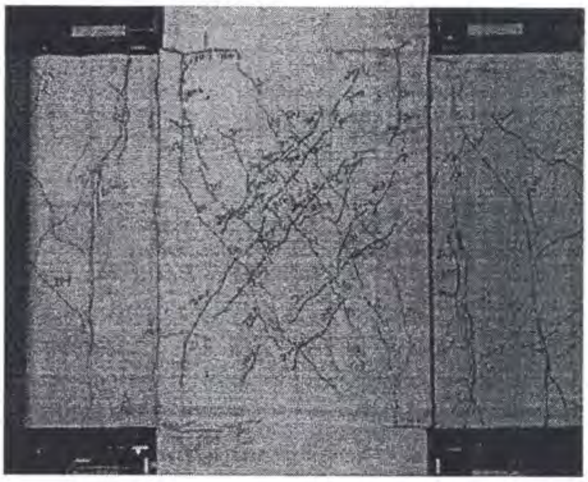

(b) At μ_Δ = -2x2

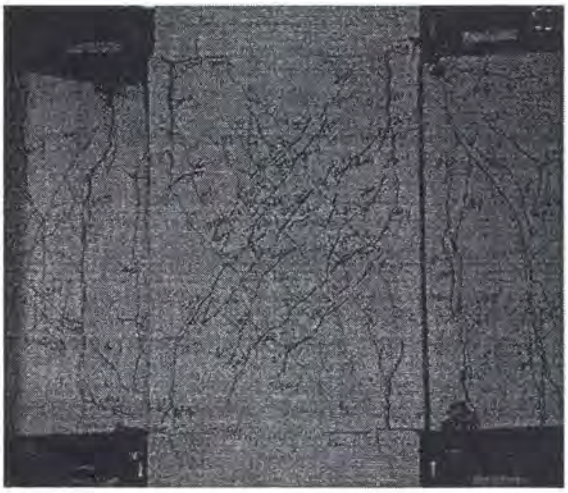

(c) At μ_Δ = -4x1

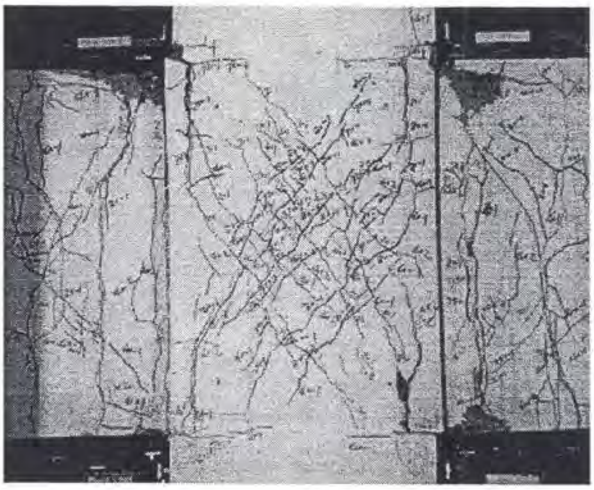

(d) At μ_Δ = -4x2

Figure 6.31 - Cracking of Unit 7 at Different Stages During the Test.

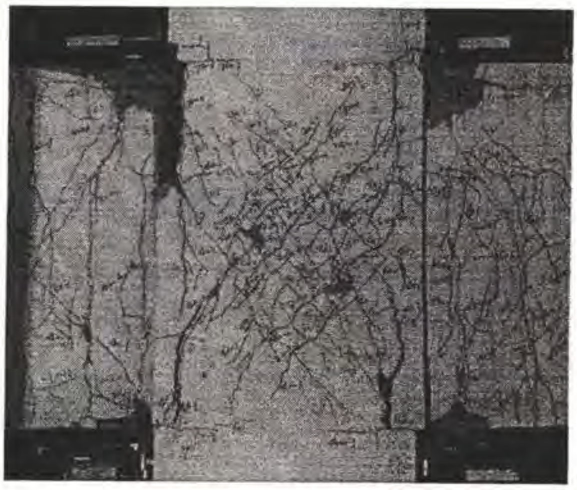

(e) At μ_Δ= -6x1

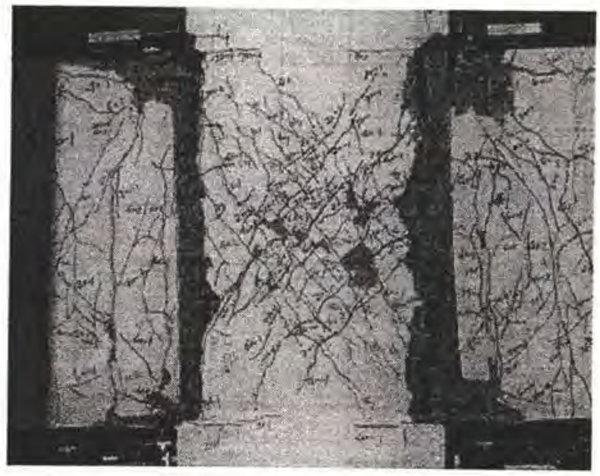

(f) At μ_Δ= -6x2

Figure 6.31(Cont.) - Cracking of Unit 7 at Different Stages During the Test.

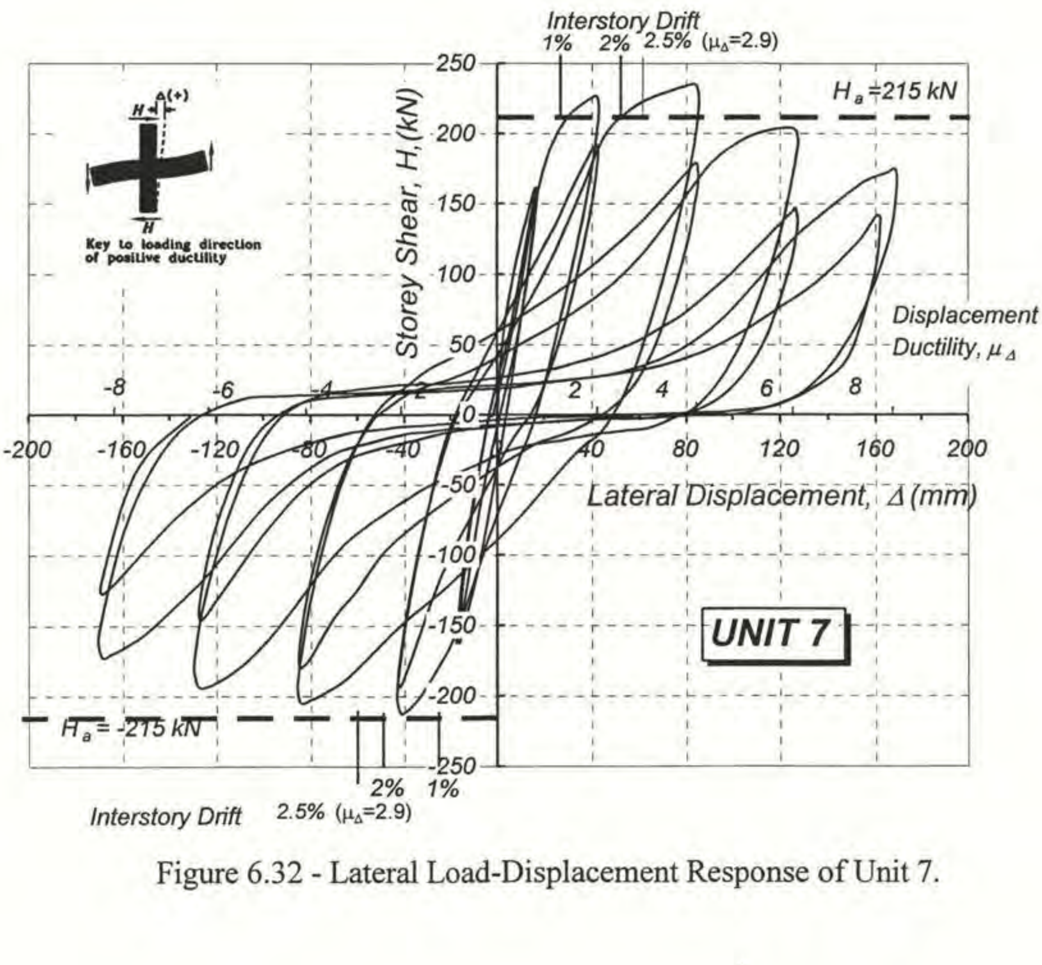

Figure 6.32 - Lateral Load-Displacement Response of Unit 7.

region became slightly dislodged. In the second load cycle to $\mu_\Delta = 4$, crushing of the concrete on the top and bottom beam chords adjacent to column faces spread along beams away from column faces. The stage of the joint at $\mu_\Delta = -4x2$ is shown in **Fig. 6.31(c)**.

In the load cycle to $\mu_\Delta = 6x1$, joint cracks became slightly wider with the main diagonal crack reaching 1.0 mm in width. Incipient damage on cover concrete in joint region was observed at this stage. Meanwhile, the dislodged cover concrete near top and bottom end of corner ducts started to fall apart. Damage on top and bottom beam chords adjacent to column faces spread further along beam span away from column faces and also toward the centre of the beam height so that some part of longitudinal beam bars was exposed. In addition, spall of the cover concrete along the outermost longitudinal beam bars was also observed. They were all indications that bond failure of these beam bars had occurred.

In the subsequent load cycle, $\mu_\Delta = 6x2$, see **Fig. 6.31(d)**, the corners in the joint panel spalled off. Crushing of concrete on the top and bottom beam chords adjacent to column faces carried on further so that gaps opening from top and bottom beam chords at column faces could be seen. Incipient crushing of the concrete in joint panel was observed in this load cycle.

6.4.3 Load Displacement Response

Figure 6.32 plots the complete lateral load-displacement response of Unit 7. The yield drift of the beam-column subassembly was 0.86%. This yield drift level implies a displacement ductility equal to $\mu_\Delta = 2.9$ when the 2.5% drift limit is attained.

The theoretical ultimate lateral load was achieved in the first inelastic load cycle, $\mu_\Delta = \pm 2x1$, in both the positive and negative load cycles. However, the measured lateral load dropped to 89% of the theoretical load in both load directions of the load cycles to $\mu_\Delta = \pm 2x2$.

Some over-strength of lateral load was recorded in the load cycle of $\mu_\Delta = 4x1$, exceeding the theoretical load by 8.3%; while the measured lateral load was equal to 95% of he theoretical ultimate value in the reversed load run. It is believed that the bond on extreme layers of beam bars started to deteriorate at this stage, causing loss of lateral load capacity in the successive load cycles.

Further reduction in the lateral load capacity occurred in the second load cycle to $\mu_\Delta = 4$. The recorded lateral load capacities in the positive and negative load directions were 77% and

83% of the measured maximum load, respectively. Note that the drop of lateral load in the positive load cycle is slightly below the 20% limit for judging failure in New Zealand [S4] [P1]. However, this criteria for judging failure might be too stringent for some cases, especially in those tests in which loss of anchorage of beam bars in joint region caused significant stiffness degradation. Since in these cases, the lateral load capacity usually can be picked up considerably if the specimen is displaced toward a larger lateral displacement. It is believed that most of the reduction of lateral load capacity occurred until this stage was mainly caused by slip of top and bottom beam bars passing through the joint region.

As expected, the measured lateral load rose significantly in the load cycle to μ_Δ = 6x1 in comparison with the recorded lateral load in the last load cycle. It reached 87% and 92% of the measured maximum load in the positive and negative load runs, respectively. In the load cycle to μ_Δ = 6x2, the lateral load capacity dropped more significantly mainly due to bond failure of top and bottom beam bars within joint region.

Specimen was loaded further toward μ_Δ = 8 in order to confirm the main reason causing drop of lateral load capacity. As expected, the lateral load capacity rose again with respect to the recorded value in last load cycle. At the end, some incipient damage of cover concrete in the joint region was observed, indicating the joint had started to deteriorate.

6.4.4 Decomposition of Lateral Displacement

Each component of lateral displacement is presented in **Fig. 6.33**.

As the specimen was loaded in the elastic range, the beam flexural deformation dominated the applied lateral displacement with a maximum percentage of 40%. Beam fixed-end rotation contributed 19-21% to the applied lateral displacement. Beam-column joint shear deformation had a comparative small percentage in comparison with that found for Units 5 and 6. The maximum percentage of it occurred in the load cycle to μ_Δ = .75x2 which was recorded as 14%. Another component of interest to be discussed is the beam shear deformation. This source of lateral displacement had a percentage of 7-8% of the applied lateral displacement, a value which is comparatively larger than the insignificant values found in Units 5 and 6. As the main difference of the detailing in beams between the three units is that less numbers but larger diameter intermediate layers of beam bars were incorporated in the beams of Unit 7. Some part of shear deformation was contributed from flexural shear

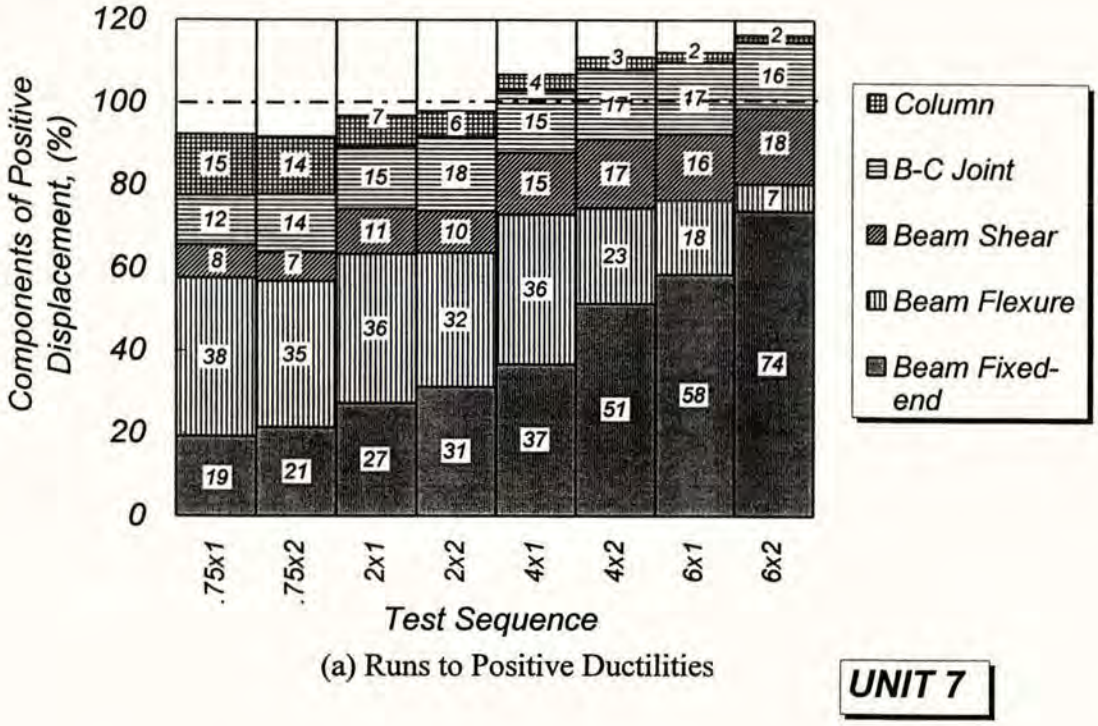

(a) Runs to Positive Ductilities

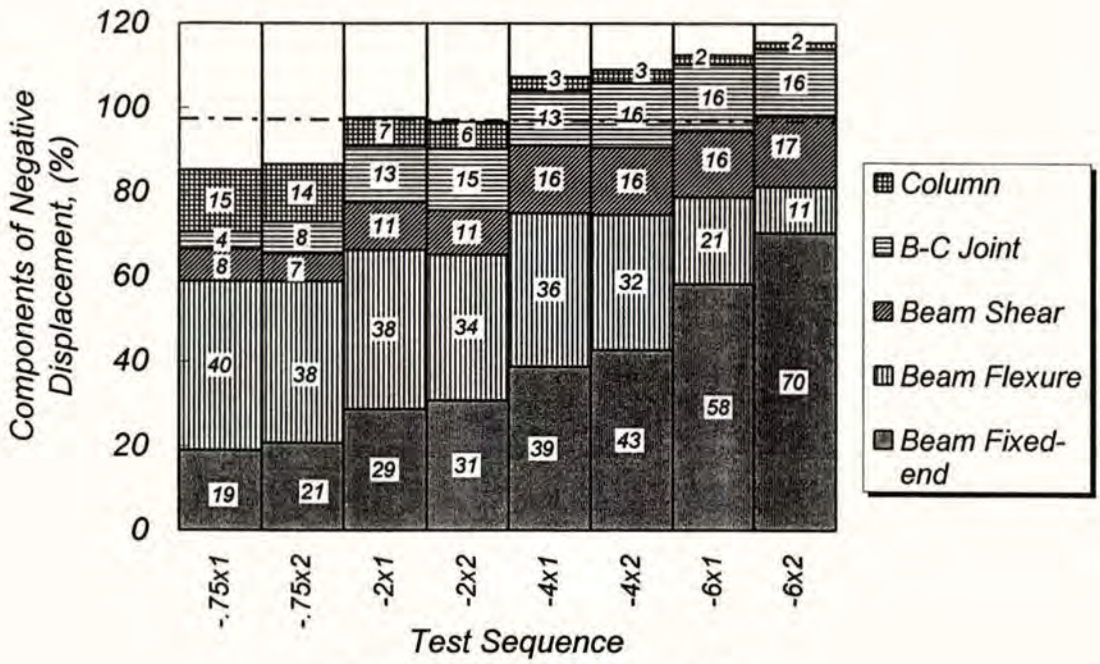

(b) Runs to Negative Ductilities

Figure 6.33 - Components of Lateral Displacement of Unit 7 at Peaks of Load Runs.

diagonal cracks forming between the larger spacing of HD16 bars distributed in the beam webs. The other source is incipient sliding shear caused by less numbers of distributed longitudinal bars in beams of Unit 7.

In the load cycle to $\mu_\Delta = 2$, beam fixed-end rotation gradually increased with beam flexural formation diminishing simultaneously. The percentages of these two components are very comparable in magnitude. The maximum value of the former one was 31% and the latter one was 38%. Beam-column joint shear distortion had a small increase up to 18%. Beam shear deformation also increase slightly, reaching 11%.

As the load cycles proceeded to $\mu_\Delta = 4$, beam fixed-end rotation continue to increase to 51% measured at the peak of $\mu_\Delta = 4x2$. In contrast, beam flexural deformation gradually diminished, with a percentage of 23% measured in the load cycle to $\mu_\Delta = 4x2$. The ascending trend of beam shear deformation also continued, reaching 17% at the peak of $\mu_\Delta = 4x2$. The beam-column joint shear deformation component remained similar to that recorded in the load cycle to $\mu_\Delta = 2$, indicating that joint did not deteriorate at this stage.

The increasing and diminishing trends of beam fixed-end and beam flexure components were progressing further in the load cycle to $\mu_\Delta = 6$. At the end, the beam fixed-end rotation predominated the lateral displacement with a percentage of 74%; while beam flexural deformation diminished to only 7%. Beam-column joint shear distortion was in a similar magnitude of percentage as recorded in the last load cycle and did not exceed 20% of applied lateral displacement until the end of test.

6.4.5 Joint Behaviour

6.4.5.1 Strains in the Horizontal Joint Reinforcement

The joint horizontal reinforcement of Unit 7 comprised 6 sets of perimeter R10 hoops plus 2 legged inner R10 ties. Strain variations of each set, including perimeter hoops and inner ties, was monitored using double electrical strain gauges during the test. Strains averaged from each pair of strain gauges at each peak of the load cycle are depicted in **Figs. 6.34** and **6.35**.

When the specimen was loaded in the elastic range, the strain profiles showed a uniform distribution with an average strain of about 700 micro-strains. As Unit 7 was loaded into the

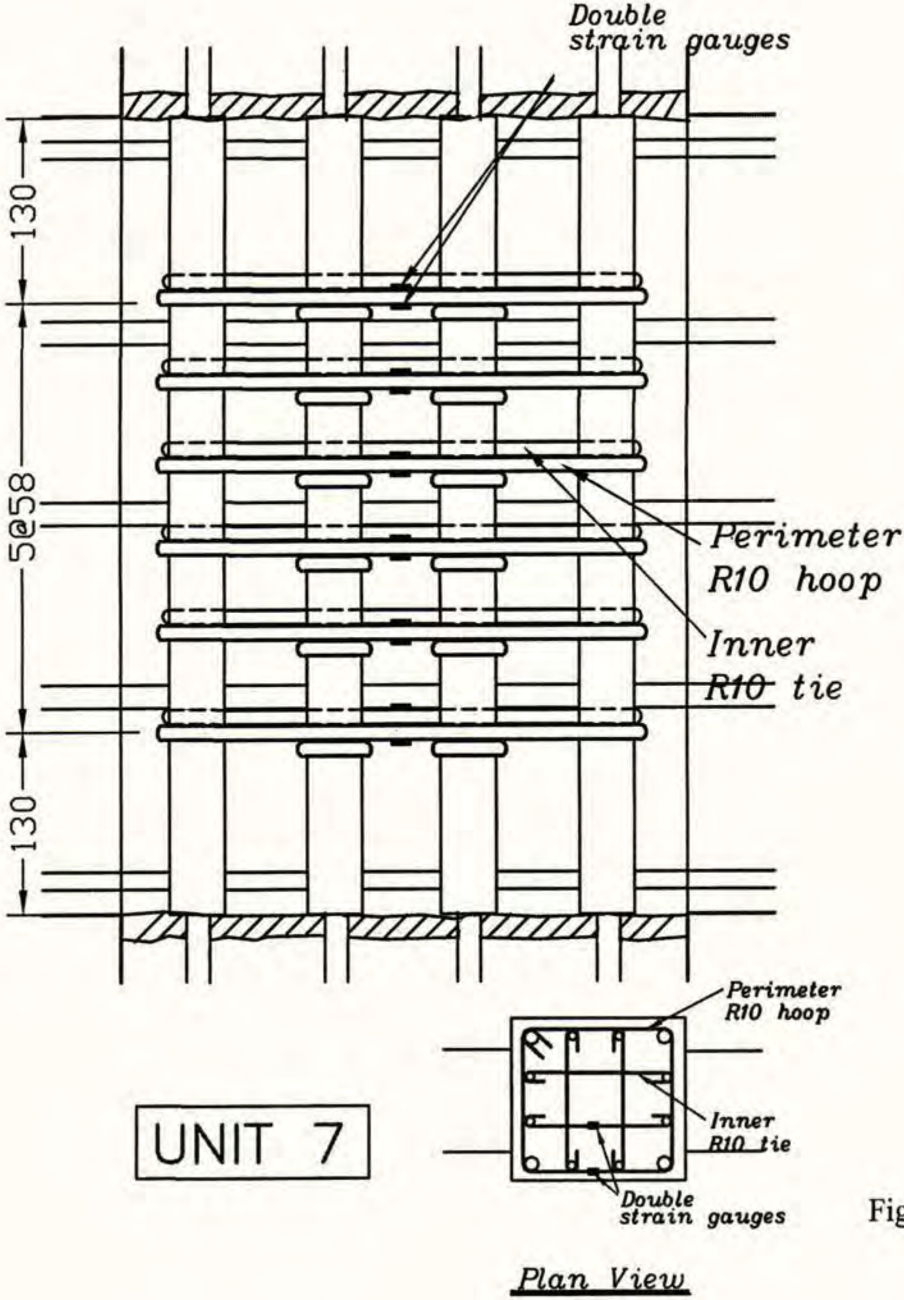

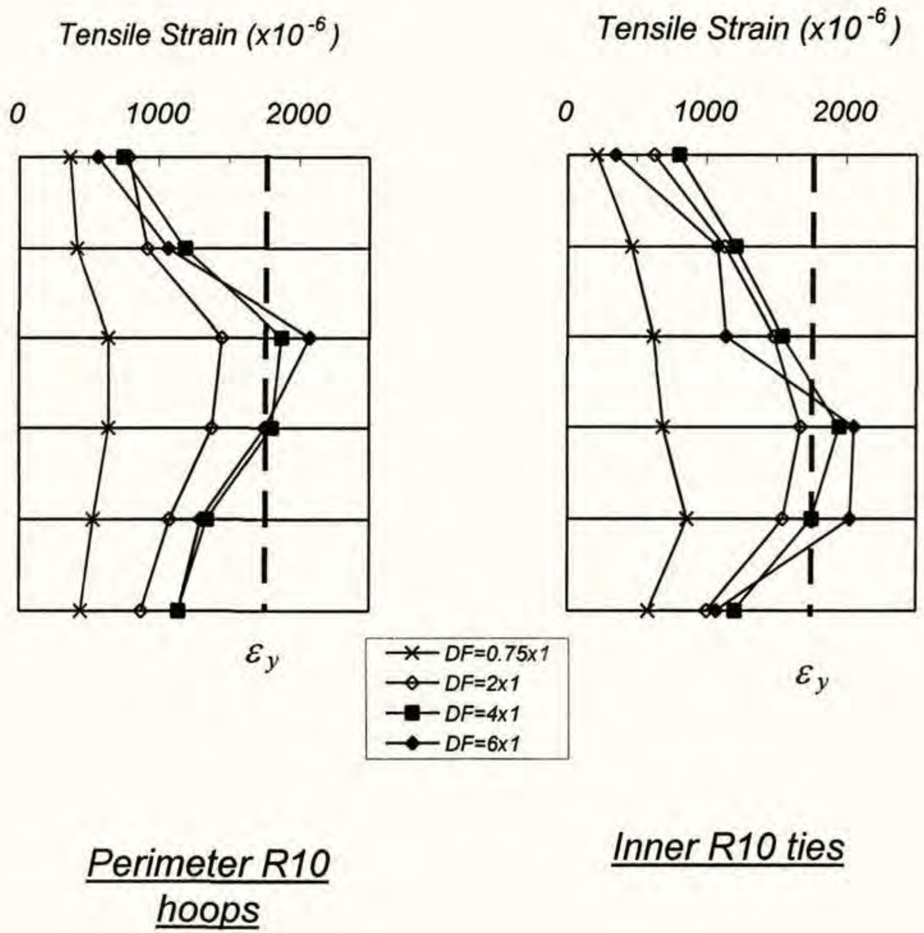

Positive Ductilities

Figure 6.34 - Measured Strain in Joint Hoops of Unit 7 During the Runs to Positive Ductilities.

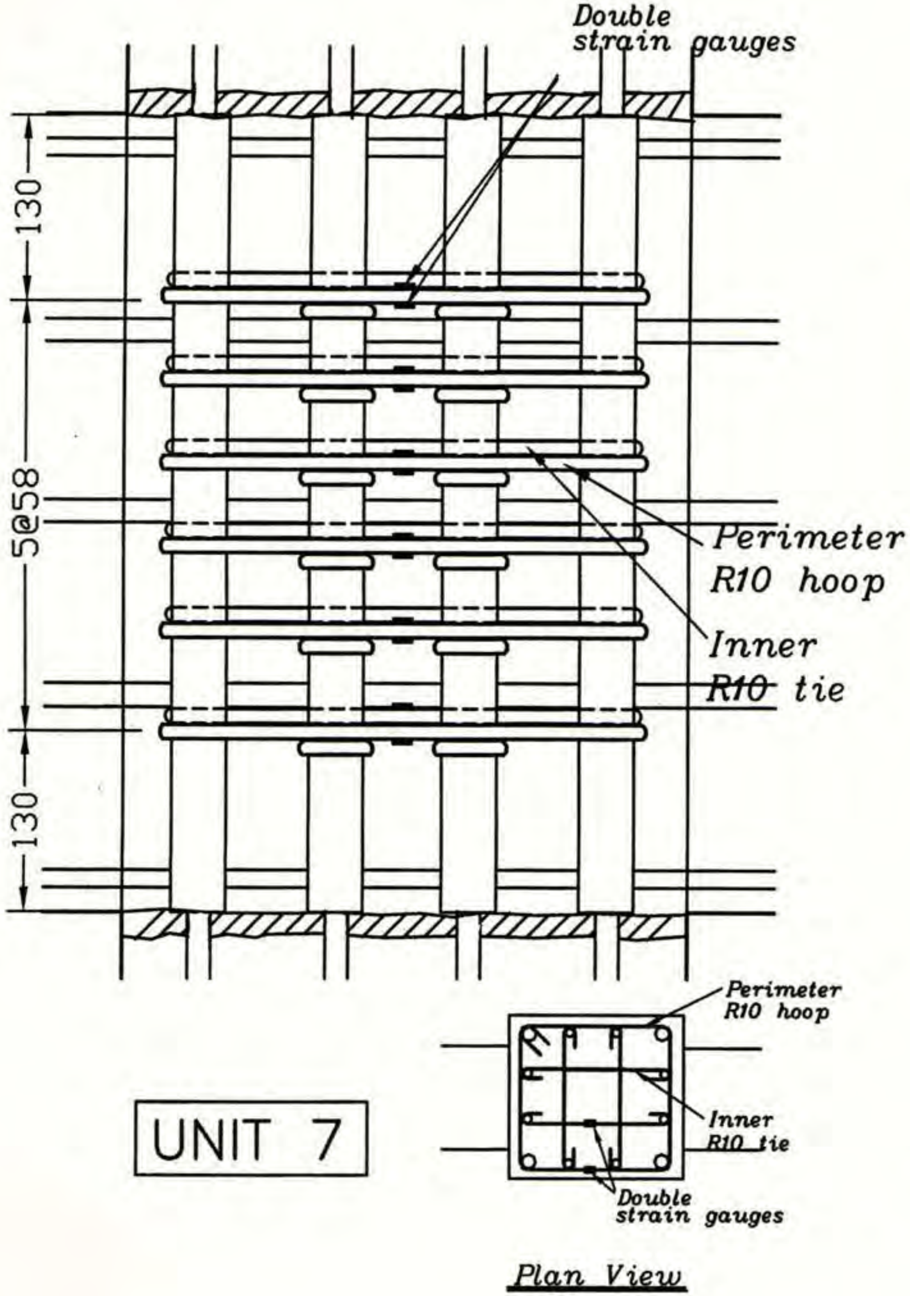

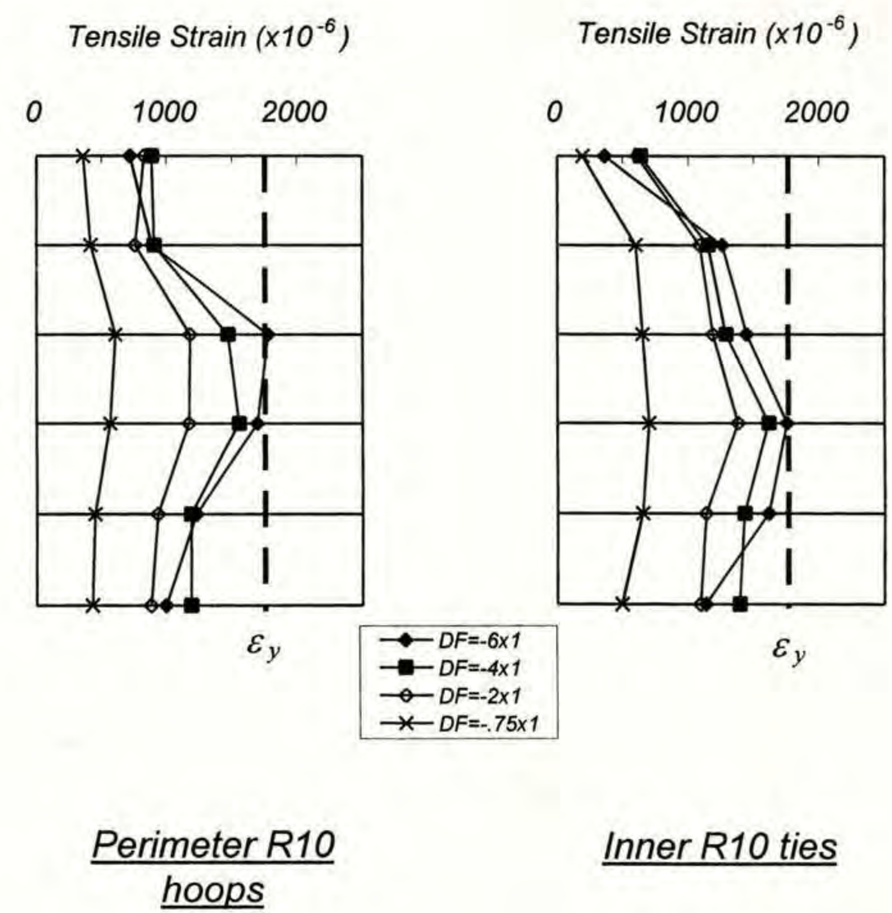

Negative Ductilities

Figure 6.35 - Measured Strain in Joint Hoops of Unit 7 During the Runs to Negative Ductilities.

inelastic range, $\mu_\Delta = 2$, a parabolic shape of strains profiles can be observed with strain values recorded in the middle set of joint transverse reinforcement reaching 1500 micro-strains. Strains measured on top and bottom sets increased only slightly, reaching 1000 micro-strains. Note that the hoops strains obtained at this stage are generally less than that obtained in Units 5 and 6. This is an indication that joint strength of this unit was controlled better than Units 5 and 6 since the transverse tensile strain in the diagonal compression stress field was smaller. The effect of enhancement observed at this stage can be attributed to the applied large column axial load and the additional set of transverse joint reinforcement.

The strain profile in the load cycles to $\mu_\Delta = 4$ showed a more apparent parabolic shape. The strains measured in the middle set reached yield strain at this stage while the top and bottom sets did not yield yet. In the subsequent load cycles, $\mu_\Delta = 6$, strains on the sets close to the middle of joint were beyond yielding but the top and bottom sets remained in a similar value as recorded in last load cycle.

It can be felt that strains recorded on transverse reinforcement placed close to the extreme layers of longitudinal beam bars strains below yielding smaller than that in Unit 5.

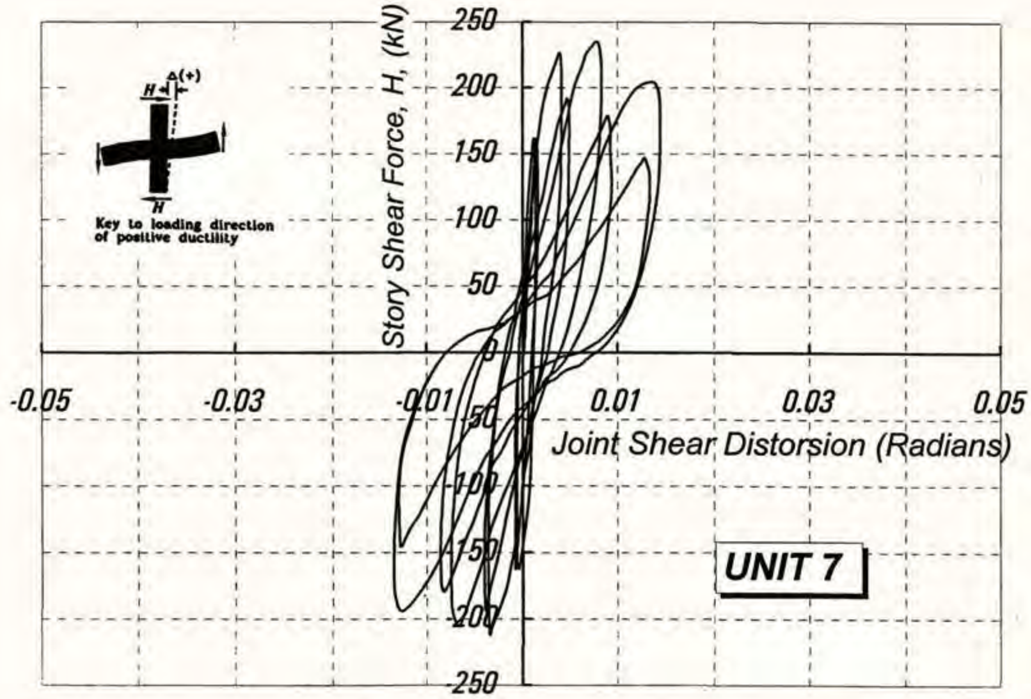

Figure 6.36 - Joint Shear Distorsion Versus Storey Shear Force.

This is because the additional one more set of joint reinforcement made the top and bottom sets closer to the extreme layers of longitudinal beam bars.

6.4.5.2 Joint Shear Distortion

Figure 6.36 presents the joint shear distortion versus lateral loads. It can be seen in this graph that the recorded joint shear deformation was generally less than that obtained in Units 5 and 6 during the test. The distortion was below 0.01 radians in the load cycles to μ_Δ = 4x2, corresponding to a inter-storey drift of 3.5%, while the maximum value measured at the end of test reached 0.015 radians, a value much less than that measured in Units 5 and 6.

6.4.5.3 Beam Bar Slip

Figures 6.37(a) and **(b)** show the measured local slip of top and bottom beam bars at three locations in the joint region.

In general, the slip measured on top beam bars was larger than that on bottom bars during the test, especially after the load cycles to μ_Δ = 4x1. This is due to the " top bar " effect caused by the vertical casting of the fresh concrete. The slip of the top beam bars exceeded the clear spacing between bar deformations in the central measurement, in the load cycle to μ_Δ = -4x1 while the bottom bars exceeded it in the load cycle to μ_Δ = 6x1. Similar to the trends found in other units, once the clear spacing of ribs was exceeded in the vertical joint centreline, significant loss of bond on beam bars would occur in the successive load cycles. The observed trends of bar slip explain the hysteresis response in **Fig. 6.32** where 17% drop of lateral load capacity recorded at the peak of μ_Δ = -4x1 was mainly due to bond failure of the top beam bars occurring in this load cycle. As the concrete surrounding the top bars between the deformations was crushed in this load cycle, the residual strength of bond would significantly decline in the reversed load run. It is thus believed that the further loss of lateral load capacity recorded in the load cycle to μ_Δ = 4x2 was mainly caused by the bond problem of top beam bars. With bond of bottom bars failing in the load cycle to μ_Δ = 6x1, the lateral load capacity could not be gained back entirely even though beam bars can be anchored in the opposite side of the beam.

The decrease of lateral load capacity after bond failure can be explained as follow.

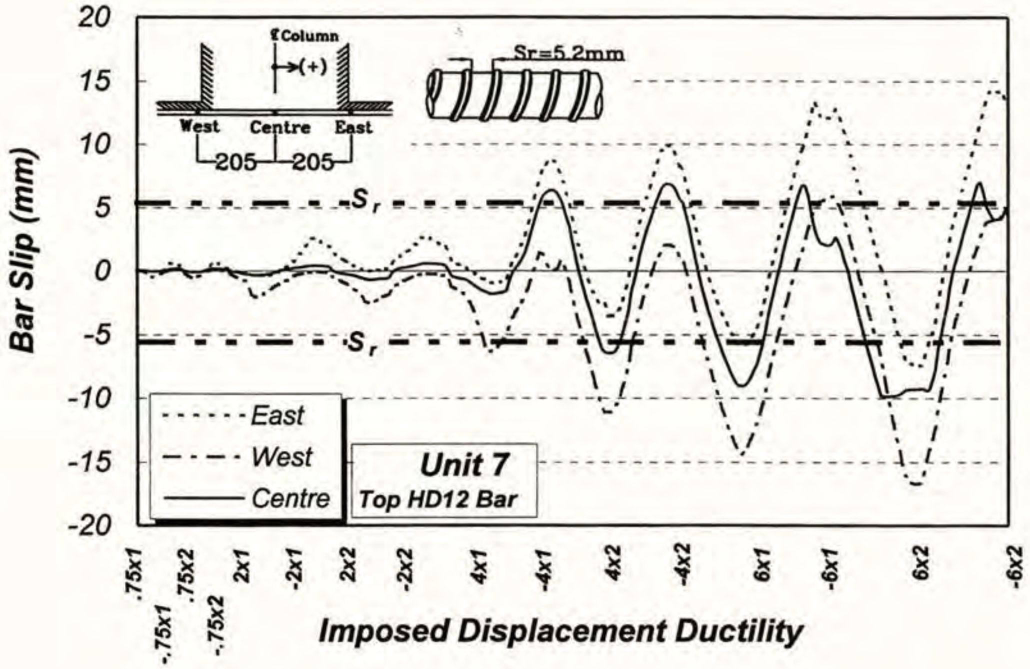

(a) Top Bars

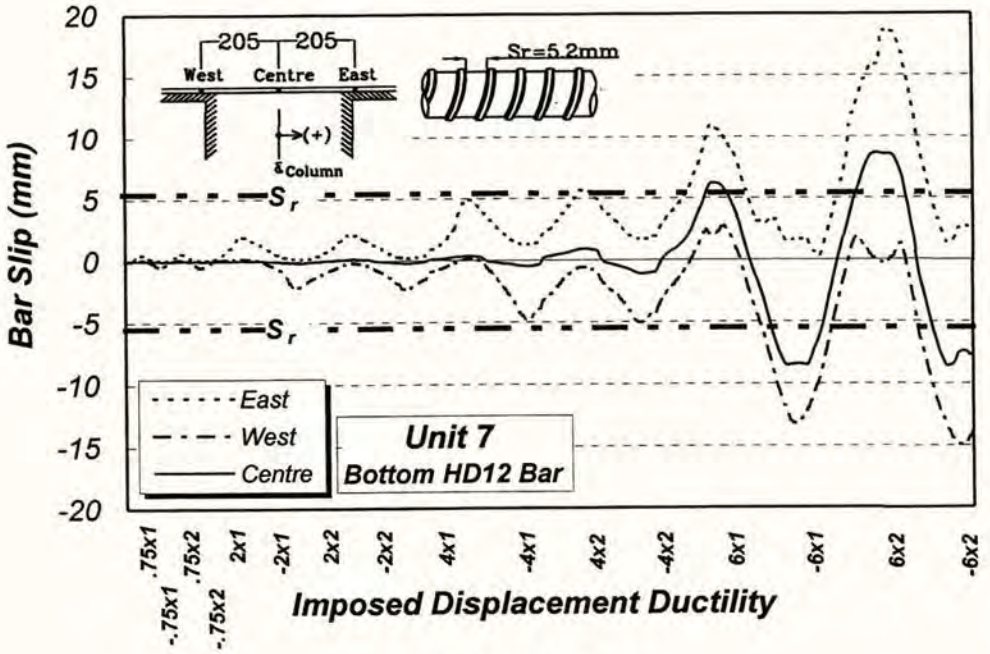

(b) Bottom Bars

Figure 6.37 - Relative Slip of Beam Longitudinal Bars in the Joint Region.

First, the beam bars can no longer develop stresses beyond yield as the deformation associated with the onset of work hardening over the depth of the joint implies a very large fixed-end rotation. Second, the resultant of the beam compressive force decreases as the force in compressive bars might decrease or even in tension due to bond failure. It decreases even further after crushing of the concrete cover. Hence, the internal lever arm decreases and so does the flexure strength.

In comparison the measured bar slip with that of Units 5 and 6, it can be known that the enhancement effect on the bond of longitudinal bars induced by the applied column compressive load was more obvious on the bottom rather than that the top beam bars.

6.4.5.4 Bar Strain And Bond Stress in Joint Region

Figure 6.38 shows the bar strains measured using electrical strain gauges along top and bottom layers of longitudinal beam bars passing through joint region. Bond stresses of those gauged bars were also calculated from the obtained strains and presented in **Fig. 6.39**.

The strain profiles are very similar to that were obtained in Units 5 and 6. Like in these two test units strain gauges were damaged prematurely as a result of relatively large bar slip. In the elastic load cycles, the tensile strain approached yielding while the maximum compressive strain was -1000 micro-strains. As the load sequence proceeded into inelastic load cycles, the recorded maximum tensile strain was larger than 4000 micro-strains, a value beyond yielding. A maximum compressive strain of -3000 micro-strains on bottom bar was recorded in the load cycle to μ_Δ = -2x1. For the top beam bars, the recorded maximum compressive strain reached -2000 micro-strains in the same load cycle. These compressive strain values imply a compressive stress reaching yield as the inelastic stress-strain relationship of the reinforcing steel is considered. This agrees with the trend found in Units 5 and 6 that the outermost layers of beam bars at column face were compressed to reach yield stress in the load cycle to μ_Δ = 2x1.The finding indicates that the beam bar diameter ratio limitation given by current Concrete Standard [S1] may not be appropriate when it is applied to the outermost layers of beam bars, as a 70% compressive yield stress of beam bars was assumed to develop at column face when deriving the Code equation [C1].

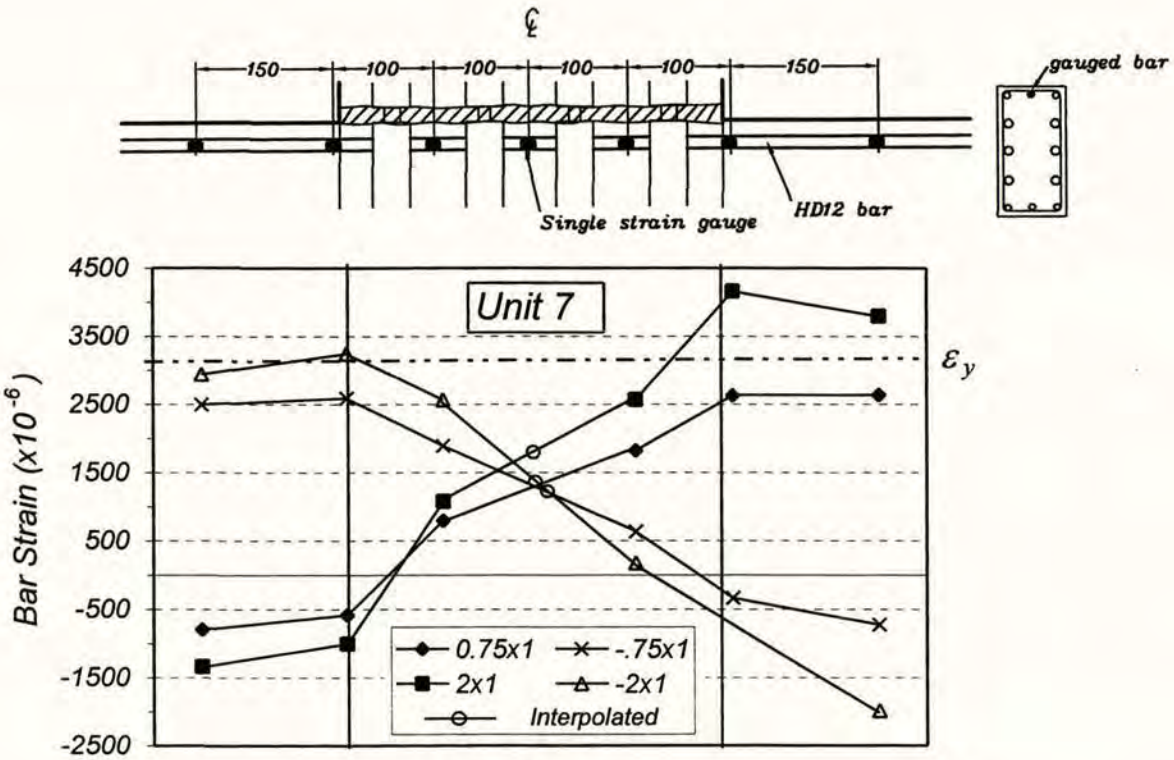

(a) Top Bars

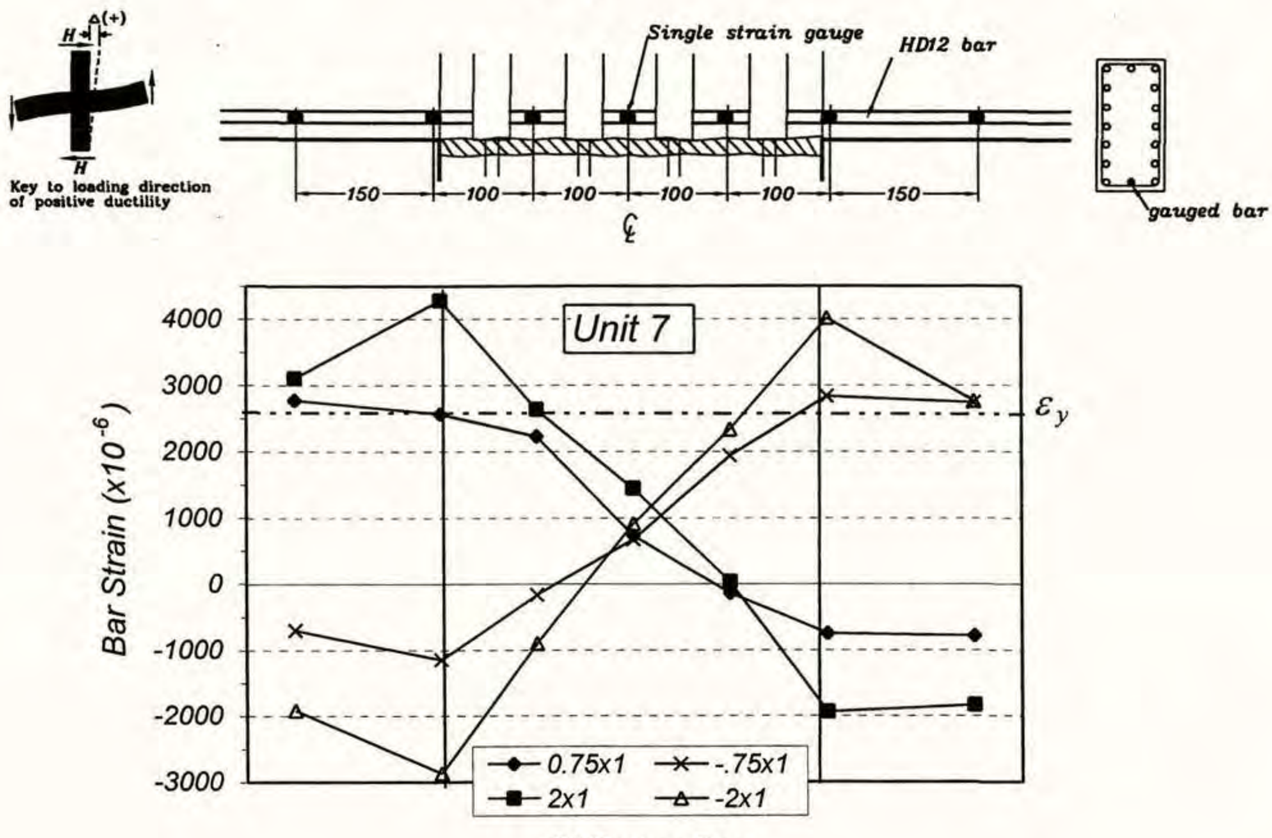

(b) Bottom Bars

Figure 6.38 - Strain Profiles of Outer Layers of Beam Bars of Unit 7.

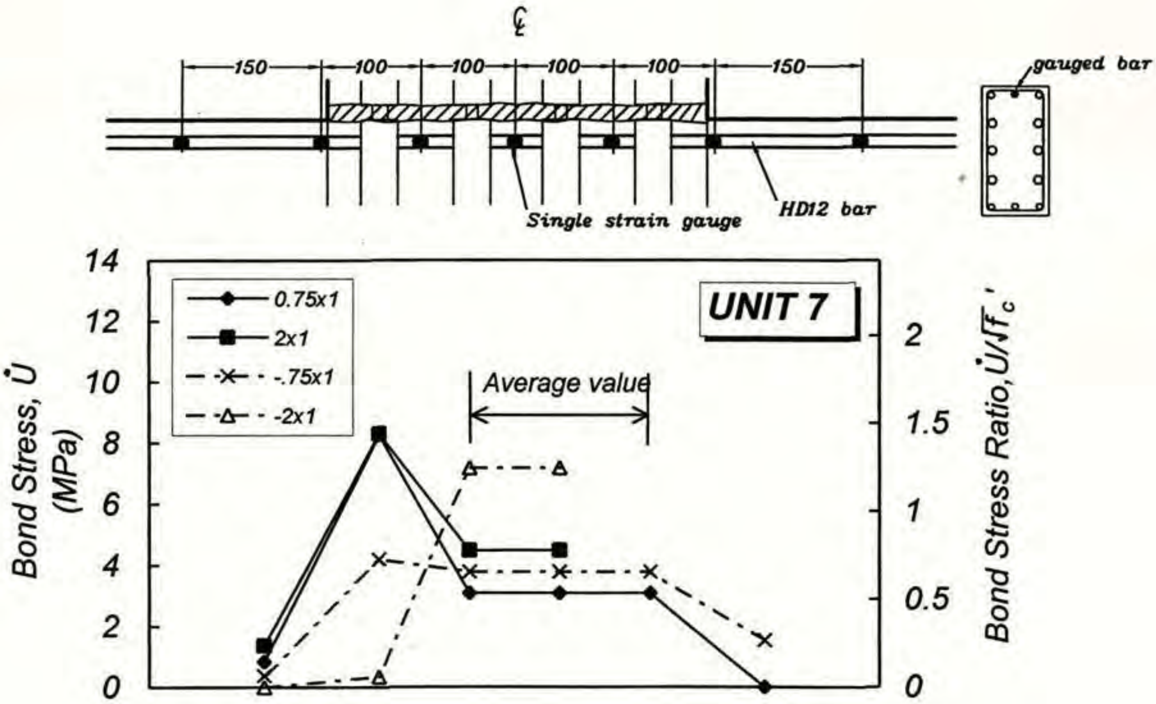

(a) Top Bars

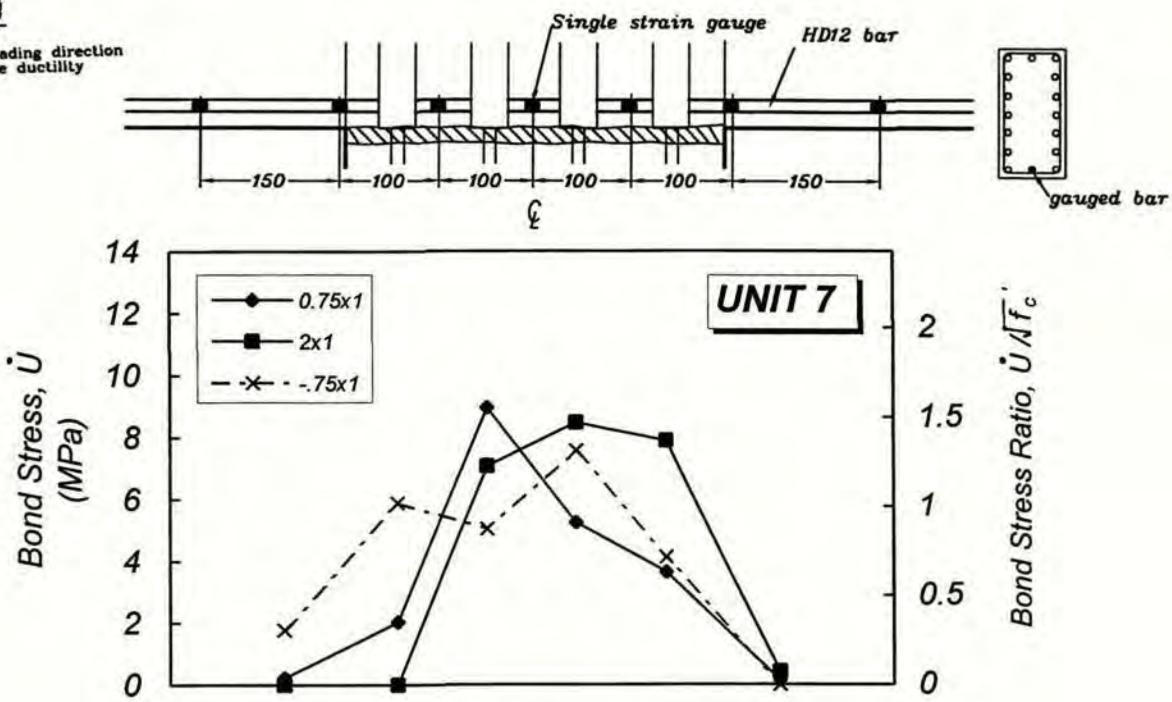

(b) Bottom Bars

Figure 6.39 - Calculated Bond Stresses.

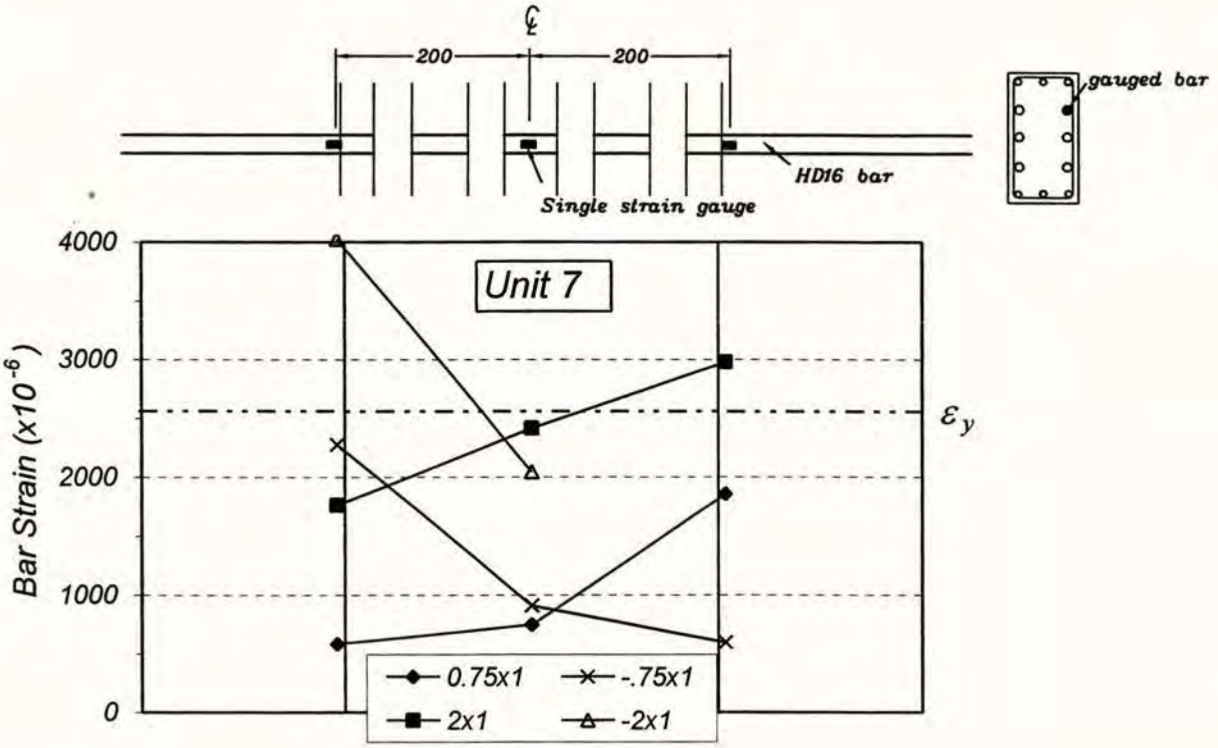

(a) Layer "a"

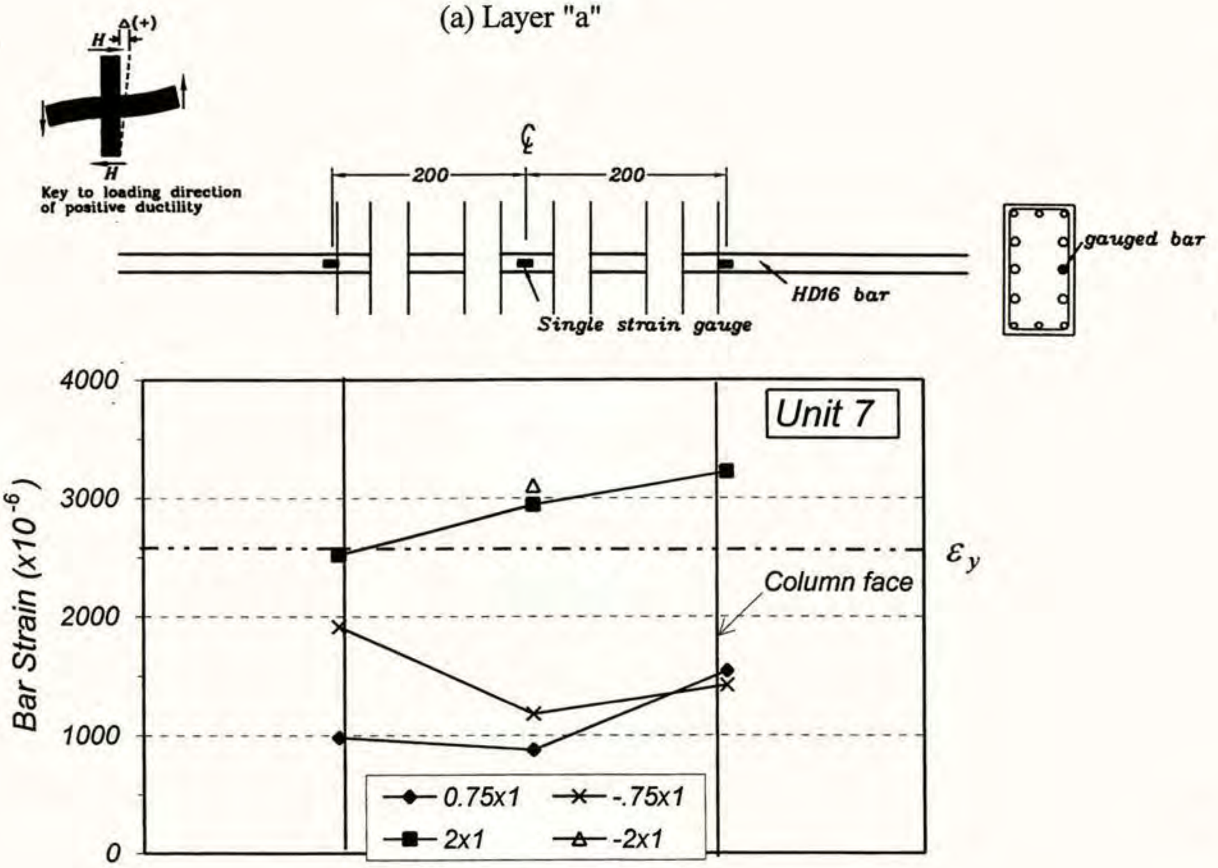

(b) Layer "b"

Figure 6.40 - Strain Profiles of Intermediate Beam Bars of Unit 7.

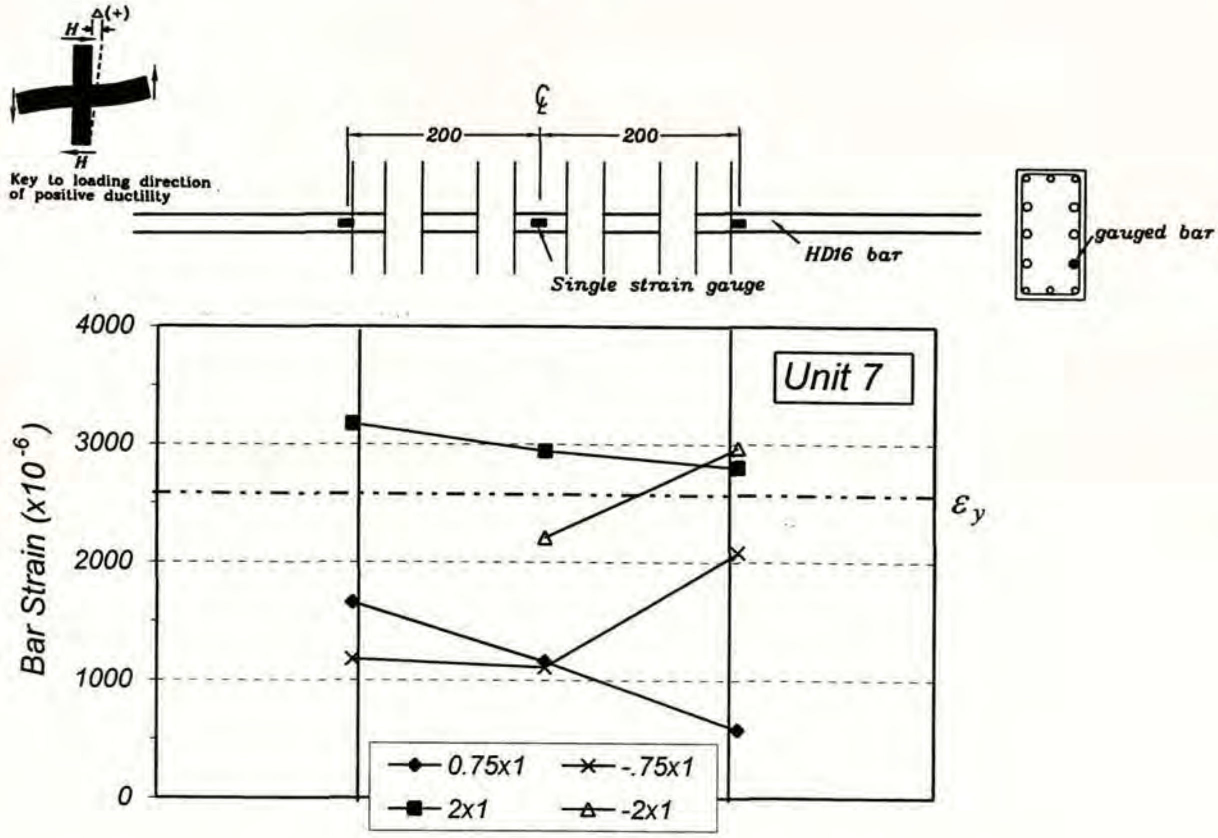

(c) Layer "c"

Figure 6.40 (Cont.) - Strain Profiles of Intermediate Beam Bars of Unit 7.

With reference to **Fig. 6.39**, it can be seen that there was no large difference of bond stress developed on top and bottom beam bars between elastic and inelastic load cycles. Based on the available limited data shown in **Fig. 6.39**, it can be known that the maximum bond stresses developed on top and bottom beam bars reached 8.5 and 11 MPa, respectively. These stresses are equivalent to 1.5, $1.9\sqrt{f_c'}$ for top and bottom bars, respectively. It should be noted that the peak values of bond stresses do not represent the maximum bond stress occurred along top and bottom beam bars within joint region, since bar strains were only available until $\mu_\Delta = \pm 2x1$. Bond stresses developing on the outermost layers of beam bars could rise further prior to the onset of bar slip exceeding ribs spacing. It is thus expected that the maximum bond stresses developed on extreme layers of longitudinal steel are likely to be larger than the above values found, especially for the bottom beam bars in which bar slip exceeded ribs spacing at a latter stage.

Strain profiles on the some bars in the inner three layers of reinforcement are depicted in **Fig. 6.40**.

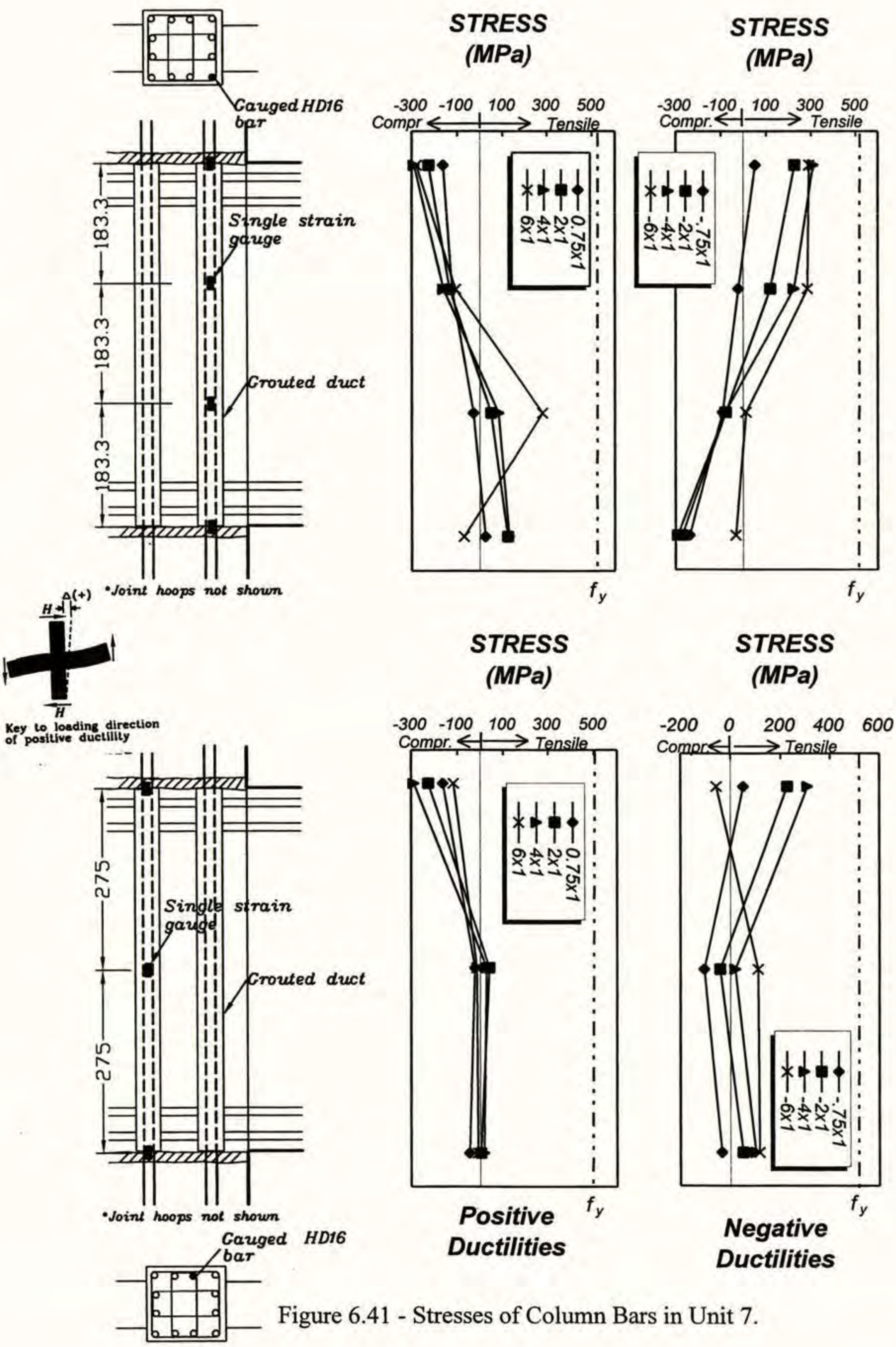

Figure 6.41 - Stresses of Column Bars in Unit 7.

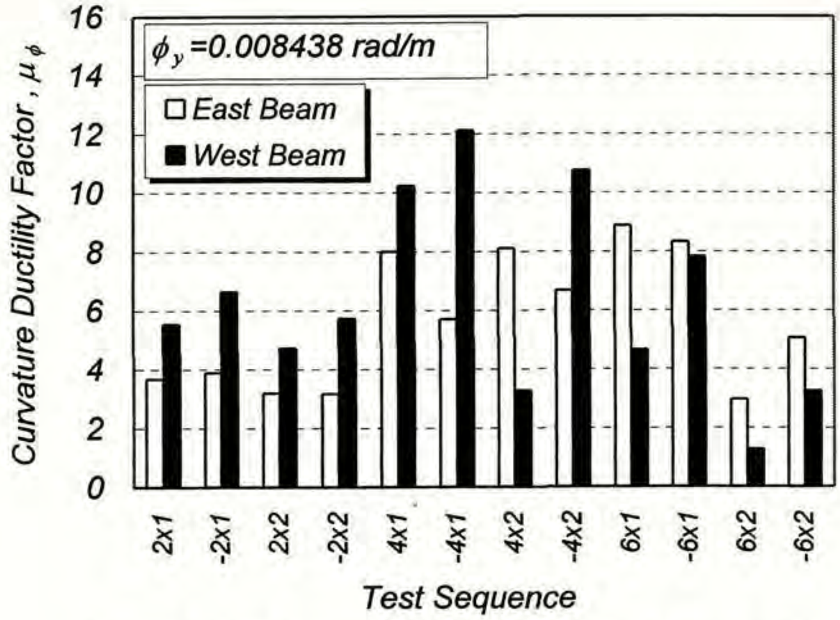

Figure 6.42 - Curvature Ductility Factors of Beams of Unit 7.

As expected, the strain profiles showed that the interior layers of longitudinal reinforcement were subjected to tension on both sides of column faces during the inelastic load cycles. The tensile strain recorded in the central layer yielded on both sides at the column faces. Although the other two layers adjacent to the central one did not yield on both sides, the smaller tensile strain recorded on one side was close to yielding. These indicates that a low bond stress demand on these layers of reinforcement may be required. The results justify the assumption made in the design stage of Unit 7 that the anchorage requirement in the joint region of inner layers of distributed beam longitudinal bars is not critical.

6.4.5.5 Bar Stresses of the Column Vertical Reinforcement Passing Through the Joint Region

The stresses of column vertical steel within joint region were converted from strain gauges readings and are presented in **Fig. 6.41**. Owing to the presence of a moderate column compressive loads, the stresses in the exterior bars were mainly in compression through nearly the entire depth of the joint in the elastic load cycles. As the unit was loaded in the inelastic range, small tensile stress recorded at one side of beam face started to increase, reaching 300

MPa in the load cycle to $\mu_\Delta = \pm 4x1$. However, the stresses obtained during the test were all below the yield stress. It can also be seen that the stress profiles at $\mu_\Delta = \pm 4x1$ had large stress variation in the middle of joint depth. This indicates that large bond stress developed in the middle region of exterior bars, which agrees with the trend observed in the analytical work depicted in Chapter 2 (see the strut-and-tie model analysis in Appendix A-1).

Stresses in interior column bars are also shown in **Fig. 6.41**. It can be seen in the graph that the stresses were all below yielding.

6.4.6 Beam Behaviour

6.4.6.1 Curvature Ductility Factors in Plastic Hinge Region

Figure 6.42 depicts the curvature ductility factors in the plastic hinge regions. The curvature ductility factors initially increase with an increase in the displacement ductility then they decrease as a result of bond failure of top beam bars. The disparity of curvature ductility factors between two beams which was caused by different bond characteristics of the top and bottom beam bars.

6.4.6.2 Beam Strain Profiles at the Level of Longitudinal Reinforcement

Figures 6.43 and **6.44** present the beam strain profiles at the level of top and bottom longitudinal reinforcement. Strain profiles followed a similar trend as that obtained in Units 5 and 6. It can be seen in **Fig. 6.43** that the decrease in of tensile strain and increase of compressive strain in the top beam bars occurred in the load cycle to $\mu_\Delta = 6x1$, after bond failure had occurred.

6.4.6.3 Beam Elongation

Figure 6.45 depicts the measured total beam elongation versus lateral load during the test. It can be seen in this graph that significant beam elongation took place in the load cycle toward a new displacement ductility factor. However, the elongation diminished in the load cycle to $\mu_\Delta = 6x1$ since bond failure on top and bottom beam bars had occurred at this stage. The maximum beam elongation measured during the test was 19 mm, equivalent to 3.4% of the overall beam depth.

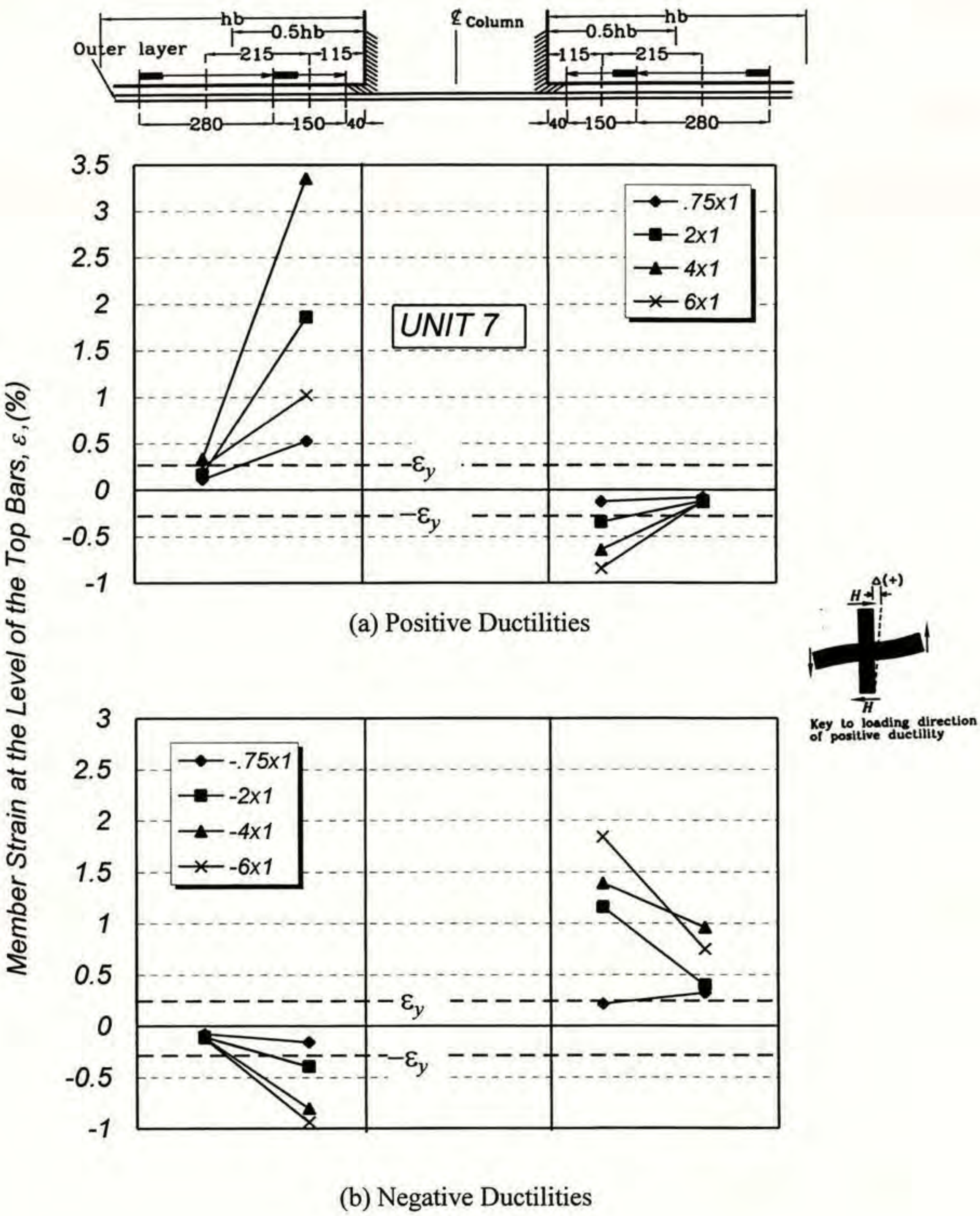

Figure 6.43 - Beam Strain Profiles at the Level of the Outer Layer of the Top Beam Bars of Unit 7.

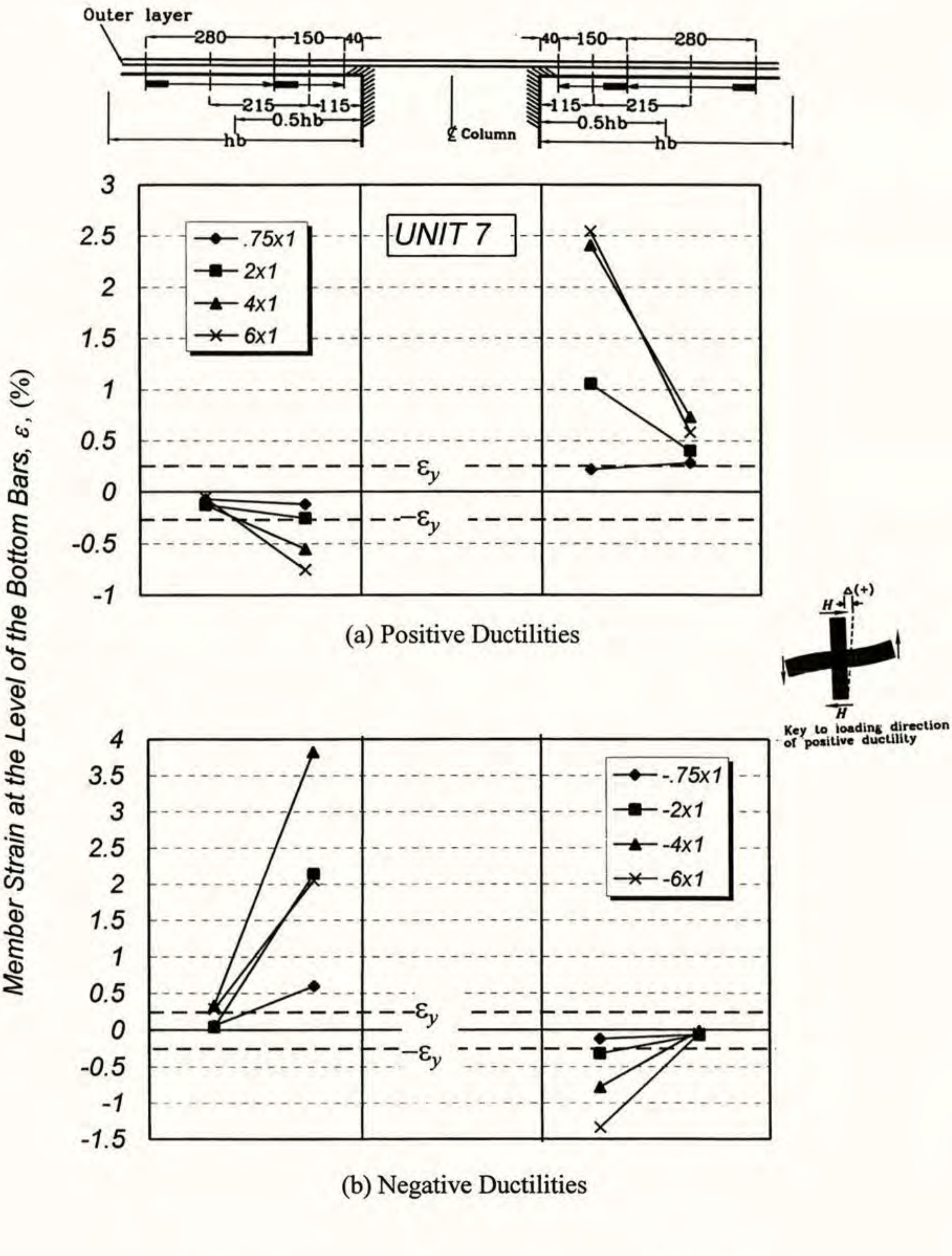

Figure 6.44 - Beam Strain Profiles at the Level of the Outer Layer of the Bottom Beam Bars of Unit 7.

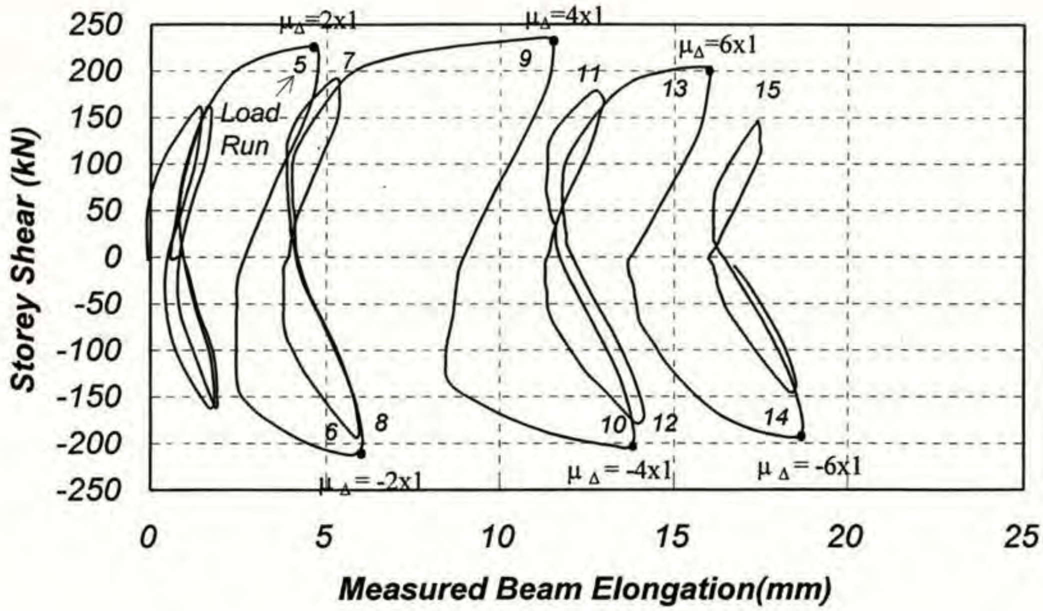

Figure 6.45 - Beam Elongation of Unit 7.

6.4.7 Column Behaviour

With reference to the measured stress profiles of column vertical bars presented in Section 6.4.5.5 and the visual observation on cracking appearance, it is concluded that the column behaved elastically during the test.

6.5 CONCLUSIONS

1. Test results of three cruciform interior beam-column joint subassemblies incorporating distributed longitudinal bars in beams, designated as Units 5, 6 and 7, were described in this chapter. Units 5 and 6 were rested under constant column axial load $N^* = 0.1f_c'A_g$ while Unit 7 was tested under $N^* = 0.25f_c'A_g$.

2. Unit 5, in which the quantity of transverse joint reinforcement was provided based on a 15% reduction with respect to the amount required by the analytical model and less than that required by the Concrete Structures Standard [S1], showed limited displacement

ductility response. Beam-column joint failure in combination with bond failure of the outermost layers of beam bars led to failure of this unit.

3. Unit 6 was similar to Unit 5 expect that deformed bars were used as joint transverse reinforcement. This unit also showed limited displacement ductility response resulting from bond and joint shear failure. However, it was found that the joint in Unit 6 did not deteriorate as much as that in Unit 5, indicating that incorporating deformed bars as joint reinforcement enhanced the joint to some extent.

4. Unit 7, in which larger diameter bars were incorporated in the inner layers of longitudinal reinforcement, showed improved performance. The beam-column joint showed acceptable performance which resulted from the higher axial compressive load applied to the column. However, this unit did not achieve fully ductile performance since bond failure of the outermost layers of beam bars lead to significant loss of lateral capacity in the load cycle to $\mu_\Delta = 6x2$.

5. The strain gauge readings of the outermost layers of beam bars in Units 5, 6 and 7 have shown that these bars are likely to yield in compression at column face and to $\lambda_o f_y$ in tension at the opposite column face. This explains the rather premature bond failure of these bars occurred in the test units.

6. Test results of Unit 7 indicate that the limitation of diameter of inner layers of beam bars is not needed when the beams are incorporated distributed reinforcement. However, the outer layers of beam bars may require more severe limit of bar diameter / column depth ratio than the current Code [S1] requirement on the other hand.

7. The displacement ductility, μ_Δ, corresponding to the 2.5% drift limitation imposed by the loading standard [S3] of Units 5, 6 and 7 is 2.3, 2.4, 2.9, respectively. These displacement ductility factors are rather small despite that these units were designed to achieve ductile performance. The large yield drift and small displacement ductility factors corresponding to the Code drift limitation are resulted from the use of Grade 500 longitudinal reinforcement.

CHAPTER 7
TEST RESULTS OF UNIT 8

7.1 INTRODUCTION

Unit 8 was a benchmark unit built for comparison with Units 5 and 6. Unit 8 had conventionally reinforced beams with equal top and bottom longitudinal reinforcement. Reinforcing details and a description of the design of these units was discussed in Section 3.2.2.3. The quantity of transverse shear reinforcement placed in joint regions of this unit was identical to that in Units 5 and 6. As in Units 5 and 6, constant compressive load of $0.1f_c{}'A_g$ was applied to the column in Unit 8. Test sequence incorporated in the testing of this unit was the standard procedure which is the same as that used in previous units.

7.2 UNIT 8

7.2.1 Overall Behaviour

Unit 8 showed limited ductility performance as a result of joint shear failure and bond failure on the top and bottom beam bars. In the second load cycle to $\mu_\Delta = 4$, corresponding to a 3.9% inter-storey drift, lateral load capacity dropped to 76% of the maximum recorded value in both positive and negative load cycles.

Cracking appearance of the joint region at different stages of loading is illustrated in **Fig. 7.1** and the lateral load-lateral displacement response is plotted in **Fig. 7.2**.

In the elastic load cycles, $\mu_\Delta = \pm .75$, most of the cracks concentrated in beams with flexural cracks distributing along beams. Cracks in columns were very limited and short. Some diagonal cracks, propagating from corner to corner, appeared in the joint panel although they were very fine with maximum width less than 0.1 mm.

By $\mu_\Delta = \pm 2x1$, not only the crack pattern was denser but also the width of cracks increased in joint region and beams. More new diagonal cracks occurred in joint region with

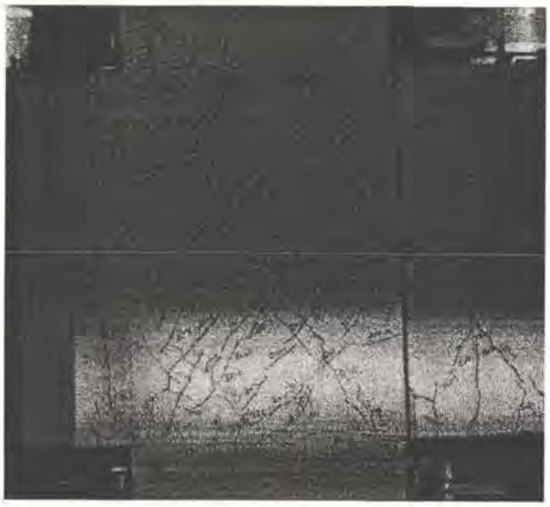

(a) At μ_Δ = -2x1

(b) At μ_Δ = -2x2

(c) At μ_Δ = -4x1

(d) At μ_Δ = -4x2

Figure 7.1 - Cracking of Unit 8 at Different Stages During the Test.

(e) At μ_Δ = -6x1

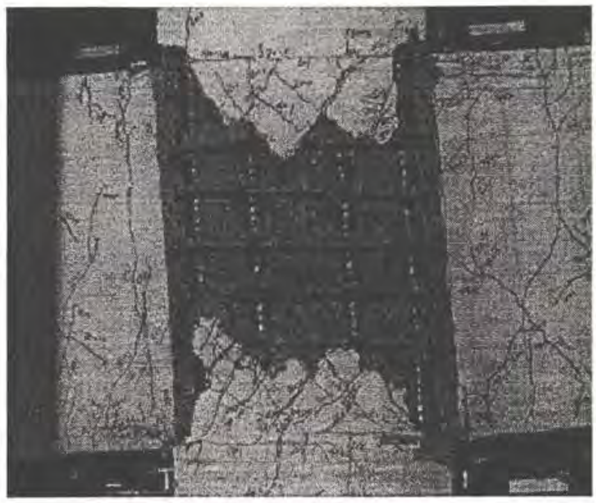

(f) At μ_Δ = -6x2

Figure 7.1(Cont.) - Cracking of Unit 8 at Different Stages During the Test.

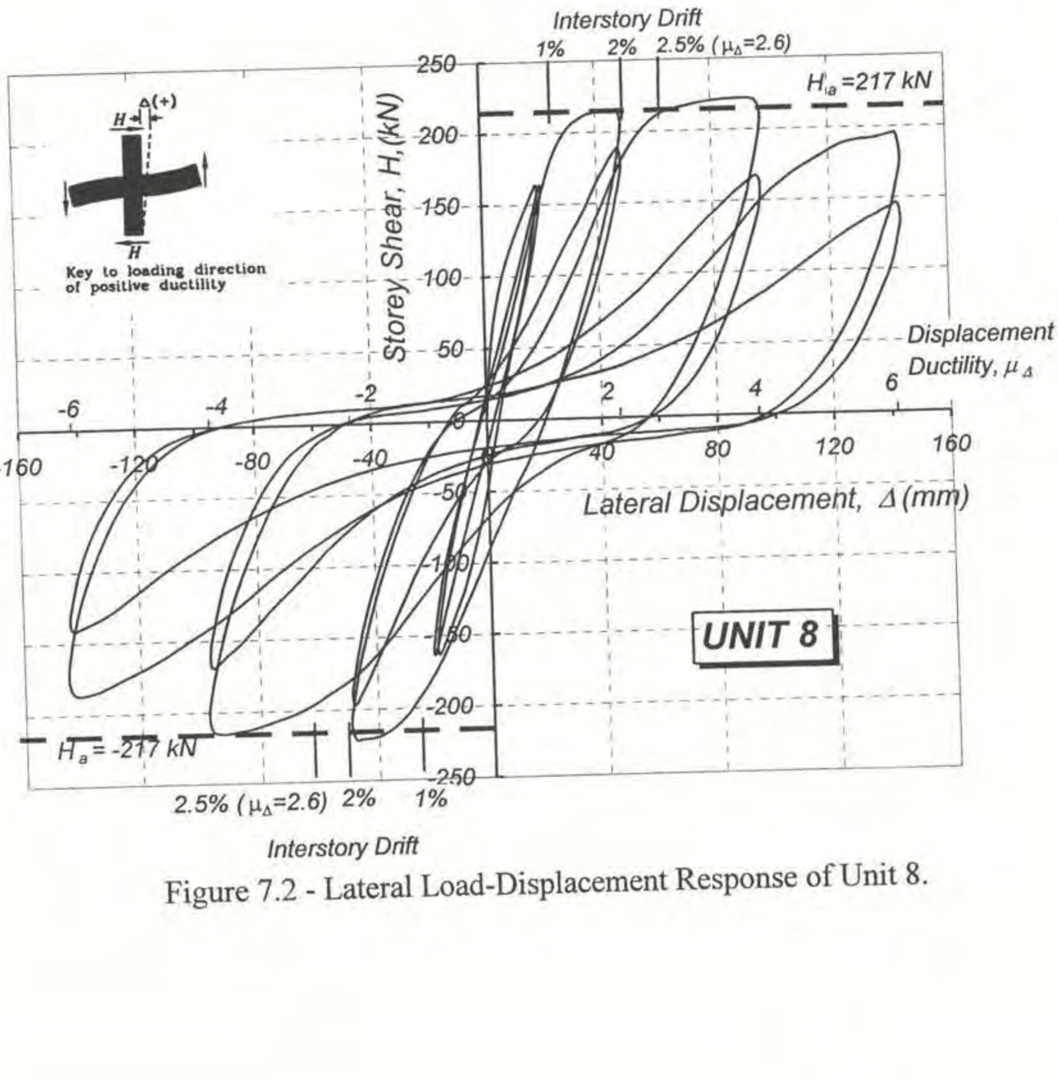

Figure 7.2 - Lateral Load-Displacement Response of Unit 8.

the maximum width reaching 0.5 mm. Two cracks developing in the beams at the column faces became comparatively wide, reaching 1.5 mm. In the subsequent load cycle, $\mu_\Delta = 2x2$, crack pattern in beams and joint became even denser although there was no noticeable change in crack widths. **Figure 7.1(a)** depicts the stage of the joint at the peak loading to $\mu_\Delta = -2x1$.

In the load cycle to $\mu_\Delta = 4x1$, the maximum width of cracks in the beams and in the joint reached 2.0 mm and 1.5 mm, respectively. Some incipient damage to the concrete cover of joint was observed at this loading stage. In addition, slight bulging of concrete in the joint was noticed, indicating that joint started to deteriorate and crushing of the concrete had occurred. Also the concrete cover around the top and bottom ends of the joint corner ducts became dislodged. It should be noted that movement of target stud welded on top beam bars was also observed, indicating that significant slip of top beam bars had occurred at this stage.

In the subsequent load cycle, $\mu_\Delta = 4x2$, some concrete in joint panel spalled off and some joint hoops were exposed around joint centre. It was also observed that cracks in the beams became thinner, indicating that joint shear deformation controlled the lateral displacement. **Figure 7.1(d)** clearly shows the extent of damage in the joint at the peak loading in the cycle to $\mu_\Delta = -4x2$.

By $\mu_\Delta = \pm 6x1$, cover concrete of joint panel carried on spalling off, in combination with falling apart of the dislodged corner concrete in joint region. In the subsequent load cycle, $\mu_\Delta = 6x2$, most of the joint cover concrete spalled off and inside joint concrete was crushed by shear. The extent of damage and the joint shear distortion at the peak loading to $\mu_\Delta = -6x2$ can easily be observed in **Fig. 7.1(f)**.

7.2.2 <u>Load Displacement Response</u>

Figure 7.2 depicts the complete lateral load-lateral-displacement response of Unit 8. The measured yield drift of this unit was 0.97%. This value of the yield drift implies a displacement ductility of $\mu_\Delta = 2.6$ when the drift reaches 2.5%.

As the specimen was displaced into the inelastic range in the load cycle to $\mu_\Delta = 2x1$, the lateral load slightly exceeded the theoretical ultimate lateral load in both, the positive and the negative load directions. In the second load cycle to the same displacement ductility, the hysteresis loops showed slight pinching and some reduction of lateral load capacity was recorded. The lateral load dropped below the theoretical ultimate load by 14% and 10% in the positive and negative load runs respectively.

In the load cycles to μ_Δ = 4x1, the measured lateral load exceeded the theoretical ultimate value by 4% in the positive load run and just reached it in the negative load run. It is noted that the unit did not develop too much lateral load over-strength. In the subsequent load cycles, μ_Δ = 4x2, considerable drop of lateral load capacity occurred. The measured lateral loads in both directions were 76% of the maximum load, leading to the failure of this unit.

In the load cycles to μ_Δ = 6x1, some lateral load capacity was picked up in both load directions with respect to the load capacity measured in the last load cycle, reaching 89% and 86% of the recorded maximum load. It is noted that this amount of pick up was moderate, indicating that part of lateral load reduction occurred in the load cycles to μ_Δ = ±4x2 was deemed to be induced by slip page of the beam bars. Since part of the failure was concentrated in the joint, the gain of lateral load capacity occurred in the load cycle to a larger displacement ductility would be insignificant.

In the load cycle to μ_Δ = 6x2, the lateral load capacity dropped more significantly, being 66%, 65% of the maximum load in the positive and negative load runs, respectively.

Comparing the lateral load-lateral displacement response of Units 8 and 5, (see **Figs. 6.2 and 7.2**), it can be seen that the behaviour of the two units under simulated seismic loading are very similar. The yield drift of Unit 8 (0.97%) is slightly smaller than that of Unit 5 (1.07%). It is believed that the larger yield drift of Unit 5 is caused by the distributed characteristics of beam longitudinal bars. It is evident that the stiffness of the frame subassembly is reduced as a result of distributed beam bars. However, the disparity is not pronounced.

In general, the lateral load-lateral displacement response of Unit 8 is slightly superior than Unit 5. The reduction of lateral load capacity in each load cycle of Unit 5 is larger than that in Unit 8 in general. It is believed that this is the result of the premature bond failure of outermost layers of beam bars in Unit 5.

7.2.3 Decomposition of Lateral Displacements

Figure 7.3 presents each component of lateral displacement as a percentage of the

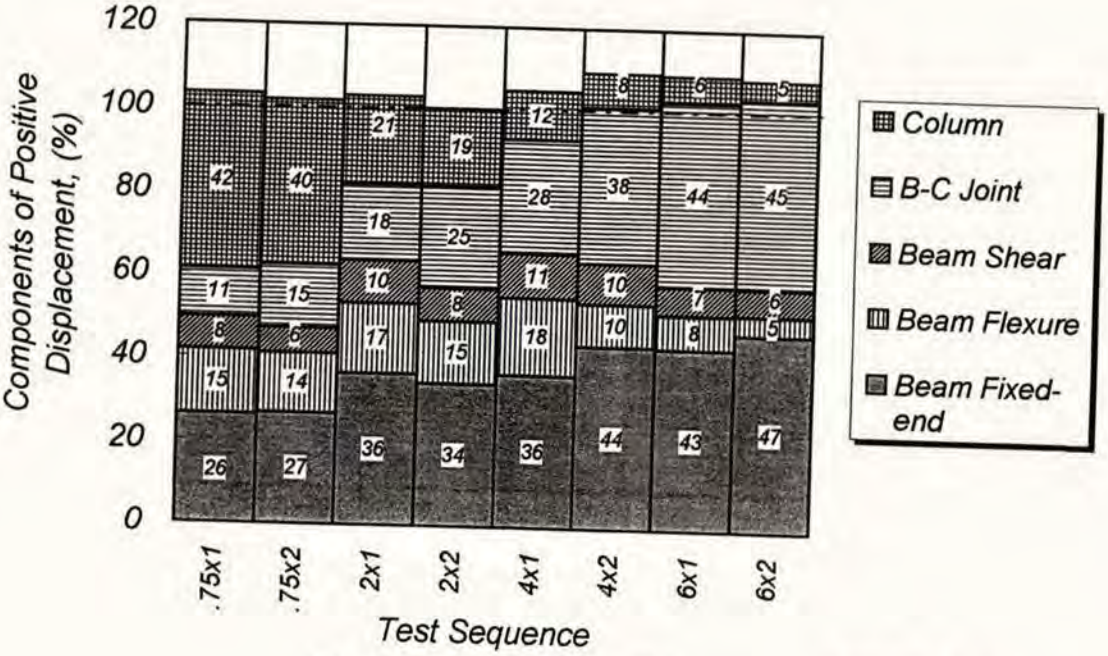

(a) Runs to Positive Ductilities

UNIT 8

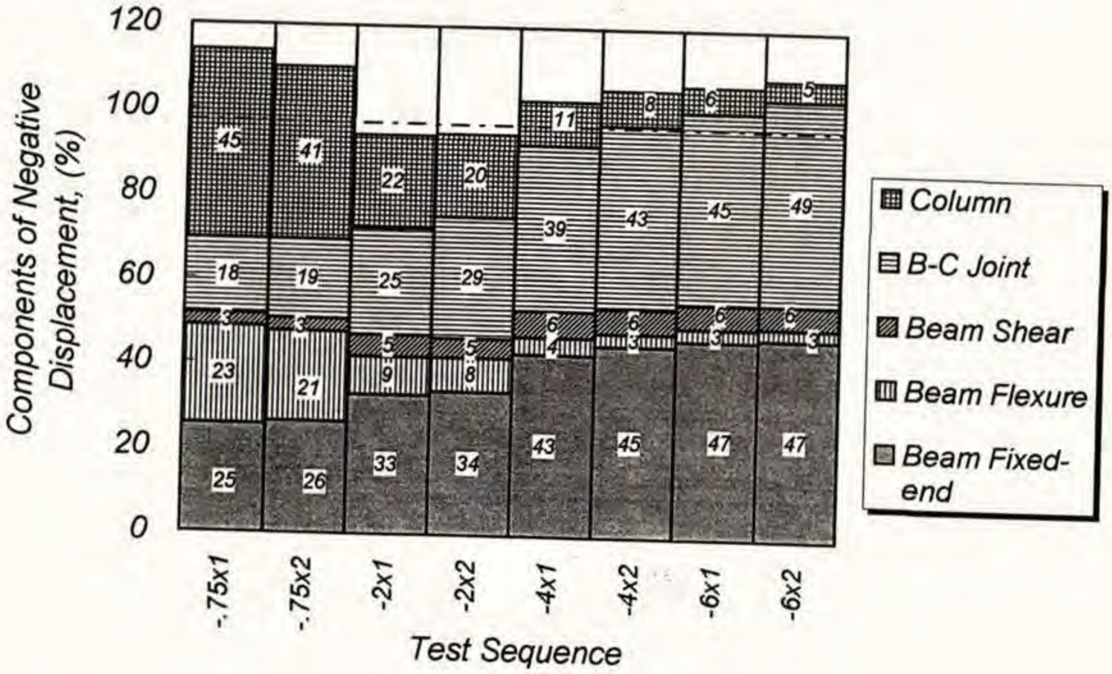

(b) Runs to Negative Ductilities

Figure 7.3 - Components of Lateral Displacement of Unit 8 at Peaks of Load Runs.

applied peak displacement in each run.

It can be seen in this graph that the component of beam fixed-end rotation contributed to the applied lateral displacement from 25% recorded in the elastic load cycle until 47% measured at the end of test. In general, this component ascended as the progressing of test sequence. However, the increasing trend was eased since load cycle to $\mu_\Delta = 4x2$.

Another source of lateral displacement which also had an ascending trend as the test progressed was the beam-column joint shear distortion. This component contributed 11-19% to the applied lateral displacement in the elastic load cycles and 18-29% in the load cycles to $\mu_\Delta = 2$. Note that until this stage the contribution due to joint shear distortion was still less than that due to beam fixed-end rotation. In the load cycles to $\mu_\Delta = 4$, the contribution of the joint shear distortion increased and reached 43% at the peak of load cycle to $\mu_\Delta = -4x2$. It should be noted that at this stage the contribution of beam-column joint shear distortion was comparable to the component of beam fixed-end rotation. Therefore, it may concluded that the cause for the significant reduction of lateral load capacity occurring in the load cycle to $\mu_\Delta =$ 4x2 was the combination of beam-column joint shear failure and bond failure of the longitudinal beam bars passing through the joint region. In the load cycles to $\mu_\Delta = 6$, the contribution of the joint shear distortion and that due to the beam fixed-end rotation increased further.

The component of beam flexural deformation had a maximum percentage of 23% recorded in elastic load cycle and diminished gradually up to 3% at the end of test. However, the diminishing trend was less apparent in load runs of positive ductility than that in load runs of negative ductility. Note that the percentage of this component calculated in each load cycle was always moderate, indicating that plastic hinges, although had formed in beams, did not evolve well for the purpose of energy dissipation. This was simply because other sources of lateral displacement, mainly were beam fixed-end and beam-column joint shear distortion, governed the lateral displacement during the test.

Column deformation, calculated from theoretical analysis and in proportional to the measured lateral load in each load cycle, had a maximum percentage of 45% recorded in the elastic load cycle. Note that this percentage occurred in elastic range was large in comparison with the 20% - 30% assumed in the analytical work. Part of the reason of this rather large percentage of column deformation in elastic load cycles was the rather slender column used in design of the units needed to obtain a high joint shear stress value.

Note that in practical, the component of column deformation may be smaller if smaller column height or larger column section is used. However, the displacement ductility at 2.5% drift limitation remains in the limited ductility level, when smaller component column deformation is considered. The relevant calculation is outlined in the below.

$\Delta_y = 0.97\%$

subtracting the column component from the yield drift,

$\Delta_y' = 0.97\text{-}0.97\text{x}0.45 = 0.53\%$

Consider a less component of column deformation, $\Delta_{col} / \Delta_y = 0.25$, the associated yield drift is

$\Delta_y'' = 0.53 / (1\text{-}0.25) = 0.71$

The displacement ductility factor when the 2.5% drift limitation is attained is

$\mu_\Delta'' = 2.5 / 0.71 = 3.5$

The calculation depicted above justifies that even if the column flexibility is only 25% of the yield drift, the displacement ductility factor of the tested frame subassembly, in which Grade 500 longitudinal reinforcement was incorporated, when the 2.5% drift limitation attained is 3.5, a value which is still far less than 6. This justifies that the cause of large yield drift, and hence the small μ_Δ associated to the 2.5% yield drift limitation, was the use of Grade 500 longitudinal reinforcement.

It may be worth to compare the components of applied lateral displacement of Units 5 and 8. (see **Figs. 6.3** and **7.3**). The components of the two units of applied lateral displacement were similar inelastic load cycles. In Unit 5, the increasing trend of beam fixed-end rotation with the progressing of loading was more pronounced than in Unit 8. In contrast, the increasing trend of beam-column joint distortion in Unit 5 was less significant than that in Unit 8. At the end of the loading cycle, the components of beam-column joint distortion and beam fixed-end rotation in Unit 8 were comparable in percentage. While in Unit 5, the component of beam fixed-end rotation was more prevailing than the beam-column joint distortion.

7.2.4 Joint Behaviour

7.2.4.1 Strains in the Horizontal Joint Shear Reinforcement

Each set of horizontal joint reinforcement, including exterior hoops and interior ties, was gauged with double strain gauges. Average strains at the peak of load cycles are presented in **Figs. 7.4** and **7.5**.

Strain profiles obtained in the elastic load cycles were rather uniform with an approximate strain level less than 1000 micro-strains. In the load cycles to $\mu_\Delta = 2$, the strains approached yield in the positive load runs and exceeded yield in the negative load runs over the entire joint depth. In the load cycle to $\mu_\Delta = 4x1$, the strains remained in the similar level as that were recorded in the previous load run. In the subsequent load cycles, strain profiles remained in a similar level without marked changes. Note that at this ductility level the lateral load capacity had begun to decrease and consequently the input joint shear force also decreased.

Comparing **Figs. 7.4**, **7.5** with **Figs. 6.4**, **6.5**, it is evident that the strain profiles recorded in joint hoops of Unit 5 showed more apparent arching shape than that in Unit 8. This is caused by the premature bond failure of outermost layers of beam bars. The outer sets of joint hoops could not develop their full strength since the strut forces which rely on the bond stress of beam bars beyond column concrete compressive region did not increase anymore as a result bond failure. In general, the hoops strains of Unit 5 reached yield while significant strain exceeding yield was observed in Unit 8. This agrees with the trend discussed in the previous section that the component of joint shear distortion in Unit 5 was not as prevalent as that in Unit 8.

7.2.4.2 Joint Shear Distortion

Figure 7.6 presents the measured joint shear distortion versus lateral loads. It can be seen in this graph that apparent increase of joint shear deformation started since the load cycles to $\mu_\Delta = 2x1$. The joint shear deformation continued to increase and reached 0.025 radians in the load cycle to $\mu_\Delta = 4x1$. It indicates that the joint strength commenced to degrade considerably at this stage. This agrees with what was observed in Section 7.2.4.1. In the load

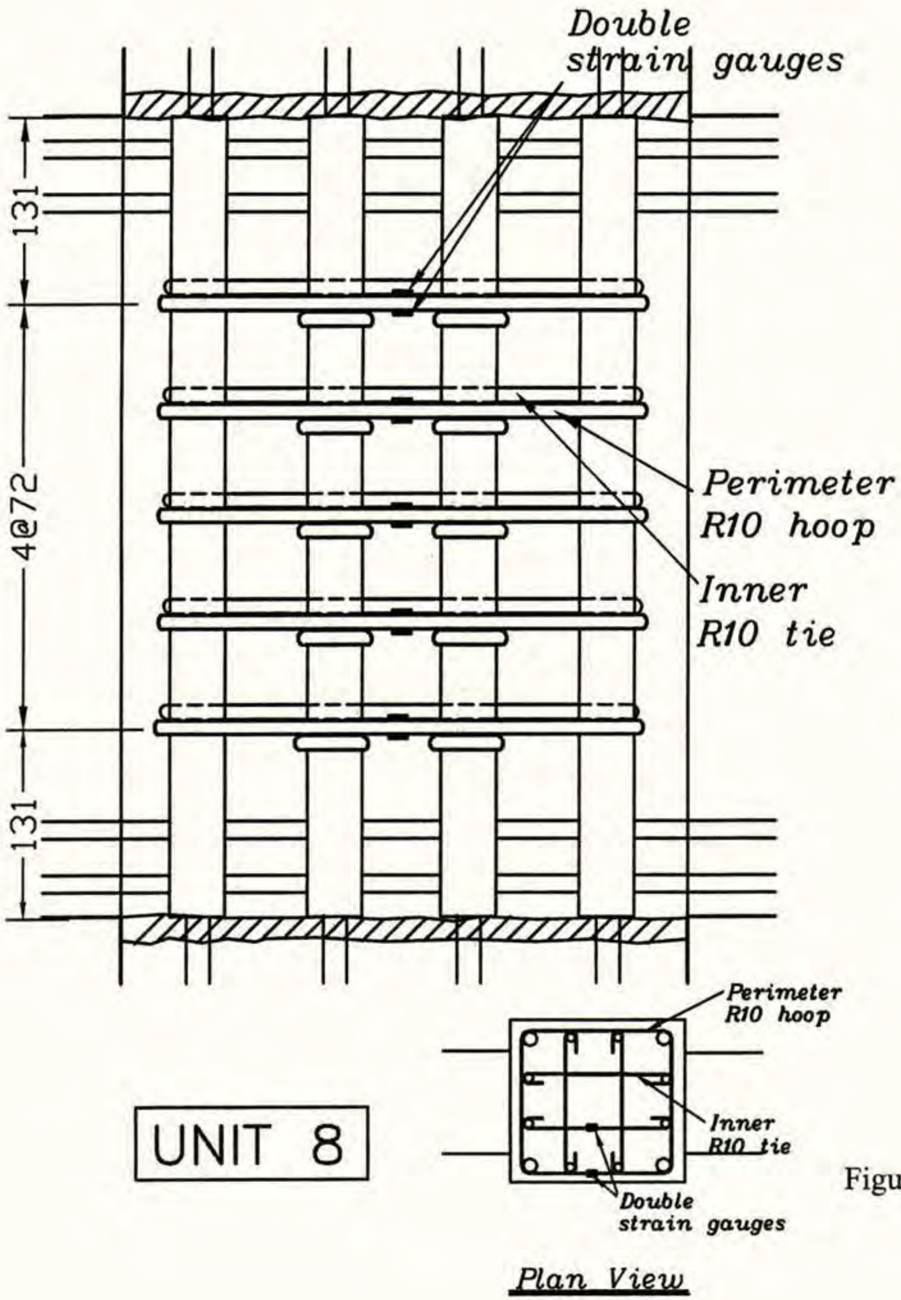

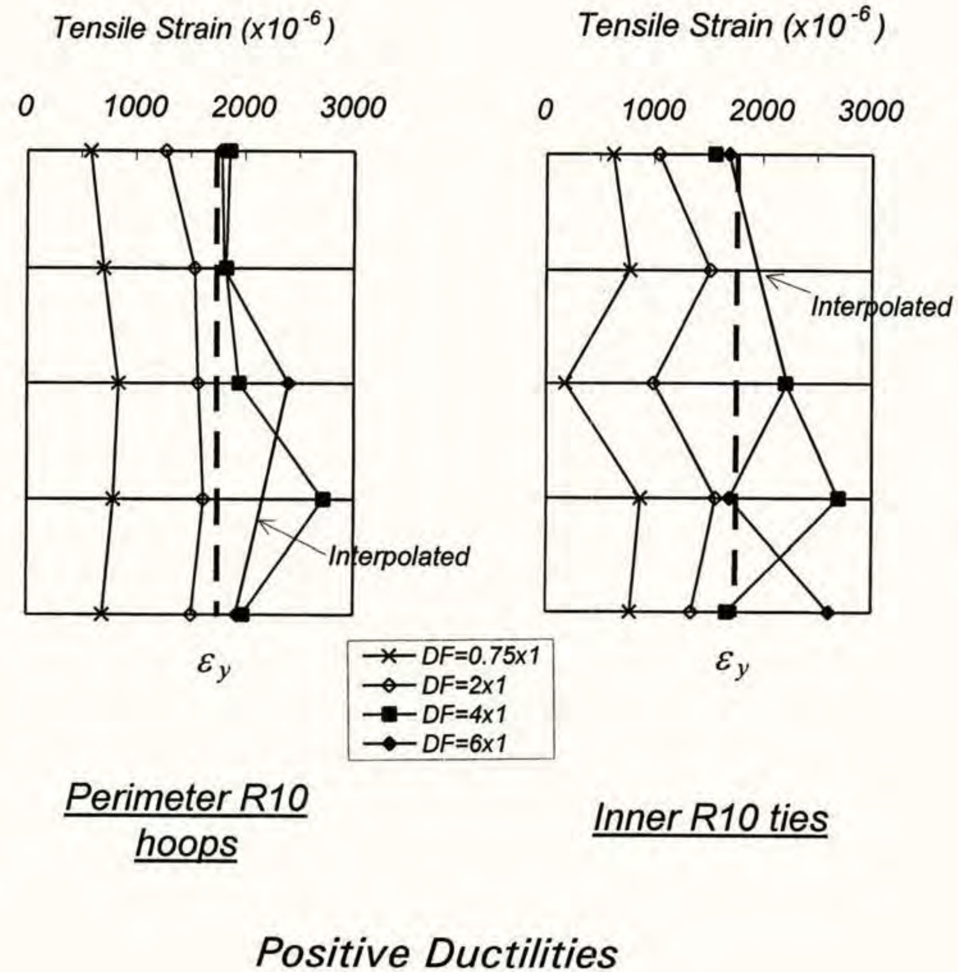

Figure 7.4 - Measured Strain in Joint Hoops of Unit 8 During the Runs to Positive Ductilities.

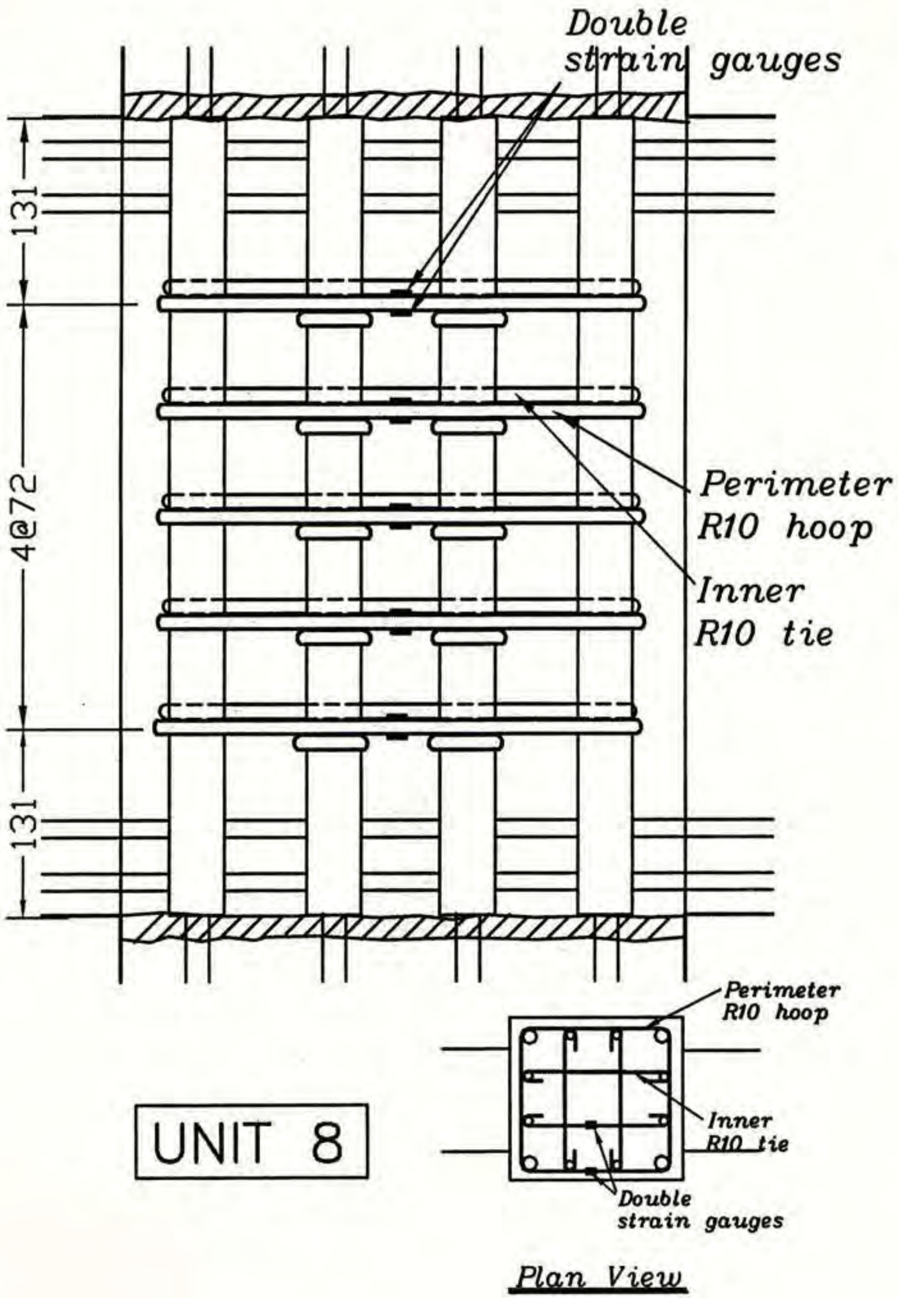

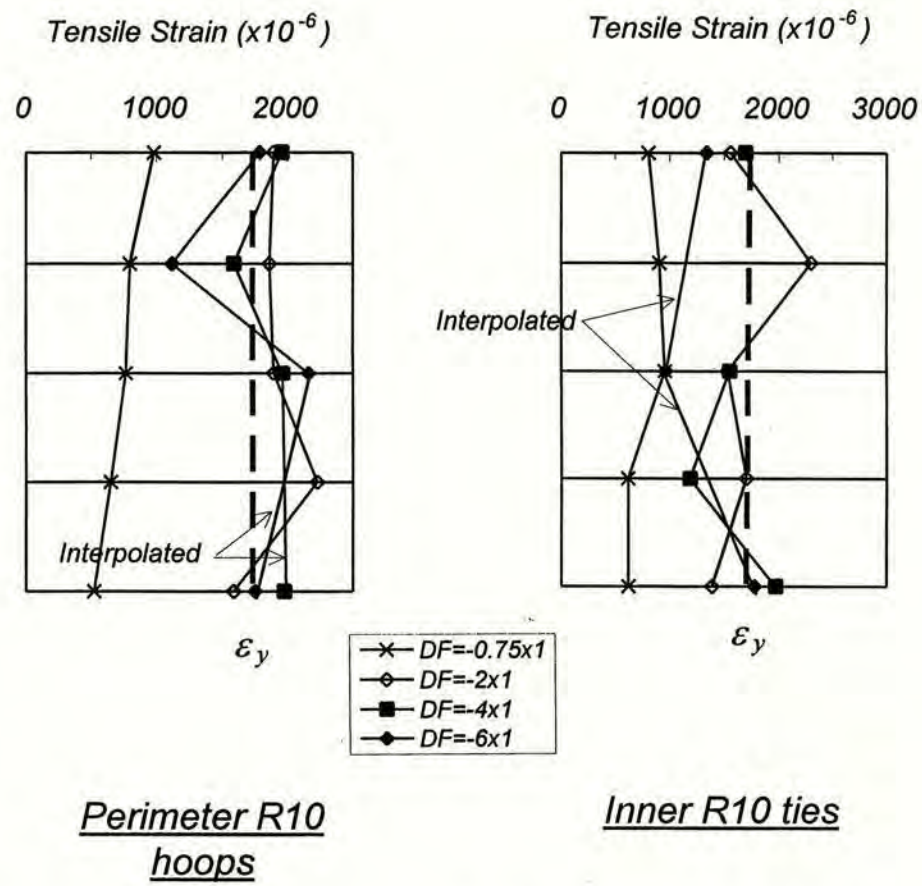

Negative Ductilities

Figure 7.5 - Measured Strain in Joint Hoops of Unit 8 During the Runs to Negative Ductilities.

cycles to $\mu_\Delta = 6$, the joint shear distortion carried on increasing in spite of the loss of lateral load capacity. It reached 0.04 radians in the final load cycle.

Comparison of recorded joint shear distortion between Units 5 and 8 (see **Figs. 6.6** and **7.6**) indicates that the joint of Unit 8 underwent larger shear distortion than that of Unit 5. The disparity of joint shear distortion between the two units commenced from the load cycle to $\mu_\Delta = 4x1$. The less joint shear distortion of the joint in Unit 5 was because of the more predominant beam fixed-end rotation as a result of premature bond failure of outermost layers of beam bars.

7.2.4.3 Beam Bar Slip

The measured local slip of top and bottom beam bars are depicted in **Figs. 7.7(a)** and **(b)**. It can be seen in **Fig. 7.7(a)** that the measured slip on the top beam bars in the centre of joint region exceeded the clear spacing between bar deformations in the load cycle to $\mu_\Delta = -4x1$. This slip threshold is related to the total bond failure of the top beam bars.

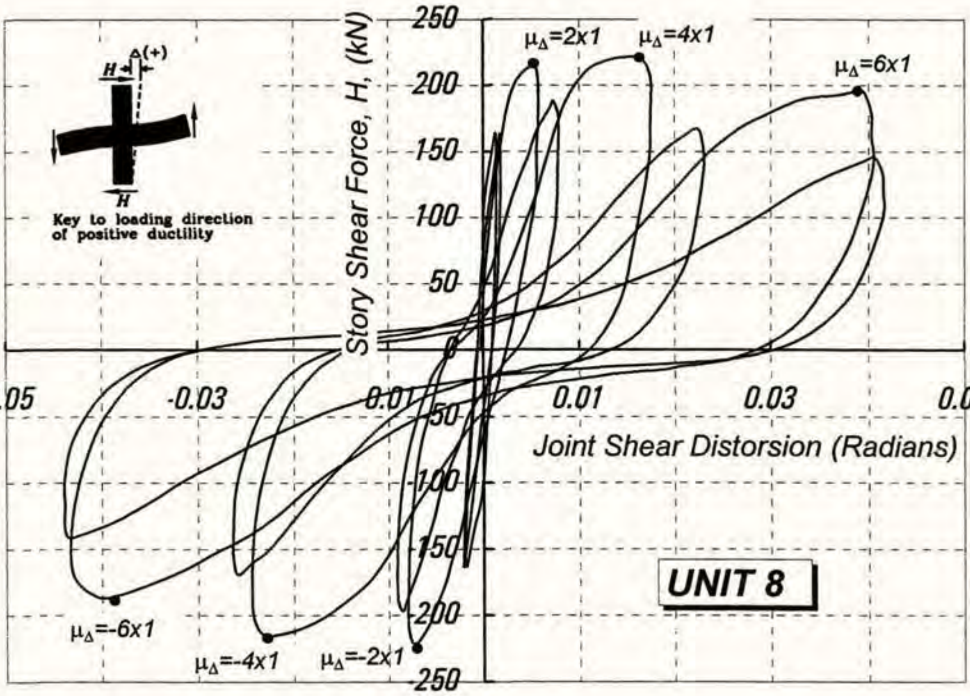

Figure 7.6 - Joint Shear Distorsion Versus Storey Shear Force.

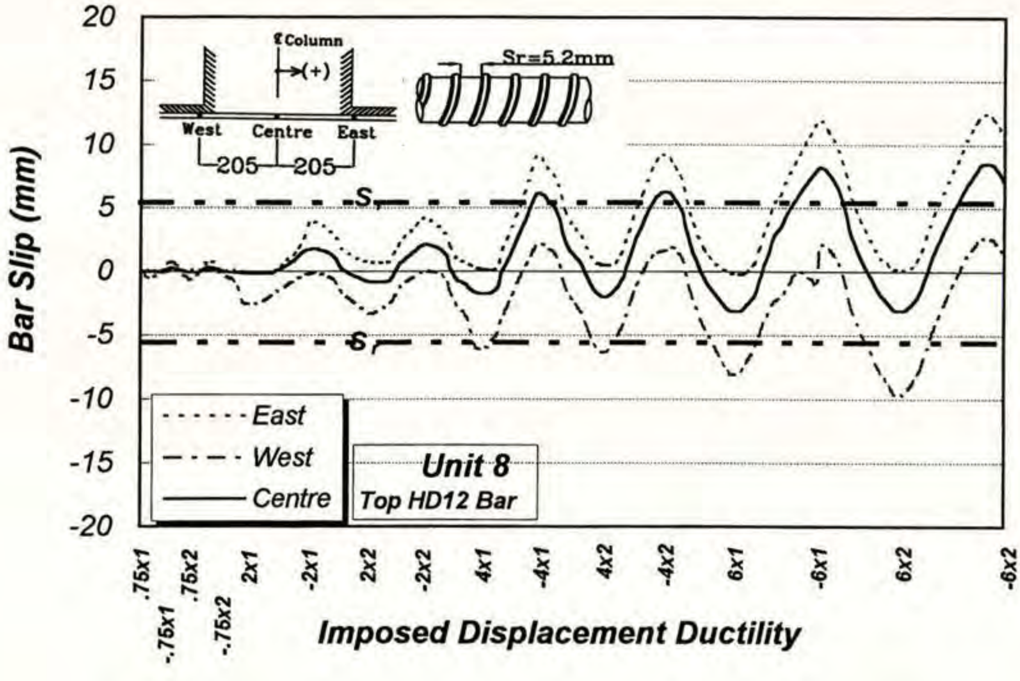

(a) Top Bars

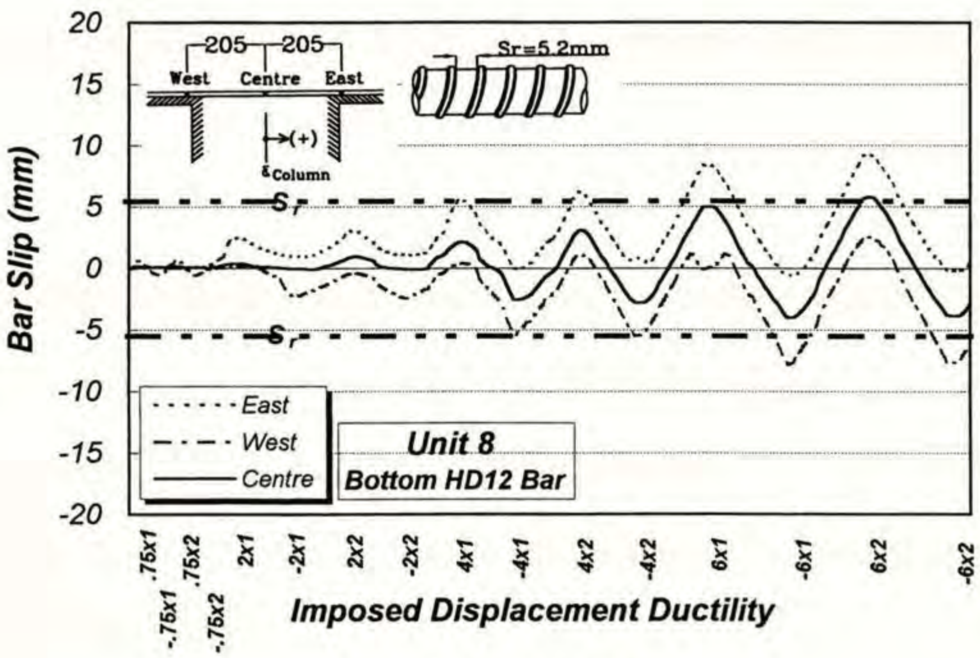

(b) Bottom Bars

Figure 7.7 - Relative Slip of Beam Longitudinal Bars in the Joint Region.

In **Fig. 7.7(b)**, it can be seen that the measured slip of bottom beam bars during the test was in general smaller than that measured on the top beam bars due to the " top bar " effect. In the load cycle to $\mu_\Delta = 6x1$, the slip exceeded the clear spacing between bar deformations. As a result, stiffness reduction and possible loss of lateral load capacity due to this failure mode was induced.

The measured slip in Unit 8 was generally smaller than that in Unit 5 on both top and bottom beam bars. Bond failure of both the top and bottom beam bars of Unit 5 occurred in earlier stages than that in Unit 8. Unit 5 and 8 had equal d_b / h_b and $N^* / A_g f_c'$ ratios and similar concrete compressive strength, f_c'. It is important to emphasize that the anchorage of outermost layers of beam bars in the joint region in which distributed longitudinal reinforcement is incorporated is more severe than that of lumped beam reinforcement. This is because in the critical section of beam in which longitudinal bars distributed, the numbers of compressive bars are much less than the numbers of bars in tension. As a result, as had been discussed in section 6.2.4.4, the outermost layers of beam bars in Unit 5 could be compressed to yield at the column face while subjected to tension beyond yielding at the opposite column face.

7.2.4.4 Beam Bar Strains And Bond Stresses in Joint Region

Figures 7.8 and **7.9** present the strain profiles of the top and bottom longitudinal beam bars at the peak of each load cycle. The average bond stresses calculated from obtained strains are shown in **Fig. 7.10**.

In the elastic load cycles, the maximum tensile strain recorded on the outer layer of top and bottom beam bars reached 2000 micro-strains while the compressive strain at column face was small. In inelastic load cycles, the recorded maximum tensile strain of the outer layers reached 4000 micro-strains while the maximum compressive strain was about -1750 micro-strains. Note that the recorded maximum compressive strain is slightly less than that was recorded on the outermost layers of beam bars in Unit 5. And it implies a compressive stress less than yield strength of reinforcing bars when the inelastic stress-strain relationship of reinforcing steel is considered.

The strain profiles on the inner layers of top and bottom beam bars showed a flatter distribution, with very small compressive or even tensile strain measured at column faces.

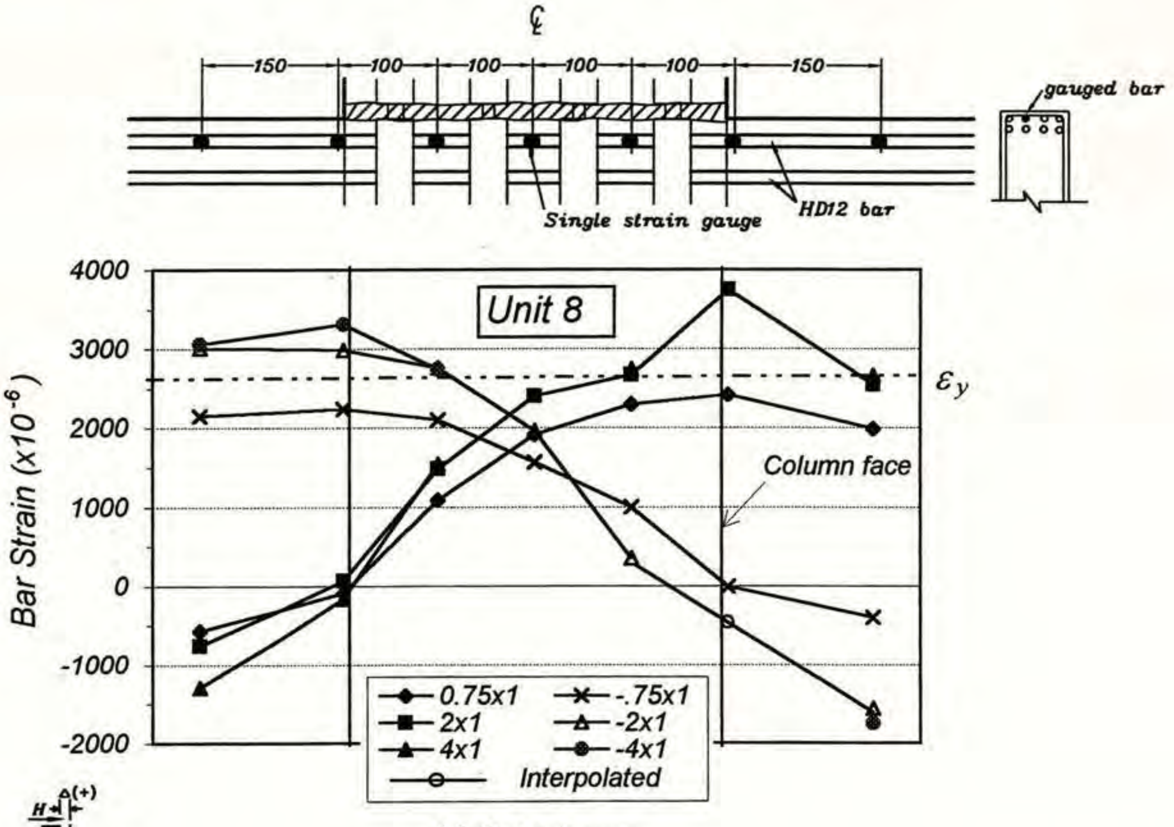

(a) Outer Layer

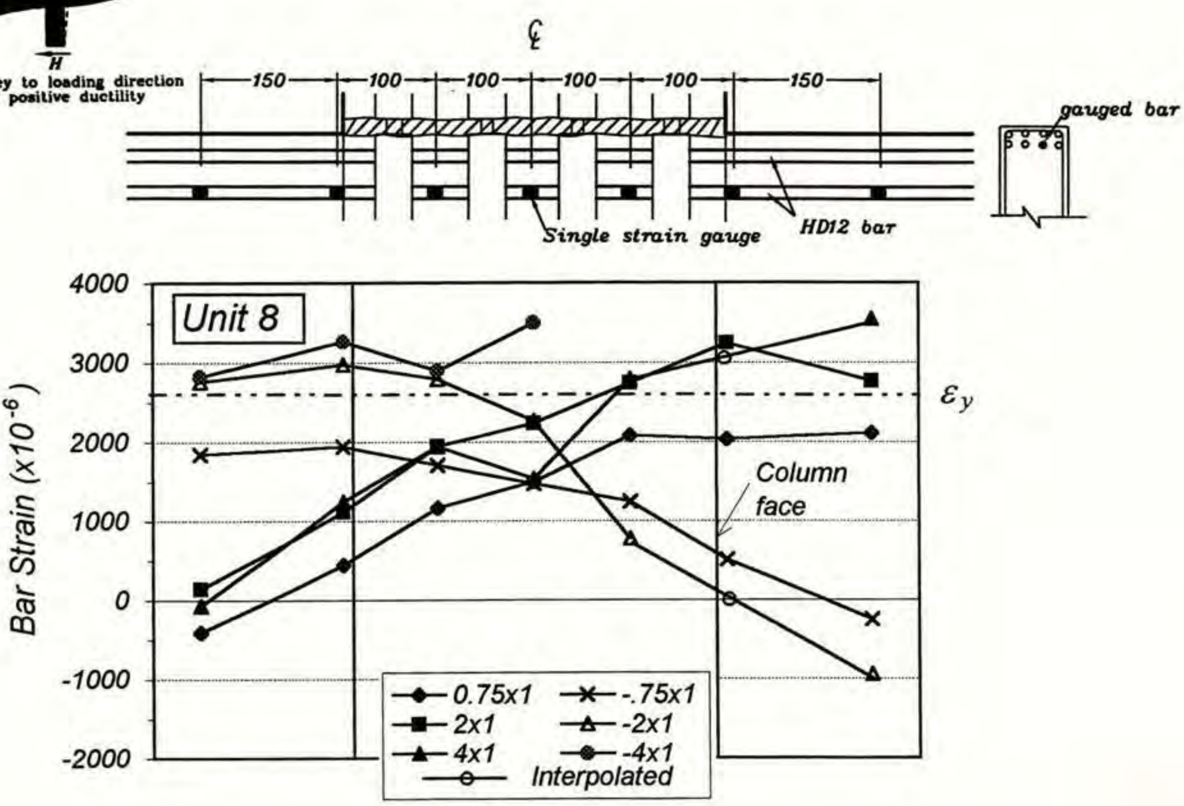

(b) Inner Layer

Figure 7.8 - Top Beam Bar Strain Profiles.

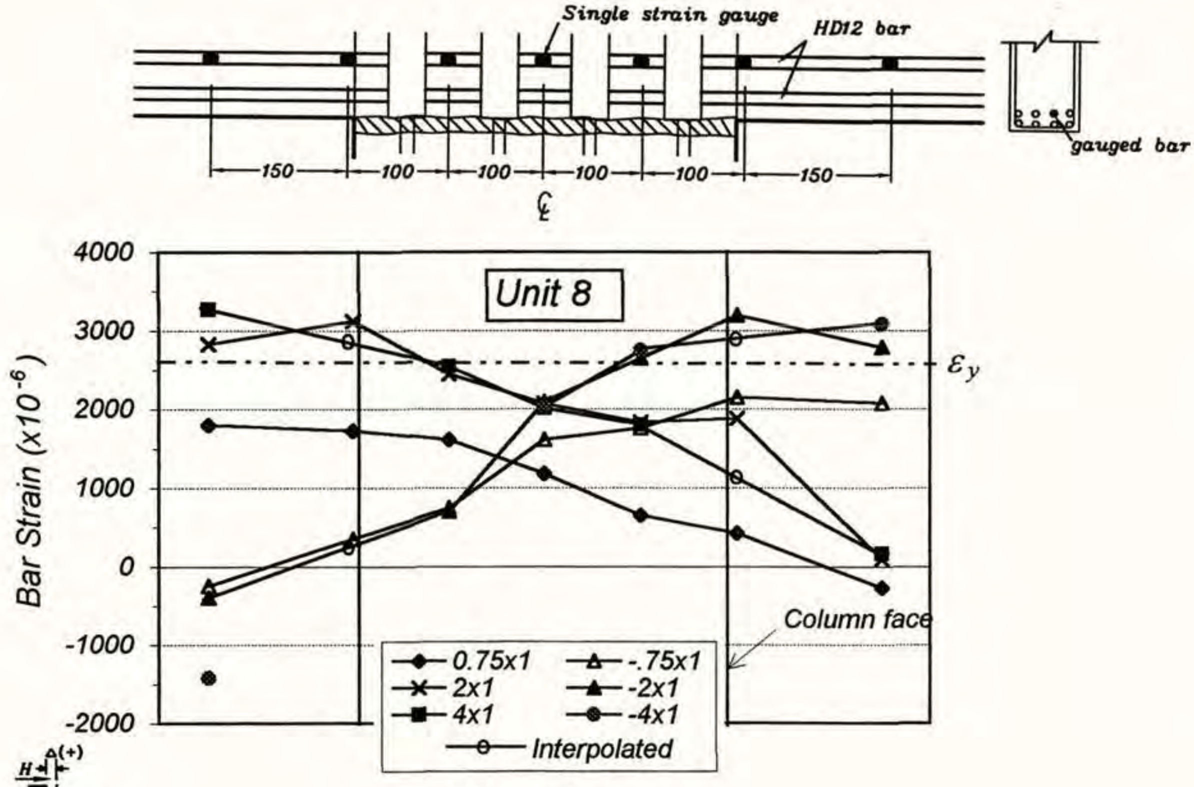

(a) Inner Layer

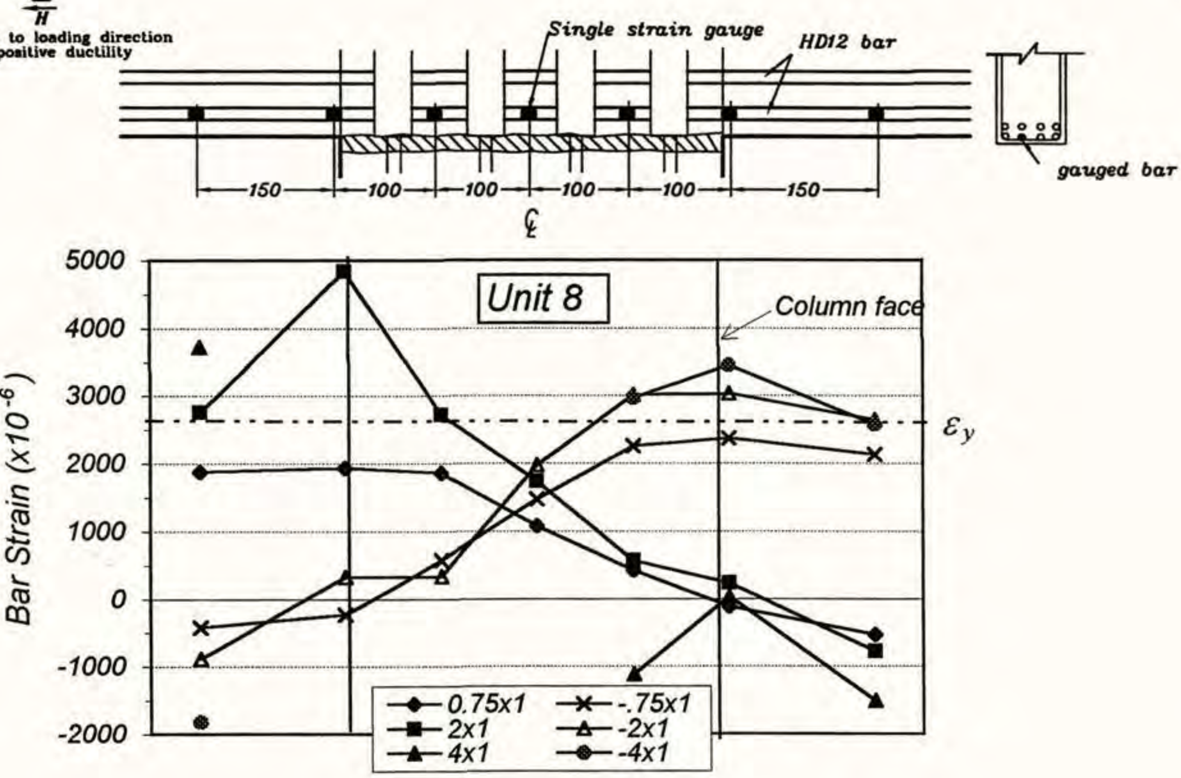

(b) Outer Layer

Figure 7.9 - Bottom Beam Bar Strain Profiles.

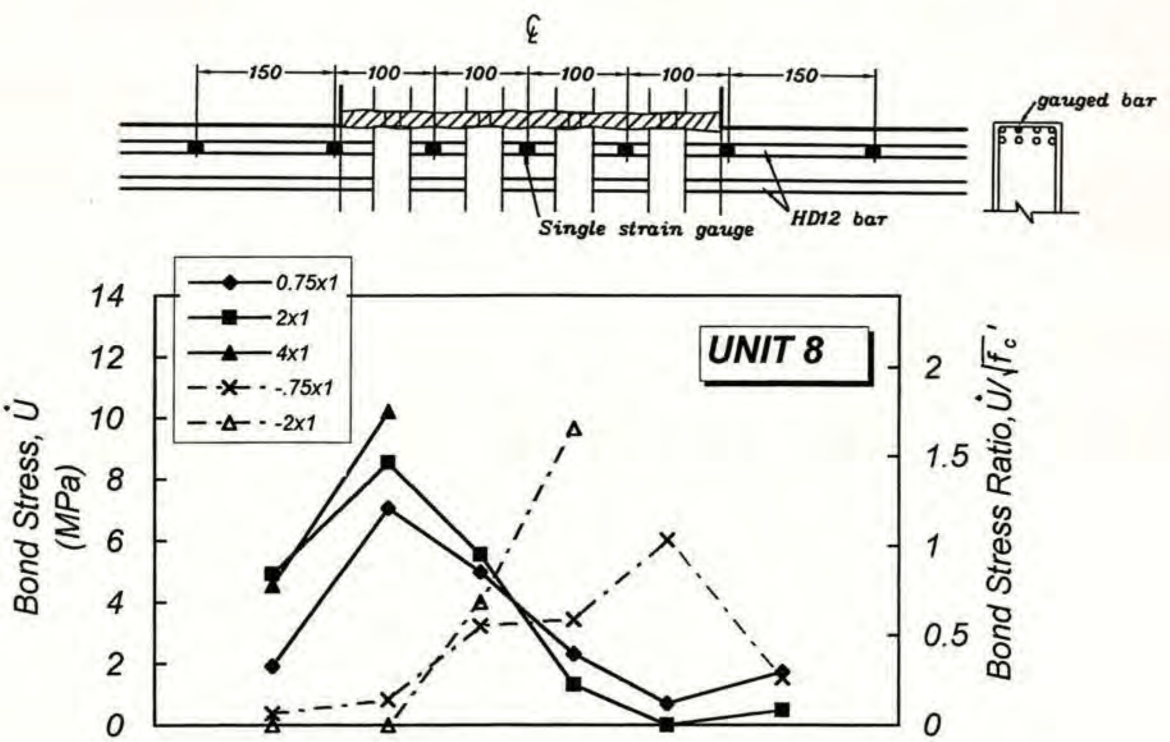

(a) Top Bars

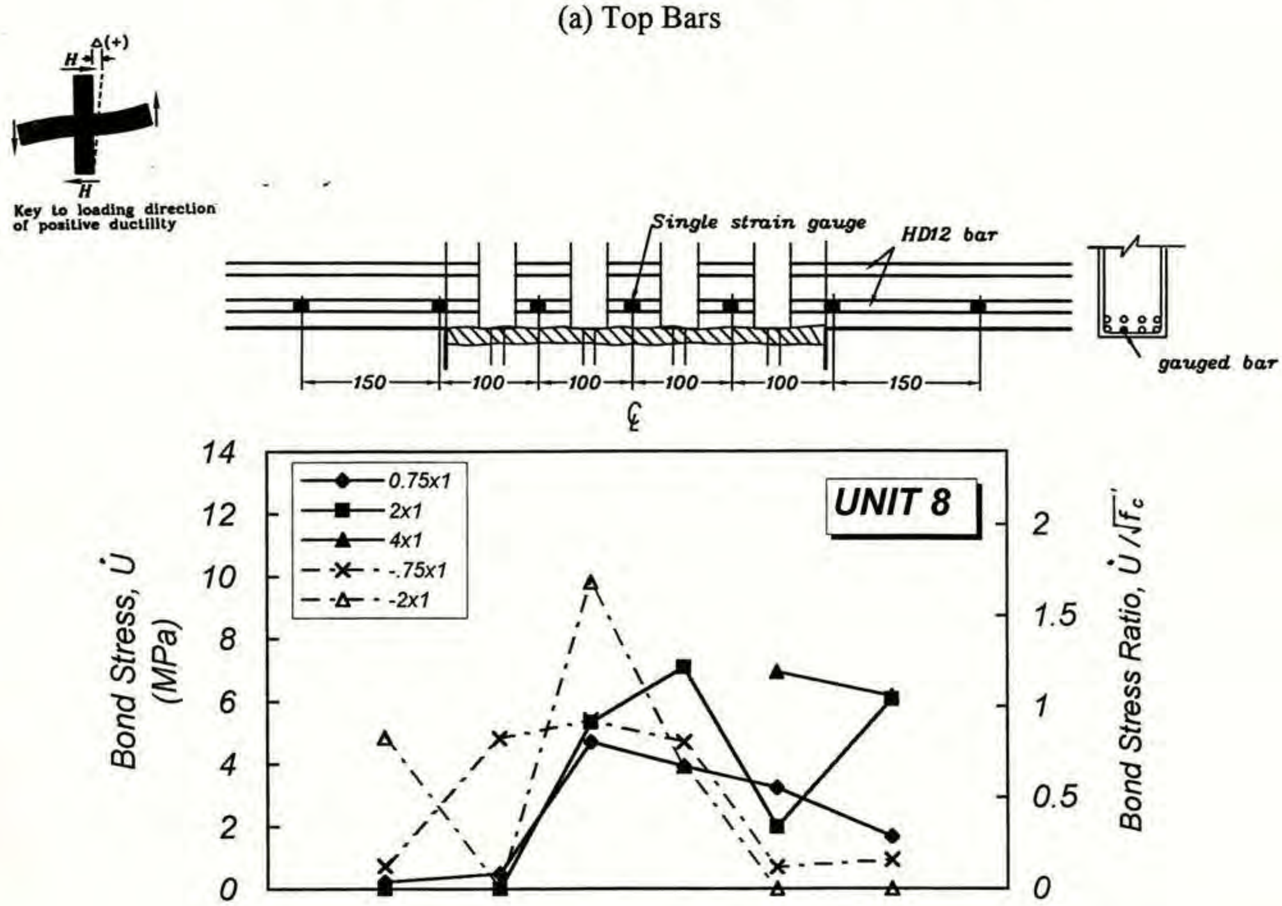

(b) Bottom Bars

Figure 7.10 - Calculated Bond Stresses.

This indicates that at this stage, the neutral axis depth of beam critical sections could be very close to the position of inner layers of beam bars.

Figure 7.10 shows that the maximum absolute bond stress of both top and bottom beam bars in joint region was 10 MPa, equivalent to $1.75\sqrt{f_c'}$. This value of peak bond stress is comparably less than the maximum value observed by Eligehausen et al. [E1] and adopted by Paulay and Priestley [P2], $2.5\sqrt{f_c'}$. The maximum bond stress of $1.75\sqrt{f_c'}$ was recorded on the top beam bars in the load cycle to $\mu_\Delta = 4x1$. Whereas larger bond stress developed in the successive load cycles was unlikely because total bond failure of top beam bars occurred in the load cycle to $\mu_\Delta = -4x1$. And beam-column joint shear distortion had accounted for a significant portion of the applied lateral displacement at this stage. As a result, local beam bars strains and bond stress did not increase continually as beam flexural deformation was diminishing.

The recorded bond stress profiles had the characteristics that tend to concentrate in the column concrete compressive region. This trend somehow agrees with the bond stress profile of beam bars passing through the joint region proposed by Restrepo et al. [R1] and used in the analytical work in Chapter 2.

Comparing the bond stress of Unit 5 (**Fig. 6.9**) and that in Unit 8 (**Fig. 7.10**), a general trend can be found that the values obtained in Unit 5 are larger than that in Unit 8 since the elastic loading run, although bond failure of beam bars in Unit 5 occurred more prematurely than that in Unit 8. This indicates that the maximum permissible bond stress of outermost layers of beam bars within the joint region would be reached earlier than that that in the lumped beam bars of conventionally reinforced joints. As a result, bond deterioration of outermost bars occurred earlier than that in the lumped bars. This agrees with what was discussed in Section 7.2.4.3.

7.2.4.5 Bar Stresses of the Column Vertical Reinforcement Passing Through the Joint Region

Figure 7.11 depicts the bar stresses of column vertical reinforcement passing through the joint region. The stresses were converted from strain gauge readings. The stresses profiles of corner bars showed very similar trends to those observed in Units 5 and 6, see **Figs. 6.11** and **6.26**. The maximum tensile stress recorded at the top beam face reached yield stress in

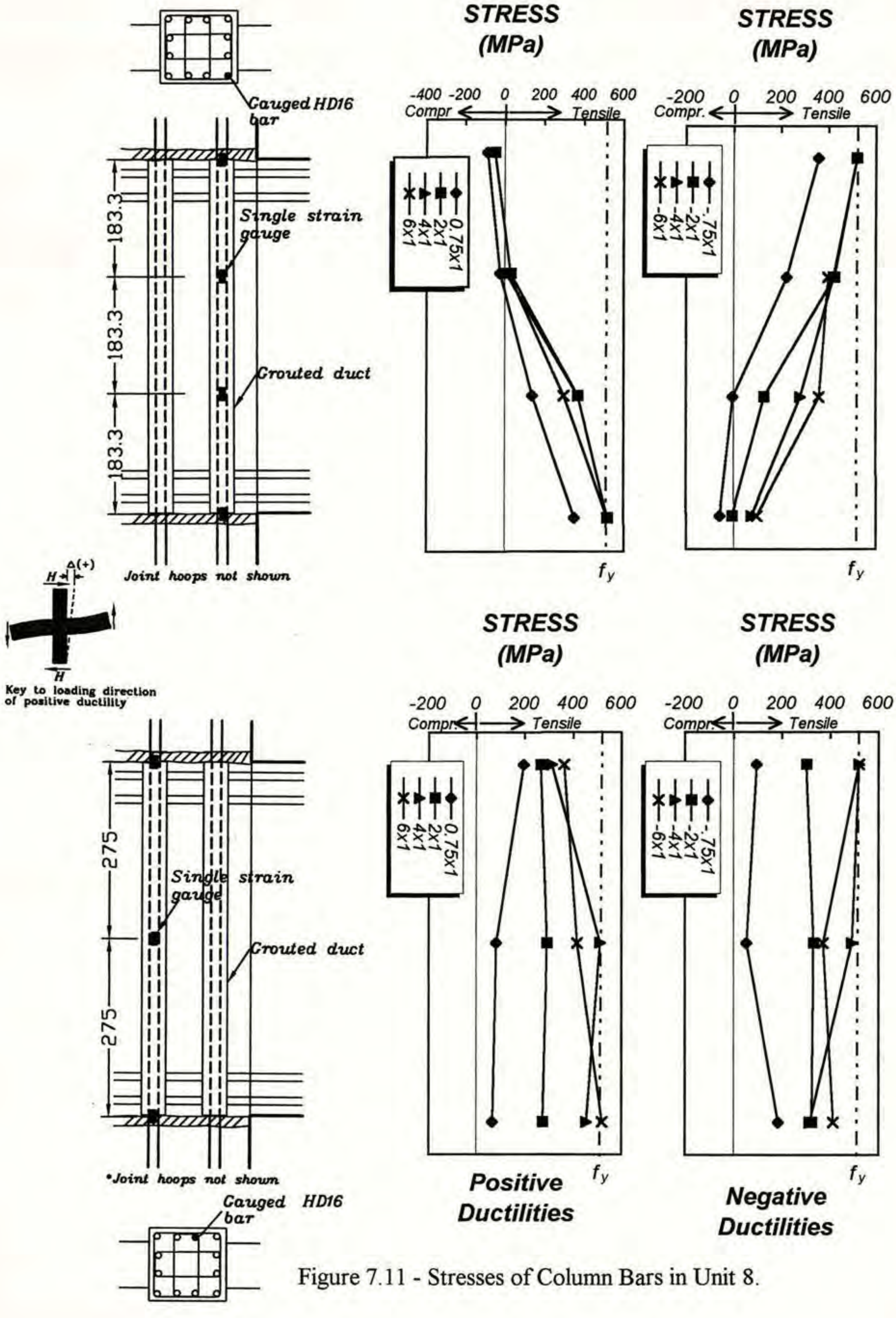

Figure 7.11 - Stresses of Column Bars in Unit 8.

inelastic load cycles while the maximum compressive stress was approximate -100 MPa. The maximum tensile strain of corner bars recorded at joint face reached 4000 micro-strains, exceeding the yielding strain. However, the tensile yielding only concentrated at the joint face and did not penetrate into joint region. Note that there is a rapid change of stress in column exterior bars within joint centre height, indicating maximum bond stress occurred there. This trend is observed in every unit and agrees with the strut-and-tie model analysis depicted in Chapter 2.

The stress profile of interior column bars show a rather uniform distribution across the joint depth. With the progression of the test, the tensile stress at the ends of the joint increased gradually. The change of stress across the joint height was not so rapid as that in corner bars, indicating that required bond stress of interior bars passing through joint region was not significant. This trend justifies the assumption made in the analytical work of having no intermediate nodes in column interior bars, unless required for equilibrium.

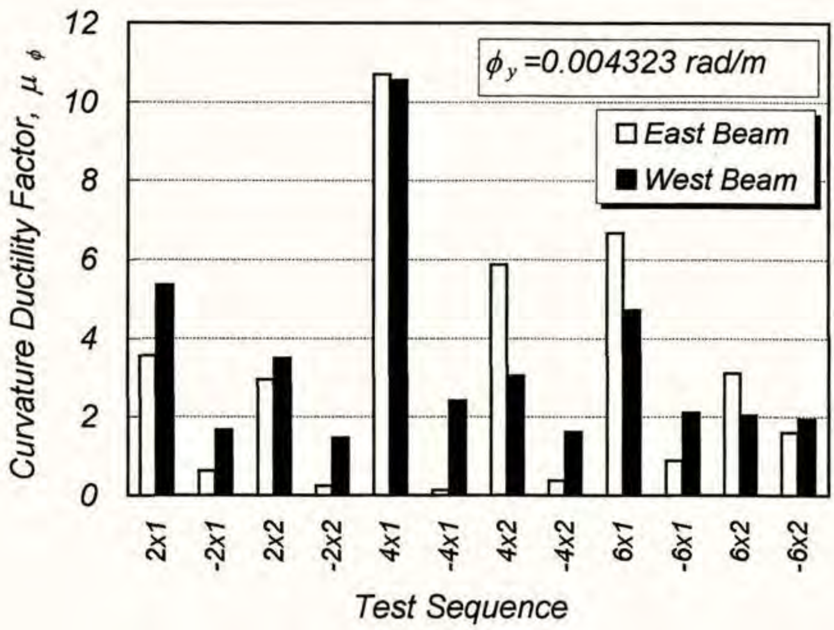

Figure 7.12 - Curvature Ductility Factors of Beam of Unit 8.

7.2.5 Beam Behaviour

7.2.5.1 Curvature Ductility Factors in Plastic Hinge

Curvature ductility factors in the plastic hinge regions are depicted in **Fig. 7.12**. A maximum value of 11 was recorded in the load cycle to $\mu_\Delta = 4x1$. It can be seen in this chart that the curvature ductility factors recorded in the positive load runs were generally larger than that in the negative load runs, particularly in the load cycle to $\mu_\Delta = \pm 4x1$. With reference to **Fig. 7.3**, it can be seen that the component of beam fixed-end rotation had a big increase in the load cycle to $\mu_\Delta = -4x1$ comparing with the component in the last load run. This is because total bond failure of top beam bars occurred in the load cycle to $\mu_\Delta = -4x1$, as had described in Section 7.2.4.3. While the component of beam fixed-end rotation increased due to bond failure of the top beam bars, the component of beam flexure deformation diminished, leading to small curvature ductility factors recorded in beams in the load cycle to $\mu_\Delta = -4x1$.

7.2.5.2 Beam Strain Profiles at the Level of the Longitudinal Reinforcement

Figures 7.13, 7.14 show the beam strain profiles at the level of the longitudinal reinforcement calculated from linear potentiometer readings. The maximum tensile strain at the level of both the top and the bottom beam bars was 2% and was recorded in the load cycle to $\mu_\Delta = 4x1$. It can be noticed that in the load cycle to $\mu_\Delta = 6x1$ the tensile strain recorded in the top and bottom bars close to the column faces did not increase anymore as compared with that was recorded in the previous load cycle. As had been discussed in the previous chapters, this phenomenon was always observed when bond failure of beam bars occurred. At this stage, the strains obtained using this method are no longer representing the average strains of the longitudinal reinforcing bars.

Strain profiles measured in the negative load runs show small values. This is possibly because in this unit, more and wider cracks occur in beams away from column faces in the positive load runs while cracks tend to concentrate on the interface cracks at the column faces in the negative load runs.

7.2.5.3 Beam Elongation

Figure 7.15 depicts the overall beam elongation measured during the test. It can be seen in this graph that the beam elongation occurred in the load cycle toward a new

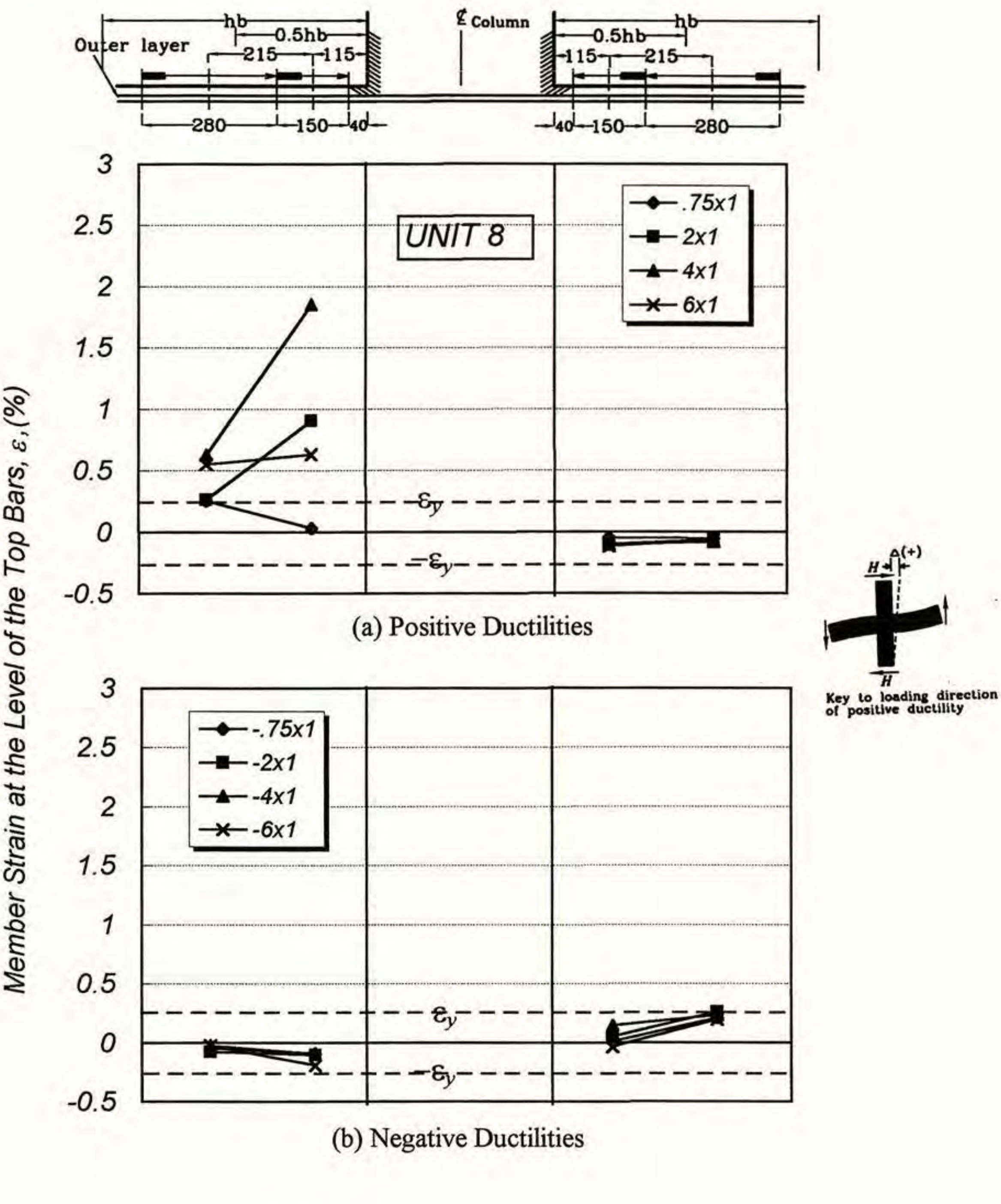

Figure 7.13 - Beam Strain Profiles at the Level of the Outer Layer of the Top Beam Bars of Unit 8.

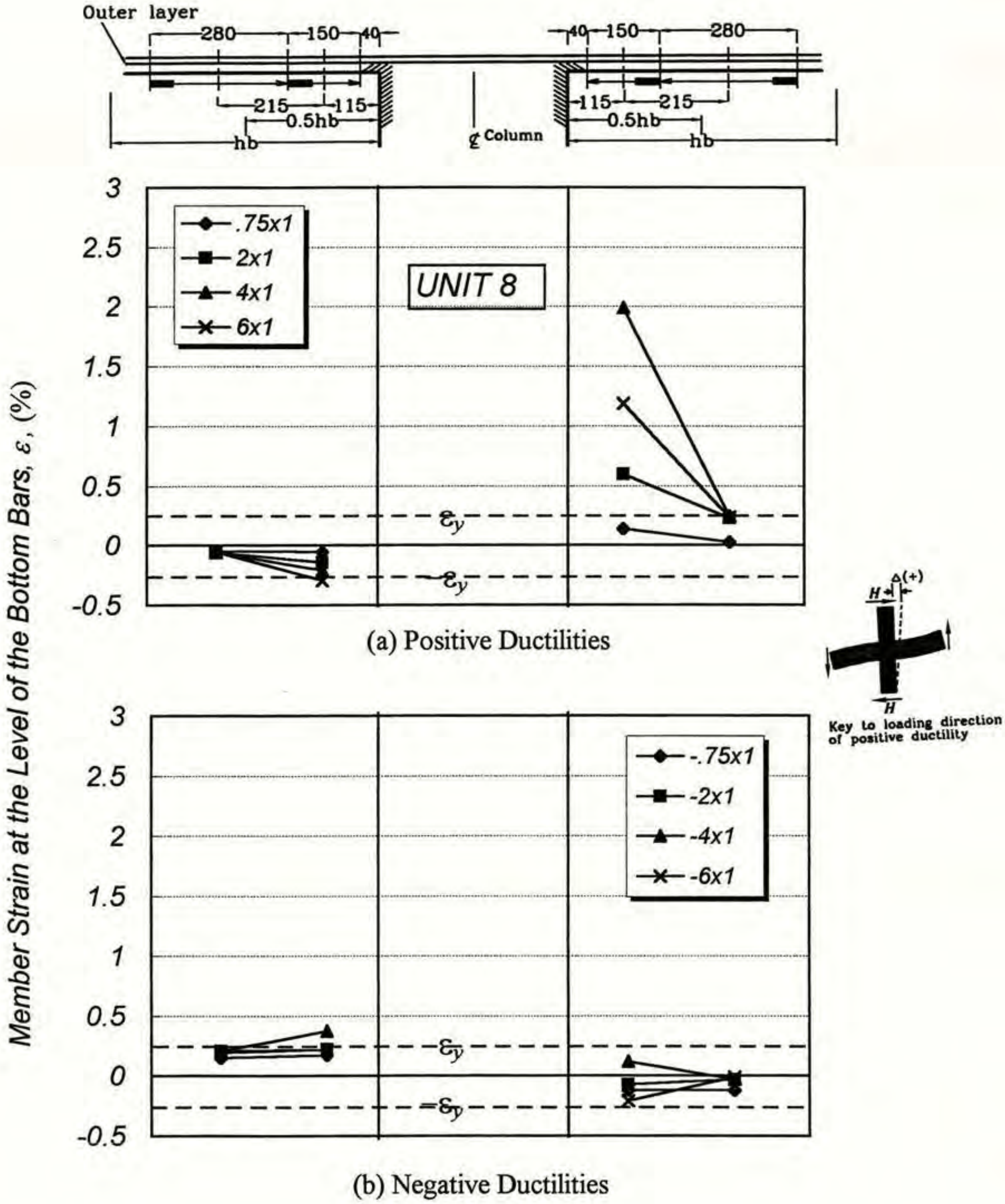

Figure 7.14 - Beam Strain Profiles at the Level of the Outer Layer of the Bottom Beam Bars of Unit 8.

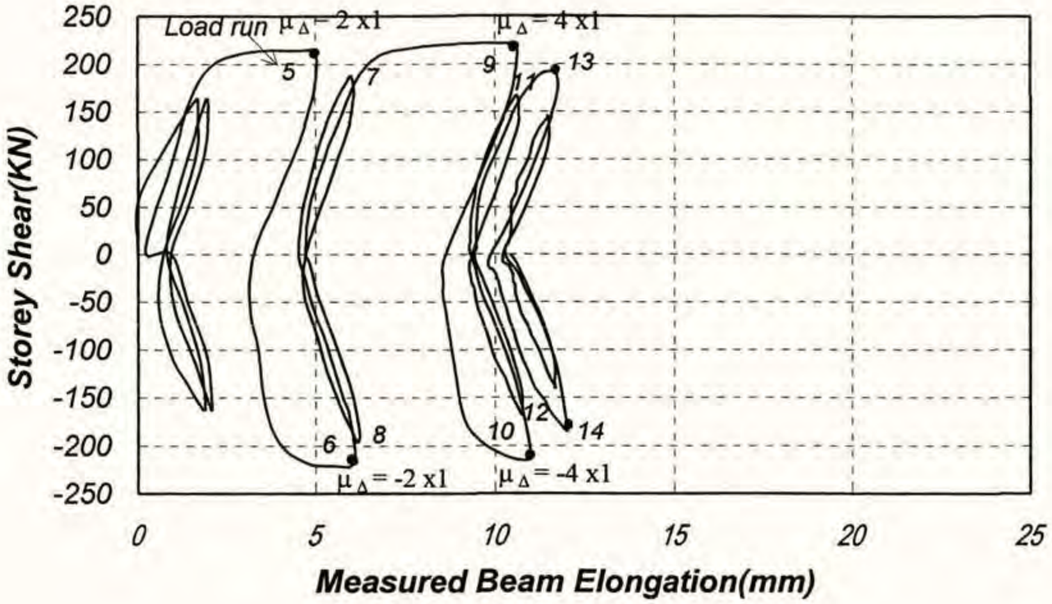

Figure 7.15 - Beam Elongation of Unit 8.

displacement ductility factor until the load cycle to $\mu_\Delta = -4x1$. In the successive load cycles, very little beam elongation took place sine other sources of lateral displacement governed the lateral displacement so that plastic hinge could not spread further along beams away from column faces. The total beam elongation measured at the end of test was 12 mm, equivalent to 2.2% of the beam height.

When comparing the beam elongation of Unit 8 and Unit 5 (see **Figs. 7.15** and **6.15**), it can be seen that the beam elongation of the two units are similar in magnitude. The maximum value recorded at the end of test in Unit 8 was slightly smaller than that in Unit 5. Note that the two units failed in similar modes. The responses of both units were dominated by beam fixed-end rotation and joint shear distortion. As a result, the beam elongation, which relates to the beam flexural yielding, of both units is very similar.

7.2.6 Column Behaviour

The columns were designed stronger than beams by taking into account the flexural over-strength of beams with a dynamic magnification factor equal to unity. As a result, the column flexural capacity, although larger, does not significantly exceed the sum of flexural capacity of framing beams. This explains the yielding of corner bars recorded at joint faces.

However, the yielding did not occur in column interior bars. Moreover, as had described in Section 7.2.4.5, the yielding of exterior column bars was not unrestricted and did not penetrate into the joint region. Note that some intrusion of yielding in some bars did not imply plastic hinges forming in columns. Also, as shown in **Fig. 7.1**, cracks in columns were much less and thinner than that in beams. Therefore, it can be known that the columns are stronger than beams in this unit, as expected.

7.3 CONCLUSIONS

1. Unit 8, had identical beam and column steel ratios and the same quantity of horizontal joint reinforcement of Units 5 and 6, except that the beam longitudinal reinforcement was lumped on the top and bottom chords. This unit was cast simultaneously with Units 5 and 6 and was tested under the same axial load ratio $N^* = 0.1A_gf_c'$. This unit, as well as Units 5 and 6, was designed to fail in the joint.

2. Test results of Unit 8 showed limited ductile performance. Beam-column joint shear failure and bond failure of top and bottom beam bars led to eventual failure of this unit.

3. Behaviour of this unit was compared with that of Unit 5. It was found that there was no significant difference between the lateral load-displacement responses of the two units. Both units failed in joint in combination with bond slip of beam bars.

4. It was found that the bond strength requirement of outermost layers of beam bars in Unit 5 is more severe than that in Unit 8. The comparison justifies the conclusion made in Chapter 6 that the design of anchorage of the outermost layers of beam bars needs to consider yielding in compression and beyond yielding in tension at the column faces.

5. Joint shear distortion in Unit 5 was less prevailing than that in the joint of Unit 8 when leading to failure. The more premature bond failure of outermost beam bars in Unit 5 resulted in larger beam fixed-end rotation, and hence, smaller joint shear distortion of Unit 5 than that in Unit 8 can be expected.

CHAPTER 8
DISCUSSION OF TEST RESULTS AND DESIGN RECOMMENDATIONS

8.1 DISCUSSION OF THE TEST RESULTS

8.1.1 Significance of the Yield Drift Level on the Seismic Design of Reinforced Concrete Moment Resisting Frames

8.1.1.1 General

In traditional force based seismic structural design, the stiffness of structural members in lateral load resisting systems needs to be adequately modeled, since the periods of vibration and, hence, the seismic forces are based on the global frame stiffness [F9]. In addition, assurance must be made for the structures to possess adequate stiffness to reduce non-structural damage during service life earthquakes and for earthquakes associated to the ultimate limit state, to prevent excessive P-delta effects from developing. Thus, attention needs to be paid to the stiffness of structures when they are designed to provide seismic resistance.

This section deals with aspects concerning the evaluation of the yield drift of components of moment resisting frames with emphasis on the yield drift of the units tested.

8.1.1.2 Theoretical Calculation of the Yield Drift of the Test Units

This section compares and discusses three methods for obtaining the inter-storey drift θ_y associated to the yield displacement Δ_y of a frame assemblie.

Method (1)

Traditionally the theoretical approach to obtain yield displacement and stiffness of a reinforced concrete frame is to use elastic theory with moment of inertia values that are based on the cross section of the member. In some cases a reduction is made to recognize the presence of cracking in the members. For example the Commentary of the Concrete

Structures Standard [S2] recommends the following values for the moment of inertia for rectangular beams and columns in frames designed for a ductility of $\mu_\Delta = 6$:

For rectangular beams, it is recommended that $I_e = 0.4I_g$, and for columns

$I_e = 0.4\ I_g$ when $N^* / A_g f_c' = -0.05$,

$I_e = 0.6\ I_g$ when $N^* / A_g f_c' = 0.2$,

$I_e = 0.8\ I_g$ when $N^* / A_g f_c' > 0.5$,

where I_e is the effective moment of inertia, I_g is the moment of inertia of the gross section and $N^*/A_g f_c'$ is the column axial load ratio taken positive in compression.

The storey yield displacement, Δ_y, and the yield drift ratio, θ_y, of a cruciform assembly can be established from elastic theory. With reference to **Fig. 8.1(a),** the storey yield displacement can be expressed as the sum of four main components.

$$\Delta_y = \Delta_b + \Delta_f + \Delta_c + \Delta_j \tag{8.1}$$

Where Δ_b is the beam flexural deformation, Δ_f is the beam fixed-end deformation, Δ_c is the column deformation and Δ_j is the joint shear deformation. Joint shear distortion Δ_j is ignored in practice. To indirectly account for this source of flexibility and to account for fixed-end rotation caused by strain penetration, the framing elements are assumed to encroach into the joint region as shown in **Fig. 8.1(e).**

If shear deformations are ignored in the beams and columns, the following equations can be deduced using elastic theorey for the assembly shown in **Fig. 8.1(e)**

$$\Delta_b = \frac{l_c}{3E_c l_b}\left[\frac{V_{b,left}\left(l''_{b,left}\right)^3}{I_{e,left}} + \frac{V_{b,rifgt}\left(l''_{b,right}\right)^3}{I_{e,right}}\right] \tag{8.2}$$

$$\Delta_c = \frac{2V_{col}\left(l''_c\right)^3}{3E_c I_{e,col}} \tag{8.3}$$

Where E_c is modulus of elasticity of concrete, which is calculated as $(3320\sqrt{f'_c}$ $+6900)$ MPa according to NZS 3101:1995 [S1]. $I_{e,left}$ and $I_{e,right}$ are the effective moment of

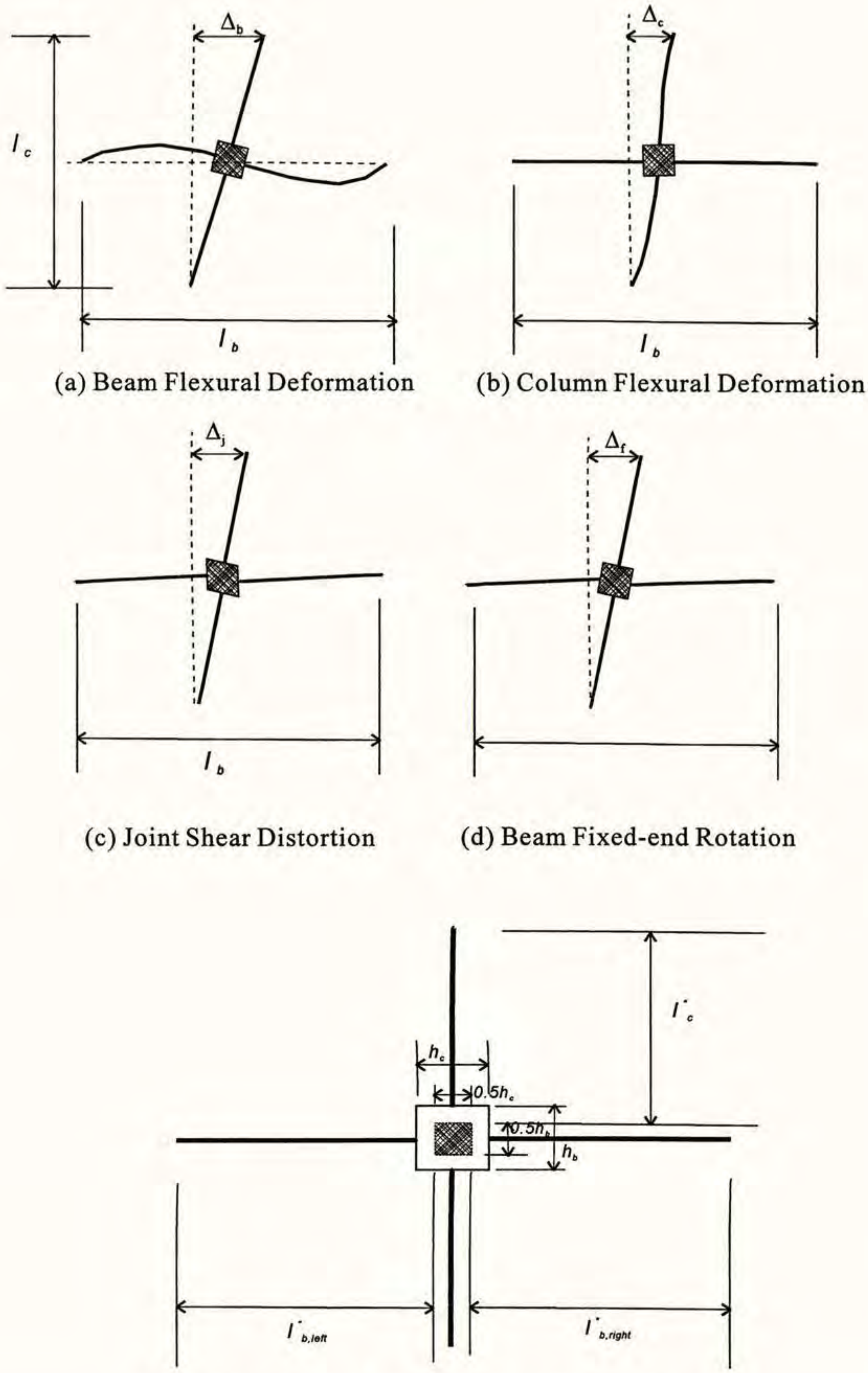

(a) Beam Flexural Deformation (b) Column Flexural Deformation

(c) Joint Shear Distortion (d) Beam Fixed-end Rotation

(e) Reduced Joint Size to Indirectly Account for Joint Shear Distortion and Yield Penetration.

Figure 8.1 - Sources of Flexibility in a Frame Assembly.

inertias of the left and right beam, respectively. $V_{b,left}$ and $V_{b,right}$ are the shear forces of left and right beam respectively when the theoretical ultimate lateral load is developed. l_c is the column height and l_b is the length of the beam measured from midspan on adjacent bays. Lengths $l''_{b,left}$ and $l''_{b,right}$ are the length of left and right beams measured from midspan to a distance of $0.25h_c$ within the joint (see **Fig. 8.1(e)**). V_{col} is the column shear force corresponding to the theoretical ultimate lateral load and l_c'' is the half column height as depicted in **Fig. 8.1(b)**.

Hence, the storey yield displacement is given by

$$\Delta_y = \frac{1}{3E_c}\left\{\frac{l_c}{l_b}\left[\frac{V_{b,left}\left(l''_{b,left}\right)^3}{I_{e,left}} + \frac{V_{b,right}\left(l''_{b,right}\right)^3}{I_{e,right}}\right] + \frac{2V_{col}\left(l''_c\right)^3}{I_{e,col}}\right\} \tag{8.4}$$

and the yield drift ratio θ_y, defined as Δ_y/l_c is

$$\theta_y = \frac{1}{3E_c l_b}\left\{\left[\frac{V_{b,left}\left(l''_{b,left}\right)^3}{I_{e,left}} + \frac{V_{b,right}\left(l''_{b,right}\right)^3}{I_{e,right}}\right] + \frac{2V_{col}\left(l''_c\right)^3}{I_{e,col}}\frac{l_b}{l_c}\right\} \tag{8.5}$$

when using the approach given by NZS 3101:1995, Eqs. 8.4 and 8.5 can be further simplified as $I_{e,right} = I_{e,left}$.

Method (2)

Method (2) is similar to Method (1) except that the effective moment of inertia, I_e is made strength-dependent. The following two equations, giving reasonable values for beams and columns with rectangular sections for use in conjunction with Eqs. 8.4 and 8.5, were derived from moment-curvature analysis,

$$\left(\frac{I_e}{I_g}\right)_{beam} = 36p + 0.07 \tag{8.6(a)}$$

$$\left(\frac{I_e}{I_g}\right)_{column} = 0.08 + 14p_t + 2\frac{N^*}{A_g f_c'}(0.6 - 8.3p_t) \leq 1 \qquad (8.6(b))$$

Where, p is the tensile longitudinal reinforcement ratio in a beam and p_t is the column total longitudinal reinforcement ratio. Equation 8.6 suggest that the effective moment of inertia decrease with a decrease in the reinforcement ratio. For a given design action the reinforcement ratio decreases as the reinforcing grade increases. As a result the effective moment of inertia is expected to decrease when high grade reinforcement is used for flexure. **Figures 8.2(a) and (b)** compare the effective moment of inertia recommended in the commentary of NZS 3101:1995 [S2] with those computed using Eq. 8.6 for the units tested in this research project. Note that when using Eq.8.4 in this approach $I_{e,left}$ is equal to $I_{e,right}$ only if the beams have equal top and bottom longitudinal reinforcement. The $(I_e/I_g)_{beam}$ value depicted in **Fig. 8.2(a)** for Unit 4 is the average value of top and bottom beam bars acting as tensile reinforcement in the left and right beams. The value of $(I_e/I_g)_{beam}$ for Units 5, 6 and 7 are based on Eq. 8.6(b) for columns with $N^* = 0$, since the longitudinal bars in these units were distributed along the web.

Method (3)

Priestley [P11] has recently proposed a procedure for estimating the yield drift ratio θ_y of a frame assemly. Such procedure is based on yield curvature calculations rather than on effective moment of inertia calculations. The use of yield curvature concept is attractive because of its simplicity. Generally the yield curvature of beams is insensitive to the longitudinal steel content. With the estimation of the beam yield curvature, the yield drift of the subassembly can be estimated by adding the flexibility of joint panel and columns. Priestley [P11] proposed the following equation for the yield drift ratios,

$$\theta_y = 0.5\varepsilon_y\left[\frac{l_b}{h_b}\right] \qquad (8.7)$$

Where h_b is the overall beam depth, ε_y is the yield strain of the longitudinal reinforcement and l_b is the beam span length as shown in **Fig. 8.1(a)**.

Note that the influence of column compressive load on the yield drift ratio was not

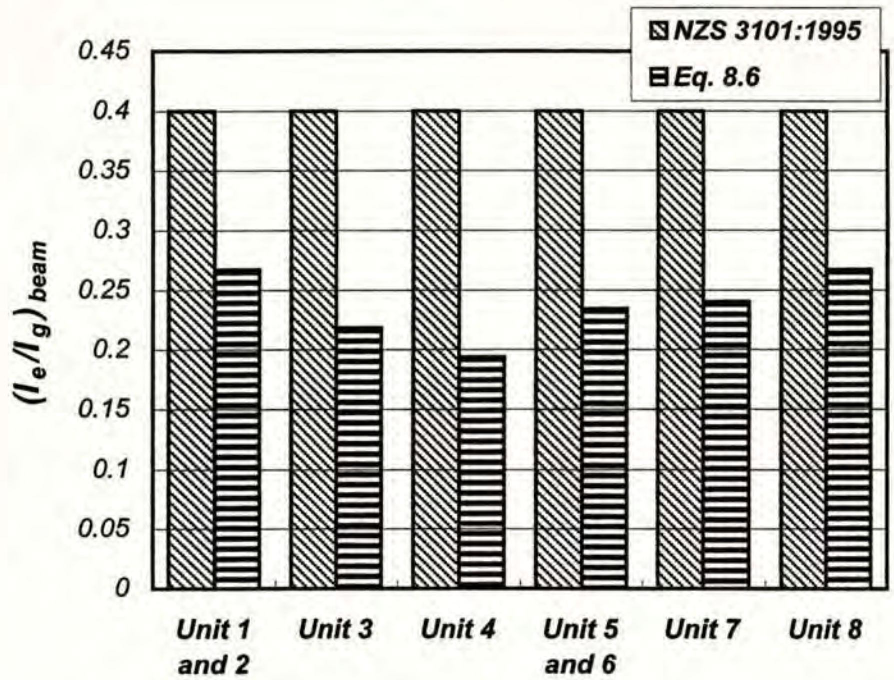

Figure 8.2 (a) - Effective Moment of Inertia of Beams of Test Units.

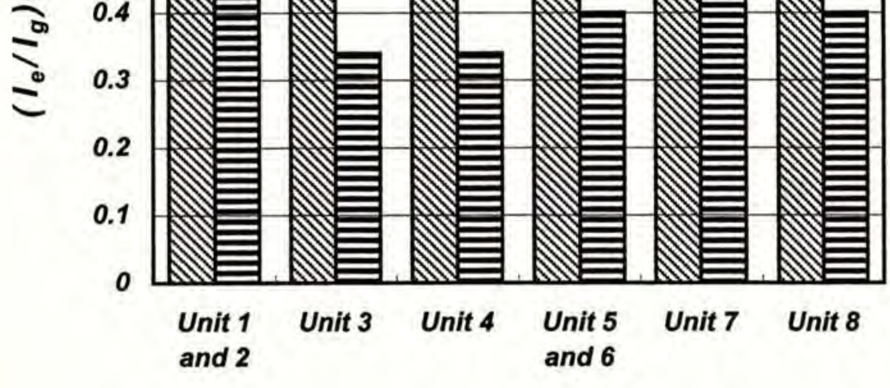

Figure 8.2 (b) - Effective Moment of Inertia of Columns of Test Units.

taken into account in Eq. 8.7 for the sake of simplicity. However, a slight dependency of the yield drift ratio and axial load in columns does exist. For example, Beckingsale [B3] had tested two units (Coded B2, B3, in Appendix B). These units were identical except for the amount of horizontal joint shear reinforcement. Unit B2 was tested under a column compressive load of $N^*/A_g f'_c = 0.045$ while the axial load for Unit B3 was $N^*/A_g f'_c = 0.442$. The measured yield drift ratios of these two units were 0.64, 0.44%, respectively. The calculate column displacement of the two units were found to contribute to 45% and 21% of the yield drift ratio at the reference yield displacement, respectively.

Tests on Units O3, O4 carried out by Otani et al. [O1] (see also Units coded O3 and O4 in **Appendix B**) also show a similar trend of reducing the yield drift ratio due to an increase on the column axial load. The column compressive loads applied on Units O3 and O4 was $N^*/A_g f'_c = 0.082$ and 0.305, respectively. These two units were basically identical except for the column compressive load and amount of horizontal joint shear reinforcement. The measured yield drift ratios of these two units were 1.08 and 0.81%, respectively. Again, the decrease of yield drift ratio was caused by the decrease of column deformation. The column deformations of the Units O3 and O4 were estimated to contributed to 19% and 9% of the yield drift ratio at the reference yield displacement, respectively.

Tests conducted in this study further justify the dependency of column compressive load and the yield drift of a frame. Taking for example Units 1 and 8, the measured yield drift ratios of these Units were 0.65 and 0.97%, respectively. The column deformations associated to the yield drift in these Units were 20% and 40% of the reference yield drift, respectively. Unit 1 was tested under a column compressive load of $0.43N^*/A_g f'_c$, while the axial load applied to Unit 8 was $N^*/A_g f'_c = 0.1$. The comparison described above conclusively shows that the increase of column axial load does reduce the yield drift due to the decrease of column deformation.

In light of the test results discussed above, Eq. 8.7 proposed by Priestley [P11] was slightly adjusted to account for the dependency of the yield drift to the axial load in columns as it is used to predict the yield drift of a frame subassembly. The proposed equation for estimating the yield drift ratio is :

$$\theta_y = \lambda \varepsilon_y \frac{l_b}{h_b} \tag{8.8}$$

where $\lambda = 0.69\text{-}0.65N^*/(A_g f_c')$ when $0.1 \le N^*/(A_g f_c') \le 0.45$.

and $\lambda = 0.63$ when $N^*/(A_g f_c') < 0.1$

It should be noted that the yield drift predicted by Eq. 8.8 is smaller than that given by Eq. 8.7 when $N^*/A_g f_c' \ge 0.3$. For joints having column compressive loads less than $0.3N^*/A_g f_c'$, the proposed equation gives slightly larger values than those predicted by Eq. 8.7. The above equation was applied to predict the inter-storey drift corresponding to the reference yield displacement of each test unit.

8.1.1.3 Comparison of Measured and Predicted Yield Drift

Figure 8.3 compares the values of the yield drift ratio θ_y predicted using the three methods with the values measured in the tests carried out in this study. The values shown in the chart have been normalized by the measured yield drift ratios. It is evident that the NZS 3101:1995 approach results always in a significant underestimation of θ_y. This is because the values of ratio I_e / I_g recommended in NZS 3101:1995 for beams were calibrated for members designed using Grade 300 reinforcement having a tensile reinforcement ratio of around 1%. Note that the experimental programme in this study used Grade 500 bars as longitudinal reinforcement in the beams and columns. As a result, the reinforcement ratios for both the beams and columns were less than that required had Grade 300 reinforcement been used. Eq. 8.6 in Method (2) closely shows the consequence of decreasing the steel content. For this reason the yield drift ratios are larger than those calculated using the I_e / I_g ratios recommended by NZS 3101:1995.

Although none of the methods can be claimed to accurately predict θ_y in all cases, Method (2) predicts well the yield drift ratios for Unit 1 to 4 and Unit 8 which had lumped top and bottom beam reinforcement. Method (2) underestimates the yield drift ratio for Unit 5 to 8 that had the beam reinforcement distributed through the web. Method (3) using Eq. 8.8 gives a reasonable prediction for all units.

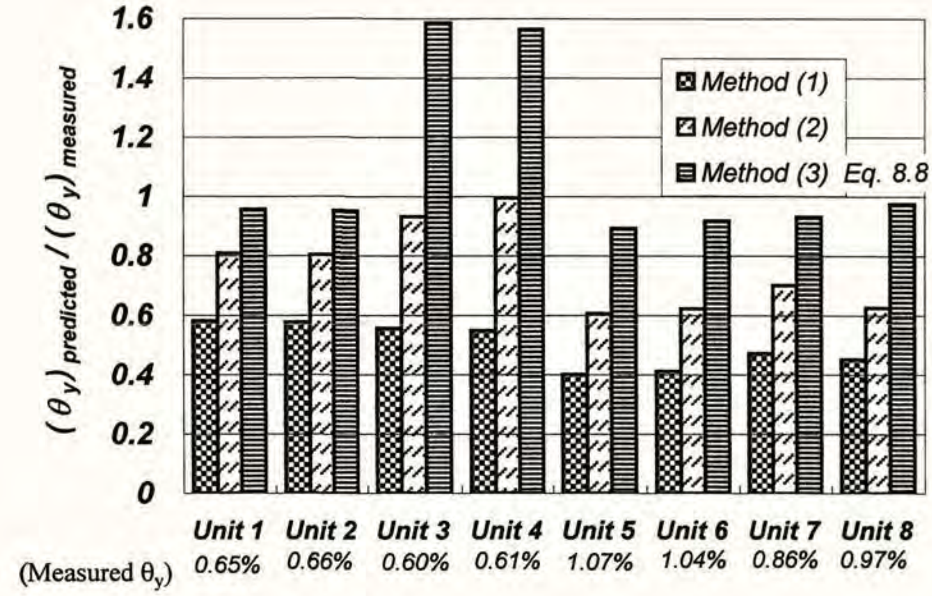

Figure 8.3 - Comparison of Predicted and Measured Yield Drift of Test Units.

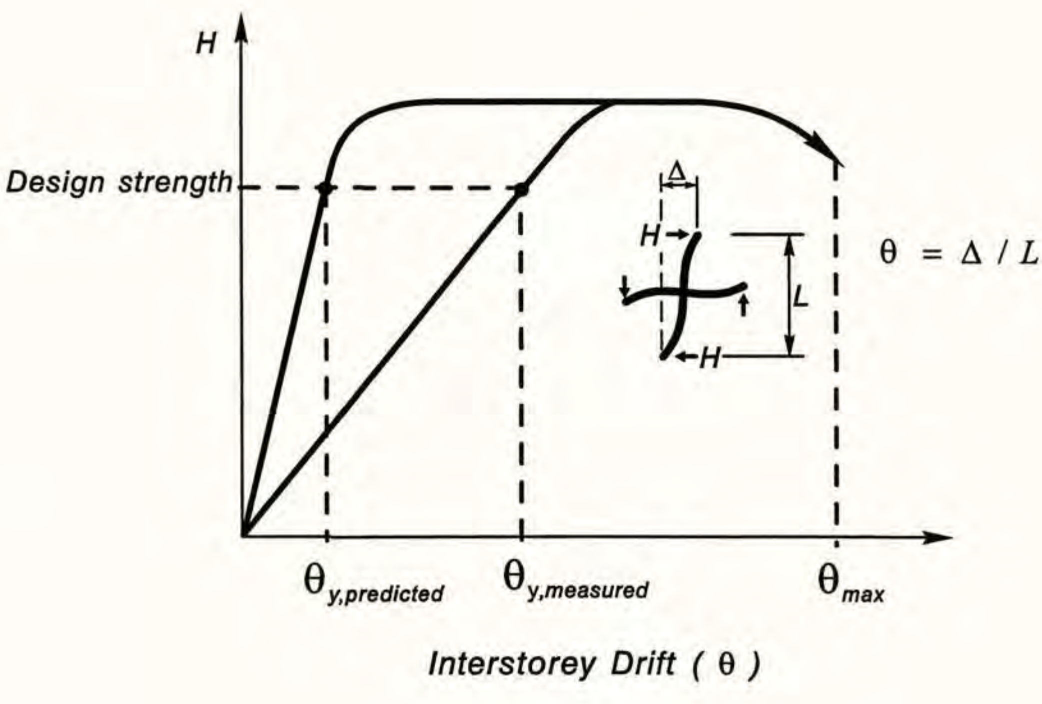

Figure 8.4 - Significance of Yield Drift on the Displacement Ductility Factor at Maximum Drift Limitation.

8.1.1.4 Available Displacement Ductility And the Significance of Using Grade 500 Longitudinal Reinforcement

It is known that structures are required to be designed and to be detailed with adequate lateral load strength and displacement ductility capacities in order to survive a major earthquake without collapse. The Concrete Structures Standard, NZS 3101:1995 [S1], permits a design displacement ductility capacity up to 6 in the design of moment resisting frames. On the other hand, the Loading Code, NZS 4203 :1992 [S3], limits the inter-storey drift at the ultimate limit state to 2% when using equivalent static analysis or to 2.5% when using time history inelastic analyses.

In the traditional force-based design method, a global ductility factor is chosen to find design lateral forces. The critical regions in the structure are then detailed according to the chosen ductility factor and on the collapse mechanism chosen. The inter-storey drifts of the structure under the design seismic actions must be within the limit permitted.

The displacement ductility of the test units corresponding at 2.5% inter-storey drift ranged between 2.6 and 4.2 for units in which beams were conventionally reinforced, as shown in Table 8.1. This range indicates that the drift limitations may control the design of many frames even if they were to be detailed for full ductility. In other words, many ductile frames will reach the interstorey drift limitations before achieving the displacement ductility factor of 6. Priestley [P11] first highlighted this issue of concern and developed a method to establish an appropriate displacement ductility factor for force-based design. He suggested that the maximum displacement ductility factor must be selected by taking into account the interstorey drift limitations. According to the test results obtained in this study and the theoretical predictions made by Method (2) and (3), it is evident that this effect will be more pronounced when Grade 500 longitudinal bars are used.

Table 8.1 - Displacement Ductility of the test Units at 2.5% Inter-storey Drift

	Unit 1	Unit 2	Unit 3	Unit 4	Unit 5	Unit 6	Unit 7	Unit 8
μ_Δ	3.7	3.7	4.2	4.2	2.3	2.4	2.9	2.6

An issue of great significance for designers is that the recommendations given in the Commentary of NZS 3101:1995 [S2] for estimating an effective moment of inertia of beams and columns will possibly lead to a significant overestimation of the member's stiffness if high grade bars are used as longitudinal reinforcement. Such disparity in stiffness will possibly lead to low inter-storey drifts in the analysis and to inter-storey drift demands in the structure larger than those initially expected. It appears that an iterative solution of stiffness modeling would be necessary. A simple alternative that may somehow recognize the effect of grade of the reinforcement is to modify the effective moment of inertia values recommended by NZS 3101:1995. Table 8.2 shows the proposed modifications. Note that the values shown are independent of the longitudinal reinforcement ratio but provide suitable values for design. No attempt should be made to use the effective moment of inertia values proposed in Table 8.2 when conducting a seismic assessment or when checking for interstorey drift limits. In these cases, actual values of I_e can easily be determined once the reinforcement layout is known.

The assessment of yield drifts of test units conclusively show that, apart from some low rise buildings in which inter-storey drift limits are easily met, frames in high rise buildings and with typical section sizes should only be designed for limited ductility response when using Grade 500 bars as longitudinal reinforcement in beams and columns.

Table 8.2 – Suggested Effective Moment of Inertia of Reinforced Concrete Members When Using Different Grades of Longitudinal Reinforcement.

Member types		**I_e (ultimate limit state)**	**Note**
Rectangular beams		$120I_g/f_y$	$(300/f_y)\leq 1$
Columns	$N^*/A_g f'_c \geq 0.4$	$0.8I_g$	
	$0\leq N^*/A_g f'_c<0.4$	Interpolate between $160\,I_g/f_y$ and $0.8I_g$	$(400/f_y)\leq 1$
	$N^*/A_g f'_c \leq 0$	$160\,I_g/f_y$	$(400/f_y)\leq 1$

8.1.2 Bond Stress Distribution of Beam and Column Bars in the Joint and Its Influence on the Joint Strength

With the observation on the test results and analytical work, it can be realized that the bond stress distribution of beam and column bars is strongly influenced by the amount of the column interior bars and the horizontal joint reinforcement. With reference to the longitudinal beam bars in joint region of the test units, it can be seen that from the elastic load cycles the bond resistance is significantly reduced and no bond stress develops over the region from the column face to the first layer of column interior bars where beam bars are subject to flexural tension. Test results indicate that the tensile strains measured on the top and bottom beam bars exceeded 76% of the yield strain in the elastic load cycles. Apparently at this stage, bond deterioration had initiated owing to the splitting of concrete surrounding the bars caused by strain penetration and by the formation of cracks in the beams at the column faces. Bond stresses rose significantly at the location of the first column interior bar (see the calculated bond stress of all test units). Obviously, the presence of column interior bars significantly improves the bond resistance of beam bars. This justifies the bond stress law postulated by Restrepo et al. [R1] (see **Fig.2.2**).

Figure 8.5 explains the influence that interior column bars have on the stress profiles and bond resistance of longitudinal beam bars. In the joint depicted in **Fig. 8.5(a)**, there are no interior column bars. The bond force in the longitudinal beam bars can only develop over the length of the joint where the column compressive stress block acts. Very little bond can develop in these bars elsewhere since bond deterioration in this region occurs prematurely due to splitting cracks along the beam bars. In this kind of joint, bond failure is likely to occur prematurely unless significant column compressive load is present. As a result, beam bars in compressive region of the beam at the column face may be in tension.

The joint depicted in **Fig. 8.5(b)**, in which interior column bars are present in the middle of the joint, bond conditions beyond the column concrete compressive stress block are improved providing the column bars remain elastic. This is because bond splitting cracks are controlled. As a result, bond deterioration of beam bars may occur less prematurely than in the joint shown in **Fig. 8.5(a)**. The enhancement of the anchorage conditions due to the presence of interior column bars enables the beam bars to develop

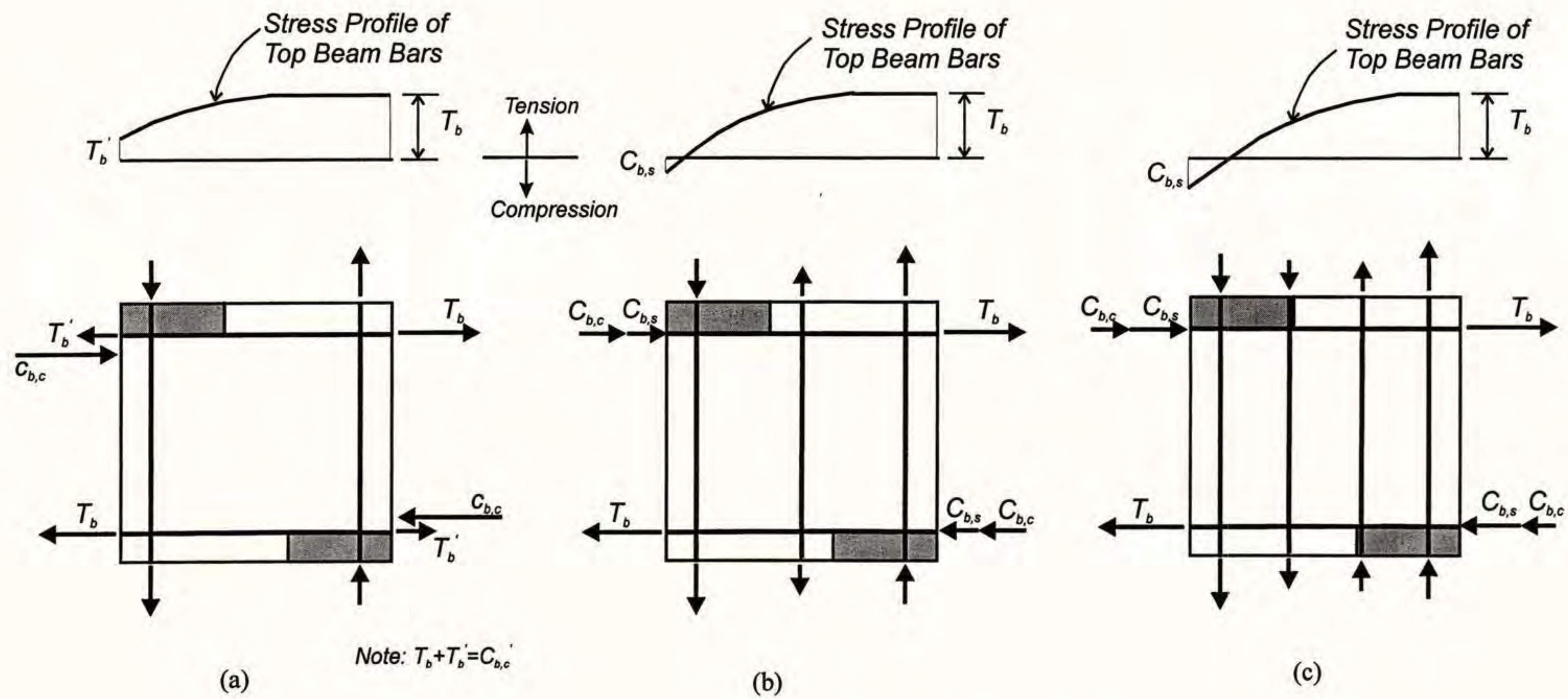

Figure 8.1 - Influence of Column Interior Bars on the Stress Profile of Beam Bars Anchored in the Joint Region.

Bmprofl.cdr

compressive stresses at the column face.

In the joint depicted in **Fig. 8.5(c)**, in which more column interior bars are added, the bond resistance of beam bars beyond column concrete compressive region is further enhanced due to the more evenly distributed clamping pressure provided by the interior column bars. In such joint, bond deterioration would be further deferred. As a result, larger bond forces, and hence, better anchorage conditions exist for the beam bars.

Figure 8.6 illustrates the influence of quantity of the horizontal joint reinforcement on the bond resistance of column exterior bars. In joint (a), in which the ratio V_{sh} / V_{jh} is small, the gradient of the column bar force is smaller than that in joint (b) in which the ratio V_{sh1}/ V_{jh} is larger is exerted. Bond stress in the joint shown in **Fig. 8.6(a)** tends to concentrate at the beam compressive region. In the joint shown in **Fig. 8.6(b)**, bond stresses develops in the region beyond beam compressive region.

Although the bond force distribution of beam and column bars passing through the joint region is affected by amount of column interior bars and by the horizontal joint reinforcement, the influence of the bond force distribution does not significantly affect the joint shear strength for commonly used deformed bars, as discussed in Chapter 2. Therefore, the limitation bar sizes passing through the joint region should be more concerned in the issue of performance rather than the joint strength. Note that some tests conducted by Hakuto [H1] showed similar trends. He tested two interior beam-column joint subassemblies without joint shear reinforcement, Unit O4 and O5. The overall column depth to beam bar diameter in the joint of Unit O4 was $h_c/d_b = 25$ and $f_c' = 53$ MPa, which satisfied the requirements of NZS 3101:1995. In the Unit O5, $h_c/d_b = 19$ and $f_c' = 33$ MPa, which did not satisfy the requirement of NZS 3101:1995. Although slip commenced at a lower ductility factor for the second unit, the lateral load versus lateral displacement hysteresis loops for the two units are almost identical for cyclic displacements up to a displacement ductility factor of $\mu_\Delta = 6$ (see page 460, 461 in **Appendix B)**. The joints in both units eventually failed in a very similar mode. The beam bar strain profiles in both units were very similar in spite of the fact that the ratio of the column depth to beam bars diameter was quite different. The only noticeable difference was that the joint shear stress at cracking of the joint region for unit with poor bond of beam bars was larger than that of the unit with better bond [H1].

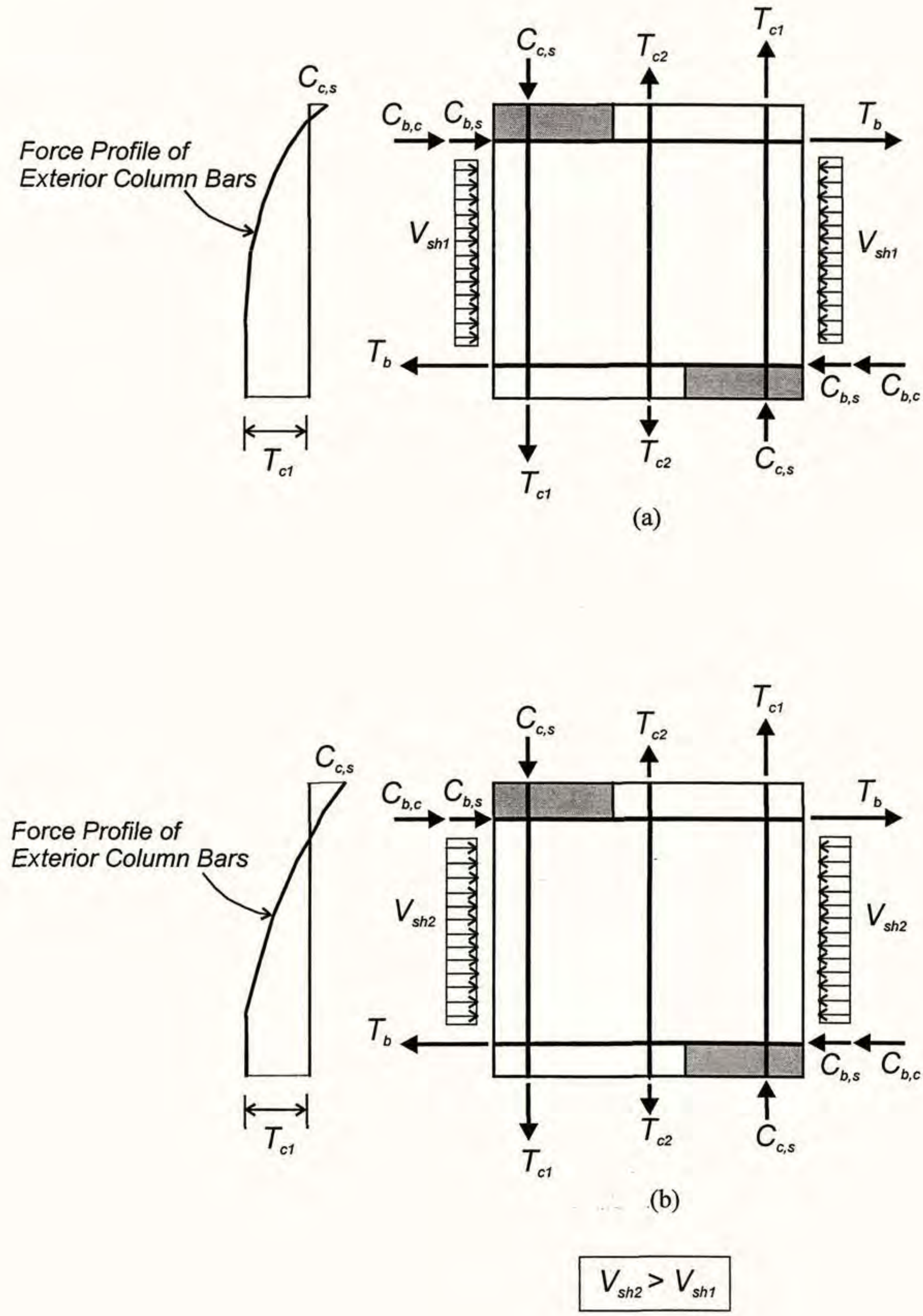

Figure 8.6 - Influence of V_{sh} on the Stress Profile of Exterior Column Bars.

8.1.3 Influence of Column Axial Load Level on the Joint Shear Strength

The behaviour of Units 1 and 2 endorses the finding of the analytical work that column compressive loads are not always beneficial to the joint strength. In those particular cases where the joint shear stress is large, column axial loads beyond some level may cause the compressive stress within the diagonal compression stress field to exceed the compressive strength of the cracked concrete in the joint. This strength is influenced by the magnitude of the strains in the transverse direction. In such joints, extra horizontal joint shear reinforcement is required to reduce the transverse strain so that premature strength degradation can be avoided. Premature joint failure in Unit 1 and adequate joint performance in Unit 2 suggest that the current design requirement of joint shear reinforcement given by the Concrete Structures Standard, NZS 3101:1995 [S1] for joints subjected to high column axial loads and high joint shear stress should be reviewed. **Figure 8.7** illustrates the quantity of horizontal joint shear reinforcement provided in Units 1 and 2 and that required by NZS 3101:1995 for ductile frames. It can be seen that the quantity of horizontal joint reinforcement provided in both units exceeds that required by NZS 3101:1995. Unit 2, which was designed according to the analytical model, had 95% more joint shear reinforcement than that required by NZS 3101:1995 [S1]. It is clear that when column compressive load reaches $0.43f_c'A_g$, the requirement of horizontal joint reinforcement given by the design standard is not sufficient to prevent diagonal compression failure of joint from occurring at ductility level lower than expected.

8.1.4 Influence of the A_s'/A_s Ratio on the Joint Shear Strength

Comparison of the test performance of Units 3 and 4 justifies the analytical finding that the influence of A_s' / A_s ratio of beam bars on the joint strength is insignificant. Unit 3 had equal bottom and top beam longitudinal reinforcement, $A_s'/A_s=1$, while Unit 4 had $A_s'/A_s = 0.5$. The hysteresis loops of Units 3 and 4 were almost identical and the cracking appearance of two units at the end of the test are very similar, see **Figs. 8.8 and 8.9**. Bond failure occurred in the top beam bars of Unit 4 at a later stage than the top bars in Unit 3. This was due to the smaller compressive stress being resisted by the beam bars at column faces in Unit 3. As a result, the lateral load capacity in the load cycle to $\mu_\Delta = 6$ of Unit 4 was larger than that of Unit 3. However, the slightly higher input joint shear force in this load cycle did not deteriorate the joint of Unit 4, indicating that the joint had been

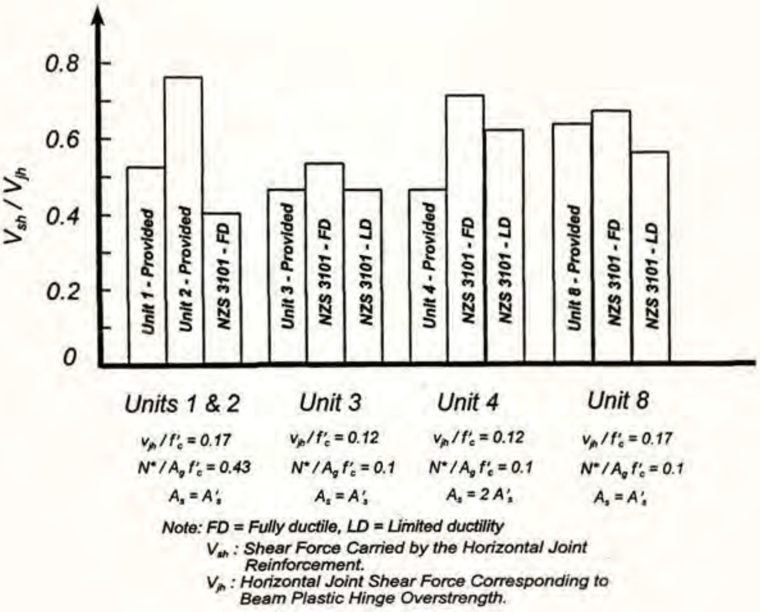

Figure 8.7 – Comparison of Horizontal Joint Reinforcement in Test Units and Code Requirements for Joints of Fully Ductile and Limited Ductility Frames.

adequately reinforced.

Figure 8.7 also compares the amount of horizontal joint reinforcement provided in Units and 4 with that required by NZS 3101:1995 for joints of fully ductile and limited ductility frames. The amount of horizontal joint reinforcement provided in Unit 3 is similar to that required by NZS 3101:1995 for joints of limited ductility frames. The amount of horizontal joint reinforcement provided in Unit 4 is only 64 and 74 % of the amount required by the standard for joints of fully ductile and limited ductility frames, respectively. Adequate behaviour of Unit 4 indicates that the requirement of horizontal joint shear reinforcement given by NZS 3101:1995 is unduly stringent. Note that the approach in NZS 3101:1995 is based on the diagonal concrete strut-steel truss model. In this model, the required quantity of horizontal joint shear reinforcement depends on the bond force of beam bars being allocated to the truss mechanism [S1] [C1]. As a result, Unit 4 in which the area of top beam longitudinal reinforcement is twice that of bottom beam bars requires 33% more horizontal joint reinforcement according NZS 3101:1995 than Unit 3. The insignificant role of bond stress and the A_s'/A_s ratio, as described in Chapter 2 and again in Section 8.1.2 suggests that the design recommendations given by NZS 3101:1995 for joints with beams

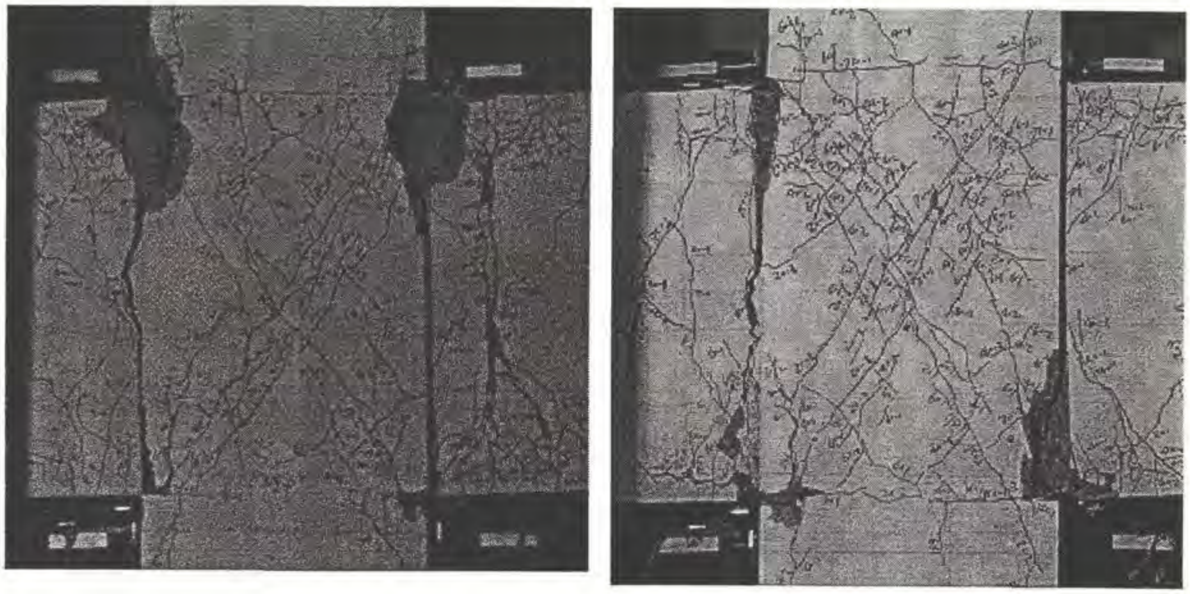

(a) Unit 3 at $\mu_\Delta = -6x2$ (b) Unit 4 at $\mu_\Delta = -6x2$

Figure 8.8 – Cracking Appearance of the Joints of Unit 3 and 4 at the end of tests.

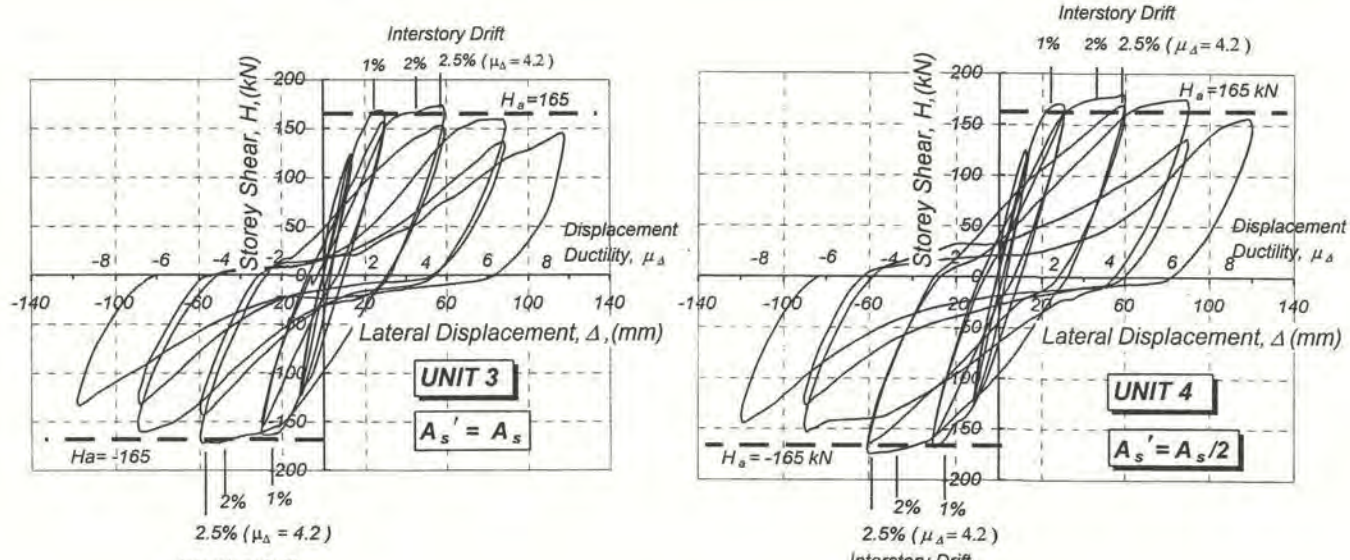

Figure 8.9 - Comparison of the Lateral Hysteresis Response of Units 3 and 4.

incorporating unequal top and bottom reinforcement should be reviewed.

8.1.5 The Role of v_{jh} / f_c'

The analytical work and test results in this research programme conclusively show that joint shear stress ratio, v_{jh} / f_c', plays an important role on the joint strength. Joint strength is normally governed by failure of the diagonal compression field that develops in the joint panel. Consequently, the joint strength would strongly depend on ratio v_{jh} / f_c' . Note that this ratio is a primary design factor in the Modified Compression Field Theory developed by Collins and Michell [C5] and is adopted in the Canadian Standards for shear design of reinforced concrete beams and columns [C4]. As mentioned in Section 2.2.4.3, the design recommendations in NZS 3101:1995 already recognizes the influence of this factor but the weight given to it is rather limited. The consequence of the low weight is that large numbers of joints possessing joint shear stress less than $0.14f_c'$ are being detailed with unnecessary amounts of horizontal joint reinforcement.

The satisfactory performance of Units 3 and 4, together with the trends given by the analytical work discussed in Chapter 2 show that joints having ratios v_{jh} / f_c' less than 0.14, the minimum requirement of joint shear reinforcement suggested by NZS 3101:1995, V_{sh} / V_{jh} = 0.4, is able to provide enough joint shear strength to ensure ductile performance in frames forming beam-sway mechanisms.

8.1.6 Study of Frame Sway Mechanisms with Joint Failures

The test of Unit 1 showed that despite that crushing of the concrete occurred in the joint, the relatively high column compressive load, $N^* = 0.43f'_cA_g$, was always sustained. In other words, the gravity load support capacity of the columns did not deteriorate due to the failure of the joint. Note that in a statically determinate structure such as a cruciform test assembly, significant loss of lateral load capacity and degradation of stiffness could cause frame instability. However, behaviour observed in Unit 1 suggests that in statically indeterminate frame structures, failure of interior beam-column joints after plastic hinges forming in the beams may not cause catastrophic failure. This is especially relevant when conducting seismic assessment of older building structures as in new designs it is inexpensive to be conservative.

It should be noted that the consequence of failure on gravity load support capacity due to failure of exterior or interior joints is quite different than an interior joint. Evidence of past earthquakes have shown that failure of exterior joints may cause loss of support to gravity loads, see for example **Fig. 1.3**. As a result, partial collapse of buildings or bridges may occur. Thus it is assumed that failure of exterior joints in the mechanisms studied below do not fail on exterior joints.

Figures 8.10 and **8.11(a)** show two possible frame sway mechanisms involving joint plasticity after a beam sway mechanism develops and is not maintained over further lateral displacement due to the shift of plasticity from the beam into the joints and into some columns. The development of such mechanisms is relevant to the seismic assessment of older buildings. **Figure 8.10** depicts a frame mechanism in which interior beam-column

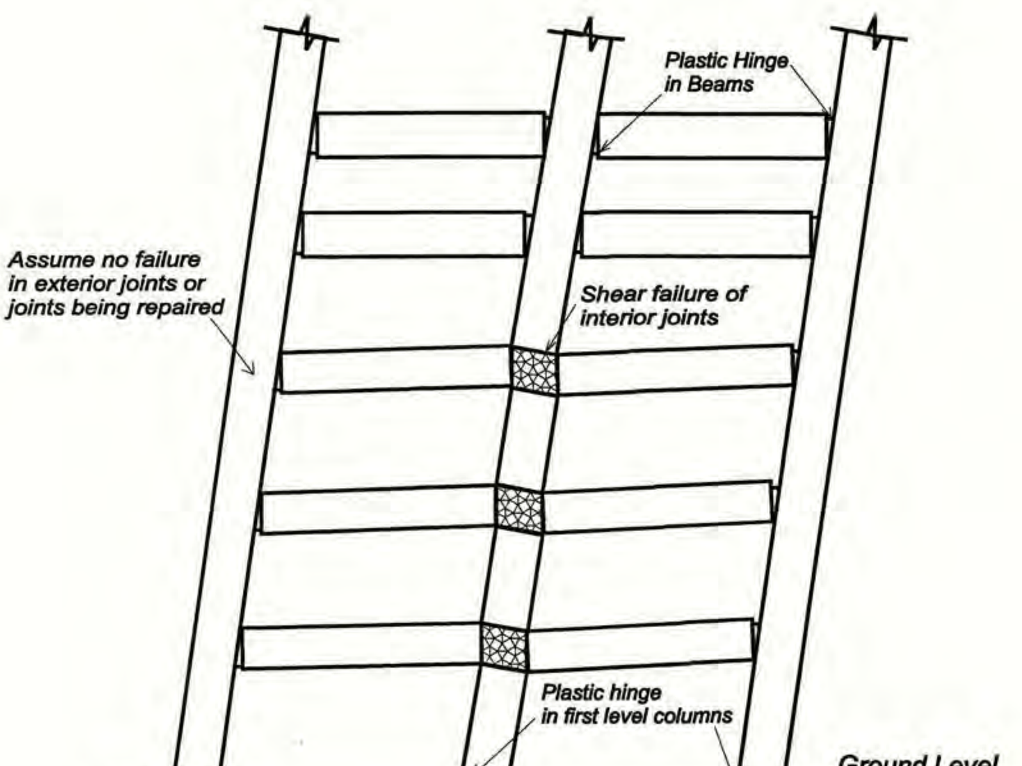

Figure 8.10 - Sway Mechanism of a Moment Resisting Frame
with Interior Joint Shear Failure Occurring in Several Levels.

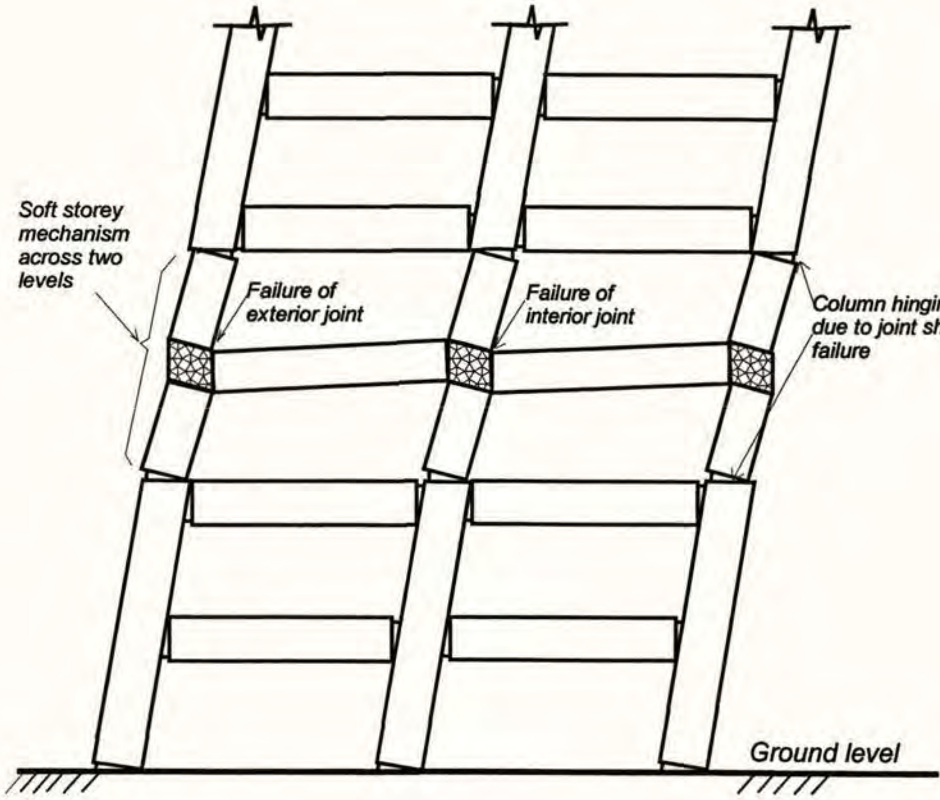

(a) - Soft Storey Mechanism Caused by Joint Shear Failures in Combination with Column Hinging.

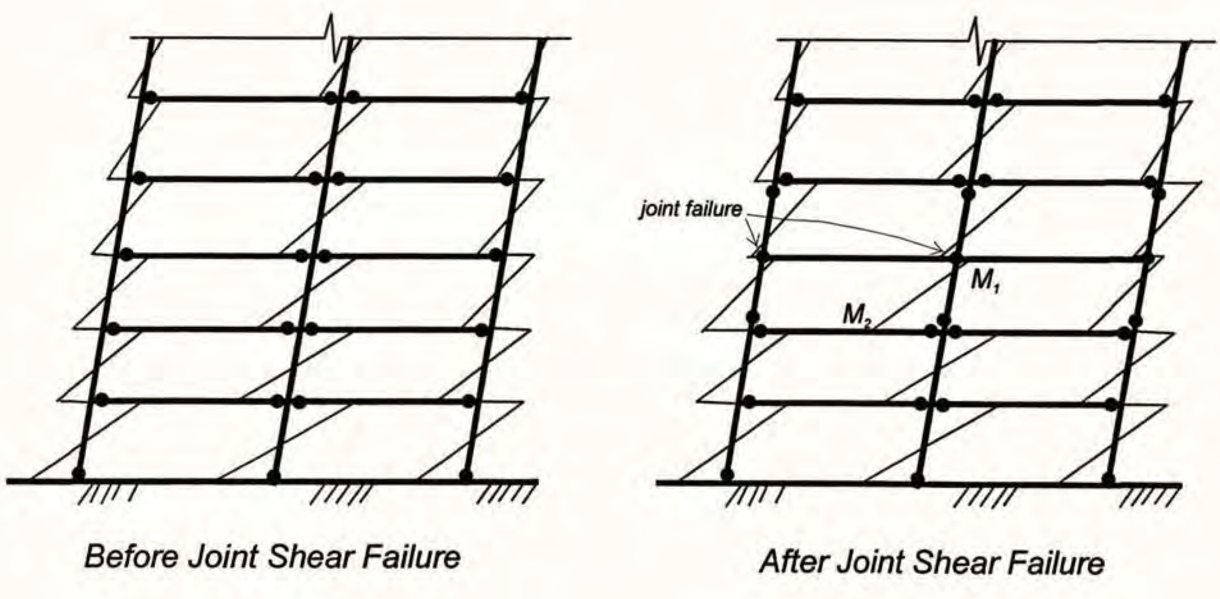

(b)- Bending Moment Diagrams in Columns before and after Joint Shear Failure.

Figure 8.11 - Soft-Storey Mechanisms Involving Beam-Column Joint Failures.

joints fail in some levels while plastic hinges form in the beams at the faces of the interior column. It should be noted that according to the test results, rotation of the beam plastic hinges diminishes after joint failure occurs. Joint shear distortion can contribute to a significant portion of the lateral displacement once joint failure develops. As shown in **Fig. 8.10**, this kind of joint failure is unlikely to cause a soft-storey mechanism.

Further study was carried out on the mechanism in which joint failure occurs together with column hinging. **Fig. 8.11(a)** depicts the mechanism studied. The development of this mechanism is described as follows. Bending moments of columns immediately above and below the failed joints may decrease due to the loss of shear strength in the joint. As a result, the columns have to carry the same shear force, which results in a considerable increase in the moment demand at the farther ends, see **Fig. 8.11(b)**. If columns are not designed with enough flexural capacity greater than M_2, plastic hinges can form at the column ends. As seen in **Fig. 8.11(a)**, the consequence of the increase of moment demand is the development of a soft storey mechanism across two stories. Because columns have small curvature ductility capacities, collapse of the building in the stories in which soft storey mechanism occurs is quite likely.

In New Zealand, where a strict capacity design procedure is followed in design, column design moments are calculated from the flexural capacities of adjacent beams taking into account flexural over-strength and multiplied by a dynamic magnification factor that accounts for higher modes [S1][P2]. Columns generally possess ample strength reserve against developing plastic hinges, except at their bases. Therefore, the frame sway mechanism depicted in **Fig. 8.11(a)** is not likely to occur in structures in which capacity design procedure has been applied.

For the frame structures designed without applying capacity design principles, columns are prone to form plastic hinges due to the failure of the joints. As a result, a soft storey mechanism involving beam-column joint failures could eventually develop. It is believed that the mechanism combined by joint shear failure and column hinging is the only possibility that catastrophic failure can be induced by deficient joints.

It should be noted that the failure mechanisms described above are associated with the survival limit state. At this stage, the corresponding maximum inter-storey drift is likely to be around 2% or greater. Poor energy dissipation and repair are no longer a main concern according to the current design philosophy. Note that according to AIJ design guidelines [A5], failure of beam-column joint is permitted as long as frames perform in a ductile manner up to more than 2% of inter-storey drift. This also recognizes that joint shear failures occur in the survival limit state the failure does not have significant effect on the overall building behaviour prior to this level of interstorey drift.

According to the above discussion, it can be said that in New Zealand, where structures are designed using capacity design principles, failure of interior joints after plastic hinges form in beams, if this ever occurs, is not likely to cause collapse, providing that failure in exterior joints is always precluded. The theoretical framework of joint design established in this study (see **Fig. 8.12(a)**) establishes that unless joints are designed with $v_{jh,e} / f'_c \leq 0.3$, joint degradation will eventually occur. The proposed design method requires horizontal joint reinforcement to preclude joint failure before plastic hinges form in the beams and defer the occurrence of joint degradation to a late stage associated with the survival limit state. Moreover, by adopting a 95% confidence limit, see **Fig. 8.9(a)**, and the failure criteria of 10% drop of lateral load capacity used in the calibration of the model, additional reserve against early joint failure is provided. As a result, it may be said that the proposed theoretical frame of joint design is able to ensure satisfactory design without violating the seismic design philosophy of reinforced concrete structures adopted in New Zealand.

8.2 DESIGN RECOMMENDATIONS FOR JOINTS INCORPORATING BEAMS WITH TOP AND BOTTOM REINFORCEMENT

8.2.1 Comparison of Test Results

Table 8.2 shows the joint stress ratios v_{jh} / f'_c for Units 1-4 and 8. These ratios were computed following the procedure discussed in Section 2.3. **Figure 8.12(a)** shows the equivalent joint shear stress ratio, $v_{jh,e} / f_c'$, versus the rotational ductility at failure, μ_θ, for these units. It can be seen that the test results closely follow the trend previously observed for other units. For example, the ratio $v_{jh,e} / f_c' = 0.3$ observed for Unit 2 suggests that only incipient joint damage would be expected. Such damage did indeed occur at a displacement ductility $\mu_\Delta = 6$. Further, Units 3 and 4 had a ratio $v_{jh,e} / f_c' < 0.3$, which implies that no

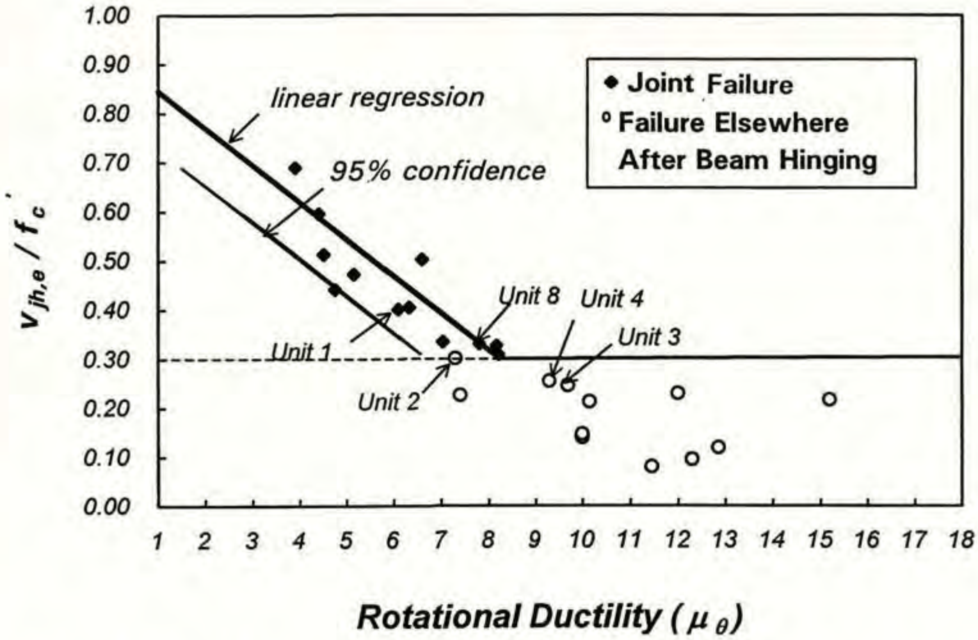

Figure 8.12(a) – Equivalent Joint Shear Stress Ratio versus Rotational Ductility Factor of Tests Including Tests in the Experimental Programme.

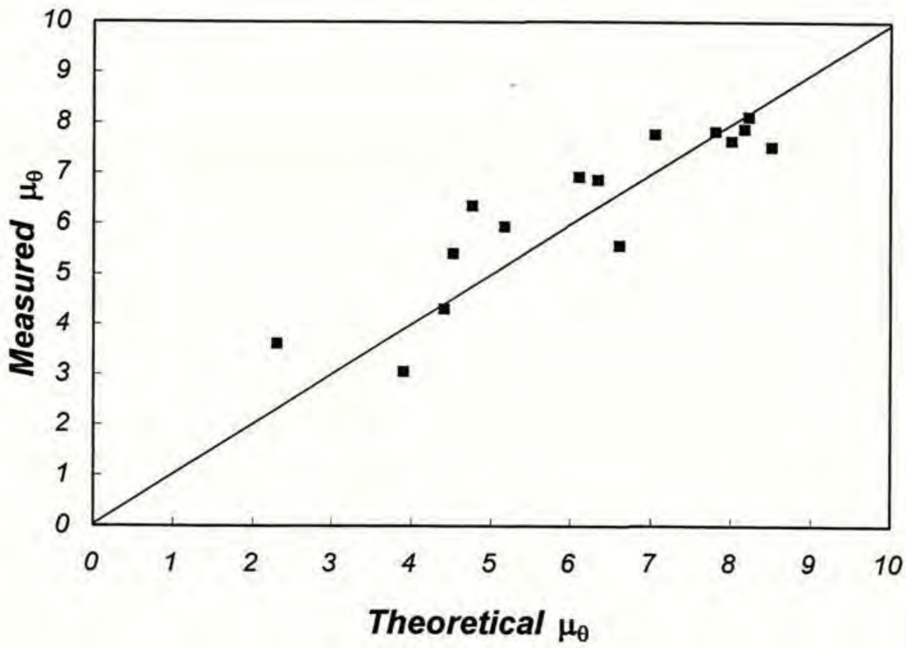

Figure 8.12(b) – Measured versus Predicted Rotational Ductility Factor.

joint failure would occur. This agrees with the experimental observation. In contrast, Units 1 and 8 had a ratio $v_{jh,e} / f_c' > 0.3$, which suggests joint failure at some stage after the development of plastic hinges in the beams. The joints in these two units failed and controlled the behaviour of the units at the end of the tests.

A statistical regression analysis was carried out to incorporate the results of units tested. conducted in this study. Those tests in which failure was mainly caused by bond failure or joints reinforced with steel not showing a well defined yield plateau are not included in this

Table 8.2 - Equivalent Joint Shear Stress Ratios and Ultimate Rotational Ductility Factors of Test Units

	$N^*/A_g f_c'$	V_{sh}/V_{jh} (1)		$v_{jh,o}/f_c'$	K_{pv}	$v_{jh,e}/f_c'$	Ultimate ductility		Failure Mode
		Provided	Effective (2)				μ_Δ	μ_θ (3)	
Unit 1	0.43	0.53	0.46	0.166	2.39	0.40	5.1	6.1	Joint failure
Unit 2	0.43	0.79	0.72	0.173	1.75	0.302	6.0	7.3	Bond Failure
Unit 3	0.1	0.46	0.46	0.111	2.22	0.246	6.2	9.7	Bond Failure
Unit 4	0.1	0.46	0.46	0.115	2.22	0.255	6.0	9.3	Bond Failure
Unit 8	0.1	0.651	0.62	0.169	1.96	0.331	5.1	7.8	Joint failure

Note: (1) V_{sh} was calculated based on measured properties.
V_{jh} is associated with measured over-strength.
(2) Calculated according to the joint hoop stress profile depicted in Fig. 8.15.
(3) Based on the component of the column displacement at first yield.

figure. **Figure 8.12(b)** shows the measured rotational ductility μ_θ versus the theoretical values calculated by the linear regression equation. It was found that the mean value of the ratio of measured and predicted rotational ductility is 0.97 and the coefficient of variation is 0.16. Clearly, the $v_{jh,e} / f_c'$ ratio is strongly correlated with the rotational ductility in those tests in which failure of the joint occurred.

The good agreement discussed above shows the capability of the model proposed in this study to predict the strength and deformation capacity of interior beam-column joints. As a result, satisfactory joint performance can be ensured when using the design recommendations made in accordance with the analytical model.

8.2.2 Observed Trends and Significance

There are two conclusive trends observed in the test results of the experimental programme. First, joint hoops yielded at the end of test in all test units. Second, joints with high joint shear stress ratios tend to degrade faster than joints with low joint shear stress ratios when failure develops.

The bilinear trend observed in **Fig. 8.12(a)** suggests that a strategy for the design of the transverse reinforcement of joints should be based on delaying joint strength failure to ensure that of beam plastic hinges can develop and be maintained during a strong earthquake.

Figure 8.12(a) indicates that unless joints are designed with an equivalent joint shear stress ratio, $v_{jh,e} / f_c' < 0.3$, joint failure will eventually occur. Consequently, the joint design philosophy should be based on delaying joint failure to ensure ductile behaviour of the frame. That is, joints should be designed to enable the development of plastic hinges in the beams and to enable the required plastic rotation without failure.

8.2.3 Relationship of $v_{jh,e} / f_c'$ versus Curvature Ductility Factors in Adjacent Beams

The theoretical model for predicting the shear strength of interior joints illustrated in **Figs. 2.9** and **8.12(a)** is in terms of rotational ductility defined in this study. While the significance of using rotational ductility to recognize that the elastic displacement of the column does not influence the strength of the joint. However, as the use of rotational ductility factor is cumbersome, it is more practical to use curvature ductility factors. The main difference between these factors is that a plastic hinge length needs to be assumed to derive curvature ductility. The relationship between rotational and curvature ductility will be discussed in the paragraphs below, so that the latter ductility can be used to assess the shear strength of an interior beam-column joint.

Figure 8.13 depicts a beam-column subassembly with plastic hinges forming in the beams at the column faces. The curvature distribution along members is also shown in the figure. The displacement ductility factor of this frame subassembly is

$$\mu_\Delta = \frac{\Delta_u}{\Delta_y} = \frac{\Delta_y + \Delta_p}{\Delta_y} = 1 + \frac{\Delta_p}{\Delta_y} \qquad (8.9)$$

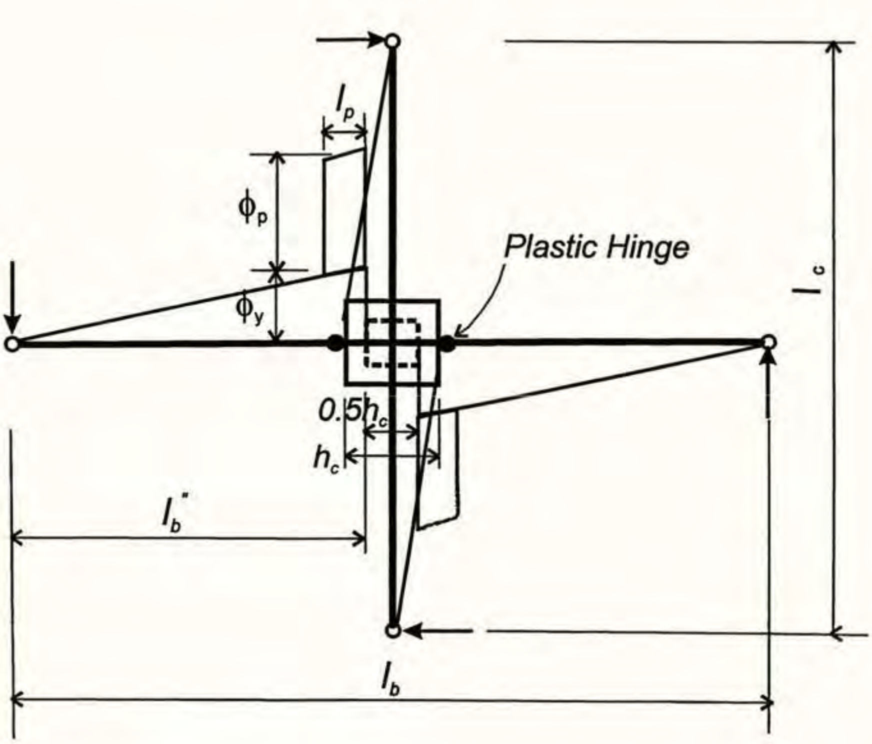

Figure 8.13 – Curvature Distribution in a Beam-column Subassembly with Plastic Hinges Forming in the Beams at the Column Faces.

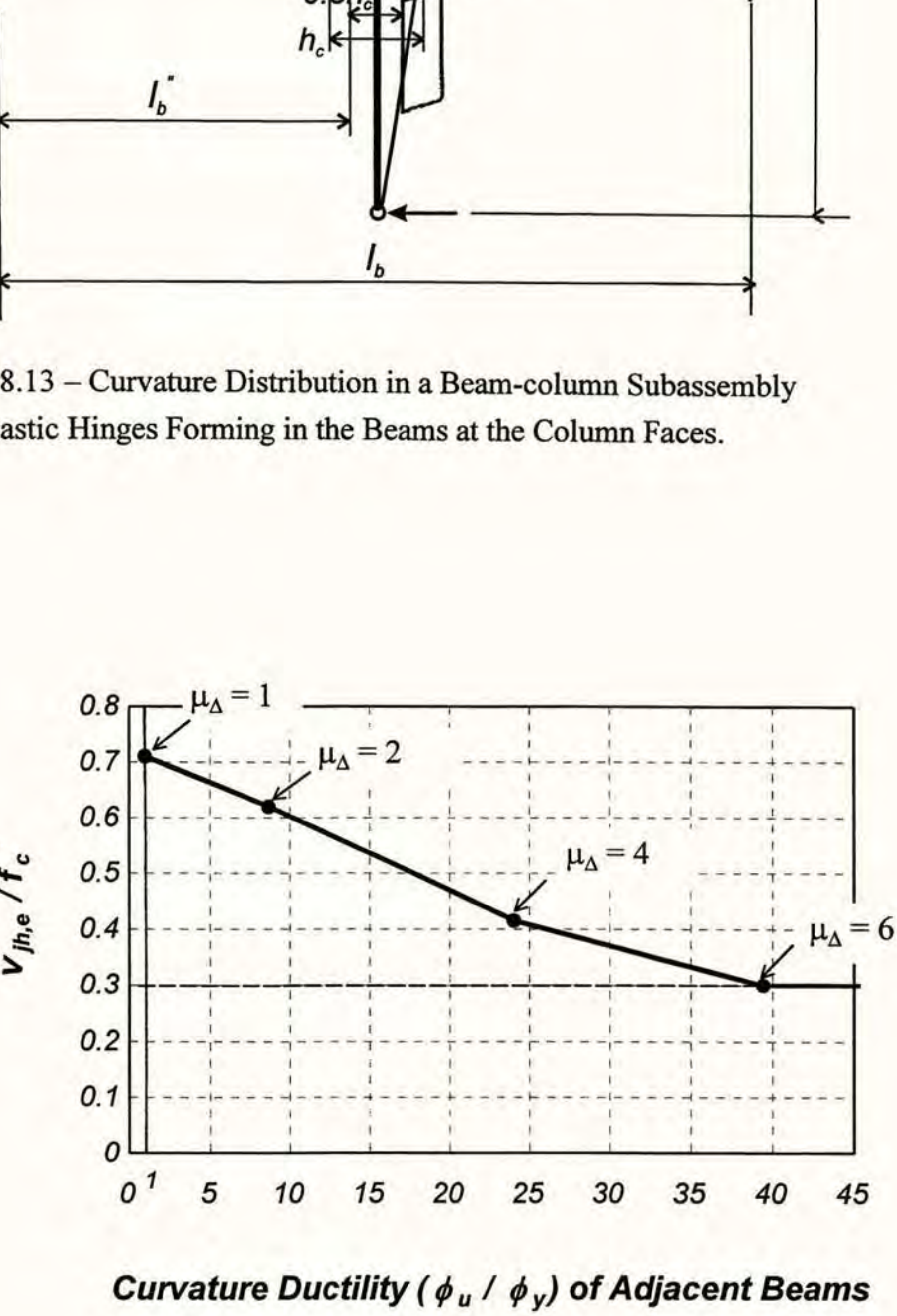

Figure 8.14 - Relationship of $v_{jh,e}/f_c'$ Versus Curvature Ductility Factors of Adjacent Beams.

where Δ_u and Δ_y are the ultimate and the yield displacement of the frame subassembly, respectively. The ultimate displacement Δ_u can be decomposed into two components, one is the yield displacement Δ_y and the other is the plastic deformation that results from beam plastic hinge rotation, Δ_p,.

let ϕ_p be the plastic curvature developing in a beam plastic hinge region and l_p is the plastic hinge length. Then the rotation in a beam resulting from the plastic deformation is,

$$\theta_p = \phi_p l_p \tag{8.10}$$

The component of plastic displacement Δ_p , in the form of lateral storey displacement, is obtained by integrating the plastic curvature over the plastic hinge length,

$$\Delta_p = 2\theta_p\left(l_b'' - 0.5l_p\right)\frac{l_c}{l_b} = 2\phi_p l_p\left(l_b'' - 0.5l_p\right)\frac{l_c}{l_b} \tag{8.11}$$

The yield displacement of the frame subassembly is

$$\Delta_y = \theta_y l_c \tag{8.12}$$

Where θ_y is the reference yield drift ratio. As will be described in Section 8.1.1.2, Priestley [P11] suggested a method to estimate the yield drifts of frame subassemblies based on the yield curvature of beams. Priestley suggested that the component of reference yield drift ratio due to deformation in beams θ_y can be approximated as,

$$\theta_{by} = \frac{1}{6}\phi_y l_b = 0.283\varepsilon_y\left[\frac{l_b}{h_b}\right] \tag{8.13}$$

Where ε_y is the yield strain of longitudinal beam bars and h_b is the beam height. Then the yield drift of the frame subassembly can be determined by making allowances for the column and joint flexibilities.

$$\theta_y = 0.5\varepsilon_y\left[\frac{l_b}{h_b}\right] \tag{8.14}$$

According to Eqs. 8.13 and 8.14, the following equation can be derived

$$\theta_y = 0.294\phi_y l_b \tag{8.15}$$

By substituting Eq.8.15 into Eq.8.12, the yield displacement becomes

$$\Delta_y = \theta_y l_c = 0.29\phi_y l_b l_c = 0.5\varepsilon_y \frac{l_b l_c}{h_b} \tag{8.16}$$

Substituting Eqs. 8.16 and 8.11 into Eq. 8.9, the displacement ductility factor can be found as,

$$\mu_\Delta = 1 + 6.8\frac{\phi_p}{\phi_y}\frac{l_p\left(l_b'' - 0.5l_p\right)}{l_b^2} \tag{8.17a}$$

But,

$$\mu_\phi = \frac{\phi_p + \phi_y}{\phi_y} = \frac{\phi_p}{\phi_y} + 1$$

or

$$\frac{\phi_p}{\phi_y} = \mu_\phi - 1$$

Hence

$$\mu_\Delta = 1 + 6.8\left(\mu_\phi - 1\right)\frac{l_p\left(l_b'' - 0.5l_p\right)}{l_b^2} \tag{8.17b}$$

The relationship between displacement and rotational ductility factors is given by Eq. 2.15. The relationship between rotational and curvature ductility can be determined by rearranging Eq. 2.15 for μ_Δ and substituting it in Eq.8.17 (b),

$$\mu_\theta = 1 + 6.8(\mu_\phi - 1)\frac{l_p\left(l_b'' - 0.5l_p\right)}{l_b^2\left(1 - \Delta_c/\Delta_y\right)} \tag{8.18}$$

Consider a frame subassembly having a typical beam span l_b = 6 m and beam and column depths h_b =h_c=500 mm, and assuming plastic hinge length approximately equal to l_p = h_b/2 [P2]. Eq. 8.18 gives a relationship between rotational ductility and curvature ductility factors.

By applying Eq. 8.18 with Δ_c / Δ_y = 0.25, the relationship between $v_{jh,e}$ / f_c' and curvature ductility in the plastic hinges of the framing beams corresponding to joint failure can be established using the 95% confidence line shown in **Fig. 8.12(a)**. This relationship is plotted in **Fig. 8.14**. This figure also shows the displacement ductility factors found from Eq. 8.17b for the different curvature ductilities.

8.2.4 Influence of the Effective Horizontal Joint Reinforcement

It was observed in the experimental programme that the strain in the horizontal joint hoops presented an arching shape. Those sets of hoops closest to the top and bottom of beam bars seldom yielded while maximum strain developed near the joint mid-depth. The analytical work discusseded in Chapter 2 recognized this trend and used an effective value of the shear force carried by the joint hoops. In Chapter 2 the top and bottom sets of horizontal joint hoops were assumed to develop only one half of its yield force.

Figures 8.15(a)-(d), depict the joint hoop stress profiles measured at the end of the test in Units 1, 2, 5 and 6, respectively. An assumed profile of stress distribution is also plotted on these figures. This profile assumes 40% of the yield strength of joint hoops can develop when they are placed immediately adjacent to the top and bottom beam bars. It is assumed that the yielding of the hoops only takes place in the central depth of the joint. Transient zones with a depth equal to 0.2h$''$ are proposed, where h$''$ is the depth of the joint core in which the joint shear is equal to V_{jh} .

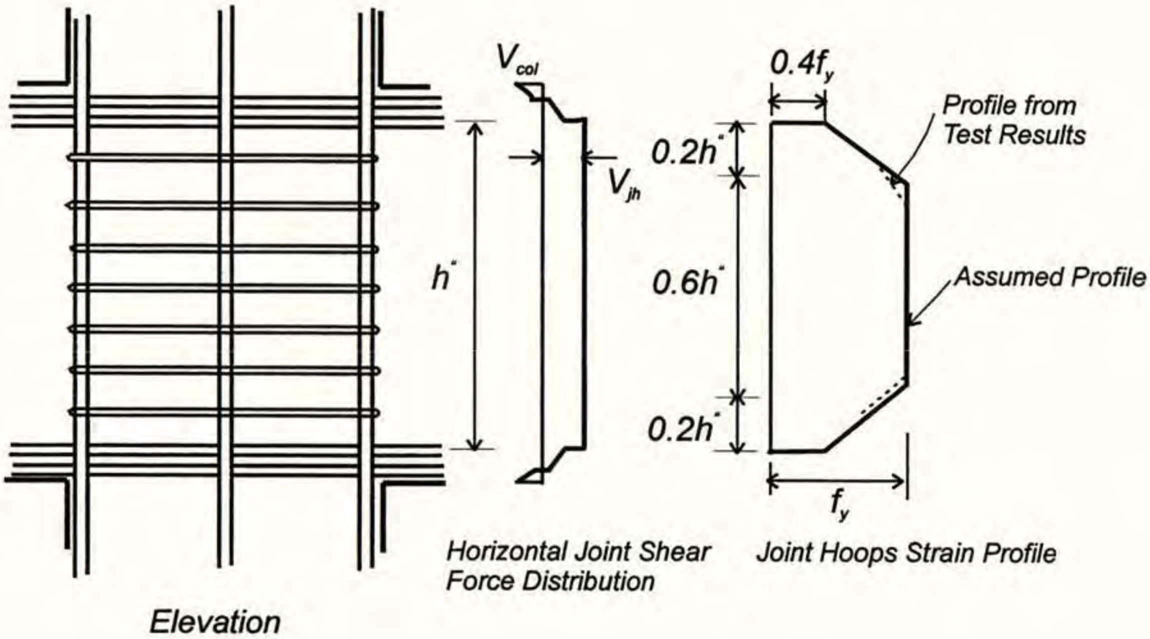

(a) Unit 1

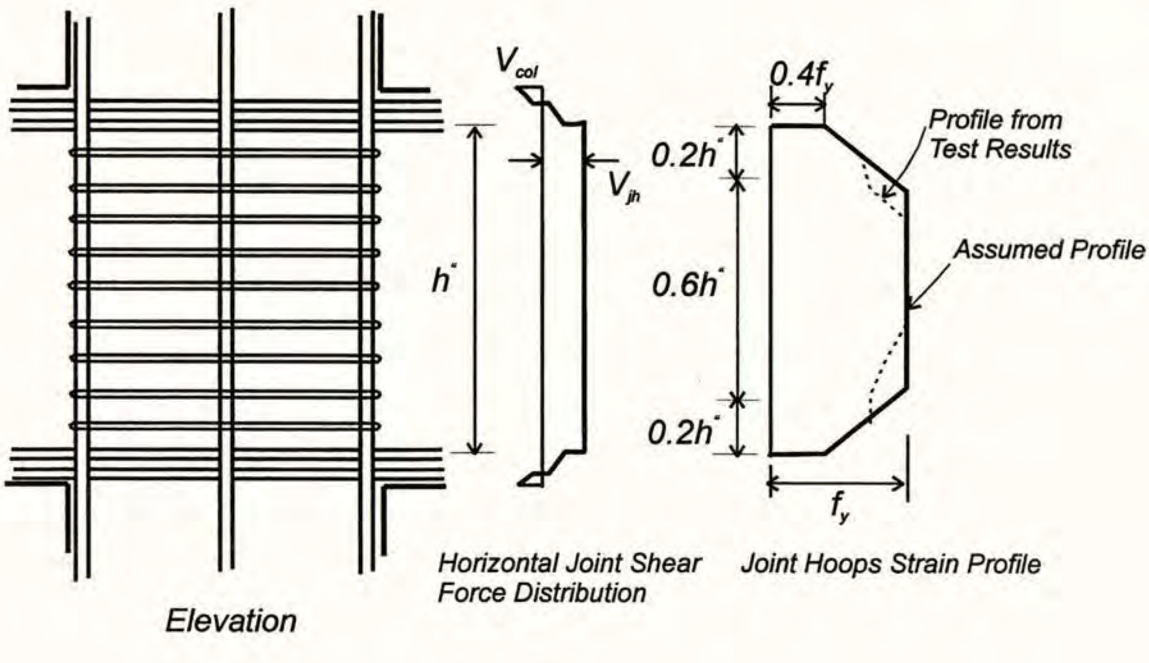

(b) Unit 2

Figure 8.15 - Measured and Assumed Stress Profiles of Joint Hoops Across the Joint Height.

Vsheff.cdr

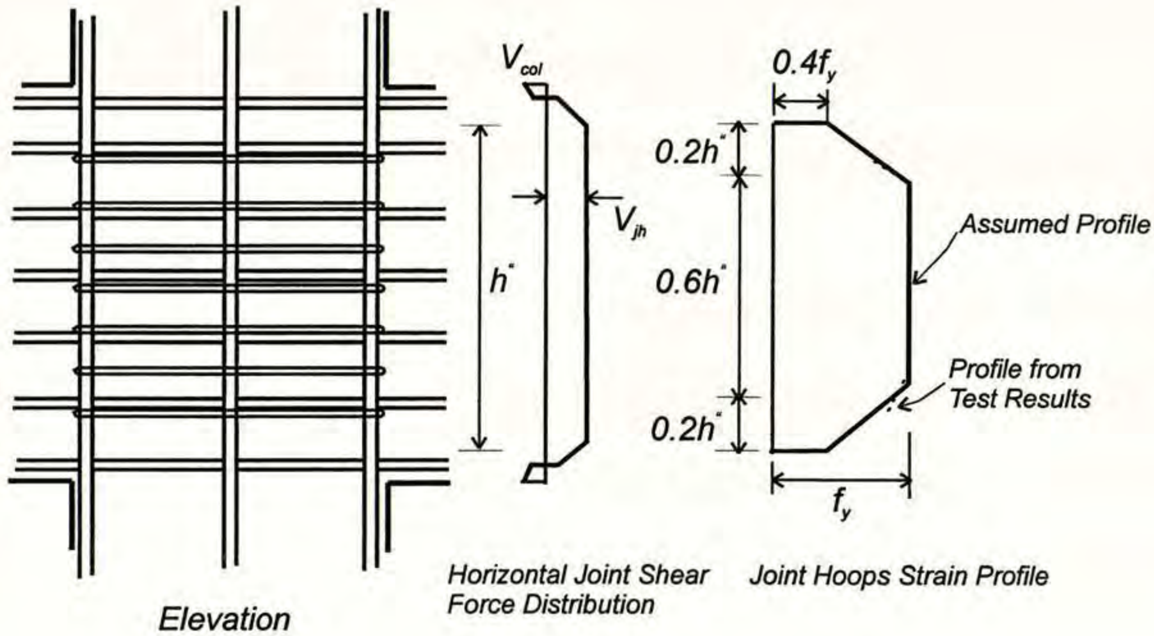

(c) Unit 5

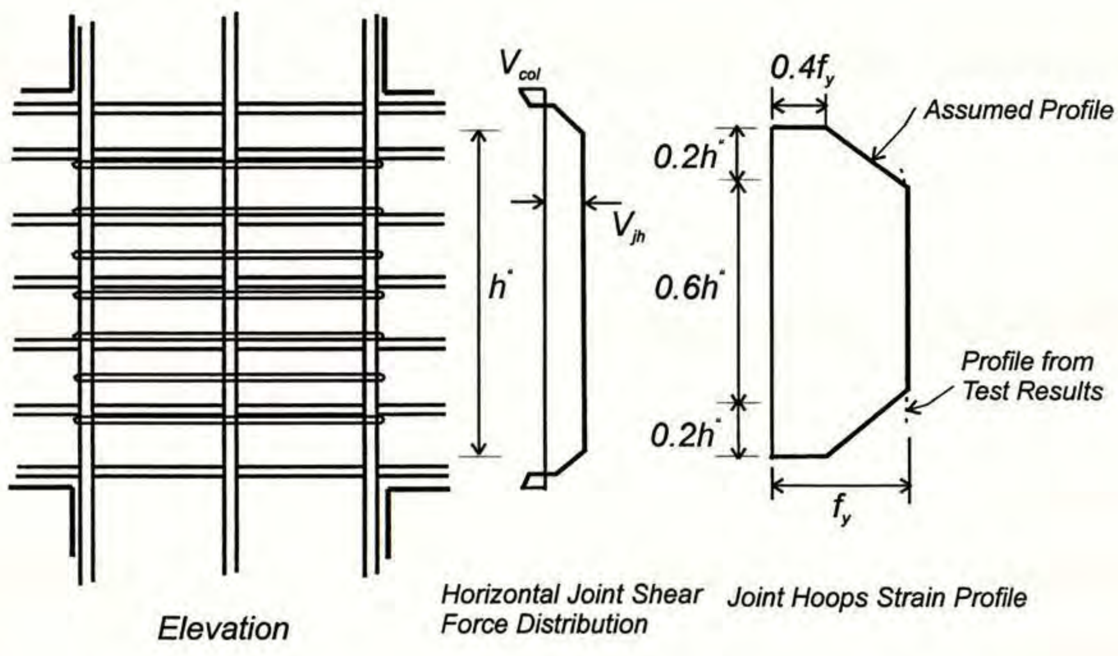

(d) Unit 6

Figure 8.15(Cont.) - Measured and Assumed Stress Profiles of Joint Hoops Across the Joint Height.

In accordance with the assumed stress profile, the joint shear force carried by the effective horizontal joint reinforcement is.

$$(V_{sh})_{eff} = \left(\frac{A_{s,j}}{h''}\right)[f_y(0.6h'') + 0.4f_y(0.2h'')2 + 0.6f_y(0.2h'')(0.5)2] = 0.88A_{s,j}f_y \qquad (8.19)$$

where $A_{s,j}$ is the area of effective legs of the horizontal joint reinforcement and f_y is the yield stress of joint reinforcement. In order to account for the effectiveness of the joint hoops the area of joint reinforcement is required to be scaled up in design according to the following equation.

$$A_{s,j}' = \left(\frac{1}{0.88}\right)A_{s,j} = 1.14A_{s,j} \qquad (8.20)$$

The magnification factor 1.14 will be introduced into the design recommendations in the following section.

The joint hoop stress profiles of Units 5 and 6 are presented in **Figs. 8.15(c) and (d)**. Owing that beam bars are distributed through the web, the transition region in which the input joint shear force increases from zero to V_{jh} is different to that of Units 1 and 2. However, for the sake of consistency the value of h'' used in **Figs. 8.15(c) and (d)** is assumed to be equal to that of joints with conventionally reinforced beams. Note that the two units are identical except that the joint reinforcement in Unit 6 consists of deformed bars. Comparing the two units, it can be observed that all joint hoops in Unit 6 yielded, including the sets adjacent to the top and bottom beam bars, while the arching shape of stress profiles in Unit 5 is evident. The strain profiles tend to be uniform. Hence, it is suggested that when deformed bars are used for joint hoops, the coefficient for taking into account the effective V_{sh} be taken as unity.

8.2.5 Refined Design Recommendations

8.2.5.1 Limitations of Joint Shear Stress Ratios

Design recommendations in NZS 3101:1995 [S1] recognize that joints with high joint shear stress ratios, v_{jh} / f_c', are vulnerable to fail in diagonal compression and limit v_{jh} / f_c' to be less than 0.2. It is recommended that this limitation of joint shear stress ratio should also be satisfied when using the design recommendations given in this study.

8.2.5.2 Ductility Based Horizontal Joint Reinforcement Design

In the traditional ductility-based design, the system displacement ductility demand of the structure is chosen by the designers. Then, the structure is detailed according to the material standard's requirements for the selected ductility demand. The Concrete Structures Standard, NZS 3101:1995 [S1], permits a system design displacement ductility factors of 6 for fully ductile structures and 3 for structures of limited ductility. The design recommendations for interior beam-column joints of fully ductile and limited ductility frames were proposed in Section 2.4.4 for the traditional ductility-based design. These recommendations are modified here in light of the effectiveness of the joint hoops discussed in previous section.

Joints of Fully Ductile Frames ($\mu_\Delta = 6$)

An efficiency factor α_e factor is introduced into Equation 2.26 to account the effect that plain round joint hoops close to the top and bottom beam bars seldom yield,

$$V_{jh} = \alpha_e V_{sh} + V_N + V_C \tag{8.22}$$

Where α_e = 0.88 if plain round bars are used as horizontal joint reinforcement.

α_e = 1.0 if deformed bars are used as horizontal joint reinforcement.

and

$$\frac{V_c}{V_{jh}} = \frac{1}{660\left(\dfrac{v_{jh}}{f_c'}\right)^3} \tag{8.22a}$$

$$\frac{V_N}{V_{jh}} = 0 \quad when \quad \frac{N^*}{A_g f_c'} \le 0.1 \tag{8.22b}$$

$$\frac{V_N}{V_{jh}} = 1.6\left(\frac{N^*}{A_g f_c'} - 0.1\right) \quad when \quad 0.1 < \frac{N^*}{A_g f_c'} \leq 0.3 \tag{8.22c}$$

$$\frac{V_N}{V_{jh}} = 1.0 - 2.27\frac{N^*}{A_g f_c'} \quad when \quad \frac{N^*}{A_g f_c'} > 0.3 \tag{8.22d}$$

Note that V_{jh} and V_N should be evaluated considering the development of over-strength in the plastic hinges. Once V_c and V_N have been found, the joint shear force carried by horizontal joint reinforcement, V_{sh}, can be obtained from Eq. 8.22. The area of horizontal joint shear reinforcement is obtained as $A_{sh}=V_{sh} / f_{yh}$, where f_{yh} is the yield strength of the horizontal joint reinforcement.

It is recommended that $V_{sh} \geq 0.4\ V_{jh}$

Joints of Limited Ductility Frames ($\mu_\Delta = 3$)

$$V_{sh} = 0.4V_{jh} \tag{8.23}$$

8.2.5.3 Performance-Based Horizontal Joint Reinforcement Design

As the performance or displacement - based design has drawn much attention on the seismic structural design, it becomes necessary to design the joints of frames in which the performance criteria has been met. The theoretical model proposed in this study and verified by the experimental programme has the capability of designing joints under different imposed ductility levels of frames. This section describes the procedure to carry out the design of joints of frames in which the performance-based design is adopted.

The most important criteria of performance of the frame structures is the inter-storey drifts. Priestley et al. [P13] suggested a direct displacement-based design method which has the advantage of avoiding estimation of initial stiffness. They claimed that with the implementation of this method, it is more likely that structures are designed to meet the drift limitation associated with the design earthquake. Most recently, Priestley [P11] proposed a method to obtain the appropriate design displacement ductility factor that should be adopted for the design structures to meet the drift limitation specified by the loading code. The expression is reproduced here,

$$\mu_\Delta = \frac{\theta_c}{0.5\varepsilon_y}\left[\frac{h_b}{l_b}\right] \tag{8.24}$$

where θ_c is the interstorey drift ratio at the ultimate limit state, h_b is the beam overall depth, l_b is the average beam span and ε_y is the yield strain of the beam longitudinal reinforcement. Ratio θ_c can be taken as 0.025, which is the maximum inter-storey drift permitted by the Loading Code, NZS 4203:1992 [S3].

The design steps are described as follows:

Step 1: Determine the design actions derived from over-strength considerations. They are $N^*/A_g f_c'$ and v_{jh}/f_c'. Check $v_{jh}/f_c' \le 0.2$.

Step 2:

Use Eq. 8.24 to determine the storey design displacement ductility associated with the drift limitation.

Step 3:

With the assumption of $\Delta_c / \Delta_y = 0.25$, the rotational ductility defined in this study can be calculated using Eq. 2.15, which is reproduced here

$$\mu_\theta = \frac{\mu_\Delta - \Delta_c/\Delta_y}{1-\Delta_c/\Delta_y} = \frac{4}{3}(\mu_\Delta - 0.25) \tag{8.25}$$

Step 4:

Input μ_θ in the chart derived in Section 2.3.6 and reproduced for convience in **Fig. 8.16**. Use the 95% confidence limit line determine the equivalent joint shear stress ratio,

$v_{jh,e} / f_c'$.

Step 5:

Determine the ratio

$$K_{pv} = \frac{v_{jh,e}/f_c'}{v_{jh}/f_c'}$$

Step 6:

Use the chart derived in Section 2.2.4.2, which is reproduced in **Fig. 8.17**, and determine the ratio $V_{sh,eff} / V_{jh}$ by entering K_{pv} and $N^*/A_g f_c'$,. The ratio $V_{sh,eff} / V_{jh}$ is designated as $C_{sh,eff}$ here.

Step 7:

Find the shear force carried by the joint hoops as

$V_{sh} = C_{sh,eff} V_{jh} / \alpha_e$

Where $\alpha_e = 1$ when using hoops with deformed bars
and $\alpha_e = 0.88$ when using hoops with plain round bars
V_{sh} should not be taken less than $0.4V_{jh}$.

Step 8:

Determine the required area of horizontal joint shear reinforcement $A_{sh} = V_{sh}/f_{yh}$.
Where f_{yh} is the yield strength of the horizontal joint reinforcement.

8.2.5.4 Prediction of the Available Displacement Ductility in Joints of Existing Buildings

Another use of the theoretical model established in this study is the ability to predict the available displacement ductility factor or available storey drift which joint failure could develop in a frame subassembly. The procedure is described in the following

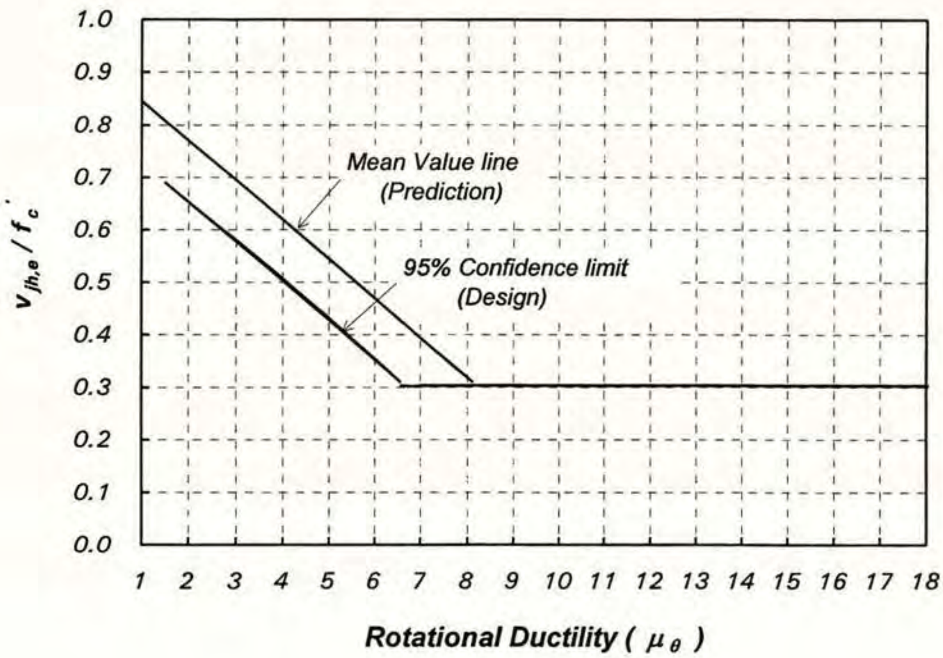

Figure 8.16 - Design Chart.

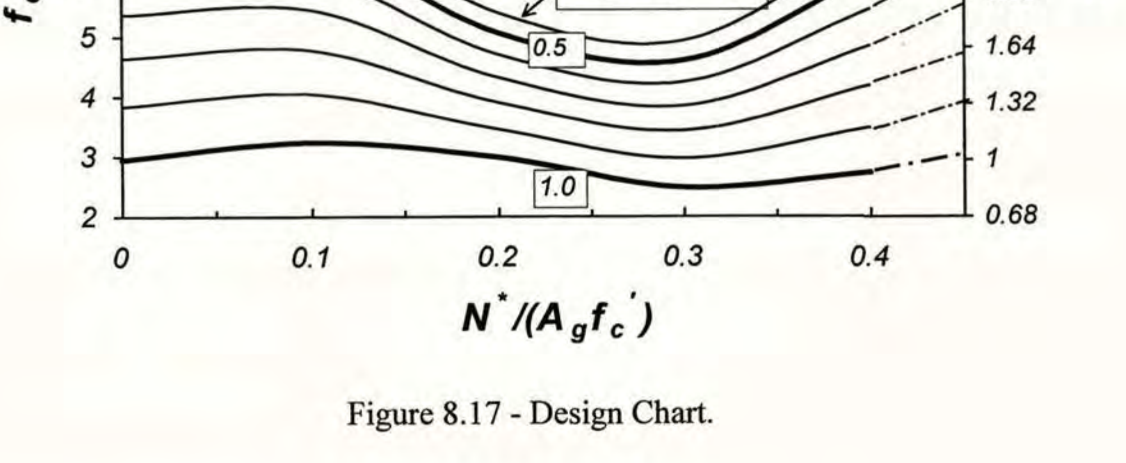

Figure 8.17 - Design Chart.

steps.

Step 1: With given $N^*/A_g f'_c$ and $V_{sh,eff}$ / V_{jh} ratios, the value of K_{pv} can be determined according to the chart shown in **Fig. 8.17**. $V_{sh,eff}$ can be calculated according to the stress profile depicted in **Fig. 8.15** if the levels of the joint hoops in the joint region are known. Otherwise, $V_{sh,eff} = 0.88\ V_{sh}$ can be assumed.

Step 2: Find the equivalent joint shear stress ratio, $v_{jh,e} / f'_c$, as $v_{jh,e} / f'_c = K_{pv}\ v_{jh} / f'_c$.

Step 3: The available rotational ductility is found from the chart shown in **Fig. 8.16**. It is suggested that the mean value line be used for the assessment of the joint strength.

Step 4: The available displacement ductility of the frame subassembly is found from Eq. 2.15 with $\Delta_c / \Delta_y = 0.25$,

$$\mu_\Delta = \frac{3}{4}\mu_\theta + 0.25 \tag{8.26}$$

Step 5: The available storey drift is obtained by multiplying the displacement ductility factor by the reference yield displacement,

$$\Delta_u = \mu_\Delta \Delta_y \tag{8.27}$$

where Δ_y is given by Eq. 8.16, which is reproduced here for clarity

$$\Delta_y = 0.5\varepsilon_y l_b l_c / h_b \tag{8.28}$$

8.2.6 Joints Incorporating Shear Reinforcement Without an Apparent Yield Plateau

Few tests collected in the database incorporated joint shear reinforcement that did not have a well defined yielding plateau. Such lack of a well defined yield plateau is often found in small diameter high strength reinforcement or in cold-worked reinforcement. Test results of those tests were processed and are presented in Table 2.1 in Chapter 2 and in Appendix B.

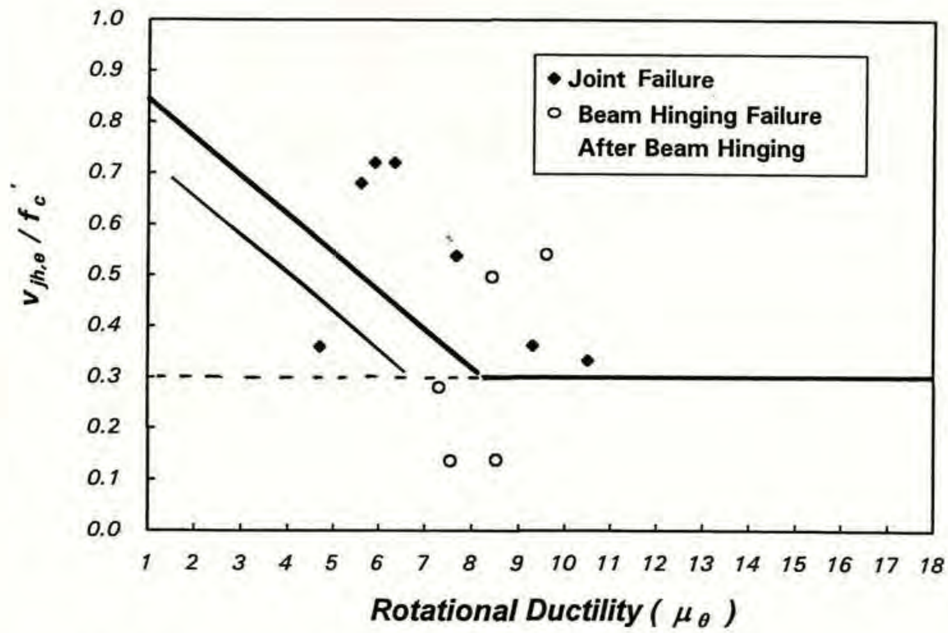

Figure 8.18 – Equivalent Joint Shear Stress Ratio versus Rotational Ductility Factors of Tests in Which the Joint Shear Reinforcement Have no Yield Plateau.

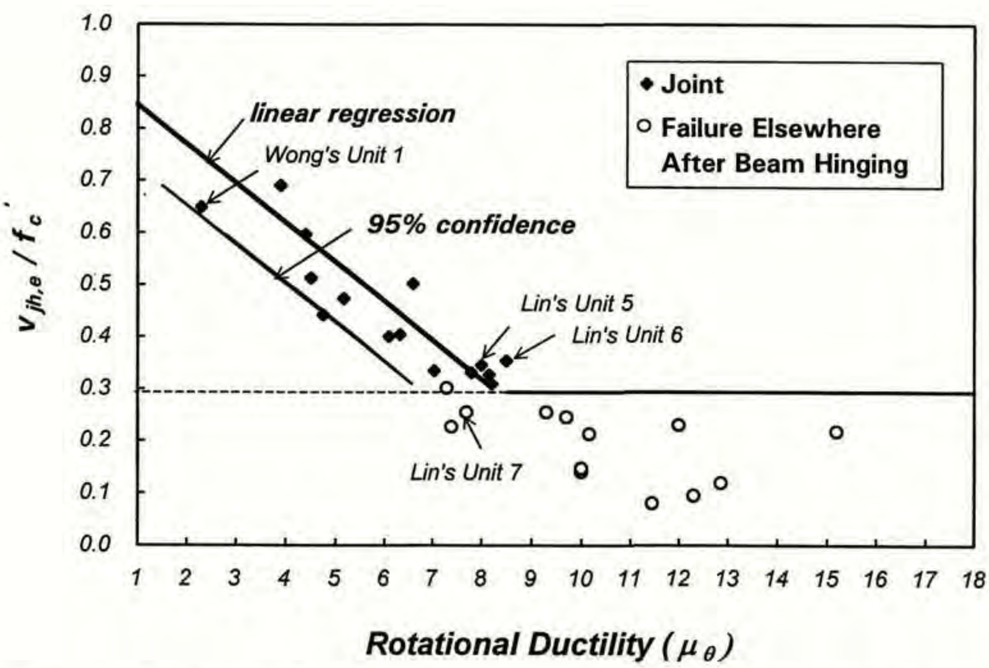

Figure 8.19 – Equivalent Joint Shear Stress Ratio versus Rotational Ductility Factor With Tests Incorporating Distributed Beam Bars Being Included.

Uzumeri and Seckin [U1] conducted tests on two exterior beam-column joint subassemblies which were identical with the exception that the joint shear reinforcement in one unit did not have a definite yield plateau while joint reinforcement in the other unit was heat treated to re-introduce a yield plateau. Comparison of the test results showed that although the behaviour of the two units are very similar, the former unit had more ductile performance than that of the latter one. They attributed the better behaviour to the confinement provided by the joint hoops without a well defined yield plateau.

However, it is known that the transverse strains become very high and the effect of confinement is activated only when the concrete is at stresses approaching the uniaxial compressive strength [P4]. The joint concrete can not be subjected to such high uniaxial compression due to the combined action of column compressive load and joint shear force and still remain essentially undamaged. Therefore, the improved performance should not be attributed to the confinement provided by the reinforcement without yield plateau. The reason to the improved behaviour is that transverse strains of such a joint are better controlled as unrestricted yielding cannot occur.

Figure 8.18 plots the equivalent joint shear stress versus rotational ductility for tests in which joint reinforcement did not show a yield plateau. The trends established by other tests are also shown in the same chart. It is evident that those tests incorporating joint shear reinforcement without flat yield plateau usually showed larger displacement ductility capacity than that are predicted by the theoretical frames. Some tests having $v_{jh,e} / f_c'$ larger than 0.3 failed in beam hinging instead of joint shear failure. The enhancement effect using such type of joint shear reinforcement can be clearly observed. This implies that using such type of reinforcement as joint shear reinforcement, the required quantity of joint shear reinforcement could possibly be reduced. However, further research is needed to quantify this effect.

8.3 BEHAVIOUR OF JOINTS INCORPORATING BEAMS WITH DISTRIBUTED REINFORCEMENT

8.3.1 Discussion of Test Results

There are two aspects of the test results of Units 5-7 that deserve to be discussed further. One is the bond strength of beam bars and the other is the joint shear strength.

8.3.1.1 Bond Strength of Beam Bars Passing Through the Joint Region

Compare the bars slip measured during the test of Units 5, 6 and 8, see Fig. 6.7, 6.22 and 7.7. A general trend can be observed that bond failure of the outermost beam bars in Units 5 and 6 occurred slightly more prematurely than that top and bottom beam bars of Unit 8. Note that these three units have the same d_b / h_b ratio, were cast simultaneously, and had a similar concrete compression strength when tested. The measured slip of the outermost beam bars measured in the column centrelines in Units 5 and 6 exceeded the clear spacing between the bar deformation in the load cycle to μ_Δ = -4x1. The slip of the top beam bars in Unit 8 reached the clear spacing between bar deformations at the peak μ_Δ = -4x1. The slip on the bottom bars did not reach the clear spacing between bar deformations until the cycle to μ_Δ = 6x1.

The strains in the outermost beam bars in Units 5-7 indicate that these bars yielded in tension at one column face and in compression at the opposite face before bond failure occurred. In contrast, in Unit 8 the bars did not yield in compression. Thus anchorage conditions are more critical when the bars are distributed through the beam web than when they are conventionally detailed as top and bottom reinforcement.

Units 5-7 conclusively showed in that almost all interior beam bars yielded in tension on both sides of the column faces. As a result, bond stresses are not required for those bars. Thus it may be concluded that for those intermediate layers of beam bars, no bar diameter limitation is required.

8.3.1.2 Joint Shear Strength of the Joint

The equivalent joint shear stress ratios and ultimate rotational ductility of Units 5-7 were calculated following the same procedure described in Section 2.3. Table 8.3. shows the main parameters evaluated for Units 5-7 and for Unit 1 tested by Wong [W1].

Figure 8.19 shows the graph of equivalent joint shear stress ratios versus rotational ductility including the units tabulated in Table 8.3. The behaviour of the joints incorporating beams with distributed reinforcement follow very closely the trend observed for joints incorporating beams with lumped top and bottom reinforcement. It is evident in figure 8.19 that the distribution of beam bars through the web does not seem to enhance the joint shear strength. According to the analytical model, the uniaxial compressive stress of the diagonal strut in the joint somehow decreases, see Section 2.6. Nevertheless, such reduction is, cancelled by the larger tensile strains somehow imposed by the inner beam bars in the concrete core of the joint.

Table 8.3 Equivalent Joint Shear Stress Ratios and Ultimate Rotational Ductility Factors of Test Units 5-7

	$N^*/A_g f_c'$	V_{sh}/V_{jh} (1)		$v_{jh,o}/f_c'$	K_{pv}	$v_{jh,e}/f_c'$	Ultimate ductility		Failure Mode
		Provided	Effective(2)				μ_Δ	μ_θ (3)	
Unit 5	0.1	0.66	0.63	0.176	1.96	0.345	5.2	8.0	Joint+bond failure
Unit 6	0.1	0.61	0.61(4)	0.176	2.01	0.354	5.5	8.5	Joint+bond failure
Unit 7	0.25	0.72	0.69	0.185	1.38	0.255	5.7	7.7	Bond Failure
Wong's Unit 1	0	0.11	0.082	0.237	2.73	0.647	2.0	2.3	Joint failure

Note: (1) V_{sh} was calculated based on measured properties. V_{jh} is associated with measured over-strength.

(2) Calculated according to the proposed profile depicted in Fig. 8.15.

(3) The percentage of column displacement as a component of yield displacement is according to the associated displacement components depicted in the Chapters depicted the test results.

(4) All deformed horizontal joint reinforcement in the joint is considered to be effective.

8.3.2 Design Recommendations

According to the observations made in previous section, it is thus known that the joint strength would be very similar no matter the framing beams are reinforced with lumped or distributed reinforcement. Therefore, it is suggested that design of joints make no difference as to the way the longitudinal beam reinforcement is layout.

8.4 SEISMIC STRENGTH ASSESSMENT OF INTERIOR BEAM-COLUMN JOINTS IN EXISTING BUILDINGS

8.4.1 Introduction

With the advance of modern seismic design technique of buildings, a great concern exists on the seismic performance of older buildings. In recent years there has been increasing emphasis on the seismic assessment and retrofit of existing buildings in United States [A2][A3], Japan [A4][S11] and New Zealand [P14][P16].

A realistic assessment procedure, which gets away from the check-list type approach, has been proposed by Priestley and Calvi [P15]. The procedure is based on determining the available static lateral load strength and available displacement ductility factor of the critical post-elastic mechanism of the structure. More recently, Park [P14] extended this static force-based procedure to assess the likely seismic performance of existing reinforced concrete moment resisting frames. A displacement-based assessment method was also suggested by Priestley [P6].

Some of the aspects of seismic assessment of reinforced concrete interior beam-column joints using the analytical method developed in Chapter 2 and the results of the experimental programme conducted in this study will be discussed in the following sections.

8.4.2 Effective Joint Shear Area

The effective joint shear area of the units tested in this experimental programme was computed following the procedures described in Section 3.8.3. These areas are tabulated in Table 8.4. Note that the information regarding the effective joint shear area is useful for structural modeling in the computer analysis when the joint flexibility is taken into account.

Let A_j be the joint area that is equal to $(h_b)(h_c)$, where h_b and h_c are the overall beam and column depth, respectively. The $A_{j,e}$ / A_j ratios depicted in Table 8.4 range from 0.10 to 0.43. It is believed that there is slight dependency between the ratio and the column axial load, joint shear stress ratios and amount of joint reinforcement. Also the $A_{j,e}$ / A_j ratios for those units in which beam bars were distributed along webs seem to be slightly lower than in joints with conventionally reinforced beams. However, a reasonable estimate for the ratio $A_{j,e}$ / A_j for well reinforced joints is $0.3 \sim 0.4$.

Table 8.4 - Evaluation of Effective Joint Shear Area of the Test Units

	Unit 1	Unit 2	Unit 3	Unit 4	Unit 5	Unit 6	Unit 7	Unit 8
γ_{75} (x10^{-3} rad)	0.67	0.67	0.39	0.53	2.63	2.47	0.93	1.76
$(V_{jh})_{75}$ (kN)	549	549	410	410	554	554	574	549
K_{joint}	819403	819403	1051282	773585	210646	224292	614561	311932
$G \approx 0.4E_c$	10881	10881	11436	11436	10551	10751	10816	10832
$A_{j,e}$	75304	75304	91931	67647	19964	20863	56819	28796
$A_{j,e} / A_j$	0.35	0.35	0.43	0.32	0.10	0.10	0.26	0.13

* See Section 3.8.3 for the notations in the above table.

8.4.3 Degradation Model of Shear Strength of Reinforced Interior Joints

In both force and displacement-based seismic assessment methods the effect of degradation of shear strength of beams and columns members and beam-column joints is required as they may limit the displacement capacity of the structures. It is thus of particular interest to investigate the degradation of shear strength degradation in interior beam-column joints.

Hakuto et al. [H1], based on the test results of beam-column subassemblies without transverse reinforcement, proposed a joint shear degradation model. Park [P14] simplified this model using a bi-linear relationship to assess the joint strength in terms of curvature ductility factors in the plastic hinges in the framing beams. Some insight on the degradation characteristics of joints with little amount of shear reinforcement may be gained from the theoretical model established in this study. Take an example of a joint with $0 \leq N^* / A_g f_c' \leq 0.1$. If the joint has a quantity of horizontal shear reinforcement of $V_{sh} / V_{jh} = 0.1$, the corresponding K_{pv} value predicted from the analytical work (see Section 8.2.5.4) is 2.71. If the joint has $v_{jh} / f_c' = 0.3$, the equivalent joint shear stress ratio, $v_{jh,e} / f_c'$, is 0.81 according to Eq. 2.1. With reference to the mean value line in **Fig. 8.12(a)**, the associated rotational ductility capacity of the joint is $\mu_\theta = 1.5$, which corresponds to a displacement ductility factor $\mu_\Delta = 1.4$, if $\Delta_c / \Delta_y = 0.25$ is assumed, see Eq. 8.26. This prediction indicates that this joint may limit the ductility capacity of the frame.

Following the same procedure described above, for a joint with $v_{jh} / f_c^{'} = 0.2$ and $0 \leq N^* / A_g f_c^{'} \leq 1$ and $V_{sh} / V_{jh} = 0.1$, the rotational ductility capacity of the frame subassembly is $\mu_\theta = 4.8$, that corresponds to $\mu_\Delta = 3.8$ if $\Delta_c/\Delta_y = 0.25$. Similarly, if the joint above has $v_{jh} / f_c^{'} = 0.15$ while the other parameters remain the same, the theoretical model predicts $\mu_\theta = 6.6$, which corresponds to $\mu_\Delta = 5.2$.

The above values can be interpreted in terms of curvature ductility if the geometry of the frame is known. This is achieved using Eq. 8.17b. Let $h_b=h_c=500$mm and $l_b=6$m and $l_p=h_b/2=250$mm, which represent typical values used in space frames built in the 1960s. The results of this example are plotted in **Fig. 8.20** together with the model proposed by Park [P14] being included. Another line derived from the theoretical model with the same V_{sh} / V_{jh} ratio but different column axial load, $N^*/A_g f_c^{'} = 0.2$, is also shown in **Fig. 8.20**. Note that the model proposed by Park and Hakuto [H1] et al. is independent of the column axial load level.

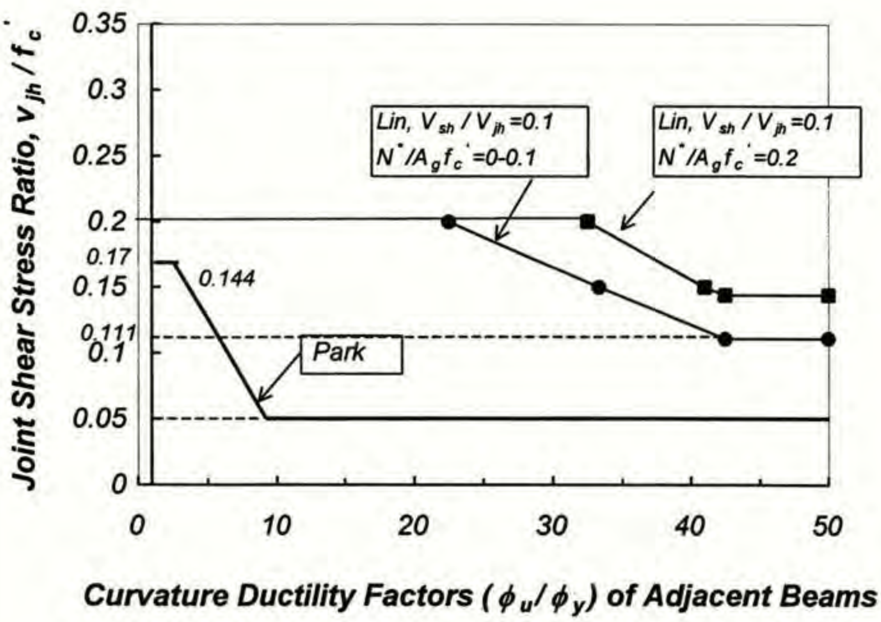

Figure 8.20 – Degradation Model for the Joint Shear Stress of Interior Joints.

Hakuto et al. [H1] estimated the maximum shear stress at failure for joints without shear reinforcement to be $v_{jh} = 0.17\ f_c'$. Park [P14] pointed out that the model was limited test evidence and require further calibration. It can be seen in Fig. 8.20 that for a given v_{jh}/f'_c ratio, the theoretical model suggests that the beam can sustain larger curvature ductility than those predicted with the Park model.

8.5 BOND STRENGTH OF INTERIOR BEAM-COLUMN JOINTS

8.5.1 Introduction

The anchorage of beam bars passing through beam-column joints is an important issue in the design of reinforced concrete moment resisting frames. Not only because it has predominant effects on the hysteresis response and energy dissipation but also because the difficulty of repairing joints suffering from bond failure. Besides, the stiffness of frames is rather sensitive to the bond performance of bars passing through a joint. Although a bond break down within interior joint is not likely to lead to catastrophic failure, it is believed that bond failure has pronounced influence on the post-earthquake behaviour of structures, particularly the residual stiffness. Thus special cautions should be taken to prevent premature bond deterioration in joints under seismic attack.

The anchorage of beam bars in beam-column joint region had been of much concern in New Zealand [S1] and overseas [A5]. In New Zealand, in the beginning, beam bars passing through the joint region were conservatively anchored there as it was deemed that bond deterioration should be precluded, thus ensuring capacity design [S13]. The limitation of diameter of the beam bars passing through an interior beam-column joint in NZS 3101:1982 [S13] was derived based on that bars would yield both in tension and compression at opposite column faces. The New Zealand approach has been to limit the bar diameter that can be anchored within the joint length. Thus Equations are given in terms of a limitation in the bar diameter-to-overall column depth ratio, d_b/h_c. The design recommendations of bond strength in NZS 3101:1995 [S1] recognized the presence of more variables. In general, the stringent limitations imposed by NZS 3101:1982 were somewhat relaxed.

It is interesting to note that most of the tests used to establish the equations of bar diameter to overall column depth ratios in the Concrete Structures Standard [S1] have been based on tests using Grade 300 reinforcing steel for the longitudinal reinforcement. The experimental programme conducted as part of this study revealed that bond deterioration may occur earlier if the current Standard bar diameter-to-column depth limitations are applied for Grade 500 reinforcing steel bars. Thus the requirements of anchorage of beam bars given by NZS 3101:1995 [S1] will be reviewed here in light of the test results obtained in this study.

Bond failure of top or bottom beam bars occurred in test units in the L series (Units 2, 3, 4 and 8) in the load cycle to $\mu_\Delta = 4$ or $\mu_\Delta = 6$. It usually caused some loss of lateral load capacity and had pronounced influence on the hysteresis response.

It is noted that in NZS 3101:1995, the ratio, d_b / h_c is assumed to be proportional to $\sqrt{f_c'}/f_y$ [S1]. With an assumed bond stress profile and prescribed maximum local bond stress, the average bond stress over the length of the joint is evaluated [P2]. Then, the required ratio d_b / h_c is obtained by realistically estimating the tensile and compressive force of beam bars at joint faces.

By applying a procedure similar to that as described above, the average beam bar bond stress can be readily evaluated. Although this value does not represent the actual bond stress occurring within the joint region, it can be used as an index of the bond strength. Such average bond stresses were calculated for a number of tests. The details of the tests and the procedure for reducing the data are described below.

8.5.2 Evaluation of the Average Bond Stress of Beam Bars Passing Through Interior Beam-Column Joint

Consider a typical interior beam-column joint, the average unit bond stress in the longitudinal beam bars can be derived from the equilibrium of forces acting on the bars, as **Fig. 8.21** shows.

for the top beam bars,

$$\alpha_o f_y A_s + C_{b,st} = n_t \pi d_{b,t} h_c u_a \tag{8.29}$$

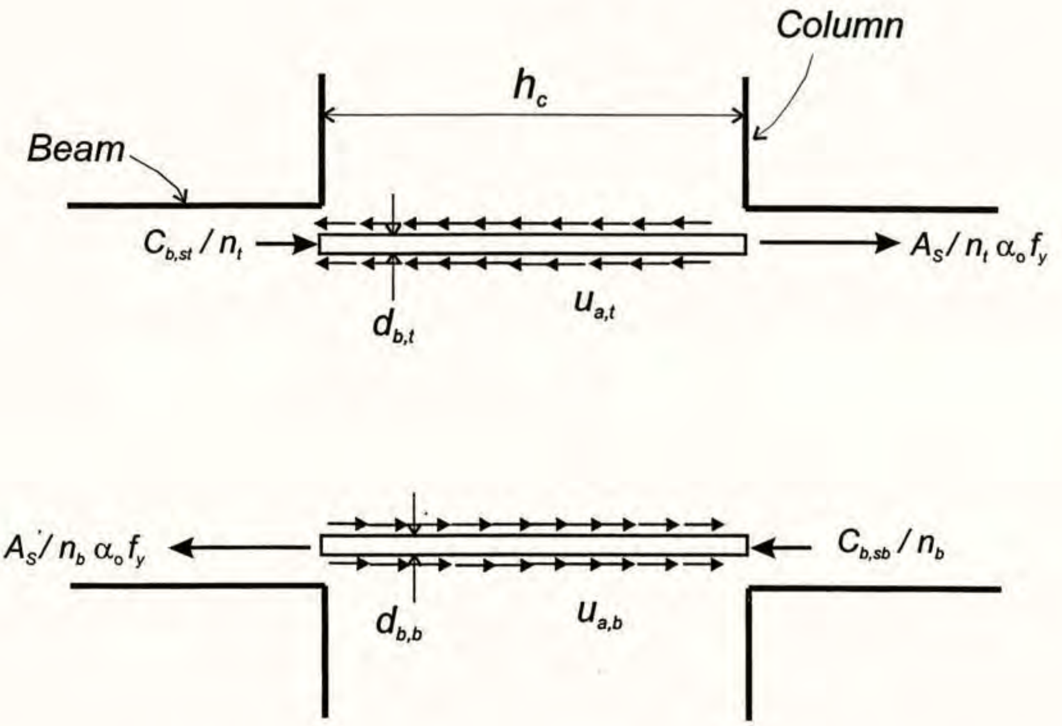

Figure 8.21 - Evaluation of Average Bond Stress of Top and Bottom Beam Bars Over the Joint Length.

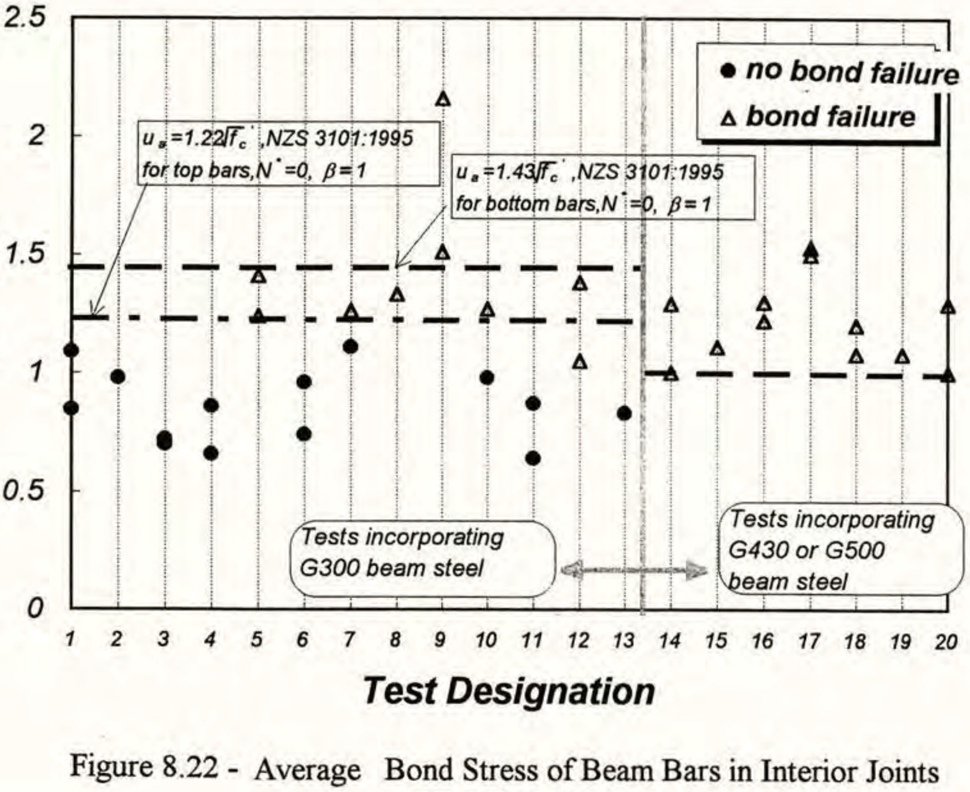

Figure 8.22 - Average Bond Stress of Beam Bars in Interior Joints of Existing Tests.

Table 8.5 - Evaluation of Average Bond Stress of Beam Bars in Interior Joints of of Existing Tests.

Test Designation	Reseacher and Test Unit	$d_{b,t}$	$d_{b,b}$	h_c	$f_{y,t}$	$f_{y,b}$	f_c'	β	$N^*/A_g f_c'$	Cast directio	Failure mode	λ	$u_{a,t} / f_c'$	$u_{a,b} / f_c'$
1	*Beckingsale, B11*	*D19*	*D19*	457	297.6	297.6	35.9	0.5	0.043	*H*	*No failure*	1.172	0.845	1.09
2	*Beckingsale, B12*	*D19*	*D19*	457	279.6	297.6	34.6	1	0.044	*H*	*No failure*	1.19	0.98	0.98
3	*Cheung, 1D-I*	*D24+D20*	*D24+D20*	600	300	300	4.8	0.63	0	*V*	*No failure*	1.196	0.72	0.7
4	*Dai Unit 1*	*D16*	*D16*	406	294	294	45.6	0.4	0	*H*	*No failure*	1.11	0.66	0.86
5	*Dai Unit 2*	*D28*	*D20*	406	314	300	36	0.51	0	*H*	*Bond failure*	1.12	1.41	1.24
6	*Dai Unit 3*	*D16*	*D16*	406	294	294	36.2	0.4	0	*H*	*No failure*	1.105	0.74	0.96
7	*Dai Unit 4*	*D28*	*D20*	406	314	300	40.1	0.51	0	*H*	*Bond failure(top bar slipped)*	1.061	1.26	1.11
8	*Fenwick& Irrine*	*D20*	*D20*	300	280	280	42.9	1	0	*H*	*Bond failure*	1.193	1.33	1.33
9	*Hakuto*	*D24*	*D24*	300	325	325	41	0.5	0	*H*	*Bond failure*	1.164	1.51	2.16
10	*Otani C1~C3*	*D10*	*D10*	300	320	320	25.6	0.5	0.077	*H*	*No failure(bot bar slipped)*	1.335	0.98	1.27
11	*Priestley IBC*	*D28+D25*	*D28*	686	280	280	48.5	0.69	0.03	*H*	*No failure*	1.184	0.64	0.87
12	*Restrepo U5*	*D24*	*D28*	600	285	321	27	1	0	*V*	*Bond failure*	1.23	1.05	1.38
13	*Restrepo U6*	*D24*	*D24*	600	285	285	44	1	0	*V*	*No failure*	1.236	0.83	0.83
14	*Xin Unit 2*	*HD16*	*HD16*	450	445	445	40.8	0.5	0	*H*	*Bond failure*	1.158	1	1.29
15	*Xin Unit 3*	*HD16*	*HD16*	450	445	445	42.5	1	0	*H*	*Bond failure*	1.175	1.11	1.11
16	*Xin Unit 4*	*HD20*	*HD16*	450	492	445	47.2	0.64	0	*H*	*Bond failure*	1.173	1.3	1.22
17	*Xin Unit 6*	*HD28*	*HD20*	450	463	492	59.3	0.51	0	*H*	*Bond failure*	1.177	1.53	1.5
18	*Lawrance&Beattie*	*HD28*	*HD20*	450	479	466	83.2	0.51	0	*V*	*Bond failure*	1.061	1.2	1.08
19	*Lin Unit 3*	*HD12*	*HD12*	390	525	525	37	1	0.1	*V*	*Bond failure*	1.044	1.08	1.08
20	*Lin Unit 4*	*HD12*	*HD12*	390	525	525	37	0.5	0.1	*V*	*Bond failure*	1.08	1	1.29
21	*Beckingsale B13A*	*D19*	*D19*	457	297.6	297.6	31.4	1	0.44	*H*	*No failure*	1.146	0.99	0.99
22	*Teraoka et al NO43*	*D19*	*D19*	400	382	382	54	1	0.2	*H*	*No failure*	1.18	1.14	1.14
23	*Joh, JHO-B8-HH*	*D13*	*D13*	300	370	370	25.6	1	0.153	*H*	*Bond failure*	1.077	1.33	1.33
24	*Joh, JHO-B8-HL*	*D13*	*D13*	300	370	370	27.4	1	0.143	*H*	*Bond failure*	1.101	1.32	1.32
25	*Joh, JHO-B8-LH*	*D13*	*D13*	300	370	370	26.9	1	0.146	*H*	*Bond failure*	1.087	1.31	1.31
26	*Joh, JHO-B8-MH*	*D13*	*D13*	300	370	370	28.1	1	0.14	*H*	*Bond failure*	1.093	1.29	1.29
27	*Otani, Kotayashi, Aoyama, J6*	*D13*	*D13*	300	346	346	28.7	0.75	0.205	*V*	*Bond failure*	1.276	1.27	1.56
28	*Viwathanatepa ,BC3*	*D19*	*D19*	432	490	490	31.1	0.53	0.361	*H*	*Bond failure*	1.138	1.53	1.98

where u_a is the average bond stress of the bar in the joint, n_t is the numbers of top beam bond stress and α_o is the over-strength factor. Let the area of the bottom beam bars be $A_s' = \beta A_s$. According to Cheung et. al [C1], the compressive force of beam bar at the other side of the column face can be realistically estimated as 70% of the yield stress.

$$C_{S2} = \beta \times \left(0.7 f_y A_S\right) \tag{8.30}$$

Equilibrium of the top bars leads to

$$\alpha_o f_y A_S + 0.7\beta f_y A_S = n_t \pi d_{b,t} h_c u_a \tag{8.31}$$

With $A_s = n_t \pi d_{b,t}^2$, the above equation can be re-arranged to obtain the ratio of bar diameter with respect to the overall column depth , h_c.

$$\frac{d_{b,t}}{h_c} = \frac{4}{\alpha_o} \frac{u_a}{f_y} \frac{1}{1+0.56\beta} \tag{8.32}$$

Similarly, the equilibrium of bottom beam bars can be written as,

$$\alpha_o f_y A_s' + C_{b,sb} = n_b \pi d_{b,b} h_c u_a \tag{8.33}$$

Where n_b is the numbers of bottom beam bars. And the tensile force of the top beam bars at column face should be equal to the sum of compressive force in the same beam section.

$$\alpha_o f_y A_S' = C_{b,sb} + C_{b,cb} \tag{8.34}$$

$$C_{b,sb} = \alpha_o f_y A_S' - C_{b,cb} = \frac{1}{\beta}\left(0.7 f_y A_S'\right) \quad where \quad 0.7 \le \beta \le 1.0 \tag{8.35}$$

Where $C_{b,cb}$ is the concrete compressive force in beams at column faces. Eq. (8.33) can be re-arranged by substituting Eq. 8.35

$$\alpha_o f_y A_S' + 0.7 \frac{1}{\beta} f_y A_S' = n_b \pi d_{b,t} h_c u_a \tag{8.36}$$

Similarly, with $A_s' = n_b \pi d_{b,b}^2$, the bar diameter ratio of the bottom beam bars can be obtained as

$$\frac{d_{b,b}}{h_c} = \frac{4}{\alpha_o} \frac{u_a}{f_y} \frac{1}{1+0.56/\beta} \qquad (8.37)$$

With adequate allowable unit bond stress, u_a, being specified, the limitations of beam bar diameter with respect to the column depth, h_c, can be readily determined using Eqs. 8.32 and 8.37. The average bond stress of beam bars was computed from a database of tests. This stress was evaluated using Eqs. 8.32 and 8.37 and was normalized in terms of $\sqrt{f_c'}$. Table 8.5 summaries the results. Tests showing clear joint failure were excluded since the equivalent bond strength might have not attained.

The stress u_a in each test is plotted in **Fig. 8.22** with the failure modes of tests being classified. It is noted that the measured material properties were used in the evaluation and the over-strength factor α_o was based on the measured over-strength using the same procedures as described in Section 2.3.1. Only those tests in which the applied axial load level was less or equal to 0.1 are included in **Fig. 8.22**. The enhancement effect of bond resistance caused by the column axial load will be discussed later.

The results shown in **Fig. 8.22** are classified in two groups. The first group consists of 13 tests in which Grade 300 steel was incorporated as longitudinal beam reinforcement. Tests incorporating Grade 430 or 500 longitudinal beam reinforcement are plotted in the second group. All units investigated incorporated interior column bars. According to Section 8.1.2 these bars influence the bond performance of the longitudinal reinforcement. It can be seen in this graph that tests in the first group having u_a smaller than $1.22\sqrt{f_c'}$ never failed in bond. It indicates that if an interior joint with plastic hinges forming adjacent to column faces is designed with u_a not larger than $1.22\sqrt{f_c'}$, ductile behaviour can be ensured without bond failure of beam bars occurring. It is worth noting that in the first group only one test, designated as no. 12, was cast upright and the "top bar effect" accelerated the bond failure. Thus, it is might be plausible to say that for top beam bar which the depth of fresh concrete cast below is larger than 300 mm, the allowable u_a for determining the bar diameter needs to be reduced further.

The second group in **Fig. 8.22** consists of 7 tests. It can be seen that the allowable average bond stress to preclude bond failure of interior joints in this group is lower than that in the first one. Note that all the tests available in the database in which Grade 430 or higher grade steel was incorporated either failed in bond or in the joint. No tests in the database showed fully ductile performance with 2 cycles to $\mu_\Delta = 6$. It seems evident in this figure that the value of u_a for joints incorporating either Grade 430 or 500 reinforcing steel is lower than for Grade 300 reinforcing steel. For Grade 430 reinforcing steel $u_a \approx 1.0\sqrt{f_c'}$ while for Grade 500 reinforcing $u_a \approx 0.95\ \sqrt{f_c'}$.

8.5.3 Enhancement Effects of the Bond Strength Caused by Column Axial Loads

It has been known that clamping pressure exerting on the anchored bars enhances the bond strength [E1]. Those recommendations in NZS 3101:1995 [S1] recognize this beneficial effect directly by making the design equations a function of the axial load and, indirectly, by requiring the use of interior column bars.

A database of test units that were subjected to axial load ratios greater than 0.1 were compiled and reduced. 7 tests were included in this category and are plotted in **Fig. 8.23**. all tests used Grade 300 reinforcement in the beams. The average bond stress increases with the column compressive load. If $u_a = 1.2\sqrt{f_c'}$ is assumed when $N^* = 0$, a lower bound straight line can be plotted to represent the allowable average bond strength as a function of column compressive load ratio. The equation of this line is.

$$u_a = 1.2\sqrt{f_c'}\left(1 + \frac{N^*}{1.8A_g f_c'}\right) \tag{8.38}$$

The term in the parentheses can be introduced into a design equation in the form of a coefficient. It is noted that the trend found here is close to that given by NZS 3101:1995 [S1]. This coefficient is similar to α_p in the recommendation of NZS 3101:1995.

8.5.4 Discussion

The bar diameter limitation in NZS 3101:1995 is proportional to $\sqrt{f_c'}/f_y$. It pointed out in the previous section that if high strength steel is used as beam longitudinal bars, the bond strength decrease slightly. A physical explanation for this phenomena is given below.

Take examples of two similar interior beam-column joints, in one the beams are reinforced with Grade 300 reinforcing steel bars, while in the other Grade 500 steel is used. Therefore, in order to meet the requirement of d_b/h_c limitation, smaller diameter beam bars are needed when Grade 500 reinforcing bars are used. Let d_{b1} be the longitudinal beam bar diameter of the first example and let d_{b2} be the bar diameter of the second example. It is obvious that d_{b2}=(300/500) d_{b1}=(3/5)d_{b1} so that the design requirement for d_b/h_c can be satisfied. For a same design moment, the required beam bar cross section area in the second example is approximately 3/5 of that required for the first example. That is, $A_{s2} \approx (3/5)\ A_{s1}$. Since the section area of a single bar available for the second example is $(3/5)^2$ times that of Unit 1, the required number of bars will be 5/3 times that of the first. This ends up with the same total circumferential length of beam bars of two units. Therefore, theoretically the two units will have identical bond strength if the same average bond stress, u_a, is assumed. This is the implication of the Concrete Structures Standard recommendation [S1] for anchorage requirement of beam bars passing through the joint region.

In capacity design, where the locations of plastic deformation are deliberately chosen and detailed for ductility, most of the storey lateral displacement arises from the plastic deformation of beam plastic hinges, in the preferable beam side-sway mechanism. Consider the two examples again. It has been pointed out by Priestley [P11] that the yield drift ratio of moment resisting frames is proportional to the yield strain of longitudinal beam bars, the yield drift ratio of the frame in the second example should be approximately (5/3) times that of the first one. If both examples are designed to have a displacement ductility factor, μ_Δ = 6, the storey drift ratio of the second example at μ_Δ = 6 would also approximately equal to (5/3) times that of the first. Therefore, with most part of lateral displacement resulting from beam plastic hinges at column faces, the Grade 500 beam bars used in the second example must be strained more than the bars in the first example in order to achieve to achieve larger storey drift at the same displacement ductility. It is expected that the fixed-end rotation or pull out of beam bars due to yielding penetration into joint region in the second example should be larger than that in the first. If the bond strength in the second example is not strong enough to avoid bond failure, beam bar slippage would eventually occur. As a result, the lateral response would be more governed by the fixed end rotation in this case.

Nevertheless, in accordance with Eligehausen et. al [E1], the cyclic bond stress-slip relationship of bars is very sensitive to the imposed slip value. Larger pull out will make

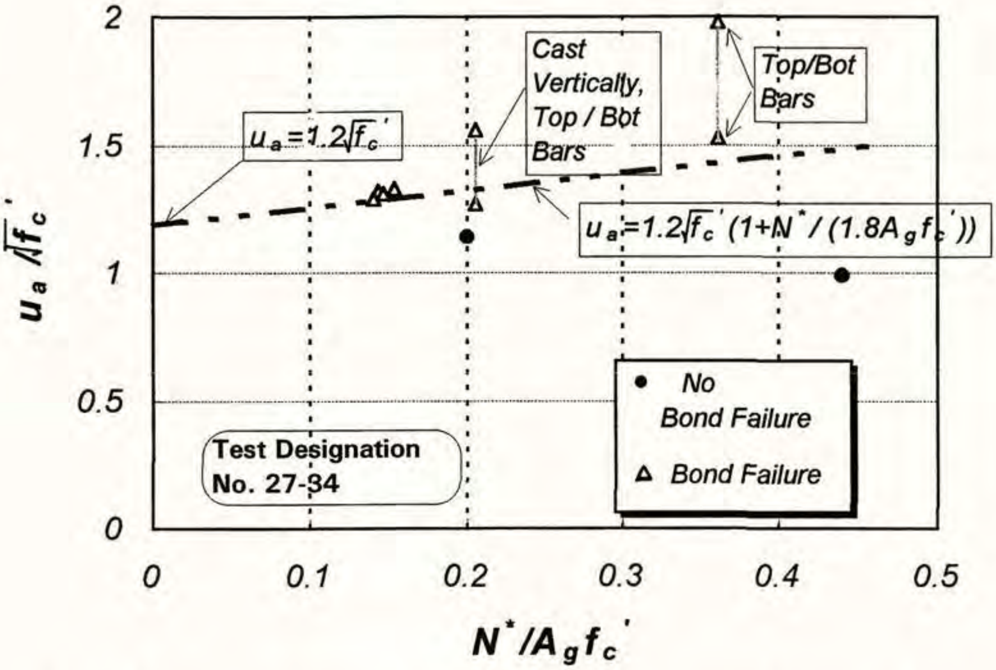

Figure 8.23 - Average Bond Stress of Beam Bars in Interior B-C Joints Versus Column Axial Loads of Existing Tests.

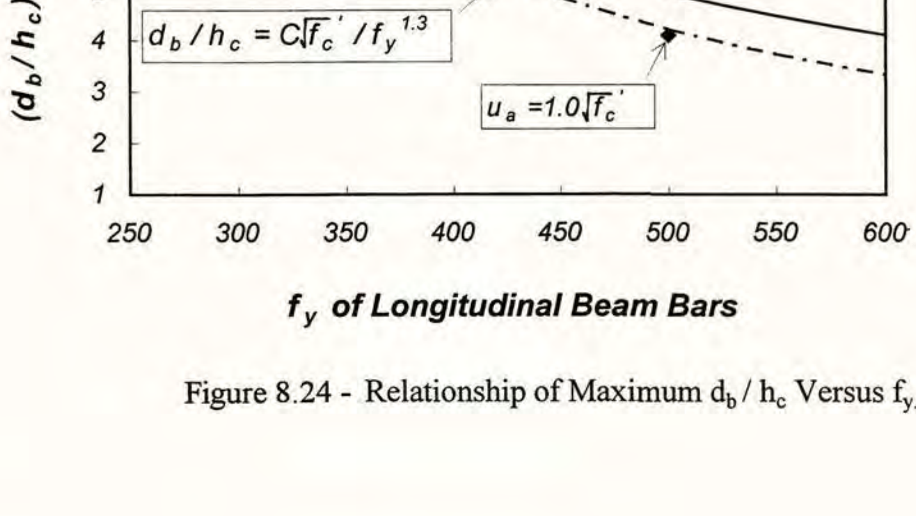

Figure 8.24 - Relationship of Maximum d_b/h_c Versus f_y.

the bond strength deteriorate quicker with the progression of cyclic loads. Therefore the bond strength of joint in the second example would be weaker than that of the first because of the larger slip as a result of the higher strains. It is believed that this is the reason why those tests in database incorporating Grade 430 or 500 steel have less allowable average bond stress.

The average bond stress u_a used in the bar ratio limitation in NZS 3101:1995 [S1] is calculated here to compare with the value evaluated in the above section. The current design equation is presented here.

$$\frac{d_b}{h_c} \le 6\left[\frac{\alpha_t \alpha_p}{\alpha_s}\right]\alpha_f \frac{\sqrt{f_c'}}{\alpha_0 f_y} \tag{8.39}$$

where α_t=0.85 for top bars with "top bar effects", other cases =1.0.

α_p= 0.95 for $N^* = 0$, α_p= $0.95 + N^* / (2A_g f_c')$

$\alpha_s = 2.55 - A_s' / A_s$

α_o : is the over-strength factor, which is taken equal to 1.25 for plastic hinges forming in the beams at the column faces.

For an interior joint reinforced with equal top and bottom beam bars subjected to zero column compressive loads, the code equation gives the bar diameter ratio for top and bottom beam bars as below.

$$\frac{d_b}{h_c} \le 2.5 \frac{\sqrt{f_c'}}{f_y} \qquad \text{for top bars} \tag{8.40}$$

$$\frac{d_b}{h_c} \le 2.94 \frac{\sqrt{f_c'}}{f_y} \qquad \text{for bottom bars} \tag{8.41}$$

Compare the equations above with Eqs. 8.32, 8.37. It is known that the average bond stress adopted in the design equation for bar diameter limitation with "top bar "effect is approximately $1.22\sqrt{f_c'}$. For bottom bars the average stress is $1.43\sqrt{f_c'}$ when $N^* = 0$ and β=1.

As shown in **Fig. 8.22**, the value of $1.43\sqrt{f_c'}$ for bottom bas is larger than the maximum u_a found from the assessment of bond of existing tests in which Grade 300 bars were incorporated and where no bond failure occurred. The stress $1.22\sqrt{f_c'}$ for top bars is just equal to the maximum u_a for beam bars without "top bars" effect. However, the difference between them is not pronounced.

According to the discussion in the above section, when higher grade reinforcement is used as longitudinal beam bars, the maximum permissible value for u_a reduced further. As a result, bond failure would be expected to occur more prematurely if the margin ratio of d_b / h_c given by the Code design recommendation is applied. Given the finding that the maximum u_a is not a constant portion of $\sqrt{f_c'}$ irrespective of f_y, it was found that it is more likely that the maximum d_b / h_c ratio is proportional to $\sqrt{f_c'} / f_y^{1.3}$. As is shown in **Fig. 8.24**, the stress u_a for Grade 300 and Grade 500 bars obtained from the series of analysis fit the line of d_b / h_b = C $\sqrt{f_c'} / f_y^{1.3}$ well, where C represents a constant coefficient. The line inherent in the Code recommendations [S1][A5] tends to slightly overestimate the stress u_a and hence, the ratio d_b / h_b . This effect becomes pronounced when high grade of reinforcement is used as beam longitudinal bars. The finding explains the test results that bond failure occurred more prematurely than what was initially expected in the test units in which Grade 500 beam bars were incorporated.

It is known that the maximum d_b / h_c values specified by standards is a matter of judgment. Some bond deterioration is inevitable and should be accepted [H2]. Although bond damage is difficult to repair and can lead to a reduction in the available flexural strength and available curvature ductility of the adjacent plastic hinges in the beams. Also, bond strength should be considered in association with the design limit state or the displacement ductility factors [R1]. It should be acceptable if bond failure occurs at large displacement ductility which corresponds to the survival limit state.

Besides, although the assessment of bond strength of existing tests reveals that the maximum d_b / h_c ratio is not proportional to $\sqrt{f_c'} / f_y$ and this has a more pronounced effect when high grade longitudinal reinforcement is used, the problem of bond failure at relatively large displacement ductility may not of significant concern, as it had been discussed in Section 8.1.1.4, the use of high grade of bars as longitudinal reinforcement in the beams and columns can only be possible for frames designed for limited ductility response.

8.6 PREDICTION AND COMPARISONS OF BEAM ELONGATION OF TEST UNITS

8.6.1 Introduction

It had been noticed by Paulay [P7] thirty years ago that longitudinal elongation at the mid-depth occurs in beams when they are subjected to flexural deformations. This is due to the offset of neutral axis. Since then elongation measurements have been made in structural tests carried out at the Universities of Canterbury and Auckland [B5] [B6] [C1] [F4] [F5] [M2] for a number of years. Other researchers outside New Zealand [Z1], [Z2] also noticed it has marked influence on the structural behaviour. In 1990, Fenwick and Megget [F6] further classified the beam elongation in accordance with two different types of plastic hinges, named uni-directional hinges and reversed hinges.

Davidson and Fenwick [D3] carried on studying the influence of beam elongation resulted from uni-directional hinges on the behaviour of frame structures based on past experimental results on individual components and sub-assemblies by means of carrying out a series of inelastic time history analysis. In a subsequent paper [F7] they reviewed the previous research regarding the effect of beam elongation, including uni-directional and reversed plastic hinges, and claimed that the beam elongation, which is normally neglected in current design practice, has important implications for the detailing of columns and the design of supports for precast components and external cladding.

In 1996, Fenwick, Ingham and Wuu [F8], based on the recognition that vast majority of existing tests have been made on statically determinate test units, conducted a test on a $2^1/_2$ storey three bay reinforced concrete frame subject to simulated cyclic lateral loads to study the effect of beam elongation as might occur during a severe earthquake. They observed that the external columns just above level one would form an additional uni-directional plastic hinge due to the elongation of beams at the second level. In light of the test results, they emphasized again that the elongation which develops in beams has a marked influence on the behaviour of the frame structures and therefore consideration associated with the influence should be made in the detailing of first level columns to ensure that ductile frames have the required level of ductility. Besides, this effect also needs to be considered when detailing the supports for precast flooring components and cladding. The current Concrete Structure Standard, NZS 3101:1995 [S1], recognizes that plastic hinges may develop in the upper end of the first storey columns in frame buildings and requires adequate detailing in this region.

As beam elongation has marked influence on both structural and non-structural systems, it might be necessary to realistically predict the quantity which is likely to occur during a severe earthquake. Elongation occurred on beams of all the test units in this programme has been measured. Some of them were chosen to demonstrate the variation trends versus inter-storey drift and compare with the predicted values.

8.6.2 Prediction of Beam Elongation

Based on extensive beam tests, Fenwick and Davidson [F7] have been able to predict the elongation characteristics produced from uni-directional hinges from conventional flexural theory using the stress and strain characteristic of concrete and reinforcement. But for reversing plastic hinges, they stated that the situation is more complex so that it is still far a distance away from accurate prediction. Nevertheless, they recognized that the elongation in the reversing plastic hinges arises from two causes; namely the extension of the longitudinal reinforcement in the compression zone and the rotation sustained by the zone. And the extension of the reinforcement in compression zone, from one cycle to the next, provides the major contribution to the elongation which occurs in reversing plastic hinges [F7]. Restrepo et al. [R1] attempted to predict the beam elongation characteristics based on the recognition that beam elongation is mainly resulted from the offset between the neutral axis depth and the mid-depth of beam. Upper and lower bond predictions were postulated on the basis of different extent of tensile residual strain remaining in the reversed load cycle. In view of the comparison of measured and predicted beam elongation made by Restrepo et. al [R1], it can be seen that the upper bond prediction provides good envelop to the measured elongation only when the beam bars were nearly perfectly anchored in joint region. For the Unit 5 tested by Restrepo, in which significant slippage of beam bars had occurred, the upper bond prediction markedly over-estimated the beam elongation of it. Thus it is known that the anchorage of beam bars passing through column does have significant influence on the characteristics of beam elongation.

In the majority of tests carried out in the past to study the characteristics of beam elongation, the anchorage of beam bars in the joint was rather conservative. In some cases, special anchorage devices were incorporated.

Bond deterioration within the joint region, initiating from yielding penetration, is inevitable unless plastic hinges are designed to be located in the beams a distance away from the column faces or special anchoring devices are incorporated [P2]. IAn practical office design work, designers normally intend to choose the largest allowable diameter of beam bars passing through joint region in terms of specified column dimension. Therefore, a realistic estimate of beam elongation should then account for the effect caused by bond deterioration.

Beam elongation arising in a frame subassembly in which plastic hinges form in the beams immediately at the column faces when bond deterioration takes place is depicted in **Fig. 8.25(a)**. The deformation in the beams is idealized as developing in two discrete cracks. The deformation resulting from beam fixed-end rotation is shown to form at the column faces. Elongation stemming from beam flexural deformations is shown to occur in a discrete crack within the beam spans. As most of the latter elongation emanates from the plastic hinges. It is assumed that this crack is located in the centre of the plastic hinge region. The plastic hinge length can be coarsely estimated to be equal to $l_p = 1/2h_b$, where h_b is the beam height (see **Fig. 8.25(a)**) . Thus the crack representing beam flexural deformation locates in the beam away from the column face in a distance of $1/4h_b$. Elongation of beams taking place in the first load cycle toward a new displacement ductility can be calculated as the following equation.

$$\delta_{el1} = 2\left[\theta_{fe1}\frac{(d-d')}{2} + \theta_{fl1}\frac{(d-d')}{2}\right] = \theta_{fe1}(d-d') + \theta_{fl1}(d-d') \tag{8.42}$$

Where θ_{fe1} is the angle of beam fixed-end rotation and θ_{fl1} is the rotation of beam section contributed from flexural deformation. (d-d') is the distance between the centroid of tensile and compressive steel. The neutral axis is assumed to coincide with the centroid of compression steel. When the sub-assembly is displaced to the reversed load cycle, based on the observation in the laboratory tests, the fixed-end rotation, θ_{fe1} has a tendency to close and open from the opposite beam chord due to beam bars slip. Only the beam elongation

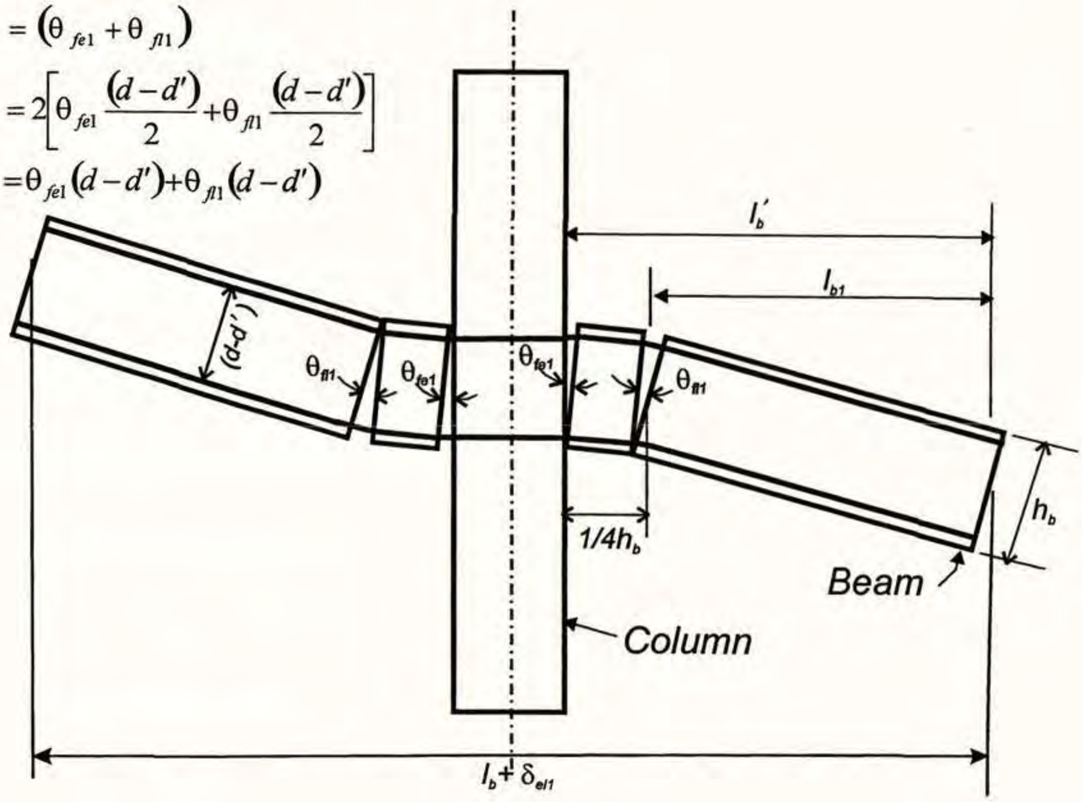

(a)

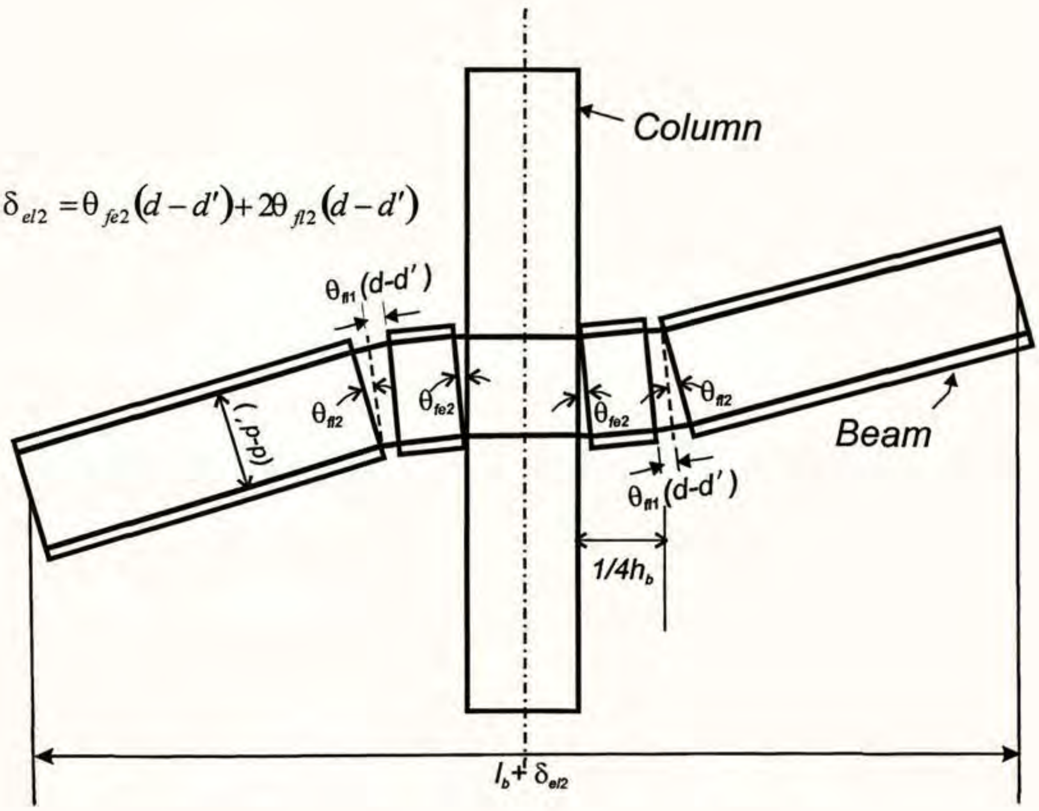

(b)

Figure 8.25 - Estimation of Beam Elongation in a Beam-column Subassembly.

caused by the flexural rotation accumulates with the reversal of loading. Assume that the residual tensile strain gained in the last load cycle remains the same, the accumulated beam elongation occurring in this load cycle is illustrated in **Fig. 8.25(b)** and can be expressed as:

$$\delta_{el2} = \theta_{fe2}(d-d') + \theta_{fl2}(d-d') + \theta_{fl1}(d-d') \tag{8.43}$$

Assuming that $\theta_{fl1} = \theta_{fl2} = \theta_{fl}$ and $\theta_{fe1} = \theta_{fe2} = \theta_{fe}$, accumulated beam elongation is

$$\delta_{el2} = \theta_{fe}(d-d') + 2\theta_{fl}(d-d') \tag{8.44}$$

Note that the first term in Eq. 8.44 represents the part of beam elongation arising from beam fixed-end rotation; while the second term is the portion resulted from beam flexural deformations. It is assumed that only the second source of elongation accumulates with the progression of cyclic loading. Unless beam bars are perfectly anchored in the joint region, some beam fixed-end rotation inevitably appears as a result of yield penetration or slippage of beam bar as the sub-assembly is displaced into inelastic range. The offset between neutral axis depth and beam mid-depth induces elongation of beam length but it does not accumulate. On the other hand, extensive tensile yielding spreading along beam span away from column faces also takes place simultaneously. Both sources contribute to the lengthening of beams but the one resulting from the residual tensile strains on the steel in compression zone is the main source due to the accumulating characteristics.

However, in order to assess the elongation of beams likely to occur during a severe earthquake in terms of the inter-storey drift angle, the relationship between the rotation in the beams and storey drift angle needs to be established. Consider the relation between beam end deflection and rotation of beam section,

$$\theta_{fl} l_{b1} + \theta_{fe} l_b' = \Delta_b \tag{8.45}$$

where Δ_b is the beam end deflection, l_b' is the half beam clear span measured to the column face and l_{b1} represents the distance between centroid of beam plastic hinge and mid-span. The storey drift angle associated with the beam deflection can be expressed as

$$\theta_{fb} = \frac{2\Delta_b}{l_b} \tag{8.46}$$

where l_b is the beam span length between two pin ends. Eq 8.45 can be rearranged in terms of θ_{fb} as

$$2\theta_{fl}\frac{l_{b1}}{l_b}+2\theta_{fe}\frac{l_b'}{l_b}=\theta_{fb} \tag{8.47}$$

When the columns are subjected to moderate compressive axial load, the column flexibility approximately contributes to 25-30% of the overall drift angle. The contribution from beam -column joint shear deformation can be estimated as 15% of the storey drift angle. As a result, the portion of storey drift angle resulting from beam deformations can be estimated as 55-60% of the total inter-storey drift. Hence,

$$\theta_{fb}=0.55\theta_f \tag{8.48}$$

where θ_f is the imposed inter-storey drift ratio. Note that the first term in Eq. 8.47 represents the component of storey drift angle contributing from beam deformation and the second term results from beam fixed-end rotation. Based on the observation of test results regarding the decomposition of lateral displacement, the two components of lateral displacement can be estimated in terms of the storey drift ratio, θ_f, as :

$$2\theta_{fl}\frac{l_{b1}}{l_b}=0.30\theta_f \tag{8.49}$$

and

$$2\theta_{fe}\frac{l_b'}{l_b}=0.25\theta_f \tag{8.50}$$

Based on the above equations, the beam rotation in beams can be expressed in terms of storey drift ratio, θ_f. Therefore, the relation between beam elongation and inter-storey drift ratio can be established by substituting Eqs. 8.49 and 8.50 into Eq.8.44,

$$\delta_{el2}=0.15\theta_f(d-d')\frac{l_b}{l_{b1}}+0.25\theta_f(d-d')\frac{l_b}{l_b'} \tag{8.51}$$

Substituting the corresponding dimensions of the test units in this study, Eq.8.51 becomes

$$\delta_{el2} = 0.95\theta_f(d - d') \tag{8.52}$$

The above equation provides an estimate of the beam elongation in which the beam fixed-end rotation is taken into account.

8.6.3 Comparison of Results

Figure 8.26 shows the comparison of the measured and predicted beam elongation, comprising the elongation taking place in two plastic hinges.

It can be seen in this graph that the predicted beam elongation using Eq. 8.52 provides a lower bound to the measured beam elongation of Units 2, 3, 4 in which longitudinal reinforcement was lumped on the top and bottom of beam section. Note that slippage of longitudinal beam bars anchored in joint region occurred in all units at a late stage during the test. When assessing the beam elongation in a frame structure, Eq. 8.51 can provide a lower bound estimate.

It can be observed in Fig. 8.26 that the measured beam elongation of Unit 7, in which beam bars were vertical distributed through the web, was always less than the predicted elongation given by Eq. 8.52. This can be attributed to two main reasons. First, according to the moment curvature analysis carried out in Chapter 2 for beams in which distributed reinforcement is incorporated, the neutral axis in beam section of Unit 7 would locate at a position closer toward the beam mid-depth instead of as what was assumed in Eq. 8.52 coinciding the centroid of the beam compression steel. Thus the shift between the neutral axis and the centre line of beam height in Unit 7 is not as large as that occurred in units in which beams bars are lumped at top and bottom beam chords. Therefore, the prediction given by Eq. 8.52 which is based on the shift of neutral axis and in terms of (d-d$'$) would certainly over-estimate the beam elongation. Second, slippage of top and bottom beam bars in Unit 7 occurred more prematurely than other units in which beams were conventionally reinforced. This caused larger component of beam fixed-end rotation and smaller rotation angle of beam flexural deformation. Consequently, the portion of beam elongation resulted from beam flexural rotation which can be accumulated during the test of Unit 7 became

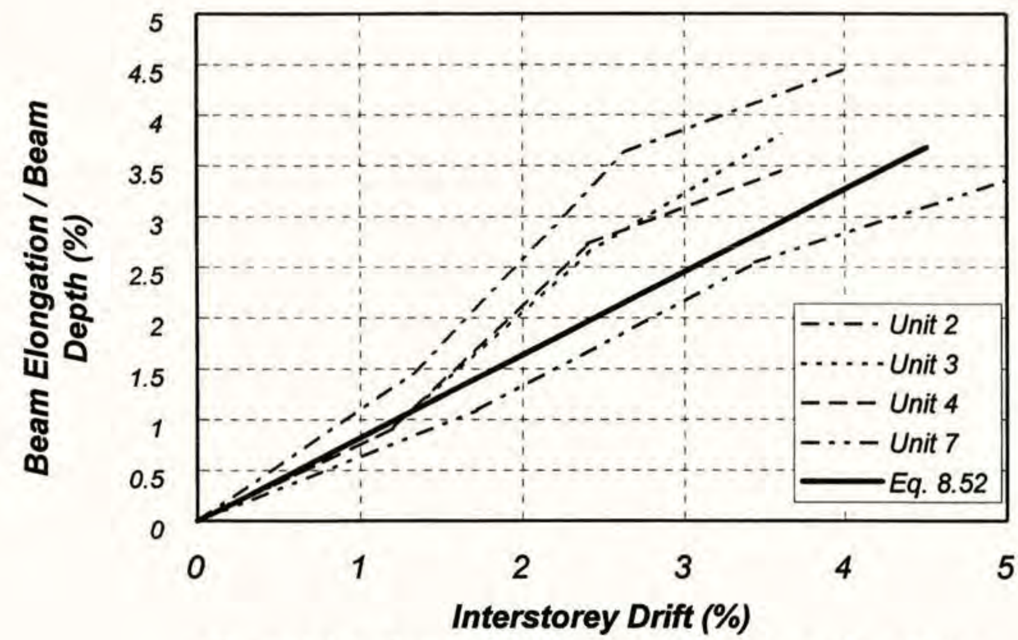

Figure 8.26 - Comparison of Beam Elongation of Test Units and the Predicted values.

less prevalent.

The detailing in which beams incorporating vertically distributed steel had been suggested by Restrepo et al. [R1] because the expected reduction in beam elongation. They claimed that the beam elongation could be reduced since beam bars in compression zone can be easily designed to yield in compression. Comparison of beam elongation described above shows that the trend of reducing beam elongation when the beam bars are distributed along the web.

8.7 CONCLUSIONS

1. The measured yield drift ratio of each test unit was compared with the theoretical values predicted by three methods. It was found that the stiffness of the frame subassembly is been considerable reduced when Grade 500 reinforcing steel is used in

beams. Relatively large yield drift ratio in fully ductile frame structures exceed the code drift limitation before achieving displacement ductility factor of 6 regardless they are detailed for full ductility. As a result, drift limit is likely to govern the design of frame structures using Grade 500 steel as longitudinal reinforcement so that the displacement ductility demand of the structures may need to be restricted.

2. Some important aspects of test results regarding the design of interior joints in which beams were conventionally reinforced are highlighted. Test results of Unit 1-4 and 8 were processed and compared with the trends of the theoretical model for predicting the strength of joints. excellent agreement was found. The capability of the theoretical model developed in Chapter 2 for predicting the joint strength is shown.

3. The relationship between $v_{jh,e} / f_c'$ of the joint and the curvature ductility factors of adjacent beams was established. The available equivalent joint shear stress ratio of the joint associated with the design curvature ductility factors of adjacent beams can be found according to this relationship.

4. The effect of the arching shape of joint reinforcement strain profile on the joint strength is discussed. A profile for evaluating the effective V_{sh} was proposed. A coefficient is suggested to be introduced into the design recommendations to take into account this effect.

5. Two different design procedures of joint design, one is for traditional ductility based design while the other one is for performance-based design, were proposed in this chapter.

6. The procedure using the theoretical model to predict the ultimate displacement ductility factor for joints with given V_{sh} / V_{jh} and $N^*/A_g f_c'$ ratios was described.

7. The effect of improving joint behaviour when using reinforcing steel without apparent yield plateau as joint reinforcement is observed in this study from the data processed from existing tests.

8. Aspects of the design of interior joints incorporating beams with distributed reinforcement were discussed. Test results show that the strength of this type of joints is very similar to that of joints incorporating conventionally reinforced beams.

9. Assessment of the joint strength in existing buildings using the theoretical model proposed in Chapter 2 was discussed. A joint shear strength degradation model was proposed.

10. Bond strength of beam bars in interior joints was studied in light of the assessment of a series of tests collected in a database. The maximum average bond stress in the joint, which is directly related to the limitation of beam bars diameter, is found to decrease slightly when high grade bars are used as beam reinforcement. The consequence is that the maximum d_b/h_c ratio is not proportional to $\sqrt{f_c'}/f_y$. The influence is pronounced when high Grade reinforcement is used in beams.

11. An equation for providing a lower bound estimation of the elongation of beams by taking into account the beam fixed-end rotation is proposed. The equation is based on a simple model that considers two main sources of beam inelastic deformation, namely fixed-end rotation and plastic hinge rotation.

CHAPTER 9
SUMMARY AND CONCLUSIONS

9.1 GENERAL

In this study analytical and experimental investigations were conducted to study the seismic behaviour of interior beam-column joints of reinforced concrete moment resisting frames.

The lower bound theorem of plasticity was used to assess the internal force flow in the panel of a joint. A database comprising 60 interior beam-column joint assemblies tested under reversed cyclic loading was compiles and processed in accordance with the methodology established from the analytical model.

Two types of beam-column joints were investigated. The first type consisted of "conventional" joints in which the framing beams have longitudinal bars lumped at the top and bottom chords. The second type of joints incorporate beams in which the longitudinal bars are distributed through the webs.

Experimental programme was carried out by testing eight 70% scaled precast interior beam-column subassemblies. Five units were designed with conventionally reinforced beams. Three units incorporated longitudinal beam bars distributed through the web. A typical quasi-static loading scheme, simulating lateral earthquake excitation, was used to test all units.

Grade 500 reinforcing steel was used as longitudinal reinforcement for the beams and columns in all units.

9.2 SEISMIC BEHAVIOUR OF INTERIOR BEAM-COLUMN JOINTS

9.2.1 Analytical Investigation

The main parameters which are likely to influence the strength of the joints were identified using the lower bound theory of plasticity. The flow of internal forces was evaluated using strut-and-tie models. A correlation between the most important parameters was found using the data extracted from the tests collected in the database.

Results obtained from the analytical work were compared with the requirements given by the New Zealand Concrete Structures Standard, NZS 3101:1995 [S1]. Four different trends were found. First, for typically used deformed bar sizes, the bond force distribution along beam bars passing through the joint region was found not to significantly affect strength of joints. Second, the required horizontal joint reinforcement, is strongly influenced by the joint shear stress ratio, v_{jh} / f_c'. Third, the influence of vertical joint reinforcement, in the form of column interior bars, was found to have an insignificant influence on the strength of joints. Instead it was found that column interior bars improve the anchorage conditions of the beam bars. Fourth, column compressive loads are not beneficial to the joint strength when $N^* / A_g f_c' \geq 0.3$. This finding implies that the required horizontal joint reinforcement should not decrease but increase when column axial loads exceed $0.3 A_g f_c'$.

A bilinear relationship between an equivalent joint strength and the rotational ductility of the frame assemblies was established. Data collected from tests subjected to reversed cyclic loading shows reasonable agreement and display a small coefficient of variation. Design recommendations derived in accordance with the theoretical model were made for joints of fully ductile and limited ductility frames.

Joints in which framing beams have the longitudinal reinforcement distributed through the web were also analyzed. In summary, the design of joints incorporating such beams can be designed using the same provisions for joints with conventionally reinforced beams.

9.2.2 Experimental Evidence

9.2.2.1 General

A common feature found in the experimental programme for all test units was the relatively large storey drifts associated with the reference yield displacement. Owing to the incorporation of Grade 500 bars as longitudinal beam and column reinforcement, the yield drifts of test units are significantly larger than that predicted using the effective moment of inertia values recommended by NZS 3101:1995. The significance of this finding is highlighted in this study.

9.2.2.2 Tests on Beam-column Joint Subassemblies Incorporating with Conventionally Reinforced Beams

Four units, Units 1 to 4, were built and tested to reconcile some discrepancies between the analytical findings and design recommendations given in NZS 3101:1995 for interior joints.

Unit 1 and 2 were tested under relatively large column axial load of $N^* / A_g f_c' = 0.43$ and a nominal joint shear stress ratio $v_{jh}/f'_c = 0.17$. NZS 3101:1995 suggests that the amount of horizontal joint reinforcement can be reduced with axial load whereas the theoretical model indicates the opposite trend when $N^* / A_g f_c' > 0.3$.

Unit 1, in which the amount of horizontal joint reinforcement slightly exceeded the requirements given by NZS 3101:1995 for joints of fully ductile frames, showed a joint shear failure at limited ductility. Unit 2, in which the amount of joint reinforcement complied the analytical results, showed satisfactory ductile performance. Bond failure of the top beam bars occurred in the load cycle to $\mu_\Delta = 6$. The experimental evidence reveals that when the applied column compressive loads exceed $0.3f_c' A_g$, and the joint is subjected to high shear stresses, the diagonally compressive stress in the joint panel increases. As a result, more joint shear reinforcement is required to sustain the diagonal compression stress field. Otherwise, the compressive capacity of the cracked concrete in the joint panel will be reached, leading to crushing of the concrete and failure of the frame subassembly.

Units 3 and 4 were tested to observe the influence of the ratio of top and bottom beam reinforcement on the amount of horizontal joint reinforcement required. The current design recommendations in NZS 3101:1995 are a function of this ratio. The analytical model indicated that this ratio has a negligible influence.

The overall behaviour of Units 3 and 4 was satisfactory. Joints performed well without much damage. Unit 4, in which the longitudinal beam top and bottom reinforcement amounts were unequal, performed very similarly to Unit 3, which had equal top and bottom reinforcement in the beams. In light of the test results of Units 3 and 4, it can be said that the provisions for horizontal joint reinforcement in NZS 3101:1995 should not depend on the ratio of the amount of top and bottom beam reinforcement.

Another finding in the tests of Units 3 and 4 was the effect of ratio v_{jh}/f'_c on the amount of horizontal joint reinforcement required. NZS 3101:1995 allows a reduction of the horizontal joint reinforcement for low values of v_{jh}/f'_c. The experimental work confirmed this trend but indicated, together with the finding of the analytical model, that more weight should be given to the ratio v_{jh}/f'_c.

9.2.2.3 Tests on Beam-column Joint Subassemblies Incorporating Beams Reinforced with Longitudinal Bars Distributed Through the Web

Units 5 to 7 were tested to obtain data for the design of beams reinforced with longitudinal bars distributed through the web. A potential advantage of such detail is the use of small diameter bars passing through the joint and a reduction of the elongation in the plastic hinge region of the beams.

Units 5 and 6 were identical except for the type of joint reinforcement. Unit 5 had plain round hoops acting as horizontal joint reinforcement whereas the hoops in Unit 6 were deformed. Both Units showed very similar limited ductility response. Joint and beam bars bond failure limited the ductility response of these Units. The presence of deformed bar reinforcement had a slight enhancement in the performance of the joint in Unit 6.

Unit 7 was similar to Unit 8 except that in Unit 5 larger diameter longitudinal bars were used in the web. Also, after the limited ductility performance observed in Units 5 and 6, Unit 7 was tested under a large axial load than the former units. Unit 7 performed better than Units 5 and 6. The joint suffered minor damage. Bond failure controlled the behaviour of this unit at the end of the test.

A reduction of the data of Units 5-7 shows that beam-column joints built using beams with longitudinal distributed reinforcement behave very similarly as joints with conventionally reinforced beams.

Unit 8 was a benchmark unit for Units 5-7. It incorporated conventionally reinforced beams. This unit showed limited ductility performance. Joint and beam bar bond failure controlled the behaviour of this unit at the end of the test. Units 5 and 6 performed very similarly to Unit 8.

9.2.3 Recommendations for the Seismic Design of Interior Beam-Column Joints

The results of the experimental work confirmed that the analytical work is capable of predicting the joint shear strength and deformation capacity of frame assemblies. As a result, the model was employed to make design recommendations. In general, it can be concluded that the current NZS 3101:1995 design recommendations for the design of interior beam-column joints are conservative and could be relaxed. An exception is the design of interior joints with reasonably large axial compressive loads in the columns combined with large joint shear stress.

The recommendation for the seismic design of interior beam-column joints proposed in this study were developed for ductility and performance based designs. Additionally, an extension of the method was proposed for the assessment of the strength and ductility capacity of joints in existing buildings.

9.2.4 Bond Strength of Beam Bars Passing through Joint Region

Units 1-4 and 8, in which Grade 500 reinforcement was used as longitudinal reinforcement in the beams and the columns met the bar anchorage requirements given by NZS 3101:1995 for joints of ductile frames. All the units showed bond failure at displacement ductilities between 4 and 6. The effect of direction of casting of the concrete was clearly observed. An analysis of bond strength data indicates that the maximum d_b / h_c ratio may more likely be proportional to $\sqrt{f_c'} / f_y^{1.3}$ rather than to $\sqrt{f_c'} / f_y$. This effect becomes pronounced when using high grade reinforcing steel.

It was found that the maximum local bond stress sustained in the outermost bars in the beams of Units 5, 6 and 7 was smaller than that in the units incorporating conventionally reinforced beams in general. Bond failure of these bars occurred slightly earlier than that in Units 1-4 and 8. Test results show that the bond demand in the joint region of outermost bars in beams incorporating distributed reinforcement is larger than that of bars in conventional beams.

9.2.5 Beam Elongation

The beam elongation measured in the test units ranged between 1.8-3.5% of the beam overall depth when the interstorey drift ratio was 2.5%.. The amount of beam elongation was affected by the different failure modes of beam-column subassemblies. The units that incorporated beams reinforced with longitudinal distributed bars showed equal or smaller beam elongation than units incorporating conventionally reinforced beams. An equation was derived for the prediction of beam elongation in recognition to the influence of beam fixed-end rotation.

9.3 SEISMIC DESIGN OF REINFORCED CONCRETE MOMENT RESISTING FRAMES USING GRADE 500 LONGITUDINAL STEEL

Experimental evidence and analytical model conclusively show that the use of Grade 500 bars as longitudinal reinforcement in beams and columns results in more flexible frame structures than those incorporating mild steel as longitudinal reinforcement. Test results of Units 1-4 and 8 showed displacement ductility factors ranging from 2.6 to 4.2 at the Code drift limit of 2.5%. Therefore, the design of such frame is likely to be governed by inter-storey drift limits when Grade 500 reinforcement is used. This is because fully ductile frame subassemblies will reach 2.5% inter-storey drift before achieving the target displacement ductility factor of 6.

An issue of great significance in design is that the effective moment area of inertia recommended by NZS 3101:1995 [S2] over-estimates the stiffness of frame subassemblies when Grade 500 longitudinal reinforcement is incorporated. The consequences if this would be to significantly under-estimate the inter-storey drift under the action of design lateral load and to over-estimate the displacement ductility demands. Designers should be aware of the significance of this issue when incorporating Grade 500 longitudinal reinforcement.

For some low rise building structures, in which the design is not likely controlled by drift limitations, Grade 500 reinforcement could possibly be used in the design of fully ductile structures. Besides, structural members which are designed to remain nominally elastic could incorporate Grade 500 reinforcement due to the cost savings.

9.4 SUGGESTED FUTURE RESEARCH

The following topics are recommended for further research.

1. The analytical work carried out in this study suggests that for joints of limited ductility frames having joint shear stress ratios, v_{jh} / f_c', less than 0.2, a minimum amount of horizontal joint reinforcement of $V_{sh} / V_{jh} = 0.4$ is sufficient. Experimental investigation on beam-column subassemblies designed with limited ductility are required to be

conducted to calibrate this minimum requirement and for checking whether these joints could sustain stresses $v_{jh} / f_c' > 0.2$.

2. Combined sway mechanisms are permitted in the design of buildings in NZS 3101:1995 [S1] [P2]. In joints of a sway mechanism involving column plastic hinges at the joint faces, significant yielding may be expected to take place in some longitudinal column bars. The current Code provisions do not cover this case and experimental work is required in this area.

3. An analysis of the database of results revealed that there is marked enhancement effect on the joint strength when the stress-strain relationship of the horizontal joint reinforcement does not show a well defined yield plateau region. As there is some possibility that such type of reinforcement will be used in New Zealand in the future [P9], tests could be carried out to investigate the apparent beneficial effect of this type of reinforcement.

4. Current design provisions for establishing the diameter of beam and column bars anchored in interior beam-column joints are based on ductility requirements. Performance-based requirements could be established with the advantage that both ductility and drift ratios could be accounted for.

REFERENCES

A1- ACI Committee 352, (1991), *Recommendations for Design of Beam-Column Joints in Monolithic Reinforced Concrete Structures*, ACI report, ACI 352R-91, American Concrete Institute, Detroit, Michigan.

A2- ATC, (1987), *Evaluating the Seismic Resistance of Existing Buildings ATC-14*, Applied Technology Council, Redwood City, California, 370 p.

A3- ATC, (1989), *A Handbook for Seismic Evaluation of Existing Buildings ATC-22*, Applied Technology Council, Redwood City, California, 169 p.

A4- Aoyama H., (1980), *A Method for the Evaluation of the Seismic Capacity of Existing Reinforced Concrete Buildings in Japan,* Bulletin of the New Zealand National Society for Earthquake Engineering, Vol. 14, No. 3, pp. 105-130.

A5- Architectural Institute of Japan, (1990), *Design Guidelines for Earthquake Resistant Reinforced Concrete Buildings Based on Ultimate Strength Concept* (in Japanese), 340 p.

A6- ACI Committee 318, (1995), *Building Code Requirements for Structural Concrete (ACI 318-95) and Commentary (ACI 318R-95)*, American Concrete Institute, Farmington Hills, USA.

B1- Blakeley R. W. C., Megget L. M. and Priestley M.J.N., (1977), *Cyclic Loading Testing of Two Reinforced Concrete Joints*, Bulletin of the New Zealand National Society for Earthquake Engineering, Vol. 12, No. 3, pp. 238-255.

B2- Bonacci J. and Pantazopoulou S. (1993), *Parametric Investigation of Joint Mechanisms*, Structural Journal, American Concrete Institute, Vol. 90, No. 1, pp. 61-71.

B3- Beckingsale C. W., (1980), *Post-Elastic Behaviour of Reinforced Concrete Beam-Column Joints*, Department of Civil Engineering, University of Canterbury, Research Report No. 80-20, 398 p.

B4- Birss G. R., (1978), *The Elastic Behaviour of Earthquake Resistant Reinforced Concrete Interior Beam-Column Joints,* Department of Civil Engineering, University of Canterbury, Research Report No. 78-13, February, 96 p.

B5- Beckhuis W. J., (1971), *An Experimental Study of Squat Shear Walls*, M.E. Thesis, Department of Civil Engineering, University of Canterbury, Christchurch, 132 p.

B6- Binney J. R., (1972), *Diagonally Reinforced Coupling Beams*, M.E. Thesis, Department of Civil Engineering, University of Canterbury, Christchurch, 131 p.

B7- Brundson D. R., (1993), *The August 8, 1993 Guam Earthquake Reconnaissance Report*, Bulletin of the New Zealand National Society for Earthquake Engineering, Vol. 26, No. 4, pp. 340-410.

C1- Cheung P. C., (1992), *Seismic Design of Reinforced Concrete Beam-Column Joints with Floor Slab*, Ph.D. thesis, Department of Civil Engineering, University of Canterbury, Christchurch.

C2- Collins M. P. and Mitchell D., (1991), *Prestressed Concrete Structures*, Prentice-Hall, Inc., 766 p.

C3- Castro J. J., Imai H. and Yamaguchi T., (1992), *Seismic Performance of Precast Concrete Beam-Column Joints*, Proc. of the 10th World Conference on Earthquake Engineering, Madrid, Spain, Vol. 6, pp. 3131-3137.

C4- Canadian Standards Association, (1984), *Design of Concrete Structures for Buildings with Explanatory Notes*, CAN3-A23.3-M84, Rexdale, Ontario.

C5- Collins M. P., Mitchell D., Adebar P. and Vecchio F. J., (1996), *A General Shear Design Method*, Structural Journal, American Concrete Institute, Vol. 93, No. 1, Detroit, Michigan.

C6- CND/EERI, (1983), *El-Asnam, Algeria Earthquake of October10, 1980*, Reconnaissance and Engineering Report, Earthquake Engineering Research Institute, Berkeley, California.

D1- Dai Ruitong and Park R., (1987), *A comparison of the Behaviour of Reinforced Concrete Beam-Column Joints Designed for Ductility and Limited Ductility,* Research Report, No. 87-4, Department of Civil Engineering, University of Canterbury.

D2- Durrani A. J. and Wight J.K., (1982), *Experimental and Analytical Study of Internal Beam to Column Connections Subjected to Reversed Cyclic Loading*, Report UmEE82R3, Department of Civil Engineering, University of Michigan, Ann Arbor, 275 p.

D3- Davidson B. J. and Fenwick R. C., (1993), *The Seismic Response of Ductile Reinforced Concrete Frames With Uni-Directional Hinges,* University of Auckland, School of Engineering Report, No. 527, 59 p.

D4- Davidson B. J. and Fenwick R. C., (1997), Ductility Demands for Reversing and Uni-directional Plastic Hinges in Ductile Concrete Frame Structures, Proceedings of Annual Technical the New Zealand National Society of Earthquake Engineering, Wairakei, Taupo.

E1- Eligehausen R., Popov E. P. and Bertero V. V., (1983), *Local Bond Stress-Slip Relationships of Deformed Bars Under Generalized Excitation,* Report UCB/EERC-83/23, Earthquake Engineering Research Center, University of California, Berkeley, 178 p.

F1- Fenwick R. C., (1982), *Shear Deformation in Reinforced Concrete Beams Subjected to Inelastic Cyclic Loading*, Research Report, No. 279, School of Engineering, University of Auckland.

F2- Fenwick R. C., (1981), *Seismic Resistant Joints for Reinforced Concrete Structures*, Bulletin of the New Zealand National Society for Earthquake Engineering, Vol. 14, No.3.

F3- Fujii S. and Morita S., (1989), *Behaviour of Exterior R.C. B-C-Slab Subassemblies Under Bi-Directional Loading, 3rd US-NZ-Japan-China Seminar on Design of RC Beam-Column Joints for Earthquake Resistance*, Christchurch, New Zealand.

F4- Fenwick R. C. and Fong A., (1979), *The Behaviour of Reinforced Concrete Beams Under Cyclic Loading,* Bulletin of the New Zealand National Society for Earthquake Engineering, Vol. 12, No. 2, pp. 158-167.

F5- Fenwick R. C. and Nguyen H. T., (1981), *Reinforced Concrete Beam-Column Joints for Seismic Loading,* Research Report, No. 220, Department of Civil Engineering, University of Auckland, 62 p.

F6- Fenwick R. C. and Megget L. M., (1993), *Elongation and Load Deflection Characteristics of Reinforced Members Containing Plastic Hinges,* Bulletin of New Zealand National Society for Earthquake Engineering, Vol. 26, No.1.

F7- Fenwick R. C. and Davidson B. J., (1995), *Elongation in Ductile Seismic Resistant Reinforced Concrete Frames*, T. Paulay Symposium, American Concrete Institute, SP 157-7, pp. 143-170.

F8- Fenwick R. C., Ingham J. M. and Wuu P.J.Y., (1996), *The performance of Ductile Reinforced Concrete Frames Under Seismic Loading*, Proceedings of the NZNSEE Annual Technical Conference, New Plymouth, pp. 20-26.

F9- Freeman S. A., Czarnecki R. M. and Honda K. K., (1980), *Significance of Stiffness Assumptions on Lateral Force Criteria*, ACI Publication SP-63, American Concrete Institute, Detroit, pp. 437-457.

G1- *Guidelines for the Use of Structural Precast Concrete in Buildings*, (1991), Report of a Study Group of the New Zealand Concrete Society and the New Zealand National Society for Earthquake Engineering, The Printery, University of Canterbury, Christchurch, 174 p.

G2- Goto Y., Joh O. and Shibata T., (1987), *Effect of Joint Reinforcement on the Shear*

Resistance of R/C Interior Beam-Column Joints, (in Japanese), Proc. of Japan Concrete Institute, Vol. 9, No. 2, pp.187-192.

H1- Hakuto S., Park R. and Tanaka H., (1995), *Retrofitting of Reinforced Concrete Moment Resisting Frames*, Research Report 95-4, Department of Civil Engineering, University of Canterbury, Christchurch.

H2- Hakuto S., Park R. and Tanaka H., (1999), *Effect of Deterioration of Bond of Beam Bars Passing Through Interior Beam-Column Joints on Flexural Strength and Ductility*, American Concrete Institute Structural Journal, Vol. 96, No. 5, pp. 858-864 .

H3- Hanson N. W. and Conner H. W., (1967), *Seismic Resistance of Reinforced Concrete Beam-Column Joints*, Journal of the Structural Division ASCE, Vol. 93, ST5, pp. 533-560.

J1- Joh O., Goto Y. and Shibata T., (1991), *Behaviour of Reinforced Concrete Beam-Column Joints with Eccentricity*, in ACI Special Publication, SP 123-12, *(Design of Beam-Column Joints for Seismic Resistance)*, Detroit, Michigan, pp. 317-357.

J2- Joh O., Goto Y. and Shibata T., (1991), *Influence of Transverse Joint and Beam Reinforcement and Relocation of Plastic Hinge Region on Beam-Column Joint Stiffness Determination*, in ACI Special Publication, SP 123-12, *(Design of Beam-Column Joints for Seismic Resistance)*, Detroit, Michigan, pp. 187-223.

K1- Kamimura T., (1993), *Shear Strength of Interior Beam-Column Joints*, Ph. D. Dissertation of Department of Architecture, Shibaura Institute of Technology, Tokyo, selected in the book, *Earthquake Resistance of Reinforced Concrete Structures,* A Volumn honoring Hiroyuki Aoyama, University of Tokyo Press.

K2- Kurose Y., (1993), *Design of Beam-column Joints for Shear*, Report of Structural Design Department, Shimizu Corporation, Tokyo, selected in the book, *Earthquake Resistance of Reinforced Concrete Structures,* A Volume honoring Hiroyuki Aoyama, University of Tokyo Press.

L1- Lawrence G. M. and Beattie G., (1993), *The Cyclic Load Performance of a High Strength Concrete Beam-Column Joint*, Central Laboratories Report 93-25130, Lower Hutt, New Zealand, 50 p.

M1- Mander J. B., Priestley M. J. N. and Park R., (1988), *Observed Stress-Strain Behaviour of Confined Concrete,* Journal of Structural Engineering, ASCE, Vol. 114, No.8, pp. 1827-1849.

M2- Megget L. M. and Fenwick R. C., (1988), *Seismic Behaviour of A Reinforced Concrete Portal Frames Sustaining Gravity Loads,* Proceedings of the Pacific Concrete Conference, Auckland, Vol. 1, pp. 4-42.

M3- Marti P., (1985), *Basic Tools of Reinforced Concrete Beam Design*, Structural Journal, American Concrete Institute, Vol. 82-4, pp. 46-56.

M4- Marti P., (1991), *Dimensioning and Detailing*, IABSE-Colloquium Stuttgart 1991: Structural Concrete, IABSE Report Vol. 62, Zurich, pp.411-443.

M5- Mueller P., (1978), *Plastic Analysis of Reinforced Concrete Walls and Beams,* Report No. 83, Institute of Structural Engineering, ETH Zurich, 160 p.

M6- Marti P., (1980), *On Plastic Analysis of Reinforced Concrete*, Report No. 104, Institute of Structural Engineering, ETH Zurich, 176 p.

M7- Marti P., (1982), Strength and Deformations of Reinforced Concrete Members Under Torsion and Combined Actions, Bulletin d'Information No. 146, Comite Euro-International du Beton, Paris, pp. 97-138.

M8- Milburn J. R. and Park R., (1982), *Behaviour of R. C. Beam Column Joints Designed to NZS 3101*, Research Report 82-7, Department of Civil Engineering, University of Canterbury, Christchurch, 107 p.

M9- Meinheit D. F. and Jirsa J. O., (1997), *The Shear Strength of R.C. Beam Column Joints*, CESRL Report 77-1, Department of Civil Engineering, University of Texas at Austin.

M10 -(1985), *The September 1985 Mexico Earthquake - Preliminary Report of the New Zealand Reconnaissance Team*, Bulletin of the New Zealand National Society for Earthquake Engineering, Vol. 18, No.4.

N1- Nielsen M. P., (1971), *On the Strength of Reinforced Concrete Discs*, Civil Engineering and Building Construction Series No. 70, Poltechnica Scandinavica, Stockholm, 261 p.

N2- Noguchi H. and Kashiwazaki T., (1992), *Experimental Studies on Shear Performance of RC Interior Column-Beam Joints with High Strength Material*, Proc. of the 10th World Conference on Earthquake Engineering, Madrid, Spain, Vol. 6, pp. 3163-3168.

N3- Norton J. A., King A. B., Bull D. K., Chapman H. E., McVerry G. H., Larkin T. J. and Spring K. C., (1994), *Northridge Earthquake Reconnaissance Report*, Bulletin of the New Zealand National Society for Earthquake Engineering, Vol. 27, No. 4, pp. 235-344.

O1- Otani S., Kobayashi Y. and Aoyama H., (1984), *Reinforced Concrete Interior Beam-Column Joints Under Simulated Earthquake Loading*, Proc. 1st US-NZ-Japan Seminar on Design of R.C. Beam-Column Joints, Monterey.

O2- Otani S., Kitayama K. and Aoyama H., (1985), *Beam Bar Bond Stress and Behaviour of Reinforced Concrete Interior Beam-Column Connections*, Proc. 2nd US-NZ-Japan Seminar on Design of R.C. Beam-Column Joints, Tokyo, 40 p.

P1- Park R., (1989), *Evaluation of Ductility of Structures and Structural Assemblages from Laboratory Testing*, Bulletin of the New Zealand National Society for Earthquake Engineering, Vol. 22-3, pp. 155-166.

P2- Paulay T. and Priestley M.J.N., (1991), *Seismic Design of Reinforced Concrete and Masonry Buildings*, John Wiley & Sons Inc., 744 p.

P3- Priestley M.J.N., Seible F. and Calvi G. M., (1995), *Seismic Design and Retrofit of Bridges*, John Wiley & Sons Inc., 686 p.

P4- Park R. and Paulay T., (1975), *Reinforced Concrete Structures*, John Wiley & Sons Inc., 769 p.

P5- Paulay T., Park R. and Priestley M.J.N., (1978), *Reinforced Concrete Beam-Column Joints Under Seismic Actions*, Journal of the American Concrete Institute, Vol. 75, No. 11, pp. 585-593.

P6- Priestley M.J.N., (1995), *Displacement-Based Seismic Assessment of Existing Reinforced Concrete Buildings*, Pacific Conference on Earthquake Engineering, Vol. 2, Melbourne, Australia.

P7- Paulay T., (1969), *The Coupling of Shear Walls*, Ph D. Thesis, Department of Civil Engineering, University of Canterbury, Christchurch, New Zealand, Vol. 1, 220 p. and Vol. 2, 210 p.

P8- Paulay T., (1982), *Lapped Splices in Earthquake-Resisting Columns*, ACI Structural Journal Vol. 79-44, pp. 458-461.

P9- Park R., (1995), *Opportunities in New Zealand for High Strength Reinforcing Steel*, Proceedings of International Conference of New Zealand Concrete Society, pp. 124-133.

P10- Park R. and Keong Y. S., (1979), *Tests on Structural Concrete Beam-Column Joints with Intermediate Column Bars, Bulletin of the New Zealand National Society for Earthquake Engineering*, Vol. 12, No.3.

P11- Priestley M.J.N., (1998), *Brief Comments on Elastic Flexibility of Reinforced Concrete Frames and Significance to Seismic Design*, Bulletin of the New Zealand Society for Earthquake Engineering, Vol. 31, No. 4, pp. 246-259.

P12- Priestley M.J.N., (1975), *Testing of Two R.C. Beam-Column Assemblies Under Simulated Seismic Loading*, Report 5-75/1. Central Laboratories, Lower Hutt, New Zealand, 114 p.

P13- Priestley M.J.N. and Calvi G. M., (1997), *Concepts and Procedures for Direct Displacement Based Design and Assessment*, Proc. International Conference on Seismic

Design Methodologies for the Next Generation of Codes, Pub. A.A. Balkema, Rotterdam, pp. 171-182.

P14- Park R., (1997), *A Static Force-based Procedure for the Seismic Assessment of Existing Reinforced Concrete Moment Resisting Frames*, Bulletin of New Zealand National Society for Earthquake Engineering, Vol. 30, No.3, pp. 213-226.

P15- Priestley M.J.N. and Calvi G. M., (1991), *Toward a Capacity Design Assessment Procedure for Reinforced Concrete Frames*, Earthquake Spectra, Vol. 7, No.3, pp. 413-437.

P16- Park R., (1992), *Seismic Assessment and Retrofit of Concrete Structures, United States and New Zealand Development*, Proc. of Annual Technical Conference of New Zealand Concrete Society, Wairakei, pp. 18-25.

P17- Popov E. P., (1984), *Bond and Anchorage of Reinforcing Bars Under Cyclic Loading*, ACI Structural Journal, American Concrete Institute, Vol. 81, No.4, pp. 21-25.

P18- Priestley M.J.N., (1995), *Myths and Fallacies in Earthquake Engineering-conflicts between design and reality, Recent Developments in Lateral Force Transfer in Buildings*, ACI SP-157, pp. 231-254.

P19- Paulay T. and Park R. and Priestley, M.J.N. (1978), *Reinforced Concrete Beam-Column Joints Under Seismic Actions*, American Concrete Institute Structural Journal, Vol. 75, No. 11, pp.585-593.

R1- Restrepo-Posada J.I., (1993), *Seismic Behaviour of Connections Between Precast Concrete Elements*, Research Report No. 93-3, Department of Civil Engineering, University of Canterbury.

S1- Standards Association of New Zealand, (1995), *Concrete Structures Standard, Part 1-The Design of Concrete Structures* NZS 3101:1995, Standards New Zealand.

S2- Standards Association of New Zealand, (1995), *Concrete Structures Standard, Part 2 -*

Commentary on The Design of Concrete Structures NZS 3101:1995, Standards New Zealand.

S3- Standards Association of New Zealand, (1992), *Code of Practice for General Structural Design And Design Loadings for Buildings, Volume 1, Code of Practice,* NZS 4203:1992, Standards New Zealand.

S4- Standards Association of New Zealand, (1992), *Code of Practice for General Structural Design And Design Loadings for Buildings, Volume 2, Commentary,* NZS 4203:1992, Standards New Zealand.

S5- Standards Association of New Zealand, (1989), *Steel Bars for the Reinforcement of Concrete*, NZS 3402:1989, Wellington, 15 p.

S6- Stevenson E. Craig, (1980), *Fibre Reinforced Concrete in Seismic Design*, Research Report No. 80-7, Department of Civil Engineering, University of Canterbury.

S7- Stevens N. B., Uzumeri, S. M. and Collins M. P., (1991), *Reinforced Concrete Subjected to Reversed Cyclic Shear - Experiments and Constitutive Model*, Structural Journal, American Concrete Institute, Vol. 88, No. 2, pp. 135-146.

S8- Schlaich J., Schafer K. and Jannew M., (1987), *Toward a Consistent Design of Structural Concrete*, PCI Journal, pp. 74-147.

S9- Satoshi B., Minoru F. and Hitoshi H., (1985), *Behaviour of Reinforced Concrete Beam-Column Joints*, Report of Kajima Institute of Construction Technology, Japan.

S10- Sugano S., Nagashima T., Kimura H. and Ichikawa A., (1991), *Behaviour of Beam-Column Joints Using High-Strength Materials*, in ACI Special Publication, SP 123-12, *(Design of Beam-Column Joints for Seismic Resistance)*, Detroit, Michigan, pp. 317-357.

S11- Sugano S. and Endo T., (1983), *Seismic Strengthening of Reinforced Concrete Building in Japan*, Final Report, International Association of Bridge and Structural Engineering Symposium on Strengthening of Building Structures-Diagnosis and Therapy, Venice, pp.

371-379.

S12- Shephard R.B., Wood, P. R., Berrill J. B., Gillon N. R., North P. J., Perry A. K. and Bent D. P., (1990), *The Loma Prieta, California, Earthquake of October. 17, 1989: Report of the NZNSEE Reconnaissance Team*, Bulletin of the New Zealand National Society for Earthquake Engineering, Vol. 23, No. 1, pp. 1-78.

S13- Standards Association of New Zealand, (1982), *Concrete Structures Standard, Part 1- The Design of Concrete Structures* NZS 3101:1982, Standards New Zealand.

S14- Sauter F., (1987), *The San Salvador Earthquake of October 10, 1986- Structural Aspects of Damage*, Earthquake Spectra, Professional Journal of the Earthquake Engineering Research Institute, Vol. 3, No. 3, pp. 563-584.

T1- Thompson K. J., (1975), *Ductility of Concrete Frames Under Seismic Loading*, Ph.D. thesis, Department of Civil Engineering, University of Canterbury.

T2- Teraoka M., Kanoh Y., Taraka K., and Hayoshi K., (1994), *Shear Strength and Deformation Behaviour of R.C. Interior Beam-Column Joint Using High Strength Concrete*, Proc. 2nd US-NZ-Japan-China Multilateral Meeting on Structural Performance of High Strength Concrete in Seismic Regions, Honolulu.

U1- Uzumeri S. M. and Seckin M., (1974), *Behaviour of Reinforced Concrete Beam-Column Joints Subjected to Slow Load Reversals*, Publication No. 74-05, Department of Civil Engineering, University of Toronto, Canada.

V1- Vecchio F. J. and Collins M.P., (1986), *The Modified Compression-Field Theory for Reinforced Concrete Elements Subjected to Shear*, Structural Journal, American Concrete Institute, Vol. 83-22, pp. 219-231.

V2- Viwathanatepa S., Popov E.P. and Bertero V. V., (1979), *Seismic Behaviour of R.C. Interior Beam-Column Subassemblages*, Report UCB/EERC-79/14, Earthquake Engineering Center, University of California, Berkeley, 184 p.

W1- Wong P. K. C., (1985), *Seismic Behaviour of Reinforced Concrete Frames Incorporating Beams with Distributed Reinforcement*, ME thesis, Department of Civil Engineering, University of Canterbury.

X1- Xian Zuo X., Park R. and Tanaka H., (1992), *Behaviour of Reinforced Concrete Interior Beam-Column Joints Designed Using High Strength Concrete and Steel,* Research Report 92-3, Department of Civil Engineering, University of Canterbury, Christchurch, 121 p.

Y1- Yanez R. and Imai H., (1992), *Bond Performance of a Lapping Joint Developed for Precast Concrete Columns*, Proc. of the 10th World Conference on Earthquake Engineering, Madrid, Spain, Vol. 6, pp. 3191-3196.

Z1- Zerke H. E. and Durrani A. J., (1989), *Seismic Response of Connections in Two Bay Reinforced Concrete Frame Sub-assemblies*, Journal of Structural Engineers, ASCE, Vol. 115, No. 11, pp. 2829-2844.

Z2- Zerke H. E. and Durrani A. J., (1990), *Seismic Response of Connections in Two Bay Reinforced Concrete Frame Sub-assemblies With a Floor,* Structural Journal, American Concrete Institute, Vol. 87, No. 4, pp. 406-415.

APPENDIX A-1

Strut-and-tie Model Analysis of Interior Joints - Part I

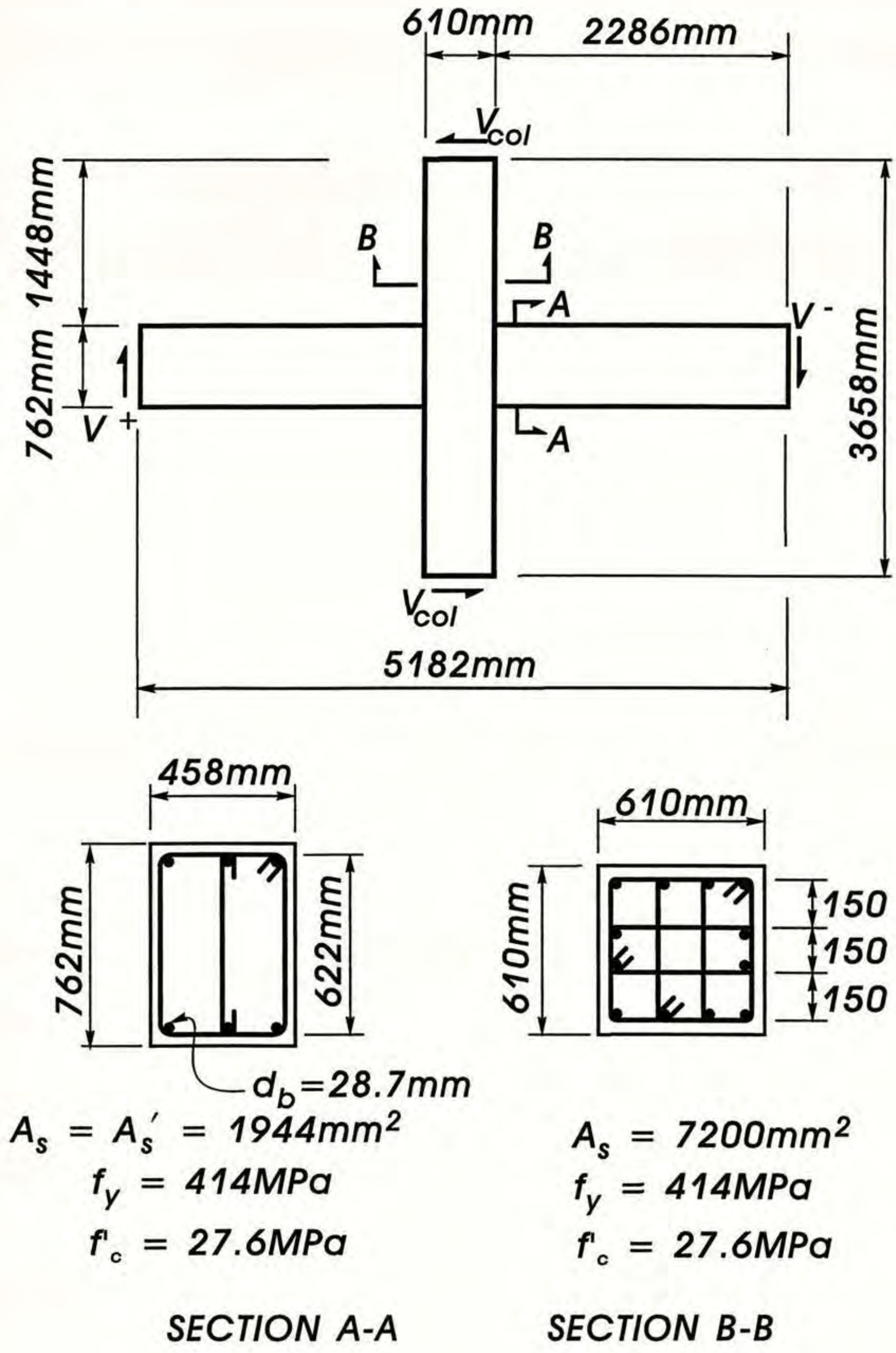

610mm
2286mm
V_{col}
1448mm
B
B
A
A
V^-
762mm
V^+
3658mm
V_{col}
5182mm
458mm
762mm
622mm
d_b=28.7mm
$A_s = A_s' = 1944mm^2$
$f_y = 414MPa$
$f'_c = 27.6MPa$
SECTION A-A
610mm
610mm
150
150
150
$A_s = 7200mm^2$
$f_y = 414MPa$
$f'_c = 27.6MPa$
SECTION B-B

Figure App-1

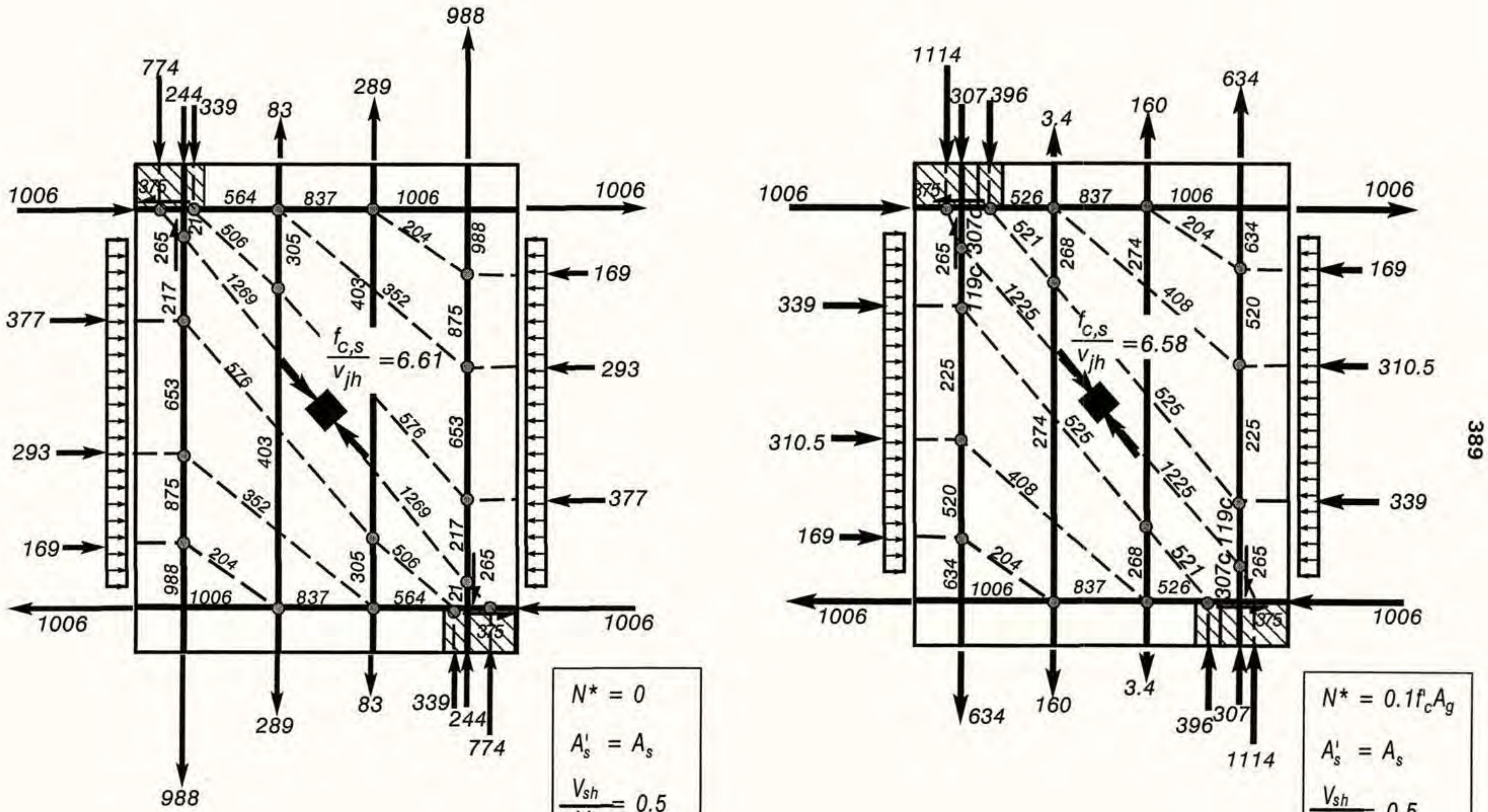
$\frac{f_{c,s}}{v_{jh}} = 6.61$
$N^* = 0$
$A_s' = A_s$
$\frac{V_{sh}}{V_{jh}} = 0.5$
$\frac{f_{c,s}}{v_{jh}} = 6.58$
$N^* = 0.1f_c'A_g$
$A_s' = A_s$
$\frac{V_{sh}}{V_{jh}} = 0.5$

Appa1_1.crd

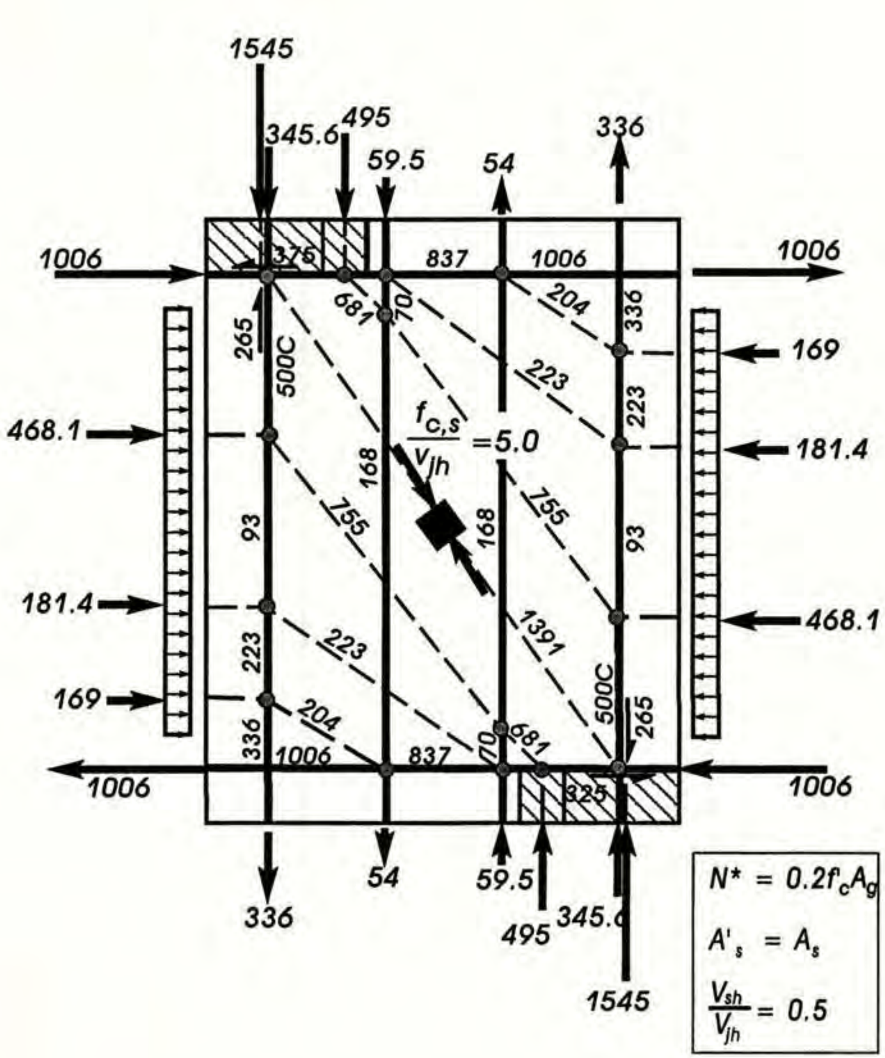
$N^* = 0.2f'_cA_g$
$A'_s = A_s$
$\frac{V_{sh}}{V_{jh}} = 0.5$
$\frac{f_{c,s}}{v_{jh}} = 5.0$

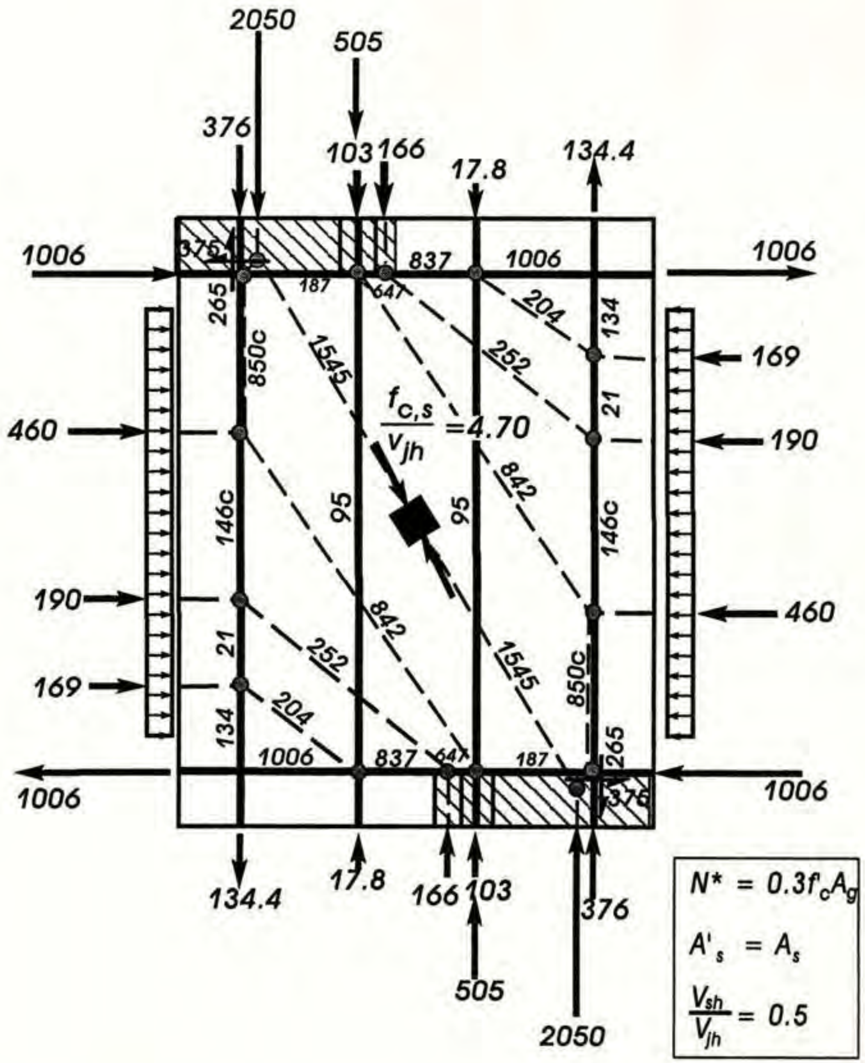
$N^* = 0.3f'_cA_g$
$A'_s = A_s$
$\frac{V_{sh}}{V_{jh}} = 0.5$
$\frac{f_{c,s}}{v_{jh}} = 4.70$

Strtie3.cdr

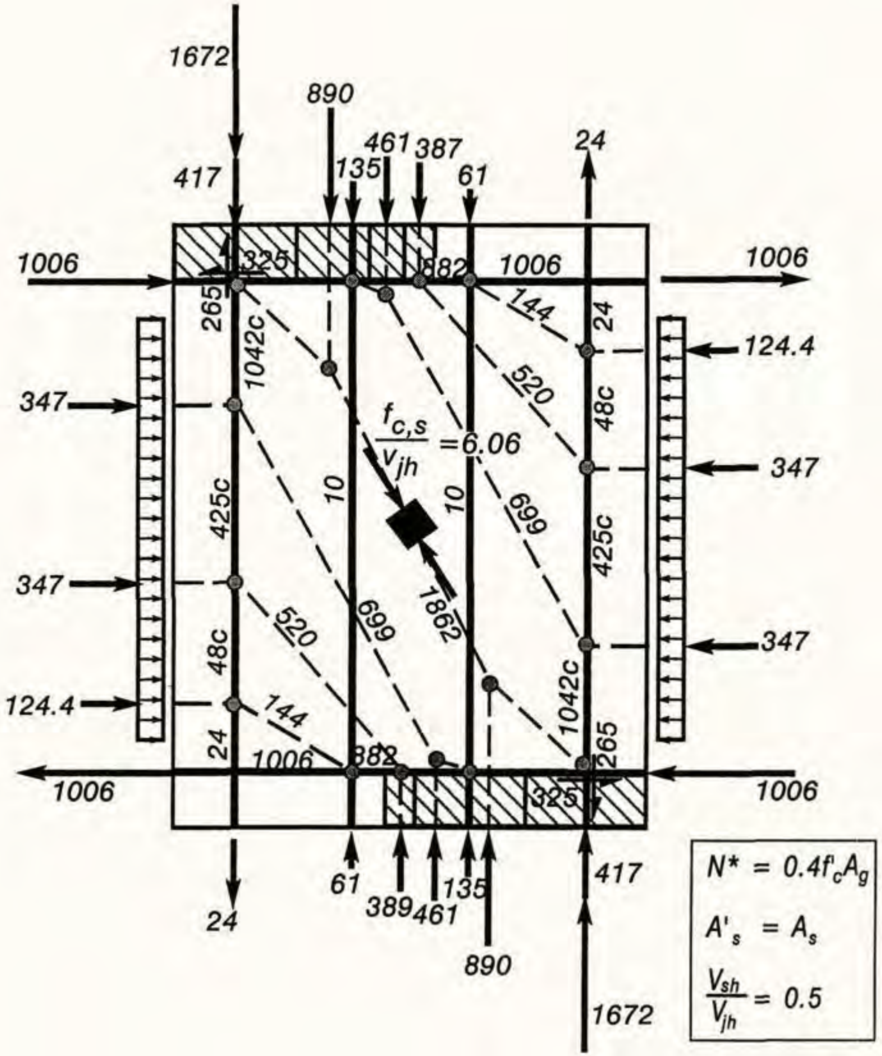
1672
890
461 387
24
417
135
61
1006
325
882
1006
1006
265
1042c
144
24
124.4
520
48c
347
$\frac{f_{c,s}}{v_{jh}} = 6.06$
10
10
699
347
425c
425c
347
347
520
699
1862
48c
1042c
124.4
144
24
265
1006
882
1006
1006
325
61
389 461
135
417
24
890
1672
$N^* = 0.4f'_cA_g$
$A'_s = A_s$
$\frac{V_{sh}}{V_{jh}} = 0.5$

Strtie2.cdr

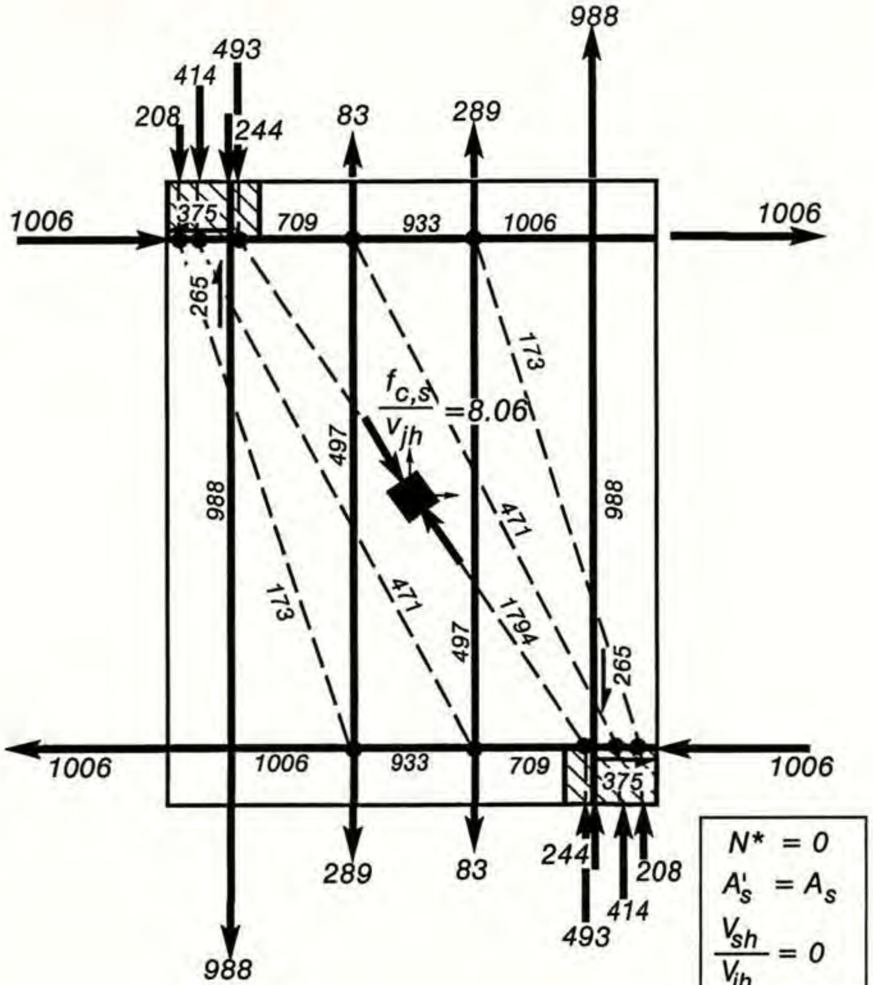

988
493
414
208
244
83
289
1006
375
709
933
1006
1006
265
173
$\frac{f_{c,s}}{v_{jh}} = 8.06$
497
988
471
1794
265
1006
1006
933
709
375
1006
244
289
83
208
414
493
988
$N^* = 0$
$A'_s = A_s$
$\frac{V_{sh}}{V_{jh}} = 0$

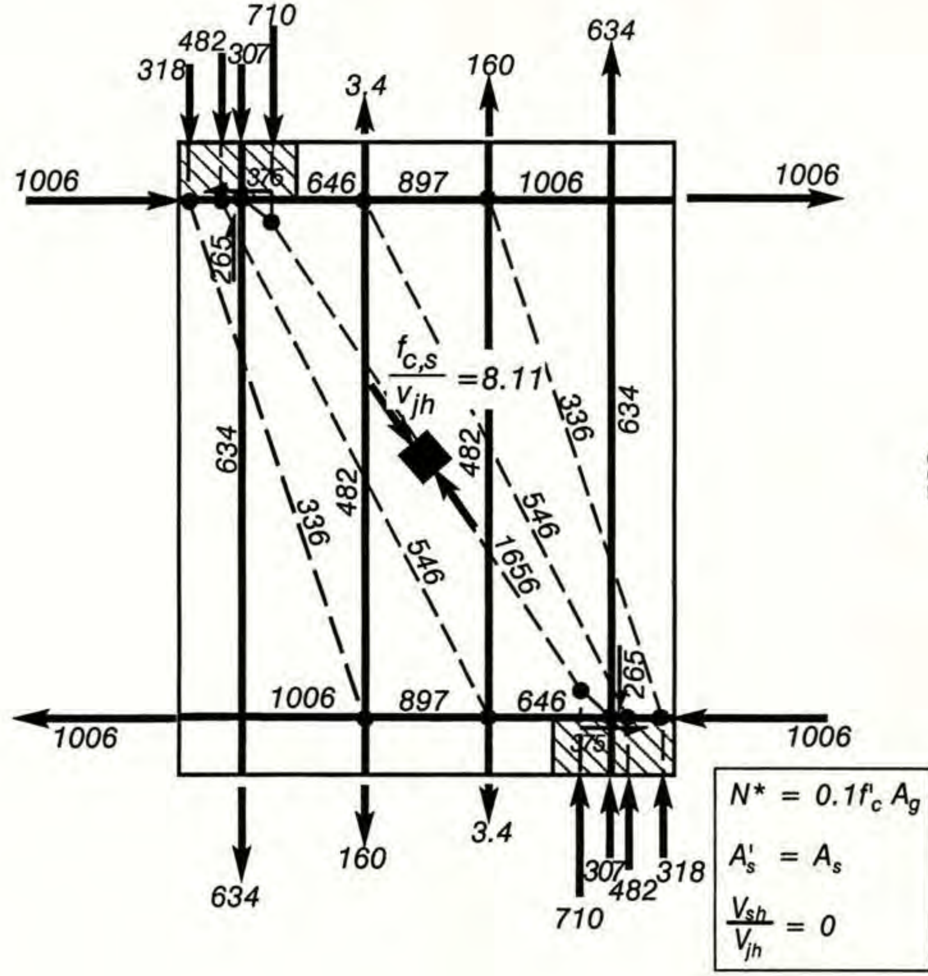

710
634
482
307
318
160
3.4
1006
376
646
897
1006
1006
265
$\frac{f_{c,s}}{v_{jh}} = 8.11$
336
634
482
546
1656
265
1006
897
646
1006
375
1006
160
3.4
634
307
482
318
710
$N^* = 0.1f'_c A_g$
$A'_s = A_s$
$\frac{V_{sh}}{V_{jh}} = 0$

AppA1_4.CDR

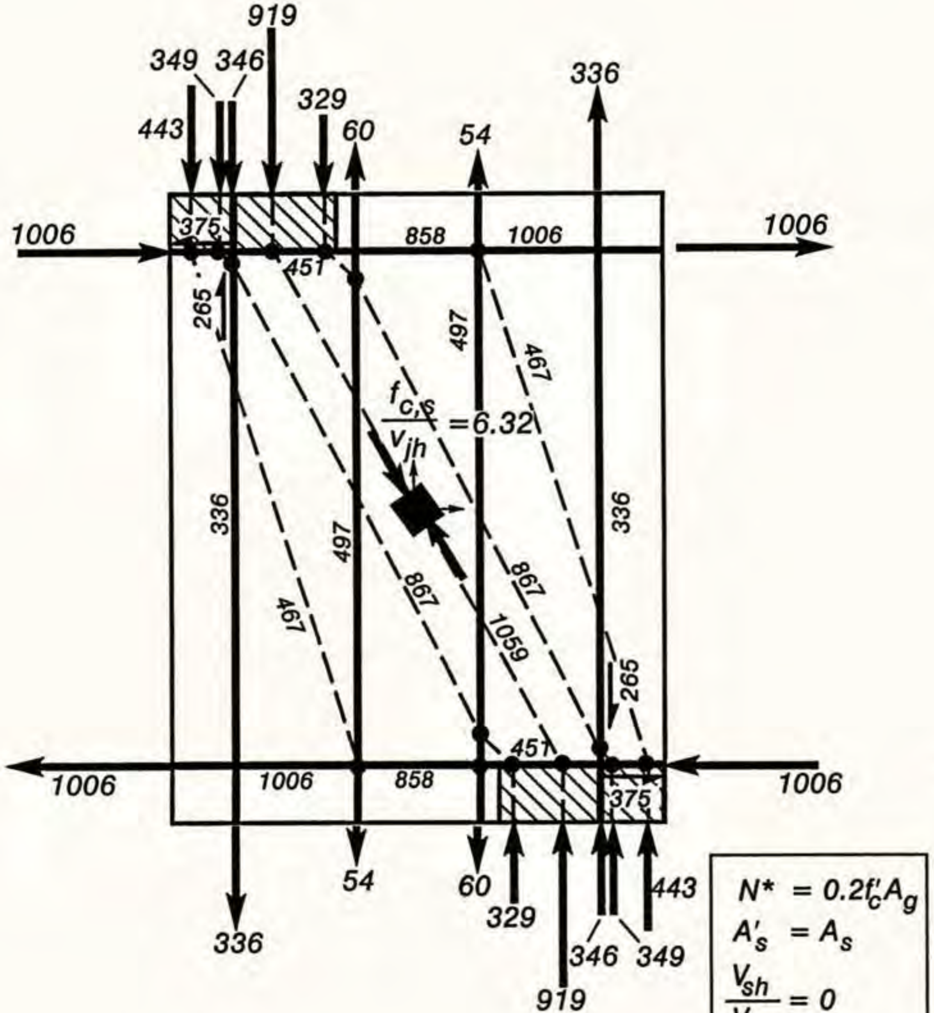
919
349 346
329
443
60
54
336
1006
375
858
1006
1006
451
265
497
467
$\frac{f_{c,s}}{v_{jh}} = 6.32$
336
497
336
467
867
867
1059
265
451
1006
1006
858
1006
375
54
60
443
329
336
346 349
919
$N^* = 0.2f'_c A_g$
$A'_s = A_s$
$\frac{V_{sh}}{V_{jh}} = 0$

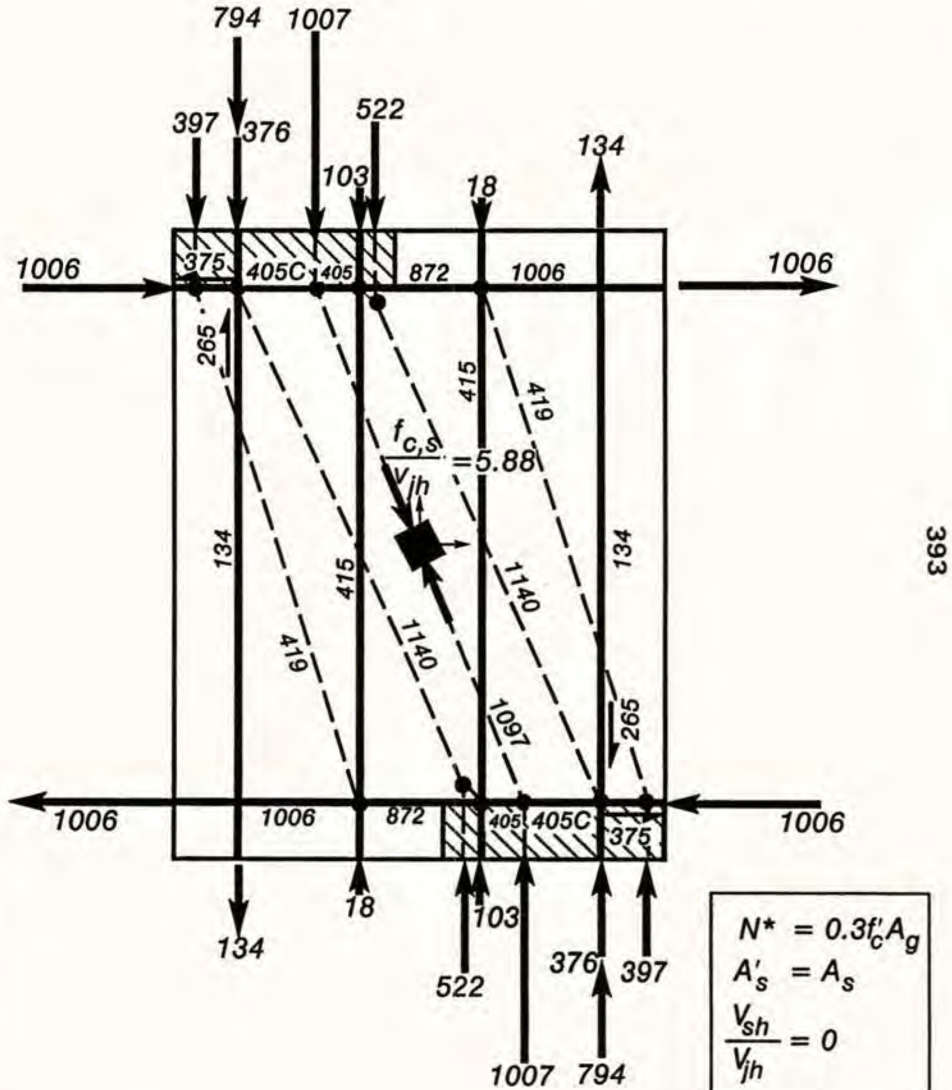
794 1007
397 376
522
103
18
134
1006
375
405C
405
872
1006
1006
265
415
419
$\frac{f_{c,s}}{v_{jh}} = 5.88$
134
415
134
419
1140
1140
1097
265
1006
1006
872
405
405C
375
1006
134
18
103
522
376 397
1007 794
$N^* = 0.3f'_c A_g$
$A'_s = A_s$
$\frac{V_{sh}}{V_{jh}} = 0$

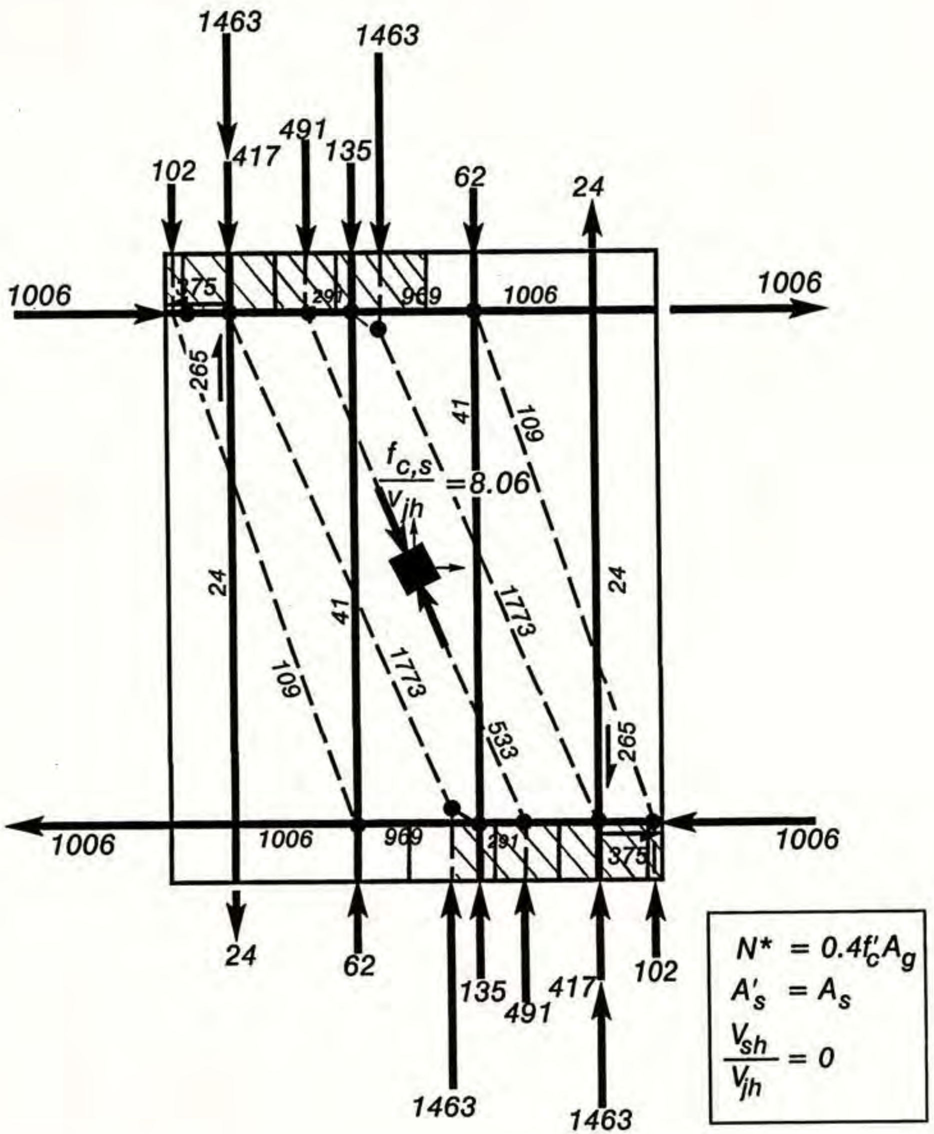

1463
1463
102
417
491
135
62
24
1006
1006
375
291
969
1006
265
41
109
$\frac{f_{c,s}}{V_{jh}} = 8.06$
24
41
1773
109
1773
533
24
265
1006
1006
1006
969
291
375
24
62
135
491
417
102
1463
1463
$N^* = 0.4f'_c A_g$
$A'_s = A_s$
$\frac{V_{sh}}{V_{jh}} = 0$

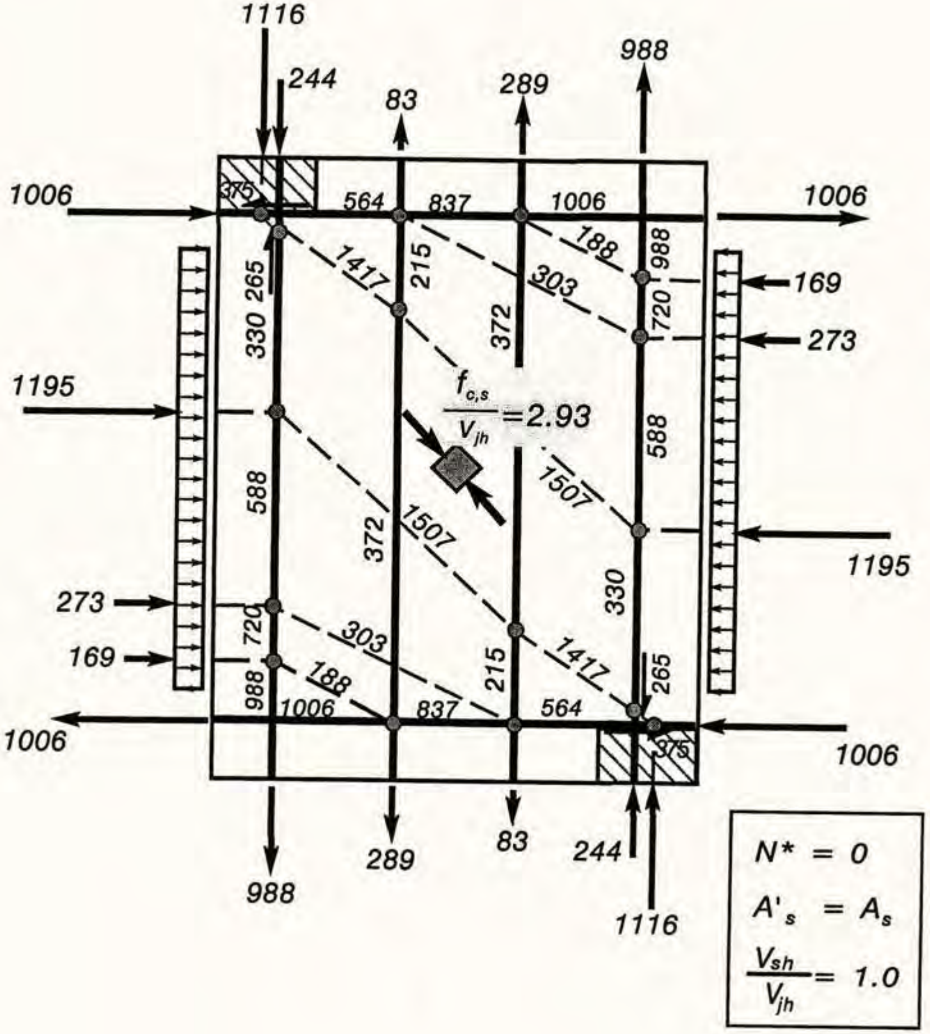
1116
244
83
289
988
1006
375
564
837
1006
1006
1417
215
188
303
988
330 265
372
720
169
273
1195
$\frac{f_{c,s}}{V_{jh}} = 2.93$
588
588
1507
1507
372
1195
330
273
169
720
303
188
215
1417
265
988
1006
837
564
375
1006
1006
988
289
83
244
1116
$N^* = 0$
$A'_s = A_s$
$\frac{V_{sh}}{V_{jh}} = 1.0$

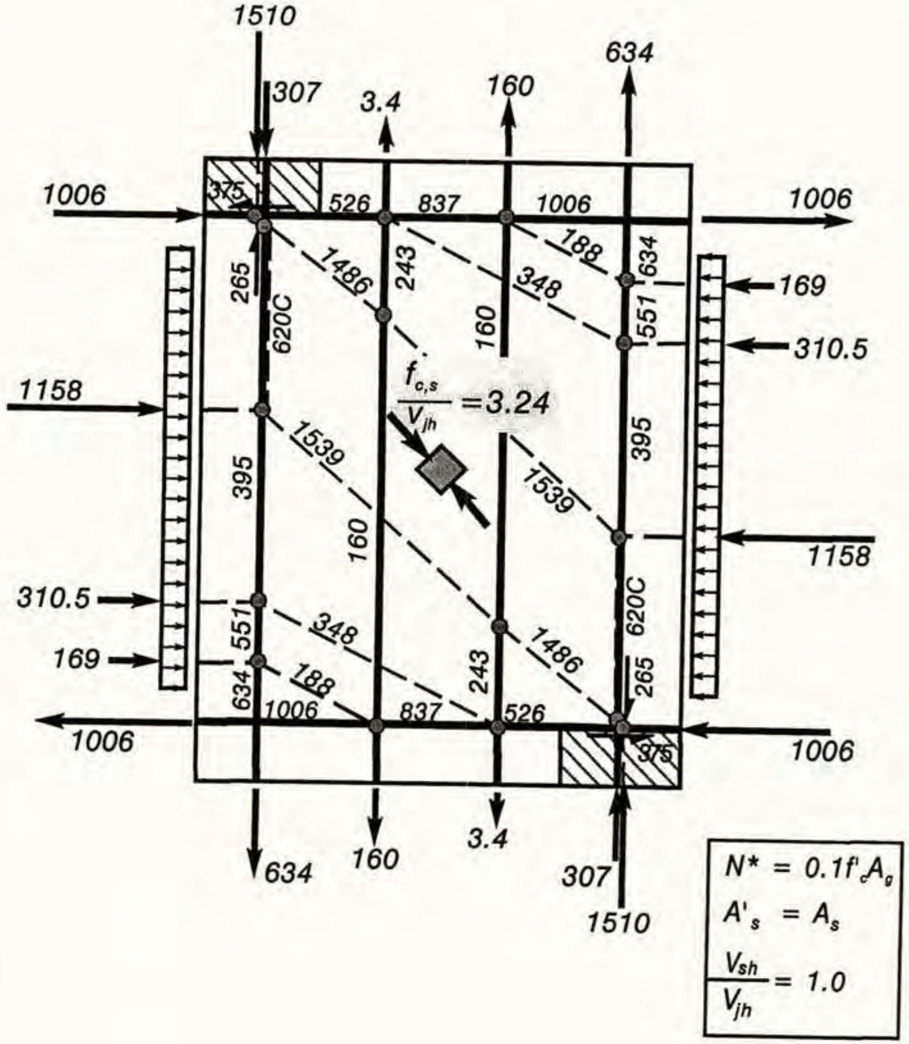
1510
307
3.4
160
634
1006
375
526
837
1006
1006
265
620C
1486
243
188
348
634
160
551
169
310.5
1158
$\frac{f_{c,s}}{V_{jh}} = 3.24$
1539
1539
395
395
160
1158
310.5
169
551
634
348
188
243
1486
620C
265
1006
837
526
375
1006
1006
634
160
3.4
307
1510
$N^* = 0.1f'_c A_g$
$A'_s = A_s$
$\frac{V_{sh}}{V_{jh}} = 1.0$

Strtie6.cdr

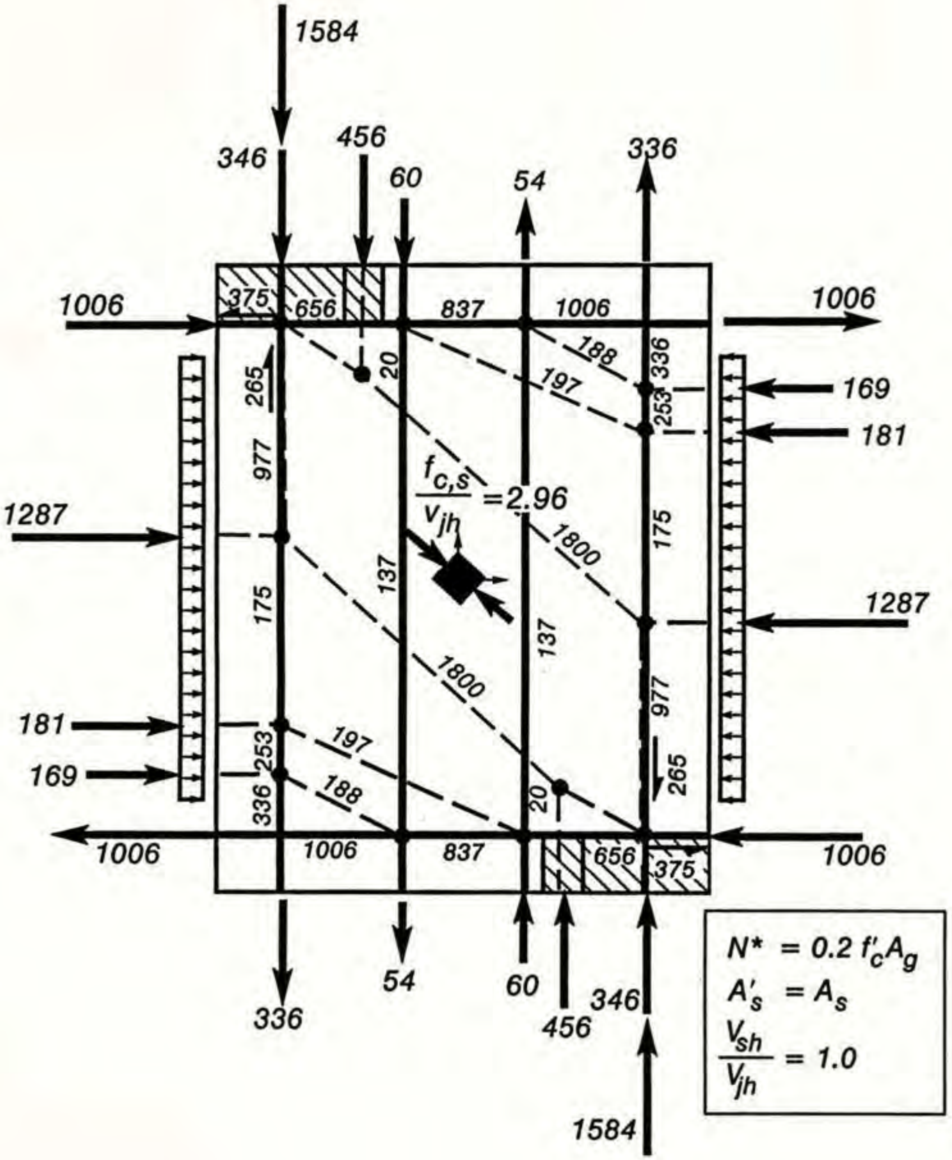
$\frac{f_{c,s}}{v_{jh}} = 2.96$
$N^* = 0.2 f'_c A_g$
$A'_s = A_s$
$\frac{V_{sh}}{V_{jh}} = 1.0$

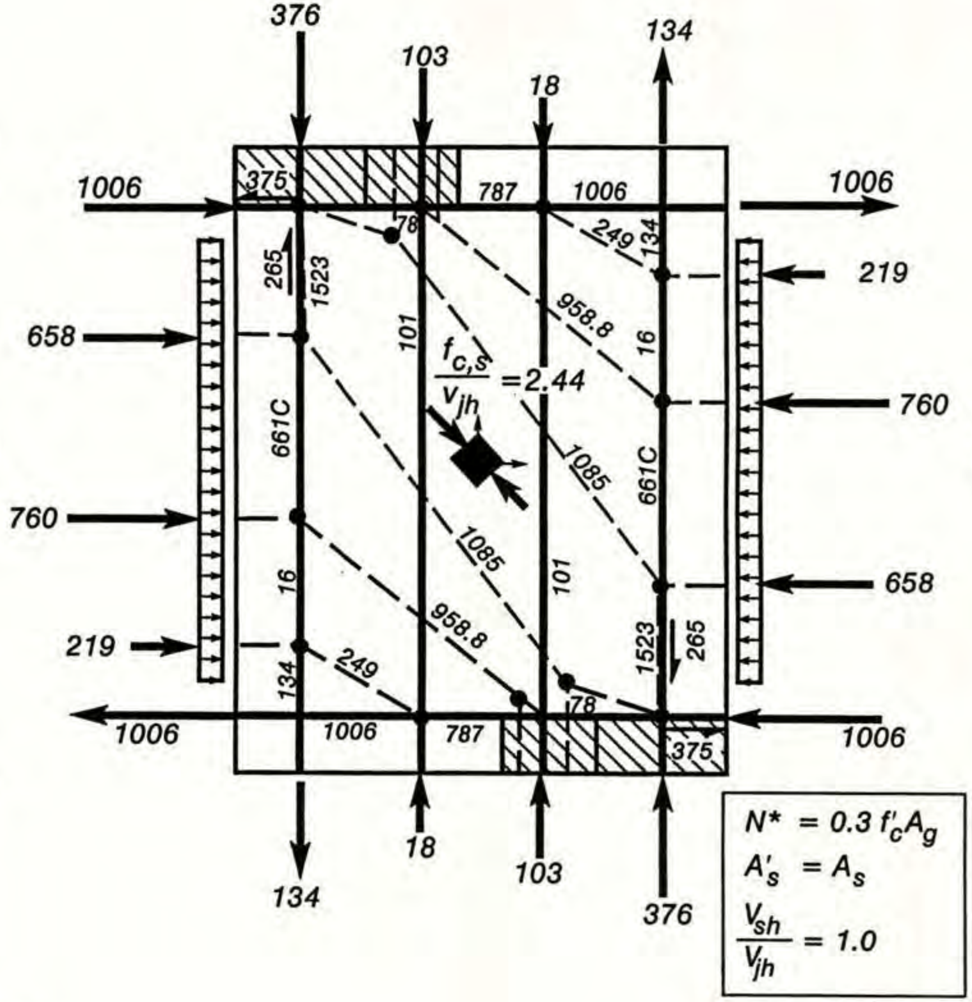
$\frac{f_{c,s}}{v_{jh}} = 2.44$
$N^* = 0.3 f'_c A_g$
$A'_s = A_s$
$\frac{V_{sh}}{V_{jh}} = 1.0$

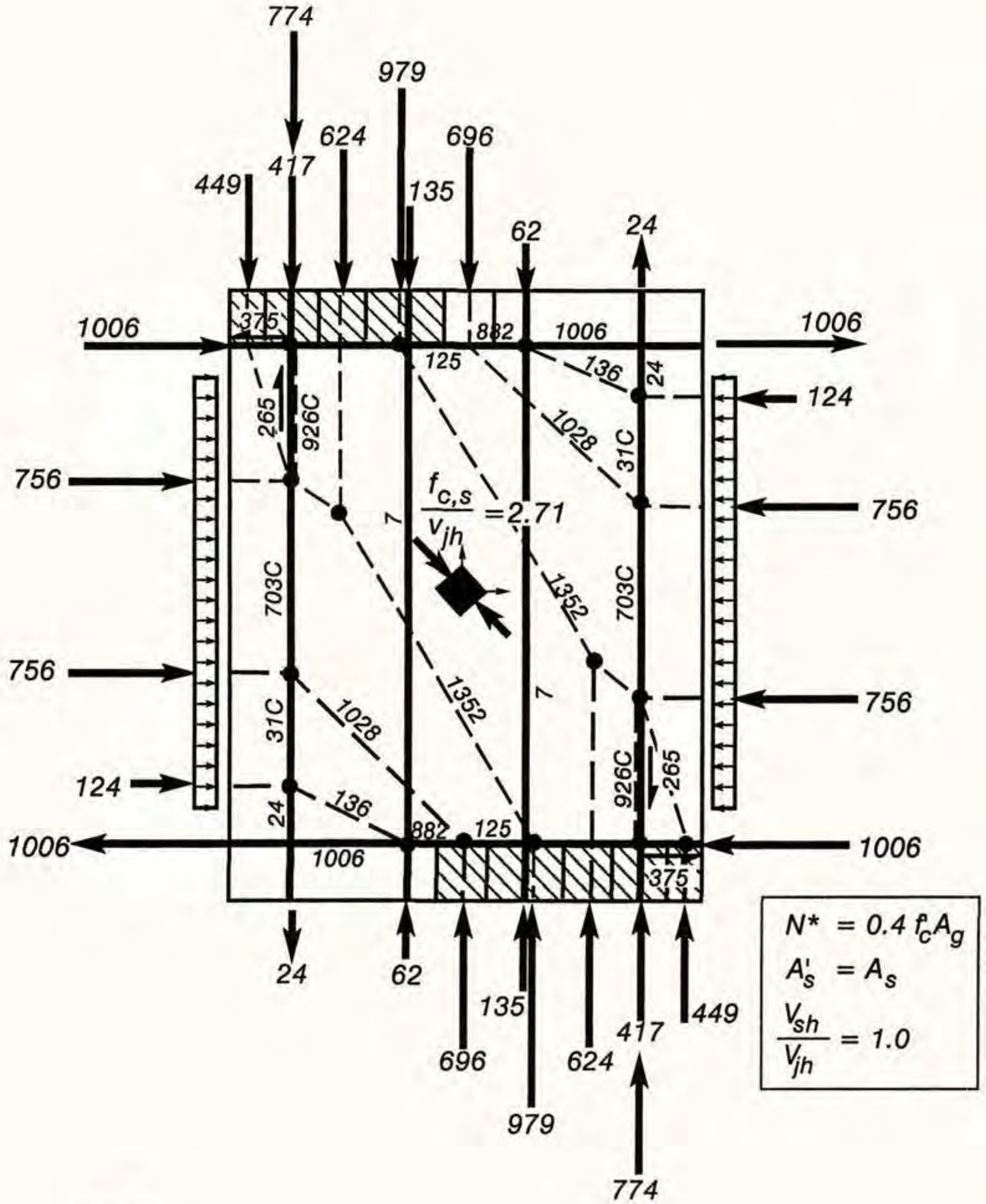
774
979
624
696
449
417
135
62
24
1006
375
882
125
136
124
756
265
926C
1028
31C
$\frac{f_{c,s}}{v_{jh}} = 2.71$
703C
1352
7
$N^* = 0.4 f'_c A_g$
$A'_s = A_s$
$\frac{V_{sh}}{V_{jh}} = 1.0$

Lin8.cdr

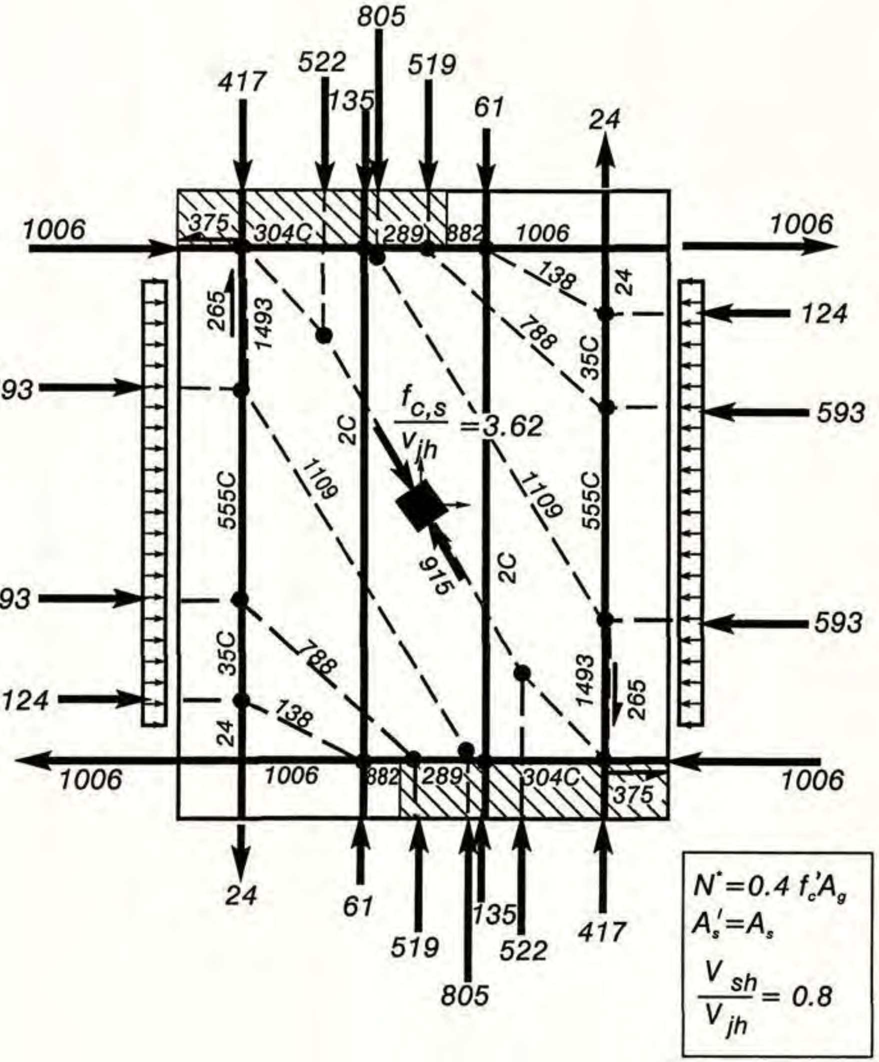
805
417
522
135
519
61
24
1006
375
304C
289
882
1006
138
24
265
1493
788
35C
124
593
$\frac{f_{c,s}}{v_{jh}} = 3.62$
2C
1109
555C
915
24
61
519
135
522
417
805
$N^* = 0.4\ f'_c A_g$
$A'_s = A_s$
$\frac{V_{sh}}{V_{jh}} = 0.8$

Lin1.cdr

APPENDIX A-2

Strut-and-tie Model Analysis of Interior Joints - Part II

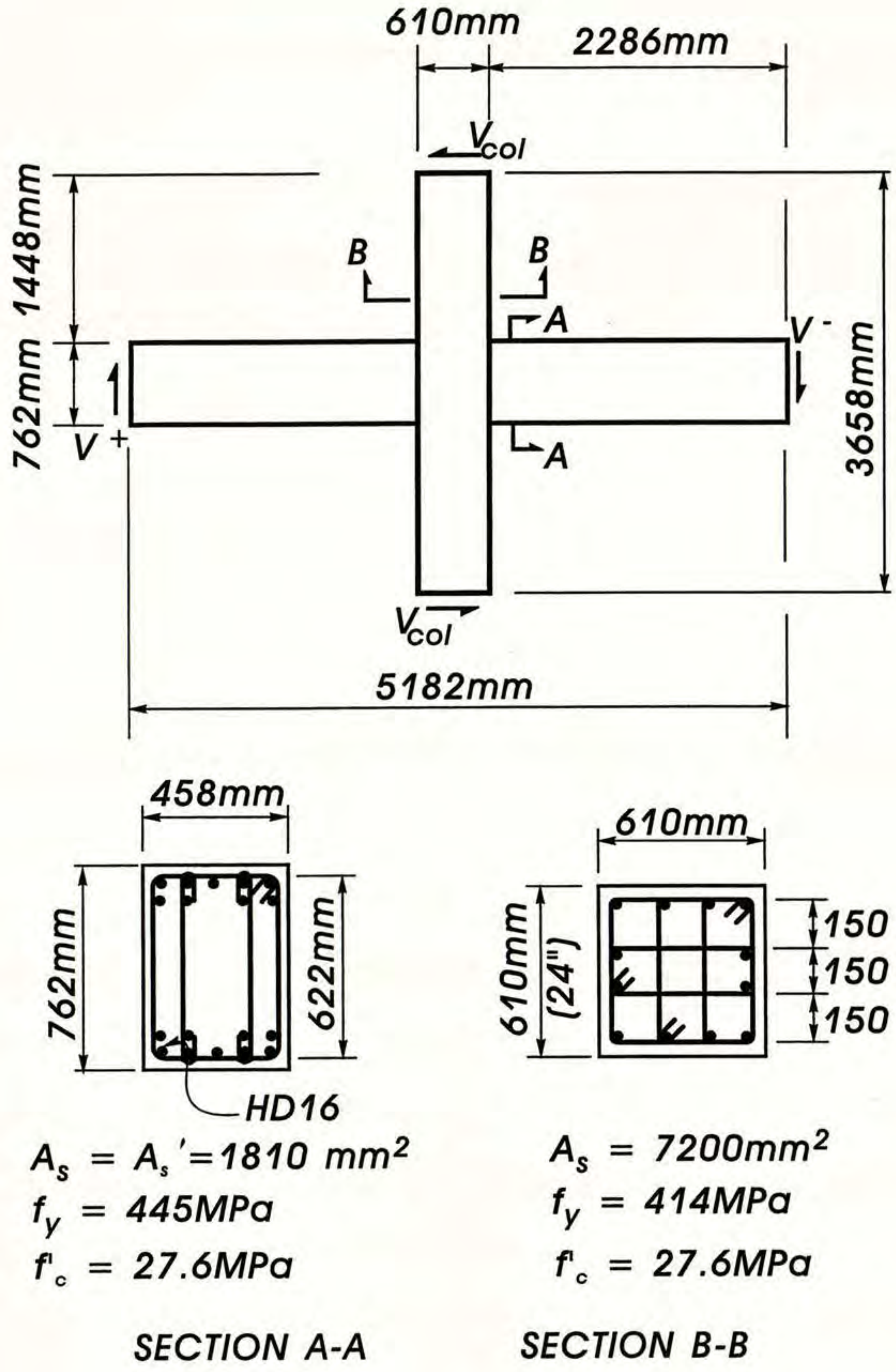
610mm
2286mm
V_{col}
1448mm
B
B
A
V^-
762mm
V^+
A
3658mm
V_{col}
5182mm
458mm
762mm
622mm
HD16
610mm
610mm
(24")
150
150
150
$A_s = A_s' = 1810\ mm^2$
$f_y = 445MPa$
$f'_c = 27.6MPa$
SECTION A-A
$A_s = 7200mm^2$
$f_y = 414MPa$
$f'_c = 27.6MPa$
SECTION B-B

Figure App-2

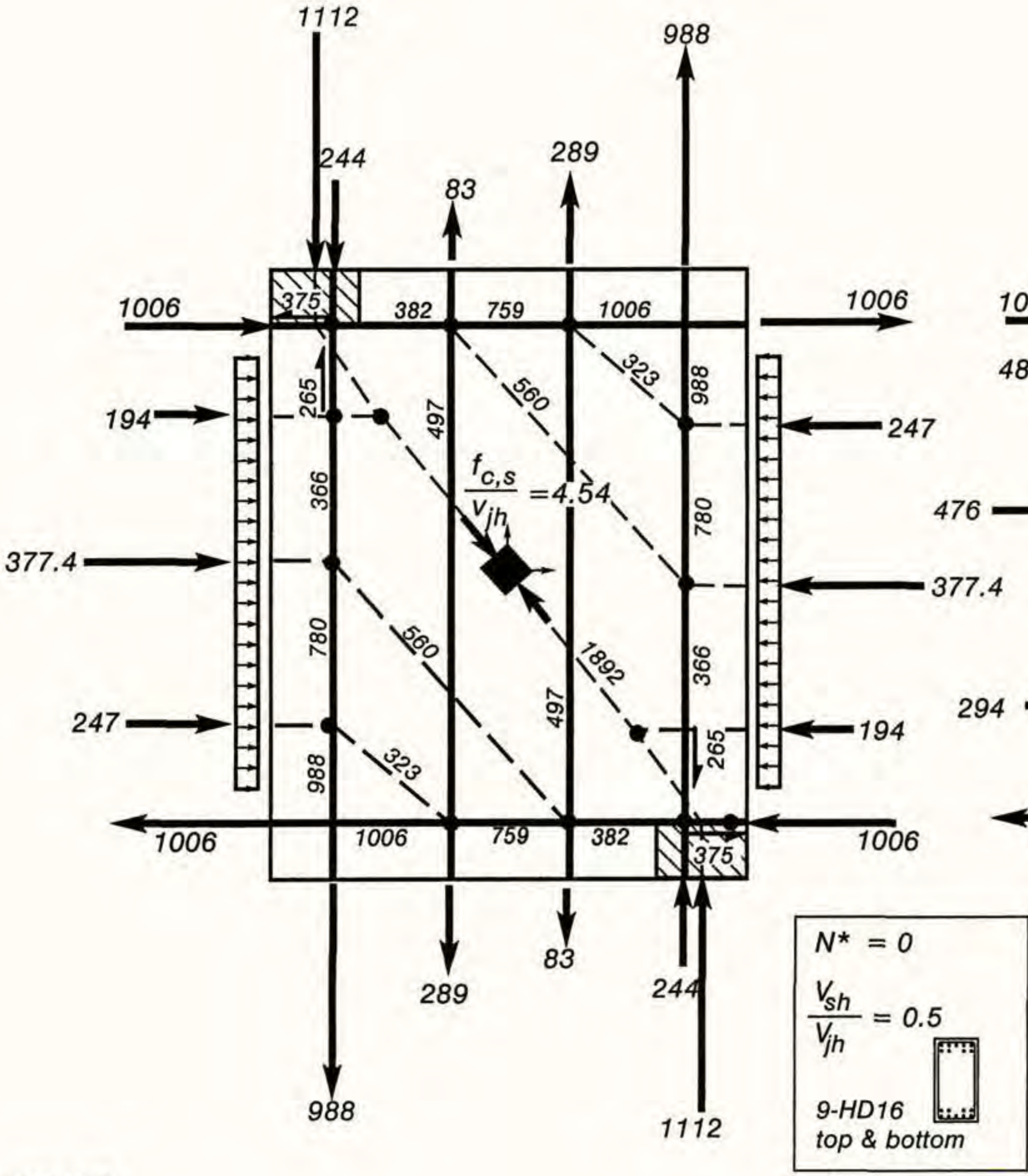

1112
988
244
83
289
1006
1006
375
382
759
1006
194
247
377.4
377.4
247
194
265
366
780
988
497
560
323
988
780
366
265
$\frac{f_{c,s}}{v_{jh}} = 4.54$
1892
560
323
497
1006
1006
759
382
375
289
83
244
988
1112
N* = 0
$\frac{V_{sh}}{V_{jh}} = 0.5$
9-HD16
top & bottom

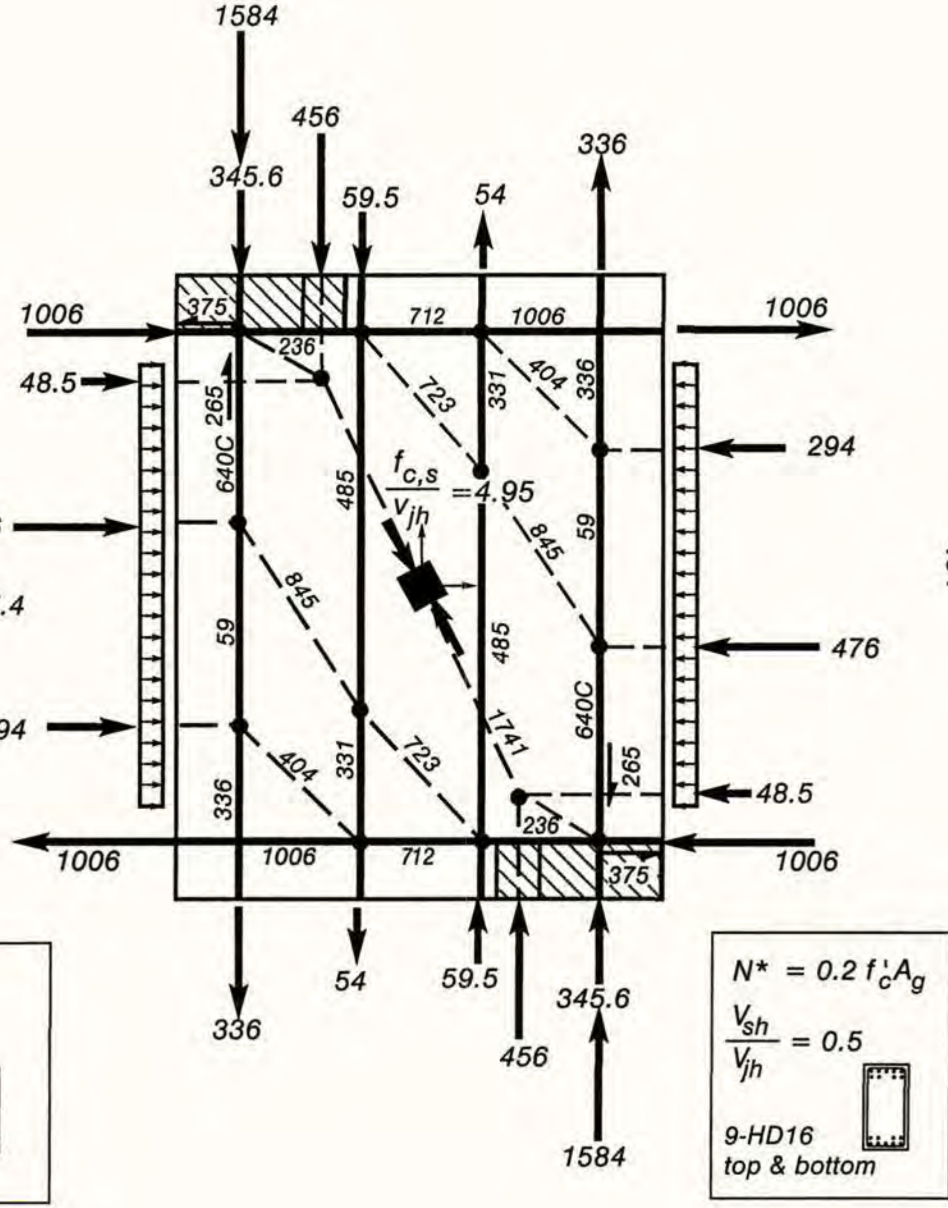

1584
456
345.6
59.5
54
336
1006
1006
375
236
712
1006
48.5
476
294
294
476
48.5
265
640C
59
336
485
331
723
404
845
$\frac{f_{c,s}}{v_{jh}} = 4.95$
1741
640C
265
236
1006
1006
712
375
336
54
59.5
345.6
456
1584
N* = 0.2 $f'_c A_g$
$\frac{V_{sh}}{V_{jh}} = 0.5$
9-HD16
top & bottom

APPA2_1.CDR

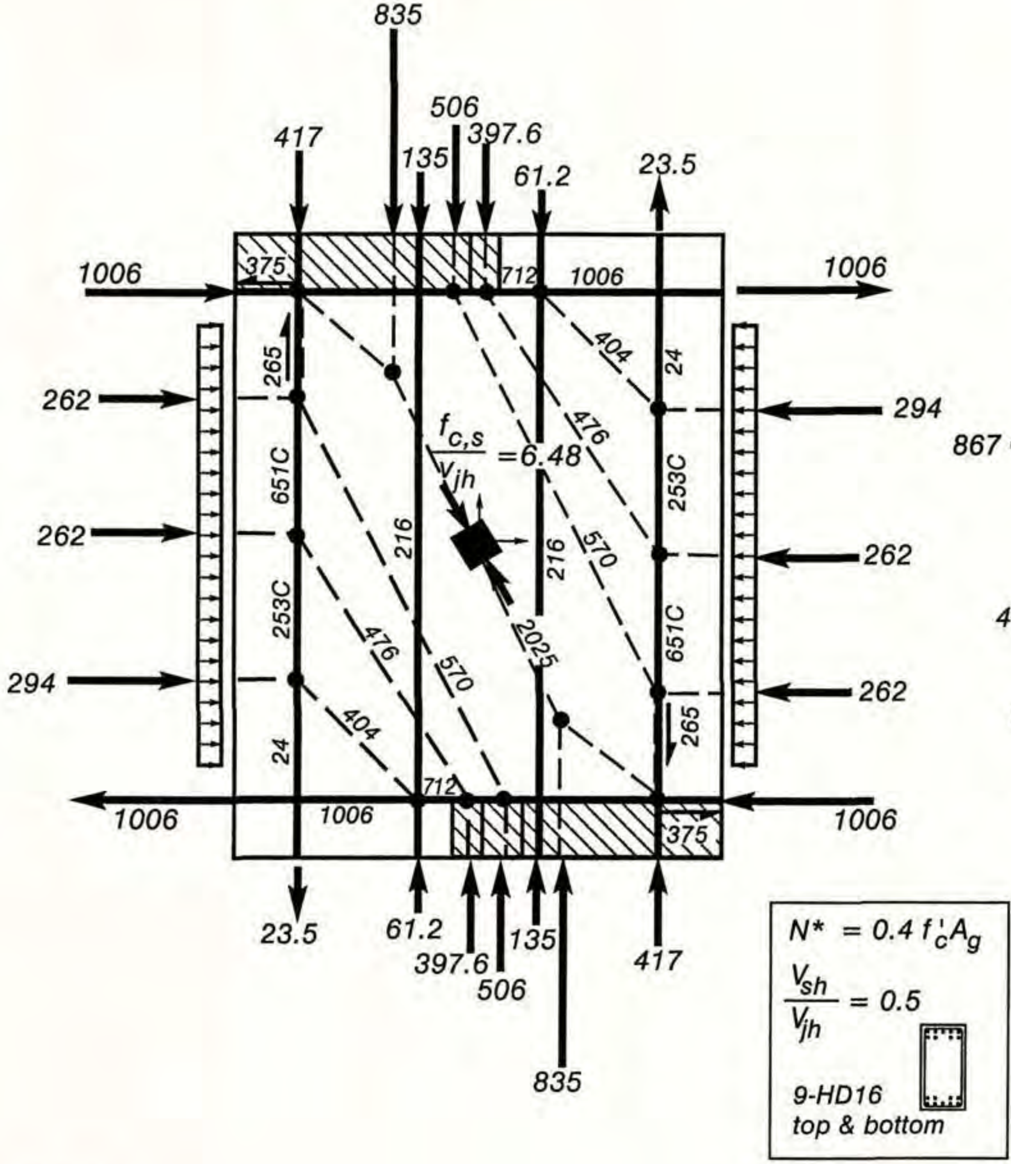
835
417
135
506
397.6
61.2
23.5
1006
375
712
1006
262
294
262
262
294
262
651C
253C
253C
651C
265
24
404
476
570
216
216
2025
$f_{c,s} / v_{jh} = 6.48$
1006
1006
1006
712
375
23.5
61.2
397.6
506
135
417
835
$N^* = 0.4 f'_c A_g$
$V_{sh} / V_{jh} = 0.5$
9-HD16
top & bottom

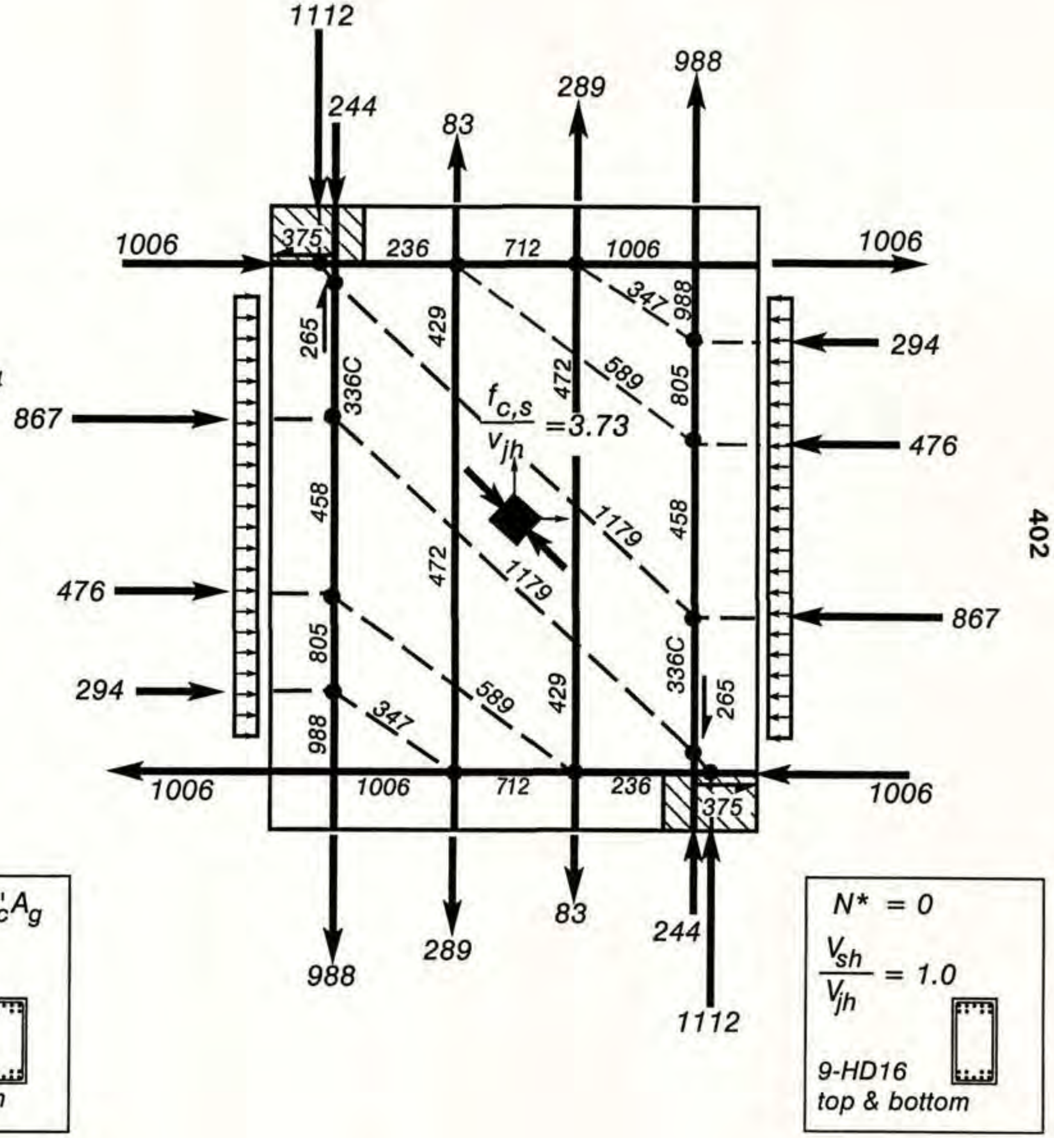
1112
244
83
289
988
1006
375
236
712
1006
1006
347
988
589
805
429
472
265
336C
458
472
458
1179
1179
$f_{c,s} / V_{jh} = 3.73$
867
476
294
294
476
867
805
988
347
589
429
336C
265
1006
1006
712
236
375
1006
988
289
83
244
1112
$N^* = 0$
$V_{sh} / V_{jh} = 1.0$
9-HD16
top & bottom

AppA2_2.cdr

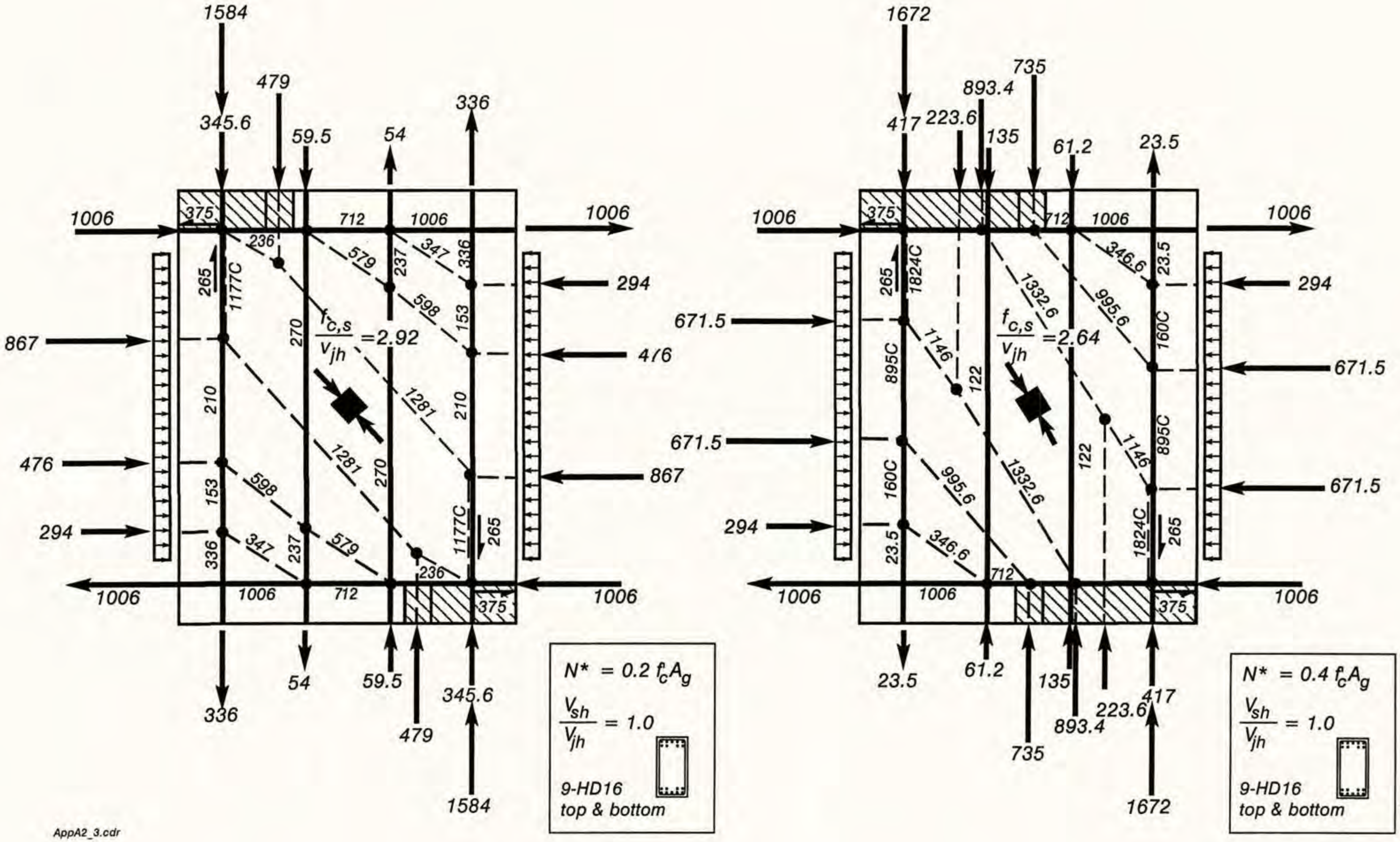

1584
479
345.6
59.5
54
336
1006
375
712
236
579
237
347
265
1177C
598
153
867
476
294
270
210
$\frac{f_{c,s}}{v_{jh}} = 2.92$
1281
236
$N^* = 0.2 f'_c A_g$
$\frac{V_{sh}}{V_{jh}} = 1.0$
9-HD16
top & bottom
1672
735
893.4
417
223.6
135
61.2
23.5
1824C
1332.6
995.6
346.6
671.5
895C
1146
122
160C
$\frac{f_{c,s}}{v_{jh}} = 2.64$
$N^* = 0.4 f'_c A_g$
$\frac{V_{sh}}{V_{jh}} = 1.0$
9-HD16
top & bottom

AppA2_3.cdr

APPENDIX A-3

Strut-and-tie Model Analysis of Interior Joints - Part III

Joints Incorporating Distributed Longitudinal Beam Bars

All the configurations and properties of the analyzed joints are identical to the Unit depicted in Fig. App-1 except that beam longitudinal beam bars are distributed along web as shown in each analyzed joint

f'_c = 27.6 MPa

Beam Bars :

HD16	f_y=445 MPa
HD28.7	f_y=414 MPa

Column Bars:

f_y=414MPa

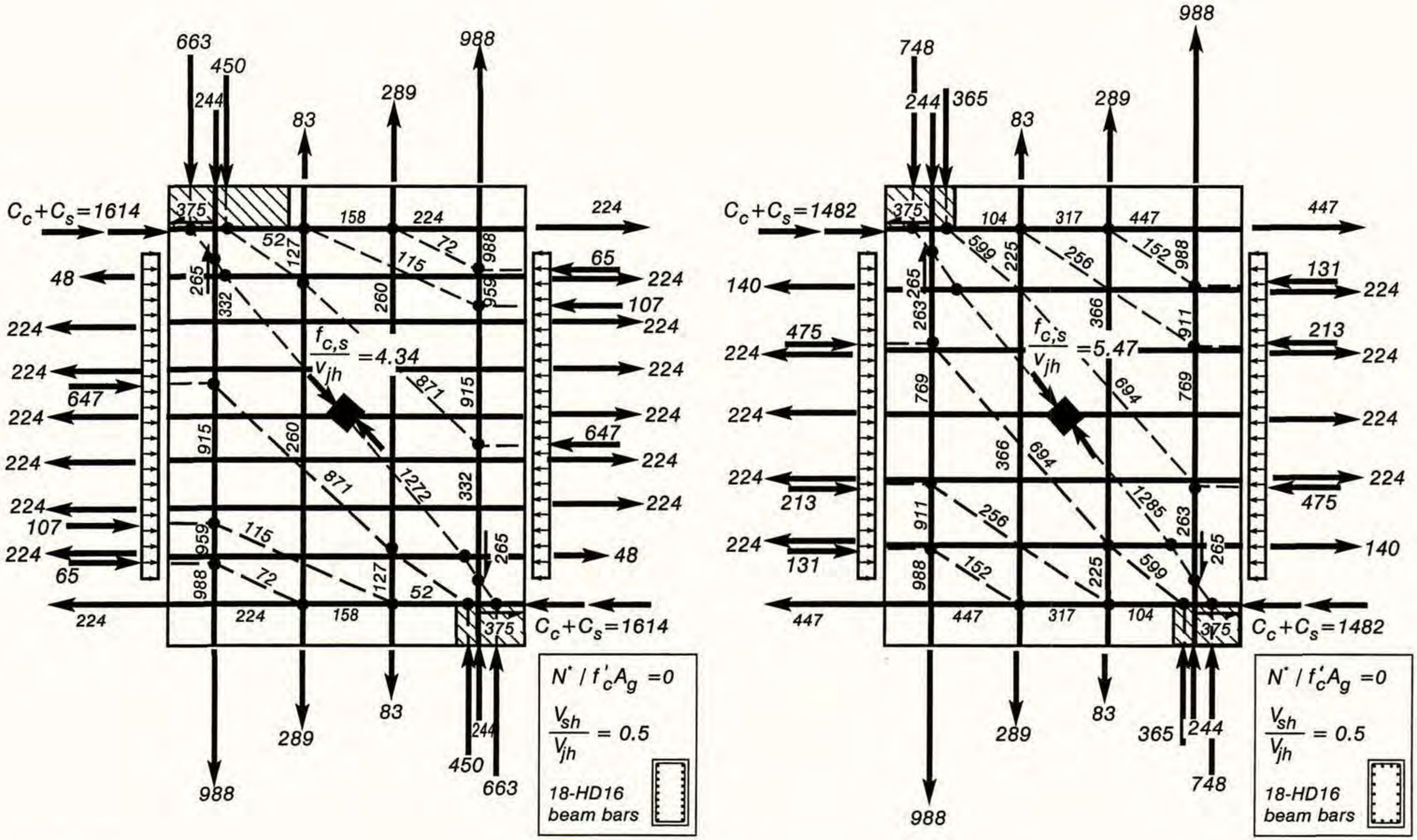

$C_c+C_s=1614$
$\frac{f_{c,s}}{v_{jh}}=4.34$
$C_c+C_s=1614$
$N^* / f'_c A_g = 0$
$\frac{V_{sh}}{V_{jh}} = 0.5$
18-HD16 beam bars
$C_c+C_s=1482$
$\frac{f_{c,s}}{v_{jh}}=5.47$
$C_c+C_s=1482$
$N^* / f'_c A_g = 0$
$\frac{V_{sh}}{V_{jh}} = 0.5$
18-HD16 beam bars

Appa3_1.cdr

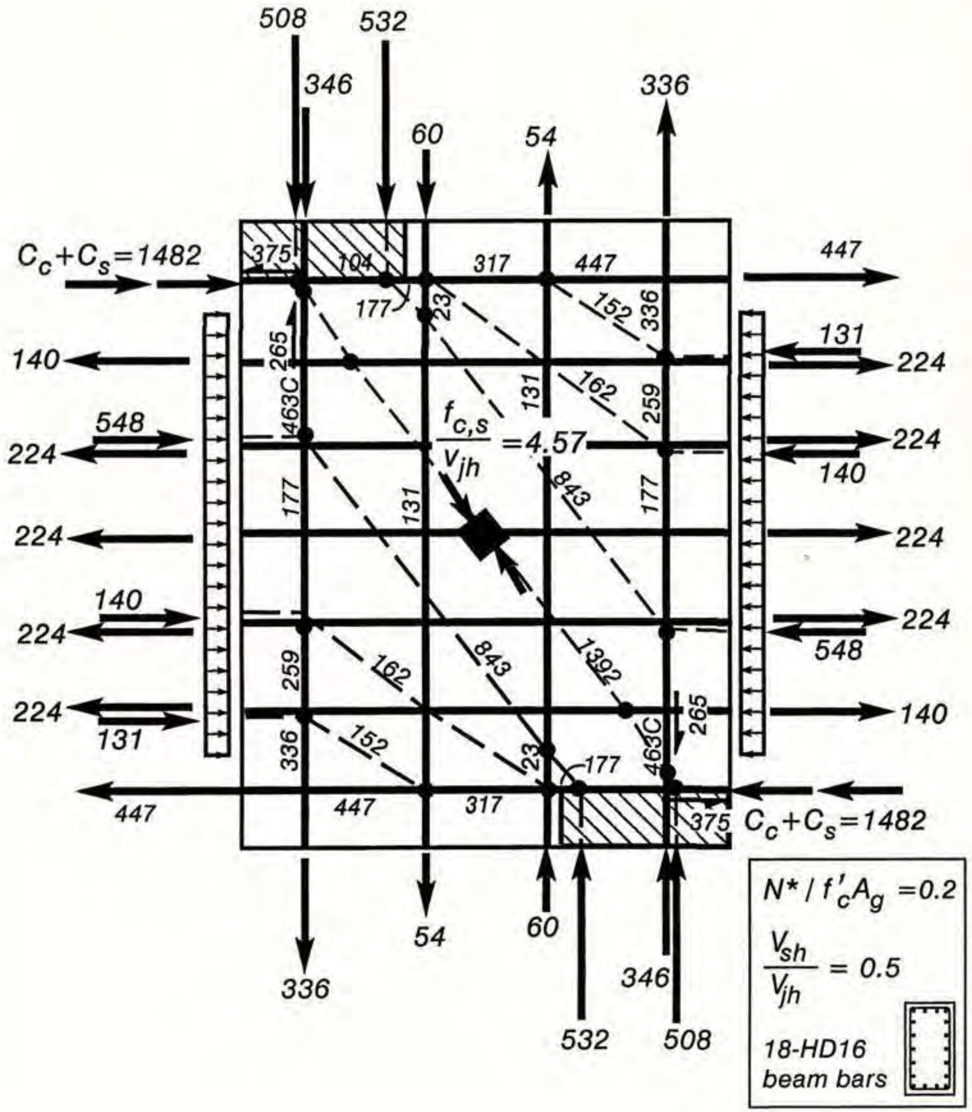

508
532
346
336
60
54
$C_c+C_s=1482$
375
104
317
447
177
23
152
336
140
131
224
265
463C
548
131
162
259
$\frac{f_{c,s}}{V_{jh}}=4.57$
843
177
1392
336
$N^*/f'_cA_g=0.2$
$\frac{V_{sh}}{V_{jh}}=0.5$
18-HD16
beam bars

Lin16.cdr

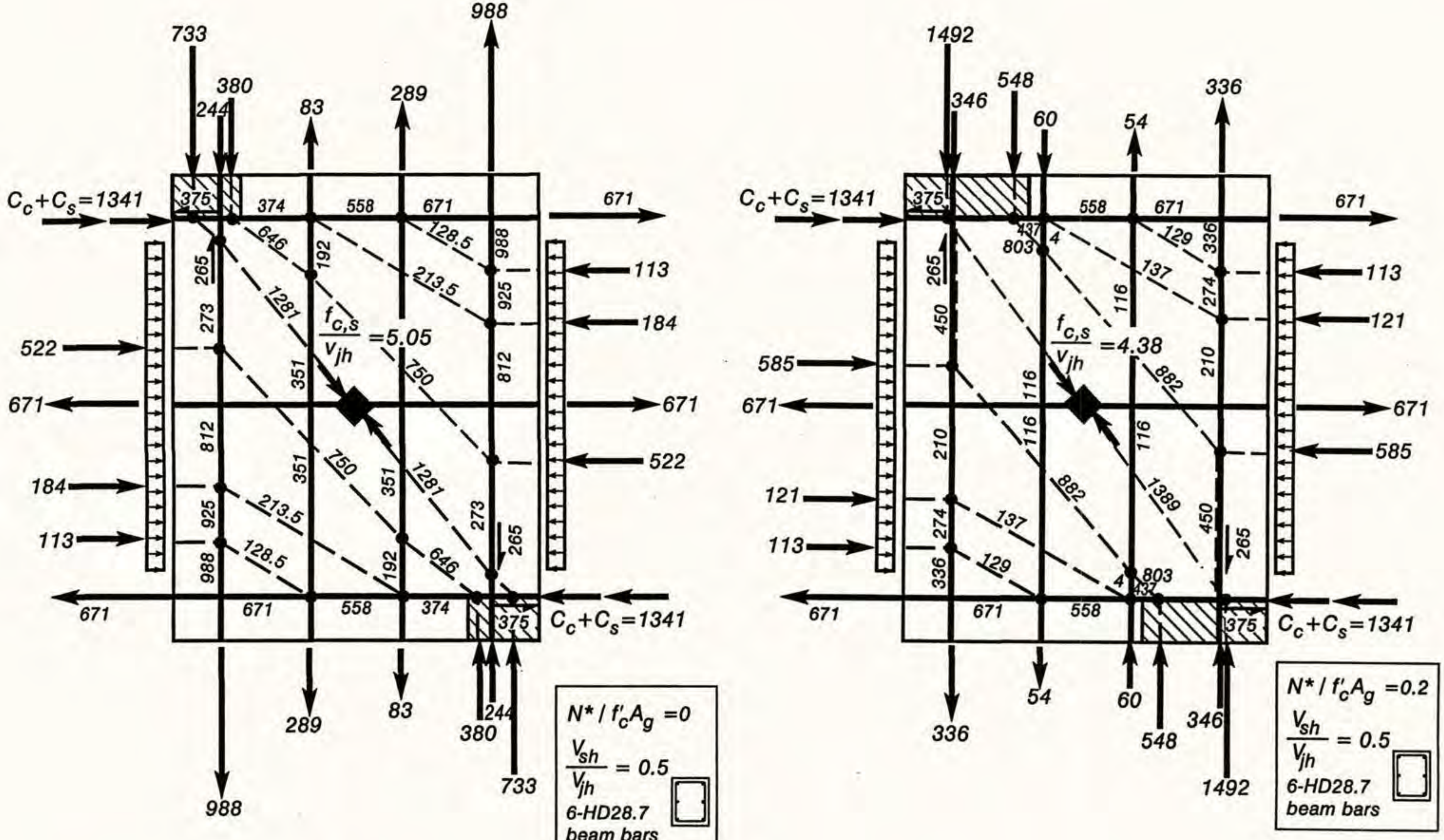

$C_c+C_s=1341$
$\frac{f_{c,s}}{v_{jh}}=5.05$
$N^*/f'_cA_g=0$
$\frac{V_{sh}}{V_{jh}}=0.5$
6-HD28.7
beam bars
$C_c+C_s=1341$
$\frac{f_{c,s}}{v_{jh}}=4.38$
$N^*/f'_cA_g=0.2$
$\frac{V_{sh}}{V_{jh}}=0.5$
6-HD28.7
beam bars

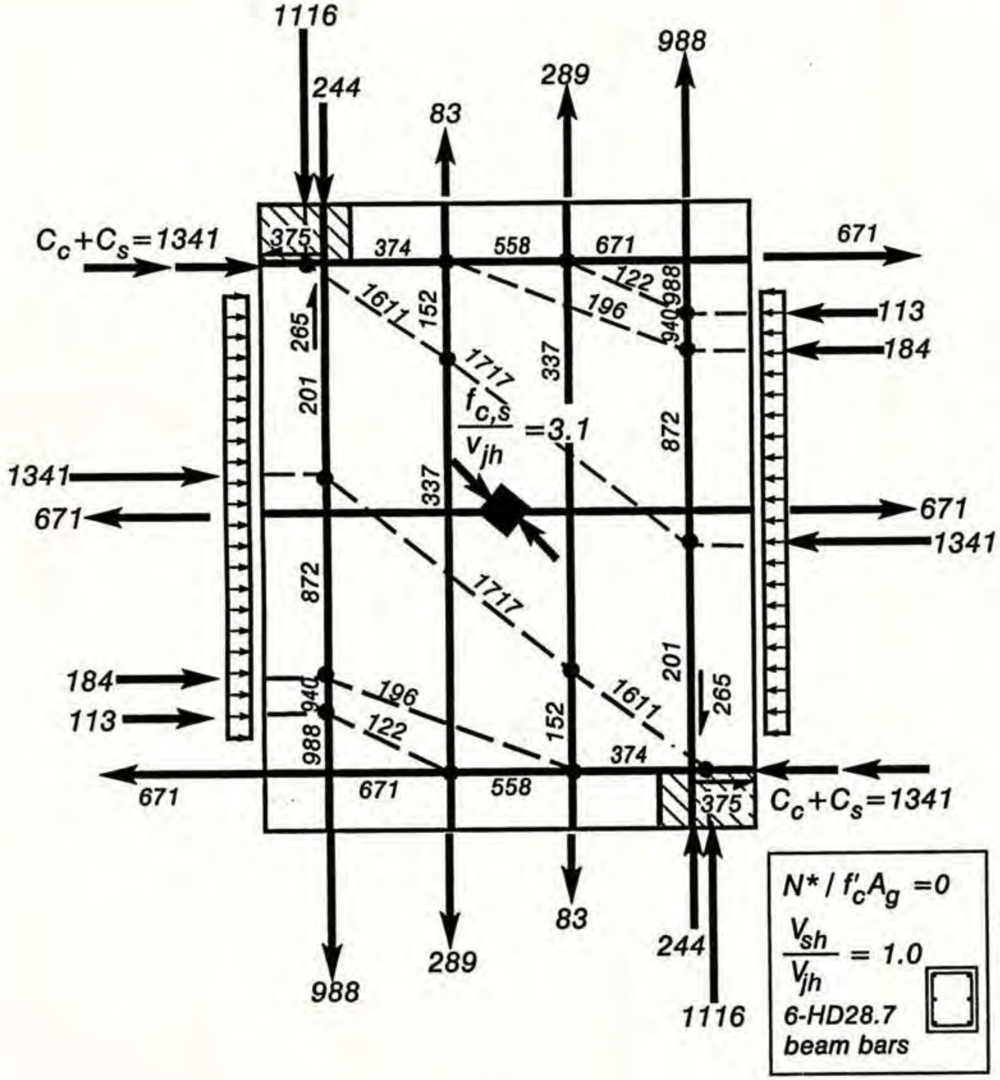

$C_c+C_s=1341$
$\frac{f_{c,s}}{v_{jh}}=3.1$
$N^* / f'_c A_g = 0$
$\frac{V_{sh}}{V_{jh}} = 1.0$
6-HD28.7
beam bars

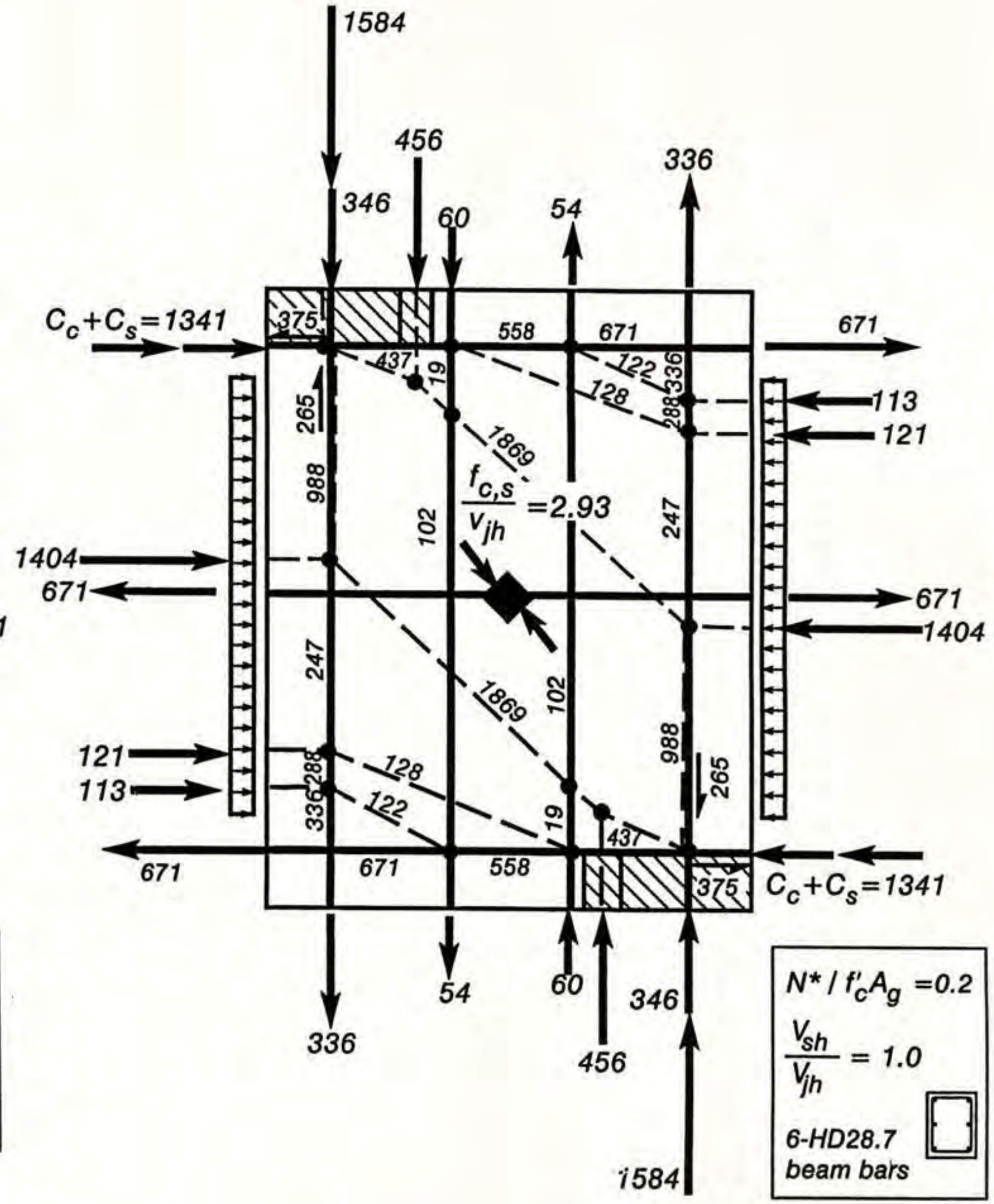

$C_c+C_s=1341$
$\frac{f_{c,s}}{v_{jh}}=2.93$
$N^* / f'_c A_g = 0.2$
$\frac{V_{sh}}{V_{jh}} = 1.0$
6-HD28.7
beam bars

APPENDIX B

Database of Tests of Interior Beam-column Joint Subassemblies

TEST: Beckingsale B11 Code: B1	
l_b	4877 mm
l_c	3354 mm
l'_b	2210 mm
l''_b	2253 mm
l'_c	1422 mm
h_b	610 mm
b_b	356 mm
h_c	457 mm
b_c	457 mm
d^- beam	550 mm
d^+ beam	569 mm
jd^- beam	519 mm
jd^+ beam	553 mm
jd^{*-}	509 mm
jd^{*+}	528 mm
f'_c	35.9 MPa
f_y beam top bars	297.6 MPa
f_y beam bottom bars	297.6 MPa
f_y slab bars	0 MPa
f_y joint hoops	336.0 MPa
$N^*/f'_c A_g$	0.043
A_s top beam bars	2280 mm^2
A_s btm beam bars	1140 mm^2
d_b, top beam bars	19 mm
d_b, btm beam bars	19 mm
A_s slab bars	0 mm^2
A_{sh} joint	4051 mm^2

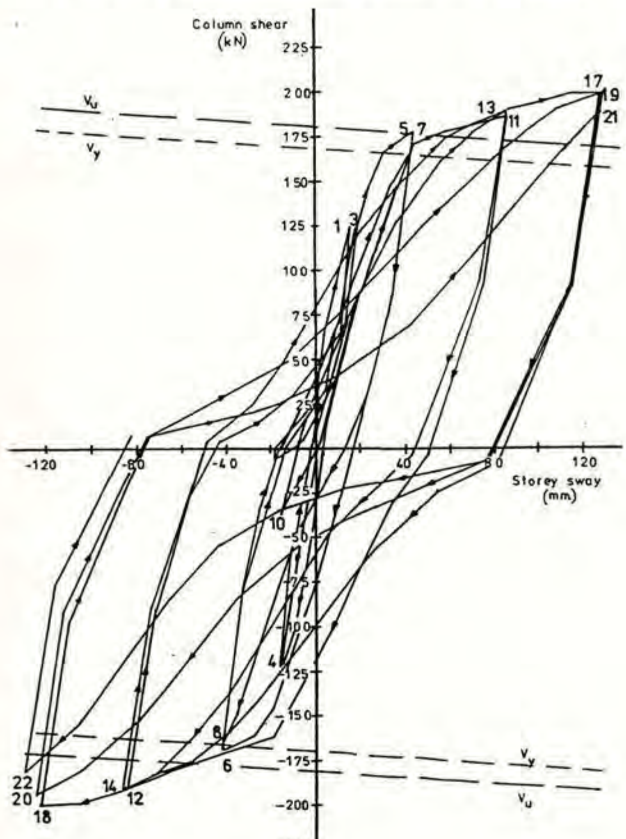

Theoretical Forces based on Measured Properties	
T_i^-	679 kN
T_i^+	339 kN
M_i^-	352 kN.m
M_i^+	188 kN.m
V_i^-	159 kN
V_i^+	85 kN
H_i	177.6 kN
$V_{jh,i}$	840.2 kN
V_{sh}	1361.0 kN
$(V_{sh})_{eff}$	1218.1 kN
Joint hoops have yield plateau	yes
$v_{jh,i} / f'_c$	0.112

Measured Strentghs	
H'_o (corr. for P-δ)	208.2 kN
H_o	196.7 kN
$\lambda_o = H'_o/H_i$	1.173
λ_{jo}	1.249
$V_{jh,o}$	1050 kN
$v_{jh,o} / f'_c$	0.140
$(V_{sh})_{eff} / V_{jh,o}$	1.000
K_{pv}	1.000
$v_{jh,e} / f'_c$	0.140

Measured Drift	
Δ_y / l_c	0.63 %
Δ_c / Δ_y	0.44
μ_Δ @ failure	>6
μ_θ @ failure	10.00
Failure Mode	no failure

Reference : [B3]

TEST: Beckingsale B12	Code:B2
l_b	4877 mm
l_c	3354 mm
l'_b	2210 mm
l''_b	2253 mm
l'_c	1425 mm
h_b	610 mm
b_b	356 mm
h_c	457 mm
b_c	457 mm
d^- beam	556 mm
d^+ beam	556 mm
jd^- beam	532 mm
jd^+ beam	532 mm
jd^{*-}	515 mm
jd^{*+}	515 mm
f'_c	34.6 MPa
f_y beam top bars	297.6 MPa
f_y beam bottom bars	297.6 MPa
f_y slab bars	0 MPa
f_y joint hoops	336 MPa
$N^*/f'_c A_g$	0.045
A_s top beam bars	1710 mm^2
A_s btm beam bars	1710 mm^2
d_b, top beam bars	19 mm
d_b, bottom beam bars	19 mm
A_s slab bars	0 mm^2
A_{sh} joint	3544.8 mm^2

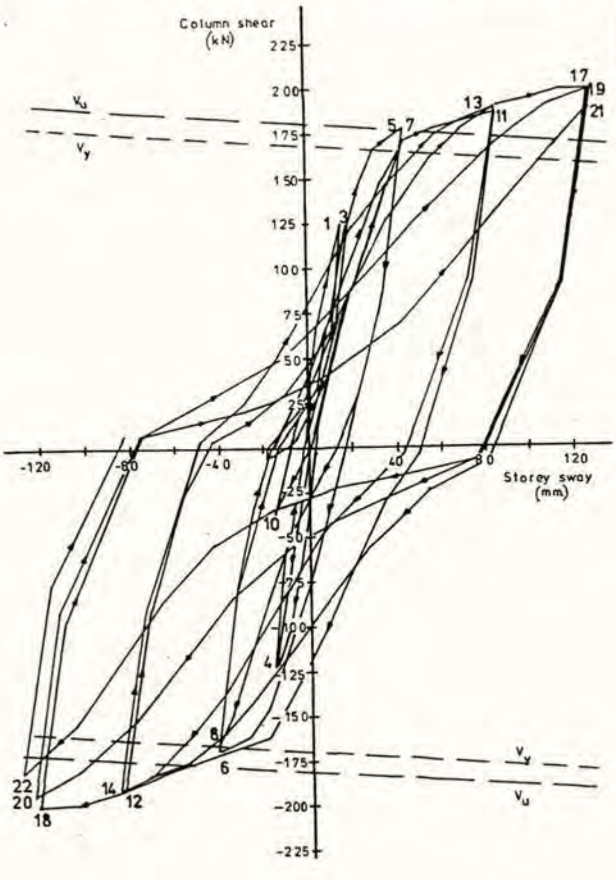

Theoretical Forces based on Measured Properties	
T_i^-	509 kN
T_i^+	509 kN
M_i^-	271 kN.m
M_i^+	271 kN.m
V_i^-	122 kN
V_i^+	122 kN
H_i	178.0 kN
$V_{jh,i}$	839.8 kN
V_{sh}	1361.0 kN
$(V_{sh})_{eff}$	1218.1 kN
Joint hoops have yield platea	yes
$v_{jh,i} / f'_c$	0.116

Measured Strentghs	
H'_o (corr. for P-δ)	211.8 kN
H_o	200.3 kN
$\lambda_o = H'_o/H_i$	1.190
λ_{jo}	1.265
$V_{jh,o}$	1063 kN
$v_{jh,o} / f'_c$	0.147
$(V_{sh})_{eff} / V_{jh,o}$	1.000
K_{pv}	1.000
$v_{jh,e} / f'_c$	0.147

Measured Drift	
Δ_y / l_c	0.64 %
Δ_c / Δ_y	0.45
μ_Δ @ failure	>6
μ_θ @ failure	>10
Failure Mode	no failure

Reference:[B3]

TEST: Beckingsale B13	Code:B3
l_b	4877 mm
l_c	3354 mm
l'_b	2210 mm
l''_b	2253 mm
l'_c	1425 mm
h_b	610 mm
b_b	356 mm
h_c	457 mm
b_c	457 mm
d^- beam	556 mm
d^+ beam	556 mm
jd^- beam	529 mm
jd^+ beam	529 mm
jd^{*-}	515 mm
jd^{*+}	515 mm
f'_c	31.4 MPa
f_y beam top bars	297.6 MPa
f_y beam bottom bars	297.6 MPa
f_y slab bars	0 MPa
f_y joint hoops	336.0 MPa
$N^*/f'_c A_g$	0.442
A_s top beam bars	1710 mm^2
A_s btm beam bars	1710 mm^2
d_b, top beam bars	19 mm^2
d_b, btm beam bars	19 mm^2
A_s slab bars	0 mm^2
A_{sh} joint	2532 mm^2

Theoretical Forces based on Measured Properties	
T_i^-	509 kN
T_i^+	509 kN
M_i^-	269 kN.m
M_i^+	269 kN.m
V_i^-	122 kN
V_i^+	122 kN
H_i	177.2 kN
$V_{jh,i}$	840.6 kN
V_{sh}	1021.0 kN
$(V_{sh})_{eff}$	895.1 kN
Joint hoops have yield plateau	yes
$v_{jh,i} / f'_c$	0.128

Measured Strenghs	
H'_o (corr. for P-δ)	203.0 kN
H_o	131.5 kN
$\lambda_o = H'_o/H_i$	1.146
λ_{jo}	1.212
$V_{jh,o}$	1018 kN
$v_{jh,o} / f'_c$	0.155
$(V_{sh})_{eff} / V_{jh,o}$	0.879
K_{pv}	1.460
$v_{jh,e} / f'_c$	0.227

Measured Drift	
Δ_y / l_c	0.44 %
Δ_c / Δ_y	0.21
μ_Δ @ failure	>6
μ_θ @ failure	>7.4
Failure Mode	no failure

Reference:[B3]

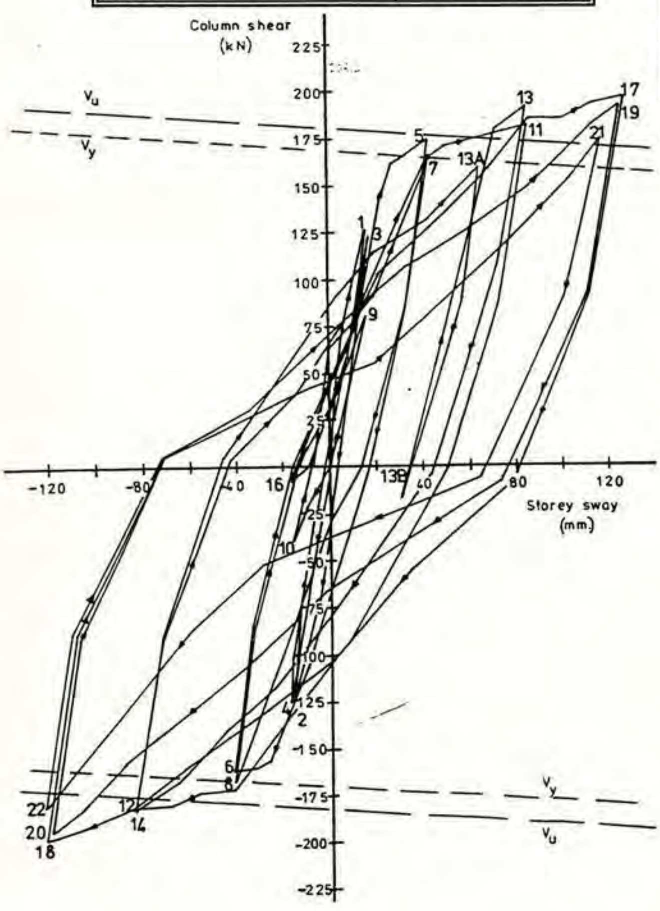

TEST: Birss B1	Code:B4
l_b	4877 mm
l_c	3430 mm
l'_b	2210 mm
l''_b	2253 mm
l'_c	1483 mm
h_b	610 mm
b_b	356 mm
h_c	457 mm
b_c	457 mm
d^- beam	537 mm
d^+ beam	537 mm
jd^- beam	494 mm
jd^+ beam	494 mm
jd^{*-}	482 mm
jd^{*+}	482 mm
f'_c	27.9 MPa
f_y beam top bars	288.0 MPa
f_y beam bottom bars	288.0 MPa
f_y slab bars	0 MPa
f_y joint hoops	345.0 MPa
$N^*/f'_c A_g$	0.053
A_s top beam bars	2512 mm2
A_s btm beam bars	2512 mm2
d_b, top beam bars	20 mm
d_b, btm beam bars	20 mm
A_s slab bars	0 mm^2
A_{sh} joint	1519 mm^2

Birss_B1.xls

Theoretical Forces based on Measured Properties	
T_i^-	723 kN
T_i^+	723 kN
M_i^-	357 kN.m
M_i^+	357 kN.m
V_i^-	162 kN
V_i^+	162 kN
H_i	230.0 kN
$V_{jh,i}$	1216.9 kN
V_{sh}	699.0 kN
$(V_{sh})_{eff}$	594.2 kN
Joint hoops have yield plateau	yes
$v_{jh,i} / f'_c$	0.209

Measured Strentghs	
H'_o (corr. for P-δ)	230.0 kN
H_o	230.0 kN
$\lambda_o = H'_o/H_i$	1.000
λ_{jo}	1.054
$V_{jh,o}$	1282 kN
$v_{jh,o} / f'_c$	0.220
$(V_{sh})_{eff} / V_{jh,o}$	0.463
K_{pv}	2.280
$v_{jh,e} / f'_c$	0.502

Measured Drift	
Δ_y / l_c	0.85 %
Δ_c / Δ_y	0.47
μ_Δ @ failure	4.00
μ_θ @ failure	6.60
Failure Mode	Joint failure

Reference: [B4]

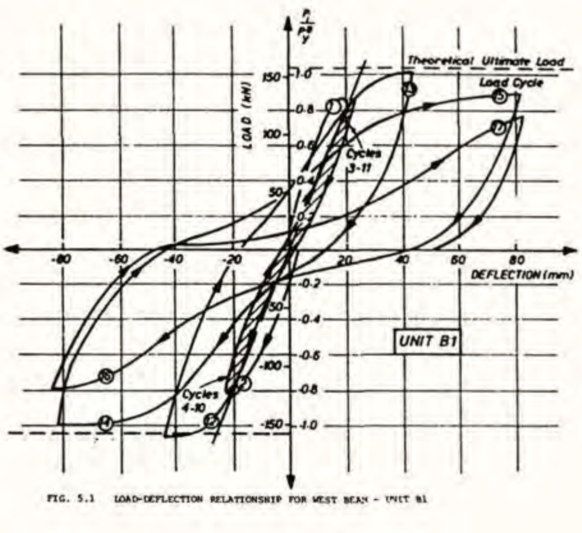

FIG. 5.1 LOAD-DEFLECTION RELATIONSHIP FOR WEST BEAM - UNIT B1

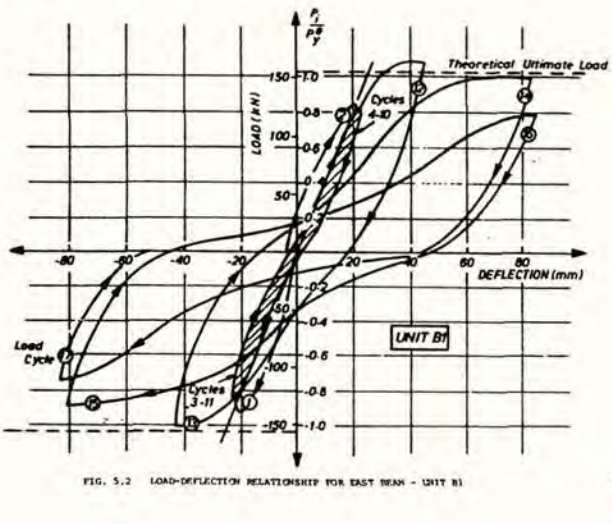

FIG. 5.2 LOAD-DEFLECTION RELATIONSHIP FOR EAST BEAM - UNIT B1

TEST: Birss B2	Code: B5
l_b	4877 mm
l_c	3430 mm
l'_b	2210 mm
l''_b	2253 mm
l'_c	1483 mm
h_b	610 mm
b_b	356 mm
h_c	457 mm
b_c	457 mm
d^- beam	537 mm
d^+ beam	537 mm
jd^- beam	499 mm
jd^+ beam	499 mm
jd^{*-}	482 mm
jd^{*+}	482 mm
f'_c	31.5 MPa
f_y beam top bars	288.0 MPa
f_y beam bottom bars	288.0 MPa
f_y slab bars	0 MPa
f_y joint hoops	397.8 MPa
$N^*/f'_c A_g$	0.439
A_s top beam bars	2512 mm^2
A_s btm beam bars	2512 mm^2
d_b, top beam bars	20 mm
d_b, btm beam bars	20 mm
A_s slab bars	0 mm^2
A_{sh} joint	398 mm^2

Birss_B2.xls

Theoretical Forces based on Measured Properties	
T_i^-	723 kN
T_i^+	723 kN
M_i^-	361 kN.m
M_i^+	361 kN.m
V_i^-	163 kN
V_i^+	163 kN
H_i	232.3 kN
$V_{jh,i}$	1214.6 kN
V_{sh}	211.0 kN
$(V_{sh})_{eff}$	179.4 kN
Joint hoops have yield plateau	yes
$v_{jh,i} / f'_c$	0.185

Measured Strengths	
H'_o (corr. for P-δ)	232.0 kN
H_o	232.0 kN
$\lambda_o = H'_o/H_i$	0.999
λ_{jo}	1.065
$V_{jh,o}$	1293 kN
$v_{jh,o} / f'_c$	0.197
$(V_{sh})_{eff} / V_{jh,o}$	0.139
K_{pv}	3.030
$v_{jh,e} / f'_c$	0.596

Measured Drift	
Δ_y / l_c	0.6 %
Δ_c / Δ_y	0.21
μ_Δ @ failure	3.70
μ_θ @ failure	4.42
Failure Mode	Joint failure

Reference : [B4]

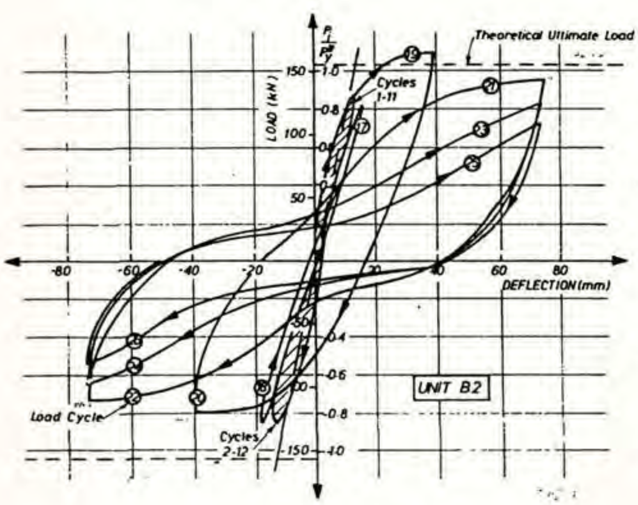

FIG. 5.3 LOAD-DEFLECTION RELATIONSHIP FOR WEST BEAM - UNIT B2

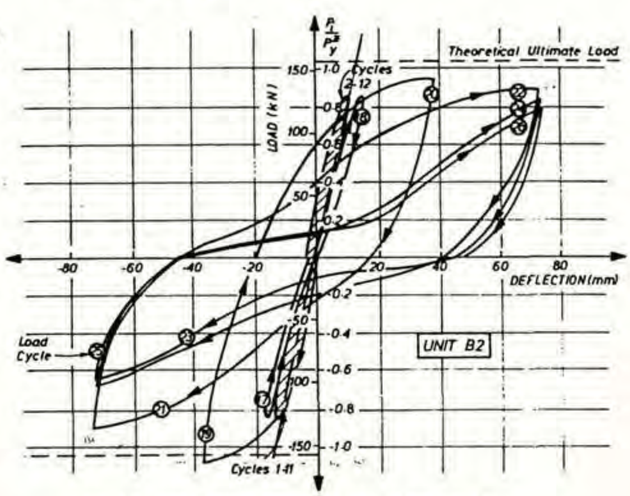

FIG. 5.4 LOAD-DEFLECTION RELATIONSHIP FOR EAST BEAM - UNIT B2

TEST: Cheung 1D-I	Code:C1
l_b	4055 mm
l_c	3500 mm
l'_b	1727 mm
l''_b	1779 mm
l'_c	1475 mm
h_b	550 mm
b_b	400 mm
h_c	600 mm
b_c	550 mm
d^- beam	498 mm
d^+ beam	498 mm
jd^- beam	461 mm
jd^+ beam	471 mm
jd^{*-}	446 mm
jd^{*+}	446 mm
f'_c	40.8 MPa
f_y beam top bars	287.4 MPa
f_y beam bottom bars	283.0 MPa
f_y slab bars	315 MPa
f_y joint hoops	318.0 MPa
$N^*/f'_c A_g$	0.000
A_s top beam bars	2436 mm^2
A_s btm beam bars	1808 mm^2
d_b, top beam bars	24+20 mm
d_b, btm beam bars	24 mm
A_s slab bars	785 mm^2
A_{sh} joint	3216 mm^2

Chng-1D-.xls

Theoretical Forces based on Measured Properties	
T_i^-	947 kN
T_i^+	512 kN
M_i^-	437 kN.m
M_i^+	241 kN.m
V_i^-	253 kN
V_i^+	140 kN
H_i	227.3 kN
$V_{jh,i}$	1231.7 kN
V_{sh}	1022.7 kN
$(V_{sh})_{eff}$	1022.7 kN
Joint hoops have yield plateau	yes
$v_{jh,i} / f'_c$	0.091

Measured Strengths	
H'_o (corr. for P-δ)	271.8 kN
H_o	271.8 kN
$\lambda_o = H'_o/H_i$	1.196
λ_{jo}	1.299
$V_{jh,o}$	1599.7 kN
$v_{jh,o} / f'_c$	0.119
$(V_{sh})_{eff} / V_{jh,o}$	0.639
K_{pv}	1.960
$v_{jh,e} / f'_c$	0.23

Measured Drift	
Δ_y / l_c	0.65 %
Δ_c / Δ_y	0.45
μ_Δ @ failure	>6
μ_θ @ failure	>12
Failure Mode	no failure

Reference : [C1]

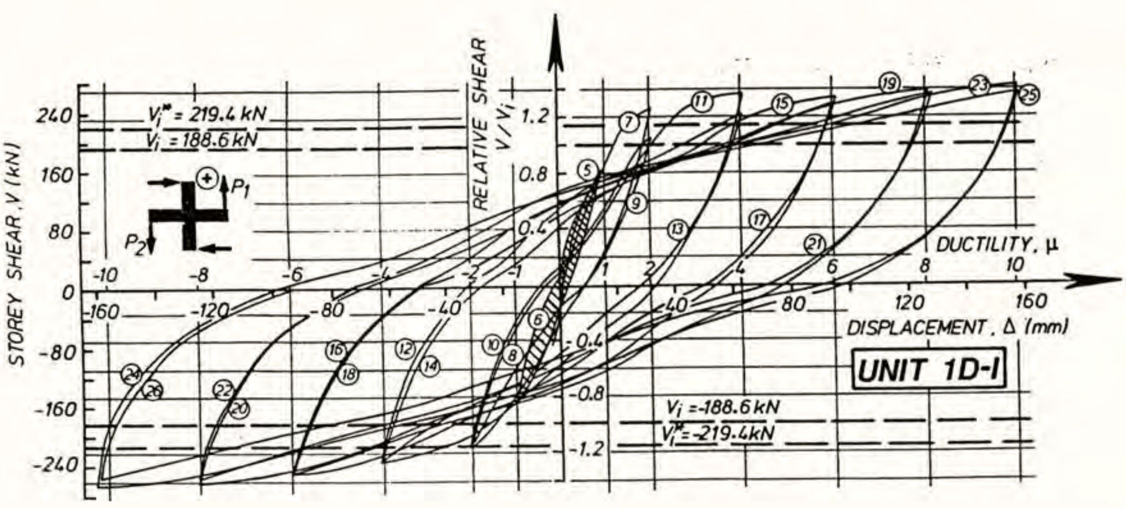

TEST: Durrani X1	Code: D1
l_b	2495.6 mm
l_c	2247.9 mm
l'_b	1066.8 mm
l''_b	1128.8 mm
l'_c	914.4 mm
h_b	419.1 mm
b_b	279.4 mm
h_c	362 mm
b_c	362 mm
d^- beam	363.6 mm
d^+ beam	366.7 mm
jd^- beam	332 mm
jd^+ beam	343 mm
jd^{*-}	311.2 mm
jd^{*+}	311.2 mm
f'_c	34.3 MPa
f_y beam top bars	331.0 MPa
f_y beam bottom bars	344.8 MPa
f_y slab bars	0 MPa
f_y joint hoops	351.7 MPa
$N^*/f'_c A_g$	0.055
A_s top beam bars	1548 mm^2
A_s btm beam bars	1136 mm^2
d_b, top beam bars	22 mm
d_b, btm beam bars	19 mm
A_s slab bars	0 mm^2
A_{sh} joint	864 mm^2

Theoretical Forces based on Measured Properties	
T_i^-	512 kN
T_i^+	392 kN
M_i^-	170 kN.m
M_i^+	134 kN.m
V_i^-	160 kN
V_i^+	126 kN
H_i	158.4 kN
$V_{jh,i}$	745.7 kN
V_{sh}	303.9 kN
$(V_{sh})_{eff}$ #	303.9 kN
Joint hoops have yield plateau	yes
$v_{jh,i} / f'_c$	0.166

Measured Strengths	
H'_o (corr. for P-δ)	164.6 kN
H_o	160.6 kN
$\lambda_o = H'_o/H_i$	1.039
λ_{jo}	1.227
$V_{jh,o}$	915.0 kN
$v_{jh,o} / f'_c$	0.204
$(V_{sh})_{eff} / V_{jh,o}$	0.332
K_{pv}	2.520
$v_{jh,e} / f'_c$	0.513

Measured Drift	
Δ_y / l_c	1.28 %
Δ_c / Δ_y	0.23
μ_Δ @ failure	3.70
μ_θ @ failure	4.51
Failure Mode	Joint Failure

Note: Levels of the sets of joint hoops in joint region are not available, it was assumed that all the two sets deveoped full yield strength.

Reference : [D2]

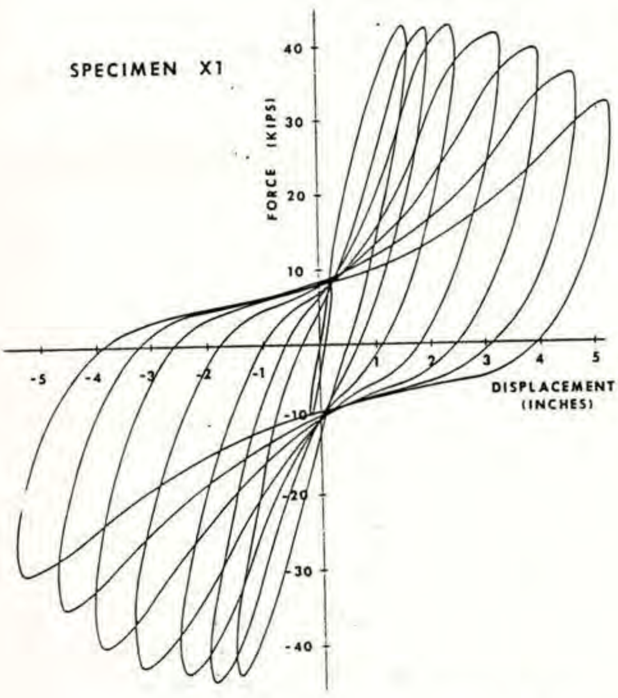

Fig. 3.3(a) Column Load vs. Column Load Point Displacement Hysteresis Curves for Specimen X1

TEST: Durrani X2	Code: D2
l_b	2495.6 mm
l_c	2247.9 mm
l'_b	1066.8 mm
l''_b	1128.8 mm
l'_c	914.4 mm
h_b	419.1 mm
b_b	279.4 mm
h_c	362 mm
b_c	362 mm
d^- beam	363.6 mm
d^+ beam	366.7 mm
jd^- beam	332 mm
jd^+ beam	342 mm
jd^{*-}	311.2 mm
jd^{*+}	311.2 mm
f'_c	33.7 MPa
f_y beam top bars	331.0 MPa
f_y beam bottom bars	344.8 MPa
f_y slab bars	0 MPa
f_y joint hoops	351.7 MPa
$N^*/f'_c A_g$	0.056
A_s top beam bars	1548 mm^2
A_s btm beam bars	1136 mm^2
d_b, top beam bars	22 mm
d_b, btm beam bars	19 mm
A_s slab bars	0 mm^2
A_{sh} joint	1297 mm^2

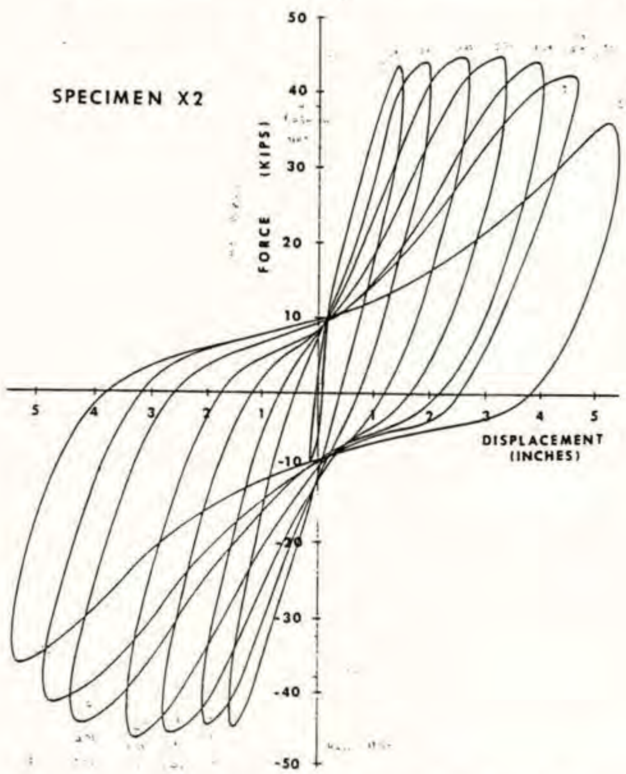

Fig. 3.3(b) Column Load vs. Column Load Point Displacement Hysteresis Curves for Specimen X2

Theoretical Forces based on Measured Properties	
T_i^-	512 kN
T_i^+	392 kN
M_i^-	170 kN.m
M_i^+	134 kN.m
V_i^-	159 kN
V_i^+	126 kN
H_i	158.2 kN
$V_{jh,i}$	745.9 kN
V_{sh}	456.0 kN
$(V_{sh})_{eff}$ #	456.0 kN
Joint hoops have yield plateau	yes
$v_{jh,i} / f'_c$	0.169

Measured Strengths	
H'_o (corr. for P-δ)	169.0 kN
H_o	164.2 kN
$\lambda_o = H'_o/H_i$	1.069
λ_{jo}	1.260
$V_{jh,o}$	940.1 kN
$v_{jh,o} / f'_c$	0.213
$(V_{sh})_{eff} / V_{jh,o}$	0.485
K_{pv}	2.220
$v_{jh,e} / f'_c$	0.473

Measured Drift	
Δ_y / l_c	1.3 %
Δ_c / Δ_y	0.23
μ_Δ @ failure	4.20
μ_θ @ failure	5.16
Failure Mode	Joint Failure

Note: Levels of the sets of joint hoops in joint region are not available, it was assumed that all the three sets deveoped full yield strength.

Reference : [D2]

TEST: Durrani X3	Code:D3
l_b	2495.6 mm
l_c	2247.9 mm
l'_b	1066.8 mm
l''_b	1128.8 mm
l'_c	914.4 mm
h_b	419.1 mm
b_b	279.4 mm
h_c	362 mm
b_c	362 mm
d^- beam	363.6 mm
d^+ beam	366.7 mm
jd^- beam	337 mm
jd^+ beam	347 mm
jd^{*-}	311.2 mm
jd^{*+}	311.2 mm
f'_c	31.0 MPa
f_y beam top bars	331.0 MPa
f_y beam bottom bars	344.8 MPa
f_y slab bars	0 MPa
f_y joint hoops	351.7 MPa
$N^*/f'_c A_g$	0.053
A_s top beam bars	1163 mm^2
A_s btm beam bars	855 mm^2
d_b, top beam bars	22 mm
d_b, btm beam bars	19 mm
A_s slab bars	0 mm^2
A_{sh} joint	864 mm^2

Durr_X3.xls

Theoretical Forces based on Measured Properties	
T_i^-	385 kN
T_i^+	295 kN
M_i^-	130 kN.m
M_i^+	102 kN.m
V_i^-	122 kN
V_i^+	96 kN
H_i	120.8 kN
$V_{jh,i}$	559.0 kN
V_{sh}	303.9 kN
$(V_{sh})_{eff}$ #	303.9 kN
Joint hoops have yield plateau	yes
$v_{jh,i} / f'_c$	0.138

Measured Strengths	
H'_o (corr. for P-δ)	124.3 kN
H_o	116.7 kN
$\lambda_o = H'_o/H_i$	1.029
λ_{jo}	1.244
$V_{jh,o}$	695.5 kN
$v_{jh,o} / f'_c$	0.171
$(V_{sh})_{eff} / V_{jh,o}$	0.437
K_{pv}	2.360
$v_{jh,e} / f'_c$	0.404

Measured Drift	
Δ_y / l_c	1.12 %
Δ_c / Δ_y	0.25
μ_Δ @ failure	5.00
μ_θ @ failure	6.33
Failure Mode	Joint Failure

Note: Levels of the sets of joint hoops in joint region are not available, it was assumed that all the two sets deveoped full yield strength.

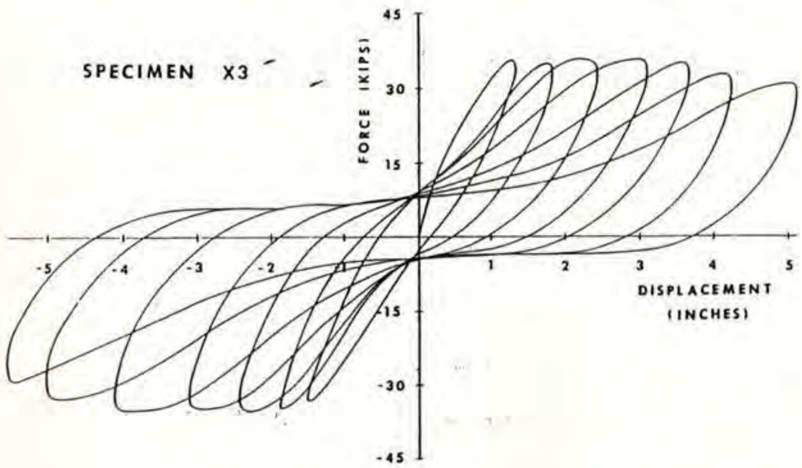

Fig. 3.3(c) Column Load vs. Column Load Point Displacement Hysteresis Curves for Specimen X3

TEST: Dai's U1	Code: D4
l_b	4238 mm
l_c	2473 mm
l'_b	1916 mm
l''_b	1958 mm
l'_c	1033.5 mm
h_b	457 mm
b_b	229 mm
h_c	406 mm
b_c	305 mm
d^- beam	402 mm
d^+ beam	415 mm
jd^- beam	385 mm
jd^+ beam	408 mm
jd^{*-}	360 mm
jd^{*+}	373 mm
f'_c	45.6 MPa
f_y beam top bars	294.0 MPa
f_y beam bottom bars	294.0 MPa
f_y slab bars	0 MPa
f_y joint hoops	304.0 MPa
$N^*/f'_c A_g$	0.000
A_s top beam bars	1005 mm^2
A_s btm beam bars	402 mm^2
d_b, top beam bars	16 mm
d_b, btm beam bars	16 mm
A_s slab bars	0 mm^2
A_{sh} joint	1235 mm^2

Dai_U1.xls

Theoretical Forces based on Measured Properties	
T_i^-	295 kN
T_i^+	118 kN
M_i^-	114 kN.m
M_i^+	48 kN.m
V_i^-	59 kN
V_i^+	25 kN
H_i	72.5 kN
$V_{jh,i}$	341.2 kN
V_{sh}	469.0 kN
$(V_{sh})_{eff}$	389.5 kN
Joint hoops have yield plateau	yes
$v_{jh,i} / f'_c$	0.060

Measured Strengths	
H'_o (corr. for P-δ)	80.4 kN
H_o	80.4 kN
$\lambda_o = H'_o/H_i$	1.109
λ_{jo}	1.253
$V_{jh,o}$	427 kN
$v_{jh,o} / f'_c$	0.076
$(V_{sh})_{eff} / V_{jh,o}$	0.911
K_{pv}	1.250
$v_{jh,e} / f'_c$	0.095

Measured Drift	
Δ_y / l_c	0.61 %
Δ_c / Δ_y	0.47
μ_Δ @ failure	>7
μ_θ @ failure	>12.32
Failure Mode	no failure

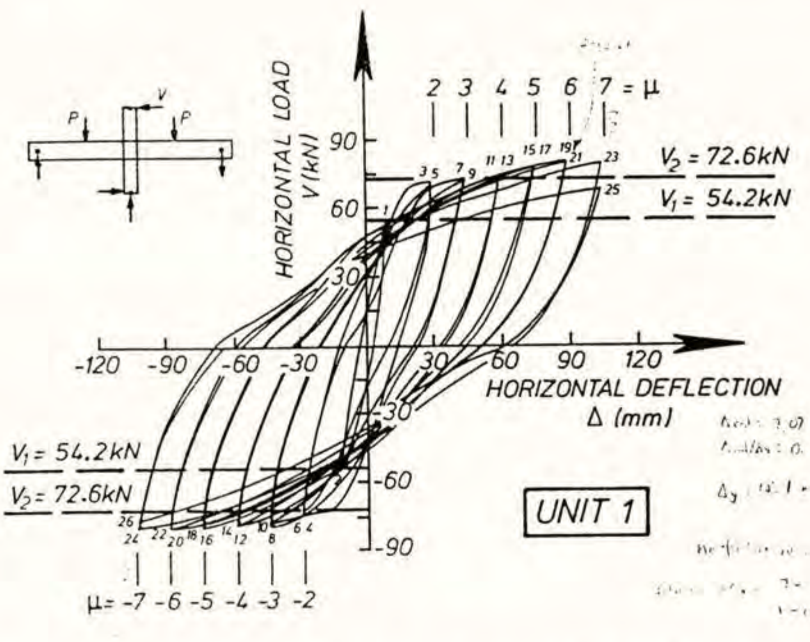

(a) Measured Horizontal Load Versus Horizontal Displacement
Hysteresis Loops for Unit 1

TEST: Dai's U2	Code: D5
l_b	4238 mm
l_c	2473 mm
l'_b	1916 mm
l''_b	1960 mm
l'_c	1033.5 mm
h_b	457 mm
b_b	229 mm
h_c	406 mm
b_c	305 mm
d^- beam	409 mm
d^+ beam	414 mm
jd^- beam	381 mm
jd^+ beam	401 mm
jd^{*-}	367 mm
jd^{*+}	367 mm
f'_c	36.0 MPa
f_y beam top bars	314.0 MPa
f_y beam bottom bars	300.0 MPa
f_y slab bars	0 MPa
f_y joint hoops	283.0 MPa
$N^*/f'_c A_g$	0.000
A_s top beam bars	1232 mm^2
A_s btm beam bars	628 mm^2
d_b, top beam bars	28 mm
d_b, btm beam bars	20 mm
A_s slab bars	0 mm^2
A_{sh} joint	1651 mm^2

Dai_U2.xls

Theoretical Forces based on Measured Properties	
T_i^-	387 kN
T_i^+	188 kN
M_i^-	148 kN.m
M_i^+	75 kN.m
V_i^-	77 kN
V_i^+	39 kN
H_i	99.7 kN
$V_{jh,i}$	475.5 kN
V_{sh}	584.0 kN
$(V_{sh})_{eff}$	490.6 kN
Joint hoops have yield plateau	yes
$v_{jh,i} / f'_c$	0.107

Measured Strengths	
H'_o (corr. for P-δ)	111.7 kN
H_o	111.7 kN
$\lambda_o = H'_o/H_i$	1.120
λ_{jo}	1.242
$V_{jh,o}$	591 kN
$v_{jh,o} / f'_c$	0.132
$(V_{sh})_{eff} / V_{jh,o}$	0.831
K_{pv}	1.449
$v_{jh,e} / f'_c$	0.192

Measured Drift	
Δ_y / l_c	0.8 %
Δ_c / Δ_y	0.352
μ_Δ @ failure	5.00
μ_θ @ failure	7.21
Failure Mode	Bond failure

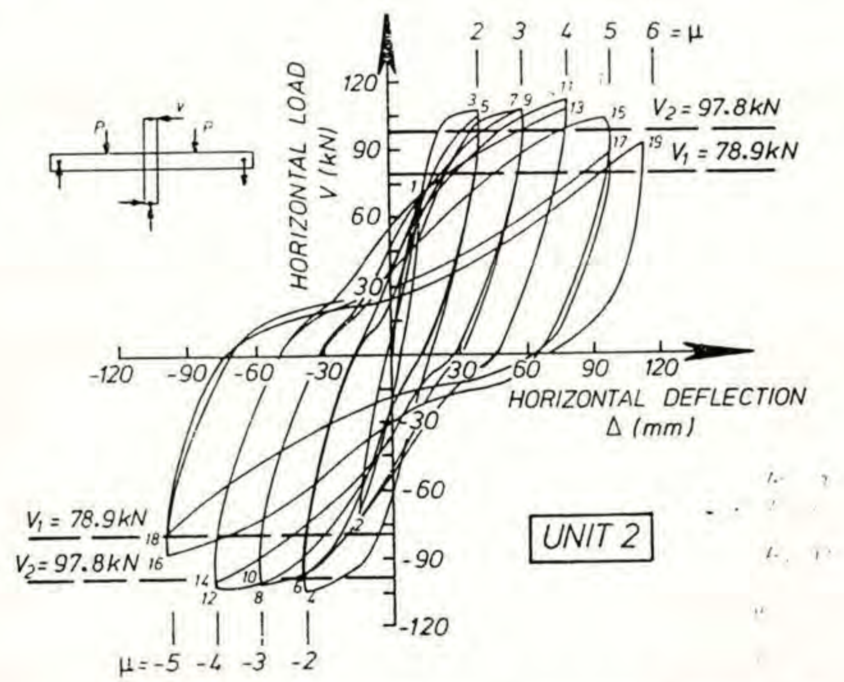

(a) Measured Horizontal Load Versus Horizontal Displacement Hysteresis Loops for Unit 2

TEST: Dai's U3	Code:D6
l_b	4238 mm
l_c	2473 mm
l'_b	1916 mm
l''_b	1958 mm
l'_c	1033.5 mm
h_b	457 mm
b_b	229 mm
h_c	406 mm
b_c	305 mm
d^- beam	402 mm
d^+ beam	415 mm
jd^- beam	381 mm
jd^+ beam	407 mm
jd^{*-}	360 mm
jd^{*+}	373 mm
f'_c	36.2 MPa
f_y beam top bars	294.0 MPa
f_y beam bottom bars	294.0 MPa
f_y slab bars	0 MPa
f_y joint hoops	336.0 MPa
$N^*/f'_c A_g$	0.000
A_s top beam bars	1005 mm^2
A_s btm beam bars	402 mm^2
d_b, top beam bars	16 mm
d_b, btm beam bars	16 mm
A_s slab bars	0 mm^2
A_{sh} joint	558 mm^2

Dai_U3.xls

Theoretical Forces based on Measured Properties	
T_i^-	295 kN
T_i^+	118 kN
M_i^-	113 kN.m
M_i^+	48 kN.m
V_i^-	59 kN
V_i^+	25 kN
H_i	71.8 kN
$V_{jh,i}$	341.8 kN
V_{sh}	229.0 kN
$(V_{sh})_{eff}$	190.2 kN
Joint hoops have yield plateau	60 % has no yield plateau
$v_{jh,i} / f'_c$	0.076

Measured Strengths	
H'_o (corr. for P-δ)	79.4 kN
H_o	79.4 kN
$\lambda_o = H'_o/H_i$	1.105
λ_{jo}	1.237
$V_{jh,o}$	423 kN
$v_{jh,o} / f'_c$	0.094
$(V_{sh})_{eff} / V_{jh,o}$	0.450
K_{pv}	2.300
$v_{jh,e} / f'_c$	0.217

Measured Drift	
Δ_y / l_c	0.58 %
Δ_c / Δ_y	0.577
μ_Δ @ failure	7.000
μ_θ @ failure	15.20
Failure Mode	no failure

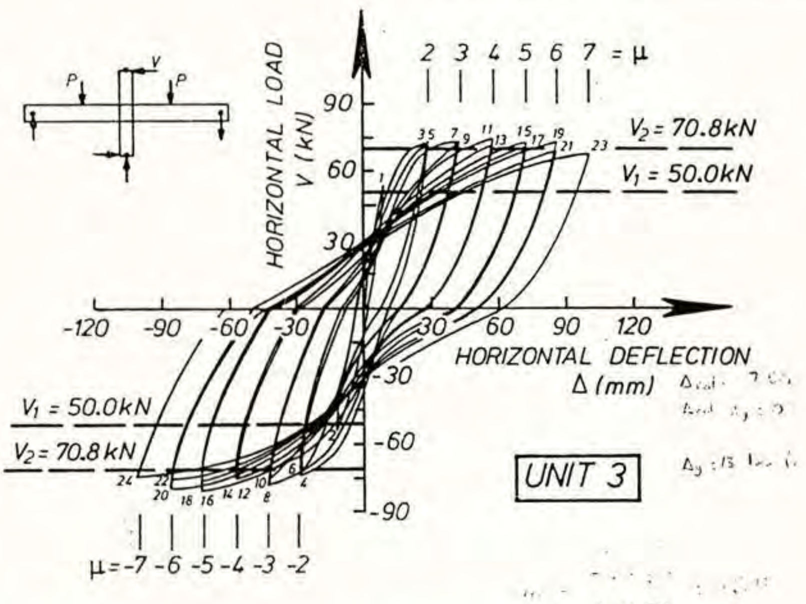

(a) Measured Horizontal Load Versus Horizontal Displacement
Hysteresis Loops for Unit 3

TEST: Dai's U4	Code: D7
l_b	4238 mm
l_c	2473 mm
l'_b	1916 mm
l''_b	1960 mm
l'_c	1033.5 mm
h_b	457 mm
b_b	229 mm
h_c	406 mm
b_c	305 mm
d^- beam	409 mm
d^+ beam	414 mm
jd^- beam	384 mm
jd^+ beam	402 mm
jd^{*-}	367 mm
jd^{*+}	367 mm
f'_c	40.1 MPa
f_y beam top bars	314.0 MPa
f_y beam bottom bars	300.0 MPa
f_y slab bars	0 MPa
f_y joint hoops	312.0 MPa
$N^*/f'_c A_g$	0.000
A_s top beam bars	1232 mm^2
A_s btm beam bars	628 mm^2
d_b, top beam bars	28 mm
d_b, btm beam bars	20 mm
A_s slab bars	0 mm^2
A_{sh} joint	815 mm^2

Dai_U4.xls

Theoretical Forces based on Measured Properties	
T_i^-	387 kN
T_i^+	188 kN
M_i^-	149 kN.m
M_i^+	76 kN.m
V_i^-	78 kN
V_i^+	40 kN
H_i	100.3 kN
$V_{jh,i}$	474.9 kN
V_{sh}	317.0 kN
$(V_{sh})_{eff}$	265.3 kN
Joint hoops have yield plateau	77 % have no yield plateau
$v_{jh,i} / f'_c$	0.096

Measured Strengths	
H'_o (corr. for P-δ)	106.5 kN
H_o	106.5 kN
$\lambda_o = H'_o/H_i$	1.061
λ_{jo}	1.185
$V_{jh,o}$	563 kN
$v_{jh,o} / f'_c$	0.113
$(V_{sh})_{eff} / V_{jh,o}$	0.472
K_{pv}	2.280
$v_{jh,e} / f'_c$	0.26

Measured Drift	
Δ_y / l_c	0.73 %
Δ_c / Δ_y	0.396
μ_Δ @ failure	5.000
μ_θ @ failure	7.62
Failure Mode	Bond Failure

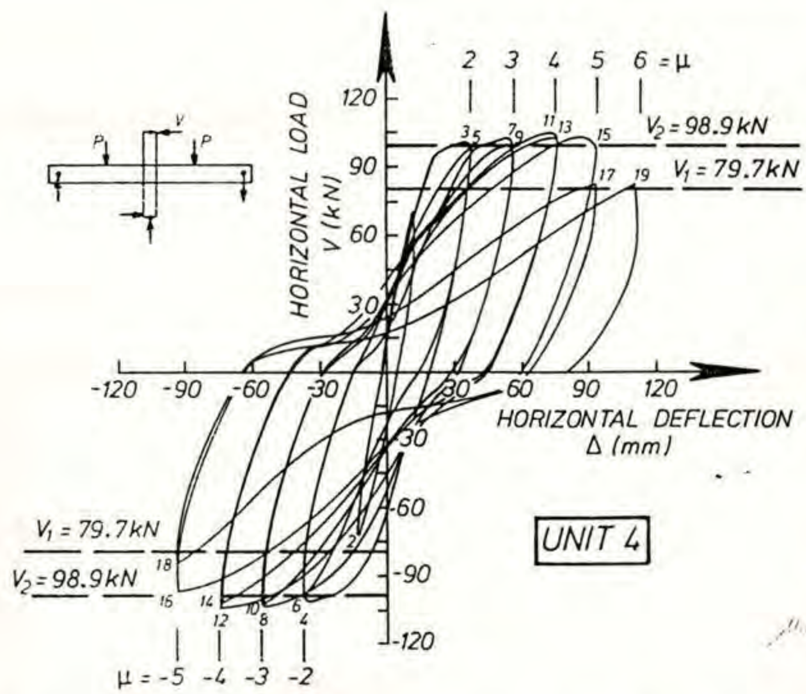

(a) Measured Horizontal Load Versus Horizontal Displacement Hysteresis Loops for Unit 4

Note: column hinging was observed. So the columns are treated here as beams and viceversa
Hakuto reinforced the Columns with 2D24+1HD24

TEST: Hakuto O1	Code: H1
l_b	3200 mm
l_c	3810 mm
l'_b	1350 mm
l''_b	1402 mm
l'_c	1755 mm
h_b	300 mm
b_b	460 mm
h_c	500 mm
b_c	300 mm
d^- beam	248 mm
d^+ beam	248 mm
jd^- beam	232 mm
jd^+ beam	232 mm
jd^{*-}	196 mm
jd^{*+}	196 mm
f'_c	41.0 MPa
f_y beam top bars	370.3 MPa
f_y beam bottom bars	370.3 MPa
f_y slab bars	0 MPa
f_y joint hoops	0.0 MPa
$N^*/f'_c A_g$	0.000
A_s top beam bars	1356 mm2
A_s btm beam bars	1356 mm2
d_b, top beam bars	2HD24+1D24
d_b, btm beam bars	2HD24+1D24
A_s slab bars	0 mm2
A_{sh} joint	0 mm2

Theoretical Forces based on Measured Properties	
T_i^-	502 kN
T_i^+	502 kN
M_i^-	117 kN.m
M_i^+	117 kN.m
V_i^-	86 kN
V_i^+	86 kN
H_i	72.6 kN
$V_{jh,i}$	931.8 kN
V_{sh}	0.0 kN
$(V_{sh})_{eff}$	0.0 kN
Joint hoops have yield plateau	-
$v_{jh,i} / f'_c$	0.099

Measured Strengths	
H'_o (corr. for P-δ)	74.8 kN
H_o	74.8 kN
$\lambda_o = H'_o/H_i$	1.030
λ_{jo}	1.286
$V_{jh,o}$	1198.5 kN
$v_{jh,o} / f'_c$	0.127
$(V_{sh})_{eff} / V_{jh,o}$	0.000
K_{pv}	2.760
$v_{jh,e} / f'_c$	0.35

Measured Drift	
Δ_y / l_c	1.16 %
Δ_c / Δ_y	0.28
μ_Δ @ failure	*
μ_θ @ failure	*
Failure Mode	**

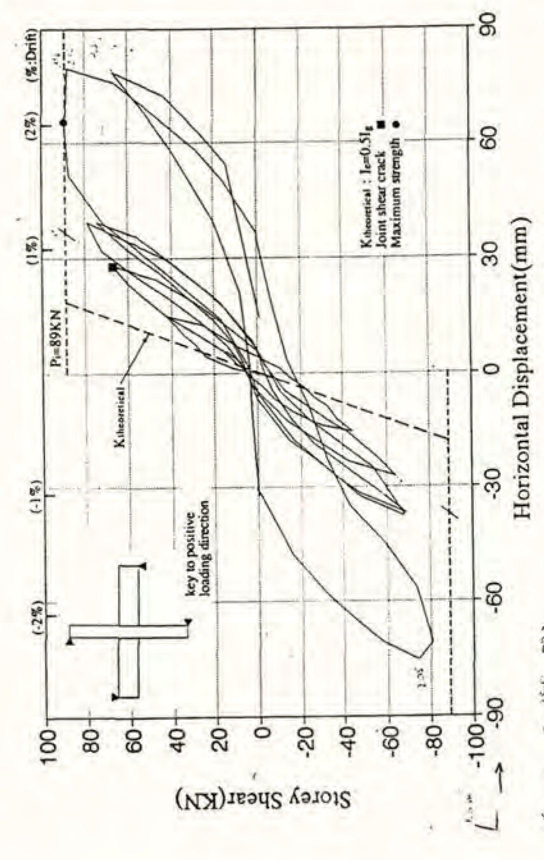

Fig. 9 Storey Shear versus Horizontal Displacement Relationship for As-Built Specimen O1

Note: * Test ceased at μ_Δ~2 , therefore ultimate displacement ductility corresponding to 0.9Hmax is not available.

** Pinching of hysteretic loops was due to bond deterioration compounded with joint diagonal cracking. Strength degradation was observed but loading sequence ceased for retrofit.

Reference: [H1]

Test : Joh JX0-B1	Code: J1
l_b	3000 mm
l_c	1750 mm
l'_b	1350 mm
l''_b	1380 mm
l'_c	730 mm
h_b	350 mm
b_b	150 mm
h_c	300 mm
b_c	300 mm
d^- beam	320 mm
d^+ beam	320 mm
jd^- beam	293 mm
jd^+ beam	293 mm
jd^{*-}	290 mm
jd^{*+}	290 mm
f'_c	21.3 MPa
f_y beam top bars	370.7 MPa
f_y beam bottom bars	370.7 MPa
f_y slab bars	0 MPa
f_y joint hoops	306.7 MPa
$N^*/f'_c A_g$	0.161
A_s top beam bars	398 mm^2
A_s btm beam bars	398 mm^2
d_b, top beam bars	13 mm
d_b, btm beam bars	13 mm
A_s slab bars	0 mm^2
A_{sh} joint	170 mm^2

Joh_jxb1.xls

Theoretical Forces based on Measured Properties	
T_i^-	148 kN
T_i^+	148 kN
M_i^-	43 kN.m
M_i^+	43 kN.m
V_i^-	32 kN
V_i^+	32 kN
H_i	54.9 kN
$V_{jh,i}$	240.2 kN
V_{sh}	52.0 kN
$(V_{sh})_{eff}$ #	52.0 kN
Joint hoops have yield plateau	no
$v_{jh,i} / f'_c$	0.125

Measured Strengths	
H'_o (corr. for P-δ)	60.7 kN
H_o	60.7 kN
$\lambda_o = H'_o/H_i$	1.106
λ_{jo}	1.150
$V_{jh,o}$	276.3 kN
$v_{jh,o} / f'_c$	0.144
$(V_{sh})_{eff} / V_{jh,o}$	0.188
K_{pv}	2.310
$v_{jh,e} / f'_c$	0.33

Measured Drift	
Δ_y / l_c	0.47 %
Δ_c / Δ_y	0.154
μ_Δ @ failure	9.00
μ_θ @ failure	10.46
Failure Mode	joint failure

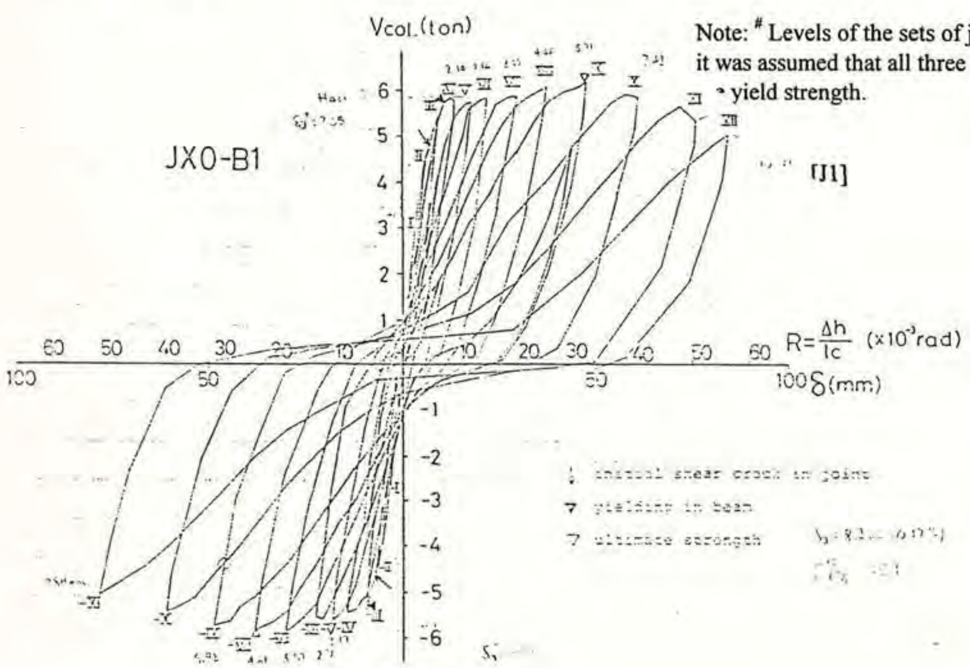

Note: # Levels of the sets of joint hoops are not available, it was assumed that all three sets of joint hoops developed [illegible] yield strength.

TEST: JXO-B2	**Code: J2**
l_b	3000 mm
l_c	1750 mm
l'_b	1350 mm
l''_b	1380 mm
l'_c	730 mm
h_b	350 mm
b_b	300 mm
h_c	300 mm
b_c	300 mm
d^- beam	320 mm
d^+ beam	320 mm
jd^- beam	306 mm
jd^+ beam	306 mm
jd^{*-}	290 mm
jd^{*+}	290 mm
f'_c	20.8 MPa
f_y beam top bars	370.7 MPa
f_y beam bottom bars	370.7 MPa
f_y slab bars	0 MPa
f_y joint hoops	306.7 MPa
$N^*/f'_c A_g$	0.161
A_s top beam bars	398 mm^2
A_s btm beam bars	398 mm^2
d_b, top beam bars	13 mm
d_b, btm beam bars	13 mm
A_s slab bars	0 mm^2
A_{sh} joint	170 mm^2

Theoretical Forces based on Measured Properties	
T_i^-	148 kN
T_i^+	148 kN
M_i^-	45 kN.m
M_i^+	45 kN.m
V_i^-	33 kN
V_i^+	33 kN
H_i	57.3 kN
$V_{jh,i}$	237.7 kN
V_{sh}	52.1 kN
$(V_{sh})_{eff}$ #	52.1 kN
Joint hoops have yield plateau	no
$v_{jh,i} / f'_c$	0.127

Measured Strengths	
H'_o (corr. for P-δ)	64.5 kN
H_o	64.5 kN
$\lambda_o = H'_o/H_i$	1.125
λ_{jo}	1.235
$V_{jh,o}$	293.6 kN
$v_{jh,o} / f'_c$	0.157
$(V_{sh})_{eff} / V_{jh,o}$	0.177
K_{pv}	2.290
$v_{jh,e} / f'_c$	0.359

Measured Drift	
Δ_y / l_c	0.31 %
Δ_c / Δ_y	0.26
μ_Δ @ failure	14.30
μ_θ @ failure	18.90
Failure Mode	joint failure

Joh_jxb2.xls

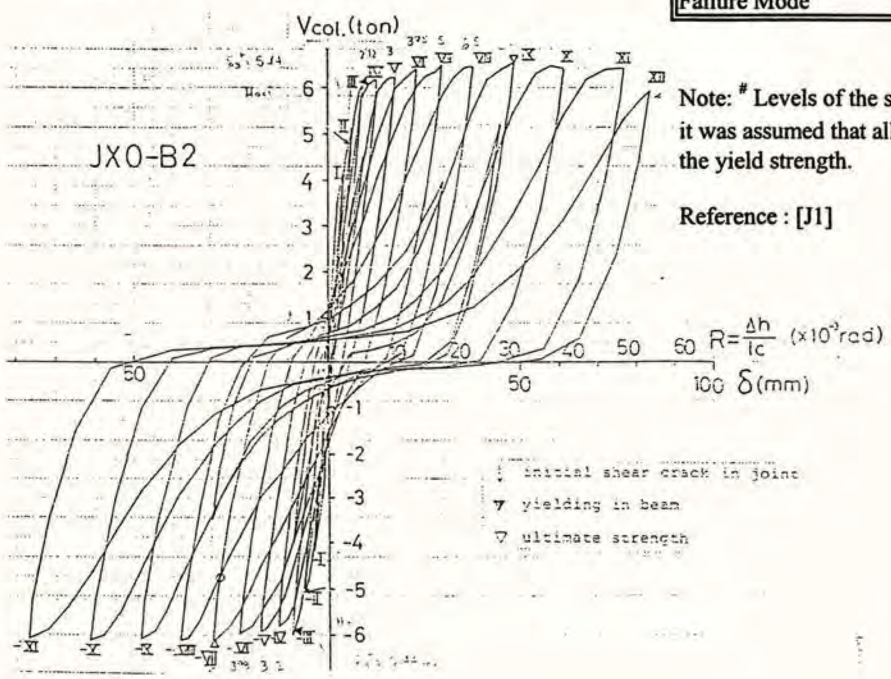

Note: # Levels of the sets of joint hoops are not available, it was assumed that all three sets of joint hoops developed the yield strength.

Reference : [J1]

TEST: Joh JXO-B8-HH Code: J3	
l_b	3000 mm
l_c	1750 mm
l'_b	1350 mm
l''_b	1380 mm
l'_c	730 mm
h_b	350 mm
b_b	200 mm
h_c	300 mm
b_c	300 mm
d^- beam	320 mm
d^+ beam	320 mm
jd^- beam	302 mm
jd^+ beam	302 mm
jd^{*-}	290 mm
jd^{*+}	290 mm
f'_c	25.6 MPa
f_y beam top bars	404.0 MPa
f_y beam bottom bars	404.0 MPa
f_y slab bars	0 MPa
f_y joint hoops	1165.0 MPa
$N^*/f'_c A_g$	0.153
A_s, top beam bars	387 mm^2
A_s, btm beam bars	387 mm^2
d_b, top beam bars	13 mm
d_b, btm beam bars	13 mm
A_s slab bars	0 mm^2
A_{sh} joint	432 mm^2

Joh_jxhh.xls

Theoretical Forces based on Measured Properties	
T_i^-	156 kN
T_i^+	156 kN
M_i^-	47 kN.m
M_i^+	47 kN.m
V_i^-	35 kN
V_i^+	35 kN
H_i	60.0 kN
$V_{jh,i}$	252.7 kN
V_{sh}	548.0 kN
$(V_{sh})_{eff}$ #	503.0 kN
Joint hoops have yield plateau	no
$v_{jh,i} / f'_c$	0.110

Measured Strentghs	
H'_o (corr. for P-δ)	64.6 kN
H_o	64.6 kN
$\lambda_o = H'_o/H_i$	1.077
λ_{jo}	1.163
$V_{jh,o}$	294.0 kN
$v_{jh,o} / f'_c$	0.128
$(V_{sh})_{eff} / V_{jh,o}$	1.000
K_{pv}	1.080
$v_{jh,e} / f'_c$	0.138

Measured Drift	
Δ_y / l_c	0.545 %
Δ_c / Δ_y	0.55
μ_Δ @ failure	7.52
μ_θ @ failure	8.520
Failure Mode	Beam Hinging

Note: # Levels of the sets of joint hoops are not available, it was assumed that the top and bottom sets of joint hoops developed 50% of the yield strength.

Reference : [J2]

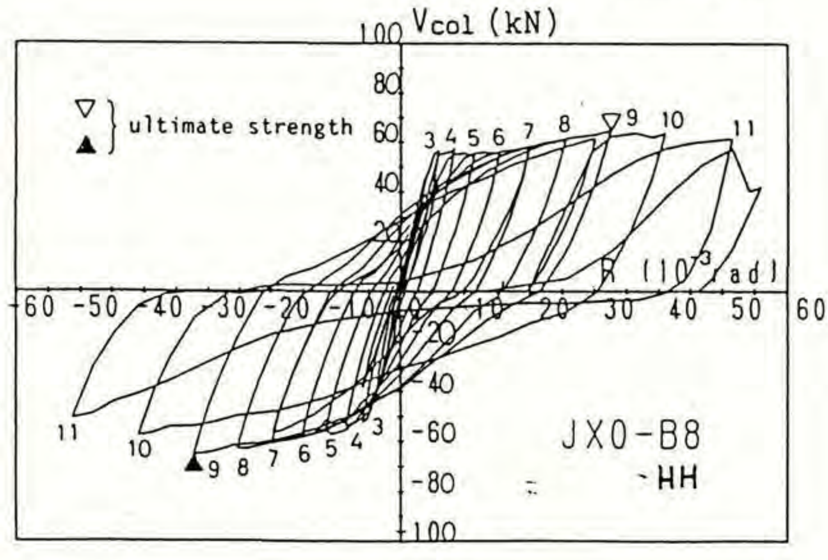

TEST: JXO-B8-HL	Code: J4
l_b	3000 mm
l_c	1750 mm
l'_b	1350 mm
l''_b	1380 mm
l'_c	730 mm
h_b	350 mm
b_b	200 mm
h_c	300 mm
b_c	300 mm
d^- beam	320 mm
d^+ beam	320 mm
jd^- beam	303 mm
jd^+ beam	303 mm
jd^{*-}	290 mm
jd^{*+}	290 mm
f'_c	27.4 MPa
f_y beam top bars	404.0 MPa
f_y beam bottom bars	404.0 MPa
f_y slab bars	0 MPa
f_y joint hoops	1165.0 MPa
$N^*/f'_c A_g$	0.143
A_s top beam bars	387 mm2
A_s btm beam bars	387 mm2
d_b, top beam bars	13 mm
d_b, btm beam bars	13 mm
A_s slab bars	0 mm2
A_{sh} joint	432 mm2

Joh_jxhl.xls

Theoretical Forces based on Measured Properties	
T_i^-	156 kN
T_i^+	156 kN
M_i^-	47 kN.m
M_i^+	47 kN.m
V_i^-	35 kN
V_i^+	35 kN
H_i	60.2 kN
$V_{jh,i}$	252.5 kN
V_{sh}	548.0 kN
$(V_{sh})_{eff}$ #	503.0
Joint hoops have yield plateau	no
$v_{jh,i} / f'_c$	0.102

Measured Strentghs	
H'_o (corr. for P-δ)	66.3 kN
H_o	66.3 kN
$\lambda_o = H'_o/H_i$	1.101
λ_{jo}	1.210
$V_{jh,o}$	305.6 kN
$v_{jh,o} / f'_c$	0.124
$(V_{sh})_{eff} / V_{jh,o}$	1.000
K_{pv}	1.100
$v_{jh,e} / f'_c$	0.136

Measured Drift	
Δ_y / l_c	0.49 %
Δ_c / Δ_y	0.148
μ_Δ @ failure	6.58
μ_θ @ failure	7.55
Failure Mode	Beam Hinging

Note: # Levels of the sets of joint hoops are not available, it was assumed that the top and bottom sets of joint hoops developed 50% of the yield strength.

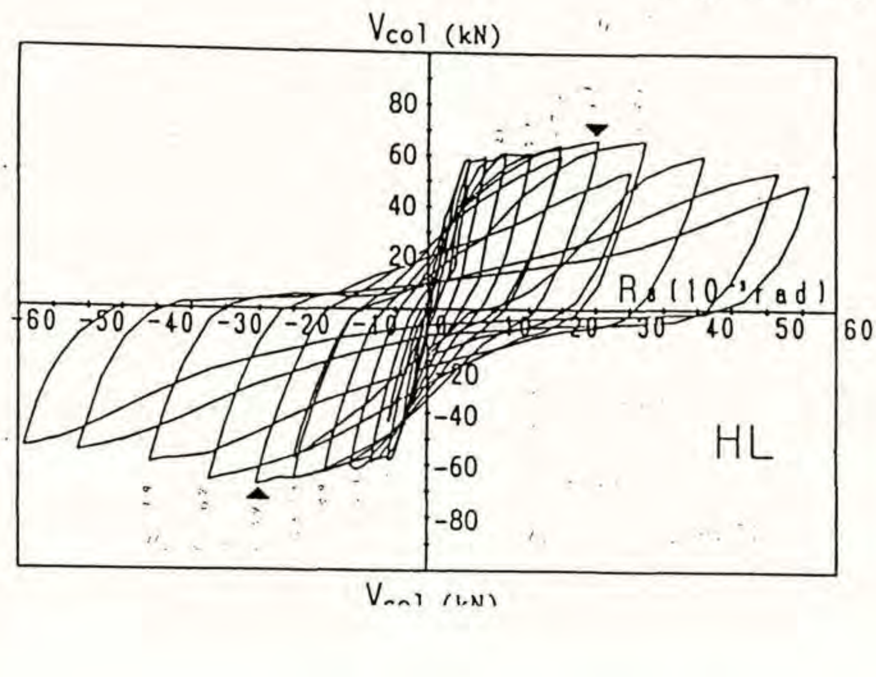

TEST: Joh-B8-LH	Code : J5
l_b	3000 mm
l_c	1750 mm
l'_b	1350 mm
l^*_b	1380 mm
l'_c	730 mm
h_b	350 mm
b_b	200 mm
h_c	300 mm
b_c	300 mm
d^- beam	320 mm
d^+ beam	320 mm
jd^- beam	303 mm
jd^+ beam	303 mm
jd^{*-}	290 mm
jd^{*+}	290 mm
f'_c	26.9 MPa
f_y beam top bars	404.0 MPa
f_y beam bottom bars	404.0 MPa
f_y slab bars	0 MPa
f_y joint hoops	377.0 MPa
$N^*/f'_c A_g$	0.153
A_s top beam bars	387 mm^2
A_s btm beam bars	387 mm^2
d_b, top beam bars	13 mm
d_b, btm beam bars	13 mm
A_s slab bars	0 mm^2
A_{sh} joint	170 mm^2

Joh_jxlh.xls

Theoretical Forces based on Measured Properties	
T_i^-	156 kN
T_i^+	156 kN
M_i^-	47 kN.m
M_i^+	47 kN.m
V_i^-	35 kN
V_i^+	35 kN
H_i	60.1 kN
$V_{jh,i}$	252.6 kN
V_{sh}	64.0 kN
$(V_{sh})_{eff}$ #	64.0 kN
Joint hoops have yield plateau	no
$v_{jh,i} / f'_c$	0.104

Measured Strenghs	
H'_o (corr. for P-δ)	65.4 kN
H_o	65.4 kN
$\lambda_o = H'_o/H_i$	1.087
λ_{jo}	1.197
$V_{jh,o}$	297.7 kN
$v_{jh,o} / f'_c$	0.123
$(V_{sh})_{eff} / V_{jh,o}$	0.215
K_{pv}	2.280
$v_{jh,e} / f'_c$	0.280

Measured Drift	
Δ_y / l_c	0.506 %
Δ_c / Δ_y	0.143
μ_Δ @ failure	6.42
μ_θ @ failure	7.32
Failure Mode	Beam Hinging

Note: # Levels of the sets of joint hoops are not available, it was assumed that all the three sets of joint hoops developed the yield strength.

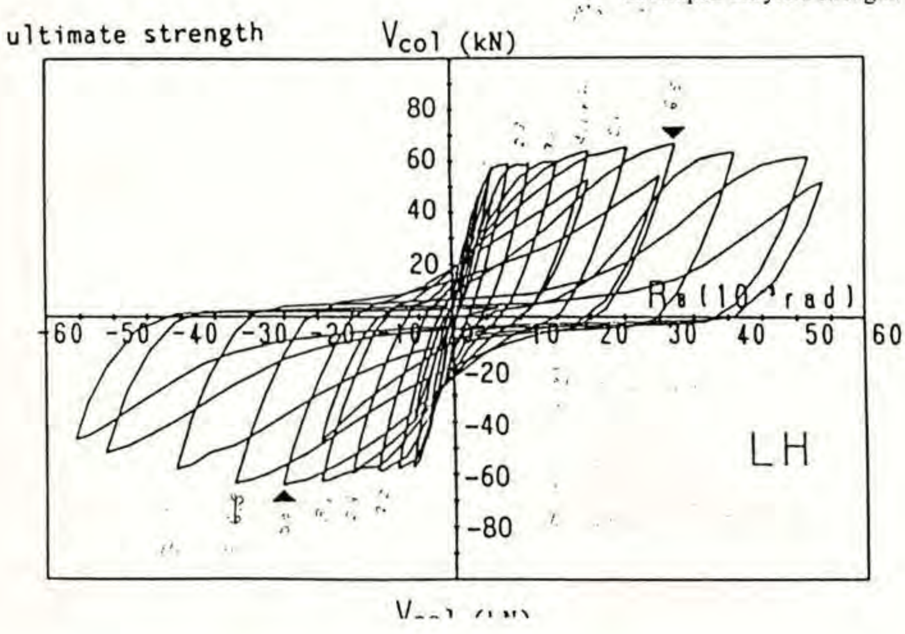

TEST: JXO-B8-MH	Code: J6
l_b	3000 mm
l_c	1750 mm
l'_b	1350 mm
l''_b	1380 mm
l'_c	730 mm
h_b	350 mm
b_b	200 mm
h_c	300 mm
b_c	300 mm
d^- beam	320 mm
d^+ beam	320 mm
jd^- beam	304 mm
jd^+ beam	304 mm
jd^{*-}	290 mm
jd^{*+}	290 mm
f'_c	28.1 MPa
f_y beam top bars	404.0 MPa
f_y beam bottom bars	404.0 MPa
f_y slab bars	0 MPa
f_y joint hoops	377.0 MPa
$N^*/f'_c A_g$	0.153
A_s top beam bars	387 mm2
A_s btm beam bars	387 mm2
d_b, top beam bars	13 mm
d_b, btm beam bars	13 mm
A_s slab bars	0 mm2
A_{sh} joint	339 mm2

Theoretical Forces based on Measured Properties	
T_i^-	156 kN
T_i^+	156 kN
M_i^-	47 kN.m
M_i^+	47 kN.m
V_i^-	35 kN
V_i^+	35 kN
H_i	60.3 kN
$V_{jh,i}$	252.4 kN
V_{sh}	149.0 kN
$(V_{sh})_{eff}$ #	123.5 kN
Joint hoops have yield plateau	no
$v_{jh,i} / f'_c$	0.100

Measured Strentghs	
H'_o (corr. for P-δ)	65.9 kN
H_o	65.9 kN
$\lambda_o = H'_o/H_i$	1.093
λ_{jo}	1.199
$V_{jh,o}$	300.0 kN
$v_{jh,o} / f'_c$	0.119
$(V_{sh})_{eff} / V_{jh,o}$	0.412
K_{pv}	2.040
$v_{jh,e} / f'_c$	0.242

Measured Drift	
Δ_y / l_c	0.51 %
Δ_c / Δ_y	0.141
μ_Δ @ failure	7.50
μ_θ @ failure	8.33
Failure Mode	Bond Failure

Joh_jxmh.xls

Note: # The available drawings show that the top and bottom sets of joint hoops were placed immediately adjacent to the beam bars, thus it was assumed that those sets developed 40% of the yield strength. Other sets deveoped full yield strength.

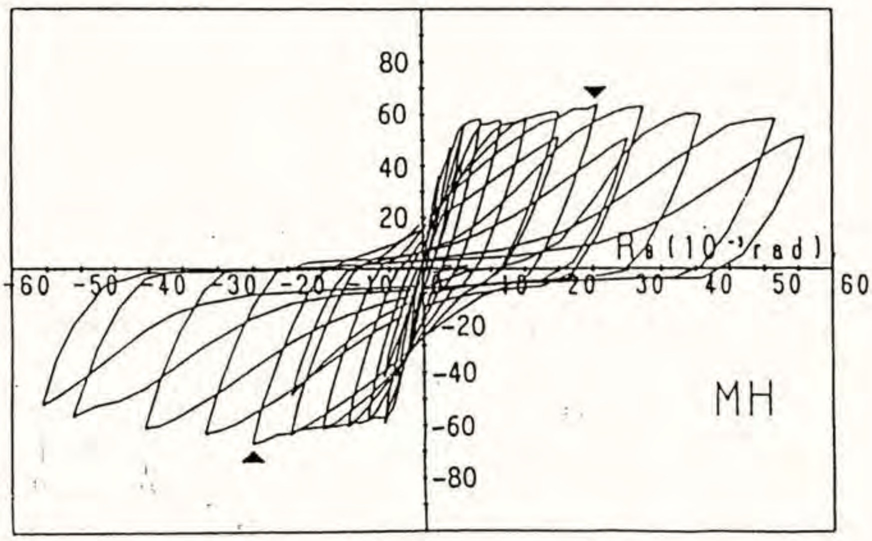

TEST: Lawrance & Beattie HSC	Code: L1
l_b	4258 mm
l_c	3658 mm
l'_b	1904 mm
l''_b	1958 mm
l'_c	1600 mm
h_b	460 mm
b_b	230 mm
h_c	450 mm
b_c	300 mm
d^- beam	406 mm
d^+ beam	410 mm
jd^- beam	388 mm
jd^+ beam	401 mm
jd^{*-}	356 mm
jd^{*+}	356 mm
f'_c	83.2 MPa
f_y beam top bars	479.0 MPa
f_y beam bottom bars	466.0 MPa
f_y slab bars	0 MPa
f_y joint hoops	446.0 MPa
$N^*/f'_c A_g$	0.000
A_s top beam bars	1232 mm^2
A_s btm beam bars	628 mm^2
d_b, top beam bars	28 mm
d_b, btm beam bars	20 mm
A_s slab bars	0 mm^2
A_{sh} joint	1474 mm^2

Lawr_hsc.xls

Theoretical Forces based on Measured Properties	
T_i^-	590 kN
T_i^+	293 kN
M_i^-	229 kN.m
M_i^+	117 kN.m
V_i^-	120 kN
V_i^+	62 kN
H_i	105.8 kN
$V_{jh,i}$	776.9 kN
V_{sh}	657.4 kN
$(V_{sh})_{eff}$ #	526.0 kN
Joint hoops have yield plateau	yes
$v_{jh,i} / f'_c$	0.069

Measured Strengths	
H'_o (corr. for P-δ)	112.3 kN
H_o	112.3 kN
$\lambda_o = H'_o/H_i$	1.061
λ_{jo}	1.138
$V_{jh,o}$	884.4 kN
$v_{jh,o} / f'_c$	0.079
$(V_{sh})_{eff} / V_{jh,o}$	0.595
K_{pv}	2.030
$v_{jh,e} / f'_c$	0.16

Measured Drift	
Δ_y / l_c	1.19 %
Δ_c / Δ_y	0.29
μ_Δ @ failure	4.00
μ_θ @ failure	5.24
Failure Mode	Bond Failure

Note: # The available drawings show that the top and bottom sets of joint hoops were placed close to the beam bars thus it was assumed that those sets developed 50% of the yield strength. Other sets deveoped full yield strength.

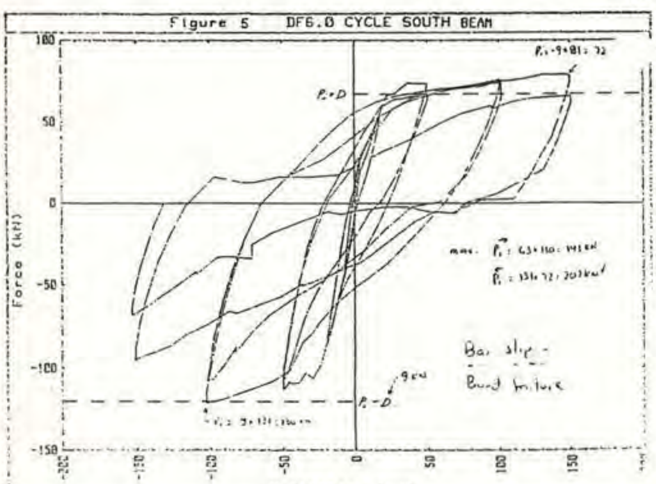

87

HIGH STRENGTH JOINT

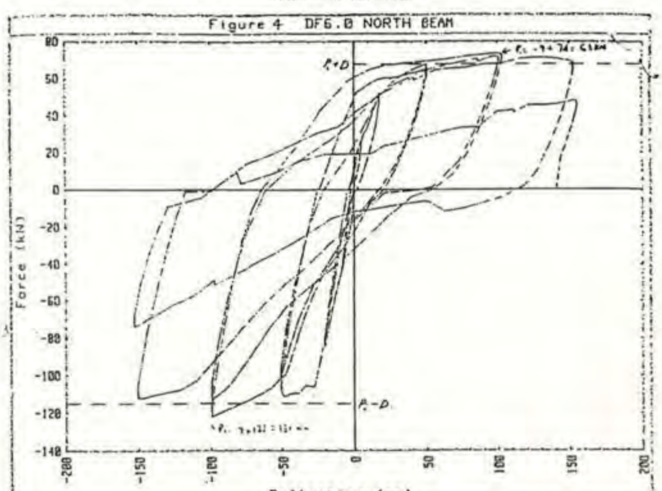

TEST: Milburn U1	Code: M1
l_b	5740 mm
l_c	3350 mm
l'_b	2667 mm
l''_b	2709 mm
l'_c	1447 mm
h_b	457 mm
b_b	229 mm
h_c	406 mm
b_c	305 mm
d^- beam	401 mm
d^+ beam	401 mm
jd^- beam	369 mm
jd^+ beam	369 mm
jd^{*-}	363 mm
jd^{*+}	363 mm
f'_c	41.3 MPa
f_y beam top bars	315.0 MPa
f_y beam bottom bars	315.0 MPa
f_y slab bars	0 MPa
f_y joint hoops	320.0 MPa
$N^*/f'_c A_g$	0.100
A_s top beam bars	1608 mm^2
A_s btm beam bars	1608 mm^2
d_b, top beam bars	16 mm
d_b, btm beam bars	16 mm
A_s slab bars	0 mm^2
A_{sh} joint	3216 mm^2

Milb_U1.xls

Theoretical Forces based on Measured Properties	
T_i^-	507 kN
T_i^+	507 kN
M_i^-	187 kN.m
M_i^+	187 kN.m
V_i^-	70 kN
V_i^+	70 kN
H_i	120.2 kN
$V_{jh,i}$	892.8 kN
V_{sh}	1029.1 kN
$(V_{sh})_{eff}$ #	900.5 kN
Joint hoops have yield plateau	yes
$v_{jh,i} / f'_c$	0.175

Measured Strentghs	
H'_o (corr. for P-δ)	128.8 kN
H_o	128.8 kN
$\lambda_o = H'_o/H_i$	1.071
λ_{jo}	1.197
$V_{jh,o}$	1069 kN
$v_{jh,o} / f'_c$	0.209
$(V_{sh})_{eff} / V_{jh,o}$	0.843
K_{pv}	1.480
$v_{jh,e} / f'_c$	0.309

Measured Drift	
Δ_y / l_c	1.06 %
Δ_c / Δ_y	0.329
μ_Δ @ failure	5.84
μ_θ @ failure	8.21
Failure Mode	joint failure

*Hysteresis loops are shown in next page

Note: # The photos show that the top and bottom sets of joint hoops were placed close to the beam bars, it was assumed that those sets developed 50% of the yield strength.

Reference: [M8]

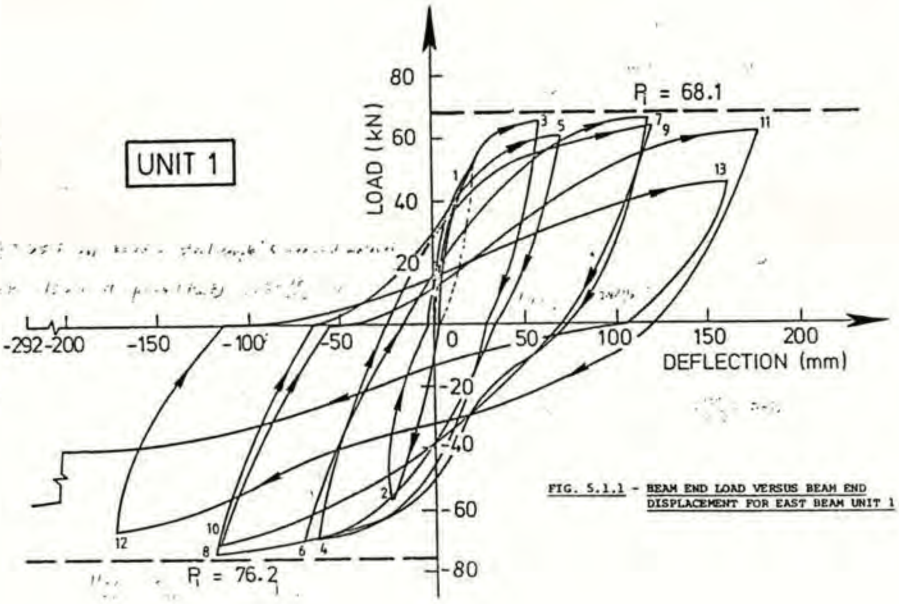

FIG. 5.1.1 - BEAM END LOAD VERSUS BEAM END DISPLACEMENT FOR EAST BEAM UNIT 1

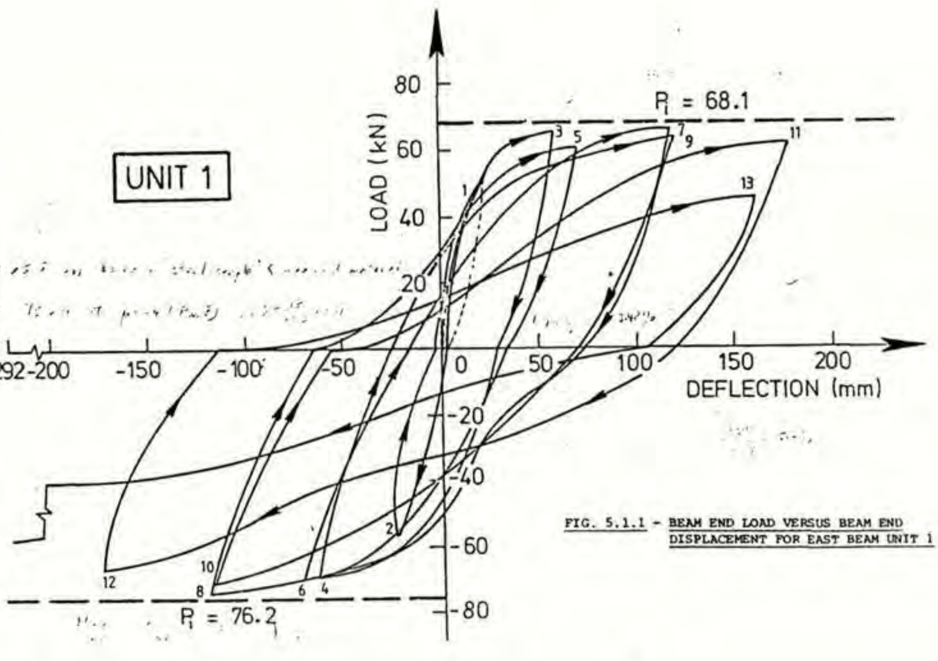
FIG. 5.1.1 - BEAM END LOAD VERSUS BEAM END DISPLACEMENT FOR EAST BEAM UNIT 1

Milburn U1 Code: M1

TEST: Meinheit and Jirsa II	Code: M2
l_b	4877 mm
l_c	3658 mm
l'_b	2210 mm
l''_b	2276 mm
l'_c	1600 mm
h_b	457 mm
b_b	279 mm
h_c	457 mm
b_c	330 mm
d^- beam	391 mm
d^+ beam	394 mm
jd^- beam	335 mm
jd^+ beam	362 mm
jd^{*-}	327 mm
jd^{*+}	327 mm
f'_c	41.8 MPa
f_y beam top bars	449.0 MPa
f_y beam bottom bars	405.5 MPa
f_y slab bars	0 MPa
f_y joint hoops	409.0 MPa
$N^*/f'_c A_g$	0.254
A_s top beam bars	2458 mm^2
A_s btm beam bars	1529 mm^2
d_b, top beam bars	32 mm
d_b, btm beam bars	25 mm
A_s slab bars	0 mm^2
A_{sh} joint	516 mm^2

Meinh_ii.xls

Theoretical Forces based on Measured Properties	
T_i^-	1104 kN
T_i^+	620 kN
M_i^-	370 kN.m
M_i^+	225 kN.m
V_i^-	167 kN
V_i^+	102 kN
H_i	179.3 kN
$V_{jh,i}$	1544.3 kN
V_{sh}	211.1 kN
$(V_{sh})_{eff}$ #	211.1 kN
Joint hoops have yield plateau	yes
$v_{jh,i} / f'_c$	0.245

Measured Strentghs	
H'_o (corr. for P-δ)	174.4 kN
H_o	174.4 kN
$\lambda_o = H'_o/H_i$	0.972
λ_{jo}	1.147
$V_{jh,o}$	1646 kN
$v_{jh,o} / f'_c$	0.261
$(V_{sh})_{eff} / V_{jh,o}$	0.128
K_{pv}	1.900
$v_{jh,e} / f'_c$	0.496

Measured Drift	
Δ_y / l_c	1.53 %
Δ_c / Δ_y	0.128
μ_Δ @ failure	2.43
μ_θ @ failure	2.64
Failure Mode	joint failure *

Note: # Levels of the sets of joint hoops are not available.
It was assumed that all two sets of joint hoops developed the full yield strength.
* Beam bars did not yield, not included in Fig. 2.9

Reference: [M9]

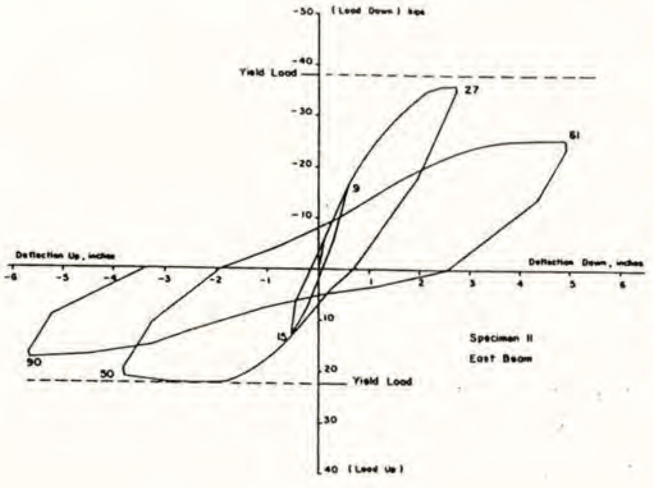

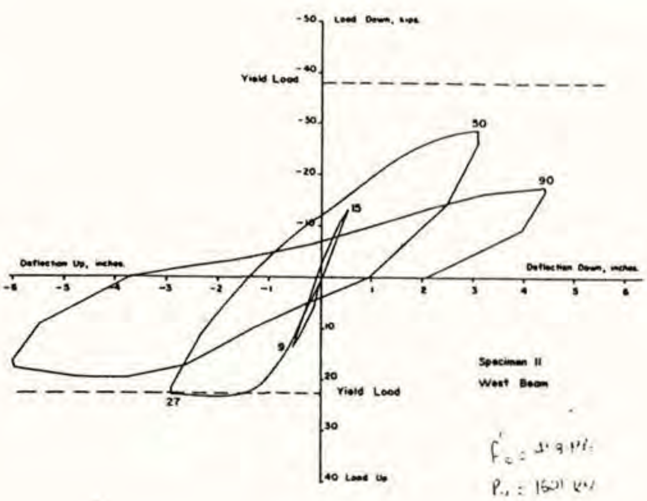

TEST: Meinheit and Jirsa VI	Code : M3
l_b	4877 mm
l_c	3658 mm
l'_b	2210 mm
l''_b	2276 mm
l'_c	1600 mm
h_b	457 mm
b_b	279 mm
h_c	457 mm
b_c	330 mm
d^- beam	391 mm
d^+ beam	394 mm
jd^- beam	327 mm
jd^+ beam	358 mm
jd^{*-}	327 mm
jd^{*+}	327 mm
f'_c	36.8 MPa
f_y beam top bars	449.0 MPa
f_y beam bottom bars	405.5 MPa
f_y slab bars	0 MPa
f_y joint hoops	409.0 MPa
$N^*/f'_c A_g$	0.483
A_s top beam bars	2458 mm^2
A_s btm beam bars	1529 mm^2
d_b, top beam bars	32 mm
d_b, btm beam bars	25 mm
A_s slab bars	0 mm^2
A_{sh} joint	516 mm^2

Meinh_vi.xls

Theoretical Forces based on Measured Properties	
T_i^-	1104 kN
T_i^+	620 kN
M_i^-	361 kN.m
M_i^+	222 kN.m
V_i^-	163 kN
V_i^+	101 kN
H_i	176.0 kN
$V_{jh,i}$	1547.6 kN
V_{sh}	211.1 kN
$(V_{sh})_{eff}$ #	211.1 kN
Joint hoops have yield plateau	yes
$v_{jh,i} / f'_c$	0.279

Measured Strenghs	
H'_o (corr. for P-δ)	180.6 kN
H_o	180.6 kN
$\lambda_o = H'_o/H_i$	1.026
λ_{jo}	1.234
$V_{jh,o}$	1705 kN
$v_{jh,o} / f'_c$	0.307
$(V_{sh})_{eff} / V_{jh,o}$	0.124
K_{pv}	3.110
$v_{jh,e} / f'_c$	0.956

Measured Drift	
Δ_y / l_c	1.46 %
Δ_c / Δ_y	0.105
μ_Δ @ failure	2.40
μ_θ @ failure	2.60
Failure Mode	joint failure

Note: # Levels of the sets of joint hoops are not available. It was assumed that all two sets of joint hoops developed the full yield strength.

Reference: [M9]

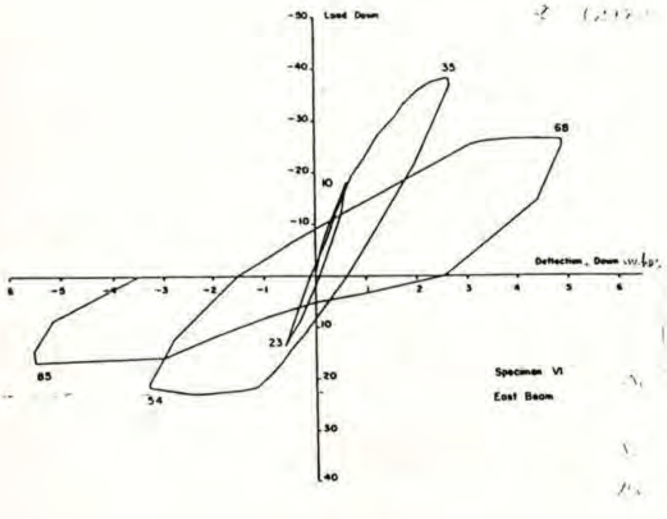

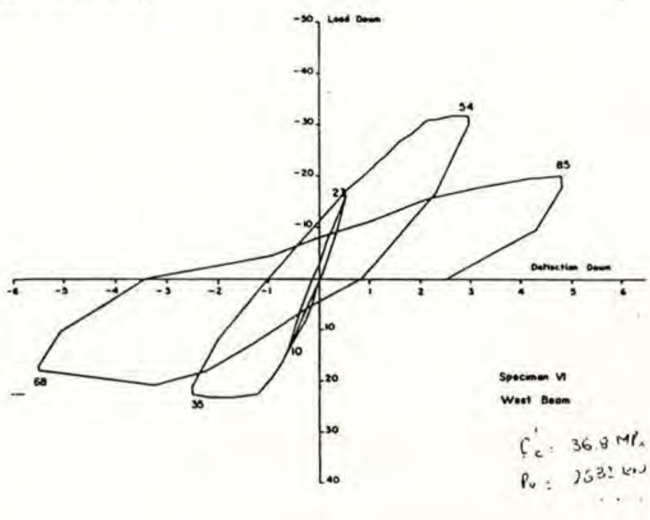

TEST: Meinheit and Jirsa XII	Code : M4
l_b	4877 mm
l_c	3658 mm
l_b'	2210 mm
l_b''	2276 mm
l_c'	1600 mm
h_b	457 mm
b_b	279 mm
h_c	457 mm
b_c	330 mm
d^- beam	391 mm
d^+ beam	394 mm
jd^- beam	325 mm
jd^+ beam	357 mm
jd^{*-}	327 mm
jd^{*+}	327 mm
f'_c	35.7 MPa
f_y beam top bars	449.0 MPa
f_y beam bottom bars	405.5 MPa
f_y slab bars	0 MPa
f_y joint hoops	422.8 MPa
$N^*/f'_c A_g$	0.300
A_s top beam bars	2458 mm^2
A_s btm beam bars	1529 mm^2
d_b, top beam bars	32 mm
d_b, btm beam bars	25 mm
A_s slab bars	0 mm^2
A_{sh} joint	2400 mm^2

Mein_xii.xls

Theoretical Forces based on Measured Properties	
T_i^-	1104 kN
T_i^+	620 kN
M_i^-	359 kN.m
M_i^+	221 kN.m
V_i^-	163 kN
V_i^+	100 kN
H_i	175.2 kN
$V_{jh,i}$	1548.4 kN
V_{sh}	1014.6 kN
$(V_{sh})_{eff}$ #	879.3 kN
Joint hoops have yield plateau	yes
$v_{jh,i} / f'_c$	0.287

Measured Strentghs	
H'_o (corr. for P-δ)	212.2 kN
H_o	212.2 kN
$\lambda_o = H'_o/H_i$	1.211
λ_{jo}	1.464
$V_{jh,o}$	2266 kN
$v_{jh,o} / f'_c$	0.420
$(V_{sh})_{eff} / V_{jh,o}$	0.388
K_{pv}	1.640
$v_{jh,e} / f'_c$	0.69

Measured Drift	
Δ_y / l_c	1.22 %
Δ_c / Δ_y	0.175
μ_Δ @ failure	3.45
μ_θ @ failure	3.90
Failure Mode	joint failure

Note: # Levels of the sets of joint hoops are not available. It was assumed that top and bottom sets of joint hoops developed 60% of the yield strength.

Reference: [M9]

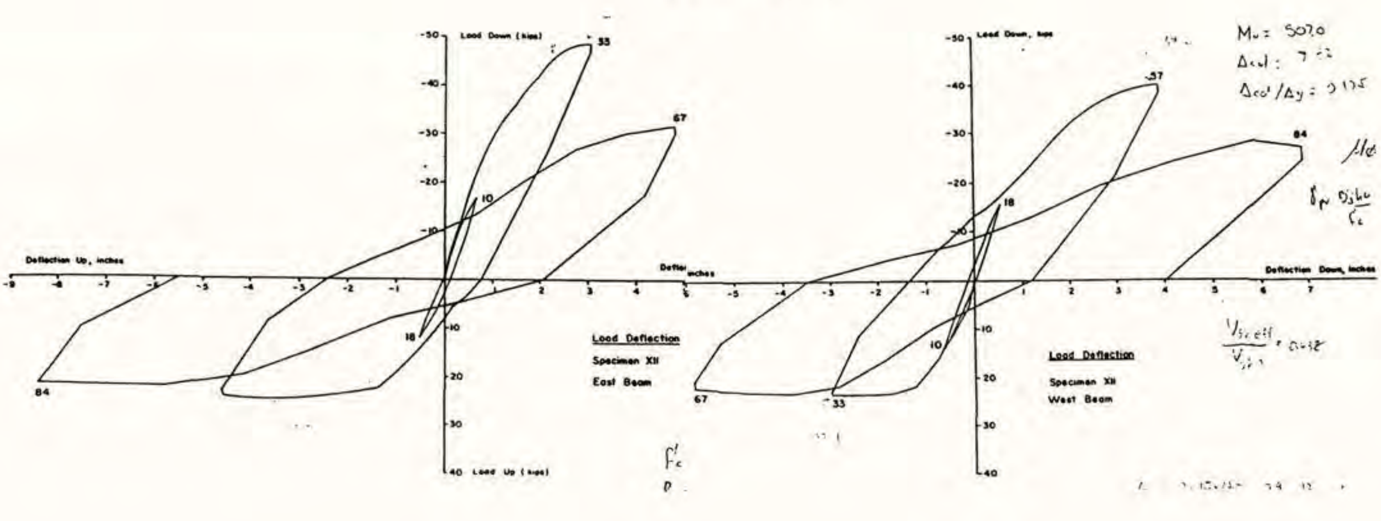

TEST: Otani, Kobayashi & Aoyama J1 Code: O1	
l_b	2700 mm
l_c	1470 mm
l'_b	1200 mm
l''_b	1230 mm
l'_c	585 mm
h_b	300 mm
b_b	200 mm
h_c	300 mm
b_c	300 mm
d^- beam	255 mm
d^+ beam	270 mm
jd^- beam	206 mm
jd^+ beam	246 mm
jd^{*-}	225 mm
jd^{*+}	240 mm
f'_c	25.7 MPa
f_y beam top bars	400.8 MPa
f_y beam bottom bars	400.8 MPa
f_y slab bars	0 MPa
f_y joint hoops	367.5 MPa
$N^*/f'_c A_g$	0.077
A_s top beam bars	1061 mm2
A_s btm beam bars	531 mm2
d_b, top beam bars	13 mm
d_b, btm beam bars	13 mm
A_s slab bars	0 mm2
A_{sh} joint	170 mm2

Otani_j1.xls

Theoretical Forces based on Measured Properties	
T_i^-	425 kN
T_i^+	213 kN
M_i^-	88 kN.m
M_i^+	52 kN.m
V_i^-	73 kN
V_i^+	44 kN
H_i	107.2 kN
$V_{jh,i}$	530.9 kN
V_{sh}	62.4 kN
$(V_{sh})_{eff}$ #	54.1 kN
Joint hoops have yield plateau	no
$v_{jh,i} / f'_c$	0.230

Measured Strentghs	
H'_o (corr. for P-δ)	120.9 kN
H_o	113.1 kN
$\lambda_o = H'_o/H_i$	1.128
λ_{jo}	1.099
$V_{jh,o}$	583.3 kN
$v_{jh,o} / f'_c$	0.252
$(V_{sh})_{eff} / V_{jh,o}$	0.093
K_{pv}	2.710
$v_{jh,e} / f'_c$	0.68

Measured Drift	
Δ_y / l_c	1.18 %
Δ_c / Δ_y	0.09
μ_Δ @ failure	5.20
μ_θ @ failure	5.60
Failure Mode	joint failure

Note: # The available drawing show that the top set of joint hoops was placed close to the top beam bars, it was assumed that the top set developed 60% of the yield strength.

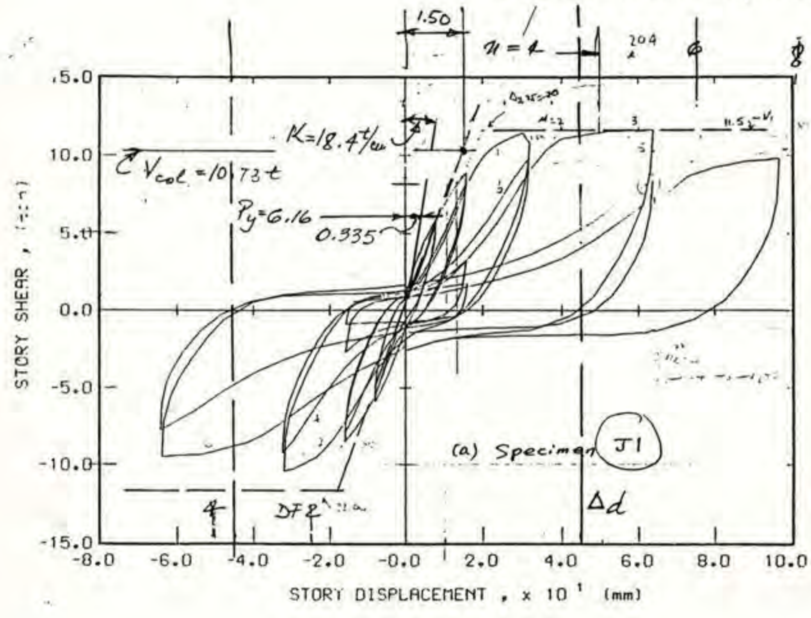

TEST: Otani, Kobayashi & Aoyama J2 Code: O2	
l_b	2700 mm
l_c	1470 mm
l'_b	1200 mm
l^*_b	1230 mm
l'_c	585 mm
h_b	300 mm
b_b	200 mm
h_c	300 mm
b_c	300 mm
d^- beam	255 mm
d^+ beam	270 mm
jd^- beam	203 mm
jd^+ beam	244 mm
jd^{*-}	225 mm
jd^{*+}	240 mm
f'_c	24.0 MPa
f_y beam top bars	400.8 MPa
f_y beam bottom bars	400.8 MPa
f_y slab bars	0 MPa
f_y joint hoops	367.5 MPa
$N^*/f'_c A_g$	0.082
A_s top beam bars	1061 mm2
A_s btm beam bars	531 mm2
d_b, top beam bars	13 mm
d_b, btm beam bars	13 mm
A_s slab bars	0 mm2
A_{sh} joint	340 mm2

Otani_j2.xls

Theoretical Forces based on Measured Properties	
T_i^-	425 kN
T_i^+	213 kN
M_i^-	86 kN.m
M_i^+	52 kN.m
V_i^-	72 kN
V_i^+	43 kN
H_i	105.8 kN
$V_{jh,i}$	532.3 kN
V_{sh}	124.8 kN
$(V_{sh})_{eff}$ #	108.2 kN
Joint hoops have yield plateau	no
$v_{jh,i} / f'_c$	0.246

Measured Strentghs	
H'_o (corr. for P-δ)	122.4 kN
H_o	118.2 kN
$\lambda_o = H'_o/H_i$	1.157
λ_{jo}	1.103
$V_{jh,o}$	586.9 kN
$v_{jh,o} / f'_c$	0.272
$(V_{sh})_{eff} / V_{jh,o}$	0.184
K_{pv}	2.660
$v_{jh,e} / f'_c$	0.72

Measured Drift	
Δ_y / l_c	1.13 %
Δ_c / Δ_y	0.18
μ_Δ @ failure	5.00
μ_θ @ failure	5.90
Failure Mode	joint failure

Note: # The available drawing show that the top set of joint hoops was placed close to the top beam bars, it was assumed that the top set developed 60% of the yield strength.

Reference: [O1]

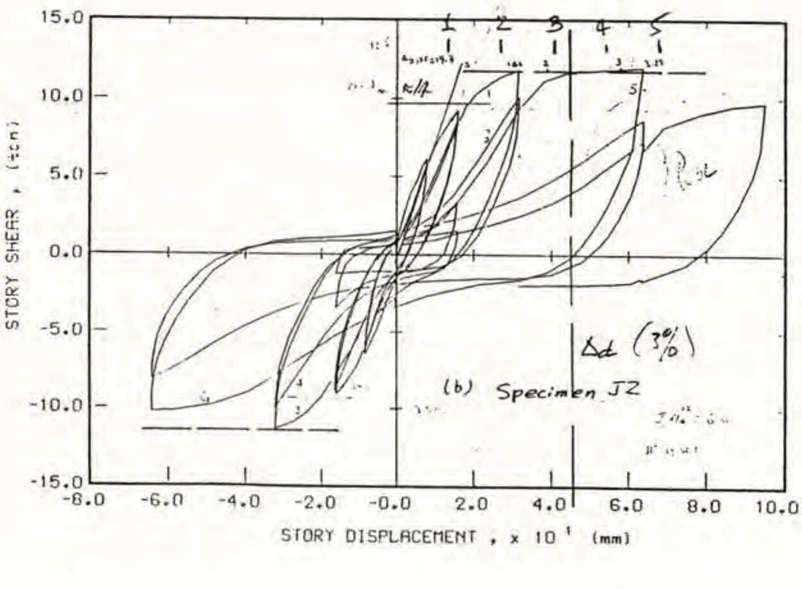

TEST: Otani, Kobayashi & Aoyama J3 Code:O3	
l_b	2700 mm
l_c	1470 mm
l'_b	1200 mm
l''_b	1230 mm
l'_c	585 mm
h_b	300 mm
b_b	200 mm
h_c	300 mm
b_c	300 mm
d^- beam	255 mm
d^+ beam	270 mm
jd^- beam	203 mm
jd^+ beam	244 mm
jd^{*-}	225 mm
jd^{*+}	240 mm
f'_c	24.0 MPa
f_y beam top bars	400.8 MPa
f_y beam bottom bars	400.8 MPa
f_y slab bars	0 MPa
f_y joint hoops	367.5 MPa
$N^*/f'_c A_g$	0.082
A_s top beam bars	1061 mm^2
A_s btm beam bars	531 mm^2
d_b, top beam bars	13 mm
d_b, btm beam bars	13 mm
A_s slab bars	0 mm^2
A_{sh} joint	792 mm^2

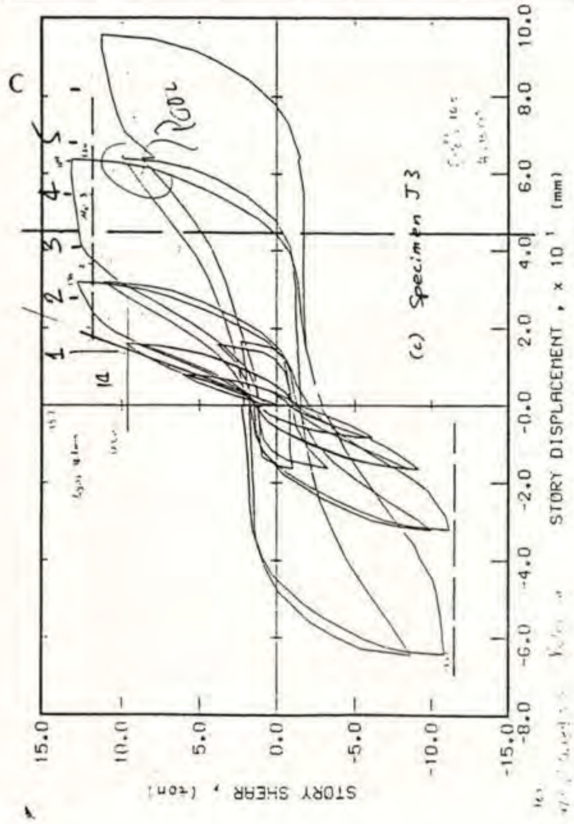

Theoretical Forces based on Measured Properties	
T_i^-	425 kN
T_i^+	213 kN
M_i^-	86 kN.m
M_i^+	52 kN.m
V_i^-	72 kN
V_i^+	43 kN
H_i	105.8 kN
$V_{jh,i}$	532.3 kN
V_{sh}	291.2 kN
$(V_{sh})_{eff}$ #	266.2 kN
Joint hoops have yield plateau	no
$v_{jh,i} / f'_c$	0.246

Measured Strengths	
H'_o (corr. for P-δ)	134.7 kN
H_o	130.0 kN
$\lambda_o = H'_o/H_i$	1.274
λ_{jo}	1.213
$V_{jh,o}$	645.9 kN
$v_{jh,o} / f'_c$	0.299
$(V_{sh})_{eff} / V_{jh,o}$	0.412
K_{pv}	2.410
$v_{jh,e} / f'_c$	0.72

Measured Drift	
Δ_y / l_c	1.08 %
Δ_c / Δ_y	0.187
μ_Δ @ failure	5.34
μ_θ @ failure	6.34
Failure Mode	joint failure

Note: # Levels of the joint hoops in the joint region are not available. Based on the available drawings, it was assumed that the top and bottom sets of the joint hoops developed 70% of the yield strength.

Reference: [O1]

TEST: Otani, Kobayashi & Aoyama J4 Code: O4	
l_b	2700 mm
l_c	1470 mm
l'_b	1200 mm
l^*_b	1230 mm
l'_c	585 mm
h_b	300 mm
b_b	200 mm
h_c	300 mm
b_c	300 mm
d^- beam	255 mm
d^+ beam	270 mm
jd^- beam	206 mm
jd^+ beam	246 mm
jd^{*-}	225 mm
jd^{*+}	240 mm
f'_c	25.7 MPa
f_y beam top bars	400.8 MPa
f_y beam bottom bars	400.8 MPa
f_y slab bars	0 MPa
f_y joint hoops	367.5 MPa
$N^*/f'_c A_g$	0.305
A_s top beam bars	1061 mm^2
A_s btm beam bars	531 mm^2
d_b, top beam bars	13 mm
d_b, btm beam bars	13 mm
A_s slab bars	0 mm^2
A_{sh} joint	170 mm^2

Theoretical Forces based on Measured Properties	
T_i^-	425 kN
T_i^+	213 kN
M_i^-	88 kN.m
M_i^+	52 kN.m
V_i^-	73 kN
V_i^+	44 kN
H_i	107.2 kN
$V_{jh,i}$	530.9 kN
V_{sh}	62.3 kN
$(V_{sh})_{eff}$ #	51.9 kN
Joint hoops have yield plateau	no
$v_{jh,i} / f'_c$	0.230

Measured Strengths	
H'_o (corr. for P-d)	130.4 kN
H_o	115.9 kN
$\lambda_o = H'_o/H_i$	1.217
λ_{jo}	1.197
$V_{jh,o}$	635.3 kN
$v_{jh,o} / f'_c$	0.275
$(V_{sh})_{eff} / V_{jh,o}$	0.082
K_{pv}	1.960
$v_{jh,e} / f'_c$	0.538

Measured Drift	
Δ_y / l_c	0.81 %
Δ_c / Δ_y	0.092
μ_Δ @ failure	7.06
μ_θ @ failure	7.67
Failure Mode	joint failure

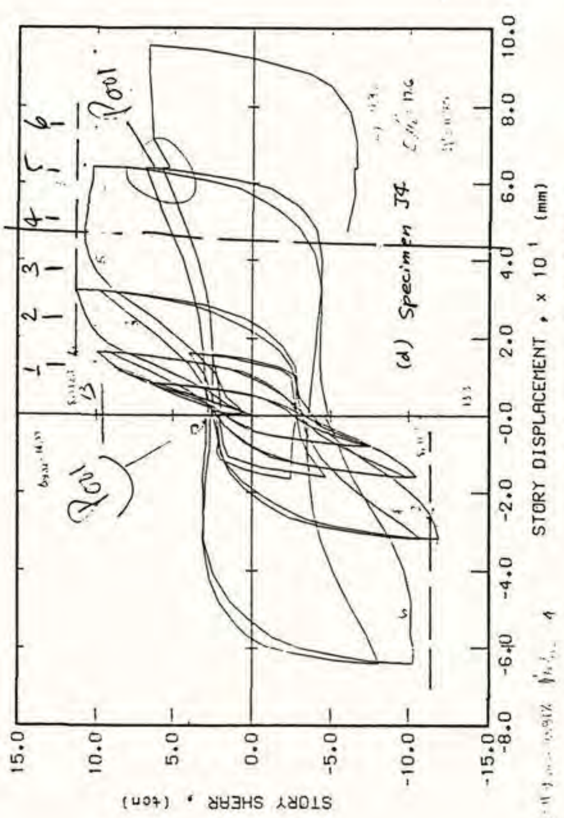

Note: # The available drawing show that the top set of joint hoops was placed close to the top beam bars, it was assumed that the top set developed 60% of the yield strength.

Reference: [O1]

TEST: Otani, Kobayashi & Aoyama J6 Code: O5	
l_b	2700 mm
l_c	1470 mm
l'_b	1200 mm
l^*_b	1230 mm
l'_c	585 mm
h_b	300 mm
b_b	200 mm
h_c	300 mm
b_c	300 mm
d^- beam	270 mm
d^+ beam	270 mm
jd^- beam	248 mm
jd^+ beam	254 mm
jd^{*-}	240 mm
jd^{*+}	240 mm
f'_c	28.7 MPa
f_y beam top bars	400.8 MPa
f_y beam bottom bars	400.8 MPa
f_y slab bars	0 MPa
f_y joint hoops	367.5 MPa
$N^*/f'_c A_g$	0.205
A_s top beam bars	531 mm2
A_s btm beam bars	398 mm2
d_b, top beam bars	13 mm
d_b, btm beam bars	13 mm
A_s slab bars	0 mm2
A_{sh} joint	283 mm2

Theoretical Forces based on Measured Properties	
T_i^-	213 kN
T_i^+	160 kN
M_i^-	53 kN.m
M_i^+	40 kN.m
V_i^-	44 kN
V_i^+	34 kN
H_i	71.4 kN
$V_{jh,i}$	300.9 kN
V_{sh}	104.0 kN
$(V_{sh})_{eff}$ #	83.2 kN
Joint hoops have yield plateau	no
$v_{jh,i} / f'_c$	0.117

Measured Strentghs	
H'_o (corr. for P-δ)	91.1 kN
H_o	70.9 kN
$\lambda_o = H'_o/H_i$	1.276
λ_{jo}	1.454
$V_{jh,o}$	437.5 kN
$v_{jh,o} / f'_c$	0.169
$(V_{sh})_{eff} / V_{jh,o}$	0.190
K_{pv}	2.070
$v_{jh,e} / f'_c$	0.351

Measured Drift	
Δ_y / l_c	0.66 %
Δ_c / Δ_y	0.06
μ_Δ @ failure	6.60
μ_θ @ failure	7.00
Failure Mode	bond failure

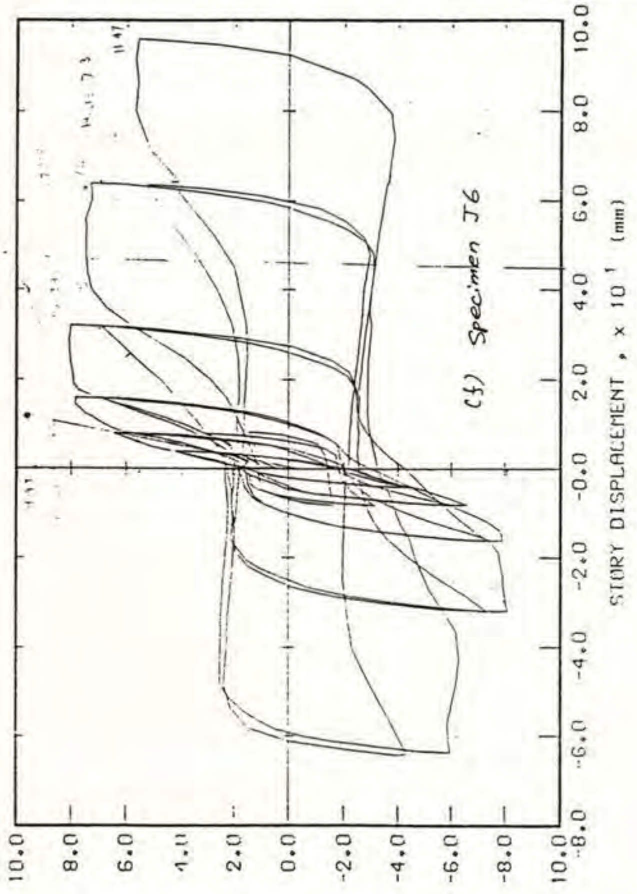

Note: # Details of levels of the joint hoops are not available, it was assumed that the top and bottom sets developed 50% of the yield strength.

Reference: [O1]

TEST: Otani, Kitayama & Aoyama C1	Code: O6
l_b	2700 mm
l_c	1470 mm
l'_b	1200 mm
l^*_b	1230 mm
l'_c	585 mm
h_b	300 mm
b_b	200 mm
h_c	300 mm
b_c	300 mm
d^- beam	255 mm
d^+ beam	270 mm
jd^- beam	224 mm
jd^+ beam	254 mm
jd^{*-}	240 mm
jd^{*+}	240 mm
f'_c	25.6 MPa
f_y beam top bars	319.8 MPa
f_y beam bottom bars	319.8 MPa
f_y slab bars	0 MPa
f_y joint hoops	323.7 MPa
$N^*/f'_c A_g$	0.077
A_s top beam bars	856 mm^2
A_s btm beam bars	428 mm^2
d_b, top beam bars	10 mm
d_b, btm beam bars	10 mm
A_s slab bars	0 mm^2
A_{sh} joint	190 mm^2

otani_c1.xls

Theoretical Forces based on Measured Properties	
T_i^-	274 kN
T_i^+	137 kN
M_i^-	61 kN.m
M_i^+	35 kN.m
V_i^-	51 kN
V_i^+	29 kN
H_i	73.5 kN
$V_{jh,i}$	337.2 kN
V_{sh}	61.5 kN
$(V_{sh})_{eff}$ #	53.3 kN
Joint hoops have yield plateau	no
$v_{jh,i} / f'_c$	0.146

Measured Strenghs	
H'_o (corr. for P-δ)	98.1 kN
H_o	87.5 kN
$\lambda_o = H'_o/H_i$	1.335
λ_{jo}	1.364
$V_{jh,o}$	460.0 kN
$v_{jh,o} / f'_c$	0.200
$(V_{sh})_{eff} / V_{jh,o}$	0.116
K_{pv}	2.710
$v_{jh,e} / f'_c$	0.541

Measured Drift	
Δ_y / l_c	0.735 %
Δ_c / Δ_y	0.165
μ_Δ @ failure	8.15
μ_θ @ failure	9.56
Failure Mode	beam hinging

Note: # The available drawing show that the top set of joint hoops was placed close to the top beam bars,
it was assumed that the top set developed 60% of the yield strength.

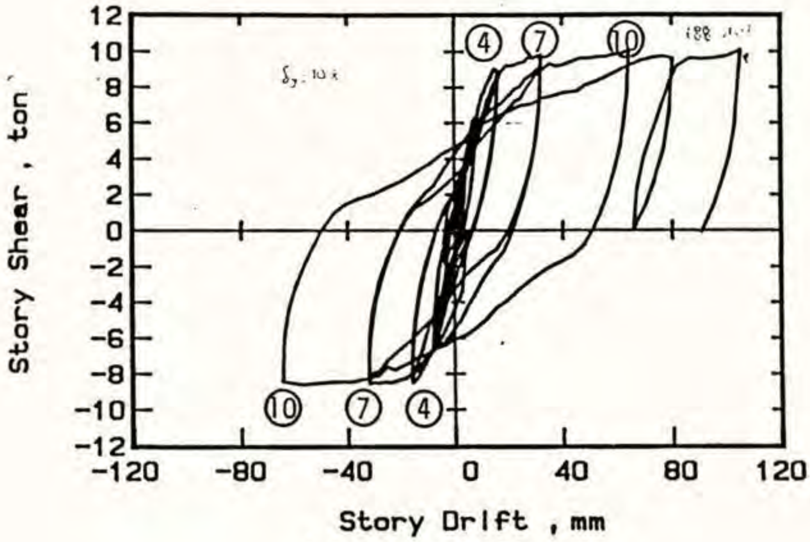

(a) Specimen C1

TEST: Otani, Kitayama & Aoyama C2 Code: O7	
l_b	2700 mm
l_c	1470 mm
l'_b	1200 mm
l^*_b	1230 mm
l'_c	585 mm
h_b	300 mm
b_b	200 mm
h_c	300 mm
b_c	300 mm
d^- beam	255 mm
d^+ beam	270 mm
jd^- beam	224 mm
jd^+ beam	254 mm
jd^{*-}	240 mm
jd^{*+}	240 mm
f'_c	25.6 MPa
f_y beam top bars	319.8 MPa
f_y beam bottom bars	319.8 MPa
f_y slab bars	0 MPa
f_y joint hoops	323.7 MPa
$N^*/f'_c A_g$	0.077
A_s top beam bars	856 mm^2
A_s btm beam bars	428 mm^2
d_b, top beam bars	10 mm
d_b, btm beam bars	10 mm
A_s slab bars	0 mm^2
A_{sh} joint	633 mm^2

Otani_c2.xls

Theoretical Forces based on Measured Properties	
T_i^-	274 kN
T_i^+	137 kN
M_i^-	61 kN.m
M_i^+	35 kN.m
V_i^-	51 kN
V_i^+	29 kN
H_i	73.5 kN
$V_{jh,i}$	337.2 kN
V_{sh}	204.9 kN
$(V_{sh})_{eff}$ #	172.2 kN
Joint hoops have yield plateau	no
$v_{jh,i} / f'_c$	0.146

Measured Strengths	
H'_o (corr. for P-δ)	100.1 kN
H_o	89.4 kN
$\lambda_o = H'_o/H_i$	1.362
λ_{jo}	1.391
$V_{jh,o}$	469.0 kN
$v_{jh,o} / f'_c$	0.204
$(V_{sh})_{eff} / V_{jh,o}$	0.367
K_{pv}	2.440
$v_{jh,e} / f'_c$	0.497

Measured Drift	
Δ_y / l_c	0.816 %
Δ_c / Δ_y	0.148
μ_Δ @ failure	7.33
μ_θ @ failure	8.43
Failure Mode	beam hinging

Note: # The available drawing show that the top & bottom sets of joint hoops were placed close to the beam bars, it was assumed that those sets developed 60% of the yield strength.

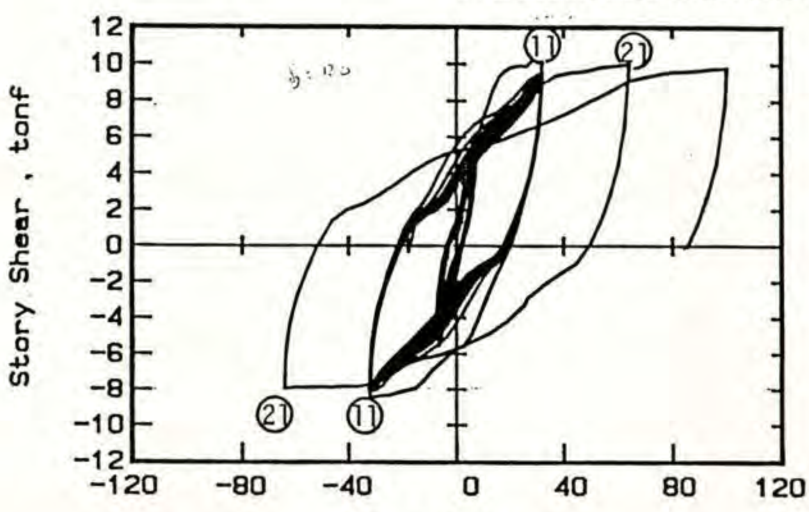

(b) Specimen C2

TEST: Otani, Kitayama & Aoyama C3	Code: O8
l_b	2700 mm
l_c	1470 mm
l'_b	1200 mm
l^*_b	1230 mm
l'_c	585 mm
h_b	300 mm
b_b	200 mm
h_c	300 mm
b_c	300 mm
d^- beam	255 mm
d^+ beam	270 mm
jd^- beam	224 mm
jd^+ beam	254 mm
jd^{*-}	240 mm
jd^{*+}	240 mm
f'_c	25.6 MPa
f_y beam top bars	319.8 MPa
f_y beam bottom bars	319.8 MPa
f_y slab bars	0 MPa
f_y joint hoops	323.7 MPa
$N^*/f'_c A_g$	0.077
A_s top beam bars	856 mm^2
A_s btm beam bars	428 mm^2
d_b, top beam bars	10 mm
d_b, btm beam bars	10 mm
A_s slab bars	0 mm^2
A_{sh} joint	1426 mm^2

Theoretical Forces based on Measured Properties	
T_i^-	274 kN
T_i^+	137 kN
M_i^-	61 kN.m
M_i^+	35 kN.m
V_i^-	51 kN
V_i^+	29 kN
H_i	73.5 kN
$V_{jh,i}$	337.2 kN
V_{sh}	461.6 kN
$(V_{sh})_{eff}$ #	387.7 kN
Joint hoops have yield plateau	yes
$v_{jh,i} / f'_c$	0.146

Measured Strenghs	
H'_o (corr. for P-δ)	98.1 kN
H_o	90.4 kN
$\lambda_o = H'_o/H_i$	1.335
λ_{jo}	1.356
$V_{jh,o}$	457.1 kN
$v_{jh,o} / f'_c$	0.198
$(V_{sh})_{eff} / V_{jh,o}$	0.848
K_{pv}	1.480
$v_{jh,e} / f'_c$	0.294

Measured Drift	
Δ_y / l_c	0.735 %
Δ_c / Δ_y	0.165
μ_Δ @ failure	8.15
μ_θ @ failure	9.56
Failure Mode	beam hinging

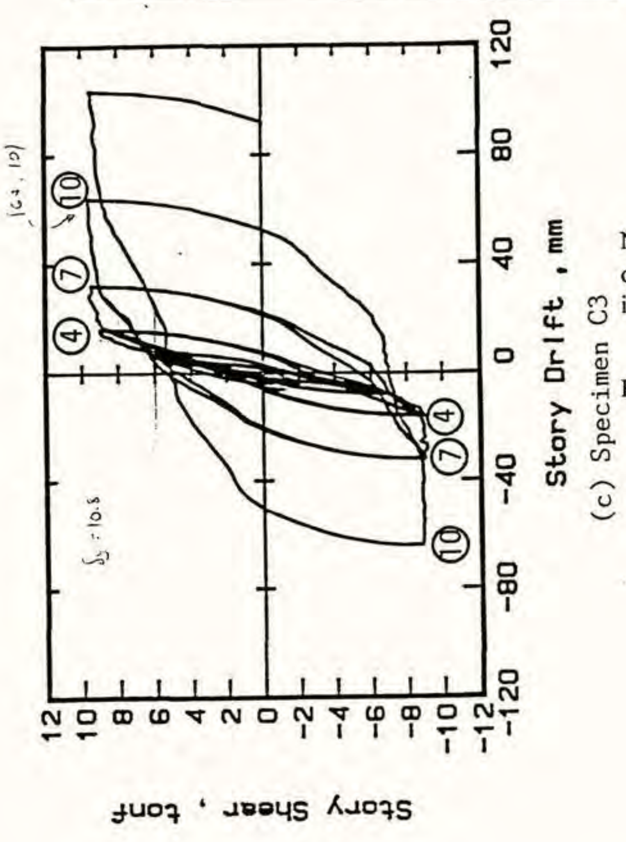

Note: # The available drawing show that the top & bottom sets of joint hoops were placed close to the beam bars, it was assumed that those sets developed 60% of the yield strength.

Reference: [O2]

TEST: Priestley IBC	Code: P1
l_b	8216 mm
l_c	3345 mm
l'_b	3460 mm
l''_b	3535 mm
l'_c	1228 mm
h_b	889 mm
b_b	457 mm
h_c	686 mm
b_c	686 mm
d^- beam	785 mm
d^+ beam	809 mm
jd^- beam	643 mm
jd^+ beam	546 mm
jd^{*-}	705 mm
jd^{*+}	705 mm
f'_c	48.5 MPa
f_y beam top bars	276.0 MPa
f_y beam bottom bars	276.0 MPa
f_y slab bars	0 MPa
f_y joint hoops	297.0 MPa
$N^*/f'_c A_g$	0.030
A_s top beam bars	4226 mm^2
A_s bottom beam bars	2570 mm^2
d_b, top beam bars	28.6+25. mm
d_b, bottom beam bars	28.6 mm
A_s slab bars	0 mm^2
A_{sh} joint	11461.0 mm^2

Theoretical Forces based on Measured Properties	
T_i^-	1304 kN
T_i^+	1128 kN
$M_i^{-\&}$	974 kN.m
$M_i^{+\&}$	618 kN.m
V_i^-	282 kN
V_i^+	152 kN
H_i	506.5 kN
$V_{jh,i}$	1389.5 kN
V_{sh}	3403.9 kN
$(V_{sh})_{eff}$ #	3063.5 kN
Joint hoops have yield plateau	yes
$v_{jh,i} / f'_c$	0.061

Measured Strentghs	
H'_o (corr. for P-δ)	592.7 kN
H_o	592.7 kN
$\lambda_o = H'_o/H_i$	1.170
λ_{jo}	1.319
$V_{jh,o}$	1832.3 kN
$v_{jh,o} / f'_c$	0.080
$(V_{sh})_{eff} / V_{jh,o}$	1.000
K_{pv}	1.000
$v_{jh,e} / f'_c$	0.080

Measured Drift	
Δ_y / l_c	0.31 %
Δ_c / Δ_y	0.33
μ_Δ @ failure	8.00
μ_θ @ failure	11.45
Failure Mode	no failure

Priest_ibc.xls

*Hysteresis Loops are shown in next page

Note: & Calculated using "Response" programe.
2 D15.9 bars (f_y=295MPa) which were placed in the middle of the the beam web were counted as calculating M^+ and M^-
The available drawing show that the top and bottom sets of joint hoops was placed close to the beam bars, it was assumed the top and bottom sets developed 50% of the yield strength.

Reference: [P12]

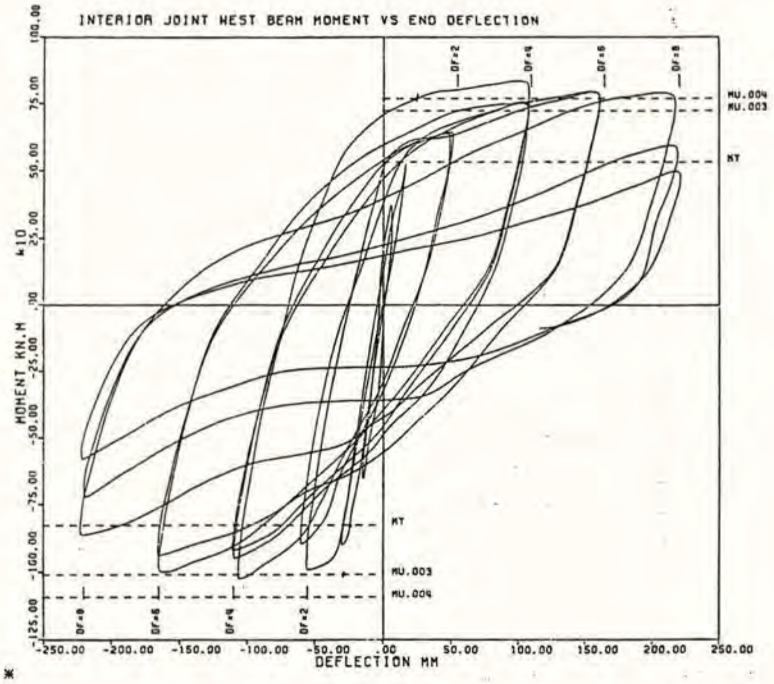

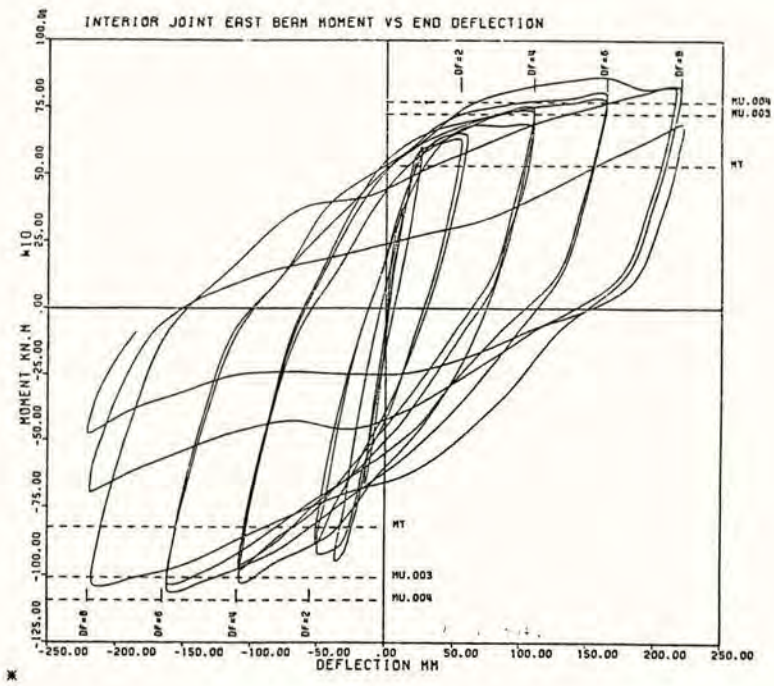

Priestley IBC Code : P1

TEST: Restrepo U6	Code: R1
l_b	3810 mm
l_c	2800 mm
l'_b	1605 mm
l''_b	1678 mm
l'_c	1050 mm
h_b	700 mm
b_b	300 mm
h_c	600 mm
b_c	450 mm
d^- beam	645 mm
d^+ beam	645 mm
jd^- beam	622 mm
jd^+ beam	622 mm
jd^{*-}	590 mm
jd^{*+}	590 mm
f'_c	44.0 MPa
f_y beam top bars	285.0 MPa
f_y beam bottom bars	285.0 MPa
f_y slab bars	0 MPa
f_y joint hoops	298.0 MPa
$N^*/f'_c A_g$	0.000
A_s top beam bars	1808 mm^2
A_s btm beam bars	1808 mm^2
d_b, top beam bars	24 mm
d_b, btm beam bars	24 mm
A_s slab bars	0 mm^2
A_{sh} joint	3216 mm^2

Rest_u6.xls

Theoretical Forces based on Measured Properties	
T_i^-	515 kN
T_i^+	515 kN
M_i^-	321 kN.m
M_i^+	321 kN.m
V_i^-	200 kN
V_i^+	200 kN
H_i	271.7 kN
$V_{jh,i}$	758.8 kN
V_{sh}	958.4 kN
$(V_{sh})_{eff}$	958.4 kN
Joint hoops have yield plateau	yes
$v_{jh,i} / f'_c$	0.064

Measured Strentghs	
H'_o (corr. for P-δ)	336.0 kN
H_o	336.0 kN
$\lambda_o = H'_o/H_i$	1.236
λ_{jo}	1.408
$V_{jh,o}$	1069 kN
$v_{jh,o} / f'_c$	0.090
$(V_{sh})_{eff} / V_{jh,o}$	0.897
K_{pv}	1.320
$v_{jh,e} / f'_c$	0.119

Measured Drift	
Δ_y / l_c	0.49 %
Δ_c / Δ_y	0.47
μ_Δ @ failure	7.30
μ_θ @ failure	12.86
Failure Mode	Beam Hinging

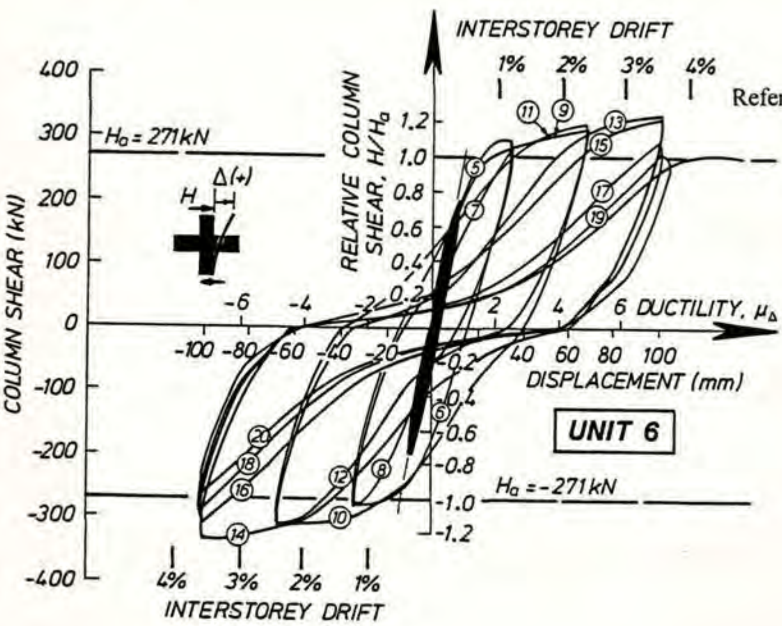

Reference : [R1]

TEST: Stevenson U1	Code: S1
l_b	5740 mm
l_c	3350 mm
l'_b	2667 mm
l''_b	2707 mm
l'_c	1446.5 mm
h_b	457 mm
b_b	229 mm
h_c	406 mm
b_c	305 mm
d^- beam	401 mm
d^+ beam	401 mm
jd^- beam	374 mm
jd^+ beam	374 mm
jd^{*-}	345 mm
jd^{*+}	345 mm
f'_c	34.0 MPa
f_y beam top bars	337.8 MPa
f_y beam bottom bars	337.8 MPa
f_y slab bars	0 MPa
f_y joint hoops	305.4 MPa
$N^*/f'_c A_g$	0.237
A_s top beam bars	1608 mm^2
A_s btm beam bars	1608 mm^2
d_b, top beam bars	16 mm
d_b, btm beam bars	16 mm
A_s slab bars	0 mm^2
A_{sh} joint	1206 mm^2

Stev_u1.xls

Theoretical Forces based on Measured Properties	
T_i^-	543 kN
T_i^+	543 kN
M_i^-	203 kN.m
M_i^+	203 kN.m
V_i^-	76 kN
V_i^+	76 kN
H_i	130.5 kN
$V_{jh,i}$	955.8 kN
V_{sh}	368.3 kN
$(V_{sh})_{eff}$ #	368.3 kN
Joint hoops have yield plateau	yes
$v_{jh,i} / f'_c$	0.227

Measured Strentghs	
H'_o (corr. for P-δ)	130.4 kN
H_o	130.4 kN
$\lambda_o = H'_o/H_i$	0.999
λ_{jo}	1.113
$V_{jh,o}$	1064 kN
$v_{jh,o} / f'_c$	0.253
$(V_{sh})_{eff} / V_{jh,o}$	0.346
K_{pv}	1.750
$v_{jh,e} / f'_c$	0.442

Measured Drift	
Δ_y / l_c	1.04 %
Δ_c / Δ_y	0.147
μ_Δ @ failure	4.20
μ_θ @ failure	4.75
Failure Mode	Joint failure

Note: # The top and bottom sets of joint hoops were placed between the first and second layers of beam bars. They are deemed not effective in resisting the joint shear. Thus, those two sets were neglected when counting $(V_{sh})_{eff}$. The yield strength of the inner three sets were fully counted.

52

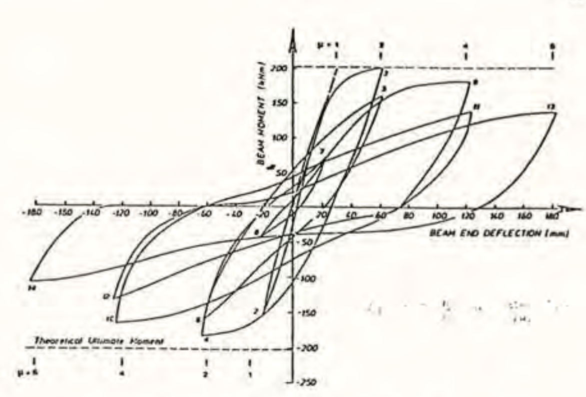

Fig. 5.1 - Unit 1 Beam Moment at Column Face Versus Right Beam End Deflection

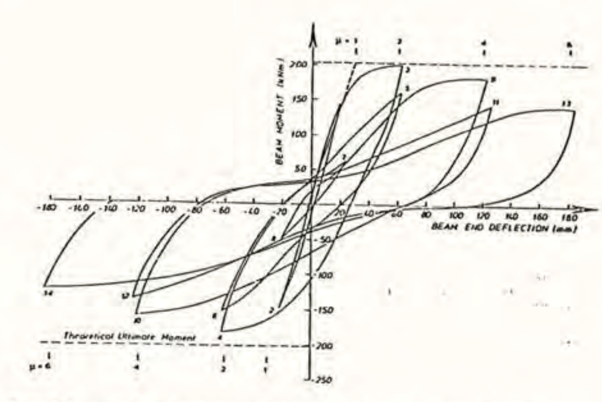

Fig. 5.2 - Unit 1 Beam Moment at Column Face Versus Left Beam End Deflection

TEST: Teraoka et al. HNO1	Code: T1
l_b	2800 mm
l_c	1800 mm
l'_b	1200 mm
l''_b	1245 mm
l'_c	700 mm
h_b	400 mm
b_b	300 mm
h_c	400 mm
b_c	400 mm
d^- beam	325 mm
d^+ beam	325 mm
jd^- beam	297 mm
jd^+ beam	297 mm
jd^{*-}	250 mm
jd^{*+}	250 mm
f'_c	88.2 MPa
f_y beam top bars	610.5 MPa
f_y beam bottom bars	610.5 MPa
f_y slab bars	0 MPa
f_y joint hoops	680.0 MPa
$N^*/f'_c A_g$	0.167
A_s top beam bars	1609 mm^2
A_s btm beam bars	1609 mm^2
d_b, top beam bars	16 mm
d_b, btm beam bars	16 mm
A_s slab bars	0 mm^2
A_{sh} joint	1030 mm^2

Theoretical Forces based on Measured Properties	
T_i^-	982 kN
T_i^+	982 kN
M_i^-	292 kN.m
M_i^+	292 kN.m
V_i^-	243 kN
V_i^+	243 kN
H_i	378.4 kN
$V_{jh,i}$	1586.0 kN
V_{sh}	700.7 kN
$(V_{sh})_{eff}$ #	583.9 kN
Joint hoops have yield plateau	no
$v_{jh,i} / f'_c$	0.112

Measured Strentghs	
H'_o (corr. for P-δ)	450.0 kN
H_o	450.0 kN
$\lambda_o = H'_o/H_i$	1.189
λ_{jo}	1.533
$V_{jh,o}$	2431 kN
$v_{jh,o} / f'_c$	0.172
$(V_{sh})_{eff} / V_{jh,o}$	0.240
K_{pv}	2.090
$v_{jh,e} / f'_c$	0.360

Measured Drift	
Δ_y / l_c	0.63 %
Δ_c / Δ_y	0.44
μ_Δ @ failure	8.90
μ_θ @ failure	9.30
Failure Mode	joint failure

Tera_hno1.xls

Note : # The available drawings showed that the top and bottom sets of the joint hoops were placed close to the beam bars. It was thus assumed that those sets developed 50% of the yield strength.

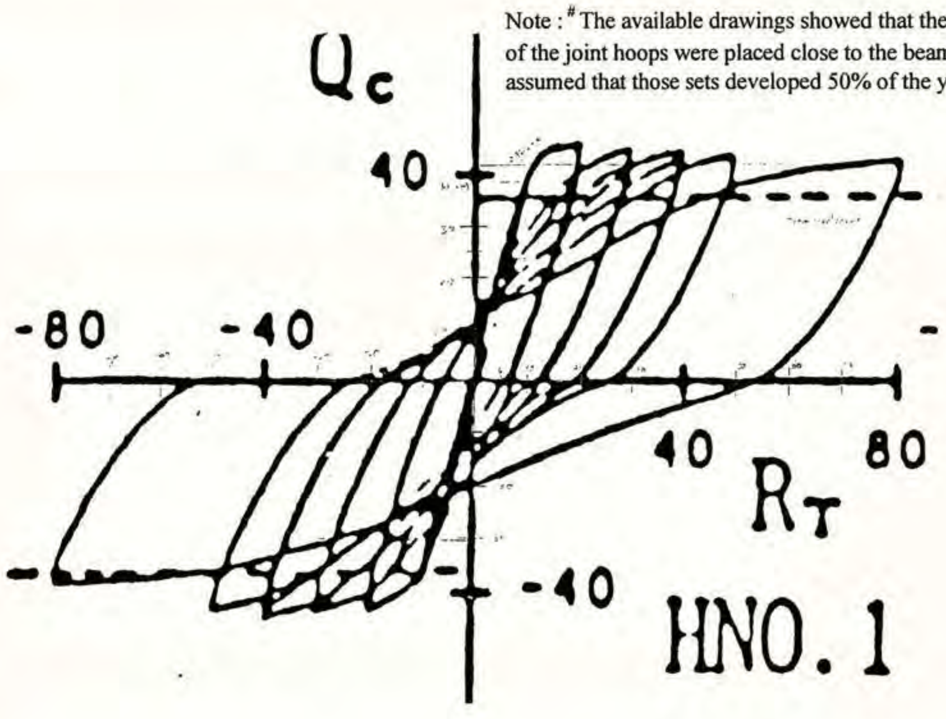

TEST: Teraoka et al. HNO3	Code: T2
l_b	2800 mm
l_c	1800 mm
l'_b	1200 mm
l''_b	1245 mm
l'_c	700 mm
h_b	400 mm
b_b	300 mm
h_c	400 mm
b_c	400 mm
d^- beam	325 mm
d^+ beam	325 mm
jd^- beam	297 mm
jd^+ beam	297 mm
jd^{*-}	250 mm
jd^{*+}	250 mm
f'_c	88.2 MPa
f_y beam top bars	441.0 MPa
f_y beam bottom bars	441.0 MPa
f_y slab bars	0 MPa
f_y joint hoops	680.0 MPa
$N^*/f'_c A_g$	0.167
A_s top beam bars	3040 mm^2
A_s btm beam bars	3040 mm^2
d_b, top beam bars	22 mm
d_b, btm beam bars	22 mm
A_s slab bars	0 mm^2
A_{sh} joint	1030 mm^2

Theoretical Forces based on Measured Properties	
T_i^-	1341 kN
T_i^+	1341 kN
M_i^-	399 kN.m
M_i^+	398 kN.m
V_i^-	332 kN
V_i^+	332 kN
H_i	516.5 kN
$V_{jh,i}$	2164.8 kN
V_{sh}	700.7 kN
$(V_{sh})_{eff}$ #	583.9 kN
Joint hoops have yield plateau	no
$v_{jh,i} / f'_c$	0.153

Measured Strenghs	
H'_o (corr. for P-δ)	592.0 kN
H_o	592.0 kN
$\lambda_o = H'_o/H_i$	1.146
λ_{jo}	1.478
$V_{jh,o}$	3198 kN
$v_{jh,o} / f'_c$	0.227
$(V_{sh})_{eff} / V_{jh,o}$	0.183
K_{pv}	2.260
$v_{jh,e} / f'_c$	0.512

Measured Drift	
Δ_y / l_c	0.9 %
Δ_c / Δ_y	0.10
μ_Δ @ failure	4.33
μ_θ @ failure	4.70
Failure Mode	joint failure

Tera_hno3.xls

Note : # The available drawings showed that the top and bottom sets of the joint hoops were placed close to the beam bars. It was thus assumed that those sets developed 50% of the yield strength.

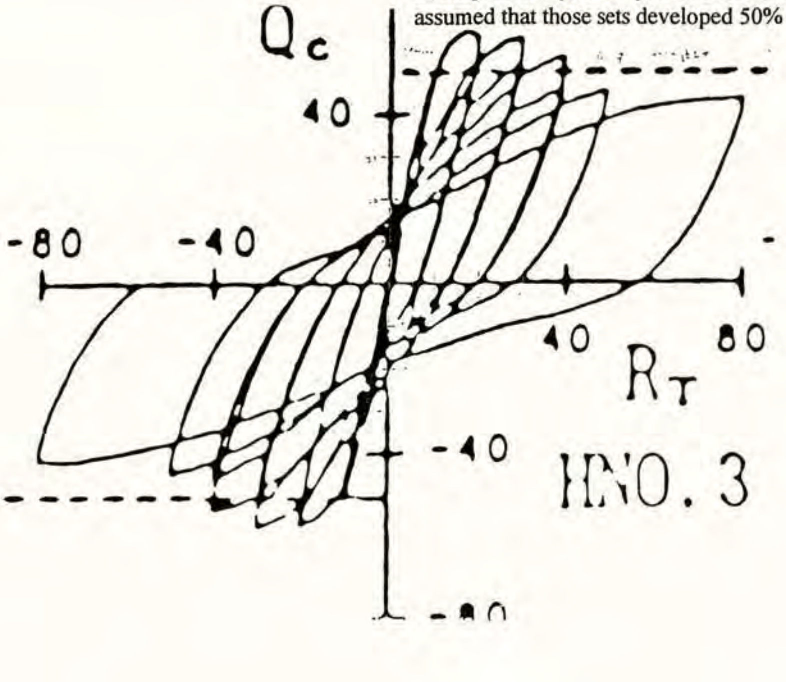

TEST: Teraoka et al. NO43	Code: T3
l_b	3000 mm
l_c	2000 mm
l'_b	1300 mm
l''_b	1345 mm
l'_c	800 mm
h_b	400 mm
b_b	300 mm
h_c	400 mm
b_c	400 mm
d^- beam	355 mm
d^+ beam	355 mm
jd^- beam	337 mm
jd^+ beam	337 mm
jd^{*-}	310 mm
jd^{*+}	310 mm
f'_c	54.0 MPa
f_y beam top bars	382.2 MPa
f_y beam bottom bars	382.2 MPa
f_y slab bars	0 MPa
f_y joint hoops	347.0 MPa
$N^*/f'_c A_g$	0.200
A_s top beam bars	1134 mm^2
A_s btm beam bars	1134 mm^2
d_b, top beam bars	19 mm
d_b, btm beam bars	19 mm
A_s slab bars	0 mm^2
A_{sh} joint	785 mm^2

Theoretical Forces based on Measured Properties	
T_i^-	433 kN
T_i^+	433 kN
M_i^-	146 kN.m
M_i^+	146 kN.m
V_i^-	112 kN
V_i^+	112 kN
H_i	168.5 kN
$V_{jh,i}$	698.3 kN
V_{sh}	272.4 kN
$(V_{sh})_{eff}$	261.5 kN
Joint hoops have yield plateau	yes
$v_{jh,i} / f'_c$	0.081

Measured Strentghs	
H'_o (corr. for P-δ)	196.0 kN
H_o	196.0 kN
$\lambda_o = H'_o/H_i$	1.163
λ_{jo}	1.343
$V_{jh,o}$	938 kN
$v_{jh,o} / f'_c$	0.109
$(V_{sh})_{eff} / V_{jh,o}$	0.279
K_{pv}	1.960
$v_{jh,e} / f'_c$	0.213

Measured Drift	
Δ_y / l_c	0.6 %
Δ_c / Δ_y	0.05
μ_Δ @ failure	9.70
μ_θ @ failure	10.16
Failure Mode	no failure

Tera_no43.xls

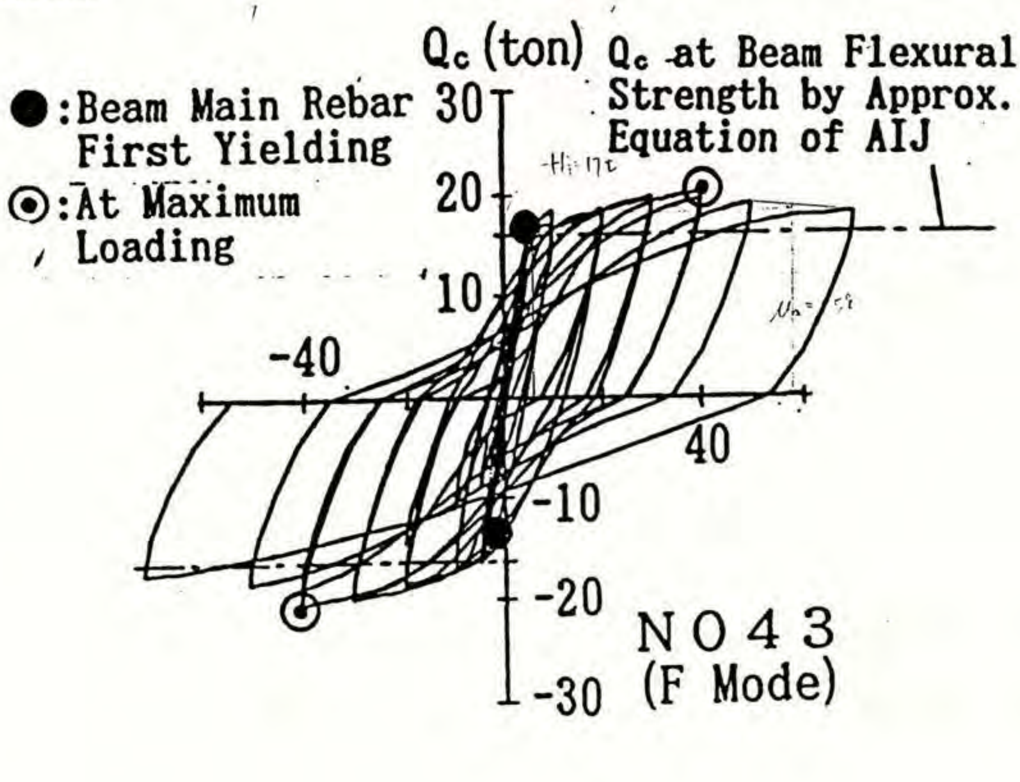

TEST: Teraoka et al. NO47	Code: T4
l_b	3000 mm
l_c	2000 mm
l'_b	1300 mm
l''_b	1345 mm
l'_c	800 mm
h_b	400 mm
b_b	300 mm
h_c	400 mm
b_c	400 mm
d^- beam	355 mm
d^+ beam	355 mm
jd^- beam	316 mm
jd^+ beam	316 mm
jd^{*-}	280 mm
jd^{*+}	280 mm
f'_c	54.0 MPa
f_y beam top bars	382.2 MPa
f_y beam bottom bars	382.2 MPa
f_y slab bars	0 MPa
f_y joint hoops	347.0 MPa
$N^*/f'_c A_g$	0.200
A_s top beam bars	1701 mm^2
A_s btm beam bars	1701 mm^2
d_b, top beam bars	19 mm
d_b, btm beam bars	19 mm
A_s slab bars	0 mm^2
A_{sh} joint	785 mm^2

Theoretical Forces based on Measured Properties	
T_i^-	650 kN
T_i^+	650 kN
M_i^-	205 kN.m
M_i^+	205 kN.m
V_i^-	158 kN
V_i^+	158 kN
H_i	236.7 kN
$V_{jh,i}$	1063.5 kN
V_{sh}	272.4 kN
$(V_{sh})_{eff}$ #	261.5 kN
Joint hoops have yield plateau	yes
$v_{jh,i} / f'_c$	0.123

Measured Strengths	
H'_o (corr. for P-δ)	265.0 kN
H_o	265.0 kN
$\lambda_o = H'_o/H_i$	1.119
λ_{jo}	1.347
$V_{jh,o}$	1432 kN
$v_{jh,o} / f'_c$	0.166
$(V_{sh})_{eff} / V_{jh,o}$	0.183
K_{pv}	2.020
$v_{jh,e} / f'_c$	0.335

Measured Drift	
Δ_y / l_c	0.6 %
Δ_c / Δ_y	0.056
μ_Δ @ failure	6.70
μ_θ @ failure	7.04
Failure Mode	joint failure

Tera_no47.xls

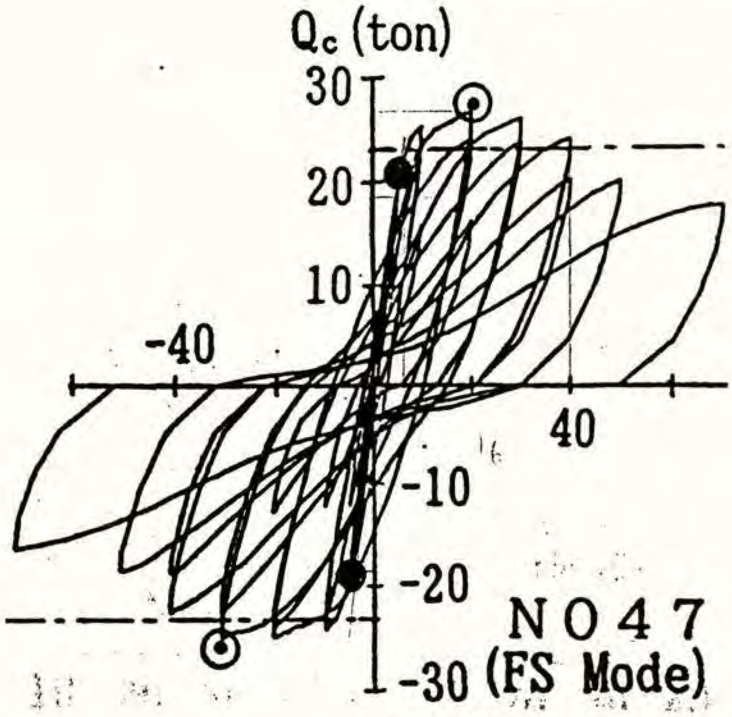

TEST: Viwathantepa et al Unit BC3	Code : V1
l_b	3657.6 mm
l_c	1828.8 mm
l'_b	1612.9 mm
l''_b	1647.4 mm
l'_c	711.2 mm
h_b	406.4 mm
b_b	228.6 mm
h_c	431.8 mm
b_c	431.8 mm
d^- beam	372.4 mm
d^+ beam	372.4 mm
jd^- beam	326 mm
jd^+ beam	348 mm
jd^{*-}	338.4 mm
jd^{*+}	338.4 mm
f'_c	31.1 MPa
f_y beam top bars	492.0 MPa
f_y beam bottom bars	490.0 MPa
f_y slab bars	0 MPa
f_y joint hoops	448.0 MPa
$N^*/f'_c A_g$	0.361
A_s top beam bars	1136 mm^2
A_s btm beam bars	600 mm^2
d_b, top beam bars	19 mm
d_b, btm beam bars	16 mm
A_s slab bars	0 mm^2
A_{sh} joint	696 mm^2

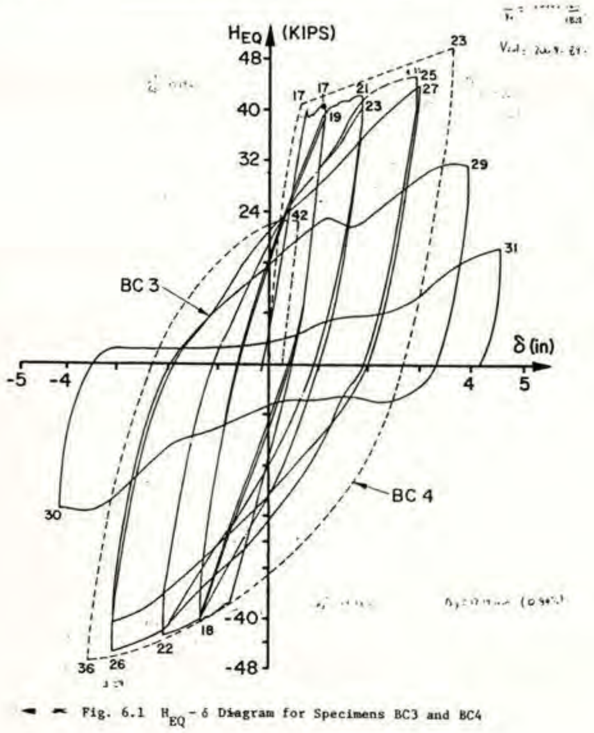

Fig. 6.1 $H_{EQ} - \delta$ Diagram for Specimens BC3 and BC4

Theoretical Forces based on Measured Properties	
T_i^-	559 kN
T_i^+	294 kN
M_i^-	182 kN.m
M_i^+	102 kN.m
V_i^-	113 kN
V_i^+	63 kN
H_i	176.5 kN
$V_{jh,i}$	676.4 kN
V_{sh}	312.0 kN
$(V_{sh})_{eff}$ #	270.4 kN
Joint hoops have yield plateau	yes
$v_{jh,i} / f'_c$	0.117

Measured Strentghs	
H'_o (corr. for P-δ)	200.9 kN
H_o	111.5 kN
$\lambda_o = H'_o/H_i$	1.138
λ_{jo}	1.281
$V_{jh,o}$	867 kN
$v_{jh,o} / f'_c$	0.149
$(V_{sh})_{eff} / V_{jh,o}$	0.312
K_{pv}	2.120
$v_{jh,e} / f'_c$	0.32

Measured Drift	
Δ_y / l_c	0.94 %
Δ_c / Δ_y	0.031
μ_Δ @ failure	4.59
μ_θ @ failure	4.70
Failure Mode	bond failure

Note: # Levels of the sets of joint hoops are not available, it was assumed that the top and bottom sets developed 60% of yield strength when calculating $(V_{sh})_{eff}$.

Reference:[V2]

TEST: Xin U1	Code : X1
l_b	3500 mm
l_c	2470 mm
l'_b	1525 mm
l''_b	1566 mm
l'_c	985 mm
h_b	500 mm
b_b	250 mm
h_c	450 mm
b_c	300 mm
d^- beam	444 mm
d^+ beam	444 mm
jd^- beam	417 mm
jd^+ beam	417 mm
jd^{*-}	394 mm
jd^{*+}	394 mm
f'_c	30.9 MPa
f_y beam top bars	453.0 MPa
f_y beam bottom bars	453.0 MPa
f_y slab bars	0 MPa
f_y joint hoops	348.0 MPa
$N^*/f'_c A_g$	0.000
A_s top beam bars	791 mm^2
A_s btm beam bars	791 mm^2
d_b, top beam bars	12 mm
d_b, btm beam bars	12 mm
A_s slab bars	0 mm^2
A_{sh} joint	1459 mm^2

Theoretical Forces based on Measured Properties	
T_i^-	358 kN
T_i^+	358 kN
M_i^-	149 kN.m
M_i^+	149 kN.m
V_i^-	98 kN
V_i^+	98 kN
H_i	138.7 kN
$V_{jh,i}$	577.9 kN
V_{sh}	507.7 kN
$(V_{sh})_{eff}$	446.8 kN
Joint hoops have yield plateau	yes
$v_{jh,i} / f'_c$	0.139

Measured Strentghs	
H'_o (corr. for P-δ)	151.0 kN
H_o	151.0 kN
$\lambda_o = H'_o/H_i$	1.088
λ_{jo}	1.205
$V_{jh,o}$	696 kN
$v_{jh,o} / f'_c$	0.167
$(V_{sh})_{eff} / V_{jh,o}$	0.642
K_{pv}	1.960
$v_{jh,e} / f'_c$	0.327

Measured Drift	
Δ_y / l_c	0.85 %
Δ_c / Δ_y	0.241
μ_Δ @ failure	5.60
μ_θ @ failure	8.16
Failure Mode	joint failure

Xin_u1.xls

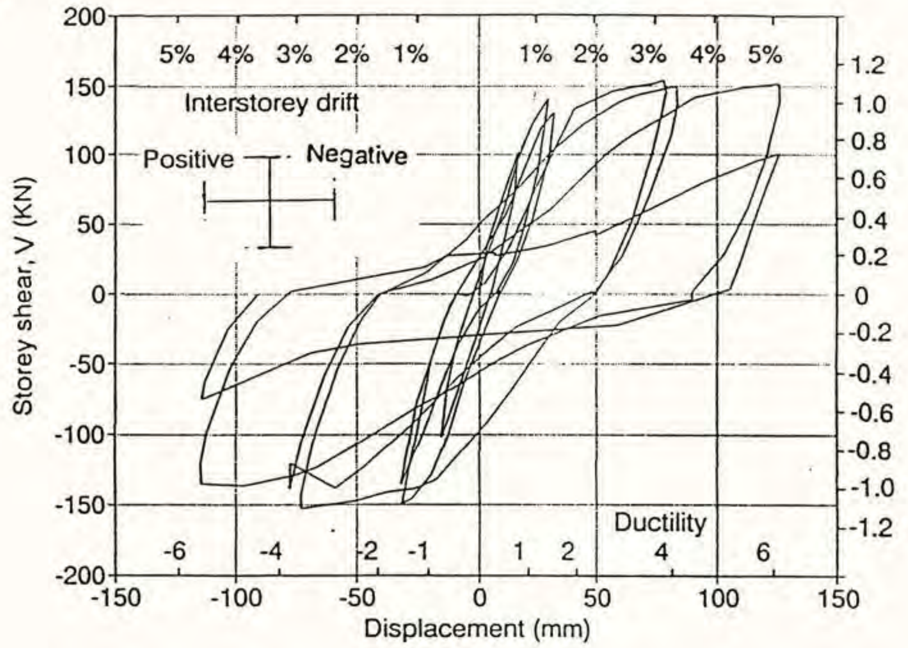

TEST: Xin U2	Code: X2
l_b	3500 mm
l_c	2470 mm
l'_b	1525 mm
l''_b	1566 mm
l'_c	985 mm
h_b	500 mm
b_b	250 mm
h_c	450 mm
b_c	300 mm
d^- beam	450 mm
d^+ beam	450 mm
jd^- beam	429 mm
jd^+ beam	440 mm
jd^{*-}	400 mm
jd^{*+}	400 mm
f'_c	40.8 MPa
f_y beam top bars	445.0 MPa
f_y beam bottom bars	445.0 MPa
f_y slab bars	0 MPa
f_y joint hoops	350.0 MPa
$N^*/f'_c A_g$	0.000
A_s top beam bars	804 mm^2
A_s btm beam bars	402 mm^2
d_b, top beam bars	16 mm
d_b, btm beam bars	16 mm
A_s slab bars	0 mm^2
A_{sh} joint	1029 mm^2

Theoretical Forces based on Measured Properties	
T_i^-	358 kN
T_i^+	179 kN
M_i^-	154 kN.m
M_i^+	79 kN.m
V_i^-	101 kN
V_i^+	52 kN
H_i	107.9 kN
$V_{jh,i}$	428.8 kN
V_{sh}	360.2 kN
$(V_{sh})_{eff}$	345.8 kN
Joint hoops have yield plateau	yes
$v_{jh,i} / f'_c$	0.078

Measured Strentghs	
H'_o (corr. for P-δ)	125.0 kN
H_o	125.0 kN
$\lambda_o = H'_o/H_i$	1.158
λ_{jo}	1.251
$V_{jh,o}$	536 kN
$v_{jh,o} / f'_c$	0.097
$(V_{sh})_{eff} / V_{jh,o}$	0.645
K_{pv}	1.960
$v_{jh,e} / f'_c$	0.191

Measured Drift	
Δ_y / l_c	0.67 %
Δ_c / Δ_y	0.306
μ_Δ @ failure	7.00
μ_θ @ failure	9.65
Failure Mode	bond failure

Xin_u2.xls

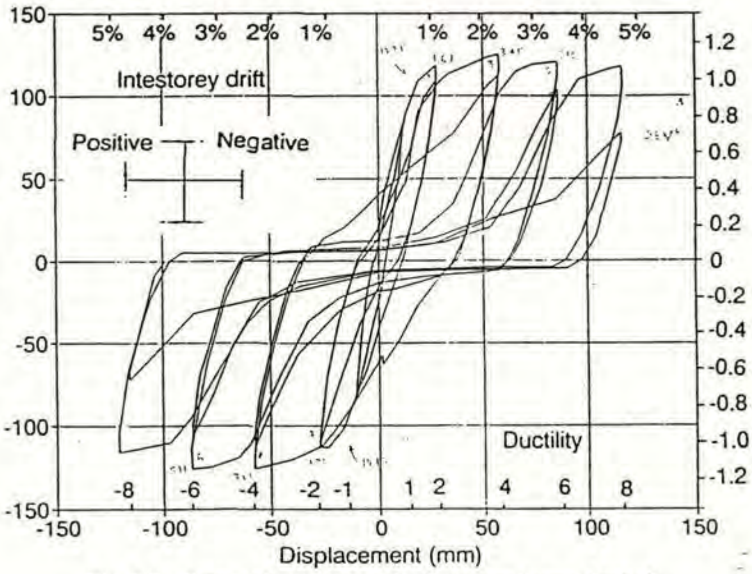

Fig. 5.8 Storey shear versus displacement loops, Unit 2

TEST: Xin U3	Code: X3
l_b	3500 mm
l_c	2470 mm
l'_b	1525 mm
l''_b	1566 mm
l'_c	985 mm
h_b	500 mm
b_b	250 mm
h_c	450 mm
b_c	300 mm
d^- beam	450 mm
d^+ beam	450 mm
jd^- beam	430 mm
jd^+ beam	430 mm
jd^{*-}	400 mm
jd^{*+}	400 mm
f'_c	42.5 MPa
f_y beam top bars	445.0 MPa
f_y beam bottom bars	445.0 MPa
f_y slab bars	0 MPa
f_y joint hoops	348.0 MPa
$N^*/f'_c A_g$	0.000
A_s top beam bars	804 mm^2
A_s btm beam bars	804 mm^2
d_b, top beam bars	16 mm
d_b, btm beam bars	16 mm
A_s slab bars	0 mm^2
A_{sh} joint	1459 mm^2

Theoretical Forces based on Measured Properties	
T_i^-	358 kN
T_i^+	358 kN
M_i^-	154 kN.m
M_i^+	154 kN.m
V_i^-	101 kN
V_i^+	101 kN
H_i	143.0 kN
$V_{jh,i}$	572.5 kN
V_{sh}	507.7 kN
$(V_{sh})_{eff}$	487.4 kN
Joint hoops have yield plateau	yes
$v_{jh,i} / f'_c$	0.100

Measured Strentghs	
H'_o (corr. for P-δ)	168.0 kN
H_o	168.0 kN
$\lambda_o = H'_o/H_i$	1.175
λ_{jo}	1.285
$V_{jh,o}$	736 kN
$v_{jh,o} / f'_c$	0.128
$(V_{sh})_{eff} / V_{jh,o}$	0.663
K_{pv}	1.900
$v_{jh,e} / f'_c$	0.244

Measured Drift	
Δ_y / l_c	0.69 %
Δ_c / Δ_y	0.255
μ_Δ @ failure	6.85
μ_θ @ failure	8.85
Failure Mode	bond failure

Xin_u3.xls

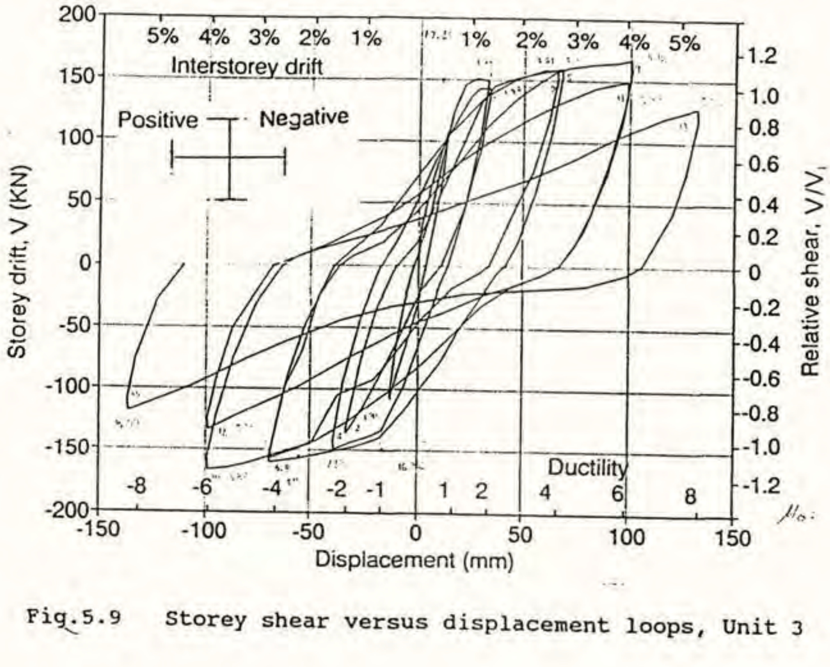

Fig.5.9 Storey shear versus displacement loops, Unit 3

TEST: Xin U4	Code: X4
l_b	3500 mm
l_c	2470 mm
l'_b	1525 mm
l''_b	1566 mm
l'_c	985 mm
h_b	500 mm
b_b	250 mm
h_c	450 mm
b_c	300 mm
d^- beam	452 mm
d^+ beam	454 mm
jd^- beam	437 mm
jd^+ beam	445 mm
jd^{*-}	402 mm
jd^{*+}	402 mm
f'_c	47.2 MPa
f_y beam top bars	492.0 MPa
f_y beam bottom bars	445.0 MPa
f_y slab bars	0 MPa
f_y joint hoops	348.0 MPa
$N^*/f'_c A_g$	0.000
A_s top beam bars	628 mm^2
A_s btm beam bars	402 mm^2
d_b, top beam bars	20 mm
d_b, btm beam bars	16 mm
A_s slab bars	0 mm^2
A_{sh} joint	1167 mm^2

Theoretical Forces based on Measured Properties	
T_i^-	309 kN
T_i^+	179 kN
M_i^-	135 kN.m
M_i^+	80 kN.m
V_i^-	88 kN
V_i^+	52 kN
H_i	99.7 kN
$V_{jh,i}$	388.2 kN
V_{sh}	406.2 kN
$(V_{sh})_{eff}$	389.9 kN
Joint hoops have yield plateau	yes
$v_{jh,i} / f'_c$	0.061

Measured Strentghs	
H'_o (corr. for P-δ)	116.9 kN
H_o	116.9 kN
$\lambda_o = H'_o/H_i$	1.173
λ_{jo}	1.255
$V_{jh,o}$	525.8 kN
$v_{jh,o} / f'_c$	0.083
$(V_{sh})_{eff} / V_{jh,o}$	0.742
K_{pv}	1.720
$v_{jh,e} / f'_c$	0.14

Measured Drift	
Δ_y / l_c	0.58 %
Δ_c / Δ_y	0.244
μ_Δ @ failure	7.03
μ_θ @ failure	8.98
Failure Mode	bond failure

Xin_u4.xls

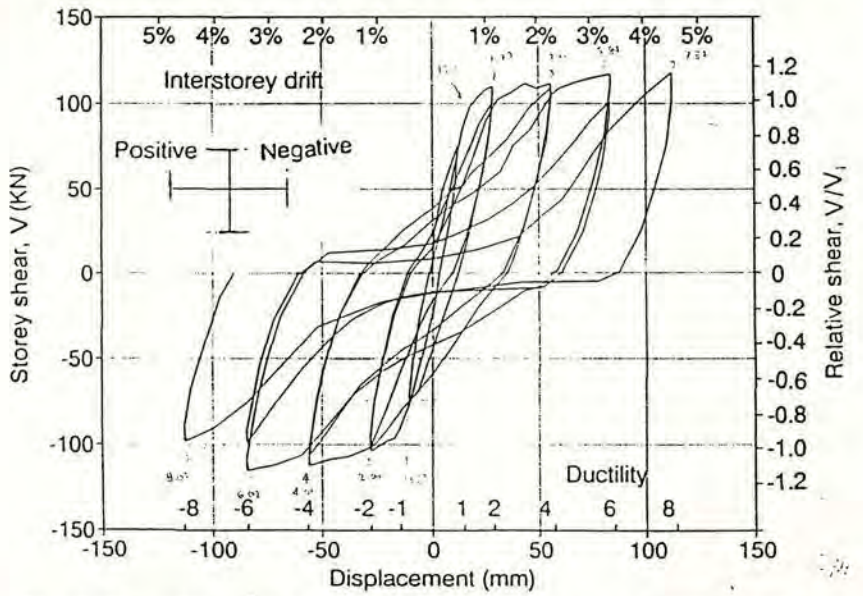

Fig.5.10 Storey shear versus displacement loops, Unit 4

TEST: Xin U5	Code: X5
l_b	3500 mm
l_c	2470 mm
l'_b	1525 mm
l''_b	1564 mm
l'_c	985 mm
h_b	500 mm
b_b	250 mm
h_c	450 mm
b_c	300 mm
d^- beam	450 mm
d^+ beam	450 mm
jd^- beam	432 mm
jd^+ beam	432 mm
jd^{*-}	400 mm
jd^{*+}	400 mm
f'_c	60.7 MPa
f_y beam top bars	492.0 MPa
f_y beam bottom bars	492.0 MPa
f_y slab bars	0 MPa
f_y joint hoops	329.8 MPa
$N^*/f'_c A_g$	0.000
A_s top beam bars	942 mm^2
A_s btm beam bars	942 mm^2
d_b, top beam bars	20 mm
d_b, btm beam bars	20 mm
A_s slab bars	0 mm^2
A_{sh} joint	1648 mm^2

Xin_U5.xls

Theoretical Forces based on Measured Properties	
T_i^-	463 kN
T_i^+	463 kN
M_i^-	200 kN.m
M_i^+	200 kN.m
V_i^-	131 kN
V_i^+	131 kN
H_i	186.1 kN
$V_{jh,i}$	740.9 kN
V_{sh}	543.4 kN
$(V_{sh})_{eff}$	521.6 kN
Joint hoops have yield plateau	yes
$v_{jh,i} / f'_c$	0.090

Measured Strengths	
H'_o (corr. for P-δ)	225.0 kN
H_o	225.0 kN
$\lambda_o = H'_o/H_i$	1.209
λ_{jo}	1.314
$V_{jh,o}$	1016.7 kN
$v_{jh,o} / f'_c$	0.124
$(V_{sh})_{eff} / V_{jh,o}$	0.513
K_{pv}	2.230
$v_{jh,e} / f'_c$	0.277

Measured Drift	
Δ_y / l_c	0.78 %
Δ_c / Δ_y	0.27
μ_Δ @ failure	6.85
μ_θ @ failure	9.01
Failure Mode	Beam hinging+bar slip

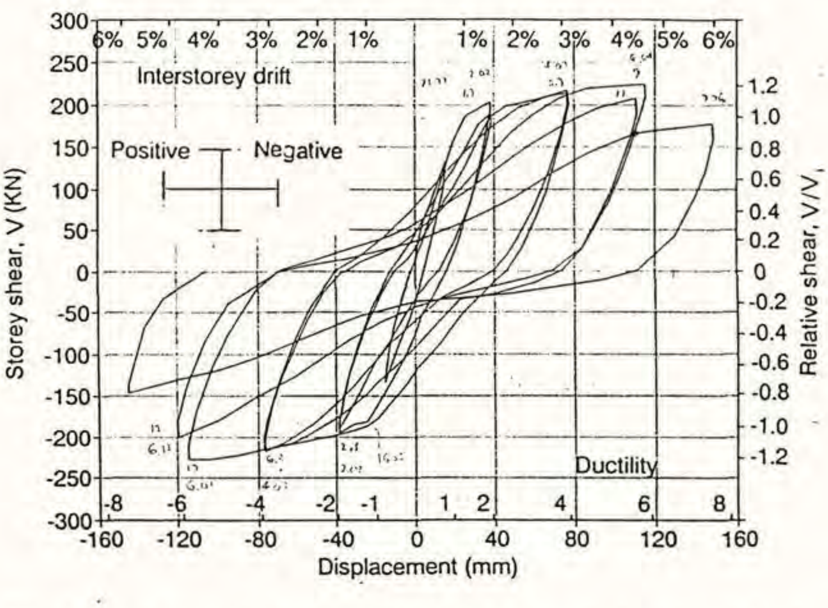

Fig.5.11 Storey shear versus displacement loops, Unit 5

TEST: Xin U6	Code: X6
l_b	3500 mm
l_c	2470 mm
l'_b	1525 mm
l''_b	1564 mm
l'_c	985 mm
h_b	500 mm
b_b	250 mm
h_c	450 mm
b_c	300 mm
d^- beam	446 mm
d^+ beam	450 mm
jd^- beam	423 mm
jd^+ beam	438 mm
jd^{*-}	396 mm
jd^{*+}	396 mm
f'_c	59.3 MPa
f_y beam top bars	463.0 MPa
f_y beam bottom bars	492.0 MPa
f_y slab bars	0 MPa
f_y joint hoops	329.8 MPa
$N^*/f'_c A_g$	0.00
A_s top beam bars	1232 mm^2
A_s btm beam bars	628 mm^2
d_b, top beam bars	28 mm
d_b, btm beam bars	20 mm
A_s slab bars	0 mm^2
A_{sh} joint	1648 mm^2

Xin_U6.xls

Theoretical Forces based on Measured Properties	
T_i^-	570 kN
T_i^+	309 kN
M_i^-	241 kN.m
M_i^+	135 kN.m
V_i^-	158 kN
V_i^+	89 kN
H_i	175.0 kN
$V_{jh,i}$	704.4 kN
V_{sh}	543.4 kN
$(V_{sh})_{eff}$	521.6 kN
Joint hoops have yield plateau	yes
$v_{jh,i} / f'_c$	0.088

Measured Strentghs	
H'_o (corr. for P-δ)	206.0 kN
H_o	206.0 kN
$\lambda_o = H'_o/H_i$	1.177
λ_{jo}	1.277
$V_{jh,o}$	942.3 kN
$v_{jh,o} / f'_c$	0.118
$(V_{sh})_{eff} / V_{jh,o}$	0.554
K_{pv}	2.120
$v_{jh,e} / f'_c$	0.250

Measured Drift	
Δ_y / l_c	0.7 %
Δ_c / Δ_y	0.299
μ_Δ @ failure	6.30
μ_θ @ failure	8.56
Failure Mode	bond failure

Reference: [X1]

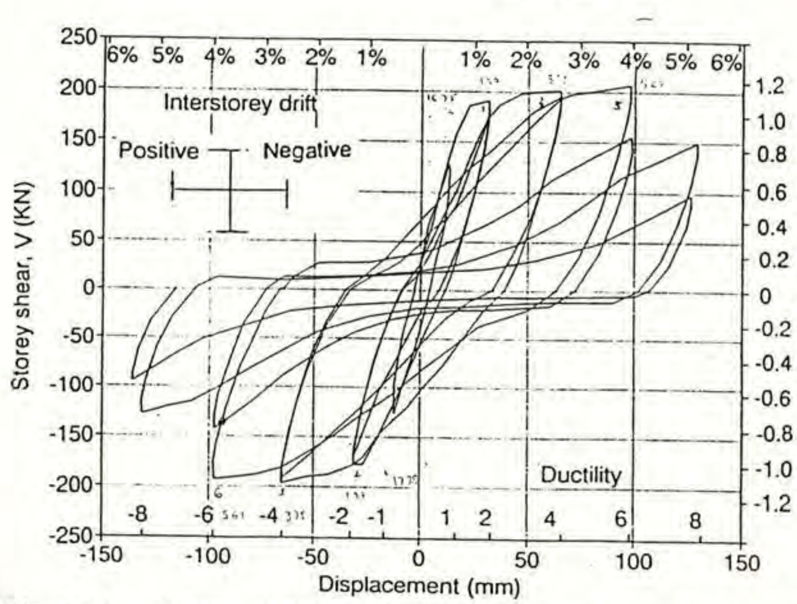

Fig.5.12 Storey shear versus displacement loops, Unit 6

TEST: P. K. C. Wong Unit 1	Code: W1
l_b	4238 mm
l_c	2473 mm
l'_b	1916 mm
l''_b	1959 mm
l'_c	1008 mm
h_b	457 mm
b_b	229 mm
h_c	406 mm
b_c	305 mm
d^- beam	421 mm
d^+ beam	421 mm
jd^- beam	395 mm
jd^+ beam	395 mm
jd^{*-}	374 mm
jd^{*+}	374 mm
f'_c	32.2 MPa
f_y beam top bars	300.0 MPa
f_y beam bottom bars	300.0 MPa
f_y slab bars	0 MPa
f_y joint hoops	339.0 MPa
$N^*/f'_c A_g$	0.000
A_s total beam bars	3217 mm^2
-	mm^2
d_b, beam bars	16 mm
-	16 mm
A_s slab bars	0 mm^2
A_{sh} joint	226.4 mm^2

Theoretical Forces based on Measured Properties	
T_i^-	- kN
T_i^+	- kN
M_i^-	171 kN.m
M_i^+	171 kN.m
V_i^-	89 kN
V_i^+	89 kN
H_i	152.5 kN
$V_{jh,i}$	812.6 kN
V_{sh}	76.7 kN
$(V_{sh})_{eff}$ #	61.4 kN
Joint hoops have yield plateau	yes
$v_{jh,i} / f'_c$	0.204

Measured Strenghs	
H'_o (corr. for P-d)	162.0 kN
H_o	162.0 kN
$\lambda_o = H'_o/H_i$	1.062
λ_{jo}	1.165
$V_{jh,o}$	946.8 kN
$v_{jh,o} / f'_c$	0.237
$(V_{sh})_{eff} / V_{jh,o}$	0.065
K_{pv}	2.730
$v_{jh,e} / f'_c$	0.648

Measured Drift	
Δ_y / l_c	1.25 %
Δ_c / Δ_y	0.233
μ_Δ @ failure	2.00
μ_θ @ failure	2.30
Failure Mode	joint failure

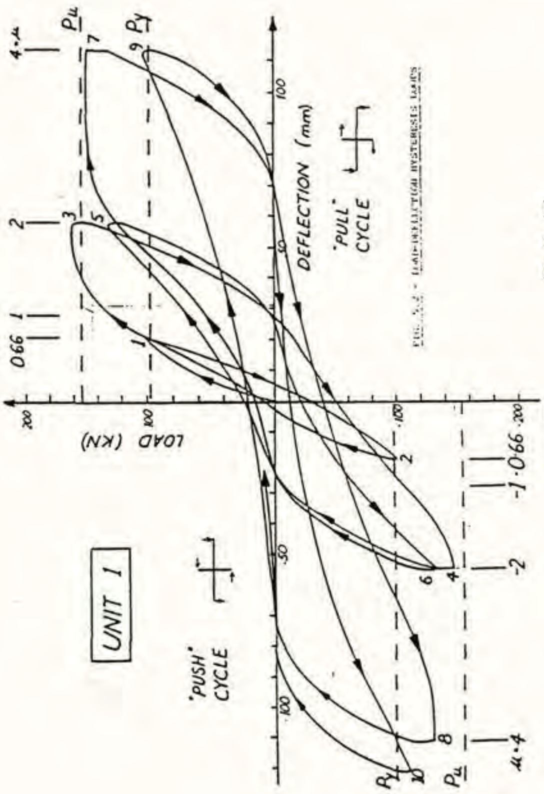

Note: # The available drawing show that the top and bottom sets of joint hoops was placed close to the beam bars, it was assumed the top and bottom sets developed 60% of the yield strength.

Reference: [W1]

Hakuto [H1], Unit O4

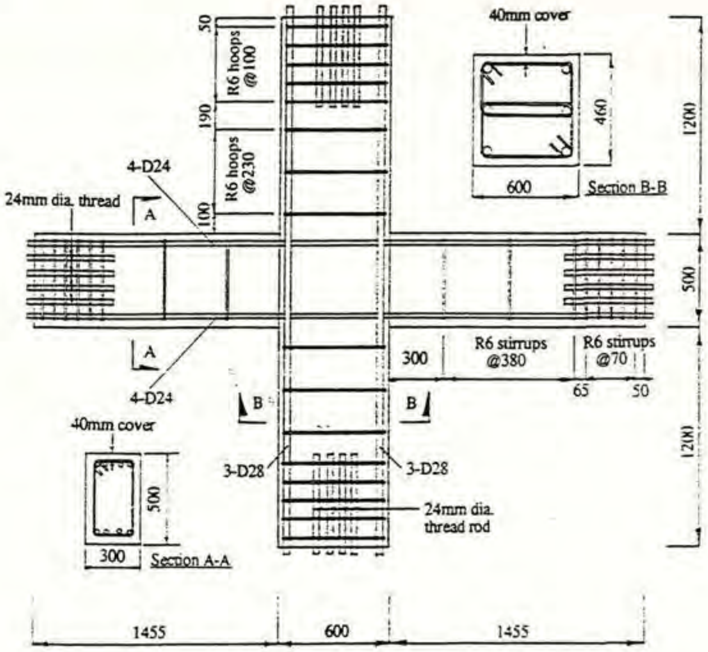

Fig.3.5 Dimensions and Reinforcement Details of Specimen O4

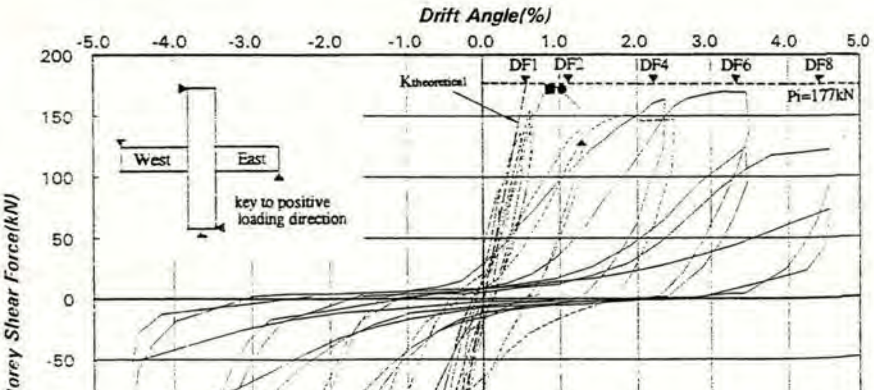

Fig.6.4 Storey Shear Force versus Horizontal Displacement Relationship for Specimen O4

Table 3.11 Measured Reinforcing Steel Properties used for Specimens R3 and O4 to O7

Grade of Steel	300				
Bar Size	R6	D12	D24	D28	D32
Yield Strength, f_y(MPa)	398	358	308	321	306
Yield Strain, ε_y	0.00206	0.00167	0.00165	0.00170	0.00160
Strain at commencing strain hardening, ε_{sh}	0.0205	0.0077	0.0206	0.0236	0.0193
Ultimate Strength, f_u(MPa)	505	476	462	480	479

Hakuto [H1], Unit O5

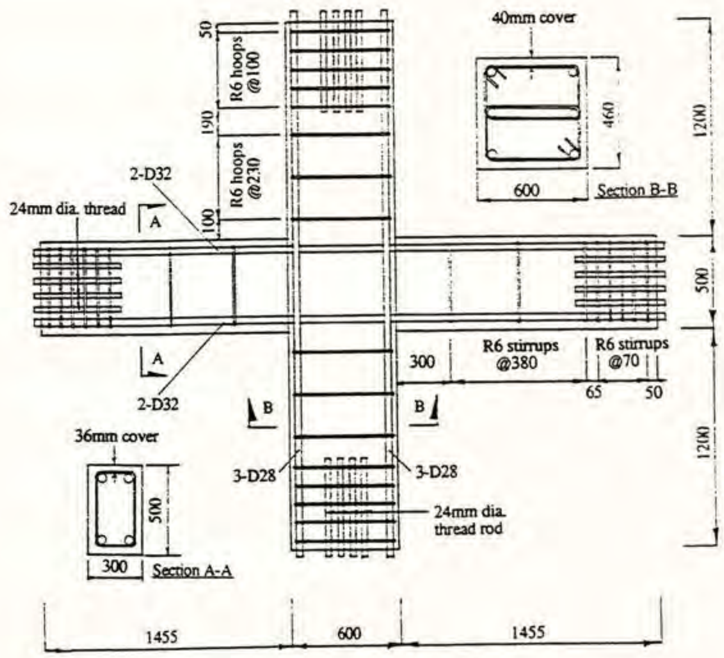

Fig.3.6 Dimensions and Reinforcement Details of Specimen O5

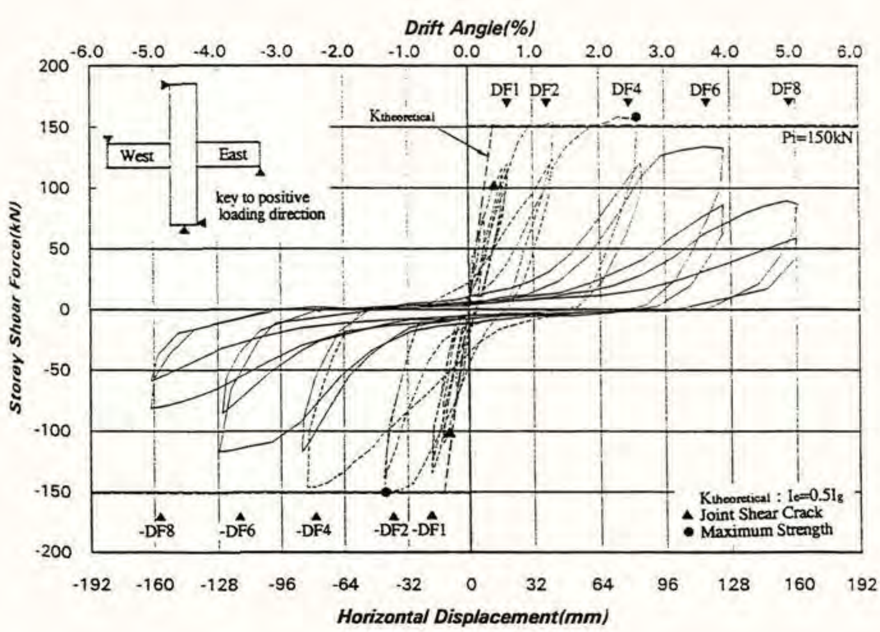

Fig.6.16 Storey Shear Force versus Horizontal Displacement Relationship for Specimen O5

APPENDIX C

Drawings of Steel Cast Fittings for DARTEC UTM

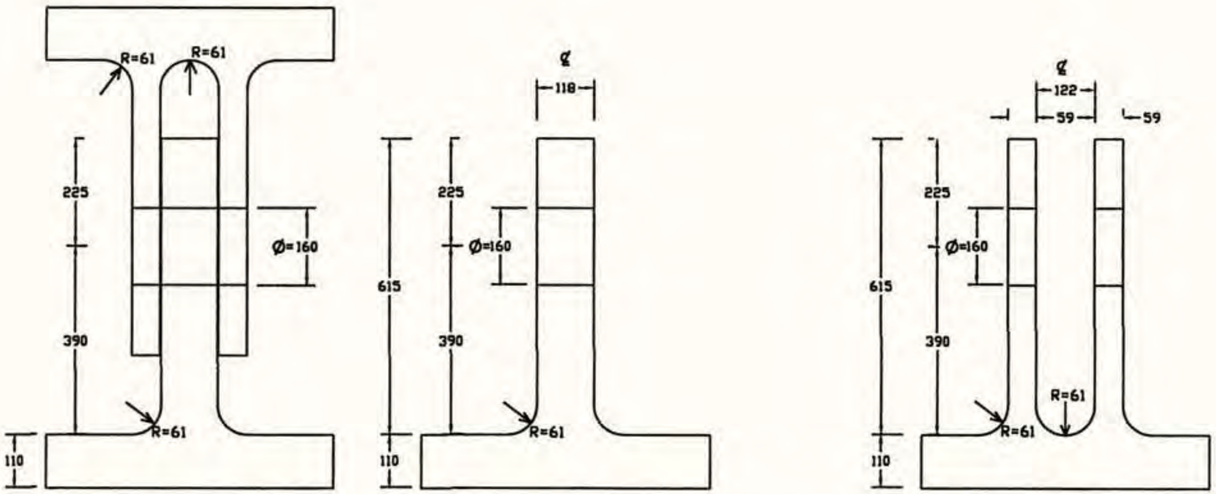

SIDE VIEW AS ASSEMBLED

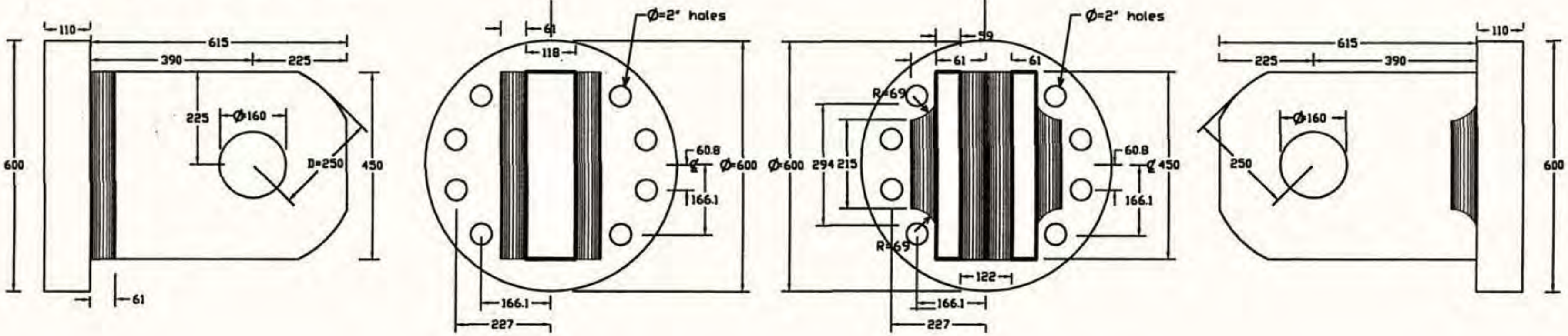

PLANE VIEW OF 1-LEG FITTING

X2

PLANE VIEW OF 2-LEG FITTING

X2

APPENDIX D

The procedure to find the internal force flow in an interior beam-column joint is explained in this Appendix. The joint shown in Fig. **D-1** will be studied. The geometry of the subassembly and general reinforcing details are shown in **Fig. App-1** in **Appendix A-1**. The following parameters are given: $f_c^{'} = 27.6$ MPa , $N^{*} = 0.2f'_cA_g$ and $V_{sh}/V_{jh} = 0.5$. The beams are reinforced with 3-HD28.7 top and bottom longitudinal bars with $f_y = 414$ MPa. The complete strut-and-tie models of this joint is reproduced in **Fig. D-1**. Seven struts are use to model the internal force flow in the joint. Struts are designated as a-a', b-b', c-c'-c'' and d-d'. Figure 2.1 and 2.2 contain the notation used in this Appendix.

Step 1: Calculate the tensile forces in the 3-HD28.7 bars at over-strength.

$T_{b,1} = T_{b,2} = 1.25 \times 0.414\ kN/mm^2 \times 1944\ mm^2 = 1006$ kN

Step 2: Calculate the horizontal joint shear force, V_{jh}

The bending moment at over-strength in the adjacent beams can be approximated as

$M^+ = M^- = 1006$ kN x 0.622 m = 626 kN-m.

the corresponding beam shear forces are calculated assuming that the critical section coincide with the outmost layer of the column longitudinal reinforcement.

$V_b^+ = V_b^- = 626$ kN-m / (2.286 m +0.08 m) = 265 kN

The column shear force required for equilibrium is

$V_{col} = 265$ kN x 5.182 m / 3.66 m = 375 kN

Hence, the horizontal joint shear force is

$V_{jh} = 2\text{x } 1006 - 375 = 1637$ kN

Step 3 : Compute the shear force V_{sh} carried by the horizontal joint reinforcement. V_{sh} = $0.5V_{jh}$= 0.5 x 1637 kN = 818.5 kN.

Assume all joint hoops yield and apply as a uniform distributed pressure over 85% of the distance between the beam top and bottom longitudinal bars, see **Fig. D-2**. This distance is equal to $\pm$265 mm from the centre of the joint. The magnitude of the pressure is 818.5 kN /(2x265) = 1.544 kN / mm. In Fig. D-2 a coordinate system with origin at the centre of the joint is assumed. Node coordinates in mm are shown in this figure.

Step 4 : Determine the potential bond forces at nodes a and b at the intersection of the longitudinal beam and column bars following the bond stress law depicted in **Fig. 2.1**. An anti-symmetrical arrangement of forces act upon the boundaries of the beam-column joints if the bond stress distribution for the top and bottom bars is assumed.

Follow with the numbers in the eq. Shown in **Fig. 2.1**. Define the variables

X_a = 225 mm

X_b = 99 mm

d_c= 530 mm, h_c = 610 mm

So = 3.14x28.7x3 mm

x_t =1.0

Then :

$U_a = 2.2 \sqrt{1.0x27.7}$ x $(225)^2$ /(2x530-610)x(3.14 x 28.7x3) /2 /1000 = 169 kN

Similarly, the bond force at node b, U_b can be calculated following the equation shown in **Fig. 2.1.**

U_b = 676 kN *((99+225)/450)^2-169=181.4 kN.

Step 5 : Find the column reinforcing steel and concrete forces due to combined bending moment and axial load. Calculate the column bending moment at the level of longitudinal beam reinforcement,

M_{col} = 375 kN x (1.448 m + 0.07 m) = 569 kN-m

The forces in the column longitudinal bars and in the concrete due to M_{col} can be obtained from a section moment-curvature analysis. The resultant column concrete compressive force is located at 103 mm from the extreme fibre in compression. Hence, the equivalent rectangular stress block extends 206 mm from the extreme compression fibre. The load per unit length of the equivalent compressive stress block is 2039 kN / 206 mm = 9.9 kN / mm.

Step 6 : Determine the geometry and forces in strut a-a$'$.

(see **Fig. D-3(a)**)

Assume that the column interior bar does not yield within the joint region and then check. Hence, the horizontal component of the diagonal strut a-a$'$ is

$H_{aa'} = U_a$ = 169 kN

Force $H_{aa'}$ has to be balanced by the uniform pressure from the joint hoops. Thus, a fraction of the uniform pressure with a resultant equal to $H_{aa'}$ is taken by this strut. The position of the resulting force measured from joint mid-depth is

$y_{a'}$ = 265 mm– (169 kN) /2 / 1.544 kN/mm = 210 mm

Once the geometry of strut a-a$'$ is determined, the vertical force carried by the strut is from geometry

$V_{aa'}$ = (311-210)mm x 169 kN/ (225-75)mm = 113.5 kN

The force in the strut is

$S_{aa'} = \sqrt{(169kN)^2+(113.5kN)^2}$ = 204 kN (compression)

The tensile force in the column interior bar at node a due to bending in the column and strut a-a$'$ is $T_{c,a}$ = 54kN + 113.5 kN = 167.5 kN

This tensile force cannot exceed the yield force of the column interior bars that is

$= 2x600mm^2$ x 414 MPa = 497 kN

$T_{c,a}$ = 167.5 kN < 497 kN , satisfactory.

Step 7 : Determine the geometry and forces in strut b-b' .

(see **Fig. D-3(b)**)

the horizontal component of the diagonal strut b-b' is $H_{bb'} = U_b$ = 181.4 kN

This force has to be balanced by a force resulting frm the hoops pressure. The position of the resulting force is measured from joint mid-depth

$y_{b''}$ = 265mm - (169 kN + 181.4/2 kN) / 1.544 kN/mm = 96.7 mm

The vertical force carried by the strut is from geometry

$V_{bb''}$ = (311-96.7)mm x 181.4 kN/ (225+75)mm = 130 kN

The force in the strut is

$S_{bb''} = \sqrt{(130kN)^2+(181kN)^2}$ = 223 kN (compression)

The tensile force in the column interior bars at node b within the joint region is

$T_{c,b}$ = 130 – 59.5 = 70.5 kN < 497 kN

Since $T_{c,a} \neq T_{c,b}$ nodes are required on interior column bars for equilibrium.

Step 8 : Determine the geometry and forces in strut c-c'-c"

(See **Fig. D-3(c)**)

Strut c-c'-c" carries the remaining joint hoop force that was not carried by struts a-a' and b-b'.

Hence

$H_{cc''} = V_{sh} - H_{aa'} - H_{bb'}$ = 818.5 – 169 –181.4 = 468 kN

The position of node c" can now be readily determined

$y_{c''}$ = -265mm + (468kN)/2/1.544kN/mm = -113.4 mm measured from joint mid-depth since $T_{c,a} \neq T_{c,b}$, nodes on column interior bars are required for equilibrium. The force of interior column bars along joint depth will be different and bond is required to balance the force difference. The force difference, $T_{c,a}$ - $T_{c,b}$ is allocated to node c'.

Strur c'-c" carries 468 kN in the horizontal direction.

There are several unknowns in this strut: (1) the magnitude and position of the fraction of the column compressive force needed for equilibrium. (2) the level of position of node c'.

Once the magnitude of the column concrete compressive force taken by strut c-c' ,C_{c1}, is specified, the position of node c' can be determined from geometry and the vertical component of strut c-c' and c'-c" can be found. The vertical component of strut c'-c" so determined, calculated from C_{c1}+ ($T_{c,a}$ - $T_{c,b}$), must satisfy the geometry of strut c'-c" that is already known. Otherwise another trial for C_{c1} is required to satisfy equilibrium.

It was found that when C_{c1} = 495 kN strut c-c'-c" is in equilibrium. The coordinates of nodes c,c' are plotted in **Fig. D-3(c)**.

The strut forces are

$S_{cc'} = \sqrt{(468)^2+(495)^2} = 681$ kN(comprssion)

$S_{c'c''} = \sqrt{(468)^2+(592.4)^2} = 755$ kN(compression)

Step 9 : Determine the geometry and forces of the diagonals strut d-d'.

This diagonal strut carries the remaining joint shear force that was not taken by the joint hoops.

$H_{dd'} = V_{jh} - V_{sh} = 1637 - 818.5 = 818.5$ kN

Strut d-d' carries the remaining column concrete compressive force

$V_{dd'} = C_{c2} = C_c - C_{c1} = 2039 - 495 = 1544$ kN

The resultant of force C_{c2} is located at 77 mm from the extreme column compressive fibre.

It is assumed that the beam shear force acts as a concentrating force at node d. Because of the anti-symmetrical feature of the struts-and-tie models in this joint, the tensile force of column exterior bars below node d (T_{cd}) must be equal to the force in the opposite column exterior bars below node c" that is already determined from strut c-c'-c" ($T_{cd'}$ = -499.5kN).

The vertical component of strut d-d' is equal to the sum of remaining column compressive force(C_{c2}) , beam shear force (V_b) and the force difference at node d on the exterior column bars

$V_{dd'} = 1544 + 345.6 - 265 - 499.5 = 1125$ kN

This force should be equal to or very close that is calculated from geometry of strut d-d'.

818.5x 622 / (450+4) = 1121 kN.

which means that this strut-and-tie model satisfies equilibrium. Due to the anti-symmetry of forces in the joint, strut d-d' shall pass through the centre of the joint.

The force of d-d' strut is

$S_{d'd'} = \sqrt{1125^2+818.5^2} = 1391$ kN

Step 10 : Calculate the uniaxial compressive stress at the centre of the joint. According to **Fig. 2.2**, the width of the strut d-d' is taken as the nearest distance measured from the joint centre to the adjacent struts. ie, $w_s = 104.1$mm

$$f_{c,s} = \frac{S_{dd'}}{d_m b_j} = \frac{1391\times 10^3}{104.1\times 534} = 25.02 \text{ MPa} = 0.91 f_c'$$

and

$$v_{jh} = \frac{V_{jh}}{b_j h_c} = \frac{1637\times 10^3}{534\times 610} = 5.0 \text{ MPa} = 0.181 f_c'$$

Thus

$$\frac{f_{c,s}}{v_{jh}} = 5.0$$

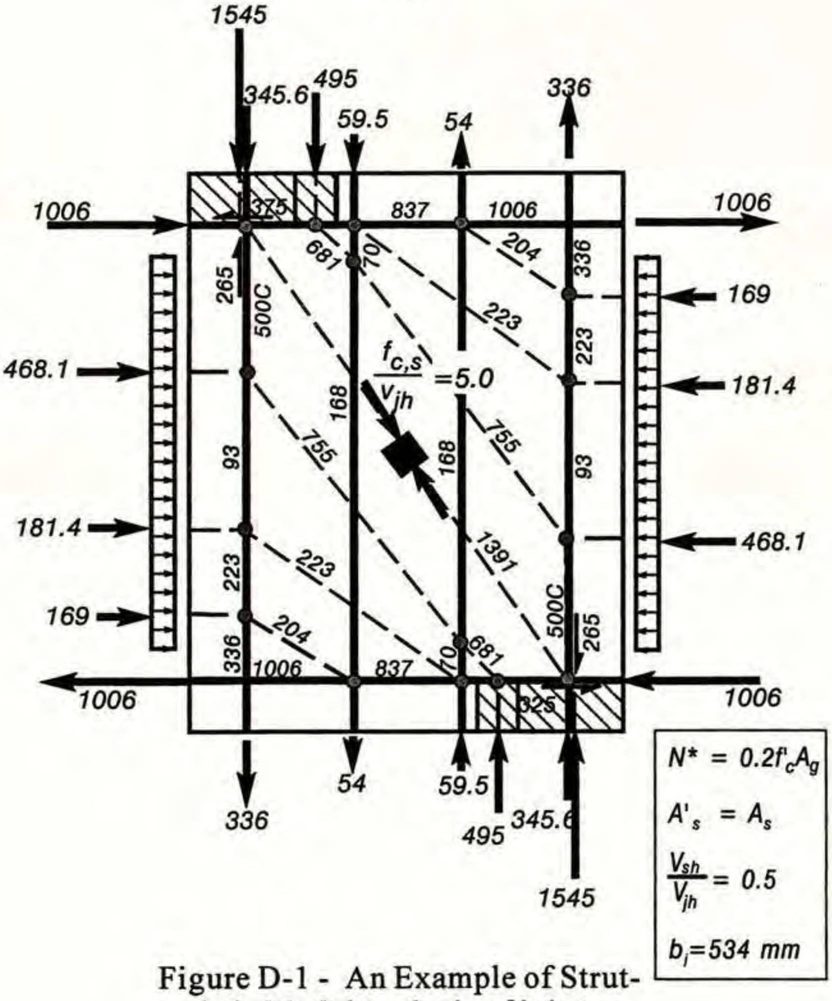

Figure D-1 - An Example of Strut-and-tie Model analysis of joints.

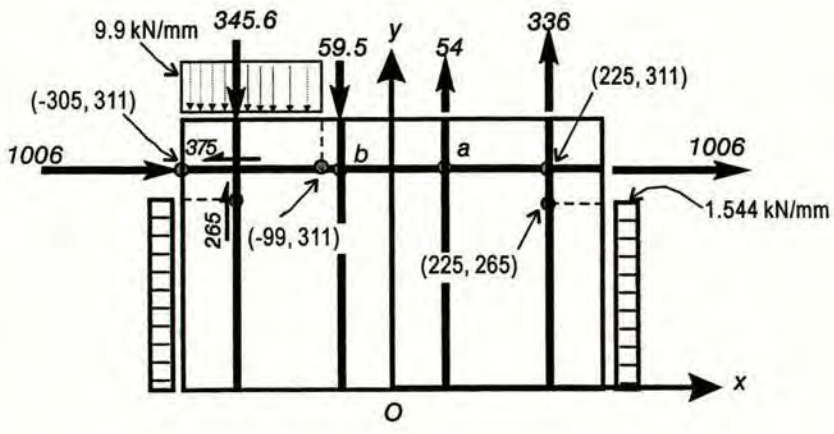

Figure D-2 - Ordinates of the Joint Analysed.

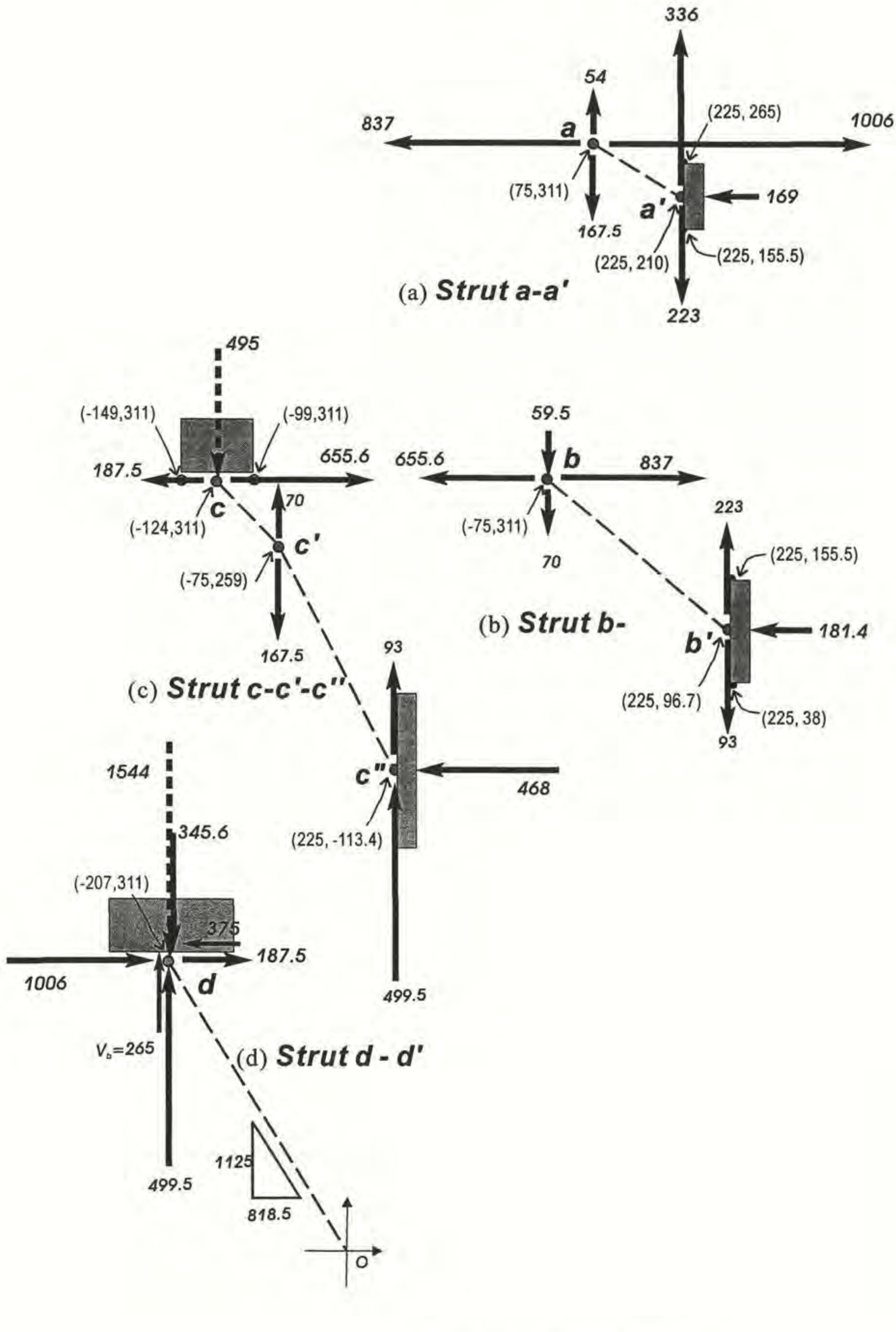

Figure D-3 - Strut Details